BEILSTEIN JOURNAL OF NANOTECHNOLOGY

Advances in nanotechnology applied to natural products

Edited by Douglas Dourado, Éverton do Nascimento Alencar, Fabio Rocha Formiga and Franceline Reynaud

Imprint

Beilstein Journal of Nanotechnology
www.bjnano.org
ISSN 2190-4286
Email: journals-support@beilstein-institut.de

The *Beilstein Journal of Nanotechnology* is published by the Beilstein-Institut zur Förderung der Chemischen Wissenschaften.

Beilstein-Institut zur Förderung der Chemischen Wissenschaften
Trakehner Straße 7–9
60487 Frankfurt am Main
Germany
www.beilstein-institut.de

BEILSTEIN JOURNAL OF NANOTECHNOLOGY

A formulation containing *Cymbopogon flexuosus* essential oil: improvement of biochemical parameters and oxidative stress in diabetic rats

Ailton Santos Sena-Júnior*[1], Cleverton Nascimento Santana Andrade[1], Pedro Henrique Macedo Moura[1], Jocsã Hémany Cândido dos Santos[1], Cauã Torres Trancoso[1], Eloia Emanuelly Dias Silva[2], Deise Maria Rego Rodrigues Silva[1], Ênio Pereira Telles[1], Luiz André Santos Silva[1], Isabella Lima Dantas Teles[1], Sara Fernanda Mota de Almeida[1], Daniel Alves de Souza[3], Jileno Ferreira Santos[4], Felipe José Aidar Martins[5], Ana Mara de Oliveira e Silva[6], Sandra Lauton-Santos[3], Guilherme Rodolfo Souza de Araujo[1], Cristiane Bani Correa[4], Rogéria De Souza Nunes[1], Lysandro Pinto Borges[1] and Ana Amélia Moreira Lira[1]

Full Research Paper

Open Access

Address:
[1]Department of Pharmaceutical Sciences, Federal University of Sergipe, São Cristóvão 49100-000, Sergipe, Brazil, [2]Department of Biology, Federal University of Sergipe, São Cristóvão 49100-000, Sergipe, Brazil, [3]Department of Physiology, Federal University of Sergipe, São Cristóvão 49100-000, Sergipe, Brazil, [4]Department of Morphology, Federal University of Sergipe, São Cristóvão 49100-000, Sergipe, Brazil, [5]Department of Physical Education, Federal University of Sergipe, São Cristóvão 49100-000, Sergipe, Brazil and [6]Department of Nutrition, Federal University of Sergipe, São Cristóvão 49100-000, Sergipe, Brazil

Email:
Ailton Santos Sena-Júnior* - juniorsena_nutri@hotmail.com

* Corresponding author

Keywords:
diabetes mellitus; essential oil; lemongrass; microemulsion

Beilstein J. Nanotechnol. **2025,** *16,* 617–636.
https://doi.org/10.3762/bjnano.16.48

Received: 12 January 2025
Accepted: 09 April 2025
Published: 07 May 2025

This article is part of the thematic issue "Advances in nanotechnology applied to natural products".

Guest Editor: D. Dourado

Abstract

Diabetes mellitus (DM) is a highly prevalent public health problem characterized by hyperglycemia that causes complications due to the generation of reactive oxygen species and oxidative damage. Studies have shown that essential oils containing citral, such as lemongrass, have various biological activities, including bactericidal, antiviral, antifungal, antioxidant, and hypoglycemic effects. Therefore, this study aims to obtain a microemulsified formulation containing the essential oil of *Cymbopogon flexuosus* (EOCF) and to evaluate its antioxidant and antidiabetic activity in diabetic rats. The microemulsion (ME) was obtained after consulting the corresponding pseudoternary phase diagram and showed stability, isotropy, Newtonian behavior, nanometric size (15.2 nm), and

pH 4.2. Both EOCF and the ME showed high antioxidant activity, but the ME resulted in greater antioxidant activity, potentiating the activity of isolated EOCF. Finally, male Wistar rats (3 months old, 200–250 g) with streptozotocin-induced type-1 DM were supplemented with EOCF and ME (32 mg/kg) for 21 days. Both EOCF and ME supplementation resulted in reduced blood glucose levels and improved lipid profiles when compared to the control group. Additionally, the ME was able to provide additional benefits, such as reduced liver damage, improved renal function, reduced systemic inflammation, and increased high-density lipoprotein levels. Overall, the results show that EOCF was efficiently incorporated into the microemulsion, improving its antioxidant activity and showing promising results for use in the treatment of DM via the oral route.

Introduction

Diabetes mellitus (DM) is one of the main public health problems. It affects around 463 million people worldwide, and it could reach 700 million cases by 2045 [1]. The main causes of DM are related to a deficit in insulin production due to a loss of pancreatic β-cell function (type-1 DM) [1], or due to insulin resistance and a partial deficit in the secretion of this hormone by pancreatic β-cells (type-2 DM).

Various therapies have been used in the treatment of patients with DM including medication using hypoglycemic agents alone or combined with the administration of exogenous insulin, associated with dietary re-education and changes in lifestyle habits, such as physical exercise [2]. Although hypoglycemic agents are widely prescribed in DM therapy, they can result in limited efficacy and cause various adverse reactions such as dyspepsia, abdominal pain, nausea, and lactic acidosis [3], which vary according to the hypoglycemic agent used and the patient's individual response.

As an alternative to conventional DM treatments, natural sources are being investigated, such as citral, the main compound in the essential oil (EO) extracted from plants of the *Cymbopogon* genus. Both citral and the essential oils of species such as *Cymbopogon flexuosus* (EOCF) and *Cymbopogon citratus* have shown antioxidant, antidiabetic, and antidyslipidemic properties in vivo [4-6]. EOs are volatile components that are sensitive to temperature, light, oxygen, and humidity [7]. Therefore, it is recommended to use them in drug delivery systems, such as nanostructured systems, which are able to guarantee stability and a better therapeutic effect after in vivo administration [8]. Among these systems, microemulsions (MEs) stand out for their ability to increase the solubility, absorption, and bioavailability of lipophilic compounds such as EOs. MEs are transparent, thermodynamically stable, low-viscosity systems containing oil and water stabilized by surfactants, with a very small droplet size (<100 nm), which facilitates their permeation through membranes [9]. In addition, MEs showed increased anti-inflammatory activity, reduced irritation, and improved the stability of EOs in previous studies [10,11].

Thus, from an innovative perspective, the aim of this work is to evaluate the antioxidant and antidiabetic activity of EOCF and a ME containing EOCF. Glycemic and lipid parameters, oxidative damage, and tissue injury in diabetic rats were evaluated.

Results and Discussion

Chemical composition of EOCF

The GC-MS analysis results of EOCF are similar to those presented in our previous study [12] and are shown in Table S1 (Supporting Information File 1). In total, 13 compounds were identified, the majority being α-citral (geranial, 53%), β-citral (neral, 19%), and geraniol (12%). EOCF also contained smaller percentages (0.07% to 4.90%) of constituents such as tricyclone, α-pinene, canphene, nonanone, linalool, isogeraniol, isoneral, isocitral, caryophyllene, and geranyl acetate. A study by Adukwu et al. [13] showed that citral (neral and geranial, 89%) and geraniol (8%) were the major constituents of EOCF, followed by linalool (2.7%), corroborating the findings of the present study. However, other minor components were not identified in this study, showing that the composition of the essential oil can change significantly when obtained from different geographical origins.

Development of microemulsions considering the pseudoternary phase diagram

Various surfactants in different combinations were tested to obtain the ME. In general, non-ionic surfactants are most commonly used because they have a low critical micelle concentration, low toxicity, and greater stability to changes in pH and charge when compared to other classes of surfactants [14]. Another important parameter is the hydrophilic–lipophilic balance (HLB). Surfactants with low HLB values between 3 and 6 generally promote the formation of water/oil (W/O) emulsions, while high HLB values between 8 and 18 predominantly result in O/W emulsions [14]. The HLB values of Eumulgin® CO 40 (14.1) and Tween® 80 (15) are suitable for O/W formulations.

Among various combinations of the components (Supporting Information File 1, Table S2), the pseudoternary phase diagram (PTPD) that best provided transparent liquid systems was obtained with Eumulgin® CO40/Tween® 80, in a ratio of 1:1 (v/v), containing distilled water as the aqueous phase and EOCF as the oil phase, as shown in Figure 1. Although the PTPD with

propylene glycol and Olivem® 300 (1:1, v/v) also showed regions characterized as ME, these regions contained only a low amount of EOCF (1%). Therefore, for the in vivo study, the required amount for oral administration would be high and could be unfeasible. Hence, the pseudoternary phase containing Eumulgin® CO40 and Tween® 80 was selected for the subsequent trials.

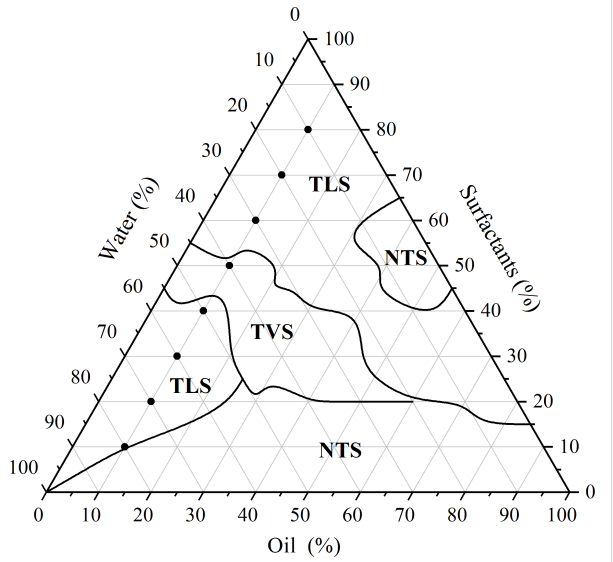

Figure 1: Pseudoternary phase diagram (PTPD) of EOCF, water, and a mixture of the surfactants Eumulgin® CO40/Tween® 80, in a 1:1 ratio. The PTPD shows demarcated regions corresponding to transparent liquid systems (TLS), transparent viscous systems (TVS) and non-transparent systems (NTS). The PTPD also shows formulations obtained with fixed oil phase concentrations (10%).

In the PTPD in Figure 1, a broad area of transparent systems is observed, suggesting that the use of these components can facilitate the development of nanometer-scale systems such as MEs and liquid crystals [15]. This region was divided into three distinct regions, with a central region of transparent viscous systems (TVS), which may be a region of lyotropic liquid crystals [16,17], and two regions of transparent liquid systems (TLS), which have low viscosity, suggesting the formation of MEs [18]. In general, the PTPD obtained with Eumulgin® CO 40 and Tween® 80 is similar to the PTPDs obtained with other similar surfactants such as shown in [8,19].

Considering the region of formation of transparent liquid systems obtained in the PTPD above, the dilution line containing 10% EOCF was selected, and the spots were prepared individually and monitored for five days (see below Table 1 and Figure 1). After this time, five formulations were classified as TLS suggesting that MEs were obtained. In addition, two SVT and one NTS were also obtained. Among the TLS, point 7 (M7-EOCF) was selected for subsequent tests, as it had the lowest amount of surfactants and the highest proportion of water in its composition.

Physicochemical characterization of the selected system

Some parameters are fundamental for characterizing nanostructured systems such as MEs, including droplet size, optical properties, and rheological profile. M7-EOCF therefore underwent tests to investigate these parameters. First, the M7-EOCF sample was analyzed by dynamic light scattering, which showed that the system had an average hydrodynamic radius of 15.24 ± 1.27 nm, which is in line with the definition of MEs, having a hydrodynamic radius between 10 and 100 nm [18]. Furthermore, it was observed that the M7-EOCF formulation had a polydispersity index (PDI) of 0.334 ± 0.054, indicating homogeneity (PDI < 0.5) in the droplet size distribution of this system. The literature reports that a PDI below 0.5 also indicates greater physical stability of the obtained formulation [20,21].

The M7-EOCF sample was also examined using polarized light microscopy to investigate its optical properties. Isotropic behavior was observed (Supporting Information File 1, Figure S1) through the visualization of a dark field. In general, microemulsions do not deflect the plane of polarized light since their optical properties are constant in all directions [18].

Rheology is the science that studies the flow characteristics and deformation of matter when exposed to different shear forces [22,23]. The parameters of rheological properties are essential in the classification and characterization of semisolids and fluids, and in the greater understanding of drug release from pharmaceutical forms [22]. Thus, the rheological behavior of M7-EOCF at two temperatures (25 and 37 °C) was analyzed. The results were expressed in rheograms (Figure 2) and represent the relationship between the shear stress and the shear rate.

The data were analyzed using the power law ($\tau = k \cdot \gamma^n$), where τ is the shear rate, k is the consistency index (viscosity), γ is the shear stress, and n is the flow index. The flow curves showed a linear correlation (n close to 1). For 25 °C, n was 1.08, while for 37 °C, it was 0.99 (i.e., Newtonian behavior). R^2 was greater than 0.996 for both tests, indicating that the data fit this model. This is expected for a microemulsion system [18,23,24]. The viscosity at 25 °C was 0.009 ± 0.001 Pa/s. The low viscosity can be justified considering the high water content present in the M7-EOCF formulation [25]. And it can be seen that increasing the temperature caused a decrease in viscosity to 0.006 ± 0.001 Pa/s (at 37 °C).

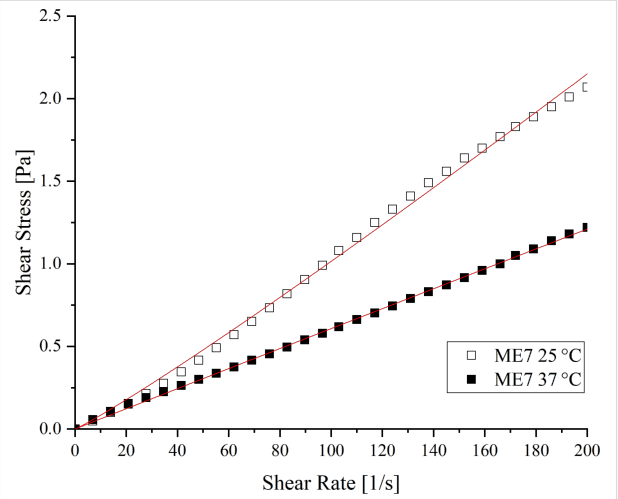

Figure 2: Rheological behavior (shear stress versus shear rate) of the microemulsion M7-EOCF at 25 and 37 °C.

The low viscosity of MEs is advantageous when taken orally as it facilitates oral application and dose adjustment; it also improves absorption and bioavailability. Additionally, MEs can be administered to humans as self-microemulsifying drug delivery systems (SMEDDSs) delivered in soft gelatin capsules as they are low-viscosity liquids. SMEDDSs are concentrated microemulsions that contain only the oil phase and the surfactant phase (without water). SMEDDSs can form MEs spontaneously through the addition of water and gentle agitation, such as movement of the gastrointestinal tract, and can be formulated into capsules [26,27], improving patient acceptance [28]. The pH value is also capable of inducing changes in stability and chemical phenomena, such as deterioration and oxidation of compounds and bacterial growth, and is a precise and specific measure for quality control of the formulation. The pH found for M7-EOCF was 4.65 ± 0.05. Orally tolerated pH values are between 2 and 10 [29]. In this context, M7-EOCF has a pH value compatible with oral use, thus demonstrating that the formulation will not cause irritation to the mucous membranes.

Altogether, considering its composition (i.e., an oil phase, an aqueous phase, and a surfactant phase), transparent appearance, low viscosity, isotropy, Newtonian behavior, and droplet size on a nanometric scale, it can be said that the M7-EOCF formulation is a microemulsion system [30,31].

Antioxidant activity

The results of the antioxidant activities of S. Mix (i.e., surfactants + water, without EOCF), EOCF, and M7-EOCF were evaluated using the DPPH, ABTS, and FRAP methods (Figure 3, see Experimental section for details). It can be seen in Figure 3A that M7-EOCF, EOCF, and S. Mix showed higher DPPH radical scavenging activities than the control. However, S. Mix showed significantly lower antioxidant activity (58.95% ± 5.95%) than M7-EOCF (91.12% ± 0.57%) and EOCF (84.73% ± 2.41%). Regarding antioxidant activity using the ABTS method (Figure 3B), M7-EOCF, EOCF and S. Mix also showed significant differences when compared to the control ($p < 0.0001$). The antioxidant potential of M7-EOCF was 93.12% ± 0.20%, that of EOCF was 76.28% ± 0.86%, and that of S. Mix was 21.60% ± 3.69%. Regarding the antioxidant activity determined through the FRAP method (Figure 3C), significant differences ($p < 0.0001$) were also found between the activities of M7-EOCF, EOCF, and S. Mix when compared to the control. It is also important to highlight the antioxidant and Fe^{2+} chelating potential of EOCF, as observed in a previous study by our research group [12].

Considering the results obtained, M7-EOCF showed the best antioxidant activity. It should also be noted that there was a statistical difference when compared to solely EOCF in the ABTS and FRAP methods, but not with DPPH, showing that the formulation potentiated the antioxidant activity of EOCF. This effect is probably due to the synergistic action between the chemical constituents present in the EO and the surfactants [32,33].

This difference between the DPPH method and the others can be explained by the different antioxidant mechanisms. DPPH is more useful in apolar surroundings and mainly involves hydrogen donation. ABTS is a method that includes electron and hydrogen donation, in addition to being useful for both non-polar and polar surroundings, covering a wider spectrum of compounds [34]. Finally, FRAP evaluates the interaction of the compounds with a ferric complex (TPTZ-Fe^{3+}), with hydrogen donation and reduction effects (TPTZ-Fe^{2+}). Another point to be raised is the saturation of the system. In the DPPH test, the antioxidant activity of M7-EOCF is very close to the activity of Trolox, that is, above 90%. Therefore, there was possibly saturation at the concentration used.

A study by Alencar et al. [35], which aimed to analyze the antioxidant activity of lemongrass (*C. citratus*) EO before and after the development of spray-dried microcapsules, showed a reduction in the antioxidant activity of the formulation when compared to the oil alone. However, the authors defend the idea that the high temperature used in the process altered the compounds in the oil and reduced the antioxidant activity. In the microemulsion formulation in this study, room temperature was used, which may also explain why the antioxidant action was maintained.

EOCF, on *E. coli* and *S. Aureus* bacteria, showed antioxidant activity and control in pathogenic species resistant to oxidative

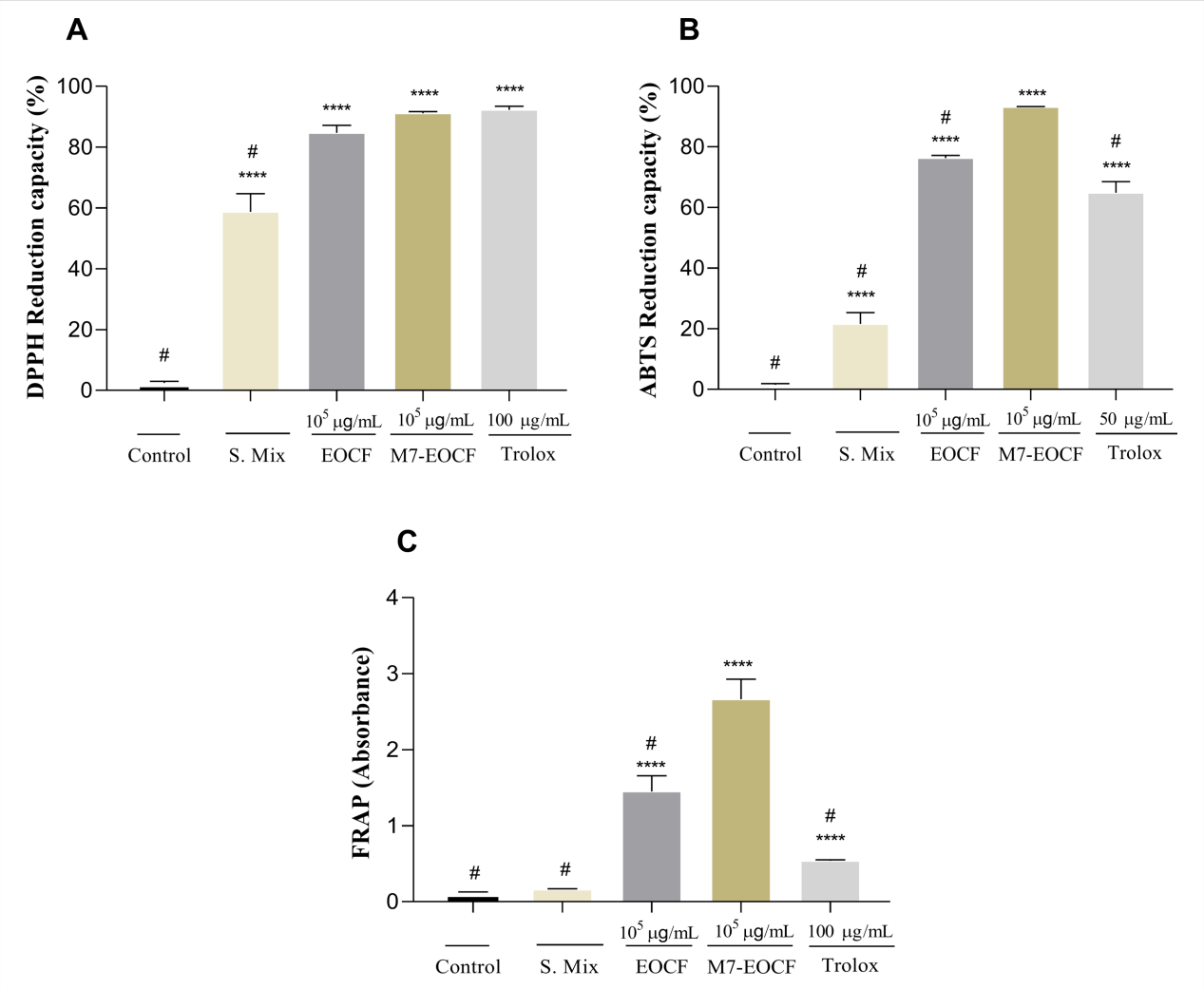

Figure 3: In vitro antioxidant activity of essential oil of *Cymbopogon flexuosus* (EOCF), its microemulsion (M7-EOCF), and S. Mix (surfactants + water, without EOCF). The analysis was carried out using the (A) DPPH, (B) ABTS, and (C) FRAP methods. Trolox was used as the standard antioxidant. The tests were carried out in quintuplicate, and the results represent the mean ± standard deviation of the values; ***$p < 0.001$, ****$p < 0.0001$ versus system (no antioxidants); #$p < 0.0001$ versus M7-EOCF – (ANOVA followed by Tukey's test).

stress. The authors also emphasized that EOCF acted as a potent attenuator of oxidative stress in in vivo models, as it has indirect antioxidants such as terpenes and terpenoids [36]. In another study using nanostructured systems containing lemongrass of the species *C. citratus*, improvements in the stability and high antioxidant content of the EO were demonstrated [37].

Evaluation of cytotoxicity

The cytotoxicity of M7-EOCF, EOCF, and S. Mix was assessed through cell viability measurements on L929 fibroblasts using the MTT method [MTT = 3-(4,5-dimethylthiazol-2yl)-2,5-diphenyltetrazoline bromide]. Figure 4 shows that EOCF was considered cytotoxic at all concentrations tested (50, 100, and 200 µg/mL), with cell viability values of less than 70% when compared to the control (100% viability). The cytotoxicity of EOCF was confirmed in the study by Al-Ghanayem [38], who showed viabilities in keratinocyte cells of 51.5% and 70.5% at concentrations of 1.25 and 0.6 µL/mL of EOCF, respectively.

In contrast, S. Mix and the microemulsion (M7-EOCF) were considered non-cytotoxic at all concentrations tested, with cell viability values greater than 70%. In the study of Sá et al. [39], MEs containing the cytotoxic essential oil of *C. zeylanicum* also showed no cytotoxicity, even with a high concentration of surfactants present in the microemulsions.

In vivo results

Anti-hyperglycemic activity

The aim of this study was to evaluate M7-EOCF supplementation and its effects on recovery, glycemic control, muscle damage, and reactive species markers in streptozotocin (STZ)-induced type-1 diabetic rats. The use of STZ in animals causes

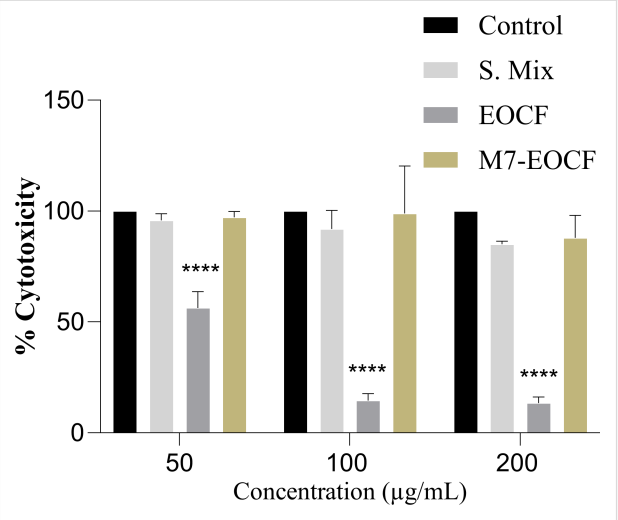

Figure 4: Evaluation of the cytotoxicity of essential oil of *Cymbopogon flexuosus* (EOCF), its microemulsion (M7-EOCF), and surfactant mix + water, without EOCF (S. Mix) on L929 fibroblasts using the MTT test. The results were presented as percentage of cell viability compared to the control group (culture medium). The tests were carried out in triplicate, and the results represent the mean ± standard deviation of the values; ****$p < 0.0001$ (ANOVA followed by Tukey's test).

conditions similar to that of some humans with type-1 diabetes without glycemic control. STZ has been shown to significantly increase blood glucose levels in Wistar rats. STZ's mechanism of action alters the DNA base sequences of pancreatic islet β-cells and stimulates polynuclear (ADP-ribose) synthetase, thus decreasing intracellular NAD and NADP levels. The depletion of NAD by STZ inhibits the synthesis of proinsulin, thus inducing experimental diabetes [40,41].

A significant increase in blood glucose levels was observed in diabetic rats in the control group (CONTROL = 452.78 mg/dL), induced by STZ, compared to supplemented animals. Treatment with the essential oil (EOCF = 234.71 mg/dL, $p < 0.0001$), the microemulsion (M7-EOCF = 283.75 mg/dL, $p < 0.001$), and metformin (MET = 300.86 mg/dL, $p < 0.01$) provided a significant reduction in glucose by, respectively, 48.16%, 37.33%, and 33.55% when compared to the control group; but there were no significant differences between EOCF, M7-EOCF, and MET. Regarding glycated hemoglobin levels, diabetic rats treated with EOCF, M7-EOCF, and MET showed no significant differences compared to diabetic animals in the control group (Figure 5B).

Corroborating the results of this research, a study carried out by Garba et al. [42], using *Cymbopogon* tea in diabetic rats, significantly reduced the induced glycemic increase. However, the data were comparable to those of the group treated with metformin, and no significant differences were observed. Sena-Junior et al. [12] evaluated the effect of citral and EOCF supplementation using different doses (32 and 64 mg/kg) in diabetic Wistar rats for 14 days. All treatments had a significant hypoglycemic effect, but with no significant differences between citral and EOCF groups.

Effect of EOCF on liver function

Exposure of rats to STZ resulted in liver dysfunction, as indicated by alanine aminotransferase (ALT) and aspartate aminotransferase (AST) activities (Figure 6). Treatments with EOCF (32 mg/kg, gavage) and M7-EOCF (32 mg/kg, gavage) significantly reduced liver dysfunction in ALT (EOCF = 97.76 U/L,

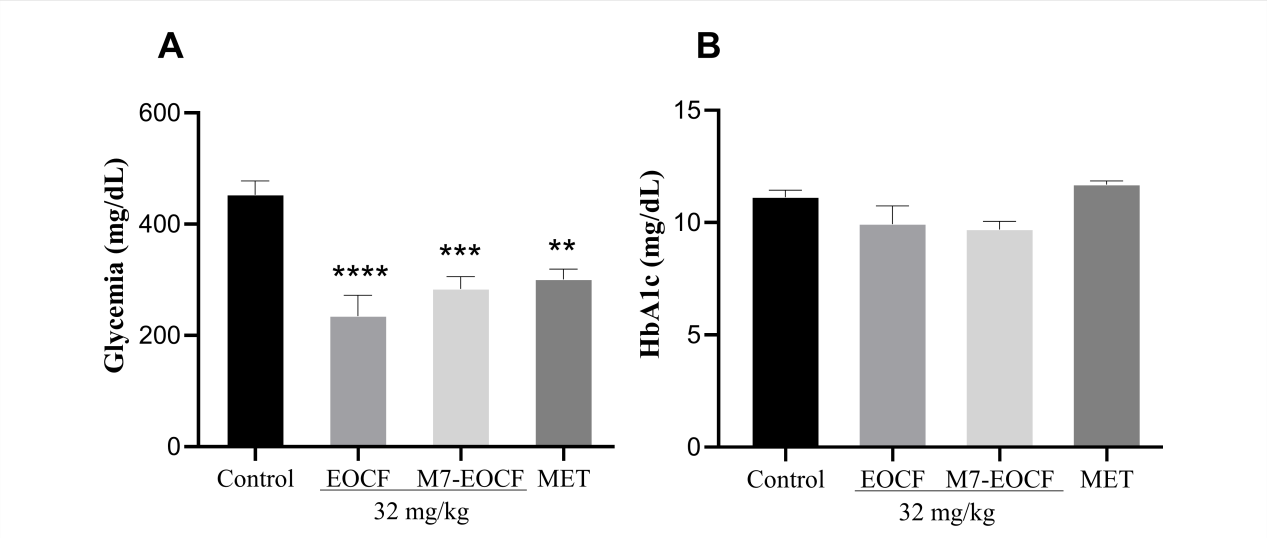

Figure 5: Glycemia (A) and glycated hemoglobin – HbA1c (B) levels of diabetic rats after 21 days of supplementation with EOCF (essential oil of *Cymbopogon flexuosus*) (32 mg/kg) and M7-EOCF (*Cymbopogon flexuosus* essential oil microemulsion) (32 mg/kg). Tween® 80 (control) was used as a negative control. Metformin (MET) was used as a positive control. The assay was carried out in quintuplicate, and the results represent the mean ± standard deviation (SD) of the values; **$p < 0.01$, ***$p < 0.001$, ****$p < 0.0001$ versus control – (ANOVA followed by Tukey's post-test).

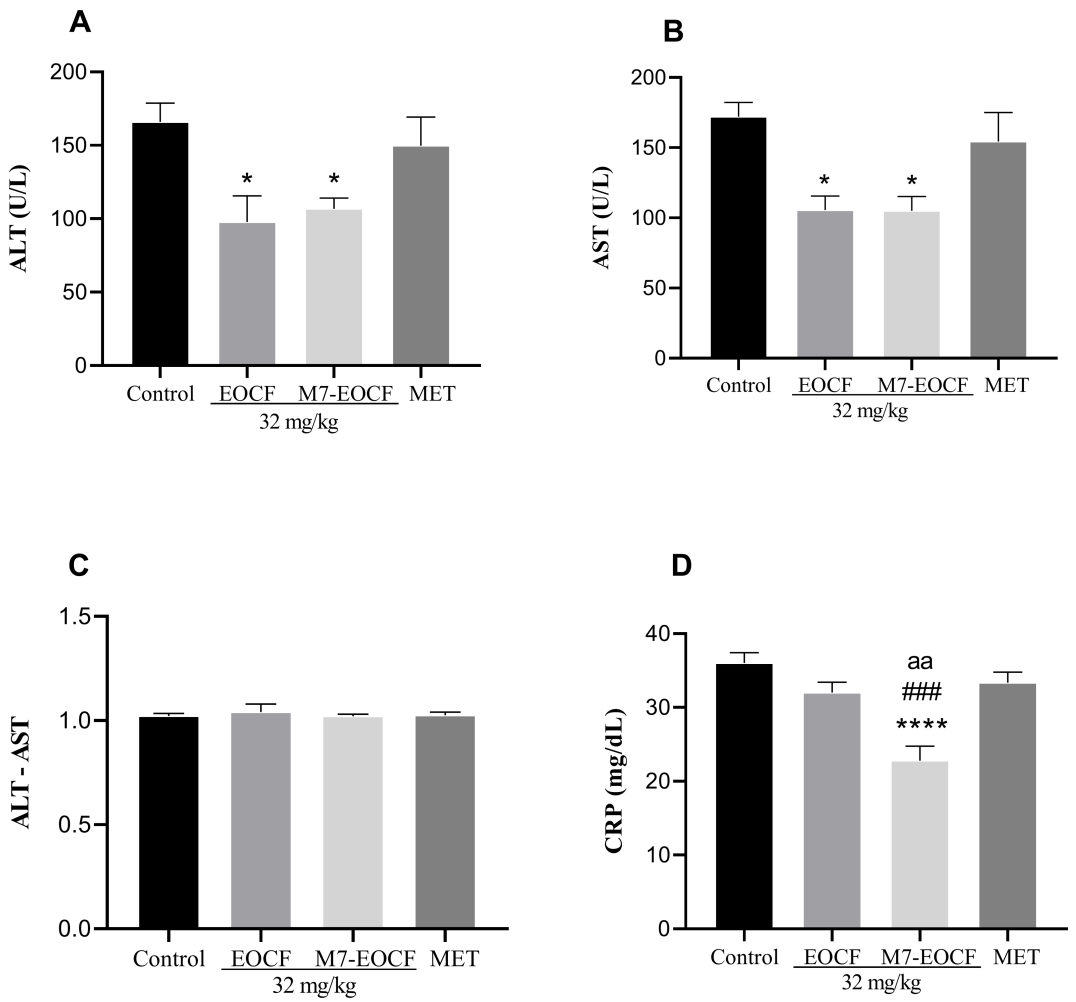

Figure 6: Liver levels of ALT (A), AST (B), ALT/AST ratio (C), and CRP (D) of diabetic rats after 21 days of supplementation with EOCF (*Cymbopogon flexuosus* essential oil) (32 mg/kg) and M7-EOCF (*Cymbopogon flexuosus* essential oil microemulsion). Tween® 80 (CONTROL) was used as a control and metformin (MET) as a positive control. The test was carried out in quintuplicate, and the results represent the mean ± standard deviation (SD) of the values; *$p < 0.05$, ***$p < 0.0001$ versus control, ###$p < 0.001$ versus MET, $^{aa}p < 0.01$ versus EOCF (ANOVA followed by Tukey's post-test).

$p < 0.05$ and M7-EOCF = 106.72 U/L, $p < 0.05$) and AST (EOCF = 105.61 U/L, $p < 0.05$ and M7-EOCF = 105.13 U/L, $p < 0.05$) when compared to the negative control group (CONTROL ALT = 165.98 U/L and AST = 172.10 U/L), as shown in Figure 6A,B. The positive control group (MET) did not significantly reduce ALT and AST liver dysfunction and showed no significant difference when compared to the negative control. Considering the ALT/AST ratio in all groups, the values remained below 1.5 at the end of treatment, with no significant differences (Figure 6C).

Considering the inflammation marker C-reactive protein (CRP), the M7-EOCF group (22.78 mg/dL) showed significant reductions when compared to the negative control group (36.0 mg/dL, $p < 0.0001$), the EOCF group (32.0 mg/dL, $p < 0.01$), and the positive control group (33.33 mg/dL, $p < 0.001$) (Figure 6D).

The significant reductions in ALT, AST, and CRP suggest attenuation of hepatic injury and systemic inflammation, which are commonly exacerbated in diabetic states. These effects may be attributed to the modulation of oxidative stress pathways, particularly through the scavenging of free radicals and the upregulation of endogenous antioxidant enzymes such as superoxide dismutase and catalase. The microemulsion likely enhances the bioavailability of key phytoconstituents such as citral, thereby potentiating their biological activity. To strengthen this interpretation, we included comparisons with prior studies involving lemongrass essential oil and phytocompounds in similar diabetic models, which reported concordant

findings in liver enzyme normalization and inflammatory marker reduction.

In a study carried out by Falode et al. [43], the crude extract of *Cymbopogon* showed similarities to the results obtained in this work regarding the effect of EOCF on the liver functions of the animals tested. In this study, there were no significant differences between the MET-positive control group and the negative control group. Furthermore, in the same study, the induction of diabetes with STZ resulted in a significant increase in the serum and liver levels of AST, ALT, alkaline phosphatase, and gamma-glutamyl transferase as shown in the diabetic control groups compared to the normal control group.

In a study by Garba et al. [42], it was observed that liver glycogen content and serum levels of AST and ALP decreased significantly, while serum ALT, total proteins, and albumin were elevated in the diabetic control group compared to the normal control group. In addition, the group of diabetic rats treated with lemongrass tea showed a modulation in liver alterations, reverting the situation to almost normal, with a reduction in the levels of liver enzymes and markers of kidney function.

More recently, Sena-Junior et al. [12] also evaluated the effect of citral (32 mg/kg) and EOCF (32 and 64 mg/kg) supplementation for 14 days on STZ-induced diabetic rats and found that all treatments protected against ALT liver dysfunction. However, AST levels were only significantly reduced in the citral group and in the group using the highest dose of EOCF (64 mg/kg). It is likely that the present study, using the 32 mg/kg dose, found a reduction in serum levels of both AST and ALP because of the longer treatment time (21 days).

Effect of EOCF on metabolic lipid parameters

Figure 7 shows that exposure of rats to STZ induced significant metabolic lipid disturbances. In the control group of diabetic rats, there was a considerable increase in plasma concentrations of total cholesterol (TC = 128.33 mg/dL), triglycerides (TG = 119.22 mg/dL), and low-density lipoprotein (LDL) cholesterol (155.67 mg/dL), along with a decrease in high-density lipoprotein (HDL) cholesterol levels (34.67 mg/dL) and an increase in Castelli-2 index (2.60 mg/dL). The positive control group (MET) only showed a difference in TC levels (102.11 mg/dL), with no significant change in the other metabolic parameters. The EOCF group showed significant reductions in TC (83.56 mg/dL), TG (69.00 mg/dL), very-low-density lipoprotein (VLDL) cholesterol (13.89 mg/dL), and Castelli-2 index (1.13 ± 0.35 mg/dL). The M7-EOCF group showed reductions in plasma concentrations of TC (95.22 mg/dL), TG (80.44 mg/dL), LDL cholesterol (128.86 mg/dL), VLDL cholesterol (13.78 mg/dL), and Castelli-2 index (1.14 mg/dL), as well as a significant 83.15% increase in HDL cholesterol levels (63.50 mg/dL).

Garba et al. [42] demonstrated in their study that serum levels of TC, TG, and LDL cholesterol were significantly reduced in the diabetic group treated with lemongrass tea compared to the control group. In addition, the tea further reduced HDL cholesterol, although not statistically different compared to the diabetic control. In comparison, the previous study of our group [12] demonstrated that EOCF at a dose of 32 mg/kg supplemented for 14 days significantly reduced TG and increased HDL cholesterol in diabetic rats.

In this study, oral administration of EOCF for 21 days also promoted an increase in HDL cholesterol levels. However, HDL cholesterol levels were higher for microemulsions than for the free essential oil. It is known that microemulsions promote greater bioavailability of hydrophobic molecules orally due to the nanometric size of the droplets. Additionally, nonionic surfactants such as Tween® and Cremophor® inhibit CYP3A metabolism or P-glycoprotein drug efflux, thus improving intestinal drug absorption. Thus, the increase in HDL cholesterol levels may be due to increased oral bioavailability [44].

Itankar et al. [45] also presented similar results to this study where the induction of DM led to a marked increase in serum levels of TG, TC, VLDL cholesterol, and LDL cholesterol, as well as to a reduction in HDL cholesterol levels. After treatment with an aqueous extract of *Cymbopogon citratus* from organically grown plants, there was a significant reduction in serum lipid levels in diabetic mice that had previously been elevated due to the induction of diabetes.

Effect of EOCF on kidney function

Exposure of rats to STZ resulted in kidney disorders, as indicated by increased creatinine, urea, and uric acid levels (Figure 8). Treatment with EOCF (32 mg/kg, gavage) and M7-EOCF significantly protected against changes in renal markers. Treatment with M7-EOCF (Figure 8B) showed significant differences in the urea level (M7-EOCF = 64.17 mg/dL), reducing it by 66.61% when compared to the negative control group (192.20 mg/dL, $p < 0.0001$) and by 46.07% when compared to the positive control group (MET = 119.00 mg/dL, $p < 0.01$). Regarding uric acid, treatment with EOCF (1.41 mg/dL) and M7-EOCF (1.36 mg/dL) significantly reduced the values when compared to the negative control group (2.76 mg/dL) and the positive control group (2.85 mg/dL) (Figure 8C).

Regarding renal markers, Dobhal et al. [46] showed in their study an increase in uric acid levels in rats after inducing diabetes and a significant reduction in these levels in the groups

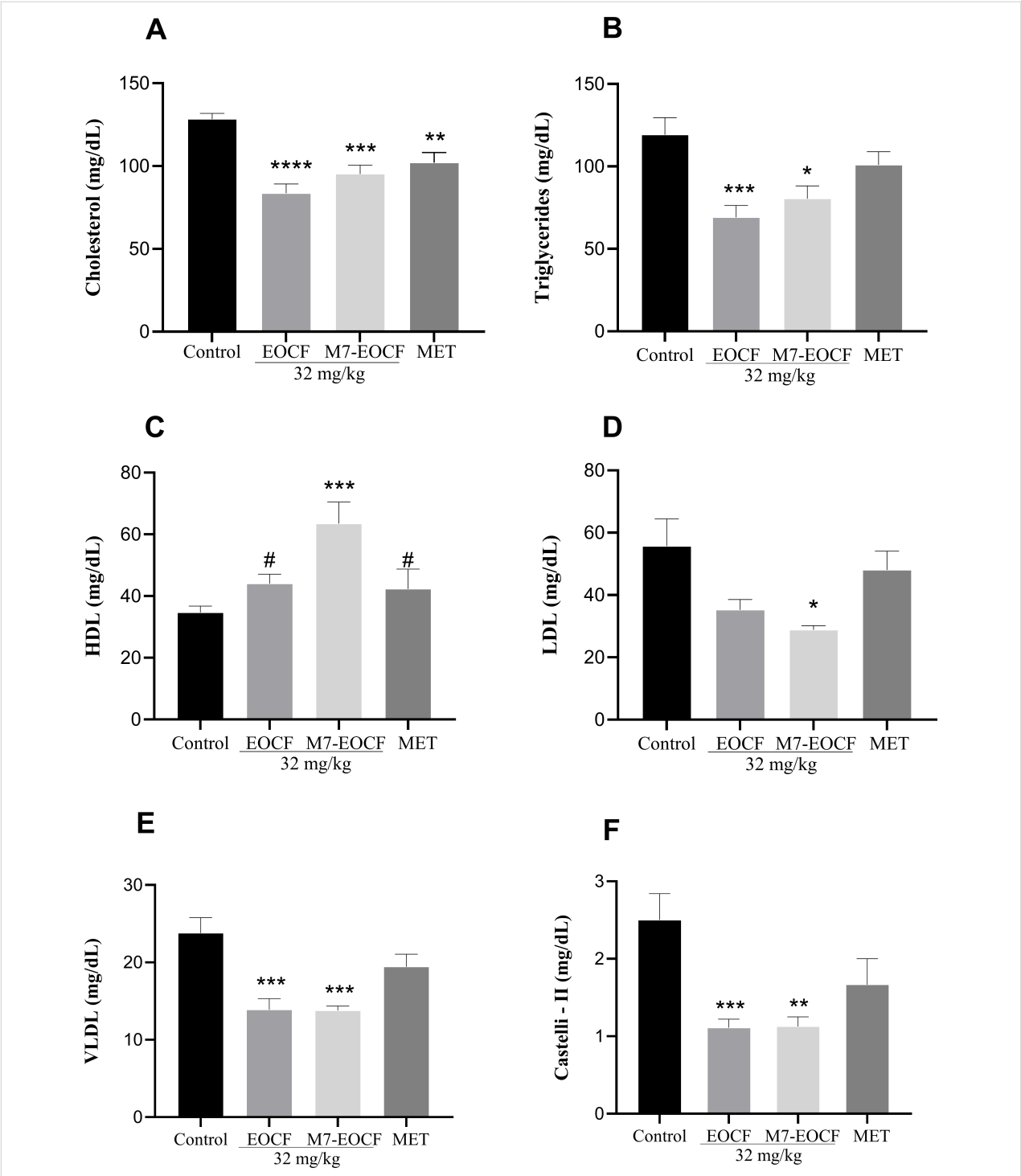

Figure 7: Lipid levels of total cholesterol (A), triglycerides (B), HDL cholesterol (C), LDL cholesterol (D), VLDL cholesterol (E), and Castelli-2 index (F) of diabetic rats after 21 days of treatment with EOCF (*Cymbopogon flexuosus* essential oil) (32 mg/kg) and M7-EOCF (*Cymbopogon flexuosus* essential oil microemulsion) (32 mg/kg). Tween® 80 (CONTROL) was used as a negative control and metformin (MET) as a positive control. The test was carried out in quintuplicate, and the results represent the mean ± standard deviation (SD) of the values; $^{*}p < 0.05$, $^{**}p < 0.01$, $^{***}p < 0.001$, $^{****}p < 0.0001$ versus control, $^{\#}p < 0.05$ versus M7-EOCF (ANOVA followed by Tukey's post-test).

treated with aqueous extract of lemongrass (100 and 200 mg/kg), ethanolic extract of lemongrass (125 and 250 mg/kg), and the essential oil of lemongrass (150 and 300 mg). Almdal and Vilstrup [47] and Mansour et al. [48] showed that induced diabetic hyperglycemia raised plasma levels of the kidney markers urea and creatinine, but there was a

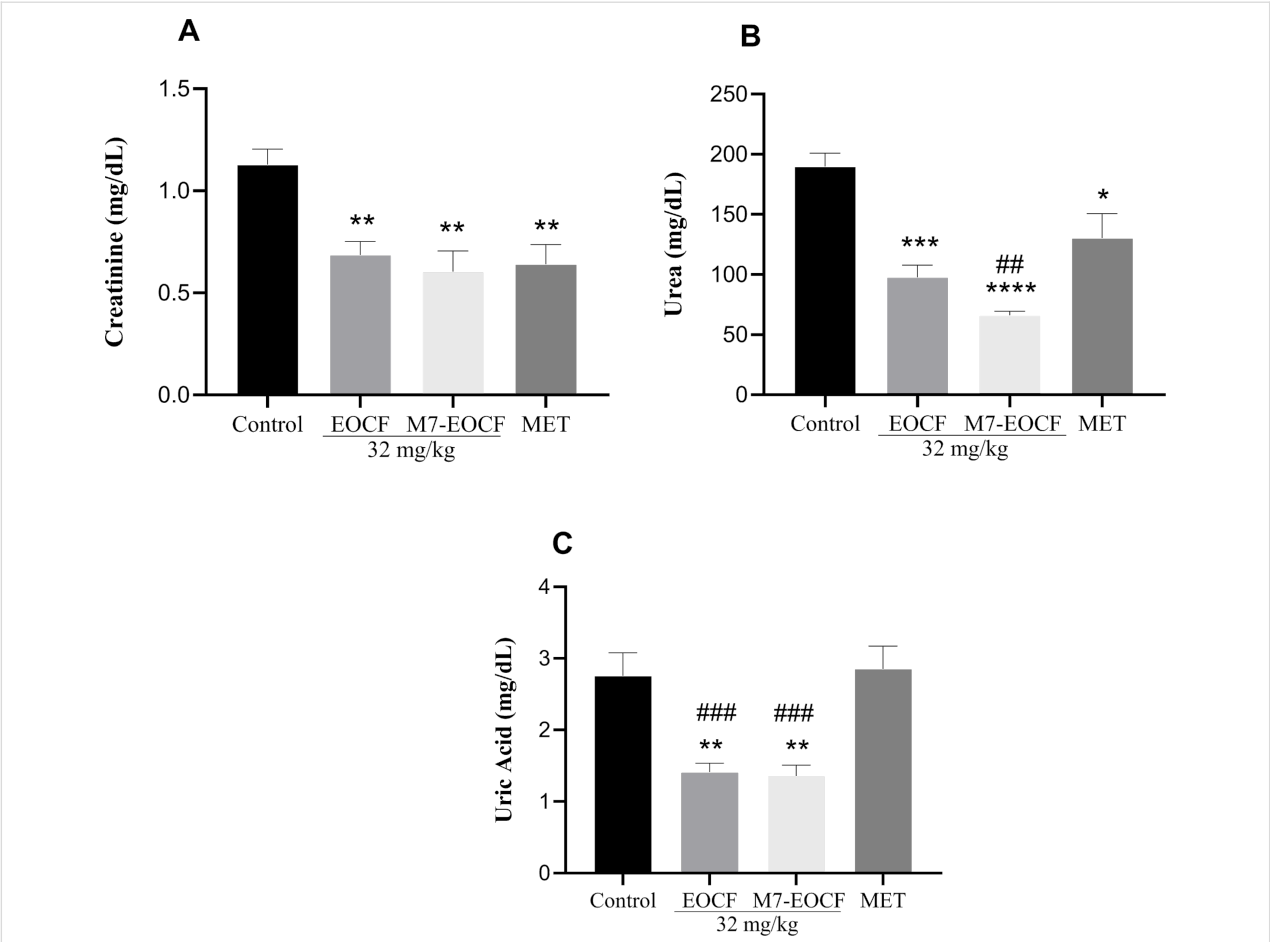

Figure 8: Renal markers creatinine (A), urea (B), and uric acid (C) of diabetic rats after 21 days of treatment with EOCF (*Cymbopogon flexuosus* essential oil) (32 mg/kg) and M7-EOCF (*Cymbopogon flexuosus* essential oil microemulsion) (32 mg/kg). Tween® 80 (CONTROL) was used as a negative control and metformin (MET) as a positive control. The test was carried out in quintuplicate, and the results represent the mean ± standard deviation (SD) of the values; $^{*}p < 0.05$, $^{**}p < 0.01$, $^{***}p < 0.001$, $^{****}p < 0.0001$ versus control (ANOVA followed by Tukey's post-test); $^{\#\#}p < 0.01$, $^{\#\#\#}p < 0.001$ versus EOCF (ANOVA followed by Tukey's post-test).

decrease in these markers after administration of *Cymbopogon proximus* suspension, made from ground seeds of the plant and suspended in double-distilled water. Sena-Junior et al. [12] found a reduction in uric acid levels in diabetic rats after 14 days of daily supplementation with EOCF (64 mg/kg), but the difference was not significant.

The observed decreases in urea and uric acid levels in this study indicate a nephroprotective effect. This may be due to a combination of improved glycemic control and antioxidant activity. Chronic hyperglycemia is known to induce oxidative damage in renal tissues via the formation of advanced glycation end products and increased reactive oxygen species (ROS) generation. By mitigating hyperglycemia, as evidenced by reductions in fasting glucose, both EOCF and M7-EOCF may indirectly reduce renal stress. Simultaneously, the enhanced antioxidant activity of the microemulsion, especially regarding ABTS and FRAP, suggests a direct protective role against oxidative damage. While our data suggest a dual mechanism, future studies using molecular markers of oxidative stress in renal tissue would further clarify the primary pathway involved.

Histological assessment

Histopathological examination revealed that the EOCF group of mice exhibited extensive lesions in the liver and pancreas, with significant structural and functional impairment of these organs. Analysis of the liver sections, illustrated in Figure 9, showed morphological alterations suggestive of an advanced pathological process. In the liver, coagulative necrosis was identified in large areas of the parenchyma, characterized by the initial preservation of cell contours, but with intensely eosinophilic cytoplasm and loss of nuclear integrity. Structural disorganization was evident, with hepatocytes (H) arranged irregularly, many of them showing vacuolized cytoplasm, indicating cell degeneration, as well as pyknotic nuclei, reflecting large-scale cell death.

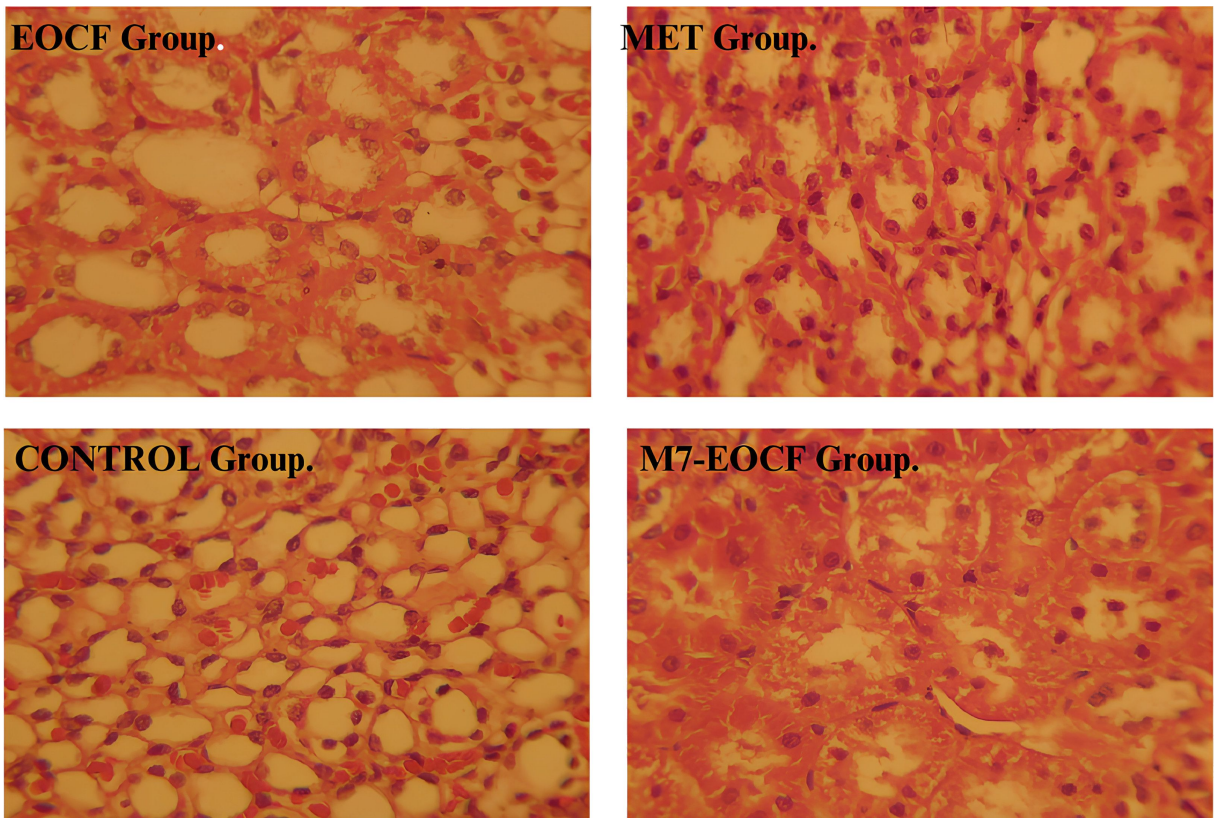

Figure 9: Histological sections of the liver from the experimental groups. The EOCF group shows extensive vacuolization and tissue disorganization. The MET group shows characteristics of necrosis and inflammation with signs of regeneration. The CONTROL group shows moderate damage, with less inflammation and necrosis. The M7-EOCF group is characterized by tissue preservation, less cell damage and regeneration.

The presence of a chronic inflammatory infiltrate was a striking finding, characterized by the accumulation of mononuclear cells, mainly lymphocytes and macrophages, around the portal spaces and areas of necrosis. In addition, the formation of cavities filled with new inflammatory cells was observed (C), suggesting a persistent and progressive inflammatory process (Figure 10). This infiltration may indicate an attempt by the body to repair the damaged tissue, although in severe cases such as the one observed, liver regeneration may be insufficient to restore the organ's homeostasis.

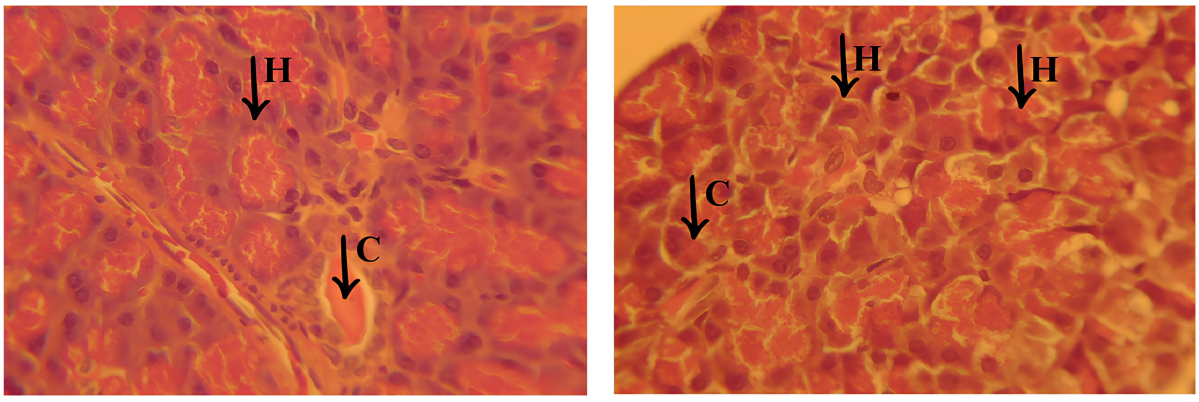

Figure 10: Histological sections of liver from the EOCF group. The images show areas of coagulative necrosis, characterized by disorganized hepatocytes (H), with vacuolized cytoplasm and degenerated or absent nuclei, indicating severe tissue damage. In addition, chronic inflammatory infiltrates (C) are observed, marked by cellular accumulations inside cavities, suggesting a persistent inflammatory response.

Another relevant aspect was the presence of vacuolar degeneration of hepatocytes, characterized by the accumulation of cytoplasmic vesicles, indicating dysfunction in metabolization and impaired cell metabolism. This finding, associated with necrosis and inflammation, suggests an exacerbated cellular response to an aggressive agent, leading to structural collapse of the liver tissue. These histopathological changes indicate that the liver has undergone a severe degenerative process, compromising its function. The combination of extensive necrosis, persistent inflammation, and tissue disruption reinforces the serious nature of the injury, as evidenced by detailed histological analysis.

Histopathological analysis also revealed significant lesions in the pancreas, as illustrated in Figure 11, with emphasis on the regions indicated by (J) and (I). One of the most obvious findings was interstitial edema, characterized by excessive accumulation of fluid in the extracellular space, which resulted in increased spacing between cells and reinforced the presence of an active inflammatory process, as well as indicating a diffuse degenerative condition (J). The cellular disorganization associated with interstitial edema was particularly pronounced in region (I), suggesting that pancreatic tissue damage was severe and progressive. The structural alteration observed, marked by the separation of cells and loss of cohesion between them, compromised the integrity of the pancreatic parenchyma, which may indicate dysfunction in enzyme production and secretion, as well as an exacerbated inflammatory response.

In addition, cell destruction associated with necrosis and local inflammation was seen in region (J). The loss of pancreatic cell integrity may have contributed to worsening interstitial edema and intensified tissue disorganization, favoring a cycle of progressive damage. The presence of these histological findings suggests an extensive degenerative process throughout the pancreatic tissue. However, the possibility should be considered that the pancreatic lesions observed in all groups were induced by streptozotocin, a cytotoxic agent selective for the β-cells of the pancreatic islets. This factor may have exacerbated the histopathological picture, intensifying cell degeneration and the inflammatory response.

Histopathological analysis of the MET group (Figure 12) revealed significant cell damage in the liver, including necrosis and inflammation, but with signs of regeneration in certain areas, suggesting a reparative response to the applied treatment. Despite the considerable degree of damage, this group showed signs of attempted tissue restoration and was classified as the second most severe group in terms of the lesions observed. Important morphological changes were identified in the liver tissue. Cell vacuolization (A) was one of the most obvious findings, characterized by the accumulation of cytoplasmic vesicles, a phenomenon often associated with degenerative and apoptotic processes. This alteration reflects an impairment of cellular homeostasis and represents an important marker of liver damage in various pathological conditions.

In addition, cell edema (B) was found, characterized by swelling of the hepatocytes due to excessive accumulation of intracellular fluid. This alteration may be associated with dysfunctions in the permeability of the plasma membrane, leading to an osmotic imbalance, which favors fluid retention and compromises cell viability. Another relevant finding was the presence of areas with an active inflammatory response. Regions with inflammatory infiltrate (C) reinforce the persistence of the inflammatory process, and the body attempts to contain tissue damage. These histological findings indicate that, despite the significant damage observed in the MET group,

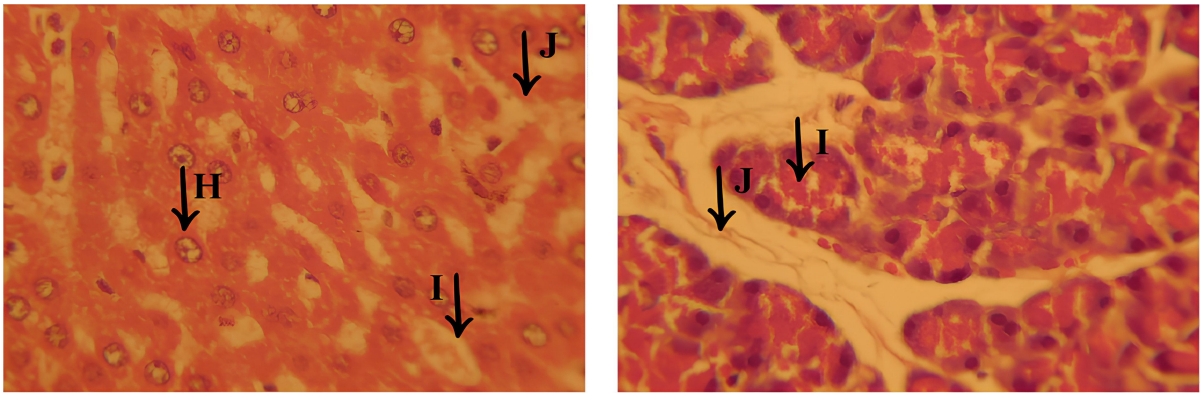

Figure 11: Significant lesions in the pancreas, highlighting interstitial edema (I). Interstitial edema contributes to cell spacing and cell disorganization, indicating a diffuse degenerative process. Presence of active inflammation (J) and destruction of pancreatic cells, suggesting local necrosis, with worsening interstitial edema and tissue disorganization.

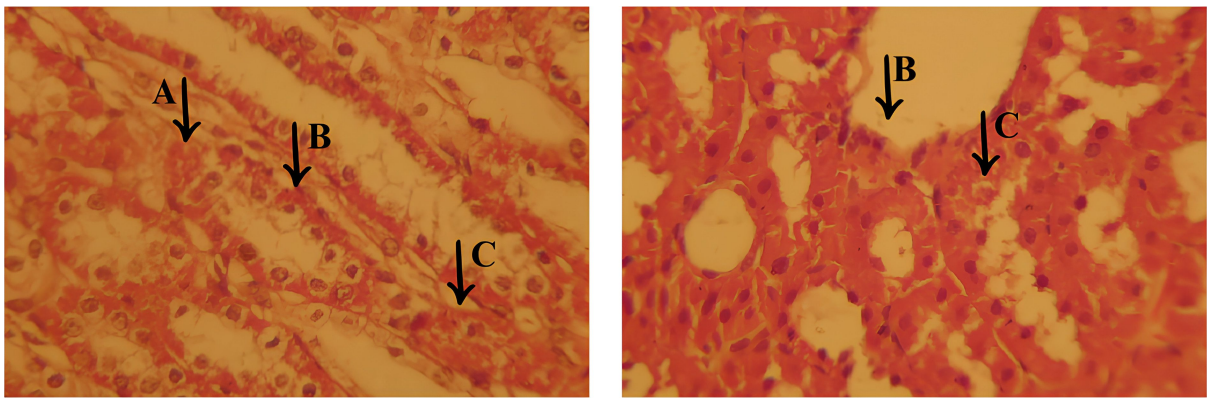

Figure 12: Histological section of the liver from the MET group, showing significant morphological changes. In (A), there is cellular vacuolization, indicating the presence of degenerative and apoptotic processes. In (B), there is the presence of cellular edema. In (C), there are areas of chronic inflammatory infiltrate, with cavities filled with inflammatory cells.

there are signs of tissue regeneration, showing a dynamic balance between inflammatory aggression and the liver's reparative response.

Histopathological analysis of the CONTROL group (Figure 13) revealed less inflammation and vascular congestion compared to the MET group, as well as moderate interstitial edema. Liver damage was less severe, with a lower incidence of necrosis and cell degeneration, indicating a reduced level of tissue impairment compared to the EOCF and MET groups. Histological examination showed moderate damage to the liver tissue, characterized by cellular vacuolization (A), an indication of cellular stress and sublethal damage, without significant progression to extensive necrosis. In addition, cellular edema was observed (B), with a slight increase in intracellular volume and the presence of prominent capillary vessels, suggesting a slight disturbance in tissue homeostasis.

Another relevant finding was the presence of a chronic inflammatory infiltrate (C), characterized by cavities containing inflammatory cells, although to a lesser extent when compared to the other experimental groups. The areas surrounding the infiltrate showed signs of cell degeneration (D), but to a limited extent, suggesting a controlled inflammatory response and less aggression to the liver tissue. These findings indicate that, despite the presence of moderate lesions, the control group showed less histological impairment compared to the other groups, with less inflammatory and degenerative impact, reflecting better preservation of the liver architecture.

The group treated with *Cymbopogon flexuosus* essential oil microemulsion (M7-EOCF) showed the least signs of liver damage of all the groups, with minimal or no histological alterations (Figure 14). The results suggest a significant potential for

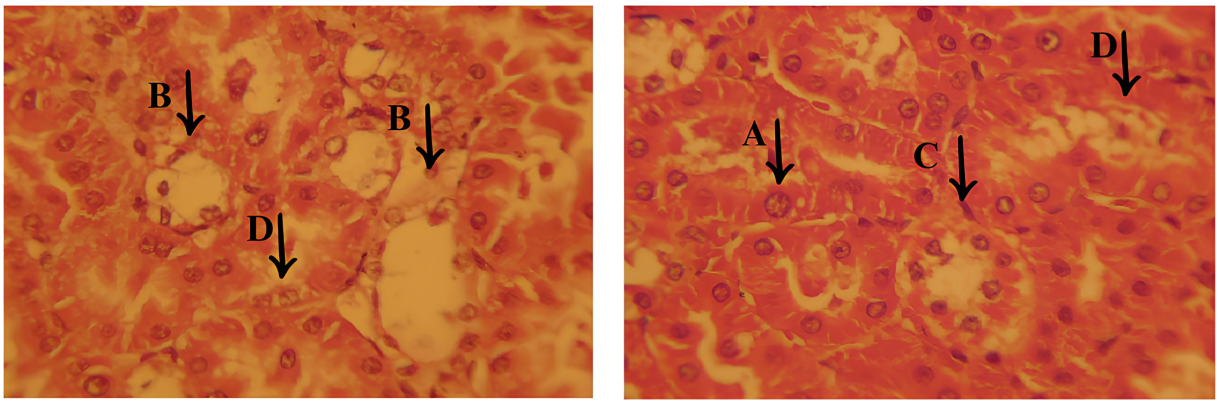

Figure 13: Histological section of the liver from the CONTROL group, showing moderate damage. In (A), cell vacuolization is observed, indicating moderate to mild damage. In (B), there is cellular edema with angiogenesis and mild inflammation. In (C), there is a chronic inflammatory infiltrate, with cavities filled with inflammatory cells. The areas adjacent to the infiltrate show signs of cellular degeneration (D), but to a lesser degree.

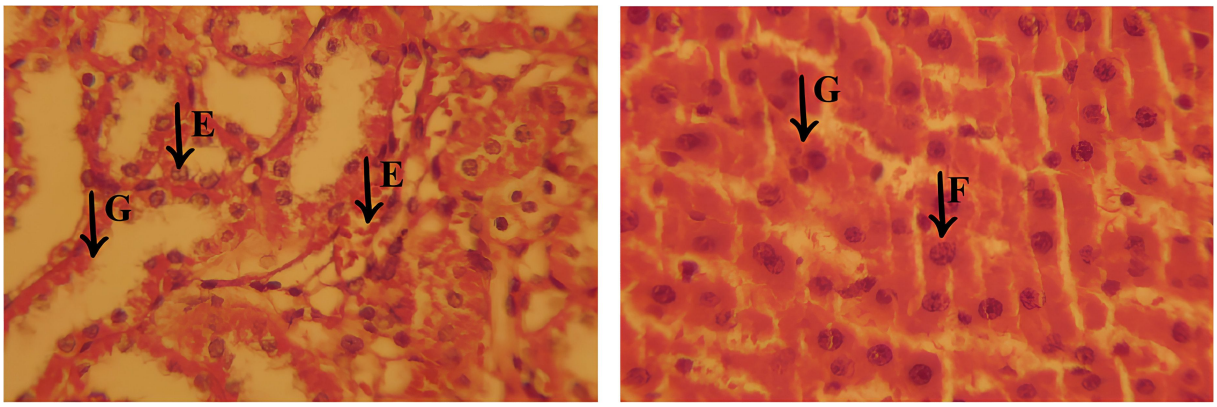

Figure 14: Histological section of the liver from the M7-EOCF group, showing relevant features of tissue preservation and cell regeneration. In (E), there is an attempt at cell regeneration, with proliferative and organized cells. In (F), there is vascular congestion and sinusoidal dilation, possibly due to inflammation or local injury. In (G), there are areas with partially preserved tissue architecture.

tissue preservation, as evidenced by the absence of severe necrosis and inflammation.

Histological analysis revealed relevant characteristics: In region (E), there was an attempt at cell regeneration, with proliferating and organized cells. Region (F) showed vascular congestion and sinusoidal dilation, possibly secondary to inflammation or local damage. In region (G), areas with partially preserved tissue architecture were identified, where the cells had small, condensed nuclei, indicating an attempt at regeneration, albeit with a loss of cellular detail. These findings reflect a favorable tissue response in the M7-EOCF group, suggesting an effective regenerative process and significant preservation of liver integrity.

Histological data indicate that treatment with M7-EOCF provided significant protection against liver damage and inflammation induced by DM. This microemulsion appears to be a promising therapeutic approach for mitigating liver complications associated with inflammatory and oxidative conditions. The literature associates DM with oxidative damage to tissues, especially the liver, due to an increase in ROS, which cause chronic inflammation. The liver, which is essential for glucose and lipid metabolism, is particularly vulnerable to the metabolic stress generated by prolonged hyperglycemia and insulin resistance, resulting in inflammation, hepatic steatosis, and fibrosis.

Based on the discussed findings, it was possible to establish a classification of the severity of the lesions observed in the different groups. The EOCF group had the most severe injuries, characterized by extensive necrosis and severe inflammation, with no signs of regeneration. The MET group showed significant lesions, but with some degree of regeneration, indicating potential for recovery. The control group showed moderate lesions, with less pronounced inflammation and necrosis compared to the previous groups. Finally, the M7-EOCF group showed the smallest lesions, with few alterations, suggesting a state of normality. This classification provides a clearer understanding of the severity of the lesions in each group.

The essential oil of *Cymbopogon flexuosus*, especially its main component, citral, has anti-inflammatory and antioxidant properties, acting to neutralize ROS and thus reduce oxidative stress and liver inflammation. The microemulsion, as a nanoformulation, improves the bioavailability of the bioactive compounds, enhancing their therapeutic efficacy and facilitating the absorption and distribution of the essential oil.

The histological results corroborate these findings, showing a significant reduction in liver damage in the group treated with the microemulsion compared to the positive and negative control groups, as well as the treatment with essential oil, which showed more significant damage. This attenuating action of ROS-mediated inflammation suggests a reduction in the risk of liver complications associated with diabetes. In addition, biochemical analysis of the rats' blood samples showed an improvement in liver and kidney parameters after treatment with the microemulsion. The cytotoxicity data also corroborate these observations, indicating that EOCF is cytotoxic, while ME-EOCF showed no cytotoxicity.

In summary, the microemulsion containing *Cymbopogon flexuosus* essential oil has emerged as a promising innovative therapy for the treatment of liver damage resulting from diabetes mellitus. However, more studies, especially human clinical trials, are needed to validate its long-term efficacy and better understand the molecular mechanisms involved.

Conclusion

The selected microemulsion containing the essential oil of *Cymbopogon flexuosus* (M7-EOCF) was obtained using Eumulgin® CO40 and Tween® 80 as the surfactant phase; it presented itself as a transparent, liquid, and isotropic system, with nanometric droplet size, good stability, low polydispersity index and pH suitable for oral administration. It was also observed that M7-EOCF exhibited high antioxidant activity, showing that the formulation acted by potentiating the bioactive activity of EOCF. Finally, the in vivo results showed that EOCF, M7-EOCF, and metformin reduced blood glucose, but without significant differences between them. EOCF and M7-EOCF improved liver parameters, unlike metformin. M7-EOCF also had a significant protective effect against liver damage and inflammation induced by DM. In terms of lipid profile, EOCF and M7-EOCF also improved the parameters evaluated, reducing total cholesterol, triglycerides, and the Castelli-2 index. However, M7-EOCF also reduced LDL cholesterol and increased HDL cholesterol by 83.15%, showing a better effect on lipid parameters compared to EOCF. Regarding kidney function, both treatments, EOCF and M7-EOCF, showed an improvement in the parameters assessed, but M7-EOCF showed a more marked improvement in the urea marker. Metformin, in contrast, was only able to reduce blood glucose, promote a slight reduction in total cholesterol and improve the renal parameters creatinine and urea.

Overall, EOCF and M7-EOCF showed significant beneficial effects on various metabolic and renal parameters in diabetic rats. However, the microemulsion was able to improve the antioxidant activity of EOCF, maintain its antidiabetic activity, and provide additional benefits, such as improved kidney function, reduced systemic inflammation, increased HDL cholesterol levels, and a hepatoprotective effect.

Experimental

Material

The EOCF was obtained commercially from local suppliers (Engenharia das Essências, lot: 451 A225841), produced by Yanih Cosmetics (ANVISA Notification 25351.25600/2017-36). The citral was purchased from Sigma-Aldrich (Brazil) with a purity content of 95%. DPPH, ABTS, and trolox were also purchased from Sigma-Aldrich, Brazil. Streptozotocin (Cayman Chemical, USA) was obtained from Induslab (Brazil). Eumulgin® CO 40 (BASF®, Brazil) and Tween® 80 (NEON®, Brazil) were purchased from local suppliers.

Identification of the chemical constituents of EOCF

To identify the chemical components, the EOCF was examined in a Thermo Scientific gas chromatograph (GC), Bremen, Germany, model TRACE 1310 coupled to a mass spectrometer (MS) model TSQ-9000, with TriPlus RSH automatic sampler. A NA-5MS column (60 m × 0.25 mm DI, 0.25 µm film thickness) was used for compound separation, with helium as a 99.999% pure carrier gas (White Martins SA) at a flow rate of 1 mL/min and a split/splitless autoinjector. For the analysis, a solution of EOCF was prepared at a concentration of approximately 10 mg/mL using hexane as a solvent, measured in a 1.5 mL glass vial. The sample then underwent chromatographic analysis. The ramp was programmed as follows: 60 °C – 3 °C/min – 240 °C (15 min). The injection mode was split (1:30), in SCAN mode, with a total analysis time of 75 min. For MS, the conditions were as follows: injector temperature 220 °C, detector temperature 240 °C, solvent cut-off time 2 min, electron ionization (EI) mode at 70 eV with a mass-to-charge ratio (m/z) range of 40 to 350 Da. The components of the essential oil were identified using their retention indices (RI), calculated for each constituent by injecting a series of linear hydrocarbon standards (C_8–C_{20}), under the same sample conditions, and compared with tabulated values, confirming the identification by comparing the compound spectra with the reference, presented by the NIST 107, 21 and Wiley 8 libraries [39] as shown in Supporting Information File 1, Table S1.

Obtaining microemulsions from pseudoternary phase diagrams and selecting formulations

The components used to develop the MEs were Tween® 80 and Eumulgin® CO40 as the surfactant phase, EOCF as the oil phase, and ultrapure water as the aqueous phase. The combination Tween 80/Eumulgin CO40 (1:1) was chosen based on a previous paper from our research group [49]. The proportions of the components were defined using the pseudoternary phase diagram [50].

First, the surfactant phase was prepared from a mixture of Tween® 80 and Eumulgin® CO40 in a ratio of 1:1 (w/w) by magnetic homogenization for 24 h. The oil phase was then added to the surfactant solution, still under magnetic stirring, and homogenized for 30 min. The oil phase and surfactant solutions were prepared in proportions of 1:9, 2:8, 3:7, 4:6, 5:5, 6:4, 7:3, 8:2, and 9:1. Each solution was titrated with pre-defined volumes of water [51]. After each addition of water, the system was left to stand for 5 min, and the macroscopic properties were used to classify the systems into transparent liquid systems, transparent viscous systems, and non-transparent systems and to delimit the regions in the pseudoternary phase diagram.

Formulations containing 10% EOCF were then prepared individually (Table 1), and the dispersions were evaluated macroscopically and characterized 48 h after they were obtained.

Table 1: Centesimal composition of formulations M1–M8, containing EOCF (essential oil *of Cymbopogon flexuosus*) and the surfactants Eumulgin® CO40 and Tween® 80 (1:1 ratio).

Formulation	EOCF (%)	Surfactant (%)	Water (%)
M1	10	85	10
M2	10	75	20
M3	10	65	30
M4	10	55	40
M5	10	45	50
M6	10	35	60
M7	10	25	70
M8	10	5	90

Physicochemical characterization of the selected microemulsions

The polydispersity index and average hydrodynamic radius of the droplets were determined by dynamic light scattering using Zetasizer Nano ZS equipment (Malvern Instruments, UK). For this purpose, about 1,000 µL of the sample, undiluted and at a temperature of 25 °C, were inserted into a cuvette suitable for carrying out the measurements [8].

The optical properties of the samples were investigated using a polarized light microscope (Olympus model BX51) equipped with a digital camera (Evolution LC Color). For analysis, a drop of the sample, undiluted, was placed on a glass slide, covered with a coverslip and analyzed under polarized light at 20,000× magnification [24].

The rheological behavior of the formulations was assessed by flow tests using the Modular Compact Rheometer (Anton Paar, MRC 302). A cone-plate geometry was used (diameter 49.9 mm, angle 1°, and gap 96 µm). The shear stress (γ) was evaluated as a function of the shear rate ranging from 0.1 to 200 s^{-1}. The experiment was carried out in triplicate at room temperature and at 37 °C.

The pH analyses were carried out after diluting the MEs (1:10). A digital pH meter (model Analion PM 608) containing a glass electrode and temperature sensor (Phtek PH 3B), previously calibrated with buffer solution (pH 4.0 and 7.0), was used at room temperature [52].

Determination of antioxidant activity

The in vitro antioxidant activities of the S. Mix. samples (surfactants + water, without EOCF), EOCF (10 mg/mL), and selected microemulsions containing EOCF (10 mg/mL) were evaluated using the 2,2-diphenyl-1-picrylhydrazyl (DPPH) free radical scavenging, 2,2′-azinobis-3-ethylbenzothiazoline-6-sulfonic acid (ABTS) radical capture, and ferric reduction antioxidant power (FRAP) methods. Trolox was used as a positive control at a concentration of 50 µg/mL for ABTS and at a concentration of 100 µg/mL for the DPPH and FRAP assays.

The DPPH method was carried out using the methodology adapted from Brand-Williams and colleagues [53]. An aliquot of 50 µL of each sample was added to 150 µL of methanolic DPPH solution (0.6 mM/L), and after 30 min, the absorbance was read in a spectrophotometer at 515 nm. The DPPH radical scavenging activity was expressed as a percentage calculated from the absorbance values of the control and the sample.

For ABTS, the methodology from Brand-Williams and colleagues was also adapted [53]. Initially, the ABTS solution was activated 16 h before the experiment by mixing 1.25 mL of ABTS stock solution and 22 µL of potassium persulfate solution. Then, 30 µL of each sample was pipetted and 300 µL of ABTS solution was added. After 6 min, the ABTS radical scavenging activity was read on a spectrophotometer at a wavelength of 734 nm and calculated from the absorbance of the control and the sample.

Using the FRAP method modified by Oyaizu [54], 9 µL of each sample, 27 µL of water, and 270 µL of FRAP reagent (a mixture of ferric chloride, TPTZ (2,4,6-tris(2-pyridyl)-*s*-triazine), and acetate buffer (0.3 M; pH 3.6) were pipetted in. The plate was incubated at 37 °C for 30 min, and the absorbance was read in a spectrophotometer at 595 nm. The results were expressed in absorbance.

Evaluation of cytotoxicity on L929 fibroblasts

Cells of the L929 strain of mouse fibroblasts were inserted into 96-well plates (EasyPath®, EP-51-25244) with a final volume of 200 µL. The fibroblasts (1×10^5 cells/mL cultured in Dulbecco MEM medium supplemented with 10% SFB (Gibco®, Thermo Fisher Scientific) and 1% antibiotic solution (5,000 UI penicillin + 5 mg streptomycin/mL, Sigma-Aldrich) were kept in an oven (5% CO_2 atmosphere at 37 °C for 24 h) [55,56].

After this period, the adherent fibroblasts were treated with the S. Mix. samples (surfactants + water, without EOCF), EOCF, and the selected microemulsion containing EOCF (M7-EOCF), at concentrations of 50, 100, and 200 µg/mL, and cultured under the previous conditions for further 24 h. At the end of this phase, the cell monolayer was washed twice with phosphate-buffered saline, and then 200 µL of MTT (0.5 mg/mL, Sigma-Aldrich) was added to each well.

The plate was incubated again under the same conditions for 3 h. After the incubation period, the MTT was aspirated, and the

formazan crystals were solubilized in 200 µL of DMSO. After placing the plate in the oven for 10 min to stabilize the color, the optical density (OD) was measured at a wavelength of 570 nm in a microplate reader. The analysis was carried out in quadruplicate, and 0.1% DMSO was considered the negative control [55,56]. The results were expressed as the percentage of viability according to the formula: %viability = (OD_{570} treated wells/OD_{570} control wells) × 100.

In vivo study in Wistar rats using a DM1 model

Animals

The trials in this study were approved by the UFS Animal Use Ethics Committee, under CEUA No. 8502100821. Male Wistar rats, aged three months and weighing approximately 250 to 300 g, were used in the study. These rats were obtained from the animal house of the Physiology Department of the Federal University of Sergipe (UFS), São Cristóvão, Sergipe, Brazil. The animals (n = 40) were housed randomly in appropriate cages under controlled temperature conditions (22 ± 3 °C) with a 12 h light/dark cycle, providing 300 lux of light. They had free access to specific rodent food (Labina®) and water ad libitum and were kept in suitable conditions for 30 days of the experiment, respecting the guidelines of CONCEA – National Council for the Control of Animal Experimentation (Normative Resolution No. 12, 20/09/2013) and the minimum number of animals necessary to achieve the scientific objectives.

Induction of diabetes mellitus

To induce DM, the animals were fasted for 12 h to improve the sensitivity and diabetogenic action of the drug, with water supplied ad libitum.

Experimental DM1 was induced as described by Wang et al. [57], Barman and Srinivasan [58], and Sena-Junior et al. [12], using the drug streptozotocin (STZ), at a dose of 40 mg/kg body weight, dissolved in 0.01 M citrate buffer, pH 4.5, injected intraperitoneally into 40 animals. STZ was administered, and all groups were offered food 30 min later to avoid hypoglycemia. Blood was collected by tail puncture to measure blood glucose using an Accu-Chek Go glucometer (Roche Diagnostics GmbH, D-68298, Mannheim, Germany) 72 and 96 h after induction. Only animals with fasting glucose levels equal to or greater than 150 mg/dL were included in the study. After confirmation of diabetes induction, the animals were randomly assigned and treatment was started.

Experimental groups

Treatment took place daily for 21 days. The animals received the treatment intragastrically (by gavage) and were divided into four groups, as described in Table 2 (10 animals/group), that is, negative control group (NCG): diabetic animals treated with vehicle (saline solution + 0.2% Tween® 80); EOCF group: diabetic animals treated with the EOCF supplementation solution at a dose of 32 mg/kg body weight; M7-EOCF group: diabetic animals treated with the EOCF microemulsion supplementation solution at a dose of 32 mg/kg body weight; positive control group (PCG): diabetic animals treated with metformin supplementation at a dose of 150 mg/kg body weight.

Supplementation

Supplementation consisted of the administration of EOCF and the selected microemulsion (M7-EOCF) at a dose of 32 mg/kg [59,60], or metformin at a dose of 150 mg/kg, and was carried out daily at the same time for 21 days.

Sample collection

After a period of 24 h from the last administration of treatment on day 21, the animals fasted for 12 h and were anaesthetized with an intraperitoneal injection of a mixture of ketamine (100 mg/kg) and xylazine (10 mg/kg). Blood and tissues (pancreas, spleen, liver, and kidneys) were collected, weighed, and stored for later analysis.

Table 2: Distribution of the animals used in this study according to the test to be carried out. NCG – negative control group: diabetic animals treated with saline solution + 0.2% Tween® 80; EOCF group: diabetic animals treated with *Cymbopogon flexuosus* essential oil; M7-EOCF group: diabetic animals treated with the EOCF Microemulsion; PCG – positive control group: diabetic animals treated with metformin.

Experimental group	Species	Number of groups	Initial number of animals/final number of animals	Total number
NCG	Wistar rats	1	10/10	10
EOCF	Wistar rats	1	10/10	10
M7-EOCF	Wistar rats	1	10/10	10
PCG	Wistar rats	1	10/10	10
Total				40

Determination of serum biochemical markers

The blood was centrifuged at 800*g* for 15 min at 4 °C, and the serum was stored at −80 °C. Serum concentrations of triglycerides (TG), total cholesterol (TC), HDL cholesterol, LDL cholesterol, VLDL cholesterol, alanine aminotransferase (ALT), aspartate aminotransferase (AST), ALT and AST ratio (ALT/AST), C-reactive protein (CRP), Castelli-2 index, fasting blood glucose (glycemia), glycated hemoglobin (HbA1c), urea, creatinine, and uric acid were determined according to the manufacturer's procedures (Labtest®, Lagoa Santa, Minas Gerais, Brazil).

Histological evaluation

Samples of pancreas, spleen, liver, and kidneys were immersed in paraffin, followed by sectioning using a microtome. The paraffin was then removed from the samples using ethanol and xylene. After washing, the samples were stained with hematoxylin and eosin. The histological sections were analyzed by microscopy and photographed (OLYMPUS BX 45, OLYMPUS).

Statistical analysis

All statistical analyses were conducted using Graph Pad Prism version 5.0 and presented as mean ± standard deviation. Data was first assessed for normality using the Shapiro–Wilk test and then statistically analyzed between groups using one-way analysis of variance (ANOVA) and Tukey post-hoc tests. Statistically significant differences between the samples adopted were considered when $p < 0.05$.

Supporting Information

Supporting Information File 1

Additional figures and tables.
[https://www.beilstein-journals.org/bjnano/content/supplementary/2190-4286-16-48-S1.pdf]

Acknowledgements

This study was part of the Ph.D. thesis of Ailton Santos Sena-Júnior, entitled “Formulação microemulsionada com óleo essencial de *Cymbopogon flexuosus*: avaliação dos impactos antioxidantes, citotóxicos e metabólicos em modelo de diabetes experimental em ratos”, defended in the Graduate Program in Pharmaceutical Sciences at the Federal University of Sergipe in 2024. The authors would like to thank CLQM (Center of Multiusers Chemistry Laboratories) and Laboratório de Corrosão e Nanotecnologia (LCNT), both from the Federal University of Sergipe, for the rheological and microscopy analysis, respectively. The Graphical Abstract was created in BioRender. Santana Santos, R. (2025) https://BioRender.com/b12v935. This content is not subject to CC BY 4.0.”

Funding

The authors would like to thank the Conselho Nacional de Desenvolvimento Científico e Tecnológico (CNPq, Brazil) for funding (Process 405142/2021-8). The authors would like to thank the Coordenação de Aperfeiçoamento de Pessoal de Nível Superior (CAPES) for the financial support through the Graduate Scholarship Program in Pharmaceutical Sciences, which made this work possible. This study was funded by CAPES - Finance Code 001.

Author Contributions

Ailton Santos Sena-Júnior: conceptualization; data curation; formal analysis; investigation; methodology; software; supervision; validation; visualization; writing – original draft. Cleverton Nascimento Santana Andrade: data curation; formal analysis; investigation; validation; visualization. Pedro Henrique Macedo Moura: data curation; formal analysis; investigation; validation; visualization. Jocsã Hémany Cândido dos Santos: data curation; formal analysis; investigation; validation; visualization. Cauãn Torres Trancoso: data curation; formal analysis; investigation; validation; visualization. Eloia Emanuelly Dias Silva: data curation; formal analysis; investigation; validation; visualization. Deise Maria Rego Rodrigues Silva: data curation; formal analysis; investigation; validation; visualization. Ênio Pereira Telles: data curation; formal analysis; writing – review & editing. Luiz André Santos Silva: data curation; investigation; methodology; validation; visualization. Isabella Lima Dantas Teles: data curation; investigation; methodology; validation; visualization. Sara Fernanda Mota de Almeida: data curation; investigation; methodology; validation; visualization. Daniel Alves de Souza: data curation; investigation; methodology; supervision; validation. Jileno Ferreira Santos: data curation; investigation; methodology; validation; visualization. Felipe José Aidar Martins: methodology; project administration; supervision; validation; visualization. Ana Mara de Oliveira e Silva: methodology; project administration; supervision; validation; visualization. Sandra Lauton-Santos: methodology; project administration; supervision; validation; visualization. Guilherme Rodolfo Souza de Araujo: methodology; project administration; supervision; validation; visualization. Cristiane Bani Correa: methodology; project administration; supervision; validation; visualization. Rogéria De Souza Nunes: methodology; project administration; supervision; validation; visualization. Lysandro Pinto Borges: methodology; project administration; supervision; validation; visualization. Ana Amélia Moreira Lira: conceptualization; funding acquisition; methodology; project administration; resources; supervision; validation; visualization.

ORCID® iDs

Ailton Santos Sena-Júnior - https://orcid.org/0000-0002-9710-9533
Jocsã Hémany Cândido dos Santos - https://orcid.org/0009-0009-6459-784X
Cauãn Torres Trancoso - https://orcid.org/0009-0000-4592-0490
Ênio Pereira Telles - https://orcid.org/0000-0003-2527-1635
Isabella Lima Dantas Teles - https://orcid.org/0000-0003-3712-8799
Daniel Alves de Souza - https://orcid.org/0000-0002-8789-1170
Felipe José Aidar Martins - https://orcid.org/0000-0001-7378-4529
Sandra Lauton-Santos - https://orcid.org/0000-0003-3373-3254
Ana Amélia Moreira Lira - https://orcid.org/0000-0003-3451-9049

Data Availability Statement

The data generated and analyzed during this study is available from the corresponding author upon reasonable request.

References

1. Cole, J. B.; Florez, J. C. *Nat. Rev. Nephrol.* **2020,** *16,* 377–390. doi:10.1038/s41581-020-0278-5
2. Padilha, A. L.; Alves Filho, J. R. *Res. Soc. Dev.* **2022,** *11,* e169111335317. doi:10.33448/rsd-v11i13.35317
3. Treviño-Almaguer, D.; Espinosa-Rodríguez, B. A.; Ramírez-Cabrera, M. A.; Winkler, R.; Garza-González, E.; Mendez-López, L. F.; Balderas-Rentería, I. *Rev. Cienc. Farm. Biomed.* **2022,** *4* (Suppl. 1), 19.
4. Avoseh, O.; Oyedeji, O.; Rungqu, P.; Nkeh-Chungag, B.; Oyedeji, A. *Molecules* **2015,** *20,* 7438–7453. doi:10.3390/molecules20057438
5. Sharma, N.; Bora, K. S. *J. Pharm. Res. Int.* **2021,** *33,* 2196–2207. doi:10.9734/jpri/2021/v33i60b34864
6. Júnior, A. S. S.; Aidar, F. J.; Silva, L. A. S.; de B. Silva, T.; de Almeida, S. F. M.; Teles, D. C. S.; de L. Junior, W.; Schimieguel, D. M.; de Souza, D. A.; Nascimento, A. C. S.; Camargo, E. A.; dos Santos, J. L.; de O. e Silva, A. M.; de S. Nunes, R.; Borges, L. P.; Lira, A. A. M. *Life* **2024,** *14,* 336. doi:10.3390/life14030336
7. Saboia, C. d. S.; Cardoso, D. T.; Santos, J. V. d.; Saboia, C. d. S.; Barbosa, R. T. P.; Teles, A. M.; Mouchrek, A. N. *Res. Soc. Dev.* **2022,** *11,* e37611730064. doi:10.33448/rsd-v11i7.30064
8. Vilas Boas de Almeida, B.; Gomes dos Santos, M.; Tescarollo, I. L. *Rev. Ensaios Pioneiros* **2023,** *7,* 1–20. doi:10.24933/rep.v7i1.291
9. Gupta, A.; Eral, H. B.; Hatton, T. A.; Doyle, P. S. *Soft Matter* **2016,** *12,* 2826–2841. doi:10.1039/c5sm02958a
10. Barros, A. M. C.; Pinto, A. C. d. S.; Santos, K. S. C. R. d.; Guilhon-Simplicio, F.; Amado, J. R. R.; Chaves, F. C. M.; Lima, E. S.; Franco, A. M. R. *Peer Rev.* **2023,** *5,* 239–252.
11. Debiasi, B. W.; Dourado, S. H. A.; Andrighetti, C. R.; Ribeiro, E. B.; Battirola, L. D.; Valladão, D. M. S. *Braz. J. Biol.* **2024,** *84,* e259451. doi:10.1590/1519-6984.259451
12. Júnior, A. S. S.; Aidar, F. J.; Silva, L. A. S.; de B. Silva, T.; de Almeida, S. F. M.; Teles, D. C. S.; de L. Junior, W.; Schimieguel, D. M.; de Souza, D. A.; Nascimento, A. C. S.; Camargo, E. A.; dos Santos, J. L.; de O. e Silva, A. M.; de S. Nunes, R.; Borges, L. P.; Lira, A. A. M. *Life* **2024,** *14,* 336. doi:10.3390/life14030336
13. Adukwu, E. C.; Bowles, M.; Edwards-Jones, V.; Bone, H. *Appl. Microbiol. Biotechnol.* **2016,** *100,* 9619–9627. doi:10.1007/s00253-016-7807-y
14. Callender, S. P.; Mathews, J. A.; Kobernyk, K.; Wettig, S. D. *Int. J. Pharm.* **2017,** *526,* 425–442. doi:10.1016/j.ijpharm.2017.05.005
15. Islam, M. R.; Uddin, S.; Chowdhury, M. R.; Wakabayashi, R.; Moniruzzaman, M.; Goto, M. *ACS Appl. Mater. Interfaces* **2021,** *13,* 42461–42472. doi:10.1021/acsami.1c11533
16. Moreira, F. V.; Bastos, J. F. A.; Blank, A. F.; Alves, P. B.; Santos, M. R. V. *Rev. Bras. Farmacogn.* **2010,** *20,* 904–909. doi:10.1590/s0102-695x2010005000012
17. Seixas, K. B.; Araujo, G. R. S. d.; de Oliveira, A. M.; Silveira Filho, A. J.; Leite, A. R. O. F.; Napoleão, T. H.; Sarmento, V. H. V.; Gonsalves, J. K. M. d. C.; Bedor, D. C. G.; Silva, M. C. S. C.; Lira, A. A. M.; Leal, L. B.; de Santana, D. P. *J. Drug Delivery Sci. Technol.* **2024,** *101,* 106166. doi:10.1016/j.jddst.2024.106166
18. Souza de Araujo, G. R.; Mendonça da Cruz Macieira, G.; Xavier de Oliveira, D.; Santos Matos, S.; Nery dos Santos, Q.; Otubo, L.; Antunes de Souza Araújo, A.; Cavalcante Duarte, M.; Moreira Lira, A. A.; de Souza Nunes, R.; Vitorino Sarmento, V. H. *Colloids Surf., B* **2022,** *214,* 112474. doi:10.1016/j.colsurfb.2022.112474
19. Tabosa, M. A. M.; de Andrade, A. R. B.; Lira, A. A. M.; Sarmento, V. H. V.; de Santana, D. P.; Leal, L. B. *AAPS PharmSciTech* **2018,** *19,* 1837–1846. doi:10.1208/s12249-018-0995-2
20. Liu, X.; Li, Q.; Gao, X.; Lu, C.; Dang, L.; Wang, Z. *J. Mol. Liq.* **2020,** *302,* 112527. doi:10.1016/j.molliq.2020.112527
21. Mahran, A.; Ismail, S.; Allam, A. A. *Pharmaceutics* **2021,** *13,* 444. doi:10.3390/pharmaceutics13040444
22. Aulton, M. E.; Taylor, K. M. G. *Aulton Delineamento de Formas Farmacêuticas,* 4th ed.; Elsevier: Rio de Janeiro, RJ, Brazil, 2016.
23. Dobos, A. M.; Filimon, A.; Bargan, A.; Zaltariov, M.-F. *J. Mol. Liq.* **2020,** *309,* 113129. doi:10.1016/j.molliq.2020.113129
24. Carvalho, A. L. M.; Silva, J. A. d.; Lira, A. A. M.; Conceição, T. M. F.; Nunes, R. d. S.; de Albuquerque Junior, R. L. C.; Sarmento, V. H. V.; Leal, L. B.; de Santana, D. P. *J. Pharm. Sci.* **2016,** *105,* 2188–2193. doi:10.1016/j.xphs.2016.04.013
25. Machado, M.; Dantas, I. L.; Galvão, J. G.; Lima, A. D.; Gonsalves, J. K. M. d. C.; Almeida, E. D. P.; de Araujo, G. R. S.; Leal, L. B.; Sarmento, V. H. V.; Nunes, R. S.; Lira, A. A. M. *Res. Vet. Sci.* **2020,** *133,* 31–38. doi:10.1016/j.rvsc.2020.08.009
26. Yan, B.; Gu, Y.; Zhao, J.; Liu, Y.; Wang, L.; Wang, Y. *Curr. Nanosci.* **2019,** *15,* 576–588. doi:10.2174/1573413715666190112122107
27. Rani, E. R.; Radha, G. V. *Crit. Rev. Ther. Drug Carrier Syst.* **2021,** *38,* 27–74. doi:10.1615/critrevtherdrugcarriersyst.2020034975
28. Dokania, S.; Joshi, A. K. *Drug Delivery* **2015,** *22,* 675–690. doi:10.3109/10717544.2014.896058
29. Strickley, R. G.; Oliyai, R. Solubilizing Vehicles for Oral Formulation Development. *Solvent Systems and Their Selection in Pharmaceutics and Biopharmaceutics;* Biotechnology: Pharmaceutical Aspects, Vol. 6; Springer: New York, NY, USA, 2007; pp 257–308. doi:10.1007/978-0-387-69154-1_9
30. de Assis, K. M. A.; da Silva Leite, J. M.; de Melo, D. F.; Borges, J. C.; Santana, L. M. B.; dos Reis, M. M. L.; Moreira, V. M.; da Rocha, W. R. V.; Catão, R. M. R.; dos Santos, S. G.; da Silva Portela, A.; de Sousa Silva, S. M.; de Oliveira, T. K. B.; de Souza da Silveira, J. W.; Pires, E. G.; Nonaka, C. F. W.; Sanches, F. A. C.; de Lima Damasceno, B. P. G. *Drug Delivery Transl. Res.* **2020,** *10,* 1748–1763. doi:10.1007/s13346-020-00850-0

31. Wan, J.; Wang, S.-m.; Gui, Z.-p.; Yang, Z.-z.; Shan, Q.-q.; Chu, X.-q.; Gui, S.-y.; Yang, Y. *Eur. J. Pharm. Sci.* **2018,** *125,* 93–101. doi:10.1016/j.ejps.2018.09.018
32. Vasco, C.; Ruales, J.; Kamal-Eldin, A. *Food Chem.* **2008,** *111,* 816–823. doi:10.1016/j.foodchem.2008.04.054
33. Al-Sagheer, A. A.; Mahmoud, H. K.; Reda, F. M.; Mahgoub, S. A.; Ayyat, M. S. *Aquacult. Nutr.* **2018,** *24,* 1006–1014. doi:10.1111/anu.12637
34. Floegel, A.; Kim, D.-O.; Chung, S.-J.; Koo, S. I.; Chun, O. K. *J. Food Compos. Anal.* **2011,** *24,* 1043–1048. doi:10.1016/j.jfca.2011.01.008
35. de Oliveira Alencar, D. D.; de Souza, E. L.; da Cruz Almeida, E. T.; da Silva, A. L.; Oliveira, H. M. L.; Cavalcanti, M. T. *Foods* **2022,** *11,* 1111. doi:10.3390/foods11081111
36. Resende, R. S. F. d.; Borba, P. A. B.; Amâncio, N. d. F. G.; Almeida, R. L. B. M. d. *Res. Soc. Dev.* **2022,** *11,* e185111738952. doi:10.33448/rsd-v11i17.38952
37. Martins, T. E. S. Avaliação morfológica do pulmão em ratos diabéticos tratados com s-metilcisteína, Universidade Federal do Rio Grande do Norte, Natal - RN, 2021.
38. Al-Ghanayem, A. A. *J. King Saud Univ., Sci.* **2022,** *34,* 102072. doi:10.1016/j.jksus.2022.102072
39. de Sá, A. Á. M.; Santos, E. W. P. d.; dos S. Santana, M. H.; Santos, A. d. J.; de Araujo, G. R. S.; Santana, D. G.; de Lara P. de M. Arguelho, M.; de O. e Silva, A. M.; Correa, C. B.; de S. Nunes, R.; Sarmento, V. H. V.; Lira, A. A. M. *Ind. Crops Prod.* **2020,** *154,* 112654. doi:10.1016/j.indcrop.2020.112654
40. Panchnadikar, A.; Bhonde, R. *Med. Hypotheses* **2003,** *60,* 356–359. doi:10.1016/s0306-9877(02)00403-6
41. Ohkuwa, T.; Sato, Y.; Naoi, M. *Life Sci.* **1995,** *56,* 1789–1798. doi:10.1016/0024-3205(95)00150-5
42. Garba, H. A.; Mohammed, A.; Ibrahim, M. A.; Shuaibu, M. N. *Clin. Phytosci.* **2020,** *6,* 19. doi:10.1186/s40816-020-00167-y
43. Falode, J. A.; Olofinlade, T. B.; Fayeun, G. S.; Adeoye, A. O.; Bamisaye, F. A.; Ajuwon, O. R.; Obafemi, T. O. *Pharmacol. Res. Mod. Chin. Med.* **2023,** *7,* 100234. doi:10.1016/j.prmcm.2023.100234
44. Hamdy, A.; El-Badry, M.; Fathy, M.; El-Sayed, A. M. *Sci. Rep.* **2024,** *14,* 22584. doi:10.1038/s41598-024-71980-5
45. Itankar, P. R.; Tauqeer, M.; Dalal, J. S. *J. Ayurveda Integr. Med.* **2019,** *10,* 233–240. doi:10.1016/j.jaim.2017.04.002
46. Dobhal, S.; Singh, M. F.; Setya, S.; Bisht, S. *Indian J. Pharm. Educ. Res.* **2022,** *56,* s281–s293.
47. Almdal, T. P.; Vilstrup, H. *Diabetologia* **1988,** *31,* 114–118. doi:10.1007/bf00395558
48. Mansour, H. A.; Newairy, A.-S. A.; Yousef, M. I.; Sheweita, S. A. *Toxicology* **2002,** *170,* 221–228. doi:10.1016/s0300-483x(01)00555-8
49. Kumar, R.; Sinha, V. R.; Dahiya, L.; Sarwal, A. *Int. J. Pharm.* **2021,** *594,* 120129. doi:10.1016/j.ijpharm.2020.120129
50. Callender, S. P.; Wettig, S. D. *J. Surfactants Deterg.* **2021,** *24,* 603–629. doi:10.1002/jsde.12510
51. Kupper, S.; Kłosowska-Chomiczewska, I.; Szumała, P. *Carbohydr. Polym.* **2017,** *175,* 347–354. doi:10.1016/j.carbpol.2017.08.010
52. Mehta, S. K.; Kaur, G.; Bhasin, K. K. *Colloids Surf., B* **2007,** *60,* 95–104. doi:10.1016/j.colsurfb.2007.06.012
53. Brand-Williams, W.; Cuvelier, M. E.; Berset, C. *Lebensm.-Wiss. Technol. (1968-2004)* **1995,** *28,* 25–30. doi:10.1016/s0023-6438(95)80008-5
54. Oyaizu, M. *Jpn. J. Nutr. Diet.* **1986,** *44,* 307–315. doi:10.5264/eiyogakuzashi.44.307
55. Hirschman, W. R.; Wheater, M. A.; Bringas, J. S.; Hoen, M. M. *J. Endod.* **2012,** *38,* 385–388. doi:10.1016/j.joen.2011.11.012
56. Mosmann, T. *J. Immunol. Methods* **1983,** *65,* 55–63. doi:10.1016/0022-1759(83)90303-4
57. Wang, X.; Li, H.; Fan, Z.; Liu, Y. *J. Physiol. Biochem.* **2012,** *68,* 563–572. doi:10.1007/s13105-012-0174-y
58. Barman, S.; Srinivasan, K. *Chem.-Biol. Interact.* **2019,** *307,* 37–50. doi:10.1016/j.cbi.2019.04.018
59. Al-Okbi, S. Y.; Mohamed, D. A.; Hamed, T. E.; Edris, A. E. *J. Med. Food* **2014,** *17,* 764–771. doi:10.1089/jmf.2013.0033
60. Mishra, C.; Khalid, M.; Fatima, N.; Singh, B.; Tripathi, D.; Waseem, M.; Mahdi, A. A. *Iran. J. Basic Med. Sci.* **2019,** *22,* 49–57. doi:10.22038/ijbms.2018.26889.6574

License and Terms

BEILSTEIN JOURNAL OF NANOTECHNOLOGY

Chitosan nanocomposite containing rotenoids: an alternative bioinsecticidal approach for the management of *Aedes aegypti*

Maria A. A. Bertonceli[1], Vitor D. C. Cristo[1], Ivo J. Vieira[2], Francisco J. A. Lemos[3], Arnoldo R. Façanha[4], Raimundo Braz-Filho[2], Gustavo V. T. Batista[5], Luis G. M. Basso[5], Sérgio H. Seabra[4], Thalya S. R. Nogueira[2], Felipe F. Moreira[4], Arícia L. E. M. Assis[4], Antônia E. A. Oliveira[1] and Kátia V. S. Fernandes[*1]

Full Research Paper

Open Access

Address:
[1]Laboratório de Química e Função de Proteinas e Peptídeos, CBB, Universidade Estadual do Norte Fluminense Darcy Ribeiro, Campos dos Goytacazes/RJ, Brazil, [2]Laboratório de Ciências Químicas, CCT, Universidade Estadual do Norte Fluminense Darcy Ribeiro, Campos dos Goytacazes/RJ, Brazil, [3]Laboratório de Biotecnologia, CBB, Universidade Estadual do Norte Fluminense Darcy Ribeiro, Campos dos Goytacazes/RJ, Brazil, [4]Laboratório de Biologia Celular e Tecidual, CBB, Universidade Estadual do Norte Fluminense Darcy Ribeiro, Campos dos Goytacazes/RJ, Brazil and [5]Laboratório de Ciências Físicas, CCT, Universidade Estadual do Norte Fluminense Darcy Ribeiro, Campos dos Goytacazes/RJ, Brazil

Email:
Kátia V. S. Fernandes[*] - cowpkat@uenf.br

* Corresponding author

Keywords:
dengue; nanoparticle; pest management; phytochemicals

Beilstein J. Nanotechnol. **2025,** *16,* 1197–1208.
https://doi.org/10.3762/bjnano.16.88

Received: 24 January 2025
Accepted: 17 July 2025
Published: 28 July 2025

This article is part of the thematic issue "Advances in nanotechnology applied to natural products".

Associate Editor: K. Koch

Abstract

Climate change has intensified the proliferation of disease vectors, such as *Aedes aegypti*, the primary transmitter of dengue, chikungunya, and zika viruses. Although the two recently licensed dengue vaccines represent a significant advancement, vector management remains the primary strategy for preventing these urban arboviruses. In this context, the development of pesticides that offer safer alternatives for the environment and human health has become urgent. In this study, a chitosan-based nanocomposite was developed as a delivery system for rotenoids isolated from *Clitoria fairchildiana* seeds, leveraging their larvicidal activity against third-instar larvae of *Ae. aegypti*. The nanocomposite was synthesized using a controlled ionic gelation method incorporating the TPP-β-CD inclusion complex, which resulted in nanoparticles with smaller size, improved polydispersity index, and enhanced stability, evidenced by a higher zeta potential. FTIR analysis confirmed rotenoid incorporation into the nanocomposite and suggested hydrogen bonding or potential covalent interaction with chitosan functional groups. Bioassays demonstrated that the

nanocomposite achieved an LC_{50} of 91.7 ppm, representing a 23.6% increase in larvicidal efficacy compared to the rotenoids in their natural form. The nanocomposite also induced dose-dependent morphological and physiological alterations in the larvae, including damage to the peritrophic matrix, evidenced by abnormal anal excretion, and tissue melanization and formation of melanotic pseudotumors. These responses may be associated with increased production of reactive oxygen species in the larval midgut, consistent with previous findings for the nonencapsulated rotenoids. Importantly, empty nanoparticles exhibited no adverse effects on larval survival, which is attributed to the biocompatibility and nontoxic nature of chitosan, a biodegradable polysaccharide structurally related to the insect exoskeleton and widely recognized for its environmental safety. Additionally, neither rotenoids nor the CS/TPP–β-CD–rot nanocomposite exerted cytotoxic effects, confirming their favorable safety profile. These findings highlight the potential of nanotechnology to enhance the efficacy of bioactive compounds while minimizing environmental and human health risks, offering a sustainable and innovative strategy for vector control.

Introduction

Climate change has significantly impacted public health, intensifying the proliferation of disease vectors such as those transmitted by the mosquito *Aedes aegypti*. Environmental conditions exacerbated by global warming, including rising temperatures, heavy rainfalls, and high humidity, have accelerated mosquito reproduction and expanded its geographic spread. In 2023, dengue reached a record 5 million cases in 80 countries, including historically non-endemic regions such as the United States, Italy, France, and Spain. Recent studies indicate that the risk of dengue transmission has increased by 11% in the past decade due to the climate crisis [1]. From even more recent data from Brazil for the year 2024, dengue cases increased by 297%, and chikungunya cases by 65% compared to the same period in 2023. These figures include 5,696 deaths from dengue and 188 deaths from chikungunya. Additionally, while no Zika cases were reported in 2023, 6,348 cases were recorded in 2024 [2]. All these alarming numbers underscore the urgent need for sustainable and innovative strategies to manage *Ae. aegypti* and mitigate the effects of this increasingly global and urgent threat.

According to the World Health Organization (WHO), two dengue vaccines have been licensed: Dengvaxia (CYD-TDV), developed by Sanofi Pasteur, and Qdenga (TAK-003), developed by Takeda. CYD-TDV is a live recombinant tetravalent dengue vaccine approved for use in individuals aged 9–45 years or 9–60 years, depending on country-specific regulatory guidelines. Due to the requirement for pre-vaccination screening, the widespread use of this vaccine has been limited. The use of TAK-003 is recommended for children aged 6 to 16 years in regions with high dengue transmission intensity. However, its use is not currently recommended for children under 6 years of age or adults aged 60 years and older, due to the lower effectiveness of the vaccine in these age groups [3]. While these vaccines represent significant advancements in dengue prevention, *Ae. aegypti* vector management remains the primary strategy for controlling dengue and other urban arboviruses, such as chikungunya and zika.

While most places are increasingly investing in the application of larger quantities of synthetic larvicides, such as the unprecedented investment of 16.9 million Brazilian reais in 2023 [4], the development of resistance by this vector to regularly used larvicides, which impact other organisms beneficial to the environment while presenting risks of poisoning to humans who handle them, is rampant. The adoption of new biotechnological tools becomes crucial to overcome these obstacles in vector control in a smarter way [5-8].

Bioactive compounds from plants have demonstrated great potential as bioinsecticidal agents. Derived from renewable sources, these compounds possess complex chemical compositions, diverse modes of action, and selective toxicity to target organisms, making them a viable alternative for developing new insecticide formulations. Combining these attributes with nanoparticle encapsulation strategies, it is possible to considerably increase the biocidal agent efficacy while reducing the environmental and human health impacts associated with traditional synthetic insecticides [9,10].

Chitosan nanoparticles, derived from a biodegradable and nontoxic polysaccharide, have proven effective in reducing post-harvest deterioration of fruits and vegetables, in addition to exhibiting well-documented antimicrobial properties [11,12]. Furthermore, a chitosan nanocomposite with fungal metabolites has been reported as a promising alternative for managing insect pests of economic importance without affecting non-target organisms [13].

In previous research by our group, two rotenoids were identified and characterized from *Clitoria fairchildiana* seeds with larvicidal activity against third-instar *Ae. aegypti* larvae. These studies revealed morphological and metabolic changes in the larvae, suggesting that V-ATPase inhibition triggers oxidative stress, resulting in high production of reactive oxygen species (ROS) in the midgut. This process causes exoskeletal alterations and ultimately leads to larval death [14].

Building on this work and aiming to develop a biotechnological product that could represent a novel tool for managing *Ae. aegypti*, a chitosan (CS)-based nanocomposite was developed as a delivery system for the isolated rotenoids. The nanocomposite represented a 23.6% increase in efficacy compared to the previously described natural rotenoids. These results highlight the potential of chitosan nanocomposites as an innovative, effective, and environmentally sustainable solution for managing the insect vector. By offering a promising alternative, this technology directly contributes to preventing diseases such as dengue, zika, and chikungunya.

Results and Discussion

Two rotenoids, identified as 11α-*O*-β-D-glucopyranosylrotenoid (CFD – RI) and 6-deoxyclitoriacetal *O*-β-D-glucopyranoside (CFD – RII), were previously isolated and characterized from *C. fairchildiana* seeds [14]. These compounds exhibited larvicidal activity against third-instar *Ae. aegypti* larvae, causing morphological changes and metabolic alterations as a result of increased production of ROS in the insect midgut [14]. It is already well-documented in the literature that larvicidal bioassays are effective tests for identifying new insecticides against this vector mosquito, as the larval stage is the longest and most vulnerable immature phase of the insect. In addition, this species is synanthropic, which means that it is adapted to live close to humans who, in their life routine, create spaces of easy access and conducive conditions for the establishment of the insect. The most frequent breeding sites are containers with accumulated water, such as plant pots, PET bottles, tires, buckets, clogged or uneven gutters, rarely used drains, poorly sealed water tanks, air conditioner trays, and other locations with stagnant and "clean" water containing organic matter [15].

In this work, with the goal of obtaining a biotechnological product that may represent a new tool for controlling *Ae. aegypti* and consequently preventing relevant arboviral diseases, we produced a chitosan nanocomposite with the isolated rotenoids.

Chitosan is an aminated polysaccharide derived from the deacetylation of chitin and is the main structural component of insect and crustacean exoskeletons. It is widely recognized as the second most abundant natural polymer, surpassed only by cellulose. Its relevance as a biopolymer is due to its properties such as biodegradability, biocompatibility, and nontoxicity to humans, characteristics that make it widely used in various scientific and technological fields [16,17]. Therefore, we used chitosan as the coating material for the nanocomposite to reduce potential environmental damage, such as those reported in the literature for some metal-decorated nanomaterials and their derivatives (silver, gold, copper, zinc, titanium, and silicon) that can be highly toxic to non-target organisms in the environment [18].

The encapsulation efficiency is estimated to be ≥99% within the detection limits of high-performance liquid chromatography (HPLC) and thin-layer chromatography (TLC) methods applied, indicating a highly effective incorporation of the rotenoids into the nanochitosan matrix. In addition to the high encapsulation efficiency, the size analysis of the produced nanochitosan particles confirmed that both ion gelation methods produced nanostructures smaller than 100 nm (Figure 1). However, in Figure 1B, the peak area is narrower, indicating a higher uniformity in particle size. Figure 2C and 2D also show that the controlled ionic gelation method using the TPP-β-CD inclusion complex resulted in smaller and more uniform nanoparticles compared to the conventional ionic gelation method (CS/TPP), illustrated in Figure 2A. This improvement can be attributed to the ability of the TPP-β-CD inclusion complex to mitigate excessive cross-linking by TPP, thereby reducing both nanoparticle size and polydispersity [19]. Furthermore, the inclusion of rotenoids in the nanocomposite seemingly improved its

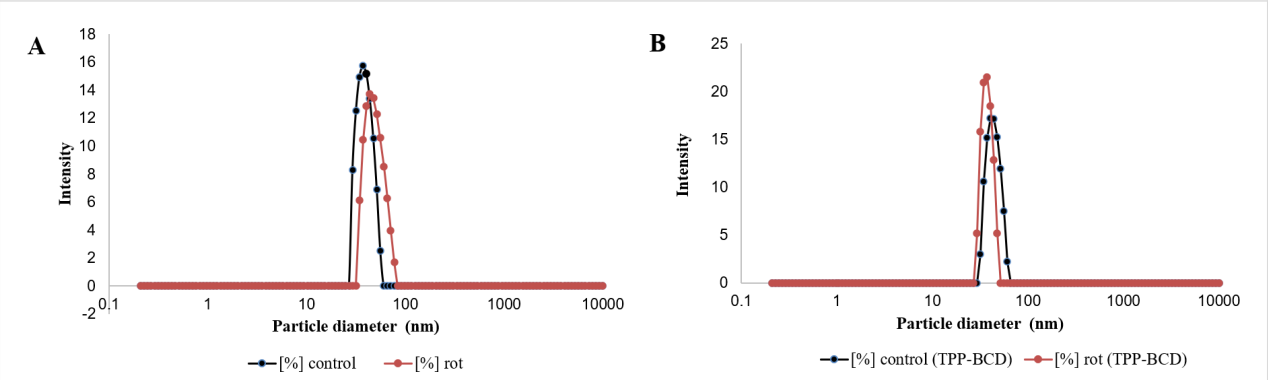

Figure 1: Size distribution and zeta potential of nanoparticles. A) Conventional ionic gelation of CS/TPP (control = empty particles; rot = rotenoid-loaded particles). B) Controlled ionic gelation of CS with TPP-β-CD inclusion complex (control and rot).

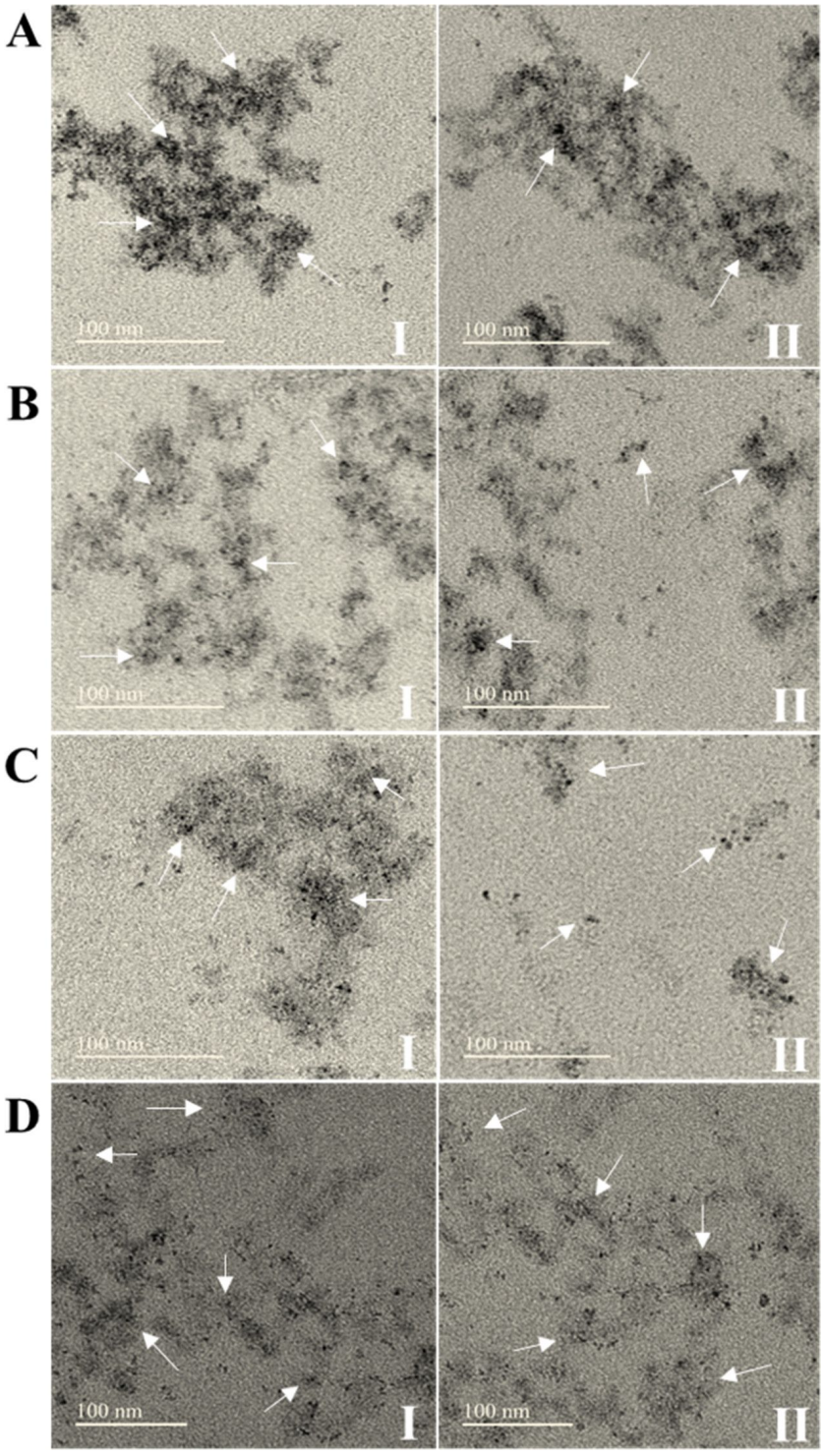

Figure 2: Transmission electron microscopy (TEM) of chitosan nanocomposites. A) Conventional ionic gelation of CS/TPP. B) Conventional ionic gelation of CS/TPP containing rotenoids (CFD – RI and RII). C) Controlled ionic gelation of CS with TPP-β-CD inclusion complex. D) Controlled ionic gelation of CS with TPP-β-CD inclusion complex containing rotenoids (CFD – RI and RII).

dispersibility (Figure 2B and 2D) compared to respective controls of empty nanoparticles (Figure 2A and 2C). The presence of rotenoids in the nanostructures also increased the zeta potential (ζ) in both ion gelation methods, which appears to influence the polydispersity index (PDI) of these nanocomposites, as the PDI values are significantly higher than those of their

respective controls (Table 1). The zeta potential is an important parameter for assessing nanoparticle stability and biodistribution. Typically, particles acquire an electric charge at the shear plane when dispersed in a liquid, which is reflected by their zeta potential, that is key to understanding dispersion and aggregation processes in nanoformulations.

Table 1: DLS analysis of chitosan nanocomposites. Average particle diameter (*d*), polydispersity index, and average zeta potential (mV) obtained by DLS.

	Samples	*d* (nm)	PDI (%)	ζ (mV)
A -	CS/TPP control	32.9	10.4	36.3
B -	CS/TPP rot	41.5	21.2	57.1
C -	CS/TPP - βCD control	35.1	21.1	44.8
D -	CS/TPP - βCD rot	29.5	27.0	51.7

Zeta potential values > ±30 mV are indicative of nanoparticle stability, as strong electrostatic repulsion prevents aggregation and ensures colloidal stability [20,21]. While these measurements provide important physicochemical insights, further evidence of the chemical incorporation and potential interactions between the rotenoids and the nanocomposite matrix was obtained through Fourier-transform infrared (FTIR) spectroscopy.

Figure 3A shows the FTIR spectra of CS/TPP-β-CD, CS/TPP-β-CD loaded with rotenoids (CS/TPP-β-CD-rot), and pure rotenoids. All three spectra display a broad absorption band in the 3600–3000 cm^{-1} region, corresponding to the stretching vibrations of hydroxyl and amide groups. In the nanoparticle spectra, characteristic bands are observed at 1640–1650 cm^{-1} and around 1550 cm^{-1}, associated with amide I (C=O stretching) and amide II (N–H bending), respectively. Peaks in the 1417–1403 cm^{-1} range are attributed to the bending vibrations of C–H in methyl and methylene groups [22-24]. The spectrum of pure rotenoids displays a complex profile with multiple peaks due to the presence of diverse functional groups [14]. Notably, 6-aromatic C=C stretching appears in the 1600–1300 cm^{-1} region, while glycosidic linkages and methoxyl groups contribute bands in the 1300–1000 cm^{-1} range [25,26]. Figure 3B presents a spectral subtraction analysis between CS/TPP-β-CD and CS/TPP-β-CD-rot, clearly revealing absorption features from the encapsulated rotenoids in the functionalized nanocomposite. Additionally, a noticeable reduction in the intensity of the amide-related bands in CS/TPP-β-CD-rot suggests possible interactions – such as hydrogen bonding or covalent bonding – between rotenoids and the chitosan matrix. These spectral features confirm the successful incorporation of rotenoids into the chitosan-based nanocomposite and suggest molecular interactions that may contribute to the enhanced stability and bioactivity of the formulation.

To complement the physicochemical characterization and confirm the efficiency of rotenoid encapsulation within the nanoparticles, a calibration curve was constructed for the raw rotenoids by HPLC using linear regression (Figure 4), enabling the quantification of rotenoids incorporated into the nanostruc-

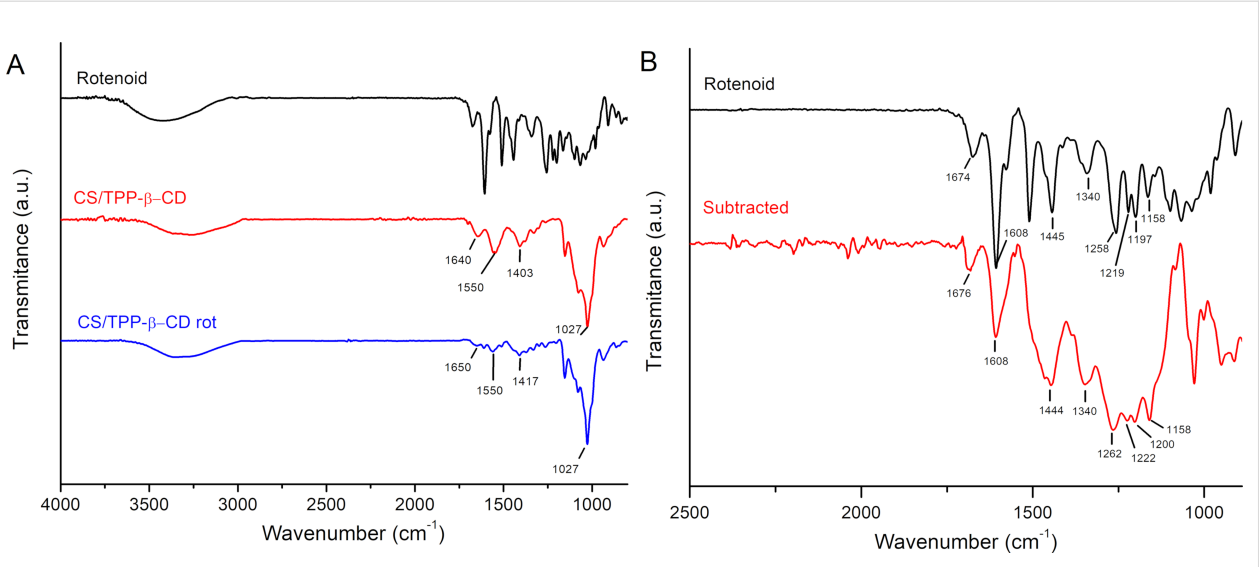

Figure 3: FTIR analysis of pure rotenoids and chitosan-based nanoparticles. A) FTIR spectra of pure rotenoids, empty nanoparticles (CS/TPP-β-CD), and rotenoid-loaded nanoparticles (CS/TPP-β-CD-rot). B) Comparison between the spectrum of in natura rotenoids and the differential spectrum obtained by subtracting the CS/TPP-β-CD spectrum from that of CS/TPP-β-CD-rot, highlighting the characteristic absorption bands of the incorporated rotenoids.

tures. Using this approach, the rotenoid concentration was determined to be 0.469 mg/mL for the conventional ionic gelation method and 0.531 mg/mL for the controlled ionic gelation method.

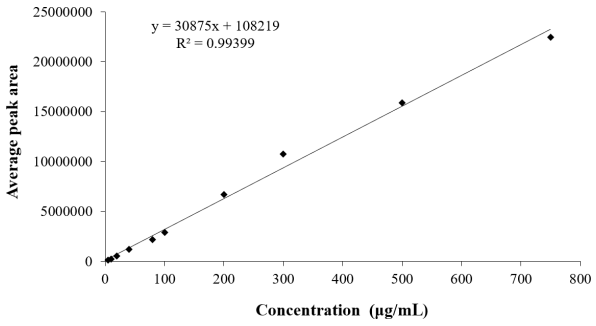

Figure 4: Calibration curve of rotenoids (CFD-RI and RII) by HPLC.

The larvicidal bioassay of the nanocomposite produced by the controlled ionic gelation method (CS/TPP–β-CD–rot, Figure 5B) revealed a significant increase in larvicidal activity, with an LC_{50} of 91.69 ppm and an LC_{90} of 149.06 ppm, indicating higher larvicidal efficacy. In comparison, the in natura rotenoids described earlier exhibited an LC_{50} of 120 ppm [14], demonstrating that the nanocomposite improved the efficacy of the rotenoids by 23.6%. These results were obtained using the classical Probit method recommended by the World Health Organization (WHO) for larvicidal bioassays, which applies the cumulative normal distribution model.

In contrast, the bioassay conducted with the nanocomposite produced by the conventional ionic gelation method (CS/TPP–rot, Figure 5A) showed an LC_{50} of 157.02 ppm and an LC_{90} of 246.52 ppm, a value notably higher than that observed for the in natura rotenoids, indicating a lower potency compared to the CS/TPP–β-CD–rot formulation. Control nanoparticles (CS/TPP and CS/TPP–β-CD) exhibited no larval mortality, confirming that the observed larvicidal activity is directly associated with the rotenoids.

Previous studies have reported similar improvements in larvicidal activity through nanocarrier systems based on botanical insecticides. For instance, silver nanoparticles (AgNPs) synthesized using aqueous leaf extract of *Ambrasia arborescens* demonstrated markedly higher toxicity against *Aedes aegypti* larvae (LC_{50} = 0.28 ppm) compared to the crude aqueous extract (LC_{50} = 1844.61 ppm) [27]. Similarly, silver nanoparticles synthesized with aqueous extracts of *Solanum mammosum* (SmAgNPs) exhibited significantly greater toxicity (LC_{50} = 0.06 ppm) than the crude aqueous extract (LC_{50} = 1631.27 ppm) [28].

According to an established classification criterion, botanical insecticides with an LC_{50} below 50 µg/mL (50 ppm) are considered highly active; those with an LC_{50} between 50 and 100 µg/mL (50–100 ppm) are classified as active; and those with an LC_{50} above 100 µg/mL (100 ppm) are regarded as weak or inactive [9]. Therefore, technically speaking, both *Ambrasia arborescens* and *Solanum mammosum* crude extracts

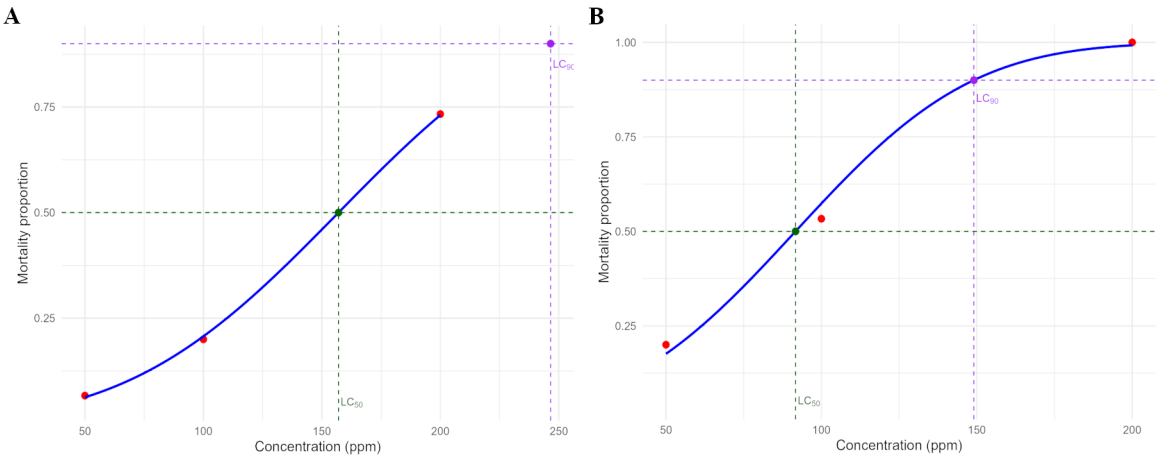

Figure 5: Mortality proportion of third-instar *Aedes aegypti* larvae as a function of concentration (ppm) of nanocomposites containing rotenoids. Negative control – vinegar (0.04% acetic acid) resulted in 0% mortality. A) Conventional ionic gelation (CS/TPP–rot) with LC_{50} = 157 ppm and LC_{90} = 247 ppm, calculated using Probit analysis performed in RStudio. B) Controlled ionic gelation (CS/TPP–β-CD–rot) with LC_{50} = 91.7 ppm and LC_{90} = 149 ppm, calculated using Probit analysis performed in RStudio. The blue line represents the fitted Probit model. Red circles represent the observed mortality proportion. The green dashed lines and green marker indicate LC_{50}, while the purple dashed lines and purple marker indicate LC_{90}. Each treatment was performed with five larvae per concentration in triplicate (n = 15 per treatment).

are classified as weak bioactive agents. However, when incorporated into nanostructures, they acquire substantially enhanced insecticidal potential. A similar pattern is observed in this study, where the incorporation of rotenoids into the CS/TPP–β-CD nanocomposite effectively improves their larvicidal activity. Furthermore, nanostructured delivery systems not only enhance the biological efficacy of botanical compounds but also improve their stability under adverse environmental conditions, such as temperature fluctuations and UV light exposure, as widely documented in the literature [29].

The analysis of third-instar *Ae. aegypti* larvae exposed to the nanocomposite CS/TPP–β-CD–rot (Figure 6) revealed notable dose-dependent morphological alterations. From 50 ppm onwards, the appearance of abnormal excretion in the anal region was observed (Figure 6, white arrows), which progressively intensified at higher concentrations (100 and 200 ppm). This phenomenon may be indicative of physiological stress related to the integrity of the peritrophic matrix (PM), a semipermeable structure that lines the midgut, playing essential roles in protecting the epithelium, facilitating digestion, and acting as a barrier against pathogens and toxic compounds [30,31].

Similar responses have been documented in previous studies, where resistant *Ae. aegypti* strains exposed to dichlorodiphenyltrichloroethane (DDT) produced abundant PM filaments to aid in the excretion of unabsorbed insecticides, unlike susceptible strains that released little or no PM [32]. Additionally, amorphous feces were reported in larvae fed with *Derris urucu* extracts (rich in rotenoids), suggesting a potential link between exposure to rotenoid-type phytochemicals and PM disruption [33].

Notably, from 100 ppm onwards, larvae exhibited melanized nodular structures interpreted as pseudotumors (Figure 6, white arrow head), a typical outcome of the activation of the phenoloxidase cascade. This immune response is frequently triggered by gut damage, epithelial barrier disruption, or the presence of damage-associated molecular patterns (DAMPs) [34,35]. Melanization serves as a fundamental defense mechanism in arthropods, contributing to the encapsulation of damaged tissues and neutralization of harmful agents, including ROS and foreign particles [36].

It is important to highlight that this tissue melanization observed in the larval midgut aligns with our previous findings, which reported the appearance of dark spots along the larval body associated with oxidative stress induced by in natura rotenoids [14]. In that study, the purified rotenoids triggered significant ROS production, causing metabolic and morphological damage particularly in the midgut, activating immune responses such as melanization [37].

The morphological alterations observed here, including abnormal excretion and tissue melanization, suggest that the nanoencapsulated rotenoids maintain, and even amplify, their ability to damage gut structures such as the PM. This damage likely contributes to the triggering of immune responses, includ-

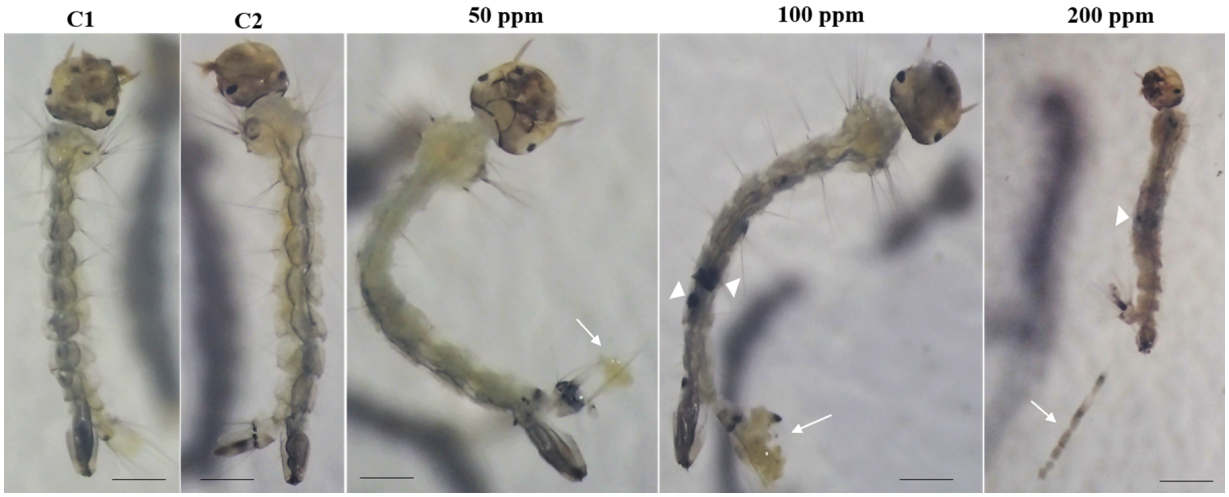

Figure 6: General morphological characteristics of 3rd instar *Aedes aegypti* larvae exposed to different concentrations (ppm) of nanocomposites (CS/TPP-β-CD–rot) observed under a stereomicroscope. C1 – negative control with ultrapure water. C2 – negative control with vinegar (acetic acid 0.04%). White arrows indicate the presence of abnormal excretion in the anal region, suggesting possible damage to the peritrophic matrix. White arrowheads point to melanized nodular structures (pseudotumors), indicative of immune activation through the phenoloxidase cascade. Scale bar = 1 mm.

ing melanization and pseudotumor formation. These findings are consistent with the hypothesis that the gut remains the primary target of rotenoid toxicity, even when delivered via nanocomposites.

The cytotoxicity analysis of natural rotenoids to HSF cells revealed no statistically significant differences in cell viability between the control group and the treatments with either in natura rotenoids or the CS/TPP-β-CD–rot nanocomposite (Figure 7; $p > 0.05$). Both treatments maintained cell viability at levels comparable to the control, indicating the absence of cytotoxic effects. These findings demonstrate that the encapsulation of rotenoids into the CS/TPP-β-CD system does not induce cytotoxicity, similarly to the free compound, suggesting that the delivery system is biocompatible with HSF cells. Therefore, both free rotenoids and the CS/TPP-BCD rot formulation are safe for use at the tested concentration. Previous studies reported that synthetic insecticides, such as type II pyrethroids (deltamethrin, cyphenothrin, λ-cyhalothrin, cyfluthrin, esfenvalerate, and α-cypermethrin) can affect cell viability by inducing the production of nitric oxide and lipid peroxides in three human cell models (SH-SY5Y, HepG2, and Caco-2), even at concentrations considered safe [38]. Nevertheless, human exposure to multiple pyrethroids routinely occurs due to the limited regulatory restrictions imposed on the use of these insecticides. The development of pesticides that provide safer alternatives for both the environment and human health is an urgent need [8]. Thus, the nanocomposite developed in this study holds promising potential for the formulation of new pesticides that could serve as an alternative tool for controlling this vector insect.

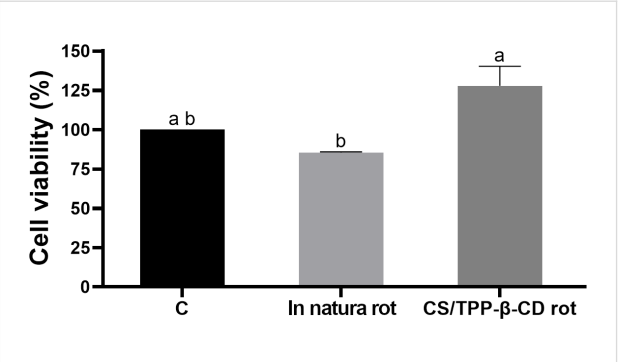

Figure 7: Cytotoxicity of in natura and nanoencapsulated rotenoids (250 ppm) to HSF cells through the MTT assay (3-(4,5-dimethylthiazol-2-yl)-2,5-diphenyltetrazolium bromide) for 24 hours at 37 °C with 5% CO_2. Statistical analysis was calculated according to ANOVA (Tukey's multiple comparison) ($P < 0.05$).

Conclusion

In this study, a chitosan-based nanocomposite was developed as a release system for isolated rotenoids, using the controlled ionic gelation method with the TPP-β-CD inclusion complex. This strategy resulted in the production of smaller, more uniform nanoparticles, with better polydispersity indices and increased stability, in comparison to conventional ionic gelation method. FTIR analysis confirmed the incorporation of rotenoids into the nanocomposite and revealed characteristic spectral features that suggest the occurrence of hydrogen bonding or potential covalent interaction with functional groups of chitosan, which may help explain the improved stability of the formulation. The high efficacy of the nanocomposite was demonstrated by bioassays which revealed an LC_{50} of 91.7 ppm, equivalent to a 23.6% improvement in the larvicidal activity rate of the rotenoids in their original forms. The nanocomposites caused morphological and biochemical alterations to the larvae similarly to those caused by in natura rotenoids, but with greater intensity. Cytotoxicity MTT assays using human skin fibroblasts demonstrated that neither rotenoids nor the CS/TPP–β-CD–rot nanocomposite exerted cytotoxic effects, confirming their favorable safety profile. The results obtained confirm that the application of nanotechnology for encapsulating bioactive compounds not only enhances larvicidal efficacy but also contributes to environmentally sustainable solutions by reducing the reliance on synthetic chemical pesticides. By integrating renewable resources such as phytochemicals and chitosan, this work reinforces the potential for the development of green technologies, offering an innovative and promising approach to the management of disease vectors and the prevention of urban arboviral diseases.

Materials and Methods

Biological material

Aedes aegypti

The larvae of *Ae. aegypti* from the Rockefeller strain were obtained from the insectary maintained at the Biotechnology Laboratory (LBT), at the Center for Biosciences and Biotechnology (CBB) of the State University of North Fluminense Darcy Ribeiro (UENF), where they were raised at room temperature between 20 and 30 °C and fed with fish food.

Production and characterization of nanocomposites

Method of production of chitosan nanocomposites

The nanocomposites for use as a vehicle of the previously isolated and characterized rotenoids [14] were prepared using chitosan (CS Sigma-Aldrich 419419) as the coating material. For comparison purposes and identification of the best method, both common ionic gelation (CS/TPP) and controlled ionic gelation (CS/TPP–β-CD) methods were employed [19], with adaptations in order to include the rotenoid.

In the common ionic gelation method, a 0.175% (w/v) chitosan solution was prepared in 20 mL of 1% (v/v) acetic acid, con-

taining 1 mg/mL of rotenoids. The mixture was maintained under constant agitation at 300 rpm, at room temperature, overnight. Subsequently, 15 mL of a 5 mM sodium tripolyphosphate (TPP) solution was prepared. The chitosan solution was then added dropwise to the TPP solution, while the mixture was continuously agitated on a magnetic stirrer at 1000 rpm, overnight, at room temperature. The resulting solution was centrifuged at 10,000*g*; the pellet was separated, lyophilized, and the obtained powder was stored at −20 °C. To evaluate whether any rotenoids remained unincorporated, the supernatant was also lyophilized and subsequently analyzed by both TLC and HPLC. No rotenoid signals were detected in the supernatant by either method, suggesting that the rotenoids were fully incorporated into the nanocomposites under the conditions employed. The same procedure was applied for the preparation of empty nanoparticles, without the addition of rotenoids. Nanoparticles containing rotenoids were then called rot.

The chitosan nanocomposites were also prepared using the TPP–β-cyclodextrin (TPP–β-CD) inclusion complex. For this, equimolar amounts of TPP and β-CD (β-cyclodextrin) were completely dissolved in ultrapure water at a molar ratio of 1:1. The obtained solution was subjected to ultrasonic bath for 1 h at room temperature. This TPP–β-CD inclusion complex replaced the pure TPP in the controlled ionic gelation process of the chitosan solution, following the same protocol previously described.

In total, four samples were obtained, two for each method. One consisted of empty nanoparticles containing only chitosan (CS/TPP and CS/TPP–β-CD, controls), while the other corresponded to nanocomposites containing rotenoids (CS/TPP rot and CS/TPP–β-CD rot).

Size, polydispersity, and zeta potential

The average size (in nm) and PDI of the nanoparticles were measured using dynamic light scattering (DLS) on the Litesizer DLS 500 instrument (Anton Paar). The same equipment was used to determine the zeta potential (ζ, in mV) of the nanoparticles under the following conditions: 25 °C operating temperature, an applied voltage of 200 V, and a total of 1,000 processed runs.

Fourier-transform infrared spectroscopy

The chemical structure of empty nanoparticles (CS/TPP-β-CD), pure rotenoids, and rotenoid-loaded nanoparticles (CS/TPP-β-CD-rot) was analyzed using a PerkinElmer Spectrum Two FTIR spectrometer equipped with an Attenuated Total Reflectance (ATR) accessory. Dried samples were scanned over a wavenumber range of 800–4000 cm^{-1}, with a resolution of 1 cm^{-1} and an accumulation of 35 scans per spectrum. A compressive force of 15 N was applied to the samples during measurement to ensure proper contact with the ATR crystal surface.

Quantification of rotenoids by high-performance liquid chromatography

The quantification of rotenoids was performed by HPLC using a SHIMADZU CBM-20A system equipped with a LC-20AD pump and SPD-M20A detector with a D2&W lamp. To construct the analytical curve, stock solutions of rotenoids were prepared in the concentration range of 5 to 750 µg/mL. Each concentration was analyzed by HPLC under previously established chromatographic conditions. An NST C18 column (250 mm × 4.6 mm; 5 µm) was used as the stationary phase, while the mobile phase consisted of solution A (50% MeOH) and solution B (100% MeOH) as eluents.

For each concentration, two HPLC runs were performed, and the average peak areas obtained were used to construct the analytical curve by linear regression of the data. The wavelength used for absorbance readings was 290 nm. As a result, a calibration curve was obtained with the equation $30875x + 108219$ ($r = 0.99399$). To determine the concentration of rotenoids in the nanoparticles, a solution containing 1 mg/mL of nanocomposites in 50% MeOH was prepared. The solution was subjected to ultrasonic bath for 10 min at room temperature. Then, the samples were filtered with a 0.22 µm filter and injected into the HPLC system. For each sample, two runs were performed, and the average peak areas obtained were used for concentration calculations.

Larvicidal activity assay

The larvicidal assay was conducted according to the standards established by the World Health Organization [39] with adaptations [14]. Starting from an initial stock solution (10 mg nanoparticles/mL in water-diluted vinegar [to reach a 0.08% acetic acid concentration]), the nanoparticles were further diluted in ultrapure water to prepare concentrations of 50, 100, and 200 ppm of rotenoids, based on calculations obtained by HPLC. Vinegar, an easily accessible source of acetic acid, was employed because chitosan is a water-insoluble polysaccharide that dissolves only in acidified solutions. Five third-instar larvae were used for 5 mL of each solution, and the tests were performed in triplicate. The negative control was prepared using 0.04% acetic acid vinegar. The larvae were incubated for 24 h at 28 °C. After the incubation period, mortality was assessed by the movement of the larvae, which were also observed under a stereomicroscope. This assay was conducted following the same standards for all four nanoparticle samples: CS/TPP control, CS/TPP–β-CD control, CS/TPP rot, and CS/TPP–β-CD rot.

The mortality data were analyzed using Probit regression performed in RStudio with the glm() function (binomial family, probit link). The lethal concentrations (LC_{50} and LC_{90}) were calculated based on the estimated model parameters [40].

Cellular viability assessment by MTT assay

The cellular viability of human skin fibroblasts (HSF) exposed to rotenoids and to the CS/TPP–β-CD–rot nanocomposite was evaluated using the 3-(4,5-dimethylthiazol-2-yl)-2,5-diphenyltetrazolium bromide (MTT) assay. The cells were cultured in 96-well plates at a density of 3×10^5 cells/mL. After adherence, the cells were treated with either in natura rotenoids, at 250 ppm, or the CS/TPP–β-CD–rot nanocomposite (equivalent to 250 ppm of rotenoids), and incubated for 24 h at 37 °C in a humidified atmosphere with 5% CO_2. Subsequently, 10 µL of MTT solution (5 mg/mL) were added to each well, and after 2 h of incubation, the supernatant was removed. The resulting formazan crystals were solubilized with acidified isopropanol, and the absorbance was measured at 570 nm using a microplate reader (Thermo Labsystems Multiskan, model 352). A positive control (2% Triton X-100) and a negative control (culture medium without treatment) were used. Cellular viability was expressed as a percentage relative to the negative control. Statistical analysis was performed using one-way ANOVA followed by Tukey's multiple comparison test ($p < 0.05$) with the GraphPad Prism 10 software.

Funding

This work was supported by the Coordenação de Aperfeiçoamento de Pessoal de Nível Superior (CAPES), the Conselho Nacional de Desenvolvimento Científico (CNPq) and the Fundação de Amparo à Pesquisa do Estado do Rio de Janeiro – FAPERJ.

Author Contributions

Maria A. A. Bertonceli: conceptualization; data curation; formal analysis; investigation; methodology; validation; writing – original draft. Vitor D. C. Cristo: data curation; validation. Ivo J. Vieira: formal analysis; supervision; validation. Francisco J. A. Lemos: data curation; validation. Arnoldo R. Façanha: data curation; validation. Raimundo Braz-Filho: data curation; formal analysis; validation. Gustavo V. T. Batista: investigation; methodology. Luis G. M. Basso: data curation; validation. Sérgio H. Seabra: data curation; validation. Thalya S. R. Nogueira: investigation. Felipe F. Moreira: investigation; validation. Arícia L. E. M. Assis: investigation. Antônia E. A. Oliveira: data curation; validation. Kátia V. S. Fernandes: conceptualization; formal analysis; funding acquisition; project administration; supervision; writing – review & editing.

ORCID® iDs

Maria A. A. Bertonceli - https://orcid.org/0000-0002-6501-4062
Ivo J. Vieira - https://orcid.org/0000-0002-2724-0106
Francisco J. A. Lemos - https://orcid.org/0000-0002-1435-4104
Arnoldo R. Façanha - https://orcid.org/0000-0002-5641-6852
Luis G. M. Basso - https://orcid.org/0000-0003-1277-1008
Thalya S. R. Nogueira - https://orcid.org/0000-0001-9287-9750
Kátia V. S. Fernandes - https://orcid.org/0000-0003-4497-4985

Data Availability Statement

All data that supports the findings of this study is available in the published article and/or the supporting information of this article.

References

1. Romanello, M.; Walawender, M.; Hsu, S.-C.; Moskeland, A.; Palmeiro-Silva, Y.; Scamman, D.; Ali, Z.; Ameli, N.; Angelova, D.; Ayeb-Karlsson, S.; Basart, S.; Beagley, J.; Beggs, P. J.; Blanco-Villafuerte, L.; Cai, W.; Callaghan, M.; Campbell-Lendrum, D.; Chambers, J. D.; Chicmana-Zapata, V.; Chu, L.; Cross, T. J.; van Daalen, K. R.; Dalin, C.; Dasandi, N.; Dasgupta, S.; Davies, M.; Dubrow, R.; Eckelman, M. J.; Ford, J. D.; Freyberg, C.; Gasparyan, O.; Gordon-Strachan, G.; Grubb, M.; Gunther, S. H.; Hamilton, I.; Hang, Y.; Hänninen, R.; Hartinger, S.; He, K.; Heidecke, J.; Hess, J. J.; Jamart, L.; Jankin, S.; Jatkar, H.; Jay, O.; Kelman, I.; Kennard, H.; Kiesewetter, G.; Kinney, P.; Kniveton, D.; Kouznetsov, R.; Lampard, P.; Lee, J. K. W.; Lemke, B.; Li, B.; Liu, Y.; Liu, Z.; Llabrés-Brustenga, A.; Lott, M.; Lowe, R.; Martinez-Urtaza, J.; Maslin, M.; McAllister, L.; McMichael, C.; Mi, Z.; Milner, J.; Minor, K.; Minx, J.; Mohajeri, N.; Momen, N. C.; Moradi-Lakeh, M.; Morrisey, K.; Munzert, S.; Murray, K. A.; Obradovich, N.; O'Hare, M. B.; Oliveira, C.; Oreszczyn, T.; Otto, M.; Owfi, F.; Pearman, O. L.; Pega, F.; Perishing, A. J.; Pinho-Gomes, A.-C.; Ponmattam, J.; Rabbaniha, M.; Rickman, J.; Robinson, E.; Rocklöv, J.; Rojas-Rueda, D.; Salas, R. N.; Semenza, J. C.; Sherman, J. D.; Shumake-Guillemot, J.; Singh, P.; Sjödin, H.; Slater, J.; Sofiev, M.; Sorensen, C.; Springmann, M.; Stalhandske, Z.; Stowell, J. D.; Tabatabaei, M.; Taylor, J.; Tong, D.; Tonne, C.; Treskova, M.; Trinanes, J. A.; Uppstu, A.; Wagner, F.; Warnecke, L.; Whitcombe, H.; Xian, P.; Zavaleta-Cortijo, C.; Zhang, C.; Zhang, R.; Zhang, S.; Zhang, Y.; Zhu, Q.; Gong, P.; Montgomery, H.; Costello, A. *Lancet* **2024,** *404,* 1847–1896. doi:10.1016/s0140-6736(24)01822-1
2. Ministério da Saúde. Painel de Monitoramento das Arboviroses. https://www.gov.br/saude/pt-br/centrais-de-conteudo/publicacoes/boletins/epidemiologicos/edicoes/2024/boletim-epidemiologico-volume-55-no-11.pdf/view (accessed July 25, 2025).
3. World Health Organization. Vaccines and immunization: Dengue. https://www.who.int/news-room/questions-and-answers/item/dengue-vaccines (accessed Jan 9, 2025).
4. Ministério da Saúde. Brasil unido contra a dengue, Zika e Chikungunya. https://www.gov.br/saude/pt-br/assuntos/noticias/2023/maio/ministerio-da-saude-lanca-campanha-de-combate-a-dengue-zika-e-chikungunya (accessed May 4, 2023).
5. Fan, Y.; Scott, J. G. *Pest Manage. Sci.* **2020,** *76,* 2251–2259. doi:10.1002/ps.5763

6. Kasai, S.; Itokawa, K.; Uemura, N.; Takaoka, A.; Furutani, S.; Maekawa, Y.; Kobayashi, D.; Imanishi-Kobayashi, N.; Amoa-Bosompem, M.; Murota, K.; Higa, Y.; Kawada, H.; Minakawa, N.; Cuong, T. C.; Yen, N. T.; Phong, T. V.; Keo, S.; Kang, K.; Miura, K.; Ng, L. C.; Teng, H.-J.; Dadzie, S.; Subekti, S.; Mulyatno, K. C.; Sawabe, K.; Tomita, T.; Komagata, O. *Sci. Adv.* **2022,** *8,* eabq7345. doi:10.1126/sciadv.abq7345
7. Nauen, R.; Bielza, P.; Denholm, I.; Gorman, K. *Pest Manage. Sci.* **2008,** *64,* 1106–1110. doi:10.1002/ps.1654
8. Rezende-Teixeira, P.; Dusi, R. G.; Jimenez, P. C.; Espindola, L. S.; Costa-Lotufo, L. V. *Environ. Pollut.* **2022,** *300,* 118983. doi:10.1016/j.envpol.2022.118983
9. da Silva Sá, G. C.; Bezerra, P. V. V.; da Silva, M. F. A.; da Silva, L. B.; Barra, P. B.; de Fátima Freire de Melo Ximenes, M.; Uchôa, A. F. *J. Pest Sci.* **2023,** *96,* 1–20. doi:10.1007/s10340-022-01507-2
10. de Oliveira, J. L.; Campos, E. V. R.; Bakshi, M.; Abhilash, P. C.; Fraceto, L. F. *Biotechnol. Adv.* **2014,** *32,* 1550–1561. doi:10.1016/j.biotechadv.2014.10.010
11. Ali, L. M.; Ahmed, A. E.-R. A. E.-R.; Hasan, H. E.-S.; Suliman, A. E.-R. E.; Saleh, S. S. *Chem. Biol. Technol. Agric.* **2022,** *9,* 80. doi:10.1186/s40538-022-00343-x
12. Divya, K.; Vijayan, S.; George, T. K.; Jisha, M. S. *Fibers Polym.* **2017,** *18,* 221–230. doi:10.1007/s12221-017-6690-1
13. Karthick Raja Namasivayam, S.; Arvind Bharani, R. S.; Karunamoorthy, K. *Int. J. Biol. Macromol.* **2018,** *120,* 921–944. doi:10.1016/j.ijbiomac.2018.08.130
14. Bertonceli, M. A. A.; Oliveira, A. E. A.; de Souza Passos, M.; Vieira, I. J. C.; Braz-Filho, R.; Lemos, F. J. A.; Martins, B. X.; Façanha, A. R.; Pireda, S.; da Cunha, M.; Fernandes, K. V. S. *Pestic. Biochem. Physiol.* **2022,** *186,* 105167. doi:10.1016/j.pestbp.2022.105167
15. Silvério, M. R. S.; Espindola, L. S.; Lopes, N. P.; Vieira, P. C. *Molecules* **2020,** *25,* 3484. doi:10.3390/molecules25153484
16. Sushma, S.; Kumar, S.; Dutta, P. K. Role of chitosan and chitosan-based nanoparticles in pesticide delivery: avenues and applications. In *Role of Chitosan and Chitosan-Based Nanomaterials in Plant Sciences;* Kumar, S.; Madihally, S. V., Eds.; Academic Press: London, UK, 2022; pp 401–434. doi:10.1016/b978-0-323-85391-0.00021-6
17. Shariatinia, Z. *Adv. Colloid Interface Sci.* **2019,** *263,* 131–194. doi:10.1016/j.cis.2018.11.008
18. Rekulapally, R.; Murthy Chavali, L. N.; Idris, M. M.; Singh, S. *PeerJ* **2019,** *6,* e6138. doi:10.7717/peerj.6138
19. Pant, A.; Negi, J. S. *Eur. J. Pharm. Sci.* **2018,** *112,* 180–185. doi:10.1016/j.ejps.2017.11.020
20. Heurtault, B.; Saulnier, P.; Pech, B.; Proust, J.-E.; Benoit, J.-P. *Biomaterials* **2003,** *24,* 4283–4300. doi:10.1016/s0142-9612(03)00331-4
21. Singhvi, M.; Singhvi, G.; Banerjee, S.; Khosa, A. Lyotropic liquid crystal nanoparticles: a novel improved lipidic drug delivery system. In *Organic Materials as Smart Nanocarriers for Drug Delivery;* Grumezescu, A. M., Ed.; William Andrew Publishing: Oxford, UK, 2018; pp 471–517. doi:10.1016/b978-0-12-813663-8.00011-7
22. Hosseini, S. F.; Zandi, M.; Rezaei, M.; Farahmandghavi, F. *Carbohydr. Polym.* **2013,** *95,* 50–56. doi:10.1016/j.carbpol.2013.02.031
23. Bezerra, J. M. N. A.; Oliveira, A. C. J.; Silva-Filho, E. C.; Severino, P.; Souto, S. B.; Souto, E. B.; Soares, M. F. L. R.; Soares-Sobrinho, J. L. *Diabetology* **2021,** *2,* 107–116. doi:10.3390/diabetology2020009
24. Zeng, R.; Tu, M.; Liu, H.-W.; Zhao, J.-H.; Zha, Z.-G.; Zhou, C.-R. *IET Nanobiotechnol.* **2009,** *3,* 8–13. doi:10.1049/iet-nbt:20080010
25. Krysa, M.; Szymańska-Chargot, M.; Zdunek, A. *Food Chem.* **2022,** *393,* 133430. doi:10.1016/j.foodchem.2022.133430
26. Pozo, C.; Rodríguez-Llamazares, S.; Bouza, R.; Barral, L.; Castaño, J.; Müller, N.; Restrepo, I. *J. Polym. Res.* **2018,** *25,* 266. doi:10.1007/s10965-018-1651-y
27. Morejón, B.; Pilaquinga, F.; Domenech, F.; Ganchala, D.; Debut, A.; Neira, M. *J. Nanotechnol.* **2018,** 6917938. doi:10.1155/2018/6917938
28. Pilaquinga, F.; Morejón, B.; Ganchala, D.; Morey, J.; Piña, N.; Debut, A.; Neira, M. *PLoS One* **2019,** *14,* e0224109. doi:10.1371/journal.pone.0224109
29. Duarte, J. L.; Maciel de Faria Motta Oliveira, A. E.; Pinto, M. C.; Chorilli, M. *Environ. Sci. Pollut. Res.* **2020,** *27,* 28737–28748. doi:10.1007/s11356-020-09278-y
30. Shao, L.; Devenport, M.; Jacobs-Lorena, M. *Arch. Insect Biochem. Physiol.* **2001,** *47,* 119–125. doi:10.1002/arch.1042
31. Berini, F.; Katz, C.; Gruzdev, N.; Casartelli, M.; Tettamanti, G.; Marinelli, F. *Biotechnol. Adv.* **2018,** *36,* 818–838. doi:10.1016/j.biotechadv.2018.01.002
32. Abedi, Z. H.; Brown, A. W. A. *Ann. Entomol. Soc. Am.* **1961,** *54,* 539–542. doi:10.1093/aesa/54.4.539
33. Gusmão, D. S.; Páscoa, V.; Mathias, L.; Vieira, I. J. C.; Braz-Filho, R.; Lemos, F. J. A. *Mem. Inst. Oswaldo Cruz* **2002,** *97,* 371–375. doi:10.1590/s0074-02762002000300017
34. Nappi, A. J.; Christensen, B. M. *Insect Biochem. Mol. Biol.* **2005,** *35,* 443–459. doi:10.1016/j.ibmb.2005.01.014
35. González-Santoyo, I.; Córdoba-Aguilar, A. *Entomol. Exp. Appl.* **2012,** *142,* 1–16. doi:10.1111/j.1570-7458.2011.01187.x
36. Hillyer, J. F. Mosquito immunity. In *Invertebrate Immunity. Advances in Experimental Medicine and Biology;* Söderhäll, K., Ed.; Springer: Boston, MA, USA, 2010; pp 218–238. doi:10.1007/978-1-4419-8059-5_12
37. Nakhleh, J.; El Moussawi, L.; Osta, M. A. The Melanization Response in Insect Immunity. In *Advances in Insect Physiology;* Ligoxygakis, P., Ed.; Academic Press: London, UK, 2017; Vol. 52, pp 83–109. doi:10.1016/bs.aiip.2016.11.002
38. Romero, A.; Ares, I.; Ramos, E.; Castellano, V.; Martínez, M.; Martínez-Larrañaga, M. R.; Anadón, A.; Martínez, M. A. *Environ. Res.* **2015,** *138,* 58–66. doi:10.1016/j.envres.2015.02.008
39. World Health Organization. Guidelines for laboratory and field testing of mosquito larvicides. WHO Document 2005, 1–41. https://iris.who.int/handle/10665/69101.
40. Ritz, C.; Baty, F.; Streibig, J. C.; Gerhard, D. *PLoS One* **2015,** *10,* e0146021. doi:10.1371/journal.pone.0146021

BEILSTEIN JOURNAL OF NANOTECHNOLOGY

Investigation of the solubility of protoporphyrin IX in aqueous and hydroalcoholic solvent systems

Michelly de Sá Matsuoka‡, Giovanna Carla Cadini Ruiz‡, Marcos Luciano Bruschi and Jéssica Bassi da Silva*

Letter

Open Access

Address:
Department of Pharmacy, State University of Maringa, Maringa, PR, Brazil

Email:
Jéssica Bassi da Silva* - jbsilva5@uem.br

* Corresponding author ‡ Equal contributors

Keywords:
5-aminolevulinic acid; photodynamic therapy; protoporphyrin IX; shake-flask; solubility test

Beilstein J. Nanotechnol. **2025,** *16,* 1209–1215.
https://doi.org/10.3762/bjnano.16.89

Received: 07 April 2025
Accepted: 14 July 2025
Published: 29 July 2025

This article is part of the thematic issue "Advances in nanotechnology applied to natural products".

Guest Editor: D. Dourado

Abstract

Photodynamic therapy (PDT) is a non-invasive treatment involving a photosensitizer (PS), light source, and tissue oxygen. Protoporphyrin IX (PpIX) is commonly used as a PS due to its tumor-targeting properties and phototoxicity. However, the physicochemical properties of PpIX foster self-aggregation, which is a challenge for its incorporation into pharmaceutical formulations. This study aimed to evaluate the solubility of PpIX in distinct solvent systems to support the development of novel pharmaceutical formulations. The shake-flask method was employed, using purified water, 50% ethanol (EtOH50), 77% ethanol (EtOH77), absolute ethanol (EtOHabs), and polymeric systems containing 10% (w/w) poloxamer 407 (P407) in water, in EtOH50 or in EtOH77. Approximately 10 to 25 mg of PpIX was added to 25 mL of the solvent, and the solutions were stirred at 100 rpm, at 37 °C, for up to 96 h. The PpIX concentration was measured by using a validated method (R = 0.9973), with equilibrium reached within 30 min. The dissolution profiles of the micellar systems were also evaluated using the Korsmeyer–Peppas model with lag time (t_{lag}), which indicated a Fickian diffusion mechanism, preceded by a thermodynamically driven accommodation stage of PpIX into the micelles. The solubility of PpIX ranged from 0.138 mg/mL in water to 0.593 mg/mL in water containing 10% (w/w) P407. The solubility of PpIX in EtOH50 and EtOH77 with 10% (w/w) P407 was 0.503 and 0.507 mg/mL, respectively, while EtOHabs yielded the lowest solubility among ethanolic solvents (0.179 mg/mL). These results indicate that water and EtOHabs are unsuitable solvents for PpIX, whereas the nanostructured systems containing P407 showed the greatest potential for future pharmaceutical applications, mainly the aqueous one because of its low toxicity considering topical preparations.

Introduction

Photodynamic therapy (PDT) is a promising therapeutic modality that has raised keen interest in the treatment of various conditions including cancer and microbial infections [1,2]. This non-invasive treatment combines a photosensitizer (PS), a suitable light source, and molecular oxygen, generating reactive oxygen species that induce cellular damage [3,4].

Among the PSs used in PDT, protoporphyrin IX (PpIX) stands out as a natural precursor of hemoglobin and porphyrins, exhibiting low toxicity in its monomeric form [5]. When exposed to light, at a specific wavelength, PpIX absorbs energy and transfers it to molecular oxygen, generating reactive oxygen species (ROS). These ROS are highly toxic to cells, inducing oxidative damage in various biomolecules such as lipids, proteins and DNA, leading to cell death [6,7].

However, PpIX and other PSs have their hydrophobicity as drawback, which can lead to the formation of aggregates in aqueous solutions, compromising bioavailability and photodynamic activity [5]. The aggregation of the PS decreases its photoactive properties since, for its action, it must be in the monomeric form, in which its bioavailability and light absorption capacity will be increased [5].

To overcome this problem, the development of drug delivery systems, such as poloxamer-based ones, has played an important role on the delivery of dyes for PDT [8-10]. Poloxamers are triblock copolymers with thermosensitive properties, capable of forming micelles that encapsulate PpIX, increasing its solubility and facilitating its administration [7,11,12].

In this context, poloxamer 407 (P407) is notable for its biocompatibility and ability to form stable nanometric micelles [8,13,14]. Its amphiphilic nature allows for the self-assembly of monomers into micelles with a hydrophobic core of polypropylene oxide (PPO) and a hydrophilic corona of polyethylene oxide (PEO), creating an environment suitable for the encapsulation of hydrophobic drugs such as PpIX [15]. These micelles enhance drug solubility, protect against aggregation, and improve bioavailability in aqueous media [5,16].

Additionally, at high concentrations, P407 can transition into more complex nanostructured systems, such as hydrogels and lyotropic liquid crystals, providing additional control over drug release and stability. The thermosensitive and self-assembling properties of P407 make it suitable for advanced nanostructures drug delivery platforms, including polymeric microneedles and hydrogels, ensuring enhanced drug retention and permeation [15,17,18].

Therefore, the present study aimed to investigate the best solvent system for PpIX, in order to optimize the development of new drug delivery systems for PDT applications. Moreover, the potential of P407 as a feasible system for PpIX delivery was also evaluated in different media.

Experimental

Preparation of the systems

The systems were prepared at least 24 h before the test and used for up to seven days. Hydroalcoholic and polymeric systems were employed. Hydroalcoholic systems were prepared by mixing water and absolute ethanol (EtOHabs). The polymeric systems were developed by adding 10% (w/w) of P407 to each solvent (water, ethanol 50% and 77% v/v), both previously weighed. The polymeric systems were refrigerated for 24 h and homogenized for 30 min prior to the addition of PpIX [19,20].

Equilibrium solubility

The solubility of PpIX disodium salt was determined using the shake-flask method. Aliquots of 10 to 25 mg of PpIX were added to 25 mL of aqueous, hydroalcoholic (EtOH50, EtOH77, EtOHAbs), or polymeric systems. Experiments were conducted in triplicate. The resulting systems exhibited concentrations of 0.4 mg/mL (EtOH50, EtOH77, and water) and 1 mg/mL (EtOHAbs). For the systems containing P407 in EtOH50, EtOH77, and water, a PpIX concentration of 0.4 mg/mL was used. The flasks were sealed, protected from light, and maintained under agitation at 37 ± 1 °C and 100 rpm. Aliquots of 50 to 500 µL were collected at time intervals up to 96 h, diluted in 77% ethanol (v/v), filtered through a 0.45 µm membrane, and quantified by spectrophotometry at λ = 400 nm. Quantification was performed using a previously validated method, yielding a correlation coefficient $R = 0.9973$ [20,21].

Transmission electron microscopy

Transmission electron microscopy (TEM) analysis was carried out using a JEM-1400 microscope (JEOL, Tokyo, Japan) with an accelerating voltage of 100 kV. The samples were diluted 50 times and negatively stained with a 2% (w/v) uranyl acetate solution before imaging. To investigate micelle formation, the samples were prepared at 37 °C. Micelle size measurements obtained by TEM were reported as the mean (± standard deviation; SD), based on the analysis of 250 micelles per system using ImageJ software [17].

Statistical analysis

Data are presented as mean ± SD. Statistical analysis was performed using Microsoft Office Excel®, version 2312, conducting Student's t-test one-way analysis of variance (ANOVA), followed by Tukey's post-hoc test. Results were considered statistically significant when $p < 0.05$, with a 95% confidence interval.

Results and Discussion

Systems containing water (0.4 mg/mL PpIX) and EtOHabs (1 mg/mL) displayed persistent visible precipitates from 30 min to 48 h, indicative of PpIX saturation in these solvents. As illus-

trated in Figure 1, while EtOH50 and EtOH77 effectively solubilized PpIX up to 0.4 mg/mL, water and EtOHabs rapidly reached saturation, demonstrating instability. Solubility equilibrium was attained within approximately 4 h for EtOH50 and EtOH77, whereas for water and EtOHabs, equilibrium was established within 30 min, followed by subsequent degradation or aggregation.

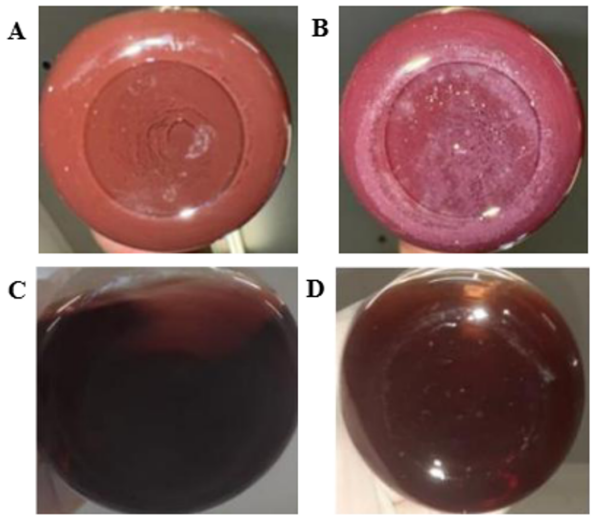

Figure 1: Macroscopic characteristics of solubilized systems: (A) water (0.4 mg/mL), (B) absolute ethanol (1 mg/mL), (C) 50% (v/v) ethanol (0.4 mg/mL), and (D) 50% (v/v) ethanol with 10% (w/w) P407 (0.4 mg/mL).

The addition of P407 significantly enhanced PpIX solubilization, particularly in aqueous systems, with no significant differences observed between water and ethanol at varying concentrations in the presence of P407. Figure 1A and Figure 1B highlight the turbidity observed in these samples, whereas samples shown in Figure 1C and Figure 1D appear clear. The sample displayed in Figure 1D was the most soluble and transparent, demonstrating the improved system performance in the presence of P407.

Although Franco [5] reported high solubility of PpIX in aqueous systems, the findings observed at 0.4 mg/mL PpIX are not in line. While spectrophotometric readings indicated high solubility, the visual inspection revealed turbidity, suggesting incomplete dissolution of the photosensitizer. This discrepancy may be attributed to the filtration step performed prior to UV–vis analysis, which intended to mitigate the limitation of the spectrophotometric techniques in the presence of aggregated species. In good agreement, similar discrepancies have been reported in the literature, such as in the study by da Silva Gonçalves and collaborators [22], where spectroscopic estimations of solubility were later contradicted by particle size distribution analysis.

Figure 2 shows the solubility behavior of PpIX in water and EtOHabs, with mean concentrations of 0.497 ± 0.054 mg/mL in water, and 0.179 ± 0.004 mg/mL in EtOHabs.

In contrast, the systems containing 0.4 mg/mL of PpIX in EtOH50 and EtOH77 remained clear and free of undissolved solids for up to 96 h, confirming the complete solubilization without saturation. Figure 3 illustrates PpIX concentration during the solubilization period in EtOH50 and EtOH77. The

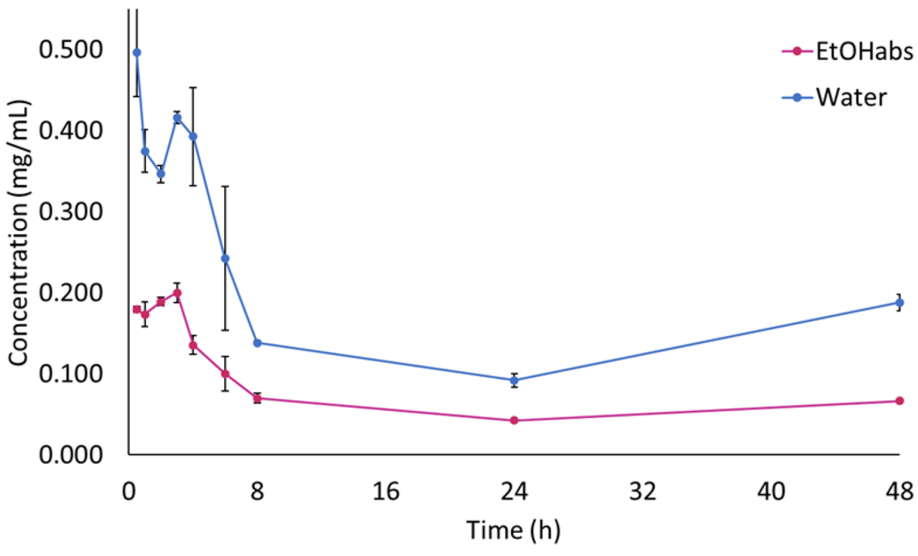

Figure 2: Solubilization kinetic curve of PpIX in water and EtOHabs. Error bars represent one standard deviation (n = 3).

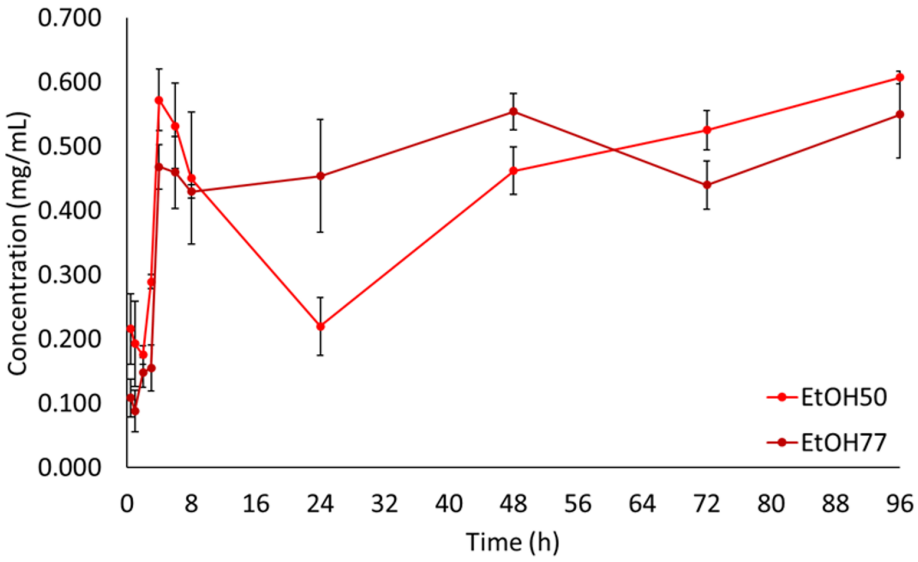

Figure 3: Solubilization kinetic curve of PpIX in EtOH50 and EtOH77 solvents. Error bars represent one standard deviation (n = 3).

average concentration over the first 8 h of analysis (stabilization period) was 0.450 ± 0.103 mg/mL for EtOH50 and 0.430 ± 0.010 mg/mL for EtOH77. These values align with findings by da Silva Gonçalves and collaborators [22], who discussed the modification of porphyrin derivatives to enhance solubility, and Rossin and colleagues [2], who reported similar solubility ranges for porphyrin-based compounds in hydroalcoholic systems.

Overall, the results indicated that while EtOH50 and EtOH77 effectively dissolve PpIX at concentrations up to 0.4 mg/mL, water and EtOHabs rapidly reach saturation and exhibit instability. The solubility equilibrium was achieved after approximately 4 h for EtOH50 and EtOH77, whereas for water and EtOHabs, the equilibrium was established within 30 min, followed by degradation or aggregation. These results support the observations made by Tima and collaborators [11], who found that ethanol–water mixtures offer an improved balance between solubility and stability for hydrophobic compounds.

In systems containing 10% (w/w) P407 with 0.4 mg/mL PpIX (EtOH50, EtOH77, and water), the complete solubilization was achieved regardless of the solvent used. Figure 4 shows the solubilization kinetics in the polymeric systems. The average con-

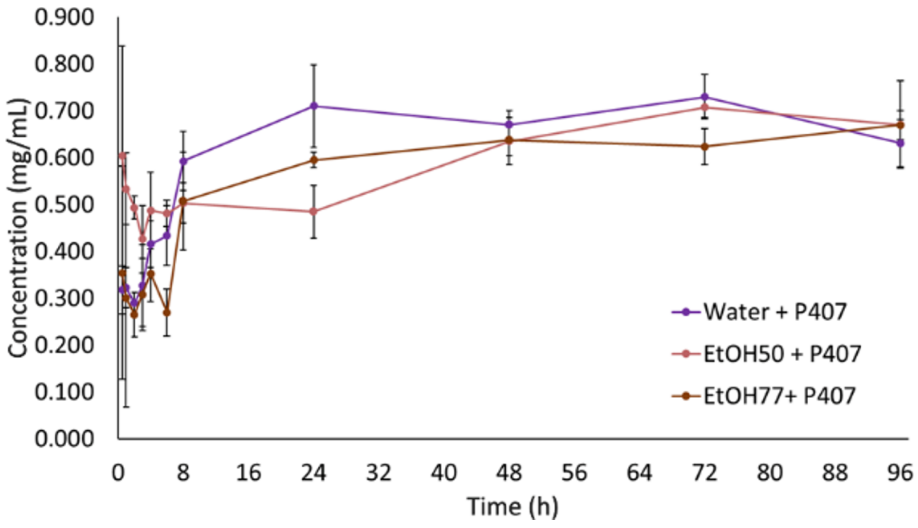

Figure 4: Kinetic curves of PpIX in polymeric systems. Error bars represent one standard deviation (n = 3).

centrations after 8 h were 0.593 ± 0.063 mg/mL for water-based systems, 0.503 ± 0.043 mg/mL for EtOH50, and 0.507 ± 0.104 mg/mL for EtOH77, which is consistent with previous reports on micellar stabilization of hydrophobic drugs [16].

These systems remained clear and free of precipitates for up to 96 h, suggesting the formation of a stable micellar solution. The presence of P407 enhanced PpIX dissolution, even in water, which otherwise exhibited some limitations. Mathematical models were employed to better understand and simplify the complex dissolution behavior of the micellar systems. Several models, including zero-order, first-order, Higuchi, and Korsmeyer–Peppas were evaluated for both conventional and micellar systems. However, most of them could not fit the results. The best fit was obtained by using the Korsmeyer–Peppas model with lag time (t_{lag}), only for the systems containing P407 (Table 1).

Table 1: Mathematical modeling of the solubilization curves of PpIX dissolution in micellar systems using the Korsmeyer–Peppas model with lag time (t_{lag}).

PpIX in polymeric systems	Korsmeyer–Peppas with t_{lag}		
	k (h^{-n})	n	*R*
water + P407	82.772	0.174	0.9007
EtOH50 + P407	124.062	0.042	0.5355
EtOH77 + P407	75.728	0.164	0.8935

The lag time parameter in the model reflects the initial phase of micelle formation and the subsequent accommodation of PpIX into the micellar core, which precedes the diffusion-driven dissolution process [23]. Among the systems evaluated, water + P407 and EtOH77 + P407 exhibited the highest correlation coefficients (R = 0.9007 and 0.8935, respectively), indicating a strong fit and supporting the hypothesis of micelle-mediated stabilization of PpIX in these environments.

The release exponent (n) values obtained were all smaller than 0.45, which is characteristic of Fickian diffusion. This suggests that the dissolution mechanism is mainly governed by simple diffusion, without significant swelling or erosion of the polymeric matrix [8], which is commonly observed in hydrophilic polymeric systems, as those produced by P407 [24]. In this context, the drug molecules diffuse through the micellar network driven by concentration gradients, while the micellar structure remains intact throughout the dissolution process [25]. The kinetic constant (k) was elevated for all the systems, although polymer, temperature, and the solvent properties may influence this parameter.

Overall, the water + P407 system demonstrated the most favorable behavior, as no micellar disintegration was observed, unlike the systems containing ethanol. These findings are consistent with other experimental results, reinforcing the stability and solubilizing potential of aqueous micellar systems for PpIX [8].

To improve the assessment of solubility, complementary methods may be performed together, such as dynamic light scattering [26] and turbidimetry [27]. Furthermore, TEM analysis can provide a more accurate understanding of the incorporation of PpIX into the micellar systems, overcoming the limitations associated with spectrophotometric estimations. These limitations include potential overestimation of solubility due to light scattering by aggregates, turbidity-related interference, and the inability to distinguish between molecularly dissolved and aggregated species [28].

Therefore, TEM micrographs of PpIX samples in different media containing P407 (water, EtOH50, and EtOH77) are displayed in Figure 5. It was possible to observe significant variations in micelle size and morphology. While in the aqueous system well-defined circular micelles are observed with an average diameter of 11.81 ± 1.71 nm, in EtOH50 and EtOH77 the samples exhibited progressively large micelles (13.56 ± 3.24 nm and 14.77 ± 3.81 nm, respectively). This suggests that ethanol, due to its dissolution properties, may partially disrupt the micelles, resulting in larger and less homogeneous structures [29].

The disrupted micelles formed in alcoholic solution may exhibit limited effectiveness in encapsulating PpIX for drug delivery in biological systems. Moreover, the small size of the micelles observed in water tend to exhibit improved permeability, which may present significant implications for the application of PpIX in biological systems [17].

Conclusion

This study demonstrated that hydroalcoholic solutions and P407-based systems effectively solubilized PpIX at 0.4 mg/mL yielding clear and stable solutions, in contrast to the low solubility and turbidity observed in aqueous and absolute ethanol systems. P407 significantly enhanced PpIX solubility, with no significant differences among water-based, 50% v/v ethanol, and 77% v/v ethanol polymeric systems. Considering the potential toxicity and the challenges of hydroalcoholic formulations, the aqueous P407 system, with its gelling and thermoresponsive properties, stands out as the most promising approach for further pharmaceutical applications. TEM micrographs revealed that PpIX micelles in water formed smaller and more uniform structures, suggesting improved drug load ability and perme-

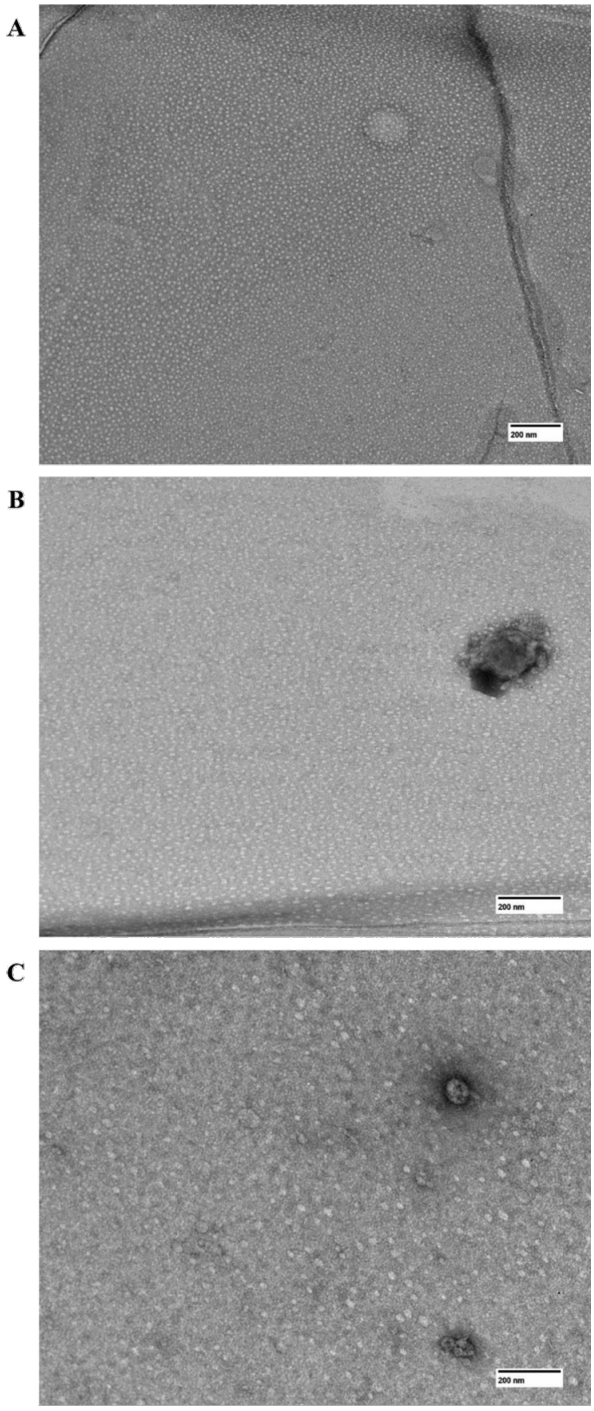

Figure 5: TEM images of PpIX in polymeric systems comprising 10% (w/w) poloxamer 407 in purified water (A), EtOH50 (B) and EtOH77 (C). The images are at a scale of 200 nm.

ability compared to alcoholic solutions. Moreover, dissolution kinetics, modeled using the Korsmeyer–Peppas equation with lag time (t_{lag}), indicated a Fickian diffusion mechanism occuring after the initial phase of micelle formation and subsequent accommodation of PpIX within the micellar core of the P407-based systems. These results reinforce the structural stability and controlled-release potential of the micellar formulations, particularly the aqueous one, strengthening their suitability for topical drug delivery strategies.

Funding

The authors are thankful to the Brazilian funding agency CNPq (Conselho Nacional de Desenvolvimento Científico e Tecnológico /National Counsel of Technological and Scientific Development of Brazil; Processes no. 307695/2020-4 and 442096/2023-2).

Author Contributions

Michelly de Sá Matsuoka: data curation; formal analysis; investigation; methodology; writing – original draft. Giovanna Carla Cadini Ruiz: data curation; formal analysis; investigation; methodology; writing – original draft. Marcos Luciano Bruschi: conceptualization; funding acquisition; project administration; resources; supervision; writing – review & editing. Jéssica Bassi da Silva: conceptualization; data curation; formal analysis; supervision; visualization; writing – original draft; writing – review & editing.

ORCID® iDs

Michelly de Sá Matsuoka - https://orcid.org/0009-0006-0966-952X
Giovanna Carla Cadini Ruiz - https://orcid.org/0009-0009-0226-7642
Marcos Luciano Bruschi - https://orcid.org/0000-0002-4838-5742
Jéssica Bassi da Silva - https://orcid.org/0000-0003-0586-7802

Data Availability Statement

Data generated and analyzed during this study is available from the corresponding author upon reasonable request.

References

1. Conrado, P. C. V.; Sakita, K. M.; Arita, G. S.; Galinari, C. B.; Gonçalves, R. S.; Lopes, L. D. G.; Lonardoni, M. V. C.; Teixeira, J. J. V.; Bonfim-Mendonça, P. S.; Kioshima, E. S. *Photodiagn. Photodyn. Ther.* **2021,** *34,* 102221. doi:10.1016/j.pdpdt.2021.102221
2. Rossin, A. R. d. S.; de Oliveira, É. L.; de Moraes, F. A. P.; Júinior, R. C. d. S.; Scheidt, D. T.; Caetano, W.; Hiokaa, N.; Dragunski, D. C. *Quim. Nova* **2020,** *43,* 613–622. doi:10.21577/0100-4042.20170524
3. Younus, L. A.; Mahmoud, Z. H.; Hamza, A. A.; Alaziz, K. M. A.; Ali, M. L.; Yasin, Y.; Jihad, W. S.; Rasheed, T.; Alkhawaldeh, A. K.; Ali, F. K.; Kianfar, E. *Braz. J. Biol.* **2024,** *84,* e268892. doi:10.1590/1519-6984.268892
4. Ou-Yang, Y.; Zheng, Y.; Mills, K. E. *Front. Med.* **2023,** *10,* 1089361. doi:10.3389/fmed.2023.1089361
5. Franco, M. D. S.; Lapierre, T. J. W. J. D.; Martinho, A. C. C.; Bessas, N. C.; Caetano, M. M.; Tasso, T. T.; Beletti, M. E.; de Lima, R. G.; Rezende Júnior, C. d. O.; Tsubone, T. M. *Dyes Pigm.* **2025,** *236,* 112649. doi:10.1016/j.dyepig.2025.112649

6. de Souza Marinho Leite, P. Â.; de Oliveira Miguel, N. C.; Pierre, M. B. R. *Braz. J. Pharm. Sci.* **2023,** *59,* e21920. doi:10.1590/s2175-97902023e21920
7. Campanholi, K. d. S. S.; Gerola, A. P.; Vilsinski, B. H.; de Oliveira, É. L.; de Morais, F. A. P.; Rabello, B. R.; Braga, G.; Calori, I. R.; Silva, E. L.; Hioka, N.; Caetano, W. *Dyes Pigm.* **2018,** *157,* 238–250. doi:10.1016/j.dyepig.2018.04.057
8. da Silva, J. B.; dos Santos, R. S.; Vecchi, C. F.; da Silva Souza Campanholi, K.; da Silva Junior, R. C.; de Castro Hoshino, L. V.; Caetano, W.; Baesso, M. L.; Simas, F. F.; Cook, M. T.; Bruschi, M. L. *Int. J. Biol. Macromol.* **2023,** *245,* 125491. doi:10.1016/j.ijbiomac.2023.125491
9. Junqueira, M. V.; Borghi-Pangoni, F. B.; Ferreira, S. B. d. S.; Bruschi, M. L. *Drug Dev. Ind. Pharm.* **2016,** *42,* 2009–2019. doi:10.1080/03639045.2016.1188111
10. Ferreira, S. B. d. S.; Slowik, K. M.; Castro Hoshino, L. V. d.; Baesso, M. L.; Murdoch, C.; Colley, H. E.; Bruschi, M. L. *Eur. J. Pharm. Sci.* **2020,** *151,* 105372. doi:10.1016/j.ejps.2020.105372
11. Tima, S.; Anuchapreeda, S.; Ampasavate, C.; Berkland, C.; Okonogi, S. *Eur. J. Pharm. Biopharm.* **2017,** *114,* 57–68. doi:10.1016/j.ejpb.2016.12.032
12. Villanova, J. C. O.; Oréfice, R. L.; Cunha, A. S. *Polim.: Cienc. Tecnol.* **2010,** *20,* 51–64. doi:10.1590/s0104-14282010005000009
13. da Silva Souza Campanholi, K.; da Silva, I. C.; dos Santos, R. S.; Vecchi, C. F.; da Silva, J. B.; Bruschi, M. L.; dos Santos Pozza, M. S.; de Castro-Hoshino, L. V.; Baesso, M. L.; Caetano, W.; Batistela, V. R. *J. Mol. Liq.* **2023,** *381,* 121807. doi:10.1016/j.molliq.2023.121807
14. Almeida, H.; Amaral, M. H.; Lobão, P.; Lobo, J. M. S. *J. Pharm. Pharm. Sci.* **2012,** *15,* 592. doi:10.18433/j3hw2b
15. Ferreira, S. B. d. S.; Braga, G.; Oliveira, É. L.; da Silva, J. B.; Rosseto, H. C.; de Castro Hoshino, L. V.; Baesso, M. L.; Caetano, W.; Murdoch, C.; Colley, H. E.; Bruschi, M. L. *Beilstein J. Nanotechnol.* **2019,** *10,* 2304–2328. doi:10.3762/bjnano.10.222
16. Markus, F.; Dreher, F.; Laschat, S.; Baudis, S.; Tovar, G. E. M.; Southan, A. *Polymer* **2017,** *108,* 21–28. doi:10.1016/j.polymer.2016.11.039
17. Bassi da Silva, J.; da Silva Souza Campanholi, K.; Braga, G.; de Souza, P. R.; Caetano, W.; Cook, M. T.; Bruschi, M. L. *Mater. Sci. Eng., C* **2021,** *130,* 112440. doi:10.1016/j.msec.2021.112440
18. Vecchi, C. F.; Said dos Santos, R.; Bassi da Silva, J.; Bruschi, M. L. *Beilstein J. Nanotechnol.* **2022,** *13,* 503–516. doi:10.3762/bjnano.13.42
19. Borman, P.; Elder, D. Q2(R1) Validation of Analytical Procedures. *ICH Quality Guidelines;* John Wiley & Sons: Hoboken, NJ, USA, 2017; pp 127–166. doi:10.1002/9781118971147.ch5
20. Zhou, L.; Yang, L.; Tilton, S.; Wang, J. *J. Pharm. Sci.* **2007,** *96,* 3052–3071. doi:10.1002/jps.20913
21. Baka, E.; Comer, J. E. A.; Takács-Novák, K. *J. Pharm. Biomed. Anal.* **2008,** *46,* 335–341. doi:10.1016/j.jpba.2007.10.030
22. da Silva Gonçalves, J. L. Caracterização Físico-Química e Fotodinâmica de Fotossensibilizadores: Efeito Da Modificação Química Para Aumentar a Solubilidade Em Meio Aquoso. Ph.D. Thesis, Universidade de São Paulo, São Carlos, Brazil, 2015. doi:10.11606/t.75.2015.tde-29062015-153459
23. Benita, S. *Appl. Biochem. Biotechnol.* **1984,** *10,* 255–258. doi:10.1007/bf02783758
24. Lopes, C. M.; Lobo, J. M. S.; Costa, P. *Rev. Bras. Cienc. Farm.* **2005,** *41,* 143–154. doi:10.1590/s1516-93322005000200003
25. Kockisch, S.; Rees, G. D.; Tsibouklis, J.; Smart, J. D. *Eur. J. Pharm. Biopharm.* **2005,** *59,* 207–216. doi:10.1016/j.ejpb.2004.07.007
26. Cerdeira, A. M.; Mazzotti, M.; Gander, B. *Int. J. Pharm.* **2010,** *396,* 210–218. doi:10.1016/j.ijpharm.2010.06.020
27. Amin, M. L. *Drug Target Insights* **2013,** *7,* 27–34. doi:10.4137/dti.s12519
28. Lipinski, C. A.; Lombardo, F.; Dominy, B. W.; Feeney, P. J. *Adv. Drug Delivery Rev.* **2001,** *46,* 3–26. doi:10.1016/s0169-409x(00)00129-0
29. Xie, B.; Liu, Y.; Li, X.; Yang, P.; He, W. *Acta Pharm. Sin. B* **2024,** *14,* 4683–4716. doi:10.1016/j.apsb.2024.08.027

License and Terms

BEILSTEIN JOURNAL OF NANOTECHNOLOGY

Acrocomia aculeata oil-loaded nanoemulsion: development, anti-inflammatory properties, and cytotoxicity evaluation

Verónica Bautista-Robles[1], Hady Keita[*2], Edgar Julián Paredes Gamero[3], Layna Tayná Brito Leite[4], Jessica de Araújo Isaías Muller[5], Mônica Cristina Toffoli Kadri[5], Ariadna Lafourcade Prada[4] and Jesús Rafael Rodríguez Amado[4,6]

Full Research Paper

Open Access

Address:
[1]College of Pharmaceutical Sciences, Food and Nutrition. Federal University of Mato Grosso do Sul, Av. Costa e Silva s/n, 79070-900, Campo Grande-MS, Brazil, [2]Postgraduate Studies Division, University of Sierra Sur, Guillermo Rojas Mijangos s/n, 70800 Miahuatlán de Porfirio Díaz, Oaxaca, México, [3]Laboratory of Cellular and Molecular Biology, Faculty of Pharmaceutical Sciences, Food and Nutrition, Federal University of Mato Grosso do Sul, Av. Costa e Silva s/n, 79070-900, Campo Grande-MS, Brazil, [4]Laboratory of Pharmaceutical Technology, Federal University of Mato Grosso do Sul, Av. Costa e Silva, s/n, 79070-900, Campo Grande-MS, Brazil, [5]Laboratory of Pharmacology and Inflammation, Federal University of Mato Grosso do Sul, Av. Costa e Silva, s/n, 79070-900, Campo Grande-MS, Brazil and [6]Postgraduate Program in Health Sciences, Faculty of Health Sciences, Federal University of Grande Dourados, Dourados 79804-970, MS, Brazil

Email:
Hady Keita[*] - hadykeith@yahoo.fr

* Corresponding author

Keywords:
Acrocomia aculeata; cytotoxicity; hemolysis; inflammation; nanoemulsion

Beilstein J. Nanotechnol. **2025,** *16,* 1277–1288.
https://doi.org/10.3762/bjnano.16.93

Received: 14 March 2025
Accepted: 11 July 2025
Published: 06 August 2025

This article is part of the thematic issue "Advances in nanotechnology applied to natural products".

Guest Editor: D. Dourado

Abstract

The oil from the pulp of the bocaiúva fruit may have several medical applications. However, little is known about its pharmacological activity. Therefore, this study aimed to develop and evaluate the anti-inflammatory activity of a nanoemulsion loaded with the oil extracted from the pulp of the fruit of *Acrocomia aculeata*. Griffin's method determined the hydrophilic–lipophilic equilibrium ratio of the nanoemulsion. It was shown to have an adequate droplet size (173.60 nm) with excellent homogeneity (polydispersity index 0.200). The anti-inflammatory activity of the nanoemulsion was evaluated by the carrageenan-induced paw edema method. Finally, the non-hemolytic and cytotoxic activity of the nanoformulation was determined to assess its safety. The nanoemulsion loaded with *Acrocomia aculeata* fruit pulp oil was shown to have parameters suitable for its characterization, impressive anti-inflammatory activity, and a safe profile.

Introduction

Acrocomia aculeata Jacq is a palm of the Arecaceae family, commonly known as bocaiúva or macaúba. It is widespread in South America and is particularly abundant in Mato Grosso do Sul, located in the Center-West region of Brazil. *A. aculeata* stands out for its wide geographic distribution, being native to tropical forests [1,2]. Its rounded fruits present sensory attractions, such as color, distinctive and intense flavor, and aroma. They are traditionally consumed by the native population, occupying an important place in the regional culture [3,4].

Bocaiúva oil contains several antioxidant compounds such as phenols, terpenes, β-carotenes, and compounds that present antioxidant properties [5,6]. It contains free fatty acids, monoglycerides, triglycerides, sterols [6-8], and saturated and unsaturated fatty acids predominantly [9]. These compounds have the potential to enhance immune response, reduce the risk of degenerative diseases, and contribute to anti-inflammatory activity [10,11], reducing the indiscriminate use of non-steroidal anti-inflammatory drugs (NSAIDs) and corticosteroids in the population [12,13]. There are several reports about the severe adverse reactions in patients taking these drugs [14,15]. In addition, the economic impact of these degenerative and inflammatory diseases, such as rheumatoid arthritis, is significant, as demonstrated by heightened healthcare resource utilization and substantially increased annual aggregate costs. This underscores the need to find effective alternative treatments to prevent and treat these pathologies [16-18].

On a global scale, vegetable oils play a fundamental role not only in human nutrition but also as strategic inputs in the chemical, pharmaceutical, and food industries. In recent decades, there has been a growing imbalance between the demand and supply of these oils, which has generated challenges in terms of sustainability and supply. In this scenario, several oil palm species have been identified as potentially efficient sources of vegetable oil production, given their high yield rates per hectare and their ability to adapt to different agroecological environments [19]. In the state of Mato Grosso do Sul, it is possible to find virgin, refined, or conventional bocaiúva oil in the market for cosmetic, food, pharmaceutical, nutraceutical, and industrial applications. However, due to the chemical and physicochemical characteristics as well as the solubility and stability of this oil, it was decided to make a nanoemulsion to enhance its already known therapeutic benefits.

Nanoemulsions are nanoemulsified systems, either oil-in-water (O/W) or water-in-oil (W/O), which are isotropic, homogeneous, and thermodynamically unstable, with droplet sizes ranging from 20 to 200 nm [20]. They present properties such as high surface area per unit volume, robust kinetic stability, and tunable rheology [21]. It has been demonstrated that emulsified systems loaded with plant extracts have better pharmacological activity than extracts when used naturally [22]. For example, plant oil-loaded nanoemulsions exhibit high water solubility, improved permeability, and enhanced bioavailability [23]. This contrasts with the limited solubility and poor bioavailability of natural oil through different routes of administration [24-27].

The possibility of developing nanotechnological products with potent pharmacological activity was considered to add more value to the oil obtained from bocaiúva pulp, which contains phenols and carotenoids. Therefore, the objective of this study was to develop, characterize, and evaluate the anti-inflammatory activity of the nanoemulsion loaded with *Acrocomia aculeata* oil.

Results and Discussion

Vegetable oils are known for their high content of fatty acids, which possess a diverse range of biological activities, including hypoglycemic [28], cholesterol-lowering, anti-inflammatory, and antioxidant effects [11,22-30]. Bocaiúva oil is widely used to treat cardiovascular, inflammatory, and renal diseases [31,32].

In addition, one of the main characteristics of this oil is its orange color due to the presence of phenols and carotenoids, which were characterized in this study. These secondary metabolites are considered to have high antioxidant activity and provide high stability to the oil [5]. These metabolites have been shown to possess anti-inflammatory and immunostimulant properties [1,33].

Physicochemical characterization of *Acrocomia aculeata* fruit pulp oil

The physicochemical parameters of bocaiúva oil, such as acidity index, iodine index, and refractive index, were analyzed. The acidity index indicates the state of conservation of oils and fats and is related to the oxidation process. Our results showed an acid index of 0.92 ± 0.10. The iodine index determines the amount of unsaturation in fatty acids [28]. Our results showed an iodine index of 74.50 ± 1.50 g I_2/100 g, values that are within the range allowed (58–75 g I_2/100 g) by OMS/FAO for oils with high oleic acid content [34].

Also, quality indicators such as refractive index, solubility in different organic solvents, and relative density showed that the bocaiúva oil used in that study had good purity [35]. Coimbra and Jorge analyzed *Acrocomia aculeata* oil and found refractive index values similar to those in this study (1.46 ± 0.01)

[19]. These results were found within the reference values established for oils rich in oleic acids, such as extra virgin olive oil, palm oil, and almond oil [34]. The presence of polyphenols and carotenoids was also identified in this oil (see Table 1).

Table 1: Physicochemical properties of *Acrocomia aculeata* fruit pulp oil.

Property	Value
relative density	0.9000 ± 0.0001
iodine value (g I_2/100 g)	74.50 ± 1.50
refractive index (30 °C)	1.456 ± 0.001
peroxide value (mEq/kg oil)	4.50 ± 0.40
saponification index (mg KOH/g)	133.00 ± 4.50
acidity	0.92 ± 0.10
total carotenoids (μg/g)	266.00 ± 12.00
polyphenols (mg/g)	12.60 ± 0.30

Table 2 shows the profile of fatty acids present in *Acrocomia aculeata* fruit pulp oil. Oleic acid is the major component (71.25%) among monounsaturated fatty acids (73.79%). Therefore, bocaiúva oil can be considered an oil with a cardioprotective effect due to its high oleic acid content [36,37]. In addition, its levels of monounsaturated fatty acids are higher than those found in extra virgin olive, soybean, corn, sunflower, and flaxseed oils [37,38].

The bocaiúva oil utilized in this study demonstrated excellent quality, as assessed by established parameters for evaluating vegetable oils reported in the literature [11,39]. The results are consistent with findings by Hiane and collaborators [40] and Lieb and collaborators [7], who also observed a high concentration of monounsaturated fatty acids in the fruit pulp. Amaral et al. further identified a notable oleic acid content of 69.07% in *Acrocomia aculeata* pulp oil [41]. Minor discrepancies in composition may be attributed to variations in environmental conditions, such as climatic conditions, temperature, and pulp drying duration before oil extraction. Additionally, the specific extraction technique employed can influence lipid degradation and promote the formation of free fatty acids [19]. Despite these variations, the compositional profiles remain comparable, underscoring the distinctive chemical characteristics of the oil studied.

Table 2: Lipid profile of *Acrocomia aculeata* fruit pulp oil.

Fatty acid	Content (%)	RE Index	LR[a] Index
saturated			
hexanoic acid	0.22 ± 0.02	974	975
octanoic acid	0.25 ± 0.02	1169	1170
decanoic acid	0.13 ± 0.01	1365	1365
dodecanoic acid	0.85 ± 0.01	1548	1547
tetradecanoic acid	0.70 ± 0.01	1747	1749
hexadecanoic acid	16.52 ± 0.15	1970	1969
octadecanoic acid	4.11 ± 0.15	2164	2165
docosanoic acid	0.06 ± 0.03	2562	2564
subtotal	22.84 ± 0.05	—	—
monounsaturated			
9-hexadecenoic acid	2.54 ± 0.01	1939	1938
9-octadecenoic acid	71.25 ± 2.21	2241	2142
subtotal	73.79 ± 1.11	—	—
polyunsaturated			
9,12,15-octadecatrienoic acid	0.80 ± 0.04	2154	2155
9,12-octadecadienoic acid	2.20 ± 0.33	2176	2175
eicosanoic acid	0.20 ± 0.03	2369	2370
subtotal	3.20 ± 0.13	—	—
total fatty acids	>99.00%	—	—

[a]Literate retention rate (from NIST chemistry webbook, SRD 69).

Preparation of nanoemulsions, required hydrophilic–lipophilic balance, droplet size, zeta potential, and shelf stability

The development of a nanoemulsion requires the determination of key formulation parameters, including the required hydrophilic–lipophilic balance (HLBr), droplet size, and polydispersity index (PDI) [42-44]. In this study, the *Acrocomia aculeata* oil nanoemulsion (AANE) exhibited a uniform droplet size distribution and a stable PDI upon formulation with the surfactant system characterized by a hydrophilic–lipophilic balance (HLB) value of 12. These physicochemical parameters are critical for defining the kinetic stability and structural integrity of the nanoemulsion system.

Surfactants or emulsifiers are characterized by their HLB values, which reflect their affinity for either aqueous or lipid phases. Hydrophilic emulsifiers typically exhibit a high HLB value, while lipophilic emulsifiers possess lower values. The HLB scale generally ranges from 1 to 20, with an approximate midpoint of 10, distinguishing emulsifiers suited for oil-in-water versus water-in-oil systems [43] (Figure 1).

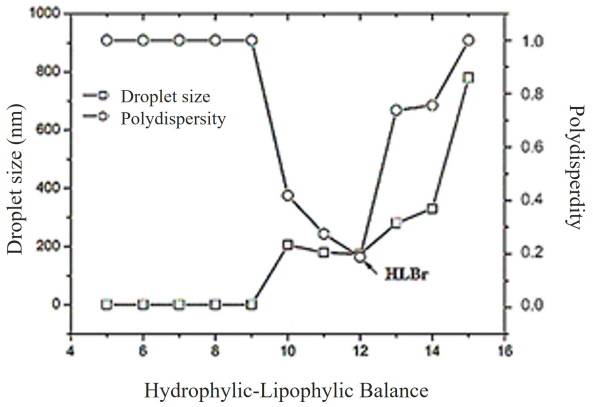

Figure 1: Droplet size and polydispersity index of nanoemulsions versus the hydrophilic–lipophilic balance of the surfactant system used for the preparation. HLBr: required hydrophilic-lipophilic balance.

A surfactant system characterized by an HLB value of 12 (Figure 1) was employed to formulate the bocaiúva oil nanoemulsion, resulting in a satisfactory polydispersity index of 0.200. The formulation exhibited excellent physical stability, maintaining consistent zeta potential and droplet size parameters over a 180-day storage period at 25 ± 2 °C. Dynamic light scattering analysis revealed a mean nanodroplet size (by intensity) of 173.6 ± 0.70 nm (Figure 2A). The nanoemulsion, composed of 0.28 parts of Span 80® and 0.72 parts of Tween 80®, exhibited a zeta potential of −14.10 ± 1.06 mV (Figure 2B), indicative of sufficient electrostatic repulsion for colloidal stability.

It should be noted that the phenolic compounds and carotenoids contained in this oil are considered potent antioxidants, which may contribute to the stability of the nanoemulsion [45,46].

Figure 3 shows the behavior of zeta potential and droplet size in Bocaiúva oil-loaded nanoemulsion over 180 days. The droplet size remained stable at around 170 nm, and no statistical differences were found at any point in time over 180 days (F_{test} = 0.18, p_{value} = 0.0804). In contrast, the zeta potential underwent a significant decrease from approximately −10 to −20 mV within the first 45 days and then stabilized for the remainder of the 180 days. The analysis of variance found statistically significant differences among the zeta potential values (F_{test} = 2.4258, p_{value} = 0.0021). The Tukey test suggests that the zeta potential values at zero and 15 days were not statistically different, forming a homogenous group statistically

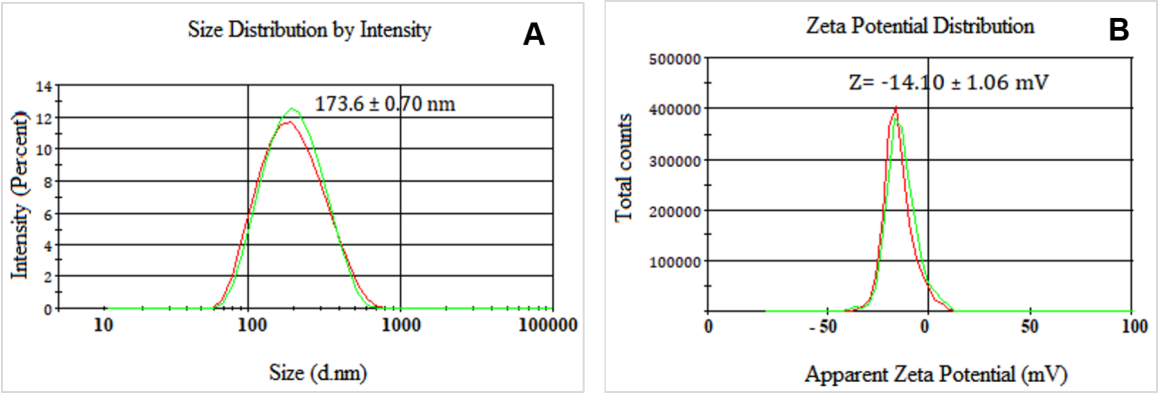

Figure 2: Droplet size distribution and zeta potential of the nanoemulsion prepared with 0.28 parts Span 80® and 0.72 parts Tween 80® (HLB = 12). Droplet size: 173.6 ± 0.70 nm. Zeta potential: 14.0 ± 1.06 mV.

different from the rest of the time points (45, 90, and 180 days), which formed another homogeneous group.

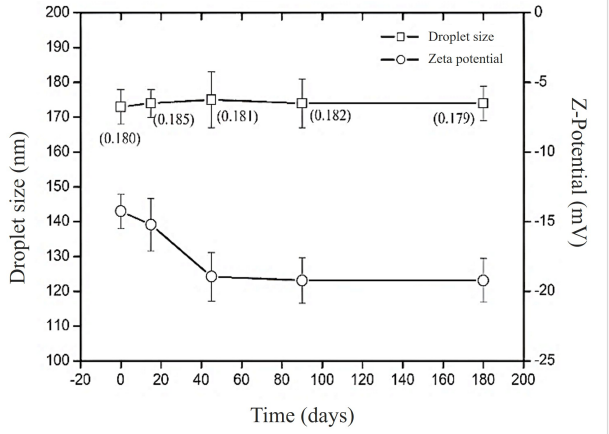

Figure 3: Stability of bocaiúva oil-loaded nanoemulsion prepared with 0.28 parts of Span 80® and 0.72 parts of Tween 80® (HLB = 12).

The progressive increase in the absolute value of zeta potential over time suggests enhanced system stability, attributed to the intensification of electrostatic repulsion among nanodroplets. Although this phenomenon is atypical for systems stabilized by nonionic surfactants (Span 80® and Tween 80®), it may result from the presence of ionizable bioactive compounds such as phenolics and carotenoids, which can associate with the droplet interface. These compounds likely expand the diffuse electrical double layer surrounding the nanodroplets, thereby increasing the magnitude of the zeta potential, enhancing stability by preventing droplet aggregation [47].

Figure 4 presents the impact of temperature (ranging from 10 to 80 °C) on the nanodroplet size of the AANE formulation over a 180-day period. Between 10 and 60 °C, the nanodroplet size remained relatively stable, ranging from 171 to 181 nm. However, temperatures exceeding 60 °C led to a marked reduction in droplet size, stabilizing between 110 and 120 nm across all time points. This reduction can be attributed to several interrelated physicochemical mechanisms. Primarily, the nonionic surfactants Span 80® and Tween 80® reduce interfacial tension between oil and aqueous phases, a phenomenon that becomes increasingly efficient at elevated temperatures, promoting the formation of smaller droplets. Additionally, elevated temperatures enhance molecular mobility and solubility, facilitating droplet disruption and dispersion effects observed in bocaiúva oil nanoemulsions above 60 °C [48]. Moreover, the surfactants exhibit temperature-responsive behavior, reorganizing at higher temperatures to stabilize finer dispersions. The concurrent decline in oil phase viscosity with increasing temperature also improves emulsification efficiency by promoting shear-induced droplet breakup, particularly under mechanical agitation [48]. Nevertheless, while these conditions favor the formation of smaller nanodroplets, temperatures above 60 °C may compromise emulsion stability, potentially triggering phase separation or degradation of labile components. This highlights the necessity for stringent temperature control during both formulation and storage to ensure the long-term stability of the nanoemulsion [49].

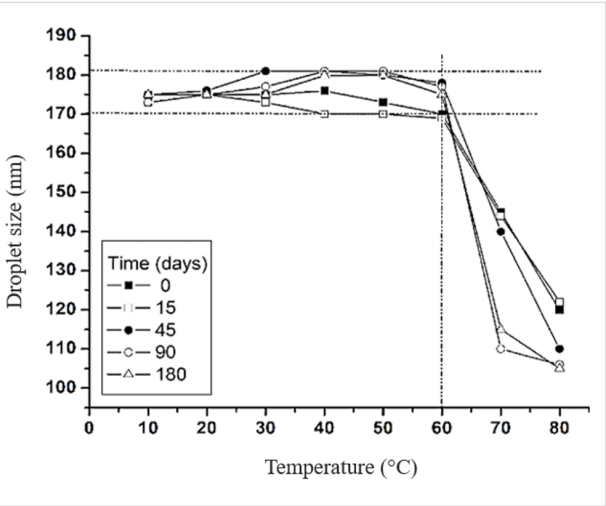

Figure 4: Effect of temperature on droplet size of nanoemulsion loaded with bocaiúva oil.

Hemolytic and cytotoxic activity of *Acrocomia aculeata* oil-based nanoemulsion

The hemolytic and cytotoxic activities of the nanoemulsion were assessed to evaluate its potential therapeutic use, with particular focus on its interaction with erythrocyte membranes. The nanoemulsion demonstrated no hemolytic activity against murine erythrocytes at concentrations of 1, 10, 100, and 1000 µg/mL. These findings were benchmarked against Triton X-100, a well-established positive control known for its potent hemolytic effect [50]. As shown in Figure 5A, AANE maintained erythrocyte membrane integrity across all tested concentrations, reinforcing its biocompatibility.

Furthermore, cytotoxicity evaluation showed that AANE did not inhibit cell growth, as cellular viability remained at 100% across all tested concentrations (1, 10, 100, and 1000 µg/mL, Figure 5B). These findings underscore the nanoemulsion's biocompatibility and support its potential for safe therapeutic applications. This is consistent with the traditional use of bocaiúva oil, which is commonly taken in or applied topically by traditional populations for managing joint inflammation and some infections [51]. Nevertheless, further comprehensive studies are necessary to confirm the long-term safety and therapeutic viability of the bocaiúva oil loaded nanoemulsions.

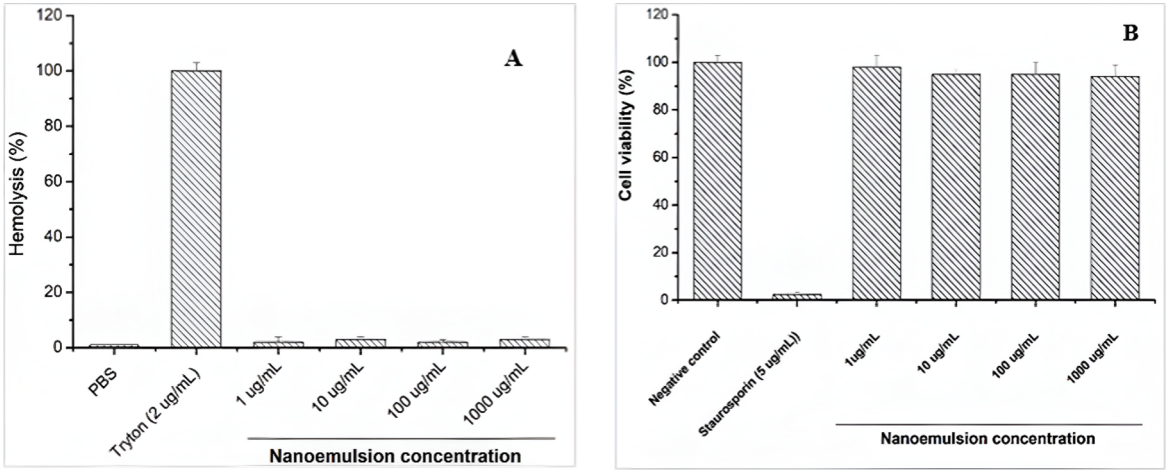

Figure 5: Hemolytic effect (A) and cell viability assay (B) of nanoemulsion loaded with *Acrocomia aculeata* fruit oil.

Anti-inflammatory activity of *Acrocomia aculeata* oil-based nanoemulsion

After confirmation of the nonhemolytic effect of the nanoemulsion, the anti-inflammatory effect was evaluated. In inflammatory processes, therapeutic interventions aim primarily to attenuate the productive phase of inflammation, particularly by inhibiting leukocyte infiltration at the injury site [52].

In this study, acute inflammation was induced via subplantar injection of carrageenan, a sulfated polysaccharide known to stimulate edema through the release of pro-inflammatory mediators associated with hyperalgesia and vascular alterations [53,54]. The paw edema model provides a reliable assessment of two key inflammatory parameters, namely, leukocyte migration and protein extravasation [55].

The assay demonstrated that *Acrocomia aculeata* nanoemulsion at a dose of 50 mg/kg has a pharmacological effect approximately two-fold greater than that of the pristine oil at 100 mg/kg (Figure 6). This finding reinforces the premise that

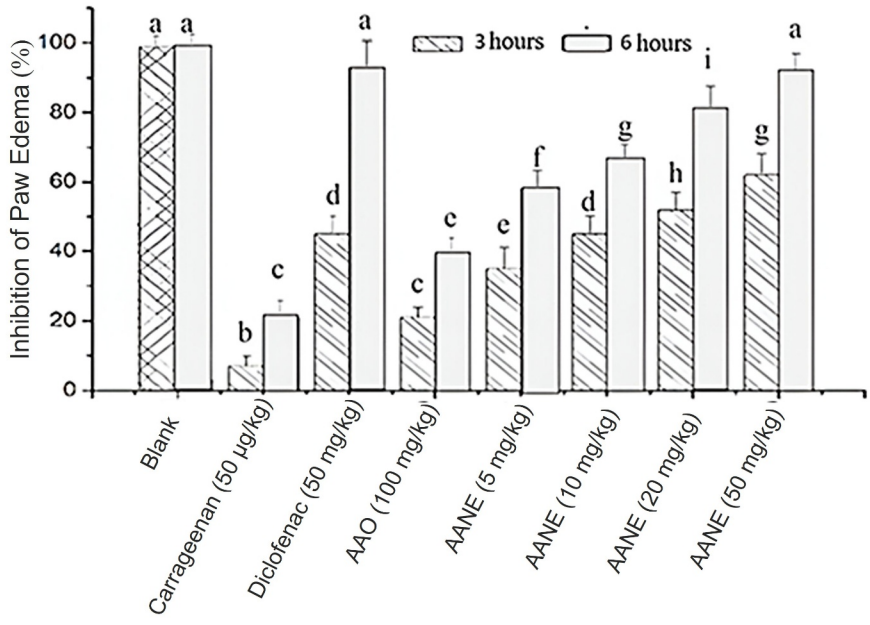

Figure 6: Anti-inflammatory effect of *Acrocomia aculeata* fruit oil and oil-loaded nanoemulsion. Different letters indicate statistically significant differences at $p \leq 0.05$.

the nanoformulation of drugs potentially enhances the biological activity of natural drugs [22]. Similar outcomes were reported by Silva et al., who observed enhanced anti-inflammatory efficacy of a *Copaifera spp*. essential oil nanoemulsion compared to its unformulated counterpart [47].

The superior pharmacological response of the nanoemulsion may be attributed to the nanoscale droplet size, which increases the surface area-to-volume ratio, enhances solubility and stability, and promotes rapid absorption and cellular uptake [56]. The nanometric scale facilitates more efficient interaction with cellular receptors, contributing to its heightened bioactivity [57]. Collectively, these findings suggest that bocaiúva oil-based nanoemulsions hold promising potential as anti-inflammatory agents.

Further analysis using the carrageenan-induced paw edema model revealed that the oil at 100 mg/kg exerted a modest anti-inflammatory effect up to 3 h post-treatment, which was considerably lower than that of both diclofenac and the nanoemulsion at 5, 10, 20, and 50 mg/kg body weight. Notably, at the 3 h time point, the nanoemulsion at 20 and 50 mg/kg elicited a more potent anti-inflammatory response than diclofenac. At 6 h post-treatment, the nanoemulsion maintained a comparable effect to diclofenac at the same dose levels (Figure 6). These results further substantiate the enhanced efficacy of the oil in the form of nanoemulsion in modulating acute inflammation in rats.

Conclusion

The *Acrocomia aculeata* oil-loaded nanoemulsion exhibited a homogeneously distributed droplet size (173.60 nm) within the nanometric range and demonstrated excellent physicochemical stability, maintaining its structural integrity and key parameters over a six-month period of shelf storage. Nanoemulsion showed a markedly greater anti-inflammatory effect compared to unformulated bocaiúva oil with an efficacy comparable to that of diclofenac. In addition, this nanoemulsion showed no cytotoxicity or hemolytic activity, indicating a favorable safety profile. These findings underscore the potential of the *Acrocomia aculeata* oil-loaded nanoemulsion as a nanotechnological innovative product that enhances the therapeutic value of *A. aculeata* oil and supports its development as a promising anti-inflammatory agent.

Experimental

Materials

Bocaiúva oil was used as the lipid core (relative density 0.9000, iodine value 74.50 g I_2/100 g, refractive index (30 °C): 1.456, peroxide value 4.50 mEq/kg, saponification index: 133.00 mg KOH/g ± 4.50) characterized in this study. The food-grade surfactant was Tween® 80 (nonionic polyoxyethylene (20) sorbitan monooleate; $C_{64}H_{124}O_{26}$; HLB = 15.0), Span 80® (2*R*)-2-[(2*R*,3*R*,4*S*)-3,4-dihydroxyoxyoxolan-2-yl]-2-hydroxyethyl (9*Z*)-octadec-9-enoate; $C_{24}H_{44}O_6$ HLB 4.3). Deionized water was used in the preparation of all experiments throughout the study.

Plant material

The fruits of *Acrocomia aculeata* were collected in Campo Grande, Mato Grosso do Sul, Brazil (20°50'00.1" S 54°36'45.7" W) after the natural fall of the first ripe fruits. The fruit pulp was manually separated from the seeds and preserved until oil extraction.

Bocaiúva oil extraction

One kilogram of fresh fruit pulp was placed in an Erlenmeyer flask and extracted with *n*-hexane (1000 mL) by mechanical agitation for 24 h. The *n*-hexane solution was separated from the pulp and preserved. Another 500 mL of *n*-hexane was added to the pulp for a second extraction under the same conditions. The two extractions were combined in a rotary evaporator system (Ika Werke, Germany). It was subjected to a slow stream of nitrogen for 24 h to obtain the solvent-free oil.

Physicochemical characterization of *Acrocomia aculeata* oil

Relative density and refractive index of *Acrocomia aculeata* oil (AAO) were evaluated according to the American Pharmacopoeia [58]. Iodine value, peroxide value, acid value, and saponification index were also evaluated following the protocols of the Brazilian Pharmacopoeia [58].

Determination of phenolic content of *Acrocomia aculeata* oil

The total phenols present in AAO were evaluated using the Folin–Ciocalteu spectrophotometric method. In this method, 3 mL of bocaiúva oil are mixed with 10 mL of a 75% ethanol solution. The mixture was stirred on a mechanical shaker for 2 h and allowed to stand in the dark for 24 h. The liquid was then centrifuged at 5000 rpm (LKP, Brazil). Aliquots of 1 mL of the ethanolic phase were used for analysis. The calibration curve was constructed using the standard addition method and a standard reference material (Sigma, USA). The results were expressed as gallic acid equivalent.

Determination of carotenoid content

Carotenoid content was evaluated spectrophotometrically (Shimatsu, Japan) following the procedure described by Rodriguez-Amaya. The molar extinction coefficient of β-carotene (β-C) in *n*-hexane at 453 nm (2592 $mol^{-1} \cdot cm^{-1}$) was used. The carotenoid content (CT), expressed as β-carotene, was calculated by the formula:

$$\mathrm{CT}_{(\mu g/100)} = \frac{(A * V * 10000)}{(\varepsilon * m)},$$

where A is the absorbance of the sample, V is the volume of the sample, ε is the molar absorbance of β-carotene in *n*-hexane at 453 nm, and m is the mass of the sample [59].

Lipid profile

A derivatization process was carried out to improve the stability of bocaiúva samples. One gram of bocaiúva oil was dissolved in *n*-hexane and vortexed for 5 min. The hexane phase was separated by centrifugation, transferred to a derivatization tube, and dried under a stream of nitrogen for 24 h. Then, 3 mL of a 2% methanolic NaOH solution was added to the tube. The tube was hermetically sealed and heated at 85 °C for 3 min. After cooling to room temperature, 2 mL of a BF_3/methanol solution was added. The tube was resealed and heated for 25 min.

Once cooled, the solution was extracted with 5 mL of *n*-hexane and centrifuged. 20 µL of supernatant (hexane phase) were injected directly into the GC-MS system (Mega 2 series gas chromatograph coupled to a SHIMADZU GC-MS-QP500 mass spectrometer (GC-MS) (Japan)) [60]. A 30 m × 0.32 mm capillary column with a 0.25 mm thick layer (66DB-5MS, Agilent Technologies, USA) was used as the stationary phase. Helium gas was used as carrier gas at a flow rate of 1.0 mL/min with a split ratio of 1:10. The injector temperature was set to 250 °C. The oven temperature was set to 130 °C for 10 min and then increased to 250 °C at a rate of 5 K/min, maintaining the final temperature for 10 min.

Mass spectra were acquired using a mass range of *m*/*z* 40–500, an interface temperature of 250 °C, and an ion source temperature of 220 °C. The solvent cutoff time was 3 min, and the event time was 0.20 min. The sweep speed was set at 2,500 mL/min. The composition (in percent) was calculated using the peak normalization method.

Preparation of nanoemulsions

Acrocomia aculeata oil nanoemulsions were prepared using the phase inversion method [61,62]. The formulations comprised 5% w/w bocaiúva oil, 5% surfactants (Span 80®: Tween 80®), and 90% deionized water. The organic phase, composed of bocaiúva oil and surfactants, was stirred at 400 rpm at 35 °C for 20 min. The aqueous phase (deionized water with conductivity below 0.4 µS and pH 6.5) was added to the organic phase at 1 mL/min under continuous magnetic stirring (400 rpm). Stirring was maintained for 20 min after adding the total volume of water. Finally, the initial volume of the nanoemulsion (50 mL) was restored with deionized water [42].

Required hydrophilic–lipophilic balance (HLBr)

Griffin's method determined the hydrophilic–lipophilic balance (HLBr) necessary to emulsify bocaiúva oil [63]. A set of nanoemulsions was prepared using HLB values from 4.3 to 15, obtained by mixing different proportions of Span 80® (HLB 4.3) and Tween 80® (HLB 15). The temperature was maintained at 25 ± 1 °C. The surfactant mixture that produced the stable nanoemulsion with the smallest droplet size was selected as the (HLBr) to emulsify bocaiúva oil [63].

Droplet size and zeta potential

Droplet size and polydispersity index (PDI) were measured by dynamic light scattering (DLS) with a Zetasizer Nano-ZS instrument (Malvern, UK). Zeta potential was determined by electrophoretic light scattering with a Zetasizer Nano-ZS instrument (Malvern, UK). AANE was diluted with Milli-Q water (1:25, v/v). All measurements were performed in triplicate, and results were presented as the mean ± standard deviation [42].

Shelf stability

The selected AANE was transferred to an amber vial and stored at 25 ± 2 °C for 180 days. Droplet size, polydispersity index, and zeta potential were measured at 0, 15, 45, 90, and 180 days. Measurements were performed in triplicate, and results were presented as the mean ± standard deviation.

The effect of temperature on droplet size was also evaluated, from 10 to 70 °C, at the same time intervals mentioned above. Measurements were performed with the Zetasizer instrument (Malvern, UK). The nanoemulsion was equilibrated at temperatures of 10, 20, 30 40, 40, 50, 60, and 70 °C for 5 min prior to measurement [42].

Hemolytic activity

Hemolytic activity was assessed using a murine erythrocyte suspension as described by Amado et al. Briefly, 190 µL of erythrocyte suspension was added to the wells of a 96-well polycarbonate plate. Then, 10 µL of nanoemulsion solution at different concentrations in PBS buffer (0, 5, 10, 20, and 50 µg/mL) was added to each well [41]. The plates were incubated for 1 h at 37 °C and were centrifuged at 3000 rpm at 5 °C for 15 min. After centrifugation, the concentration was suspended in 50 mL of phosphate-buffered saline (PBS, pH 7.4). The amount of hemoglobin was determined at 540 nm using a docetaxel (DTX) 880 multi-mode detector (Beckman, UK). A solution of 10 µg/mL Triton X-100 was used as a positive control, and 10 µL of PBS was used as a negative control. The assay was performed in triplicate.

The hemolytic activity (% of Hemolysis) was calculated using:

$$\%\ \text{of hemolysis} = \frac{\text{AM} - \text{AS}}{\text{AC} - \text{AS}} \times 100,$$

where AM is the absorbance of the sample; AS is the absorbance of the solvent, and AC is the absorbance of the positive control [61,62].

Cytotoxic activity

The cytotoxic activity of AANE was evaluated in murine macrophages of the J774 strain (ATCC USA) according to the technique described by Nakayama and colleagues [64]. Staurosporine (5 µg/mL) was used as a positive control, whereas cells from the culture without the nanoemulsion served as a negative control. Different concentrations of the nanoemulsion (1.65, 3.30, 6.60, 12.5, 25, 50, and 100 µg/mL) were added to the cultured cells and kept in contact for 24 h. Assays were performed in triplicate, and cell viability was expressed as a percentage according to International Organization for Standardization ISO 10993-5 guidelines [65].

Anti-inflammatory activity of *Acrocomia aculeata* oil-based nanoemulsion

Animals

The anti-inflammatory effect was evaluated using carrageenan-induced paw edema. Six- to eight-week-old female Swiss mice weighing 22 to 28 g were used [66]. Animals were acclimatized under laboratory conditions (25 ± 3 °C, 65 ± 5% humidity) with a 12/12 h light/dark cycle. Animals had free access to food and water at all times and were deprived of food 6 h before the experiment.

Formation of experimental groups and induction of paw edema

Eight experimental groups were randomly formed, with five animals per group (n = 5). 30 min before edema induction, groups 3, 4, 5, 6, 7, and 8 received the test substances (diclofenac sodium, AAO, or AANE). Group 1 received a blank (obtained under the same conditions, but without AAO) and group 2 received only carrageenan as it is explained in Table 3.

Therefore, the experimental groups were organized as follows:

- Group 1 recieved a blank (i.e., no carrageenan) but AANE treatment.
- Group 2 received only water before carrageenan administration.
- Group 3 received diclofenac sodium before carrageenan administration.
- Group 4 received AAO before carrageenan administration.
- Groups 5, 6, 7, and 8 received AANE before carrageenan administration.

Table 3 details how the experiment (Figure 7) was conducted with the corresponding doses of each treatment.

Edema volume was measured by plethysmometry (NovaLab, Brazil) at 3 and 6 h after carrageenan injection [67]. Inhibition of paw edema was expressed (in percentage) as the difference between the control value (paw volume of each animal before carrageenan injection) and the volumes measured at each time point after the treatments [63].

The expression of the results obtained, which is calculated using the formula:

$$\%\ \text{of inhibition of paw edema} = 100 \times \left[1 - \left(\frac{a - x}{b - y}\right)\right],$$

where a = mean hind paw volume of test/standard group animals after carageenan injection, b = mean hind paw volume of positive control animals after carageenan injection, x = mean

Table 3: Experimental groups of the paw edema protocol induced by carrageenan.

Groups	Treatment orally	Induction of edema
Group 1 (blank) (mg/kg body weight)	50	—[a]
Group 2 (D.W.[b]) (µL)	200	50 µL carrageenan
Group 3 (D.S.[c]) (mg/kg body weight)	50	50 µL carrageenan
Group 4 (AAO[d]) (mg/kg body weight)	100	50 µL carrageenan
Group 5 (AANE[e]) (mg/kg body weight)	5	50 µL carrageenan
Group 6 (AANE[e]) (mg/kg body weight)	10	50 µL carrageenan
Group 7 (AANE[e]) (mg/kg body weight)	20	50 µL carrageenan
Group 8 (AANE[e]) (mg/kg body weight)	50	50 µL carrageenan

[a]50 µL injected saline; [b]D.W. = distilled water; [c]D.S. = diclofenac sodium; [d]AAO = *Acrocomia aculeata* oil; [e]AANE: *Acrocomia aculeata* oil nanoemulsions.

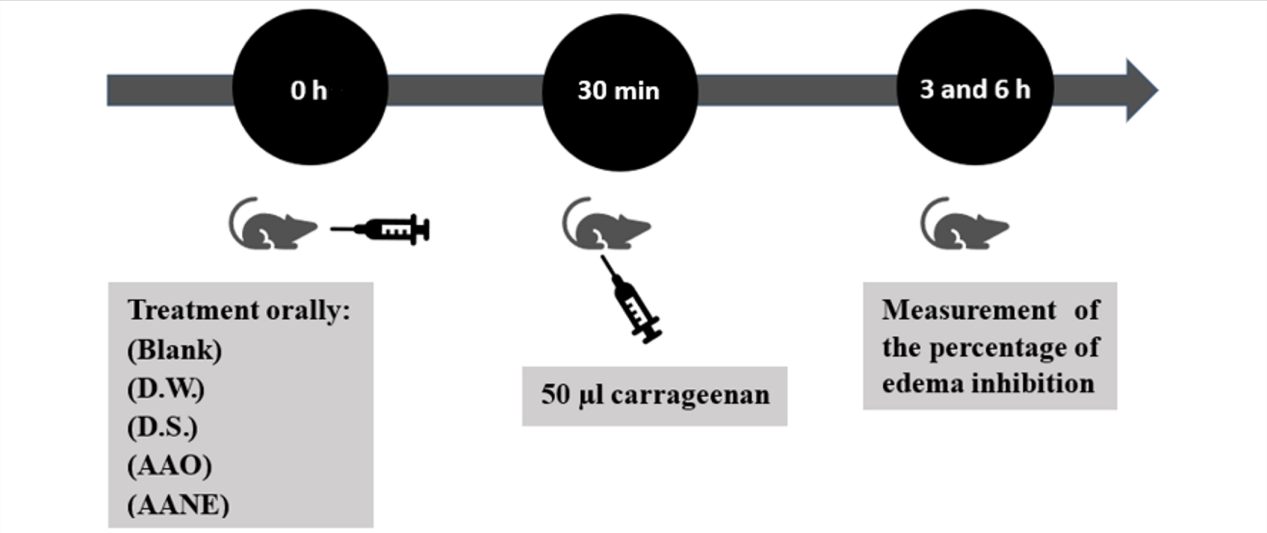

Figure 7: Representative scheme of the experimental protocol of paw edema induced by carrageenan. D.W. = distilled water; D.S. = diclofenac sodium; AAO = *Acrocomia aculeata* oil; AANE = *Acrocomia aculeata* oil nanoemulsions.

hind paw volume of test/standard group animals before carageenan injection, y = mean hind paw volume of positive control animals before carageenan injection [51].

Statistical analysis

A one-way ANOVA followed by Tukey's HSD test was performed to determine statistical differences between experimental groups. A statistically significant difference was considered at $p \leq 0.05$. StatGraphics® Centurion XV.1 software (StatEase, USA) was used for the analyses.

Ethical approval

All experiments were performed in accordance with the Ethics Committee for the Experimental Use of Animals of the Federal University of Mato Grosso do Sul, Brazil (Reference number: 1.250/2022).

Funding

The authors thank the Postgraduate Program in Biotechnology of the Federal University of Mato Grosso do Sul (UFMS), Brazil. The authors thank the Cordenação de Aperfeiçoamento de Pessoal de Nível Superior (CAPES) - Funding Code 001.

Conflict of Interest

The authors confirm that there is no conflict of interest related to the article.

Author Contributions

Verónica Bautista-Robles: conceptualization; data curation; formal analysis; investigation; visualization; writing – original draft. Hady Keita: conceptualization; data curation; investigation; writing – review & editing. Edgar Julián Paredes Gamero: conceptualization; data curation; project administration; supervision; validation. Layna Tayná Brito Leite: conceptualization; formal analysis; investigation. Jessica de Araújo Isaías Muller: data curation; formal analysis; investigation. Mônica Cristina Toffoli Kadri: data curation; formal analysis; investigation; supervision; validation. Ariadna Lafourcade Prada: conceptualization; formal analysis; investigation; writing – original draft. Jesús Rafael Rodríguez Amado: conceptualization; formal analysis; project administration; supervision; validation; writing – review & editing.

ORCID® iDs

Verónica Bautista-Robles - https://orcid.org/0000-0003-1338-7657
Hady Keita - https://orcid.org/0000-0001-9168-8995
Edgar Julián Paredes Gamero - https://orcid.org/0000-0003-3686-8402
Layna Tayná Brito Leite - https://orcid.org/0009-0000-6173-1649
Jessica de Araújo Isaías Muller - https://orcid.org/0000-0003-2493-9330
Mônica Cristina Toffoli Kadri - https://orcid.org/0000-0003-4160-4444
Ariadna Lafourcade Prada - https://orcid.org/0000-0003-1648-0865
Jesús Rafael Rodríguez Amado - https://orcid.org/0000-0001-7574-6219

Data Availability Statement

Data generated and analyzed during this study is available from the corresponding author upon reasonable request.

Preprint

A non-peer-reviewed version of this article has been previously published as a preprint: https://doi.org/10.3762/bxiv.2025.18.v1

References

1. Dario, M. F.; Oliveira, F. F.; Marins, D. S. S.; Baby, A. R.; Velasco, M. V. R.; Löbenberg, R.; Bou-Chacra, N. A. *Ind. Crops Prod.* **2018,** *112,* 305–312. doi:10.1016/j.indcrop.2017.12.021

2. Borges, C. E.; dos Santos, J. C. B.; Evaristo, A. B.; da Cunha, T. G.; Von dos Santos Veloso, R.; Barroso, G. M.; Souza, P. G. C.; da Silva, R. S. *Theor. Appl. Climatology* **2021,** *146,* 1069–1078. doi:10.1007/s00704-021-03788-6
3. Andrade, A. C.; Marinho, J. F. U.; de Souza, A. C.; de Sousa Tavares, T.; Dias, D. R.; Schwan, R. F.; Nunes, C. A.; Bastos, S. C. *Food Res. Int.* **2020,** *136,* 109595. doi:10.1016/j.foodres.2020.109595
4. Sanjinez-Argandoña, E. J.; Chuba, C. A. M. *Rev. Bras. Frutic.* **2011,** *33,* 1023–1028. doi:10.1590/s0100-29452011000300040
5. del Río, J. C.; Evaristo, A. B.; Marques, G.; Martín-Ramos, P.; Martín-Gil, J.; Gutiérrez, A. *Ind. Crops Prod.* **2016,** *84,* 294–304. doi:10.1016/j.indcrop.2016.02.018
6. Bressan, J.; Hermsdorff, H. H. M.; Zulet, M. Á.; Martínez, J. A. *Arq. Bras. Endocrinol. Metabol.* **2009,** *53,* 572–581. doi:10.1590/s0004-27302009000500010
7. Lieb, V. M.; Schex, R.; Esquivel, P.; Jiménez, V. M.; Schmarr, H.-G.; Carle, R.; Steingass, C. B. *NFS J.* **2019,** *14–15,* 6–13. doi:10.1016/j.nfs.2019.02.002
8. Souza, L. T. A.; Oliveira, J. S.; Rodrigues, M. Q. R. B.; dos Santos, V. L.; Pessela, B. C.; Resende, R. R. *Microb. Cell Fact.* **2015,** *14,* 87. doi:10.1186/s12934-015-0266-9
9. César, A. d. S.; Almeida, F. d. A.; de Souza, R. P.; Silva, G. C.; Atabani, A. E. *Renewable Sustainable Energy Rev.* **2015,** *49,* 1213–1220. doi:10.1016/j.rser.2015.04.125
10. Oliveira, U. F.; Costa, A. M.; Roque, J. V.; Cardoso, W.; Motoike, S. Y.; Barbosa, M. H. P.; Teofilo, R. F. *Food Chem.* **2021,** *351,* 129314. doi:10.1016/j.foodchem.2021.129314
11. Lescano, C. H.; Iwamoto, R. D.; Sanjinez-Argandoña, E. J.; Kassuya, C. A. L. *J. Med. Food* **2015,** *18,* 656–662. doi:10.1089/jmf.2014.0077
12. Abduljaleel, Y. R.; Jwaid, A. H.; Hussein, A. K. *J. Med. Life* **2023,** *16,* 1519–1526. doi:10.25122/jml-2023-0107
13. Hussain, S.; Ur-Rehman, M.; Arif, A.; Cailleau, C.; Gillet, C.; Saleem, R.; Noor, H.; Naqvi, F.; Jabeen, A.; Atta-ur-Rahman; Iqbal Choudhary, M.; Fattal, E.; Tsapis, N. *Int. J. Pharm.* **2023,** *643,* 123227. doi:10.1016/j.ijpharm.2023.123227
14. Temporelli, P. L.; Zito, G. B.; Pedretti, R. F.; Belisarii, F. I.; Putortì, G.; Faggiano, P. *Monaldi Arch. Chest Dis.* **2014,** *82,* 165–170. doi:10.4081/monaldi.2014.58
15. Ventura, M. T.; Cenci, L.; Giuliano, G.; Di Corato, R.; Matino, M. G.; Tursi, A. *Immunopharmacol. Immunotoxicol.* **1999,** *21,* 455–468. doi:10.3109/08923979909007120
16. Hsieh, P.-H.; Wu, O.; Geue, C.; McIntosh, E.; McInnes, I. B.; Siebert, S. *Ann. Rheum. Dis.* **2020,** *79,* 771–777. doi:10.1136/annrheumdis-2019-216243
17. Roodenrijs, N. M. T.; Welsing, P. M. J.; van der Goes, M. C.; Tekstra, J.; Lafeber, F. P. J. G.; Jacobs, J. W. G.; van Laar, J. M. *Rheumatology (Oxford, U. K.)* **2021,** *60,* 4681–4690. doi:10.1093/rheumatology/keab078
18. Verstappen, S. M. M. *Rheumatology (Oxford, U. K.)* **2017,** *56,* 1051–1052. doi:10.1093/rheumatology/kew428
19. Coimbra, M. C.; Jorge, N. *J. Food Sci.* **2011,** *76,* C1156–C1161. doi:10.1111/j.1750-3841.2011.02358.x
20. Choi, S. J.; McClements, D. J. *Food Sci. Biotechnol.* **2020,** *29,* 149–168. doi:10.1007/s10068-019-00731-4
21. Patel, R. B.; Patel, M. R.; Thakore, S. D.; Patel, B. G. Nanoemulsion as a Valuable Nanostructure Platform for Pharmaceutical Drug Delivery. In *Nano- and Microscale Drug Delivery Systems;* Grumezescu, A. M., Ed.; Elsevier: Amsterdam, Netherlands, 2017; pp 321–341. doi:10.1016/b978-0-323-52727-9.00017-0
22. Prada, A. L.; Amado, J. R. R.; Keita, H.; Zapata, E. P.; Carvalho, H.; Lima, E. S.; de Sousa, T. P.; Carvalho, J. C. T. *Biomed. Pharmacother.* **2018,** *103,* 421–428. doi:10.1016/j.biopha.2018.04.059
23. Salvia-Trujillo, L.; Soliva-Fortuny, R.; Rojas-Graü, M. A.; McClements, D. J.; Martín-Belloso, O. *Annu. Rev. Food Sci. Technol.* **2017,** *8,* 439–466. doi:10.1146/annurev-food-030216-025908
24. Ansari, S. H.; Islam, F.; Sameem, M. *J. Adv. Pharm. Technol. Res.* **2012,** *3,* 142–146. doi:10.4103/2231-4040.101006
25. Gupta, A.; Eral, H. B.; Hatton, T. A.; Doyle, P. S. *Soft Matter* **2016,** *12,* 2826–2841. doi:10.1039/c5sm02958a
26. Kumari, A.; Kumar, V.; Yadav, S. K. *Trends Med. Res.* **2012,** *7,* 34–42. doi:10.3923/tmr.2012.34.42
27. McClements, D. J. *Curr. Opin. Colloid Interface Sci.* **2012,** *17,* 235–245. doi:10.1016/j.cocis.2012.06.002
28. Nunes, Â. A.; Buccini, D. F.; dos Santos Jaques, J. A.; Portugal, L. C.; Guimarães, R. C. A.; Favaro, S. P.; de Araújo Caldas, R.; Carvalho, C. M. E. *J. Funct. Foods* **2020,** *75,* 104295. doi:10.1016/j.jff.2020.104295
29. Duarte, J. L.; Amado, J. R. R.; Oliveira, A. E. M. F. M.; Cruz, R. A. S.; Ferreira, A. M.; Souto, R. N. P.; Falcão, D. Q.; Carvalho, J. C. T.; Fernandes, C. P. *Rev. Bras. Farmacogn.* **2015,** *25,* 189–192. doi:10.1016/j.bjp.2015.02.010
30. Silva, P. V. B. Caracterização química e avaliação do potencial antidiabético e citotóxico de óleo extraído de *Acrocomia aculeata* (macaúba). Dissertação (Mestrado). Dourados-MS. Brasil, 2012.
31. da Silva, P. V. B.; Ramiro, M. M.; Iriguchi, E. K. K.; Corrêa, W. A.; Lowe, J.; Cardoso, C. A. L.; Arena, A. C.; Kassuya, C. A. L.; Muzzi, R. M. *Nat. Prod. Res.* **2019,** *33,* 2413–2416. doi:10.1080/14786419.2018.1446006
32. Monteiro-Alfredo, T.; Oliveira, S.; Amaro, A.; Rosendo-Silva, D.; Antunes, K.; Pires, A. S.; Teixo, R.; Abrantes, A. M.; Botelho, M. F.; Castelo-Branco, M.; Seiça, R.; Silva, S.; de Picoli Souza, K.; Matafome, P. *Nutrients* **2021,** *13,* 2856. doi:10.3390/nu13082856
33. Belmonte-Herrera, B. H.; Domínguez-Avila, J. A.; Wall-Medrano, A.; Ayala-Zavala, J. F.; Preciado-Saldaña, A. M.; Salazar-López, N. J.; López-Martínez, L. X.; Yahia, E. M.; Robles-Sánchez, R. M.; González-Aguilar, G. A. *Nutrients* **2022,** *14,* 3663. doi:10.3390/nu14173663
34. OMS/FAO. *Organización de las Naciones Unidas para la Alimentación y la Agricultura,* 1999. https://www.fao.org/fao-who-codexalimentarius/sh-proxy/en/?lnk=1&url=https%253A%252F%252Fworkspace.fao.org%252Fsites%252Fcodex%252FStandards%252FCXS%2B210-1999%252FCXS_210s.pdf.
35. Barros Gomes, P. R.; Mouchrek Filho, V. E.; Ferreira Rabêlo, W.; Albuquerque do Nascimento, A.; Costa Louzeiro, H.; Da Silva Lyra, W.; Alves Fontenele, M. *Rev. Colomb. Cienc. Quim.-Farm.* **2018,** *47,* 37–52. doi:10.15446/rcciquifa.v47n1.70657
36. Faria e Souza, B. S.; Carvalho, H. O.; Taglialegna, T.; Barros, A. S. A.; da Cunha, E. L.; Ferreira, I. M.; Keita, H.; Navarrete, A.; Carvalho, J. C. T. *J. Med. Food* **2017,** *20,* 830–837. doi:10.1089/jmf.2017.0027
37. Keita, H.; Ramírez-San Juan, E.; Paniagua-Castro, N.; Garduño-Siciliano, L.; Quevedo, L. *Diabetol. Metab. Syndr.* **2013,** *5,* 53. doi:10.1186/1758-5996-5-53

38. Brito Mariano, R. G.; Da Silva, C. M.; Couri, S.; Nogueira, R. I.; Freitas, S. P. *Defect Diffus. Forum* **2011,** *312–315,* 554–559. doi:10.4028/www.scientific.net/ddf.312-315.554
39. ANVISA. Agencia Nacional de Vigilancia. Agencia Nacional de Vigilancia Sanitaría, ed. 2019, 1. 2019; https://bibliotecadigital.anvisa.gov.br/jspui/bitstream/anvisa/12396/1/Manual%20de%20reda%c3%a7%c3%a3o%20da%20Farmacopeia%20Brasileira%20-%20vers%c3%a3o%20final%20-%20formato%20ANVISA%20.pdf.
40. Hiane, P. A.; Ramos Filho, M. M.; Ramos, M. I. L.; Macedo, M. L. *Braz. J. Food Technol.* **2005,** *8,* 256–259.
41. Amaral, F. P. d.; Broetto, F.; Batistella, C. B.; Jorge, S. M. A. *Energy Agric.* **2011,** *26,* 12–20. doi:10.17224/energagric.2011v26n1p12-20
42. Amado, J. R. R.; Prada, A. L.; Diaz, J. G.; Souto, R. N. P.; Arranz, J. C. E.; de Souza, T. P. *Environ. Sci. Pollut. Res.* **2020,** *27,* 9410–9423. doi:10.1007/s11356-020-07608-8
43. Gadhave, A. *Int. J. Sci. Res.* **2014,** *3,* 573–575.
44. Silva, G. C. R.; Andrade, M. H. C. *J. Food Process Eng.* **2013,** *36,* 134–145. doi:10.1111/j.1745-4530.2011.00657.x
45. Liu, Q.; Huang, H.; Chen, H.; Lin, J.; Wang, Q. *Molecules* **2019,** *24,* 4242. doi:10.3390/molecules24234242
46. Garavand, F.; Jalai-Jivan, M.; Assadpour, E.; Jafari, S. M. *Food Chem.* **2021,** *364,* 130376. doi:10.1016/j.foodchem.2021.130376
47. Silva, E. A.; Prada, A. L.; Boechat, A. L.; Lima, E. S.; Simplício, F. G.; de Souza, T. P.; Rodriguez-Amado, J. R. *Bol. Latinoam. Caribe Plant. Med. Aromat.* **2022,** *21,* 323–342.
48. Astaraki, A. M.; Shirvani, F. *Russ. J. Appl. Chem.* **2020,** *93,* 916–919. doi:10.1134/s1070427220060191
49. Jintapattanakit, A. *Pharm. Sci. Asia* **2018,** *45,* 1–12.
50. Unver, Y.; Yildiz, S.; Acar, M. *Bioprocess Biosyst. Eng.* **2022,** *3,* 553–561. doi:10.1007/s00449-021-02678-5
51. Preté, P. S. C.; Gomes, K.; Malheiros, S. V. P.; Meirelles, N. C.; de Paula, E. *Biophys. Chem.* **2002,** *97,* 45–54. doi:10.1016/s0301-4622(02)00042-x
52. de Souza, F. G.; de Araújo, F. F.; de Paulo Farias, D.; Zanotto, A. W.; Neri-Numa, I. A.; Pastore, G. M. *Food Res. Int.* **2020,** *138,* 109690. doi:10.1016/j.foodres.2020.109690
53. Sousa, L. P.; Alessandri, A. L.; Pinho, V.; Teixeira, M. M. *Curr. Opin. Pharmacol.* **2013,** *13,* 625–631. doi:10.1016/j.coph.2013.03.007
54. Morris, C. J. Carrageenan-Induced Paw Edema in the Rat and Mouse. In *Inflammation Protocols. Methods in Molecular Biology;* Winyard, P. G.; Willoughby, D. A., Eds.; Humana Press: Totowa, NJ, USA, 2003; pp 115–121. doi:10.1385/1-59259-374-7:115
55. Doğan, A.; Yanılmaz, E. M. B.; Karakoc, G.; Parlar, A.; Annaç, E.; Lolak, N.; Akocak, S. *J. Biochem. Mol. Toxicol.* **2025,** *39,* e70217. doi:10.1002/jbt.70217
56. Sandri, G.; Bonferoni, C.; Ferrari, F.; Rossi, S.; Caramella, C. M. The Role of Particle Size in Drug Release and Absorption. In *Particulate Products;* Merkus, H. G.; Meesters, G. M. H., Eds.; Particle Technology Series, Vol. 19; Springer International Publishing: Cham, Switzerland. doi:10.1007/978-3-319-00714-4_11
57. Gertsch, J.; Leonti, M.; Raduner, S.; Racz, I.; Chen, J.-Z.; Xie, X.-Q.; Altmann, K.-H.; Karsak, M.; Zimmer, A. *Proc. Natl. Acad. Sci. U. S. A.* **2008,** *105,* 9099–9104. doi:10.1073/pnas.0803601105
58. United States Pharmacopeia (USP). United States Pharmacopeial Convention, 42nd ed. 2020. http://www.usp.org (accessed Aug 25, 2024).
59. Rodriguez-Amaya, D. B. *A guide to carotenoids analysis in foods;* ILSI Press: Washington, D.C., USA, 2001.
60. Moigradean, D.; Poiana, M. A.; Alda, L. M.; Gogoasa, I. *J. Agroaliment. Processes Technol.* **2013,** *19,* 459–463.
61. Ostertag, F.; Weiss, J.; McClements, D. J. *J. Colloid Interface Sci.* **2012,** *388,* 95–102. doi:10.1016/j.jcis.2012.07.089
62. Prada, A. L.; Amado, J. R. R.; Reis, E. T. d. N.; Bicudo, G.; Perdomo, R. T.; Martines, M. A. U. *Biotechnol. Res. Innovation* **2023,** *7,* e2023014. doi:10.4322/biori.0142023
63. Griffin, W. C. *J. Soc. Cosmet. Chem.* **1954,** *5,* 249–256.
64. Nakayama, G. R.; Caton, M. C.; Nova, M. P.; Parandoosh, Z. *J. Immunol. Methods* **1997,** *204,* 205–208. doi:10.1016/s0022-1759(97)00043-4
65. International Organization for Standardization “(ISO) 10993-5:2009 2009”. https://www.iso.org/obp/ui/en/#iso:std:iso:10993:-5:ed-3:v1:en (accessed Sept 7, 2024).
66. Pitsillides, A. A. *Rheumatology (Oxford, U. K.)* **2004,** *43,* 814. doi:10.1093/rheumatology/keh165
67. Winter, C. A.; Risley, E. A.; Nuss, G. W. *Proc. Soc. Exp. Biol. Med.* **1962,** *111,* 544–547. doi:10.3181/00379727-111-27849

License and Terms

BEILSTEIN JOURNAL OF NANOTECHNOLOGY

Venom-loaded cationic-functionalized poly(lactic acid) nanoparticles for serum production against *Tityus serrulatus* scorpion

Philippe de Castro Mesquita[1], Karla Samara Rocha Soares[1], Manoela Torres-Rêgo[1], Emanuell dos Santos-Silva[1], Mariana Farias Alves-Silva[1], Alianda Maira Cornélio[2], Matheus de Freitas Fernandes-Pedrosa[1] and Arnóbio Antônio da Silva-Júnior[*1]

Full Research Paper

Open Access

Address:
[1]Laboratory of Pharmaceutical Technology and Biotechnology, Department of Pharmacy, Federal University of Rio Grande do Norte (UFRN), Natal, RN, Brazil and [2]Department of Morphology, Federal University of Rio Grande do Norte-UFRN, Natal, RN, Brazil

Email:
Arnóbio Antônio da Silva-Júnior[*] - arnobio.silva@ufrn.br

* Corresponding author

Keywords:
cationic nanoparticles; immunoadjuvant; polyethylenimine; poly(lactic acid); *Tityus serrulatus*

Beilstein J. Nanotechnol. **2025,** *16,* 1633–1643.
https://doi.org/10.3762/bjnano.16.115

Received: 31 May 2025
Accepted: 11 September 2025
Published: 17 September 2025

This article is part of the thematic issue "Advances in nanotechnology applied to natural products".

Guest Editor: D. Dourado

Abstract

Reported accidents involving scorpion poisoning by *Tityus serrulatus* are the most frequent in Brazil. The only specific treatment for envenomation is the administration of antivenoms associated with traditional adjuvants. Novel adjuvants are studied to reduce or avoid side effects and potentialize the efficacy of conventional serum. In this study, poly(lactic acid) nanoparticles were functionalized with polyethylenimine for loading peptides and proteins of *T. serrulatus* venom, and their use as a potential immunoadjuvant was evaluated. The protein loading efficiency of about 100% and the polyacrylamide gel electrophoresis assay confirmed the success of venom loading. Dynamic light scattering and zeta potential analysis supported small and narrow-sized cationic functionalized nanoparticles. Atomic force microscopy and scanning electron microscopy images showed nanoparticles with a spherical and smooth shape. The stability of tested formulations was accessed for six weeks, and the sustained release of proteins controlled by diffusion mechanism was also measured. Finally, in vivo immunization in BALB/c mice showed superior efficacy of the *T. serrulatus* venom protein-loaded nanoparticles compared to the traditional aluminum hydroxide immunoadjuvant. Thus, the formulations shown are promising nanocarriers to be used as a biotechnological approach to immunotherapy against scorpion envenomation.

Introduction

Accidents caused by scorpion envenoming are recognized as an important public health problem in tropical and subtropical regions, due to the high incidence and/or severity of cases, especially for children and elders, and difficulty of management by public health services [1-4]. In Brazil, although 22 species of the scorpion genus *Tityus* have been described in the country,

Tityus serrulatus is a Brazilian scorpion species with great medical significance [2,5], responsible for the highest number of accidents and also the most severe ones [6,7].

Scorpion toxins represent a vast collection (≈100,000) of pharmacologically relevant peptide toxins that have provided an important foundation for advancing the studies in this field [8]. *Tityus serrulatus* venom is comprised of several compounds such as mucus, salts, proteins with high molecular mass, nucleotides, lipids, amino acids, hyaluronidase, hypotension factors, metalloproteases, and neurotoxins [7,9]. However, neurotoxins are considered the main responsible for the envenoming syndrome as well as the most studied [10].

With regard to treatment, in severe scorpion envenoming cases, immunotherapy is the most common approach to protect populations from lethal effects [1,10,11]. Aluminum-based adjuvants have been extensively used to induce long-lasting protective immunity through vaccination [12,13]. However, reported incidences of toxicity and side effects of aluminum have raised concerns regarding their safety in childhood vaccines [13]. Consequently, there is a growing need for alternative immunization strategies that not only improve safety but also effectively deliver complex venom proteins.

The bioactive proteins that compound the *Tityus serrulatus* venom are complex molecules that should have the structural integrity preserved for the specific biological activity. The poor stability of these proteins, both in vivo and in vitro, creates a challenge for drug delivery systems aiming to effectively target affected tissues or cells [14,15]. Nanocarriers have been widely studied for enabling prolonged circulation and sustained drug release over time, depending on their structural properties [16,17]. Therefore, protein delivery through nanoparticles is an effective way to control drug release as well as to design an efficient protein delivery system [16].

Among different materials used for nanocarriers, several polymers have been investigated for producing cationic nanocarriers due to their ability to cross biological barriers, their biocompatibility, and low toxicity [18]. Their manipulation at the nanoscale changes specific surface properties, possibly improving the ability to cross biological barriers targeting the affected tissues [18,19].

In this context, nanoparticle controlled release based on biodegradable polymers such as poly(lactic acid) (PLA) has been investigated [13]. The nanoparticles produced using these synthetic polyesters show neutral or negative zeta potential, which limits the loading of negatively charged macromolecules such as proteins, polypeptides, or DNA [14,20]. The surface of nanoparticles can be modified to achieve high protein loading or avoid a rapid cellular uptake. Using different strategies, nanoparticles have been functionalized with a variety of ligands such as small molecules, surfactants, polymers, and biomolecules [21,22].

The use of cationic molecules, as polyethylenimine (PEI), to change the surface of nanoparticles to a positive potential, improving the interaction with negatively charged biomolecules, is one strategy successfully employed for gene delivery [20,23,24]. These cationic nanoparticles have an absent or weak electrostatic interaction with negatively charged peptides, proteins, antigens, oligonucleotides, polypeptides, or DNA [18].

The PLA is well established to produce nanoparticles as carriers for drugs or biomolecules from a biotechnology source due to its natural metabolism pathway [25,26]. In a recent study, PLA was successfully employed to detoxify, preserve antigenicity, and enhance immune protection against scorpion toxins [11]. At the same time, it has always been a constant effort and focus to either search for alternative adjuvants or to reduce the quantity of aluminum in the vaccines. In this direction, controlled release of micro- and nanoparticulate formulations based on biodegradable polymers such as PLA have been investigated [13,27-32].

A more detailed approach for use of a delivery system as a new nontoxic and non-inflammatory immunoadjuvant is of great importance to public health. The present study was designed with the aim to evaluate the effectiveness of biodegradable PLA polymeric nanoparticles functionalized with PEI as an adjuvant and potential candidate for vaccine delivery against *T. serrulatus* venom.

Results

Protein loading efficiency of the *Tityus serrulatus* scorpion venom

The *T. serrulatus* venom protein-loaded PLA nanoparticles were fabricated by nanoprecipitation methods. In this technique, the PLA nanoparticles (NPs) were produced by low-energy solvent displacement and functionalized with polyethylenimine (cationic polymer) for the *T. serrulatus* protein adsorption.

The NPs showed a mean diameter of 165 nm and a positive zeta potential of 7.0 mV. After the addition of venom, the PLA nanoparticles loaded with *T. serrulatus* venom proteins remained with a narrow particle size distribution. Moreover, an increase in size of the particles occurred after the addition of the venom for both concentrations ($*p < 0.05$), without significantly altering the zeta potential (Table 1). A polydispersity index

(PDI) smaller than 0.3 was required for all the analyses. The quantification of proteins by the bicinchoninic acid (BCA) assay showed an encapsulation efficiency (EE) of 100% for all samples containing *T. serrulatus* venom (Table 1).

The high percentage of protein incorporation was confirmed by the electrophoretic profiles in sodium dodecyl sulfate polyacrylamide gel (SDS-PAGE), after the gel was stained with Coomassie brilliant blue R-250. In this methodology, the nanoparticles are retained in the wells and only the proteins that were not incorporated in the nanoparticles will migrate through the gel. The *T. serrulatus* venom (Tsv) protein presented a molecular mass range of approximately 2 to 66.4 kDa. Comparing the electrophoretic profiles of *T. serrulatus* venom protein-loaded PLA nanoparticles at 0.5% and 1.0% (w/w) with *T. serrulatus* venom was possible to evidence that all proteins of the venom were incorporated within the polymeric matrix, since the protein bands were not evidenced in the gel. The PLA nanoparticles and bovine serum albumin (BSA) were used as controls (Figure 1). This assay corroborates the high encapsulation efficiency obtained by the BCA assay.

Field emission gun scanning electron microscopy and atomic force microscopy analyses

Field emission gun scanning electron microscopy (FEGSEM) and atomic force microscopy (AFM) analyses were realized to access shape and surface features of NPs and *T. serrulatus* venom protein-loaded PLA nanoparticles at 0.5% and 1.0%. For both techniques, the particles showed uniform characteristics with smooth surface, spherical shape, and great encapsulation efficiency. The addition of *T. serrulatus* venom did not alter the spherical shape, as well as the mean diameters of nanoparticles (Figure 2).

Table 1: Encapsulation efficiency (EE), mean diameter and zeta potential of PLA nanoparticles (NPs), *T. serrulatus* venom protein-loaded PLA nanoparticles at 0.5% (NPs + Tsv 0.5%) and *T. serrulatus* venom protein-loaded PLA nanoparticles at 1.0% (NPs + Tsv 1.0%).

Samples	EE (%)	Mean diameter	Zeta potential (mV)
NPs	—	165.0 ± 25.3	7.00 ± 4.10
NPs + Tsv 0.5%	100.0	226.4 ± 13.6*	3.58 ± 1.56
NPs + Tsv 1.0%	100.0	230.9 ± 15.59*	4.40 ± 1.99

Values are the mean ± standard deviation, n = 3; *$p < 0.05$ for the venom group compared to the NPs group.

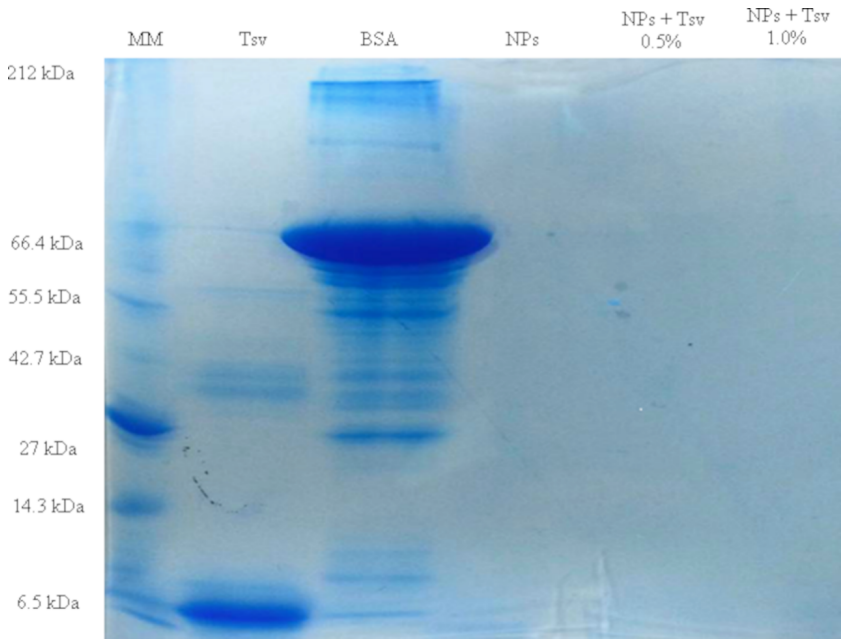

Figure 1: Electrophoretic profile of *Tityus serrulatus* venom (Tsv), bovine serum albumin (BSA), PLA nanoparticles (NPs), *T. serrulatus* venom protein-loaded PLA nanoparticles at 0.5% (NPs + Tsv 0.5%), and *T. serrulatus* venom protein-loaded PLA nanoparticles at 1.0% (NPs + Tsv 1.0%). MM: molecular mass marker. Gel stained with Coomassie brilliant blue R-250.

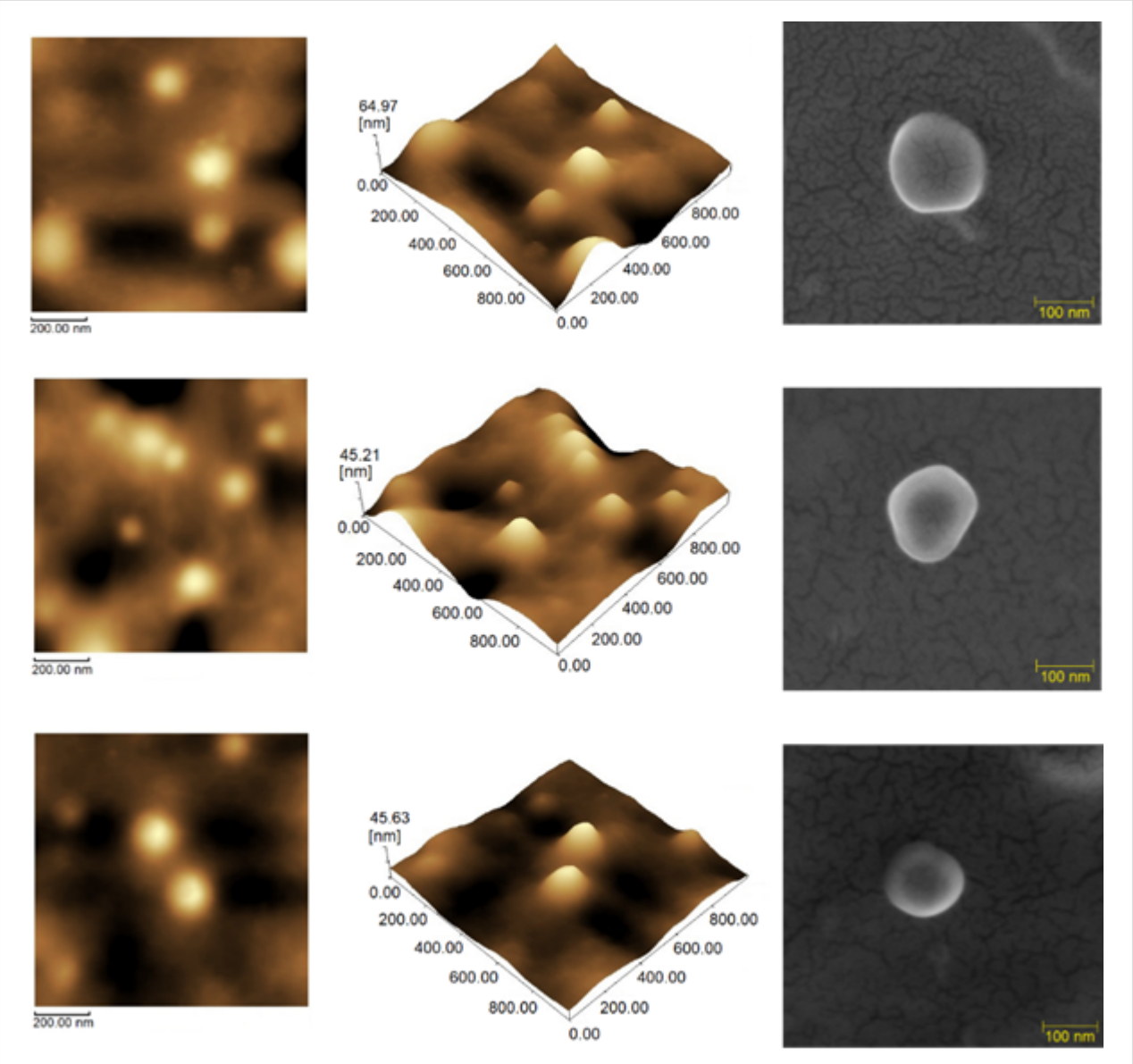

Figure 2: 2D and 3D atomic force microscopy and field emission gun scanning electron microscopy images, respectively, of formulations of *Tityus serrulatus* venom-loaded PLA nanoparticles. (A) PLA nanoparticles, (B) *T. serrulatus* venom protein-loaded PLA nanoparticles at 0.5%, and (C) *T. serrulatus* venom protein-loaded PLA nanoparticles at 1.0%.

Physical stability assay

Distinct NPs with venom-loaded formulations were analyzed for particle size and PDI (Figure 3). The tracking was accomplished for 42 days (six weeks) and the formulations do not show significant differences in particle size (≈225 nm) and PDI (<0.3).

In vitro protein release

The Figure 4 shows the release profile of *T. serrulatus* venom protein-loaded PLA cationic nanoparticles with two different formulations containing 0.5% (Figure 4a) and 1.0% (Figure 4b) (w/w) of Tsv in the nanoparticle suspension. The in vitro protein release studies showed that all samples exhibited a slight initial burst effect, releasing 30–60% of the total protein mass, followed by the subsequent slow release phase. After 144 h, the *Tityus serrulatus* venom-loaded PLA nanoparticles have released about 88% and 50% of the initial loaded protein for the samples containing 0.5% and 1.0% of *T. serrulatus* venom, respectively.

The mechanism of release of venom protein-loaded PLA nanoparticles profile was studied by applying different mathematical models to the experimental data. The data were subject to four different diffusion kinetic linear models: zero order, first

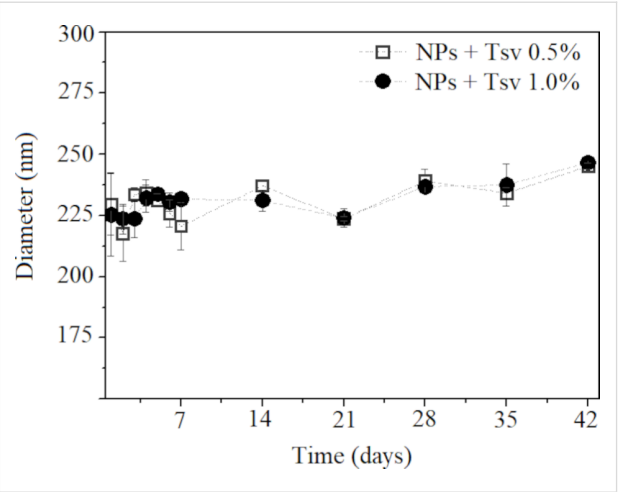

Figure 3: Colloidal stability of *T. serrulatus* venom protein-loaded PLA nanoparticles at 0.5% (NPs + Tsv 0.5%) and *T. serrulatus* venom protein-loaded PLA nanoparticles at 1.0% (NPs + Tsv 1.0%) in the period of six weeks. The data are expressed as mean ± standard deviation.

order, Korsmeyer–Peppas, and parabolic diffusion (Table 2). The zero order, first order, and Korsmeyer–Peppas models exhibiting determination coefficient (r^2) values demonstrate that the release mechanism cannot be explained by these models. The parabolic diffusion model better fitted the venom release from PLA cationic nanoparticles, providing a linear correlation coefficient of 0.975 and 0.967 for 0.5% and 1.0% venom concentrations, respectively.

Serum antibody responses

The immunization protocol was based in subcutaneous administration for six weeks with 100 µL of venom-loaded NPs or aluminum hydroxide (AH) at concentrations of 0.5% or 1.0% (w/w). The blood samples were treated and subjected to serial dilutions with a PBS/BSA 0.1% solution, and the antibody production was evaluated by enzyme-linked immunosorbent assay (ELISA). The antibody dilutions were detected in the serum of mice immunized with NPs and AH, both venom loaded. At first, NP formulations can produce more antibodies than AH formulations when analyzed in the first dilution (1:25), $^{**}p < 0.01$. Venom-loaded nanoparticles at 1.0% showed higher

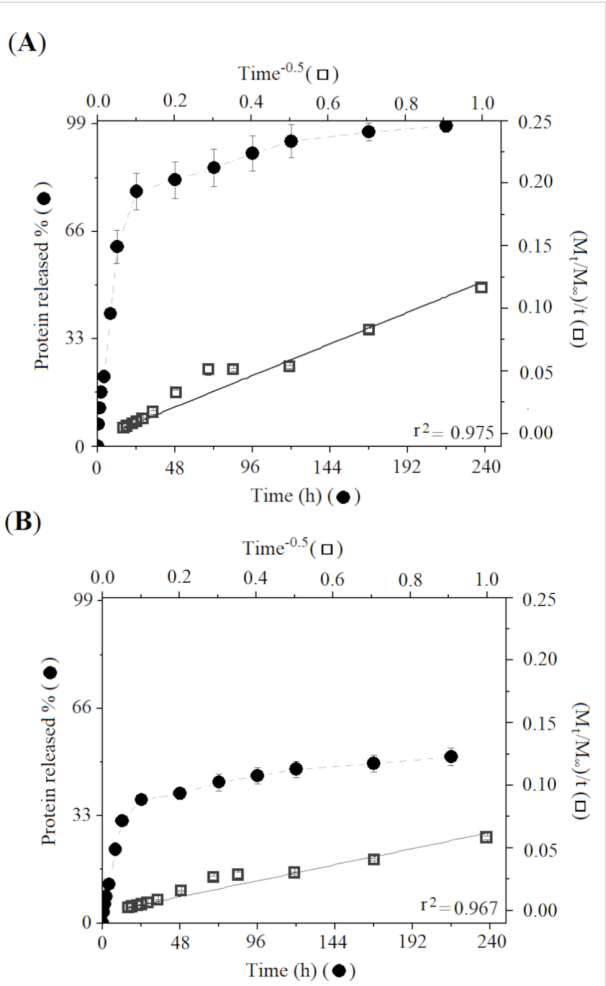

Figure 4: Experimental in vitro release profile of *T. serrulatus* venom-loaded PLA nanoparticles at 0.5, r^2: 0.975 (A) and 1.0%, r^2: 0.967 (B). The release profile of each sample is represented by dots. The data are expressed as mean ± standard deviation.

effectiveness when compared to venom-loaded AH at 1.0%, while the nanosystems at 0.5% demonstrated to be equipotent to AH 0.5%. The NP formulation produced antibodies that were detected until the 1:3,200 dilution, whereas the AH formulation produced antibodies that were detected until the 1:1,600 dilution. The Figure 5 shows the antibody production results from

Table 2: Different kinetic mathematical models for the in vitro release *T. serrulatus* venom protein-loaded PLA nanoparticles at 0.5% (NPs + Tsv 0.5%) and *T. serrulatus* venom protein-loaded PLA nanoparticles at 1.0% (NPs + Tsv 1.0%).

Kinetic models	NPs + Tsv 0.5% (r^2)	NPs + Tsv 1.0% (r^2)
zero order	0.701	0.648
first order	0.412	0.401
Korsmeyer–Peppas	0.940	0.922
parabolic diffusion	0.975	0.967

mice immunized with venom-loaded nanoparticles and aluminum hydroxide, demonstrating higher effectiveness of NPs at a 1.0% concentration compared to that of AH. Nanoparticle results were statistically different to those of the AH immunized groups, and demonstrated that the nanoparticles can stimulate the immune system with low concentration of antigens/venom.

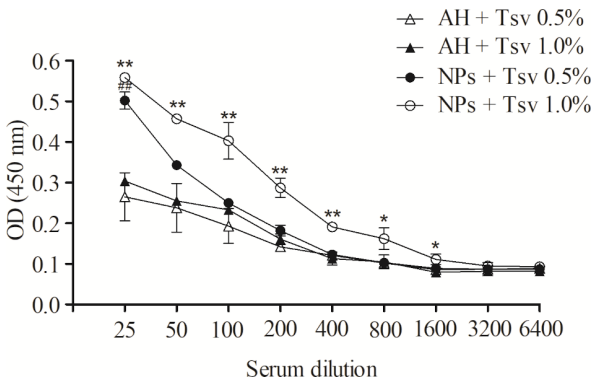

Figure 5: Evaluation of antibody production from mice immunized subcutaneously for six weeks with *Tityus serrulatus* venom-loaded NPs or AH at concentrations of 0.5% or 1.0% determined by ELISA. The data are expressed as mean ± standard deviation. $^{**}p < 0.01$ and $^{*}p < 0.05$ compared to NPs + Tsv 1.0% group with AH + Tsv 1.0%. $^{\#\#}p < 0.01$ compared to NPs + Tsv 0.5% group with AH + Tsv 0.5%.

Discussion

Figure 1 shows the electrophoretic profiles in an SDS-PAGE gel, which suggests high percentage of protein incorporation in cationic nanoparticles and total encapsulation. It is possible to observe the absence of any free protein migrate through the gel for *T. serrulatus* venom protein-loaded PLA nanoparticles at 0.5% and 1.0% (w/w) compared with non-encapsulated proteins. This achievement corroborates with encapsulation efficiency experiments. In the present approach, PLA nanoparticles loaded with *Tityus serrulatus* venom proteins were successfully obtained using parameters selected for the nanoprecipitation method. This low-energy technique allowed the spontaneous self-assembling of PLA nanoparticles, which were functionalized with polyethyleneimine (PEI) to enable the adsorption of venom proteins. Experimental results demonstrated the potential for use in therapeutic serum production against *T. serrulatus*, one of the most dangerous scorpions in South America.

Poly(lactic acid) nanoparticles show neutral or negative zeta potential, which limits the loading of negatively charged species [33]. For this, the surface of the PLA nanoparticles was functionalized with PEI, a hydrophilic polymer that provides a positive surface charge. This modification enhances high macromolecule loading or improves the cell interaction and cellular uptake [22,33,34]. The cationic character induces biomolecules with negative charges, such as proteins, peptides, DNA, RNA, antigens, and oligonucleotides to be efficiently incorporated through electrostatic interactions [35,36]. Moreover, some studies showed the interesting association of nanoparticles containing PEI for incorporation of DNA in gene transfection and BSA protein [14,37].

The physicochemical characterization of the nanoparticles revealed mean diameters below 230 nm, positive zeta potentials, and PDI below 0.3, corroborating other reports of PLA–PEI systems [14,38]. In addition, the high encapsulation efficiency can be attributed to the functionalizing agent (PEI), which demonstrates a certain advantage over the polymer, and it is responsible for the nanoparticle cationic character, ensuring binding of venom proteins. Similar results were obtained using the ionic affinity interaction to bind negatively charged proteins of the *T. serrulatus* scorpion venom to the amine groups of cationic nanoparticles prepared by ionic gelation with 100% encapsulation efficiency [1,2]. Additionally, PEI with high branching density has been shown to enhance complexation and transfection efficiency [23].

The morphology obtained by AFM and FEGSEM showed particles with a smooth surface, spherical shape, uniform aspects, and sizes compatible with the results obtained by dynamic light scattering. These morphological features are known to influence the biological activity of nanoparticles loaded with bioactive molecules, directly affecting their release. The release profile of a substance depends on the particle size; thus, small particles have a larger surface area for dissolution, providing faster release kinetics [39]. Uniformity of particle size is also important for the stability of the formulation, as well as for the choice of administration route. The intravenous and intramuscular routes are very common for the administration of proteins with pharmacological activity and with particle sizes of around 200 nm [40].

Regarding stability, only minimal changes in physicochemical parameters were observed, indicating colloidal stability of the nanoparticle formulation. This is particularly relevant as nanoparticles have a natural tendency to agglomerate, often leading to the formation of larger aggregates [41]. It is interesting to report that the presence of electrostatic charges on the surface of particles plays a crucial role in maintaining physical stability. However, long-term colloidal stability observed in the formulations with low zeta potential values can be attributed to steric stabilization provided by poly(vinyl alcohol) (PVA) and an additional electrostatic repulsion introduced by surface-bound PEI. This behavior is consistent with previous reports on nanoprecipitation systems that utilize surfactants [26]. The stability

of venom-loaded nanoparticles did not exhibit significant changes in particle size, which can be explained by the complex interplay of charges derived from the polycation (PEI) and venom proteins. The net repulsive forces between particles offer a barrier to aggregation and support long-term colloidal stability [14,37].

The protein release study of venom-loaded PLA cationic nanoparticles occurred in two stages. In the first stage, a burst release effect was due to surface-adsorbed proteins, followed by the diffusion through the external swollen layer of particles, and a slow release equilibrium state was demonstrated for distinct formulations [1]. Successful protein-loaded PLA cationic nanoparticles, previously demonstrated, ensured the desired slow-release protein profile effect for all tested formulations. As shown in Figure 4A and Figure 4B, based on the analysis of the determination coefficient (r^2), obtained from the application of four mathematical models to experimental data, the model that explains the release profile of the venom-loaded PLA nanoparticles has been identified, and a more accurate adjustment was observed for the parabolic diffusion model. This mathematical model suggests that the release mechanism of venom-loaded PLA nanoparticles was controlled by diffusion dependent on the protein-loading level [18]. These results corroborate with previous studies that used nanoparticles for venom protein delivery [42,43].

During an immune response against poisoning, some toxins are poorly immunogenic, and due to that, they are associated with immunoadjuvants. Information about the efficiency of immunoadjuvants can be accessed by immunization protocols [44]. Venom-loaded NPs obtained better efficiency in the stimulation to the immune system when compared to that of AH. Similar results were found in experiments performed by Ayari-Riabi (2016) using a PLA nanoparticle formulation to stimulate immune response against the venom from *Androctonus australis hector* and *Buthus occitanus tunetanus* scorpions. However, PLA nanoparticles had the same response when compared with that of AH standard formulation [11]. Cationic PLA nanoparticles produced in this study demonstrated better immune stimulation behavior. These results can be found in other chitosan-based cationic nanoparticle formulations [1,45]. The cationic properties probably explain the immune response improvement since different nanoparticle types generated stronger Th1 and Th2 immune responses compared to other antigen types [45].

Although the present study provides physicochemical and immunological data supporting the potential of PLA–PEI nanoparticles as antigen carriers, further investigation is required to assess their safety profile. In vitro cytotoxicity assays on relevant cell lines, particularly immune or epithelial cells and long-term biocompatibility studies, including histopathological analysis following repeated administration, will be essential to evaluate the potential of these nanosystems. These aspects are part of our ongoing research and will be addressed in future studies, aiming to support the translational advancement and industrial applicability of this nanoplatform.

Conclusion

In conclusion, the enhanced immunoadjuvant effect by functionalized cationic PLA nanoparticles adsorbed with negatively charged proteins was successfully developed by low-energy solvent diffusion method, producing effective and stable spherical cationic nanoparticles. The positive surface charge enabled a high protein incorporation into particles. The prolonged release effect showed a slow release of venom-loaded nanoparticles. Moreover, the biological efficacy of the nanosystems showed that cationic nanoparticles can stimulate the immune system to increase the immune response against *T. serrulatus* venom when compared to the most used immunoadjuvant, aluminum hydroxide. Thus, all data demonstrate a good performance of the nanoprecipitation method to generate small-sized protein-loaded polymeric nanoparticles which can be used as a novel immunoadjuvant.

Experimental

Material

Poly(D,L-lactic acid) (D,L-PLA) 50:50 (inherent viscosity 0.63 $dL \cdot g^{-1}$ at 30 °C) was purchased from Birmingham Polymers Inc. (Birmingham, United States of America). Poly(vinyl alcohol) with molecular weight of 30 to 70 kDa and 86.5 to 89.5 kDa when hydrolyzed, hyper-branched PEI with average molecular weight of 25 kDa, BSA, and aluminum hydroxide were purchased from Sigma-Aldrich® (Saint Louis, Missouri, United States of America). The BCA Protein Assay Kit was purchased from Pierce Biotechnology (Woburn, Massachusetts, United States of America) and mouse IgG total ELISA was purchased from eBioscience (San Diego, California, United States of America). Purified water (1.3 $\mu S \cdot cm^{-1}$) was prepared from a reverse osmosis purification equipment (model OS50 LX, Gehaka, São Paulo, Brazil). All other reagents were of analytical grade.

Venom

Lyophilized *Tityus serrulatus* scorpion venom was generously supplied by the Instituto Butantan, São Paulo, Brazil. The scientific use of the biological material was approved by the Brazilian Access Authorization and Dispatch Component of Genetic Patrimony (CGen) (Process 010844/2013-9, 25 October 2013). The venom was weighed and dissolved with PBS at 1 mg/mL, aliquoted, and stored at −20 °C until used.

Preparation of cationic PLA nanoparticles for *Tityus serrulatus* venom delivery

In a manner similar to [14], PLA NPs) were prepared by nanoprecipitation, up to a 30:70 (%) ratio of organic and aqueous phase (OP:AP). The organic phase was set up with 6 mL of acetone solution containing PLA (0.1% w/v) and PEI (0.1% w/v) to 14 mL of the aqueous phase containing PVA (1.0% w/v), at an output flux of 3.0 mL·min^{-1}. After titrations, the acetone organic solvent evaporation occurred under a 700 rpm of magnetic stirring overnight. After solvent evaporation, colloidal dispersions were centrifuged at 22,000*g* for 5 minutes. The *T. serrulatus* venom loading in the cationic nanoparticles was tested at two different formulations containing 0.5% and 1.0% (w/w) of Tsv in the nanoparticle suspension. The venom aqueous solution was added to the colloidal dispersion containing the cationic-functionalized NPs at 22 °C, which remained under magnetic stirring at 360 rpm for 5 h.

Physicochemical aspects of nanoparticles

The mean particle size, PDI, zeta potential, and stability of the nanoparticles were assessed by using the cumulative analysis method, according to the intensity of DLS with a particle size analyzer (ZetaPlus, Brookhaven Instruments Corporation, New York, United States of America), equipped with a 90 Plus/BI-MAS apparatus, at a wavelength of 659 nm with a scattering angle of 90°. For the analysis, 100 µL of the nanoparticle suspension was diluted in 900 µL of deionized water (1:10 dilution) to ensure dispersions within a suitable experimental range (100–500 kcps). For the colloidal stability assay, the nanoparticles were stored at a temperature of 4.0 ± 2.0 °C, and every seven days particle sizes were analyzed during six weeks. A polydispersity index smaller than 0.5 was required for all the experiments. All analyses were performed in triplicate and data expressed as mean ± standard deviation.

The shape and surface of nanoparticles were assessed by AFM (SPM-9700 Shimadzu, Tokyo, Japan) and FEGSEM (Zeiss Microscopy, Auriga, Jena, Germany) images. For the AFM analyzes, a drop of dispersion was placed on a clean microscope slide and dried under a desiccator for 24 h. The images were obtained with a silicon tip, operating in the attractive region of a cantilever in non-contact mode. For the FEGSEM analyzes, a drop of dispersion was placed in a microscope slide with carbon tapes and dried under a desiccator for 24 h [46].

Protein-loading efficiency

The different concentration samples of protein-loaded PLA nanoparticles were carefully transferred to 1.5 mL centrifuge tubes, and then centrifuged at 20,000*g* at 4 °C for 30 min. The protein concentration of the supernatant was quantified using a BCA Protein Assay Kit (Thermo Fisher Scientific) according to the manufacturer recommendations, and a microplate reader (Epoch, BioTek®, Winooski, Vermont, United States of America) at 562 nm [47] was used. The encapsulation efficiency performed was calculated using Equation 1. All analyses were performed in triplicates and data expressed in percentage.

$$\mathrm{EE\%} = \left[\frac{\text{total proteins} - \text{free proteins}}{\text{total proteins}}\right] \times 100, \quad (1)$$

where "total proteins" is the total protein amount added and "free proteins" is the non-entrapped protein in the supernatant after centrifugation.

Sodium dodecyl sulfate in polyacrylamide gel electrophoresis

The electrophoretic profile of *T. serrulatus* venom, free-protein nanoparticles, and different concentrations of protein-loaded nanoparticles were recorded by SDS-PAGE electrophoresis using a minigel system (Mini-Protean® II, BIO-RAD, Hercules, California, United States of America). The molecular weight markers were commercially obtained (Gibco-BRL Life Technologies, Gaithersburg, Maryland, United States of America). The gel was stained with Coomassie Brilliant Blue R-250 solution and scanned [48].

In vitro protein release

To monitor the protein release profile, 1.5 mL of venom-loaded nanoparticles (0.1% PLA w/v, 1% venom w/w) were suspended in 1 mL of phosphate buffer solution (pH 7.4, KH_2PO_4 0.05 mol·L^{-1}), in a thermostatic bath (SL-150/22; Solab, Piracicaba, Brazil) at 37 °C. At predetermined time intervals, 100 µL of the suspension was collected and centrifuged at 16,000*g* for 30 min to sediment any residual particles. The supernatant was carefully removed for analysis, and the total protein released was quantified using the BCA Protein Assay Kit (Thermo Fisher Scientific), following the manufacturer instructions. After each collection, the same volume of fresh buffer was added to the tube to maintain constant volume and sustain sink conditions throughout the experiment [14].

Animals

BALB/c mice (about 30 g, 6–8 weeks old), from both sexes were used for the studies. The animals were maintained at 22 ± 2 °C and in a 12 h dark/12 h light cycle, with free access to standard laboratory chow and water. Each experimental group was composed of five animals (n = 5). After the experiments, all animals were euthanized with an overdose of thiopental (100 mg/kg) associated with an intraperitoneal injection of lidocaine 2% (10 mg/kg) followed by cervical dislocation. The experimental protocol was approved by the Committee for Ethics

in Animal Experimentation of the Federal University of Rio Grande do Norte (UFRN), Brazil (Protocol No. 015/2015).

Immunization

Mice received 100 µL of PBS, free-cationic nanoparticles, aluminum hydroxide, *Tityus serrulatus* venom (0.5 or 1.0% w/w) loaded nanoparticles or associated with AH. The immunization was performed once per week for six times via subcutaneous administration in the lumbar region [2].

Serum production

Blood samples in the absence of anticoagulants were incubated at 37 ºC. After 30 min, the samples were incubated at 4 ºC for 2 h and then were centrifuged at 15,000*g* at 4 ºC for 5 min. The supernatant (serum) was then collected and stored at −20 ºC.

Antibody titer evaluation

The antibody titers were determined according to Fernandes-Pedrosa et al. 2002 [31]. The plate was sensitized with 100 µL/well of a venom solution in PBS (10 µg/mL w/v), followed by incubation overnight at 4 °C. Afterward, the wells were washed twice with 200 µL of washer buffer (PBS/Tween 0.05%) and a 100 µL of blocking solution (PBS/BSA 5%) was added, followed by incubation at 37 °C for 2 h. The plate was washed and 100 µL/well of each pre-diluted serum (PBS/BSA 0.1%) were added and then incubated at 37 °C for 1 h. Subsequently, 100 µL/well of conjugated antibodies were added and the plate was incubated at 37 °C for 1 hour. The plate was washed and 50 µL/well of diluted detection antibodies was added and incubated for 3 h. The plate was then washed again, the substrate was added, and the plate was incubated at room temperature for 15 min. The reaction was stopped (H_2SO_4 4 M) and the plate was read at 450 nm.

Statistical analysis

The results are expressed as mean ± standard deviation. Statistical analyses were realized using one-way analysis of variance (ANOVA) with Tukey's test using GraphPad Prism version 5.00 (San Diego, CA, USA). Differences in the mean values with *** or $^{###}p < 0.001$, ** or $^{##}p < 0.01$, or * or $^{#}p < 0.05$ were considered statistically significant.

Acknowledgements

The authors acknowledge the Department of Materials and Engineering of the Federal University of Rio Grande do Norte for the SEM and AFM analyses.

Funding

The authors are grateful for the financial support from the National Council for Scientific and Technological Development (CNPq) (process numbers: 436051/2018-4; 311209/2020-3). They also thank the National Institute of Science and Technology of the Health Economic-Industrial Complex - iCEIS (CNPq,406264/2022-8). This study was also financed in part by the Coordenação de Aperfeiçoamento de Pessoal de Nível Superior – Brasil (CAPES) – Finance Code 001".

Author Contributions

Philippe de Castro Mesquita: conceptualization; investigation. Karla Samara Rocha Soares: investigation; methodology. Manoela Torres-Rêgo: investigation; methodology. Emanuell dos Santos-Silva: investigation; methodology. Mariana Farias Alves-Silva: writing – original draft. Alianda Maira Cornélio: visualization; writing – review & editing. Matheus de Freitas Fernandes-Pedrosa: conceptualization; funding acquisition; resources; writing – original draft; writing – review & editing. Arnóbio Antônio da Silva-Júnior: conceptualization; funding acquisition; project administration; resources; supervision; visualization; writing – review & editing.

ORCID® iDs

Manoela Torres-Rêgo - https://orcid.org/0000-0002-8535-1533
Mariana Farias Alves-Silva - https://orcid.org/0000-0001-9373-3585
Alianda Maira Cornélio - https://orcid.org/0000-0001-5762-2538
Matheus de Freitas Fernandes-Pedrosa - https://orcid.org/0000-0003-4221-9580
Arnóbio Antônio da Silva-Júnior - https://orcid.org/0000-0002-7516-1787

Data Availability Statement

All data that supports the findings of this study is available in the published article and/or the supporting information of this article.

References

1. Rocha Soares, K. S.; Oliveira, A. R.; Daniele-Silva, A.; Glaucia-Silva, F.; Caroni, A. L. P.; Fernandes-Pedrosa, M. F.; da Silva-Júnior, A. A. *J. Mol. Liq.* **2017,** *241,* 540–548. doi:10.1016/j.molliq.2017.06.071
2. Araújo, K. A. M. d.; Torres-Rêgo, M.; Gurgel-Medeiros, T.; Silva-Júnior, A. A. d.; Leite, R. d. S.; Daniele-Silva, A.; Fernandes-Pedrosa, M. d. F. *Heliyon* **2024,** *10,* e24190. doi:10.1016/j.heliyon.2024.e24190
3. Nait Mohamed, F. A.; Laraba-Djebari, F. *Vaccine* **2016,** *34,* 2692–2699. doi:10.1016/j.vaccine.2016.04.035
4. Chippaux, J.-P.; Goyffon, M. *Acta Trop.* **2008,** *107,* 71–79. doi:10.1016/j.actatropica.2008.05.021
5. Carmo, A. O.; Oliveira-Mendes, B. B. R.; Horta, C. C. R.; Magalhães, B. F.; Dantas, A. E.; Chaves, L. M.; Chávez-Olórtegui, C.; Kalapothakis, E. *Toxicon* **2014,** *90,* 45–55. doi:10.1016/j.toxicon.2014.07.014
6. Bucaretchi, F.; Fernandes, L. C. R.; Fernandes, C. B.; Branco, M. M.; Prado, C. C.; Vieira, R. J.; De Capitani, E. M.; Hyslop, S. *Toxicon* **2014,** *89,* 17–25. doi:10.1016/j.toxicon.2014.06.022
7. Pucca, M. B.; Cerni, F. A.; Peigneur, S.; Bordon, K. C. F.; Tytgat, J.; Arantes, E. C. *Toxins* **2015,** *7,* 2534–2550. doi:10.3390/toxins7072534

8. Bergeron, Z. L.; Bingham, J.-P. *Toxins* **2012,** *4,* 1082–1119. doi:10.3390/toxins4111082
9. Cerni, F. A.; Pucca, M. B.; Peigneur, S.; Cremonez, C. M.; Bordon, K. C. F.; Tytgat, J.; Arantes, E. C. *Toxins* **2014,** *6,* 892–913. doi:10.3390/toxins6030892
10. Pucca, M. B.; Cerni, F. A.; Pinheiro Junior, E. L.; Bordon, K. d. C. F.; Amorim, F. G.; Cordeiro, F. A.; Longhim, H. T.; Cremonez, C. M.; Oliveira, G. H.; Arantes, E. C. *Toxicon* **2015,** *108,* 272–284. doi:10.1016/j.toxicon.2015.10.015
11. Tonin dos Santos, R. H.; González, A. D.; Guidoni, C. M.; Rufino, J. V.; Tirolla, R. M.; Girotto, E. *Toxicon* **2025,** *258,* 108305. doi:10.1016/j.toxicon.2025.108305
12. Danielsson, R.; Eriksson, H. *Semin. Cell Dev. Biol.* **2021,** *115,* 3–9. doi:10.1016/j.semcdb.2020.12.008
13. Zhao, T.; Cai, Y.; Jiang, Y.; He, X.; Wei, Y.; Yu, Y.; Tian, X. *Signal Transduction Targeted Ther.* **2023,** *8,* 283. doi:10.1038/s41392-023-01557-7
14. Mesquita, P. C.; dos Santos-Silva, E.; Streck, L.; Damasceno, I. Z.; Maia, A. M. S.; Fernandes-Pedrosa, M. F.; da Silva-Júnior, A. A. *Colloids Surf., A* **2017,** *513,* 442–451. doi:10.1016/j.colsurfa.2016.11.013
15. Tibery, D. V.; Nunes, J. A. A.; da Mata, D. O.; Menezes, L. F. S.; de Souza, A. C. B.; Fernandes-Pedrosa, M. d. F.; Treptow, W.; Schwartz, E. F. *Toxins* **2024,** *16,* 257. doi:10.3390/toxins16060257
16. Gupta, R.; Mohanty, S. *Mater. Sci. Eng., C* **2017,** *70,* 327–333. doi:10.1016/j.msec.2016.09.012
17. Haroon, H. B.; Hunter, A. C.; Farhangrazi, Z. S.; Moghimi, S. M. *Adv. Drug Delivery Rev.* **2022,** *188,* 114396. doi:10.1016/j.addr.2022.114396
18. dos Santos-Silva, A. M.; de Caland, L. B.; de S. L. Oliveira, A. L. C.; de Araújo-Júnior, R. F.; Fernandes-Pedrosa, M. F.; Cornélio, A. M.; da Silva-Júnior, A. A. *Mater. Sci. Eng., C* **2017,** *78,* 978–987. doi:10.1016/j.msec.2017.04.053
19. Ji, Y.; Wang, Y.; Wang, X.; Lv, C.; Zhou, Q.; Jiang, G.; Yan, B.; Chen, L. *J. Hazard. Mater.* **2024,** *468,* 133800. doi:10.1016/j.jhazmat.2024.133800
20. Park, Y.-M.; Shin, B.-A.; Oh, I.-J. *Arch. Pharmacal Res.* **2008,** *31,* 96–102. doi:10.1007/s12272-008-1126-5
21. Sanità, G.; Carrese, B.; Lamberti, A. *Front. Mol. Biosci.* **2020,** *7,* 587012. doi:10.3389/fmolb.2020.587012
22. Kim, M.; Choi, R.; Kim, L.; Kim, Y.-C.; Noh, I. *J. Controlled Release* **2025,** *382,* 113752. doi:10.1016/j.jconrel.2025.113752
23. Medeiros, T. S.; Bezerra de Lima, L. E.; Alves-Pereira, E. L.; Alves-Silva, M. F.; Dourado, D.; Fernandes-Pedrosa, M. d. F.; Figueiredo, R. C. B. Q. d.; da Silva-Junior, A. A. *Biomed. Pharmacother.* **2025,** *183,* 117782. doi:10.1016/j.biopha.2024.117782
24. Yang, S.; Wang, Z.; Ping, Y.; Miao, Y.; Xiao, Y.; Qu, L.; Zhang, L.; Hu, Y.; Wang, J. *Beilstein J. Nanotechnol.* **2020,** *11,* 1728–1741. doi:10.3762/bjnano.11.155
25. Khouri, N. G.; Bahú, J. O.; Blanco-Llamero, C.; Severino, P.; Concha, V. O. C.; Souto, E. B. *J. Mol. Struct.* **2024,** *1309,* 138243. doi:10.1016/j.molstruc.2024.138243
26. Casalini, T.; Rossi, F.; Castrovinci, A.; Perale, G. *Front. Bioeng. Biotechnol.* **2019,** *7,* 259. doi:10.3389/fbioe.2019.00259
27. Gupta, R. K. *Adv. Drug Delivery Rev.* **1998,** *32,* 155–172. doi:10.1016/s0169-409x(98)00008-8
28. Moni, S. S.; Abdelwahab, S. I.; Jabeen, A.; Elmobark, M. E.; Aqaili, D.; Gohal, G.; Oraibi, B.; Farasani, A. M.; Jerah, A. A.; Alnajai, M. M. A.; Mohammad Alowayni, A. M. H. *Vaccines (Basel, Switz.)* **2023,** *11,* 1704. doi:10.3390/vaccines11111704
29. Wu, Z.; Liu, K. *Med. Drug Discovery* **2021,** *11,* 100103. doi:10.1016/j.medidd.2021.100103
30. Santos-Silva, E. d.; Torres-Rêgo, M.; Gláucia-Silva, F.; Feitosa, R. C.; Lacerda, A. F.; Rocha, H. A. d. O.; Fernandes-Pedrosa, M. d. F.; Silva-Júnior, A. A. d. *Toxins* **2022,** *14,* 888. doi:10.3390/toxins14120888
31. Fernandes Pedrosa, M. d. F.; Junqueira de Azevedo, I. d. L. M.; Gonçalves-de-Andrade, R. M.; van den Berg, C. W.; Ramos, C. R. R.; Lee Ho, P.; Tambourgi, D. V. *Biochem. Biophys. Res. Commun.* **2002,** *298,* 638–645. doi:10.1016/s0006-291x(02)02521-4
32. Setyawati, D. R.; Sekaringtyas, F. C.; Pratiwi, R. D.; Rosyidah, A.; Azhar, R.; Gustini, N.; Syahputra, G.; Rosidah, I.; Mardliyati, E.; Tarwadi; El Muttaqien, S. *Beilstein J. Nanotechnol.* **2024,** *15,* 1105–1116. doi:10.3762/bjnano.15.89
33. Thomsen, T.; Klok, H.-A. *ACS Appl. Bio Mater.* **2021,** *4,* 2293–2306. doi:10.1021/acsabm.0c01619
34. Austria, E., Jr.; Bilek, M.; Varamini, P.; Akhavan, B. *Nano Today* **2025,** *60,* 102552. doi:10.1016/j.nantod.2024.102552
35. Kuhn, D. A.; Vanhecke, D.; Michen, B.; Blank, F.; Gehr, P.; Petri-Fink, A.; Rothen-Rutishauser, B. *Beilstein J. Nanotechnol.* **2014,** *5,* 1625–1636. doi:10.3762/bjnano.5.174
36. Bian, T.; Gardin, A.; Gemen, J.; Houben, L.; Perego, C.; Lee, B.; Elad, N.; Chu, Z.; Pavan, G. M.; Klajn, R. *Nat. Chem.* **2021,** *13,* 940–949. doi:10.1038/s41557-021-00752-9
37. Gan, Q.; Wang, T. *Colloids Surf., B* **2007,** *59,* 24–34. doi:10.1016/j.colsurfb.2007.04.009
38. Munier, S.; Messai, I.; Delair, T.; Verrier, B.; Ataman-Önal, Y. *Colloids Surf., B* **2005,** *43,* 163–173. doi:10.1016/j.colsurfb.2005.05.001
39. Öztürk, K.; Kaplan, M.; Çalış, S. *Int. J. Pharm.* **2024,** *666,* 124799. doi:10.1016/j.ijpharm.2024.124799
40. Silva-Júnior, A. A.; Scarpa, M. V.; Pestana, K. C.; Mercuri, L. P.; de Matos, J. R.; de Oliveira, A. G. *Thermochim. Acta* **2008,** *467,* 91–98. doi:10.1016/j.tca.2007.10.018
41. Chakraborty, S.; Panigrahi, P. K. *Appl. Therm. Eng.* **2020,** *174,* 115259. doi:10.1016/j.applthermaleng.2020.115259
42. DeLeon, V. H.; Nguyen, T. D.; Nar, M.; D'Souza, N. A.; Golden, T. D. *Mater. Chem. Phys.* **2012,** *132,* 409–415. doi:10.1016/j.matchemphys.2011.11.046
43. Gláucia-Silva, F.; Torres-Rêgo, M.; Rocha Soares, K. S.; Damasceno, I. Z.; Tambourgi, D. V.; Silva-Júnior, A. A. d.; Fernandes-Pedrosa, M. d. F. *Int. J. Biol. Macromol.* **2018,** *120,* 1917–1924. doi:10.1016/j.ijbiomac.2018.09.203
44. Chavez-Olortegui, C.; Amara, D. A.; Rochat, H.; Diniz, C.; Granier, C. *Vaccine* **1991,** *9,* 907–910. doi:10.1016/0264-410x(91)90012-u
45. Kumar, S.; Anselmo, A. C.; Banerjee, A.; Zakrewsky, M.; Mitragotri, S. *J. Controlled Release* **2015,** *220,* 141–148. doi:10.1016/j.jconrel.2015.09.069
46. Soares, K. S. R.; Gláucia-Silva, F.; Daniele-Silva, A.; Torres-Rêgo, M.; Araújo, N. K. d.; Menezes, Y. A. S. d.; Damasceno, I. Z.; Tambourgi, D. V.; Da Silva-Júnior, A. A.; Fernandes-Pedrosa, M. d. F. *Toxins* **2018,** *10,* 158. doi:10.3390/toxins10040158
47. Pan, Y.; Li, Y.-j.; Zhao, H.-y.; Zheng, J.-m.; Xu, H.; Wei, G.; Hao, J.-s.; Cui, F.-d. *Int. J. Pharm.* **2002,** *249,* 139–147. doi:10.1016/s0378-5173(02)00486-6
48. Laemmli, U. K. *Nature* **1970,** *227,* 680–685. doi:10.1038/227680a0

BEILSTEIN JOURNAL OF NANOTECHNOLOGY

Prospects of nanotechnology and natural products for cancer and immunotherapy

Jan Filipe Andrade Santos[*1,2], Marcela Bernardes Brasileiro[1,2], Pamela Danielle Cavalcante Barreto[1,2], Ligiane Aranha Rocha[1,2] and José Adão Carvalho Nascimento Júnior[1,2,3]

Review

Open Access

Address:
[1]Department of Pharmacy, Federal University of Sergipe, São Cristóvão, Brazil, [2]Laboratório de Ensaios Farmacêuticos e Toxicidade, Federal University of Sergipe, São Cristóvão, Brazil and [3]Postgraduate Program in Health Sciences, Federal University of Sergipe, Aracaju, Sergipe, Brazil

Email:
Jan Filipe Andrade Santos[*] - janfilipe21@academico.ufs.br; Marcela Bernardes Brasileiro - marcelabrasileiro@academico.ufs.br; Pamela Danielle Cavalcante Barreto - pamela.danielle@academico.ufs.br; Ligiane Aranha Rocha - Ligiane2004@academico.ufs.com.br; José Adão Carvalho Nascimento Júnior - adaocarv95@gmail.com

* Corresponding author

Keywords:
cancer; immunotherapy; nanotechnology; natural products; patent; review

Beilstein J. Nanotechnol. **2025,** *16,* 1644–1667.
https://doi.org/10.3762/bjnano.16.116

Received: 12 April 2025
Accepted: 19 August 2025
Published: 22 September 2025

This article is part of the thematic issue "Advances in nanotechnology applied to natural products".

Guest Editor: D. Dourado

Abstract

Nanotechnology is revolutionizing pharmaceutical industry and drug development by providing significant advantages in controlling drug release, enhancing stability, and reducing adverse effects. Concurrently, natural products are being extensively researched for their anticancer and immunomodulatory properties. This patent review aims to analyze publications that integrate nanotechnology with natural products to develop cancer treatments and immunotherapies. In this context, 17 patents were identified through the free online databases of the European Patent Office (EPO) and the World Intellectual Property Organization (WIPO). The review discusses various types of nanotechnology, including nanoparticles, nanocarriers, and nanocapsules, as well as bioactive compounds primarily extracted from plants. Among the most frequently identified natural products were ursolic acid, hyaluronic acid, and catechins. These bioactive compounds have been shown to promote cell cycle arrest, reduce tumor size, and exhibit synergistic effects with other anticancer agents. Consequently, the combination of natural products with nanotechnology holds significant therapeutic potential.

Introduction

Cancer is a disease characterized by the uncontrolled proliferation of abnormal cells, which have the ability to invade neighboring tissues and to metastasize to distant organs [1] (Figure 1). This pathology results from accumulated genetic alterations in proto-oncogenes, tumor suppressor genes, and DNA repair-related genes [2]. According to the International Agency

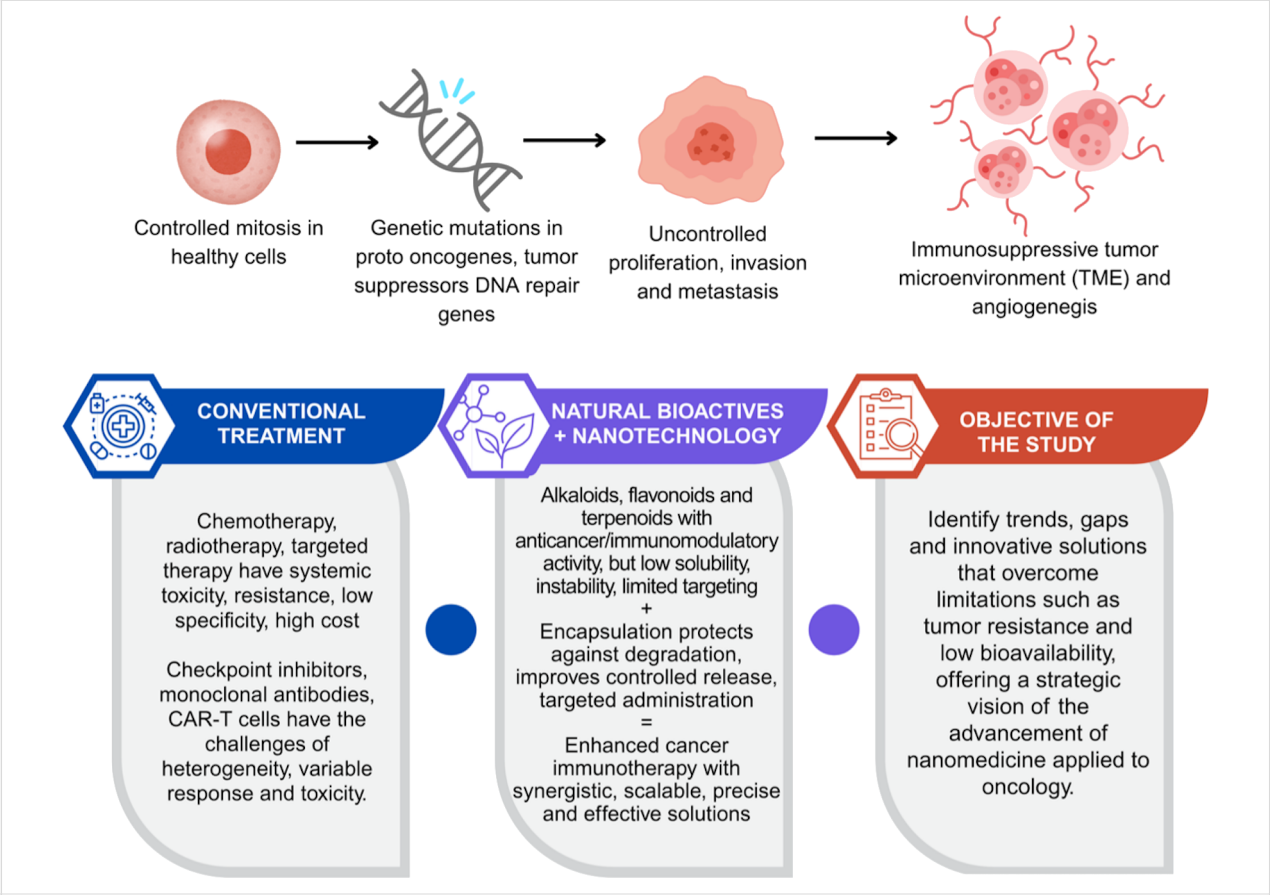

Figure 1: Pathophysiology of Cancer and Emerging Therapeutic Innovations. Graphical element Watercolor Illustration of a Pin: ©irasutoya via Canva.com; Graphical element Genetic Mutation Vector Icon D: ©123stock via Canva.com; Graphical element Cancer cells vector illustration: ©faridyulian via Canva.com; Graphical element cancer cell growth. cancer disease: ©surachet99 via Canva.com; Graphical element treatment outline icon: ©tulpahn via Canva.com; Graphical element Molecule Icon: ©rendicon via Canva.com; Graphical element Plant Leaves Icon: ©sirvectorr via Canva.com; Graphical element Infographic Table: ©creative-visionery via Canva.com; Graphical element Check list icon. Revision icon: ©vitaliikras-noselskyi via Canva.com. These elements are not subject to CC BY 4.0.

for Research on Cancer (IARC), approximately 20 million new cancer cases were reported in 2022, with lung cancer being the leading cause of death, resulting in an estimated 1.8 million deaths (18.7%) during the same period [3]. The unequal distribution of incidence and mortality across different regions reflects the influence of genetic and environmental factors, while common cancer types, such as lung, breast, and prostate cancer, present significant therapeutic challenges due to their biological heterogeneity and resistance to conventional treatments [4].

The immune system is crucial for identifying and eliminating tumor cells. This highly specialized network includes cells such as T lymphocytes, dendritic cells, macrophages, and natural killer (NK) cells, as well as soluble mediators like cytokines and chemokines, which regulate inflammatory and adaptive responses [5,6]. However, cancer often employs strategies to evade the immune system, such as expressing immunosuppressive molecules and creating a hostile tumor microenvironment that suppresses antitumor activity [7]. One of the most exploited mechanisms by tumors involves immune checkpoints, such as PD-L1 (programmed death-ligand 1) and CTLA-4 (cytotoxic T-lymphocyte associated protein 4), which inhibit T-cell activation, allowing cancer cells to escape immune-mediated destruction [8].

Immunotherapy shows promise as a cancer treatment approach, encompassing strategies such as monoclonal antibodies, immune checkpoint inhibitors, antitumor vaccines, and cell-based therapies, including chimeric antigen receptor T (CAR-T) cells [9]. However, these therapies face limitations, including systemic toxicity, high cost, variable clinical responses, and tumor resistance, often associated with the genetic and phenotypic heterogeneity of tumors [10-12]. Given this scenario, bioactive compounds from natural products, such as alkaloids, flavonoids, and terpenoids, have garnered interest due to their anticancer and immunomodulatory properties [13,14]. Derivatives from plants, fungi, and microorganisms offer diverse

mechanisms of action, including immune system activation and tumor growth inhibition [14]. Nevertheless, challenges like low bioavailability, chemical instability, and difficulty in targeting specific tissues hinder their effective clinical application [15].

Nanotechnology has emerged as an innovative solution to overcome the limitations of traditional therapies. Advances in cancer nanotechnology include the development of smart nanocarriers capable of responding to internal stimuli (such as pH, redox potential, and enzymes) and external stimuli (such as magnetic fields, heat, or ultrasound), enabling precise and controlled drug release [16,17]. Additionally, the use of biomimetic nanoparticles, including exosome-based delivery systems and cell membrane-coated nanoparticles, has shown promise in improving targeting efficiency and immune evasion [18,19]. Despite these advances, significant challenges remain, including nanoparticle stability in biological environments, potential immunogenicity, scalability of manufacturing processes, and the need for comprehensive long-term toxicity studies [20,21]. Overcoming biological barriers, such as penetration through the dense tumor extracellular matrix, also remains a major hurdle [19].

Nevertheless, nanotechnology opens up unprecedented opportunities in cancer immunotherapy by facilitating the co-delivery of chemotherapeutic agents, immunomodulators, and gene editing tools [22]. These multifunctional platforms can modulate the tumor microenvironment, enhance antigen presentation, reverse local immunosuppression, and improve the efficacy of cell-based therapies such as CAR-T and NK cells [23]. In this scenario, combining natural bioactive compounds with nanotechnological platforms represents a promising strategy. This approach enhances the therapeutic potential of natural molecules by improving their pharmacokinetic properties, increasing bioavailability, protecting them from degradation, and allowing for site-specific delivery [24]. Consequently, this combination addresses both the limitations of natural products and the complex challenges of cancer therapy [25].

Unlike conventional literature reviews, this study employs a technology foresight approach based on patent analysis to provide a strategic overview of emerging trends in the application of nanotechnology to natural products for cancer treatment and immunotherapy. This method allows for the identification of innovation gaps, technological barriers, and commercial opportunities, generating insights that are often overlooked in academic publications. The study systematically maps and analyzes recent patents focused on the integration of nanotechnology platforms with natural bioactive compounds in oncology and immunotherapy, highlighting technological progress and, at the same time, revealing current limitations, future directions, and perspectives for the development of effective and scalable therapeutic strategies.

Methods

In this patent review, the free online databases of the European Patent Office (EPO) and the World Intellectual Property Organization (WIPO) were used to carry out the search using the descriptors “nano* AND cancer AND natural product” for research associated with cancer treatment, while the descriptors “nano* AND immun* AND natural product” was implemented to analyze patents related to immunotherapy. Furthermore, a time filter was applied to both surveys, with patents collected from 2016 to 2024. Given that both databases are well established and widely recognized in the field of intellectual property, and to avoid significant data duplication, we considered their inclusion sufficient for the scope of this review. In view of the subject matter addressed, the IPC classification was not used, since the search criteria implemented provided patents from different IPCs that were related to the topic addressed in the review. Also, PCT (Patent Cooperation Treaty) applications were considered, as can be seen in the inclusion of patent WO2016178224. This initial search identified 240 preliminary patents, of which 90 were excluded as duplicates. After reading the title and abstract, 106 documents were excluded due to their content being different from the focus of the review (nanotechnology formulations containing natural products for cancer treatment and immunotherapy). Subsequently, four were excluded for not having full text available. Additionally, 23 patents were eliminated for being outside the scope of the review. Finally, 17 patents were selected for critical analysis according to the objective of the study. Figure 2 shows the guidelines used for searching and screening the patents in this review, based on the PRISMA methodology.

Results and Discussion

Researching and screening of selected patents

Based on the review criteria, the 17 selected patents were initially classified by their year of publication, covering the period from 2016 to 2024. In the first year, one document was published, a figure that remained consistent until 2021, when there was a decline, with no documents published that year. This decline can be attributed to the global impact of the COVID-19 pandemic, which began in 2020 and redirected research activities toward combating the virus. The pandemic particularly affected countries such as the United States of America and China, two major contributors to immunotherapy, related cancer research and patent production, potentially delaying research progress and patent filings. A strong recovery is evident in 2022 and 2023, with five patents published each

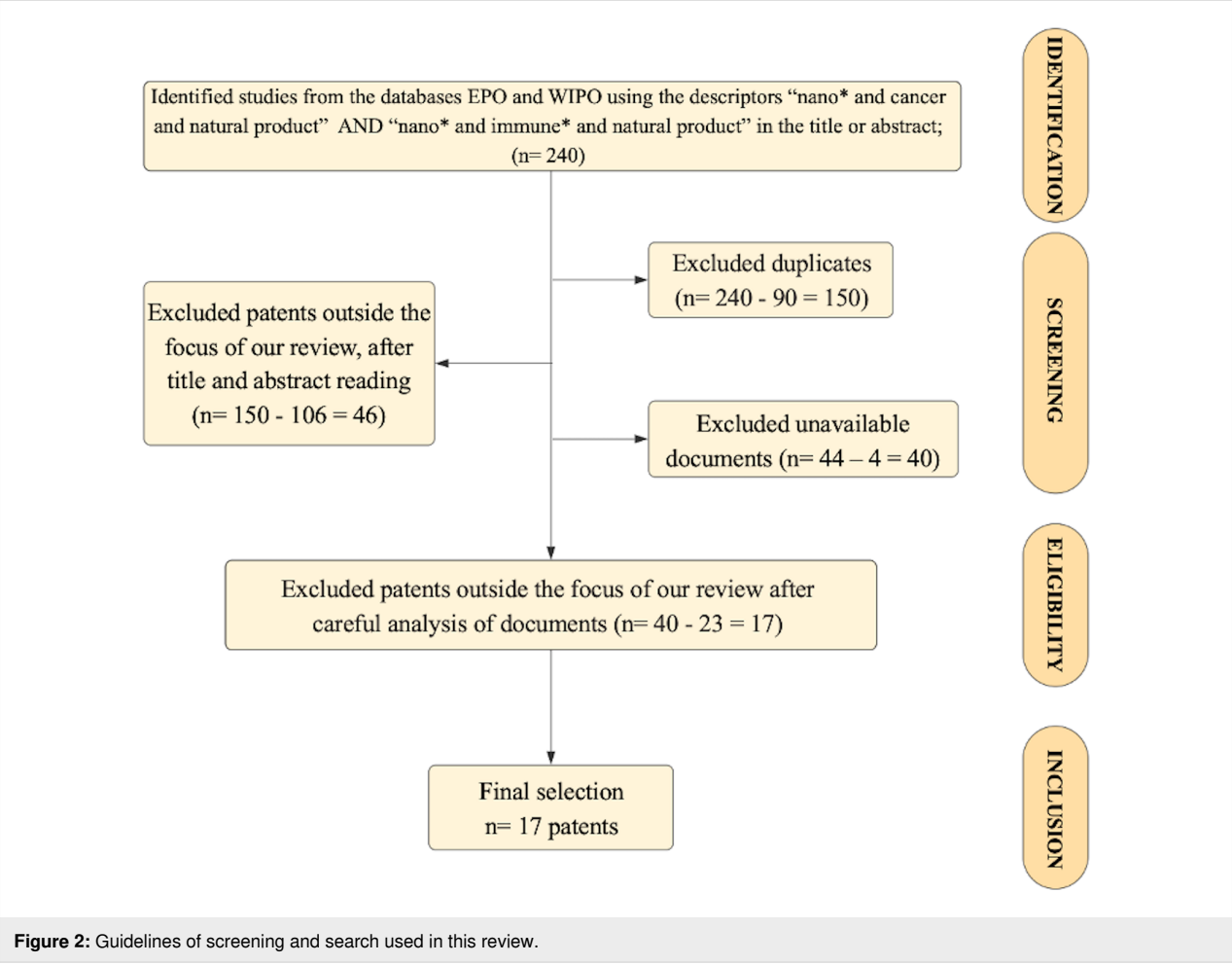

Figure 2: Guidelines of screening and search used in this review.

year, suggesting a resumption of research efforts and innovation following the pandemic-induced slowdown. In 2024, the number of patents dropped again to one, although it is important to consider that data for this year may be incomplete or still in progress, especially considering the waiting time until a patent is published in the databases [26] (Figure 3A).

These results may be related to the necessity of improving treatments for health issues such as cancer. Conventional treatments like chemotherapy and radiotherapy are highly cytotoxic and nonspecific, affecting both cancerous and healthy cells. Consequently, the scientific community is seeking alternatives, one of which is the use of nanotechnology in combination with other treatments. The advent of nanotechnology has revolutionized both diagnosis and treatment, enhancing factors such as bioavailability and stability, while also reducing toxicity [27].

China (CN) leads the ranking of published inventions with 14 documents, followed by the World Intellectual Property Organization (WO), the Republic of Korea (KR), and the United States of America (USA), each with one patent (Figure 3B). The oldest selected patent was published by WO in November 2016, while the most recent was published by CN in 2024. China's leadership in global patent activity is strongly supported by extensive public investment in research and innovation at both national and regional levels. The government offers reimbursement for patent filing and maintenance fees, along with substantial fiscal incentives, including reduced corporate income tax rates and generous super deductions for enterprises recognized as high-tech. Notably, China allocates approximately USD 1 billion annually to support scientific publications. These policy measures collectively reduce the financial barriers associated with securing patent protection, particularly in strategic sectors such as biotechnology and cancer immunotherapy, thereby reinforcing China's prominent position in the global landscape of patent filings [28,29].

US and the Republic of Korea also have economic incentives for biotechnology research and innovation, with the US investing over 3% of its GDP in research and development and Korea allocating approximately 4.5% of its GDP to research and development [30]. Although most patents were published

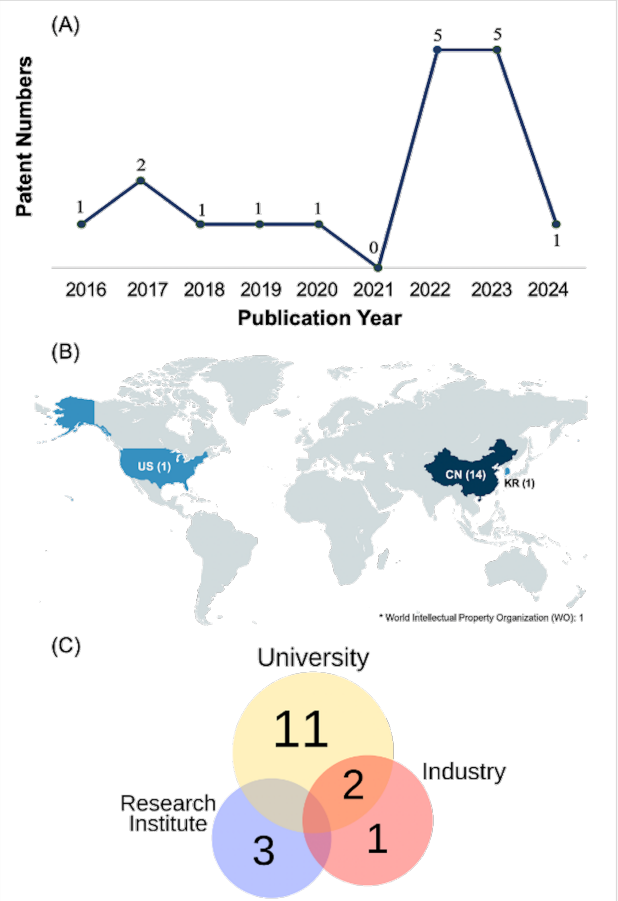

Figure 3: (A) Distribution of patents by publication year. (B) Distribution of patents by application country (CN: China; KR: Korea of Republic; US: United States of America; WO: World Intellectual Property Organization); (C) Distribution of patents by type of applicants. Figure 3B was created with https://www.mapchart.net/ and is distributed under the terms of the Creative Commons Attribution-ShareAlike 4.0 International License (https://creativecommons.org/licenses/by-sa/4.0/). This content is not subject to CC BY 4.0.

by the US and China, patents from other countries were also found by searching the EPO database, such as the patent KR20220169108 from South Korea, and patent WO2016178224, which is a PCT (Patent Cooperation Treaty) application.

In terms of protecting their inventions, various entities, including universities, industries, and research institutes, file for the publication of their patents. The results indicate eleven patents registered by universities such as Fuzhou University (CN), South China University of Technology (CN), Sun Yat-sen University (CN), Kyung Hee University (KR), King Abdulaziz University (US), Guizhou University of Traditional Chinese Medicine (CN), Hebei University of Technology (CN), China Three Gorges University (CN), China Pharmaceutical University (CN), South China Normal University (CN), and Sichuan University (CN). Additionally, research institutes such as Harbin Institute of Technology (CN) and The Institute of Medicinal Plant Development (CN) have published around three patents; the industry is represented by a single patent from BG Negev Technologies & Applications Ltd (WO) (Figure 3C).

The predominance of patents filed by universities in cancer research based on natural products certainly reflects the industry's insecurity in investing in early-stage projects involving extraction, isolation, characterization, and reproducibility, as they are technically complex and costly, with little initial commercial appeal. Consequently, pharmaceutical companies tend to avoid these high-risk ventures and prefer to enter later, when the therapeutic application has already been proven, often through partnerships with universities. This trend also explains the two patents between universities and industry observed and why the industry filed only one patent [31-33].

Figure 4 shows that the patents analyzed primarily focused on carrier-free self-assembly nanoparticle technology, which was present in eight inventions. Other types of nanotechnology, including nanovaccine, polymeric nanocapsules, and nanodrug complexes, were each identified in a single publication. The 14 inventions based on nanoparticles can be subdivided into five groups according to the type used in the product. Patents WO2016178224 and CN117534780 utilized polysaccharide nanoparticles, while patent KR20220169108 used gold nanoparticles, CN427216811 implemented quantum dot nanoparticles, CN367902299 and CN115887415 employed polymeric nanoparticles, and the remaining inventions used carrier-free self-assembly nanoparticles.

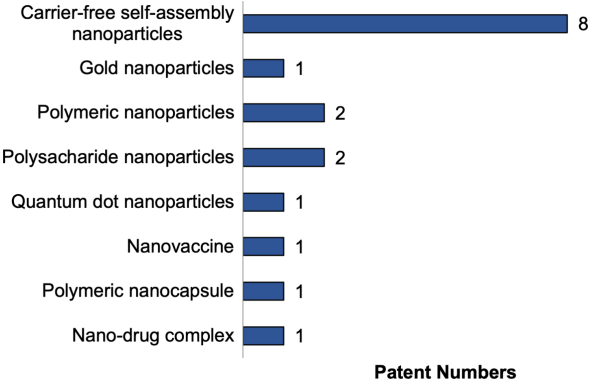

Figure 4: Type of technology present in the selected publications.

The greater number of inventions based on nanoparticles can be attributed to the longer period over which this carrier system has been studied and utilized. Indeed, the scientific literature contains reports dating back to the early 2000s that describe the application of nanoparticles in cancer treatment [34]. In

contrast, other technologies such as nanovaccines and nanocapsules are relatively recent developments, which may account for their lower representation in the current patent landscape [35].

Following this analysis, polysaccharide nanoparticles have high biocompatibility and the ability to encapsulate therapeutic molecules, representing an alternative to the use of natural products [36]. However, although polysaccharides are often studied in pharmaceutical systems, this has not been reflected in patent searches, as only two publications were found. Self-assembled nanoparticles are structures with adapted particle interactions to achieve desired purposes [37]. In the pharmaceutical field, these nanoparticles have potential as vehicles for anticancer drugs due to their biocompatibility, cellular absorption, and slow release of drugs [38]. Polymeric nanoparticles are colloidal polymer systems used as drug carriers for targeted therapies and diagnostics [39]. Gold nanoparticles have properties such as chemical reactivity, anti-inflammatory effects, and protein-binding abilities, while quantum dot nanoparticles are fluorescent semiconductor compounds that can act as drug carriers [40,41].

Nanotechnology, natural products, cancer, and immunotherapy

Natural products are chemicals produced by living organisms such as microbes, marine organisms, animals, fungi, and plants. They are widely used as therapeutic agents to treat diseases and maintain health and wellness [42]. In recent years, treatments involving natural products have seen significant growth in academia. Historically, natural products have made up 23.5% of approved medicines over the past 40 years. However, current technological development and an interdisciplinary approach have led to the more widespread implementation of these natural products in pharmaceutical research, as they are preferred for their favorable therapeutic efficacy, low adverse effects, and cost-effectiveness compared to synthetic products [43-45].

The use of natural products in cancer treatment and immunotherapy is mainly represented by the use of certain classes of compounds. Among them are saponins, which can remodel the tumor microenvironment, polysaccharides, such as lentinan, which increase immune cell activity, and polyphenols that can modulate immune checkpoints, such as curcumin seen in patents CN111202719 and US240447339, and terpenoids with direct anticancer activity, such as paclitaxel, observed in patent CN111202719 [46-50].

Moreover, natural products play a promising role in cancer treatment and immunotherapy. Their potential effects include tumor cell death, inhibition of proliferation, increased autophagy, and enhanced immune system response [51]. Furthermore, natural products can also promote the regulation of immune cells and cytokines, increasing immunogenic cancer cell death, natural killer cell activity, and dendritic cell activity. Other effects include the immunomodulatory function of natural products, which enhances their benefits as immune checkpoint inhibitors [52].

Based on this, analyzing the bioactive compounds responsible for these effects, such as saponins, polysaccharides, flavonoids, and natural products from traditional Chinese medicine like baicalin and wogonin, which reverse the immunosuppressive environment of tumors [48,50]. In addition to their active effects, natural products can be used as adjuvants and aids to conventional treatments, helping to boost antitumor capacity and reduce adverse effects [53,54].

Therefore, the use of natural products for cancer treatment and immunotherapy formulation presents a promising option for the pharmaceutical industry. One of the main technologies implemented in pharmaceutical development for incorporating natural products in cancer and immunotherapy is nanotechnology, as it presents physicochemical benefits for drugs. Among the advantages, nanotechnology can eliminate the limitations of using bioactive compounds in cancer treatment formulations, leading to increased bioavailability and pharmacokinetics [55]. The mechanisms behind the improvement in bioavailability and pharmacokinetics are based on increased solubility, observed, for example, by Chittasupho et al., improved permeation through biological barriers, as seen in the work of Huang et al., and protection against premetabolism and early elimination, as analyzed by Miguel et al. [56-58]. Additionally, the controlled release of the drug provided by pharmaceutical technologies can help reduce the toxicity and adverse effects of cancer treatments [59]. Consequently, the implementation of nanotechnology is seen as fundamental to the production of antineoplastic and immunomodulatory drugs from natural products. Table 1 shows the main information extracted from the patents, while Figure 5 shows the chemical structures of the active compounds used [60-76]. Some patents lack information about their preclinical formulation evaluation tests, such as data on the species, strains, and doses used. This reduces the reliability of the results, as it limits access to the reliability, reproducibility, and predictive value of the findings. Especially in the field of oncology, it is essential to have information about the procedures and results, as this allows researchers to analyze whether the study models represent human biology, whether the results are biased, and whether the research can enable the prediction of clinical outcomes [77-79].

By analyzing the chemical structures of the natural compounds illustrated in Figure 5, it is possible to identify their relation-

Table 1: Selected patents that use nanotechnology and natural products for cancer treatment and immunotherapy.

Patent number		Country/year of publication		
nanotechnology/physico-chemical properties[a]	natural product	biological activity	in vitro and in vivo tests	outcomes
WO2016178224 [60]		WO/2016		
polyssacharide nanoparticle PZ: 300 nm ZP: Negative surface charge at physiological pH (7.2–7.5)	hyaluronanic acid and alginate	targeting and uptake by certain tumor cells, peptides, integrin receptors, growth factor receptors and antibodies	in vitro cytotoxicity and antitumor efficacy were assessed using CT26 and MDA-MB-231 cancer cells; in vivo antitumor activity was evaluated in female athymic nude mice with MDA-MB-231 cells	significantly reduced cell viability, reduced tumor size, low cardiotoxic effect and lower IC_{50} values compared to the free drug
US240447339 [61]		US/2017		
polymeric nanocapsule PZ: 100–500 nm PDI: <15% (monodisperse) ZP: +5 to +30 mV or −30 to −5 mV EE: Not specified DL: Not specified RP: Controlled release via shell properties (pore size: 0.01–2 nm, viscosity: 3–6 mPa·s)	diindolylmethane and ellagic acid	anticancer efficacy	in vitro CAM model was used for pancreatic cancer cell implantation; additional in vitro tests were conducted with SUIT-2, colon, breast, ovarian, and bladder cancer cells	Encapsulated forms inhibited cell viability by 50–70%, showing a significantly higher effect than unencapsulated forms. They also reduced tumor size and angiogenesis.
CN222367609 [62]		CN/2017		
carrier-free self-assembly nanoparticle PZ: 115 nm	epicatechin gallate, gallocatechin, epicatechin and procyanidin	epicatechin gallate, gallocatechin and epicatechin: inhibitory activity on telomerase; procyanidin: inhibition effects on cancer cells and induced apoptosis mechanism	in vitro cytotoxicity test, staining of dead living cells, cell migration detection and targeting test with MCF-7 cell strains	better killing effect on breast cancer cells MCF-7 compared with the individual nanoparticles, effectively targeting breast cancer cells effect and inhibition of migration of breast cancer cells MCF-7
CN225561345 [63]		CN/2018		
nanodrug complex N.S.	tannic acid, catechin, epigallocatechin or procyanidin	remotion of free radicals in the body, resistance of oxidation, inflammation and cardiovascular diseases, preventing and treating cancers.	in vitro survival rate test of MBA-MD-231 cells; in vivo test with mice inoculated with MBA-MD-231 tumors and with bone tumors	significant inhibitory effect on cancer cells in vitro, tumor tracing effect, reduction of the tumor size, with inhibition of the growth of tumor cells, inhibitory effect on bone tumors
CN109846857 [64]		CN/2019		
carrier-free self-assembly nanoparticle PZ: 273 nm (β-sitosterol), 154 (ergosterol), 585 nm (stigmasterol) PDI: – ZP: – EE: – DL: 3.4%, 2.4% and 4.3% RP: –	sterol natural products like β-sitosterol, ergosterol or stigmasterol	anticancer, and synergistic effects with photosensitizers	in vivo effect with Balb-c female mice with 4T1 tumor cells; in vitro anticancer activity with murine 4T1 and human MCF-7 breast cancer cells	increased phototoxicity compared to the single drug, and synergistic anticancer effects, with reduction of the tumor volume higher than the drugs alone

Table 1: Selected patents that use nanotechnology and natural products for cancer treatment and immunotherapy. (continued)

CN111202719 [65]		CN/2020		
carrier-free self-assembly nanoparticle PZ: 150–190 nm EE: 94.41 ± 4.28% (UA-PTX NPs), 58.76 ± 2.54% (OA-PTX NPs) DL: 23.12 ± 1.07% (UA-PTX NPs), 12.95 ± 0.51% (OA-PTX NPs) RP: ≈40% (pH 7.3), ≈30% (pH 5.5) (UA-PTX NPs); ≈18% (pH 7.3), ≈10% (pH 5.5) (OA-PTX NPs)	ursolic acid and oleanolic acid	effects in blocking cell cycles and in reducing tissue damage by chemotherapy	in vitro release experiment: measured at 37 °C and pH 7.3 and 5.5; in vitro cell experiments with MCF-7 cells; in vivo antitumor with 4T1 tumor-bearing mice	ursolic acid and paclitaxel achieved a synergistic effect by inhibiting MCF-7 cells growth, with a significantly higher effect than that of the single drug group and the single carrier group
CN114129571 [66]		CN/2022		
carrier-free self-assembly nanoparticle PZ: 80–120 nm	ursolic acid	low toxicity, high efficiency, and multi-link regulated antitumor properties	in vitro flow cytometry with HepG2 cells; in vivo mouse H22 liver cancer transplant tumor model	synergistic anticancer effect superior to any single therapy, with increase of the water solubility and bioavailability of the drug
KR20220169108 [67]		KR/2022		
gold nanoparticle N.S.	ginseng and black cumin extract	black cumin: anticancer and antiproliferative activities	in vitro test with AGS human gastric cancer cells and toxicity test with macrophage RAW264.7 and HaCaT cells	no serious toxic effects and increased inhibitory activity against AGS cells compared to black cumin alone
CN367902299 [68]		CN/2022		
polymeric nanoparticle N.S.	procyanidin	inhibiting TMEM16A ion channels effect, promoting the inhibition of cancer	in vivo test with L795 lung adenocarcinoma tumor model in BALB/c mice	Good drug targeting and significantly reduced the tumor volumes compared to free drugs.
CN114470229 [69]		CN/2022		
carrier-free self-assembly nanoparticle N.S.	ursolic acid	increase of sensitivity of tumor cells to chemotherapy and synergistic effect	in vitro cytotoxicity experiment with HepG2 cells, and in vitro cellular uptake experiment with LO2 cells and HepG2 cells	A synergistic effect with sorafenib inhibited HepG2 cell proliferation and growth more effectively than individual drugs. It also improved targeting capability
CN115252560 [70]		CN/2022		
carrier-free self-assembly nanoparticle PZ: 100–300 nm PDI: 0.05–0.28 RP: Slow and prolonged release at pH 7.4 and pH 6.5	berberine, lonidamine and gambogic acid	inhibition of respiratory chain complex, hexokinase 2, glycolysis, mitochondrial targeting, cytotoxicity and glutamine metabolism	in vitro cytotoxicity and antitumor effect test with breast cancer cells 4T1 and normal human liver cells, hexokinase activity assay, determination of glutamine content, mitochondrial respiratory chain activity assay, and mitochondrial targeting ability	The treatment exhibited low cytotoxicity, high biocompatibility, and selectivity, enhancing anticancer activity. It inhibited glycolysis, reduced glutamine levels, and decreased mitochondrial respiratory chain activity.

Table 1: Selected patents that use nanotechnology and natural products for cancer treatment and immunotherapy. (continued)

CN117064865 [71]		CN/2023		
carrier-free self-assembly nanoparticle PZ: 150 nm	ursolic acid	inhibition of the differentiation of tumor cells, and immune-activating effect, with stimulation of cytokines	in vitro antitumor HepG2 cells and flow cytometry 293T cells experiment; in vivo effect with Balb-c female mice with 4T1 tumor cells; in vitro anticancer activity with Mouse 4T1 and human MCF-7 breast cancer cells	targeting gene knockout effect and killing effect on tumor cells
CN426774477 [72]		CN/2023		
polymeric nanoparticle PZ: 100 nm	astragalus polysaccharide	antiviral, antitumor, anti-aging, anti-radiation, anti-stress, and antioxidant effects	in vitro immune checkpoint inhibitor testing, NF-κB pathway blocking effect and cytotoxicity test with B16F10 tumor cells	promotes delivery of PD-L1 antibodies, great immune checkpoint target effect, toxic and side effects reduced, immune activation effect improved, and synergistic effect achieved
CN115671277 [73]		CN/2023		
nanovaccine PZ: 170–300 nm RP: sustained release with acid sensitivity	astragalus polysaccharide	antiviral, antitumor, anti-aging, anti-radiation, anti-stress, and antioxidant effects	flow cytometry with antibodies; in vitro BMDC maturation effect test; immunotherapeutic in vivo effect on mouse B16F10 melanoma model and mouse Lewis lung cancer model	upregulation effect on the expression of co-stimulatory molecules, lower tumor size compared to the control group, treating tumor effect, activation of immune responses
CN427216811 [74]		CN/2023		
quantum dot nanoparticle PZ: 2.68 ± 0.54 nm PDI: 14.68 ± 0.99 mV EE: 95.8% RP: 18.23% (pH 7.4, laser), 21% (pH 5.0, laser)	berberine	anti-inflammatiory, protection of the liver, improvement of immunity and antitumor activity	in vitro cytotoxicity test with L929 cells and in vitro photothermal antitumor effect on LLC cells	photothermal therapy effect and a chemotherapy effect under laser irradiation, efficiently killing LLC cells, having synergistic effect
CN115887415 [75]		CN/2023		
polymeric nanoparticle PZ: <100 nm PDI: 0.012 ZP: >20mV EE: 53.28% DL: 10.23% RP: Continuous release	dehydro-curvularin	inhibition of the growth, reproduction migration, transformation and cloning of tumor cells	in vitro cytotoxicity and cellular uptake test with MCF-7 cells and MM-231 cells; in vivo tumor inhibition effect in female Balb/c mice with a breast cancer tumor (4T1 cell) model	tumor cell growth inhibition effect better than that of free drugs, good targeting, promotion of release of the drug inside the cells, and slowing effect of the growth of tumor volume
CN117534780 [76]		CN/2024		
nanopolysaccharide nanoparticle PZ: 125–300 nm	chitin and β-1,3-D-glucan	stimulate immune cells and improve its interaction with cell receptors in the body	in vitro antitumor HepG2 cells experiment, immunoassay with RAW 264.7 macrophages	significantly increased cell inhibition rate and immune-promoting effects on cells by increasing cytokines levels

[a]Abbreviations: DL, drug load; EE, encapsulation efficiency; N.S., not specified; NPs, nanoparticles; OA, oleanolic acid; PDI, poly dispersion index; PTX, paclitaxel; PZ, particle size; RP, release profile; UA, ursolic acid; ZP, zeta potential.

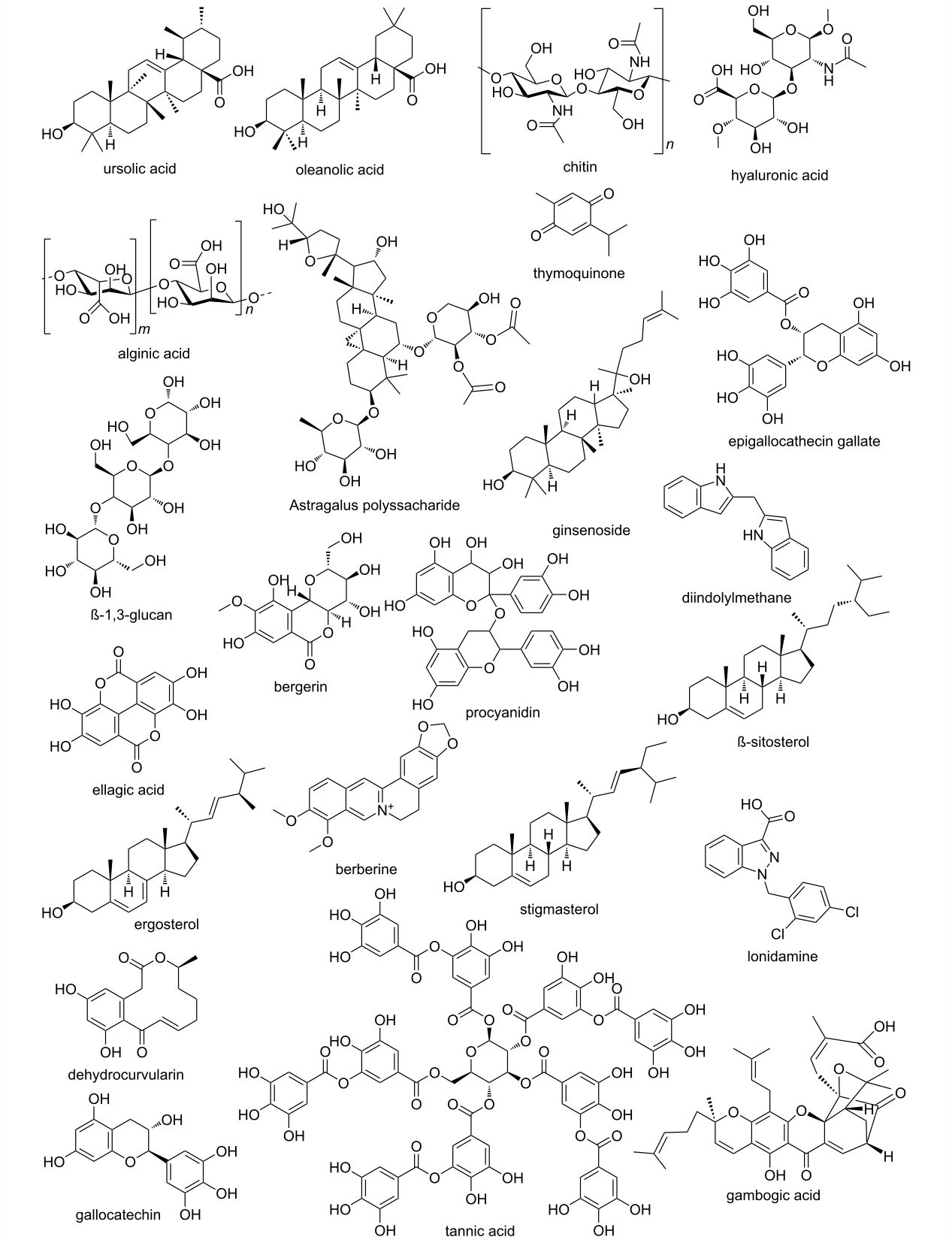

Figure 5: Chemical structures of selected compounds. Source: Made by the authors using ChemDraw Professional 16.0.

ships with cancer control and immunotherapy. For instance, terpenoids such as ursolic acid, oleanollonidamine, exhibit variations in selectivity and potency against cancer cells, depending on the presence of methoxylations at positions 3 and 20 [80-82]. In phenolic compounds such as catechins, procyanidin, tannic acid, and thymoquinone, the arrangement and presence of the aromatic ring, along with hydroxy, methoxy, and carboxyl groups, directly influence the antioxidant activity of these substances and their ability to induce apoptosis [83-85]. Furthermore, in polysaccharides such as chitin, hyaluronic acid, and alginate, factors such as molecular weight, degree of branching, monosaccharide composition, and processes like sulfation or phosphorylation significantly influence their ability to modulate the tumor microenvironment and activate the immune system [86-88]. Finally, alkaloids and their derivatives, such as lonidamine, exhibit variations in selectivity and potency against cancer cells, depending on the presence and position of hydroxy, methoxy, or alkyl groups, as well as modifications to the nitrogen atom [89-91].

Patents WO2016178224 and US240447339 show robust results, with solid data both in vitro and in vivo, suggesting high efficacy compared to the free drug and lower toxicity. Patents CN222367609 and CN225561345, although their results are limited to specific cell lines, also show good results in terms of targeting and tumor inhibition.

Following this perspective, patents CN111202719, CN114470229, and CN115252560 represent advances in tumor therapy, since they combine cell cycle blockade and inhibition of metabolic pathways, which are considered complex cellular mechanisms. Nevertheless, patent CN109846857 stands out for combining the natural compound with photosensitizers, presenting a synergistic effect that is better than the isolated effect of the substances, with a methodology not seen in the others formulations. Finally, patents CN117064865, CN426774477, and CN115671277 combine immunotherapies containing immunomodulators and checkpoint inhibitors to achieve a synergistic effect and consequently expand the clinical potential of nanotechnology containing natural products.

Patent KR20220169108 was discussed in the article published by Dhandapani et al., which addresses the synthesis, physicochemical characterization, and therapeutic evaluation of nanotechnology [92]. The formulation of patent CN114470229 was discussed in an article by Guo et al., which showed that the nanoparticle, as in the patent, achieved better solubility, synergistic effect, and better targeting [93]. In addition, the article published by Li et al. discussed patent CN115671277 [94].

Nanoparticles

Nanoparticles are materials with at least one dimension ranging from 1 to 999 nm [95]. This technology possesses a high contact surface, a high concentration of surface-active centers, and low toxicity due to promoting a reduction in the dose of its active ingredients [96]. These characteristics have made nanoparticles widely used in medicines, medical applications, and the food industry, as they provide increased shelf life, improved drug delivery, and enhanced therapeutic efficacy [97]. Various methods, such as chemical reduction, microemulsion and inverse microemulsion, hydrothermal method, seeding, sonoelectrodeposition, and coprecipitation can be implemented for the synthesis of nanoparticles [98].

In the context of cancer treatment, nanoparticles promote enhanced biocompatibility, reduced toxicity, and increased stability and permeability, which can help overcome challenges like multidrug resistance [23]. Moreover, this technology enables better encapsulation of active pharmaceutical ingredients (APIs), contributing to improved drug delivery to the tumor region and promoting new therapeutic approaches for cancer treatment [99]. In the field of immunotherapy, nanoparticles can increase antitumor immunity, reduce immune system evasion, suppress tumor growth, and diminish metastasis by ameliorating the tumor microenvironment [100]. Additionally, this technology promotes the activation of cytotoxic T cells, enhances antigen presentation, facilitates immune cell trafficking, and reduces toxic side effects on non-target cells [101,102]. However, nanoparticles have disadvantages, such as lack of routes of administration, concerns about crossing biological barriers, and tempering biodistribution. In addition, they can cause inflammatory and oxidative effects, posing a risk to the lungs, liver, and kidneys [27].

Regarding the use of natural products, nanoparticles can increase the bioavailability, pharmacokinetics, and selectivity of compounds toward cancer cells, thereby improving their solubility and delivery [103]. Moreover, nanoparticles can be subdivided into various structures, such as carrier-free self-assembly nanoparticles, polymeric nanoparticles, polysaccharide nanoparticles, gold nanoparticles, and quantum dot nanoparticles.

Carrier-free self-assembly nanoparticles

Carrier-free self-assembly nanoparticles are formed spontaneously from the organization of active or natural compounds, without the presence of a carrier material or excipients. Their stability is due to the presence of intermolecular interactions, such as electrostatic forces, hydrogen bonding, π–π stacking, and hydrophobic interactions [104,105]. Among the benefits of this technology are reduced toxicity and immunogenicity, as

well as less complexity, since they do not implement synthetic carriers in their composition.

However, carrier-free self-assembly nanoparticles may have some limitations, such as the limitation of natural products used, since the compounds must have properties that contribute to a stable formulation, difficulty in controlling physicochemical characteristics, such as particle size, which can affect reproducibility and scalability, and problems related to rapid clearance and interaction with non-target tissues, mainly due to the absence of a carrier substance [104,106,107]. In short, this technology reduces adverse effects and environmental risks, mainly due to the greater use of natural products over synthetic ones, and promotes increased stability and drug load efficiency [104,108].

For example, patent CN114129571 (2022) describes the formation of metal–organic co-assembly nanoparticles without a carrier. The formulation contains sorafenib, a molecularly targeted anticancer drug, ursolic acid as an API, and iron ions. Ursolic acid, a naturally occurring pentacyclic triterpenoid, exhibits a variety of biological activities and potential health benefits, and it can be found in herbs, fruits, and traditional Chinese medicinal plants [109]. The compound can be extracted through various methods, such as maceration, heat reflux, and Soxhlet and ultrasonic extraction, with dichloromethane considered the most efficient and selective solvent [110]. Ursolic acid exhibits anti-inflammatory, antimicrobial, antiviral, antioxidant, and antiproliferative properties, making it a potential antitumor agent [111]. It inhibits tumor cell proliferation, prevents metastasis and angiogenesis, and induces cell death [112]. The therapeutic mechanisms involve inhibiting cell proliferation by disrupting the lysosomal system, increasing pH, and altering the lipid profile of cancer cells [113]. Additionally, ursolic acid can inhibit the differentiation of Th17 cells from the STAT3/RORβt pathway and the migration of these cells by down-regulating CXCL9/10 expression in Schwann cells [114]. Particle size and stability of the formulation in the patent were characterized using scanning electron microscopy (SEM). The nanoparticles demonstrated enhanced uptake in HepG2 cells, as confirmed by flow cytometry and confocal microscopy, and achieved a tumor inhibition rate of 75.9% in 15 days, significantly higher than ursolic acid and sorafenib alone [66].

Patent CN117064865 (2023) claims a nano bionic CRISPR/Cas9 drug co-assembly system to treat liver cancer. The technology is composed of ursolic acid as an API, a Cas9 ribonucleoprotein (RNP) complex that targets the PD-L1 gene, a cell-penetrating peptide, and a tumor cell membrane derived from HepG2 cells. Characterization of the nanoparticles showed that the nanocomplex was stabilized by hydrogen bonds, van der Waals forces, and hydrophobic forces. In addition, confocal microscopy, gene editing efficiency, MTT assay, and flow cytometry tests were carried out to observe the therapeutic activity of the technology. The results demonstrated that the nanoparticles increased targeting and internalization, had a knockout rate of 80%, and exhibited better inhibition of HepG2 cell proliferation compared to the individual components, revealing a synergistic activity for cancer treatment [71].

Patent CN114470229 (2022) describes carrier-free double-drug self-assembled nanoparticles for treating liver cancer. This technology contains indocyanine green, a cell-penetrating peptide, a nucleic acid aptamer, sorafenib, and ursolic acid as an API at 4 $mg{\cdot}mL^{-1}$ in methanol. Physicochemical tests showed that the nanoparticles have a spherical shape, confirmed by atomic force microscopy (AFM), and are stable in ultrapure water and Dulbecco's modified eagle medium (DMEM) with 10% FBS. Procedures to evaluate the nanoparticles' antitumor activity included fluorescence intensity and combination index to determine drug synergy. The results indicate the nanoparticles exhibit a synergistic effect, effectively target HepG2 cells as observed by fluorescence, and show a higher inhibition of cell proliferation than the free drugs, demonstrating superior therapeutic potential [69,115-117].

Furthermore, nanoparticles containing antineoplastic drugs have demonstrated the ability to act against cancer. They do so by inhibiting the cell cycle, blocking the depolymerization of microtubules, and stimulating the development of reactive oxygen species (ROS) [118]. Hyaluronic acid can inhibit local recurrence and distant tumor growth when used in immunotherapy scenarios in conjuction with CAR-T cells and anti-PDL1-conjugated platelets [119]. Transmission electron microscopy (TEM) and dynamic light scattering (DLS), and UV–visible (UV–vis) spectroscopy were used for characterization. The nanoparticles showed increased cellular uptake compared to free PD-L1, suppression of the NF-κB pathway as indicated by reduced PHO-P65 protein expression, and enhanced tumor inhibition due to immune activation and targeted delivery [72].

Patent CN222367609 (2017) describes targeted amphiphilic nanoparticles composed lecithin, procyanidine, and doxorubicin condensated with epigallocatechin gallate in *N*-hydroxysuccinimide solution, which were developed to inhibit breast cancer. The procyanidine and epigallocatechin gallate act as APIs, while lecithin is an excipient. Catechins and their derivatives are natural polyphenolic compounds that are found in foods such as chocolate, red grapes, wine, and apples, as well as especially in green tea from *Camellia sinensis* (*C. sinensis*) and *C. assumica* [120,121]. These compounds present remarkable properties in treating and preventing cancer, including antioxi-

dant, anti-inflammatory, and antiangiogenic effects, as well as inhibitory effects on protein kinases. This results in cancer cell apoptosis, suppression of proteinases, strong inhibition of telomerase, and inhibition of cancer cell migration, invasion, and metastasis [122,123]. The patent characterizes the NPs through DLS and TEM, confirming a uniform size distribution. Additionally, in vitro studies using MCF-7 breast cancer cells demonstrated inhibition of cell proliferation, with the NP inducing apoptosis through their targeted mechanism [62].

Patent CN115252560 (2022) describes self-assembled nanoparticles composed of berberine, lonidamine, and gambogic acid in a 3:1:4 ratio, all acting as APIs, encapsulated with vitamin E polyethylene glycol succinate (VE-TPGS), an excipient, for stability. *Berberis vulgaris* and *B. aquifolium* are some of the main sources of berberine, a quaternary isoquinoline alkaloid compound with a range of pharmacological properties, including antioxidant, anti-inflammatory, antimicrobial, and, most importantly, antitumor effects [124,125]. The drug's potential for cancer treatment lies especially in its activation of the apoptotic pathway and the blocking of HIF-1α expression [126].

This combination of drugs in the formulation yields multiple mechanisms against cancer. Berberine provides mitochondrial targeting, lonidamine inhibits hexokinase, and gambogic acid offers cytotoxicity. The nanoparticles showed inhibition of the proliferation of breast cancer cells, with lower cytotoxicity to normal liver cells compared to standard drug and free drug. This is due to the nanoparticles' enhanced permeability and retention, which improves tumor-specific targeting. Mitochondrial membrane potential investigation using 2 $\mu g \cdot mL^{-1}$ of NPs for 12 h determined that the formulation induced early apoptosis in the targeted cells [70].

Patent CN111202719 (2020) utilized a nanosystem containing ursolic acid and oleanolic acid, paclitaxel, curcumin, camptothecin, and polyvinyl alcohol as APIs and drug carriers, and methanol, ethanol, and acetone as solvents. Both nanoparticle systems exhibited high biocompatibility and low cytotoxicity to normal cells. Additionally, the results demonstrated the technology had a tumor inhibition greater than 70% in mice with a synergistic antitumor effect, significantly improved blood indicators compared to paclitaxel injection ($p < 0.01$), extended circulation, improved targeting to tumor sites, and reduced toxic side effects [65].

CN109846857 (2019) describes the development of a natural photosensitizer derived from chlorophyllin e6 (Ce6). Self-assembled nanoparticles containing sterol compounds, such as β-sitosterol, ergosterol, or stigmasterol, were employed to enhance the stability and bioavailability of the active ingredient. Ce6 has the ability to selectively accumulate in cancer cells, attributed to the increased metabolic activity and permeable vasculature of these cells compared to healthy ones. Upon absorption of light during photodynamic therapy, Ce6 generates ROS, causing damage to the cell membrane, proteins, and DNA of the cancer cells, ultimately leading to their destruction. Additionally, the ROS produced by Ce6 destroys the vascular layer surrounding the tumor, thereby inhibiting its continued growth and stimulating immune cells to recognize and target the mutated cells [127,128]. Regarding the natural compounds mentioned in the patent, sitosterol is particularly noteworthy. Preclinical studies have demonstrated that sitosterol can induce cell cycle arrest, regulate oxidative stress, enhance metabolic reprogramming, inhibit invasion and metastasis, and modulate immunity and inflammation [129]. The developed nanoparticles underwent physicochemical characterization by SEM, UV–vis spectroscopy, and encapsulation testing, in which the nanoparticles demonstrated stability, spherical shape, and homogeneous size distribution. The use of nanoparticles with sterol compounds associated with Ce6 yielded higher tumor inhibition rates compared to the isolated compounds, especially the nanocarrier with ergosterol, which reached a rate of 86.4% [27,64,130-133].

Polymeric nanoparticles

Polymeric nanoparticles are solid colloidal systems of synthetic or natural polymers, which can be organized in hollow, occluded, multilobed, and core–shell structures, depending on their thermodynamic and kinetic characteristics [130]. Polymeric nanoparticles can be synthesized using methods such as direct polymerization of monomers, nanoprecipitation, solvent evaporation emulsification, dispersion of preformed polymers, or salting-out [27]. For cancer and immunotherapy, polymeric nanoparticles offer advantages such as biocompatibility, stimulation of T cells, controllable size, and protection of the tumor environment [131]. They also help by reducing adverse effects, increasing antitumor response, as well as increasing solubility and precision in drug delivery [132,133].

Seeking a new pharmaceutical application for procyanidines (PCs) as APIs, the patent CN367902299 (2022) describes photo-thermally responsive PC-loaded polymeric nanoparticles designed to prevent and/or treat lung adenocarcinoma by inhibiting TMEM16A. TMEM16A is a calcium-activated chloride ion channel that appears to be a suitable biomarker and target for lung cancer treatment. PCs, also known as proanthocyanidin, are phenolic compounds of the flavonoid family and are a class of natural polymers formed by catechins and epicatechins [134]. They exhibit a variety of bioactive properties, including anti-inflammatory, antimicrobial, cardioprotective, and neuroprotective effects, which could contribute to cancer

prevention and treatment [135]. In cancer therapy, PCs show potential for inhibiting cancer cell proliferation, inducing apoptosis, modulating oxidative stress, suppressing angiogenesis, and interfering with signaling pathways involved in tumor progression [136]. The formulation includes temperature-responsive and non-temperature-responsive amphiphilic molecules (weight ratio of 7:3). UV–vis spectroscopy, TEM, and DLS experiments demonstrated that administration of 14.37 $mg \cdot kg^{-1}$ of the nanoparticles inhibited lung adenocarcinoma proliferation and migration after 24 h [68].

Similarly, patent CN426774477 (2023) developed an immune checkpoint inhibitor nano-delivery system using natural polyphenols. The formulation contained sulfhydrylated hyaluronic acid (HA-SH), which acts as an adjuvant carrier, and epigallocatechin gallate (EGCG) as an API to form HA-EGCG, as well as manganin, $FeCl_3$, and the PD-L1 antibody. Hyaluronic acid is a non-sulfated glycosaminoglycan component of the extracellular matrix and has diverse biomedical applications [115]. It can be obtained through the fermentation of bacteria and yeasts, as well as animal sources, using chemical, enzymatic, and combined extraction methods [116,117].

CN115887415 (2023) describes a methoxypoly(ethyleneglycol)-poly(lactic-*co*-glycolic acid) (mPEG-PLGA) nanocarrier containing dehydrocurvularin; the latter is the API of the formulation and exhibits sustained release. Dehydrocurvularin is a natural benzenediol produced by many fungi as a secondary metabolite. Its therapeutic activity is focused on antitumor capacity through its synergistic activity with drugs, increasing efficacy and tumor targeting capacity [127,137]. The formulation combines mPEG-PLGA, acetonitrile, and Tween-80. The nanoparticles were obtained by precipitation and freeze-drying and were analyzed by HPLC and DLS. Additionally, the in vivo studies performed in a mice model with breast cancer tumor (4T1 cell) showed that the drug exhibits a level of biosafety while reaching 44% tumor inhibition [75].

Polysaccharide nanoparticles

Polysaccharides are a class of polar polymers frequently employed in polymeric systems and nanotechnologies, including the creation of polysaccharide nanoparticles [28]. Substances such as chitosan, hyaluronic acid, alginate, starch, and their derivatives are most commonly used in nanoparticles for therapeutic applications [138]. Organic solvents, ionic liquids, inorganic strong alkalis and acids, enzymes, and hydrothermal treatment are used to obtain polysaccharide nanoparticles [139]. Consequently, polysaccharide-containing nanoparticles offer an alternative for cancer treatment, promoting antitumor immune responses with reduced toxicity and fewer side effects [140]. Moreover, this technology can be applied to various cancer therapies, such as chemotherapy, photothermal therapy, photodynamic therapy, gene therapy, and immunotherapy [141].

For instance, patent WO2016178224 (2016) describes the development of anionic polysaccharide nanoparticles designed for the delivery of anionic small-molecule anticancer drugs. The formulation consists of anionic polymers, such as hyaluronic acid (HA), alginate (Alg), HA-sulfate, and Alg-sulfate, which acts as adjuvants for drug delivery, as well as anionic small-molecule drugs, including methotrexate (MTX) and doxorubicin (DOX), and divalent cations like calcium (Ca^{2+}). Alginate is a cross-linked polymeric network derived from algae and shows potential for cancer treatment due to its improved bioavailability, sustained release, and environmentally benign properties [142,143]. The tests showed that the nanoparticles containing MTX and DOX were around 400 times more effective and yielded higher cytotoxicity in CT26, MDA-MB-231, and NAR cancer cells, compared to the free drugs [60].

CN117534780 (2024) uses chitosan–glucan nanopolysaccharide complexes (CGCs) obtained from fungi to prepare antitumor and immunomodulatory drugs, with chitosan–glucan being an API. Chitosan–glucan is a biopolymer complex composed of chitosan, a deacetylated derivative of chitin, and glucan, a polysaccharide commonly found in fungal cell walls, cereals, and seaweed. Chitosan possesses a combination of properties that include antioxidant and antitumor effect, giving it potential to prevent and/or treat cancer by stimulating apoptosis [144]. Meanwhile, glucan presents potential in cancer therapy due to its immunomodulatory influence, which can increase the recruitment of neutrophils or infiltration of $CD4^+$ T cells to destroy tumors [145]. The process of nanosizing the CGCs in the patent involves shearing at high speed and ultrasonic cycles followed by freeze-drying. This resulted in a yield of 12.73% and a purity of 96.32%. The increased surface area due to the reduction in particle size, along with improved interaction with cellular receptors, enables a significantly increase of the cell inhibitory effect (tumor cells were HepG2 and MCF-7), with the complex exhibiting an increased amount of cytokine secretion when used at a concentration of 10 $mg \cdot mL^{-1}$ [76].

Gold nanoparticles

Gold nanoparticles are nanometer-scale structures composed of a gold core with surface ligands, which can be structured into nanospheres, nanocages, nanorods, and nanoshells [146,147]. There are various manufacturing processes such as vacuum sputtering, biosynthesis, methods based on ultraviolet light, synthesis in reverse micelles, and condensation processes [148]. Gold nanoparticles have great benefits for cancer and immunotherapy, providing increased efficiency and effective-

ness by acting as immune regulators, enhancing the delivery of antitumor drugs, and improving biocompatibility, durability, and innate immune responses [149,150]. In addition, gold nanoparticles lead to more selective oncological treatments with biocompatibility and low toxicity and their use in association with natural products is promising [151,152].

The patent KR20220169108 (2022) claims that gold nanoparticles were developed using membrane vesicles from a *Curtobacterium proimmune* K3 strain, isolated from ginseng, and black cumin seed extract, which are presented in the formulation in the form of stabilizing adjuvants. The use of ginseng is based on the fact that its components may have anticancer effects, especially on apoptosis, cell cycle regulation and the PI3K/AKT and MAPK pathways, while black cumin extract is used because its main components, such as thymoquinone, show anti-inflammatory, antioxidant, and immune system stimulating potential [89,90]. The compound was characterized using UV–vis spectroscopy, TEM, DLS, X-ray diffraction (XRD), and Fourier-transform infrared (FTIR) spectroscopy, revealing a polygonal or oval morphology. To evaluate the antitumor effects, cytotoxicity assays, cellular uptake assays, apoptosis detection, ROS production, qRT-PCR, and Western blotting for gene and protein expression, and autophagy inhibition studies were applied. The results showed that gold nanoparticles promoted an increase in apoptosis markers, such as stimulation of p53, Bax, cytochrome c, caspase-9, and caspase-3, as well as a decrease in Bcl2, a greater production of ROS in CC-AuNP-treated cells compared to black cumin alone, and synergistic anticancer effects when combined with rapamycin [67]. Therefore, nanoparticles containing natural products are a promising technology for cancer and immunotherapy with synergistic effects and reduced side effects.

Quantum dot nanoparticles

Quantum dot nanoparticles are semiconductor structures smaller than typical nanoparticles, ranging from 2 to 10 nm in size. They are composed of heavy metal or inorganic material and exhibit fluorescent activity, making them commonly used for pharmaceutical applications [153,154]. The technology's composition is characterized by two free functional groups responsible for drug binding, while a semiconductor shell helps reduce toxicity [106]. Quantum dot nanoparticle synthesis processes involve colloidal and plasma systems, which allow for the utilization of bioactive compounds such as fructose, chitosan, citric acid, lignin, cellulose, and starch [155,156]. Furthermore, quantum nanoparticles offer advantages for cancer treatment. They can manipulate emission properties near the infrared region, improving drug targeting and solubility, enhancing tumor detection, and reducing adverse effects on adjacent healthy tissues [157,158]. Regarding the use of natural products, carbon quantum dots, the main type of nanoparticles derived from bioactive compounds, show promising activity for cancer treatment due to their biocompatibility, photostability, and fluorescent characteristics [159].

Bergenin (BER) is a natural compound extracted from cinnabar root. It has been combined with carbon quantum dots to treat lung cancer in the patent CN427216811 (2023). BER is a glycosidic derivative of hydroxybenzoic acid found in various plant families and species worldwide, with *Bergenia purpurascens* and *Ardisia japonica* being its primarily natural sources [160]. The compound and its derivatives have shown antimalarial, trypanocidal, antibacterial, antileishmanial, anti-inflammatory, antioxidant, analgesic, and anticancer activities [161]. BER acts against cancer by inhibiting cell proliferation, inducing apoptosis, suppressing glycolysis, reducing angiogenesis, and promoting the degradation of oncogenic proteins [162,163]. The invention proposes the use of carbon dots (CDs) loaded with BER as an API, with a sustained drug release that increases upon contact with the acidic conditions surrounding tumors. Both non-loaded CDs and free BER exhibited antitumor effects on Lewis lung carcinoma (LLC) cells, which were further improved with CDs–BER. This combination was able to enhance the inhibitory effect on the cells subjected to photothermal therapy, reducing the cell survival rate to 34.5%, while being biocompatible with a survival rate of 80% for normal L929 cells [64,65,74,75,127-129,137,164-175].

Polymeric nanocapsules

Polymeric nanocapsules (PNCs) are vesicular systems between 1 and 999 nm in size, composed of an internal oily reservoir surrounded by polymeric membranes, non-ionic surfactants, macromolecules, and phospholipids [176,177]. The properties of the pharmaceutical form are governed by size, shape, core structure, and ligands, which can alter factors such as solubility, charge density, hydrophobicity, stability, and binding affinity [178]. The methods for developing PNCs involve appropriate materials and various production techniques, including emulsion polymerization, layer-by-layer self-assembly, interface polymerization, nanoprecipitation, spray-drying, and supercritical fluids [179,180]. This technology offers the ability to encapsulate hydrophilic or lipophilic pharmaceutical drugs, as well as surface modification, making PNCs advantageous for controlled drug delivery systems [132]. PNCs hold potential applications for cancer treatment and immunotherapy. They can provide sustained drug release while decreasing cytotoxicity and modifying tumor retention for tumor treatment. They can also serve as formulations that encapsulate synergistic combinations of drugs and other substances, such as natural products [181,182]. In the field of immunotherapy, PNCs good biocompatibility and the ability to present antigens and activate the

T-cell response, while being efficiently distributed in the lymphatic vessels, contributing to the local and systemic antitumor effects of small molecules [183].

However, PNCs face some challenges for therapeutic use, especially regarding the lack of methods for characterizing the shell, which is important for drug release, toxicity due to the use of organic solvents, the tendency to aggregate in aqueous media, and difficulties in sterilizing the formulation [184]. Furthermore, the technology has advantages when associated with natural products, as phytochemicals show antioxidant and anti-inflammatory activity against cancer. For polyphenols, the use of PNCs enhances pro-apoptotic activity, especially against breast, lung, prostate, cervical, and colorectal tumors [185,186]. Therefore, PNCs are a powerful alternative for the use of natural products in cancer and immunotherapy due to their properties such as controlled drug release.

The patent US240447339 (2017) involves the creation of PNCs. These PNCs utilized a range of bioactive compounds, such as diindolylmethane (DIM) and ellagic acid (EA), both as APIs, curcumin, green tea polyphenols, resveratrol, sulforaphane, and tocopherols. DIM is one of the main metabolites of indole-3-carbinol, found in cruciferous vegetables like broccoli, cauliflower, and cabbage; it exhibits antineoplastic properties such as suppression of cell proliferation, migration, and growth [187,188]. Additionally, EA is a phenolic bioactive compound found in fruits, nuts, and herbs, which can help cancer treatment by targeting mitochondrial metabolism and inducing apoptosis through the inhibition of cyclin-dependent kinase 6 [189-191]. Following the development of the patent, the inventors also incorporated biocompatible polymers, such as PLGA and polyethylene glycol, optionally combined with chitosan or polyvinyl alcohol, and an anticancer agent such as cisplatin, doxorubicin, or temozolomide. The characterization of this technology involved analyses of size distribution, surface charge, morphology by TEM, and monodispersity. The data showed that the PNCs promoted a reduction in pancreatic cancer cell proliferation of 50% and in colon cell proliferation of 50–60%, anti-angiogenic effects with suppression of the vascular pattern. Also, a greater suppression with encapsulated drugs compared to free drugs, sustained delivery profiles, improved bioavailability, and reduced rapid clearance were observed [61].

Nanovaccines

Nanovaccines (NVs) are composed of nanoparticles whose structure contains substances responsible for stimulating the host's immune system [131]. NVs can be lipid or non-lipid formulations. Although they vary according to the personalization for each patient, they mainly feature micrometer-sized tumor cells and diverse antigens inside and on their surface to promote the stimulation of the immune system [192,193]. Mechanisms such as covalent conjugation of antigen peptides and flash nanocomplexation can be implemented [194,195]. The use of NVs offers advantages like improved target delivery, antigen presentation, strong T cell response, and safety to combat infectious diseases and cancers [196]. Additionally, the NVs can induce tumor cell death, relieve immune suppression, increase antitumor immune activity, and inhibit metastasis [197]. Nevertheless, NVs have technical and biological limitations. Examples include tumor heterogeneity, which reduces the effectiveness of immune responses, problems with antigen delivery, rapid degradation of molecules, tumor evasion processes, and low persistence in the blood. In addition, NVs face challenges related to treatment complexity, high cost, and complications regarding effective cytotoxicity, requiring a combination of different therapeutic approaches [198].

Patent CN115671277 (2023) describes a nanovaccine with the aim of offering an oncological treatment using astragalus polysaccharides as an adjuvant immune response stimulator and drug release promoter. This natural product has potential for anticancer activity, as it can be applied as an immune adjuvant, responsible for inhibiting tumor growth and increasing immune function [199]. The NV was composed of astragalus polysaccharides as delivery vehicles, ovalbumin as a tumor antigen, and microfluidics, which allows for the formation of nanoparticles, size control, and morphology. SEM, TEM, and in vitro release tests were implemented. In order to evaluate the immunomodulatory activity, the researchers carried out migration tests to lymph nodes, activation of dendritic cells, antigen uptake capacity, and antitumor efficacy in C57 mice and nude mice inoculated with B16F10 melanoma and Lewis lung carcinoma model. The outcomes showed that the NV inhibited tumor growth better than vaccines with conventional adjuvants, such as aluminum, and increased the expression of CD80/CD86 co-stimulators in C57 mice [73]. In addition to reducing tumor progression in the Lewis lung carcinoma model, the vaccine had no effect in nude mice lacking adaptative immunity, confirming that its efficacy depends on specific activation of the immune system. Therefore, it can be inferred that the NV containing astragalus polysaccharide showed better efficacy than conventional adjuvants [54].

Nanodrug complexes

Nanodrug complexes are nanometer-scale assemblies composed of two or more biomolecules, such as active compounds, antibodies, polymers, and polysaccharides, which exhibit unique biological properties [200]. Polysaccharides and proteins are particularly promising vehicles for delivering active compounds as they can protect these molecules and enhance encapsulation,

delivery, and release [201]. In the context of cancer therapy, nanocomplexes containing molecules like anti-HER2 antibody, tamoxifen, cisplatin, polyphenols, and DNA have demonstrated increased cellular uptake, improved anticancer efficiency, enhanced tumor penetration, reduced tumor hypoxia, and tumor suppression, while minimizing adverse effects [202-204]. Nonetheless, nanocomplexes face disadvantages regarding their implementation, as they may present low stability, cause accumulation in tissues, and difficulties in controlling drug release [205].

CN225561345 (2018) combines natural polyphenols that act as APIs (tannic acid, catechin, epigallocatechin, or procyanidine), bortezomib, and iron ions to form a traceable boric acid nanodrug complex for tumor tracing and treatment. Tannic acid, a polyphenolic compound consisting of gallic acid esterified to a glucose core, can be found in various plant sources such as grapes, Sicilian sumac leaves, tea, nuts, and oak bark [206]. Tannic acid demonstrates diverse bioactive properties, including antimicrobial, anti-inflammatory, and antioxidant effects, which could play an important role in cancer prevention and therapy [207]. When tested for its pharmacological use in cancer therapy, this compound demonstrated antitumor and molecular targeting capabilities with the capacity to inhibit cell proliferation, induce apoptosis, modulate oxidative stress, suppress angiogenesis, and interfere with signaling pathways associated with tumor growth [208]. The iron ions stabilize the formulation and improve the tracing effect.

The nanodrug complex responds differently to human breast cancer cell lines (MBA-MD-231) based on the pH value, exhibiting stable release in the tumor microenvironment, which has a pH close to 6.5 (ensuring site-specific activation) and a significant inhibitory effect of up to 26.7%. When tested against mouse bone tumors, the BTZ/Ta Iron complex showed an obvious inhibitory effect without causing mice death, which can occur using high concentrations of bortezomib, and avoided damage caused by tumors on healthy bone tissue [63].

Obstacles to using nanotechnology containing natural products in cancer treatment

Between the idea of a new treatment and its commercialization, there are many obstacles to overcome. When it comes to complex diseases like cancer and technologies such as nanomedicine, there are even more challenges. Cancer is not a simple condition, it is a multifaceted combination involving genetic, molecular, and clinical profiles that vary for each patient. This instance alone can compromise the search for patients to participate in clinical trials. Patient recruitment for an ideal trial with significant results would require a large-scale random selection of people with identical disease parameters, necessitating an adapted clinical trial [209]. This, along with ethical considerations, makes clinical trials a tough process [210].

The commercialization of a medicine also requires scale-up of production to an industrial level and sufficient stability for transportation and storage, which are not easily achieved with all nanotechnologies. This emerging field of therapeutic products still misses robust and well-developed regulatory guidelines from policy-making agencies [211]. There are no standardized guidelines to follow or minimum parameters to meet, as these types of drugs have unique properties and are not equivalent to other categories already consolidated in the market. Bioaccumulation of nanomaterials is a concerning aspect of this category of medicine to be considered. The regulatory guidelines provided by the European Medicines Agency, whatsoever, lack to mention clear reference figures for such accumulation in terms of risk for the environment and leave that assessment of risk-benefit ratio up to the inventors [212]. Moreover, traditional methods of environmental risk assessment may not be sensitive enough to detect the specific impacts of nanomaterials, making this an urgent issue to be addressed in the process of developing nanotechnology medicine [213]. The absence of these guidelines means a lack of criteria for quality control, safety, and efficacy [214]. Therefore, the field of natural products within nanotechnology for cancer treatment is still poorly explored, and those who have developed a product in this area face high costs and uncertainties in regulatory approvals.

Despite US$24.5 billion being invested in research about cancer throughout the years of 2016–2020, its treatment remains at a high cost in development, production, and acquisition, which compromises patient care [215,216]. High expenses are associated with not only the complexity of cancer, but also of nanotechnology and natural product acquisition. Isolation and assuring purity of natural compounds demand a variety of solvents and specialized resources, which results in an increase in value of the final product but also production of waste. Extraction and purification processes involve multiple steps, such as liquid–solid and partition chromatography and high-performance liquid chromatography (HPLC), each demanding specific solvents and materials to achieve the desired selectivity and purity of the compound [217,218]. Traditional nanoparticle synthesis methods often rely on dangerous chemicals, leading to the release of toxic byproducts and environmental pollution [219]. Additionally, these processes typically require substantial energy input for extraction, purification, and nanoparticle formation, further increasing their environmental footprint [220]. Advanced techniques such as ultrasonication, spray drying, and freeze-drying are energy-intensive processes

frequently used to create nanoformulations and are not easily substituted as they determine stability and particle size [221].

Abraxane® is an albumin bonded with nanoparticles of paclitaxel, an alkaloid extracted and isolated from *Taxus brevifolia* bark, that is, a drug based on nanotechnology with a natural product indicated for breast cancer treatment [222,223]. One of the main challenges in using natural products in cancer nanomedicine is poor water solubility, which limits bioavailability and therapeutic efficacy [103]. Traditional paclitaxel formulations required organic solvents to solubilize the compound, leading to significant toxicity and hypersensitivity reactions [224]. Abraxane overcomes this by binding the nanoparticles with albumin, therefore changing the delivery system of the drug rather than the structure of it. Additionally, it indicates a success story in the application of nanotechnology of natural based products for cancer therapy.

Conclusion

In recent years, the demand for innovations that offer improved safety, fewer adverse effects, and greater efficacy in cancer treatments and immunotherapy has increased. In this way, the use of natural products has shown itself to be growing, associated with the implementation of nanotechnologies that seek to enhance the physicochemical properties of formulations. This review analyzed 17 patents for antineoplastic drugs where nanoparticles were the main technology utilized. The formulations developed were observed to promote tumor cell cycle blockage, inhibit metastasis and tumor growth, stimulate the immune system, and exhibit a synergistic effect with anticancer compounds. These formulations also demonstrated enhanced solubility, stability, and controlled drug release while reducing treatment risks. In conclusion, the combination of natural products and nanotechnology has great potential and offers substantial benefits for cancer treatment and immunotherapy. However, issues like high cost, environmental impacts, complex clinical trials, and unclear or inexistent regulations are obstacles for the successful development and commercialization of these therapies.

Acknowledgements

The authors dedicate this article to the entire scientific community that fights for quality science. The authors would like to thank the contributors of Canva.com, which was used to create the Graphical Abstract: Graphical element Illustration Cancer Cells: © muttaqin-images via Canva.com; Graphical element radiation radioactive cancer: ©pepermpron via Canva.com; Graphical element 3D Isometric Flat Illustration: ©tarikvision via Canva.com; Graphical element Scalpel gradient icon: ©amethyststudio via Canva.com; Graphical element cancer cell growth. cancer disease: ©surachet99 via Canva.com; Graphical element Watercolor Illustration of a Pin: ©irasutoya via Canva.com; Graphical element cancer cell icon: ©xella92 via Canva.com; Graphical element Mortar 3D Illustration: ©permadicreative via Canva.com; Graphical element 3D Serum Bottle: ©yansone via Canva.com; Graphical element Syringe Treatment Injection Vaccines Vaccination Icon: ©photo3idea via Canva.com; Graphical element 3D blue sphere element: ©hartonocreativestudio via Canva.com; Graphical element 3D Half Sphere: ©agungamiansyah via Canva.com; Graphical element Yellow sphere 3d: ©tetiana-mykhailenko via Canva.com; Graphical element Thumb Down or Dislike Icon: ©prettygirll via Canva.com. These elements are not subject to CC BY 4.0.

Funding

This study was financed in part by the Coordenação de Aperfeiçoamento de Pessoal de Nível Superior – Brasil (CAPES) – Finance Code 001. The authors thank CAPES, CNPq and FAPITEC/SE for their financial support.

ORCID® iDs

Jan Filipe Andrade Santos - https://orcid.org/0009-0006-2573-5566
Marcela Bernardes Brasileiro - https://orcid.org/0009-0007-8828-6590
José Adão Carvalho Nascimento Júnior - https://orcid.org/0000-0001-8243-5849

Data Availability Statement

Data sharing is not applicable as no new data was generated or analyzed in this study.

References

1. Brown, J. S.; Amend, S. R.; Austin, R. H.; Gatenby, R. A.; Hammarlund, E. U.; Pienta, K. J. *Mol. Cancer Res.* **2023,** *21,* 1142–1147. doi:10.1158/1541-7786.mcr-23-0411
2. Kontomanolis, E. N.; Koutras, A.; Syllaios, A.; Schizas, D.; Mastoraki, A.; Garmpis, N.; Diakosavvas, M.; Angelou, K.; Tsatsaris, G.; Pagkalos, A.; Ntounis, T.; Fasoulakis, Z. *Anticancer Res.* **2020,** *40,* 6009–6015. doi:10.21873/anticanres.14622
3. Bray, F.; Laversanne, M.; Sung, H.; Ferlay, J.; Siegel, R. L.; Soerjomataram, I.; Jemal, A. *Ca-Cancer J. Clin.* **2024,** *74,* 229–263. doi:10.3322/caac.21834
4. Baliu-Piqué, M.; Pandiella, A.; Ocana, A. *Cancers* **2020,** *12,* 3271. doi:10.3390/cancers12113271
5. Huntington, N. D.; Cursons, J.; Rautela, J. *Nat. Rev. Cancer* **2020,** *20,* 437–454. doi:10.1038/s41568-020-0272-z
6. Zeng, Z.; Chew, H. Y.; Cruz, J. G.; Leggatt, G. R.; Wells, J. W. *Int. J. Mol. Sci.* **2021,** *22,* 2907. doi:10.3390/ijms22062907
7. Labani-Motlagh, A.; Ashja-Mahdavi, M.; Loskog, A. *Front. Immunol.* **2020,** *11,* 940. doi:10.3389/fimmu.2020.00940
8. Zhang, H.; Dai, Z.; Wu, W.; Wang, Z.; Zhang, N.; Zhang, L.; Zeng, W.-J.; Liu, Z.; Cheng, Q. *J. Exp. Clin. Cancer Res.* **2021,** *40,* 184. doi:10.1186/s13046-021-01987-7
9. Alard, E.; Butnariu, A.-B.; Grillo, M.; Kirkham, C.; Zinovkin, D. A.; Newnham, L.; Macciochi, J.; Pranjol, M. Z. I. *Cancers* **2020,** *12,* 1826. doi:10.3390/cancers12071826

10. Tan, S.; Li, D.; Zhu, X. *Biomed. Pharmacother.* **2020,** *124,* 109821. doi:10.1016/j.biopha.2020.109821
11. Bai, R.; Chen, N.; Li, L.; Du, N.; Bai, L.; Lv, Z.; Tian, H.; Cui, J. *Front. Oncol.* **2020,** *10,* 1290. doi:10.3389/fonc.2020.01290
12. Rieth, J.; Subramanian, S. *Int. J. Mol. Sci.* **2018,** *19,* 1340. doi:10.3390/ijms19051340
13. Naeem, A.; Hu, P.; Yang, M.; Zhang, J.; Liu, Y.; Zhu, W.; Zheng, Q. *Molecules* **2022,** *27,* 8367. doi:10.3390/molecules27238367
14. Nan, Y.; Su, H.; Zhou, B.; Liu, S. *Front. Oncol.* **2023,** *12,* 1049888. doi:10.3389/fonc.2022.1049888
15. Singab, A. N. B.; Amr, K.; Elissawy, A. M. *Bioequiv. Bioavailab. Int. J.* **2024,** *8,* 000226. doi:10.23880/beba-16000226
16. Jin, C.; Wang, K.; Oppong-Gyebi, A.; Hu, J. *Int. J. Med. Sci.* **2020,** *17,* 2964–2973. doi:10.7150/ijms.49801
17. Murugan, B.; Sagadevan, S.; Fatimah, I.; Oh, W.-C.; Motalib Hossain, M. A.; Johan, M. R. *Nanotechnol. Rev.* **2021,** *10,* 933–953. doi:10.1515/ntrev-2021-0067
18. Azizi, M.; Jahanban-Esfahlan, R.; Samadian, H.; Hamidi, M.; Seidi, K.; Dolatshahi-Pirouz, A.; Yazdi, A. A.; Shavandi, A.; Laurent, S.; Be Omide Hagh, M.; Kasaiyan, N.; Santos, H. A.; Shahbazi, M.-A. *Mater. Today Bio* **2023,** *20,* 100672. doi:10.1016/j.mtbio.2023.100672
19. López-Estévez, A. M.; Lapuhs, P.; Pineiro-Alonso, L.; Alonso, M. J. *Adv. Mater. (Weinheim, Ger.)* **2024,** *36,* 2309355. doi:10.1002/adma.202309355
20. Northwick, A. B.; Carlson, E. E. *Chem. Res. Toxicol.* **2025,** *38,* 7–14. doi:10.1021/acs.chemrestox.4c00220
21. Pandit, C.; Roy, A.; Ghotekar, S.; Khusro, A.; Islam, M. N.; Emran, T. B.; Lam, S. E.; Khandaker, M. U.; Bradley, D. A. *J. King Saud Univ., Sci.* **2022,** *34,* 101869. doi:10.1016/j.jksus.2022.101869
22. Irvine, D. J.; Dane, E. L. *Nat. Rev. Immunol.* **2020,** *20,* 321–334. doi:10.1038/s41577-019-0269-6
23. Chen, Y.; Zhou, Q.; Jia, Z.; Cheng, N.; Zhang, S.; Chen, W.; Wang, L. *Acta Pharm. Sin. B* **2024,** *14,* 3834–3854. doi:10.1016/j.apsb.2024.05.032
24. Vieira, I. R. S.; Conte-Junior, C. A. *Crit. Rev. Food Sci. Nutr.* **2024,** *64,* 381–406. doi:10.1080/10408398.2022.2106471
25. Hadkar, V. M.; Mohanty, C.; Selvaraj, C. I. *RSC Adv.* **2024,** *14,* 25149–25173. doi:10.1039/d4ra03911d
26. *World Intellectual Property Indicators 2022;* World Intellectual Property Organization. doi:10.34667/tind.47082
27. Gavas, S.; Quazi, S.; Karpiński, T. M. *Nanoscale Res. Lett.* **2021,** *16,* 173. doi:10.1186/s11671-021-03628-6
28. Owens, B. *Nature* **2024,** *630,* S2–S4. doi:10.1038/d41586-024-01596-2
29. Li, Q.; Di, J.; Liu, Q. *Front. Public Health* **2023,** *11,* 1087830. doi:10.3389/fpubh.2023.1087830
30. National Center for Science and Engineering Statistics (NCSES). U.S. R&D Totaled $892 Billion in 2022; Estimate for 2023 Indicates Further Increase to $940 Billion. https://ncses.nsf.gov/pubs/nsf25327/ (accessed June 24, 2025).
31. Singh, S. B.; Martin, G. E.; McKittrick, B.; Crowther, J.; Fraenkel, H.; Lunn, C.; Bayne, M.; Perkins, J. B.; Gullo, V. *J. Nat. Prod.* **2024,** *87,* 1235–1245. doi:10.1021/acs.jnatprod.4c00081
32. Cordell, G. A. *Natl. Sci. Rev.* **2022,** *9,* nwac075. doi:10.1093/nsr/nwac075
33. Atanasov, A. G.; Zotchev, S. B.; Dirsch, V. M.; Orhan, I. E.; Banach, M.; Rollinger, J. M.; Barreca, D.; Weckwerth, W.; Bauer, R.; Bayer, E. A.; Majeed, M.; Bishayee, A.; Bochkov, V.; Bonn, G. K.; Braidy, N.; Bucar, F.; Cifuentes, A.; D'Onofrio, G.; Bodkin, M.; Diederich, M.; Dinkova-Kostova, A. T.; Efferth, T.; El Bairi, K.; Arkells, N.; Fan, T.-P.; Fiebich, B. L.; Freissmuth, M.; Georgiev, M. I.; Gibbons, S.; Godfrey, K. M.; Gruber, C. W.; Heer, J.; Huber, L. A.; Ibanez, E.; Kijjoa, A.; Kiss, A. K.; Lu, A.; Macias, F. A.; Miller, M. J. S.; Mocan, A.; Müller, R.; Nicoletti, F.; Perry, G.; Pittalà, V.; Rastrelli, L.; Ristow, M.; Russo, G. L.; Silva, A. S.; Schuster, D.; Sheridan, H.; Skalicka-Woźniak, K.; Skaltsounis, L.; Sobarzo-Sánchez, E.; Bredt, D. S.; Stuppner, H.; Sureda, A.; Tzvetkov, N. T.; Vacca, R. A.; Aggarwal, B. B.; Battino, M.; Giampieri, F.; Wink, M.; Wolfender, J.-L.; Xiao, J.; Yeung, A. W. K.; Lizard, G.; Popp, M. A.; Heinrich, M.; Berindan-Neagoe, I.; Stadler, M.; Daglia, M.; Verpoorte, R.; Supuran, C. T. *Nat. Rev. Drug Discovery* **2021,** *20,* 200–216. doi:10.1038/s41573-020-00114-z
34. Davis, M. E.; Chen, Z.; Shin, D. M. *Nat. Rev. Drug Discovery* **2008,** *7,* 771–782. doi:10.1038/nrd2614
35. Sakdiset, P.; Okada, A.; Todo, H.; Sugibayashi, K. *J. Drug Delivery Sci. Technol.* **2018,** *44,* 58–64. doi:10.1016/j.jddst.2017.11.021
36. Plucinski, A.; Lyu, Z.; Schmidt, B. V. K. J. *J. Mater. Chem. B* **2021,** *9,* 7030–7062. doi:10.1039/d1tb00628b
37. Rao, A.; Roy, S.; Jain, V.; Pillai, P. P. *ACS Appl. Mater. Interfaces* **2023,** *15,* 25248–25274. doi:10.1021/acsami.2c05378
38. Yang, J.; Zhang, L.; Zhou, Q.; Chen, F.; Stenzel, M.; Gao, F.; Liu, C.; Yuan, H.; Li, H.; Jiang, Y. *Nanoscale Adv.* **2021,** *3,* 2812–2821. doi:10.1039/d0na01066a
39. Pulingam, T.; Foroozandeh, P.; Chuah, J.-A.; Sudesh, K. *Nanomaterials* **2022,** *12,* 576. doi:10.3390/nano12030576
40. Ko, W.-C.; Wang, S.-J.; Hsiao, C.-Y.; Hung, C.-T.; Hsu, Y.-J.; Chang, D.-C.; Hung, C.-F. *Molecules* **2022,** *27,* 1551. doi:10.3390/molecules27051551
41. Phafat, B.; Bhattacharya, S. *Mini-Rev. Med. Chem.* **2023,** *23,* 1257–1272. doi:10.2174/1389557522666220405202222
42. Bontempo, P.; De Masi, L.; Rigano, D. *Nutrients* **2023,** *15,* 2961. doi:10.3390/nu15132961
43. Najmi, A.; Javed, S. A.; Al Bratty, M.; Alhazmi, H. A. *Molecules* **2022,** *27,* 349. doi:10.3390/molecules27020349
44. Elkordy, A. A.; Haj-Ahmad, R. R.; Awaad, A. S.; Zaki, R. M. *J. Drug Delivery Sci. Technol.* **2021,** *63,* 102459. doi:10.1016/j.jddst.2021.102459
45. Ma, L.; Diao, L.; Peng, Z.; Jia, Y.; Xie, H.; Li, B.; Ma, J.; Zhang, M.; Cheng, L.; Ding, D.; Zhang, X.; Chen, H.; Mo, F.; Jiang, H.; Xu, G.; Meng, F.; Zhong, Z.; Liu, M. *Adv. Mater. (Weinheim, Ger.)* **2021,** *33,* 2104849. doi:10.1002/adma.202104849
46. Nuzzo, G.; Senese, G.; Gallo, C.; Albiani, F.; Romano, L.; d'Ippolito, G.; Manzo, E.; Fontana, A. *Mar. Drugs* **2022,** *20,* 386. doi:10.3390/md20060386
47. Alqathama, A. *Front. Immunol.* **2024,** *15,* 1410300. doi:10.3389/fimmu.2024.1410300
48. Cai, C.; Wu, Q.; Hong, H.; He, L.; Liu, Z.; Gu, Y.; Zhang, S.; Wang, Q.; Fan, X.; Fang, J. *Sci. Rep.* **2021,** *11,* 3332. doi:10.1038/s41598-021-82857-2
49. Deng, L.-J.; Qi, M.; Li, N.; Lei, Y.-H.; Zhang, D.-M.; Chen, J.-X. *J. Leukocyte Biol.* **2020,** *108,* 493–508. doi:10.1002/jlb.3mr0320-444r
50. Dong, S.; Guo, X.; Han, F.; He, Z.; Wang, Y. *Acta Pharm. Sin. B* **2022,** *12,* 1163–1185. doi:10.1016/j.apsb.2021.08.020

51. Yang, L.; Chen, Y.; Liu, K.; Chen, Y.; Zhang, Y.; Zhang, Z.; Li, H. *Front. Pharmacol.* **2024,** *15,* 1289957. doi:10.3389/fphar.2024.1289957
52. Vijayan, Y.; Sandhu, J. S.; Harikumar, K. B. *Curr. Med. Chem.* **2024,** *31,* 5165–5177. doi:10.2174/0109298673274796240116105555
53. Kan, L. L.-Y.; Chan, B. C.-L.; Leung, P.-C.; Wong, C.-K. *Molecules* **2023,** *28,* 5804. doi:10.3390/molecules28155804
54. Komorowska, D.; Radzik, T.; Kalenik, S.; Rodacka, A. *Int. J. Mol. Sci.* **2022,** *23,* 10627. doi:10.3390/ijms231810627
55. Tang, L.; Li, J.; Zhao, Q.; Pan, T.; Zhong, H.; Wang, W. *Pharmaceutics* **2021,** *13,* 1151. doi:10.3390/pharmaceutics13081151
56. Miguel, R. d. A.; Hirata, A. S.; Jimenez, P. C.; Lopes, L. B.; Costa-Lotufo, L. V. *Pharmaceutics* **2022,** *14,* 1722. doi:10.3390/pharmaceutics14081722
57. Huang, L.; Huang, X.-H.; Yang, X.; Hu, J.-Q.; Zhu, Y.-Z.; Yan, P.-Y.; Xie, Y. *Pharmacol. Res.* **2024,** *201,* 107100. doi:10.1016/j.phrs.2024.107100
58. Patel, P.; Garala, K.; Singh, S.; Prajapati, B. G.; Chittasupho, C. *Pharmaceuticals* **2024,** *17,* 329. doi:10.3390/ph17030329
59. Ion, D.; Niculescu, A.-G.; Păduraru, D. N.; Andronic, O.; Muşat, F.; Grumezescu, A. M.; Bolocan, A. *Pharmaceutics* **2021,** *14,* 18. doi:10.3390/pharmaceutics14010018
60. Cohen, S.; Kryukov, O.; Forti, E.; Ruvinov, E. Anionic nanoparticles for use in the delivery of anionic small molecule drugs. WO Patent WO2016178224, Nov 10, 2016.
61. Saddiq, A. A. N.; Mousa, S. A.; Mousa, D. S. Nanocapsule containing a bioactive compound, and a method of reducing toxicity resulting from cancer therapy. U.S. Patent US240447339, Nov 2, 2017.
62. Guan, Y.; Du, S.; Hu, Z. Targeted Nano-Particle for Inhibiting Breast Cancer, and Preparation Method and Application Thereof. Chin. Patent CN222367609, Dec 15, 2017.
63. Cheng, Y.; Sang, H.; Wang, C.; Li, C. Traceable Boric Acid Nano-Drug Compound, Preparation Method and Use Thereof. Chin. Patent CN225561345, Feb 11, 2018.
64. Yang, X.; Cheng, J. Preparation Method and Application of Active Natural Super-Molecular Photosensitizer. Chin. Patent CN109846857, June 7, 2019.
65. Yang, X.; Wang, J. Active Natural Product Nano Drug Carrier System and Preparation Method and Application Thereof. Chin. Patent CN111202719, May 29, 2020.
66. Shao, J.; Zhang, W.; Zhao, R.; Fang, Y. Carrier-Free Nano-Drug Based on Metal-Organic Co-Assembly as Well as Preparation and Application of Carrier-Free Nano-Drug. Chin. Patent CN114129571, March 4, 2022.
67. Kim, Y. J. Method for producing gold nanoparticle using strain from ginseng and nigella sativa extract and pharmaceutical composition for treating cancer comprising the gold nanoparticle. Korean Pat. Appl. KR20220169108 (A), Dec 27, 2022.
68. Xing, C.; Li, C.; Gao, D.; Ahn, H.; Chen, Y. Photo-Thermal Response Drug-Loaded Nano Particle as Well as Preparation and Application Thereof. Chin. Patent CN367902299, April 8, 2022.
69. Shao, J.; Yue, J.; Yang, F. Preparation and Application of Carrier-Free Double-Drug Self-Assembled Nanoparticles. Chin. Patent CN114470229, May 13, 2022.
70. Qu, W.; Zhang, K.; Zhu, J.; Wang, R.; Feng, F.; Wang, C. Self-Assembled Nanoparticles Based on Natural Products as Well as Preparation Method and Application of Self-Assembled Nanoparticles. Chin. Patent CN115252560, Nov 1, 2022.
71. Shao, J.; Zhang, B.; Tan, X. CRISPR/Cas9-Drug Co-Assembly Bionic Nano System as Well as Preparation and Application Thereof. Chin. Pat. Appl. CN117064865 (A), Nov 17, 2023.
72. Zeng, X.; Li, Z.; Shi, K.; Chen, H. Immune Checkpoint Inhibitor Nano-Delivery System Composed of Natural Polyphenol and Preparation Method of Immune Checkpoint Inhibitor Nano-Delivery System. Chin. Patent CN426774477, Dec 20, 2023.
73. Dong, Z.; Zhang, Y.; Li, N. Nano Tumor Vaccine Formed Based on Self-Assembly of Astragalus Polysaccharide and Application of Nano Tumor Vaccine. Chin. Patent CN115671277, Feb 3, 2023.
74. Li, J.; Feng, T.; Feng, X.; Zhou, Y.; Chen, L.; Jiang, H.; Zhao, C. Novel CDs-Ber Nano Material as Well as Preparation Method and Application Thereof. Chin. Patent CN427216811, Dec 28, 2023.
75. Deng, Z.; Cui, X.; Qin, Y.; He, Z.; Du, S. Preparation Method of Breast Cancer Targeted Nano Drug Delivery System. Chin. Patent CN115887415, April 4, 2023.
76. Wang, Z.; Wang, J.; Liu, L.; Wei, B.; Shen, K.; Zheng, Q. Chitin-Glucan Nano-Polysaccharide Compound as Well as Preparation Method and Application Thereof. Chin. Patent CN117534780, Feb 9, 2024.
77. Sorzano, C. O. S.; Hamilton, D. G.; Mendez, E. *Lab. Anim.* **2025,** *59,* 276–282. doi:10.1177/00236772241271039
78. Honkala, A.; Malhotra, S. V.; Kummar, S.; Junttila, M. R. *Nat. Rev. Drug Discovery* **2022,** *21,* 99–114. doi:10.1038/s41573-021-00301-6
79. Gunjur, A.; Balasubramanian, A.; Hafeez, U.; Menon, S.; Cher, L.; Parakh, S.; Gan, H. K. *J. Neuro-Oncol.* **2022,** *159,* 539–549. doi:10.1007/s11060-022-04092-7
80. Kamran, S.; Sinniah, A.; Abdulghani, M. A. M.; Alshawsh, M. A. *Cancers* **2022,** *14,* 1100. doi:10.3390/cancers14051100
81. Ren, Y.; Kinghorn, A. D. *J. Med. Chem.* **2020,** *63,* 15410–15448. doi:10.1021/acs.jmedchem.0c01449
82. Singh, A.; Debnath, R.; Sharma, A.; Saini, A.; Seni, K.; Chawla, V.; Chawla, P. A. *Curr. Med. Chem.* **2025,** in press. doi:10.2174/0109298673315133240830055507
83. Liu, W.; Cui, X.; Zhong, Y.; Ma, R.; Liu, B.; Xia, Y. *Pharmacol. Res.* **2023,** *193,* 106812. doi:10.1016/j.phrs.2023.106812
84. Abotaleb, M.; Liskova, A.; Kubatka, P.; Büsselberg, D. *Biomolecules* **2020,** *10,* 221. doi:10.3390/biom10020221
85. Bakrim, S.; El Omari, N.; El Hachlafi, N.; Bakri, Y.; Lee, L.-H.; Bouyahya, A. *Foods* **2022,** *11,* 3323. doi:10.3390/foods11213323
86. Ying, Y.; Hao, W. *Front. Immunol.* **2023,** *14,* 1147641. doi:10.3389/fimmu.2023.1147641
87. Li, Y.; Wang, X.; Ma, X.; Liu, C.; Wu, J.; Sun, C. *Front. Pharmacol.* **2021,** *12,* 621813. doi:10.3389/fphar.2021.621813
88. Guo, R.; Chen, M.; Ding, Y.; Yang, P.; Wang, M.; Zhang, H.; He, Y.; Ma, H. *Front. Nutr.* **2022,** *9,* 838179. doi:10.3389/fnut.2022.838179
89. Huang, Y.; Li, G.; Hong, C.; Zheng, X.; Yu, H.; Zhang, Y. *Front. Oncol.* **2021,** *11,* 733369. doi:10.3389/fonc.2021.733369
90. Stærk, D.; Lykkeberg, A. K.; Christensen, J.; Budnik, B. A.; Abe, F.; Jaroszewski, J. W. *J. Nat. Prod.* **2002,** *65,* 1299–1302. doi:10.1021/np0106384
91. Luan, S.; Gao, Y.; Liang, X.; Zhang, L.; Yin, L.; He, C.; Liu, S.; Yin, Z.; Yue, G.; Zou, Y.; Li, L.; Song, X.; Lv, C.; Zhang, W.; Jing, B. *Bioorg. Chem.* **2021,** *109,* 104699. doi:10.1016/j.bioorg.2021.104699
92. Dhandapani, S.; Xu, X.; Wang, R.; Puja, A. M.; Kim, H.; Perumalsamy, H.; Balusamy, S. R.; Kim, Y.-J. *Mater. Sci. Eng.: C* **2021,** *127,* 112214. doi:10.1016/j.msec.2021.112214

93. Guo, Y.; Jiang, K.; Shen, Z.; Zheng, G.; Fan, L.; Zhao, R.; Shao, J. *ACS Appl. Mater. Interfaces* **2017,** *9,* 43508–43519. doi:10.1021/acsami.7b14755
94. Li, N.; Zhang, Y.; Han, M.; Liu, T.; Wu, J.; Xiong, Y.; Fan, Y.; Ye, F.; Jin, B.; Zhang, Y.; Sun, G.; Sun, X.; Dong, Z. *Sci. China: Life Sci.* **2024,** *67,* 680–697. doi:10.1007/s11427-023-2465-x
95. Rezić, I. *Polymers (Basel, Switz.)* **2022,** *14,* 4961. doi:10.3390/polym14224961
96. Shabatina, T. I.; Gromova, Y. A.; Vernaya, O. I.; Soloviev, A. V.; Shabatin, A. V.; Morosov, Y. N.; Astashova, I. V.; Melnikov, M. Y. *Pharmaceuticals* **2024,** *17,* 587. doi:10.3390/ph17050587
97. Yusuf, A.; Almotairy, A. R. Z.; Henidi, H.; Alshehri, O. Y.; Aldughaim, M. S. *Polymers (Basel, Switz.)* **2023,** *15,* 1596. doi:10.3390/polym15071596
98. Nam, N. H.; Luong, N. H. Nanoparticles: Synthesis and Applications. *Materials for Biomedical Engineering;* Elsevier: Amsterdam, Netherlands, 2019; pp 211–240. doi:10.1016/b978-0-08-102814-8.00008-1
99. Mundekkad, D.; Cho, W. C. *Int. J. Mol. Sci.* **2022,** *23,* 1685. doi:10.3390/ijms23031685
100. Hu, Y.; Nie, W.; Lyu, L.; Zhang, X.; Wang, W.; Zhang, Y.; He, S.; Guo, A.; Liu, F.; Wang, B.; Qian, Z.; Gao, X. *ACS Nano* **2024,** *18,* 3295–3312. doi:10.1021/acsnano.3c10037
101. Wells, K.; Liu, T.; Zhu, L.; Yang, L. *Nanoscale* **2024,** *16,* 17699–17722. doi:10.1039/d4nr01780c
102. Zhou, L.; Zou, M.; Xu, Y.; Lin, P.; Lei, C.; Xia, X. *Front. Oncol.* **2022,** *12,* 864301. doi:10.3389/fonc.2022.864301
103. Manzari-Tavakoli, A.; Babajani, A.; Tavakoli, M. M.; Safaeinejad, F.; Jafari, A. *Cancer Med.* **2024,** *13,* e7010. doi:10.1002/cam4.7010
104. Ji, H.; Wang, W.; Qiao, O.; Hao, X. *ACS Appl. Nano Mater.* **2024,** *7,* 4564–4587. doi:10.1021/acsanm.3c03315
105. Yao, Y.; Xu, Z.; Ding, H.; Yang, S.; Chen, B.; Zhou, M.; Zhu, Y.; Yang, A.; Yan, X.; Liang, C.; Kou, X.; Chen, B.; Huang, W.; Li, Y. *J. Nanobiotechnol.* **2025,** *23,* 108. doi:10.1186/s12951-025-03146-y
106. Zhang, X.; Li, N.; Zhang, S.; Sun, B.; Chen, Q.; He, Z.; Luo, C.; Sun, J. *Med. Res. Rev.* **2020,** *40,* 1754–1775. doi:10.1002/med.21669
107. Kyu Shim, M.; Yang, S.; Sun, I.-C.; Kim, K. *Adv. Drug Delivery Rev.* **2022,** *183,* 114177. doi:10.1016/j.addr.2022.114177
108. Liu, C.; Liu, Q.; Chen, L.; Li, M.; Yin, J.; Zhu, X.; Chen, D. *Adv. Healthcare Mater.* **2020,** *9,* 2000899. doi:10.1002/adhm.202000899
109. Nguyen, H. N.; Ullevig, S. L.; Short, J. D.; Wang, L.; Ahn, Y. J.; Asmis, R. *Antioxidants* **2021,** *10,* 1161. doi:10.3390/antiox10081161
110. Grabowska, K.; Żmudzki, P.; Wróbel-Biedrawa, D.; Podolak, I. *Planta Med.* **2021,** *87,* 305–313. doi:10.1055/a-1345-9377
111. Panda, S. S.; Thangaraju, M.; Lokeshwar, B. L. *Molecules* **2022,** *27,* 8981. doi:10.3390/molecules27248981
112. Alam, M.; Ali, S.; Ahmed, S.; Elasbali, A. M.; Adnan, M.; Islam, A.; Hassan, M. I.; Yadav, D. K. *Int. J. Mol. Sci.* **2021,** *22,* 12162. doi:10.3390/ijms222212162
113. Fogde, D. L.; Xavier, C. P. R.; Balnytė, K.; Holland, L. K. K.; Stahl-Meyer, K.; Dinant, C.; Corcelle-Termeau, E.; Pereira-Wilson, C.; Maeda, K.; Jäättelä, M. *Cells* **2022,** *11,* 4079. doi:10.3390/cells11244079
114. Xu, H.; Yu, A.-l.; Zhao, D.-p.; Meng, G.-y.; Wang, L.; Shan, M.; Hu, N.-x.; Liu, Y.-l. *Innate Immun.* **2022,** *28,* 155–163. doi:10.1177/17534259221094559
115. Yasin, A.; Ren, Y.; Li, J.; Sheng, Y.; Cao, C.; Zhang, K. *Front. Bioeng. Biotechnol.* **2022,** *10,* 910290. doi:10.3389/fbioe.2022.910290
116. Rodriguez-Marquez, C. D.; Arteaga-Marin, S.; Rivas-Sánchez, A.; Autrique-Hernández, R.; Castro-Muñoz, R. *Int. J. Mol. Sci.* **2022,** *23,* 6038. doi:10.3390/ijms23116038
117. Graciela, C.-Q.; José Juan, E.-C.; Gieraldin, C.-L.; Xóchitl Alejandra, P.-M.; Gabriel, A.-Á. *Polymers (Basel, Switz.)* **2023,** *15,* 3473. doi:10.3390/polym15163473
118. Wang, W.; Zhang, X.; Li, Z.; Pan, D.; Zhu, H.; Gu, Z.; Chen, J.; Zhang, H.; Gong, Q.; Luo, K. *Carbohydr. Polym.* **2021,** *267,* 118160. doi:10.1016/j.carbpol.2021.118160
119. Hu, Q.; Li, H.; Archibong, E.; Chen, Q.; Ruan, H.; Ahn, S.; Dukhovlinova, E.; Kang, Y.; Wen, D.; Dotti, G.; Gu, Z. *Nat. Biomed. Eng.* **2021,** *5,* 1038–1047. doi:10.1038/s41551-021-00712-1
120. Bae, J.; Kim, N.; Shin, Y.; Kim, S.-Y.; Kim, Y.-J. *Biomed. Dermatol.* **2020,** *4,* 8. doi:10.1186/s41702-020-0057-8
121. Sheng, Y.; Sun, Y.; Tang, Y.; Yu, Y.; Wang, J.; Zheng, F.; Li, Y.; Sun, Y. *Front. Pharmacol.* **2023,** *14,* 1144878. doi:10.3389/fphar.2023.1144878
122. Oh, J.-W.; Muthu, M.; Pushparaj, S. S. C.; Gopal, J. *Molecules* **2023,** *28,* 2151. doi:10.3390/molecules28052151
123. Talib, W. H.; Awajan, D.; Alqudah, A.; Alsawwaf, R.; Althunibat, R.; Abu AlRoos, M.; Al Safadi, A.; Abu Asab, S.; Hadi, R. W.; Al Kury, L. T. *Molecules* **2024,** *29,* 1373. doi:10.3390/molecules29061373
124. Li, Z.; Geng, Y.-N.; Jiang, J.-D.; Kong, W.-J. *Evidence-Based Complementary Altern. Med.* **2014,** 289264. doi:10.1155/2014/289264
125. Kazemipoor, M.; Fadaei Tehrani, P.; Zandi, H.; Golvardi Yazdi, R. *Clin. Exp. Dent. Res.* **2021,** *7,* 601–608. doi:10.1002/cre2.379
126. Bhanumathi, R.; Manivannan, M.; Thangaraj, R.; Kannan, S. *ACS Omega* **2018,** *3,* 8317–8328. doi:10.1021/acsomega.7b01347
127. Cui, X.; He, Z.; Liang, J.; Wei, M.; Guo, Z.; Zhou, Y.; Qin, Y.; Deng, Z. *J. Drug Targeting* **2024,** *32,* 325–333. doi:10.1080/1061186x.2024.2309566
128. Hak, A.; Ali, M. S.; Sankaranarayanan, S. A.; Shinde, V. R.; Rengan, A. K. *ACS Appl. Bio Mater.* **2023,** *6,* 349–364. doi:10.1021/acsabm.2c00891
129. Wang, H.; Wang, Z.; Zhang, Z.; Liu, J.; Hong, L. *Adv. Nutr.* **2023,** *14,* 1085–1110. doi:10.1016/j.advnut.2023.05.013
130. Sundberg, D. *Biomacromolecules* **2020,** *21,* 4388–4395. doi:10.1021/acs.biomac.0c00549
131. Fu, L.; Zhou, X.; He, C. *Macromol. Biosci.* **2021,** *21,* 2100075. doi:10.1002/mabi.202100075
132. Wan, Z.; Zheng, R.; Moharil, P.; Liu, Y.; Chen, J.; Sun, R.; Song, X.; Ao, Q. *Molecules* **2021,** *26,* 1220. doi:10.3390/molecules26051220
133. Chang, D.; Ma, Y.; Xu, X.; Xie, J.; Ju, S. *Front. Bioeng. Biotechnol.* **2021,** *9,* 707319. doi:10.3389/fbioe.2021.707319
134. Zhang, F.; Zhong, H.; Zhou, X.; Pan, M.; Xu, J.; Liu, M.; Wang, M.; Liu, G.; Xu, T.; Wang, Y.; Wu, X.; Xu, Y. *Hortic. Res.* **2022,** *9,* uhac055. doi:10.1093/hr/uhac055
135. Nie, F.; Liu, L.; Cui, J.; Zhao, Y.; Zhang, D.; Zhou, D.; Wu, J.; Li, B.; Wang, T.; Li, M.; Yan, M. *Antioxidants* **2023,** *12,* 1004. doi:10.3390/antiox12051004
136. Yao, Z.; Liu, N.; Lin, H.; Zhou, Y. *J. Clin. Transl. Hepatol.* **2023,** *11,* 1329–1340. doi:10.14218/jcth.2023.00071
137. Zhou, F.; Zhou, Y.; Guo, Z.; Yu, X.; Deng, Z. *Mini-Rev. Med. Chem.* **2022,** *22,* 836–847. doi:10.2174/1389557521666210428132256
138. Fan, Y.; Liu, Y.; Wu, Y.; Dai, F.; Yuan, M.; Wang, F.; Bai, Y.; Deng, H. *Int. J. Biol. Macromol.* **2021,** *192,* 1240–1255. doi:10.1016/j.ijbiomac.2021.10.074

139. Kou, T.; Faisal, M.; Song, J.; Blennow, A. *Crit. Rev. Food Sci. Nutr.* **2024,** *64,* 1–15. doi:10.1080/10408398.2022.2104209
140. Zeng, Y.; Xiang, Y.; Sheng, R.; Tomás, H.; Rodrigues, J.; Gu, Z.; Zhang, H.; Gong, Q.; Luo, K. *Bioact. Mater.* **2021,** *6,* 3358–3382. doi:10.1016/j.bioactmat.2021.03.008
141. Li, M.; Zhao, Y.; Zhang, W.; Zhang, S.; Zhang, S. *Carbohydr. Polym.* **2021,** *269,* 118323. doi:10.1016/j.carbpol.2021.118323
142. Abka-khajouei, R.; Tounsi, L.; Shahabi, N.; Patel, A. K.; Abdelkafi, S.; Michaud, P. *Mar. Drugs* **2022,** *20,* 364. doi:10.3390/md20060364
143. Iravani, S.; Varma, R. S. *Mar. Drugs* **2022,** *20,* 598. doi:10.3390/md20100598
144. Wan, S.; Fan, Q.; Wu, Y.; Zhang, J.; Qiao, G.; Jiang, N.; Yang, J.; Liu, Y.; Li, J.; Chiampanichayakul, S.; Tima, S.; Tong, F.; Anuchapreeda, S.; Wu, J. *Pharmaceutics* **2023,** *15,* 631. doi:10.3390/pharmaceutics15020631
145. Wu, L.; Zhao, J.; Zhang, X.; Liu, S.; Zhao, C. *Int. J. Biol. Macromol.* **2021,** *179,* 116–124. doi:10.1016/j.ijbiomac.2021.02.207
146. Moura, R. P.; Sousa, F.; Almeida, A.; Pinto, S.; Sarmento, B. Theranostic Biomaterials for Regulation of the Blood–Brain Barrier. *Theranostic Bionanomaterials;* Elsevier: Amsterdam, Netherlands, 2019; pp 303–319. doi:10.1016/b978-0-12-815341-3.00013-4
147. Kim, H.; Park, Y.; Stevens, M. M.; Kwon, W.; Hahn, S. K. *J. Controlled Release* **2019,** *303,* 55–66. doi:10.1016/j.jconrel.2019.04.003
148. Slepička, P.; Slepičková Kasálková, N.; Siegel, J.; Kolská, Z.; Švorčík, V. *Materials* **2019,** *13,* 1. doi:10.3390/ma13010001
149. He, J.-s.; Liu, S.-j.; Zhang, Y.-r.; Chu, X.-d.; Lin, Z.-b.; Zhao, Z.; Qiu, S.-h.; Guo, Y.-g.; Ding, H.; Pan, Y.-l.; Pan, J.-h. *Front. Pharmacol.* **2021,** *12,* 687399. doi:10.3389/fphar.2021.687399
150. Chen, X.-Y.; Yung, L.-Y. L.; Tan, P. H.; Bay, B. H. *Front. Immunol.* **2022,** *13,* 865554. doi:10.3389/fimmu.2022.865554
151. Goddard, Z. R.; Marín, M. J.; Russell, D. A.; Searcey, M. *Chem. Soc. Rev.* **2020,** *49,* 8774–8789. doi:10.1039/d0cs01121e
152. Sargazi, S.; Laraib, U.; Er, S.; Rahdar, A.; Hassanisaadi, M.; Zafar, M. N.; Díez-Pascual, A. M.; Bilal, M. *Nanomaterials* **2022,** *12,* 1102. doi:10.3390/nano12071102
153. Gidwani, B.; Sahu, V.; Shukla, S. S.; Pandey, R.; Joshi, V.; Jain, V. K.; Vyas, A. *J. Drug Delivery Sci. Technol.* **2021,** *61,* 102308. doi:10.1016/j.jddst.2020.102308
154. Tiwari, P. K.; Sahu, M.; Kumar, G.; Ashourian, M. *Comput. Intell. Neurosci.* **2021,** 2096208. doi:10.1155/2021/2096208
155. Ondry, J. C.; Philbin, J. P.; Lostica, M.; Rabani, E.; Alivisatos, A. P. *ACS Nano* **2021,** *15,* 2251–2262. doi:10.1021/acsnano.0c07202
156. Kurniawan, D.; Sharma, N.; Rahardja, M. R.; Cheng, Y.-Y.; Chen, Y.-T.; Wu, G.-X.; Yeh, Y.-Y.; Yeh, P.-C.; Ostrikov, K. K.; Chiang, W.-H. *ACS Appl. Mater. Interfaces* **2022,** *14,* 52289–52300. doi:10.1021/acsami.2c15251
157. Uprety, B.; Abrahamse, H. *Front. Chem. (Lausanne, Switz.)* **2022,** *10,* 946574. doi:10.3389/fchem.2022.946574
158. Uthman, A.; AL-Rawi, N.; Saeed, M. H.; Eid, B.; Al-Rawi, N. H. *PeerJ* **2024,** *12,* e16732. doi:10.7717/peerj.16732
159. Naik, K.; Chaudhary, S.; Ye, L.; Parmar, A. S. *Front. Bioeng. Biotechnol.* **2022,** *10,* 882100. doi:10.3389/fbioe.2022.882100
160. Liu, X.-Y.; Wang, Y.-N.; Du, J.-S.; Chen, B.-H.; Liu, K.-Y.; Feng, L.; Xiang, G.-S.; Zhang, S.-Y.; Lu, Y.-C.; Yang, S.-C.; Zhang, G.-H.; Hao, B. *Front. Plant Sci.* **2024,** *14,* 1259347. doi:10.3389/fpls.2023.1259347
161. Salimo, Z. M.; Yakubu, M. N.; da Silva, E. L.; de Almeida, A. C. G.; Chaves, Y. O.; Costa, E. V.; da Silva, F. M. A.; Tavares, J. F.; Monteiro, W. M.; de Melo, G. C.; Koolen, H. H. F. *Biomolecules* **2023,** *13,* 403. doi:10.3390/biom13030403
162. Gan, Y.; Li, X.; Han, S.; Zhou, L.; Li, W. *Pharmaceuticals* **2023,** *16,* 241. doi:10.3390/ph16020241
163. Li, X.; Xie, L.; Zhou, L.; Gan, Y.; Han, S.; Zhou, Y.; Qing, X.; Li, W. *Am. J. Chin. Med.* **2023,** *51,* 1905–1925. doi:10.1142/s0192415x23500842
164. Abed, S. N.; Deb, P. K.; Surchi, H. S.; Kokaz, S. F.; Jamal, S. M.; Bandopadhyay, S.; Tekade, R. K. Nanocarriers in Different Preclinical and Clinical Stages. *Basic Fundamentals of Drug Delivery;* Academic Press: London, UK, 2019; pp 685–731. doi:10.1016/b978-0-12-817909-3.00017-0
165. Morales-Becerril, A.; Aranda-Lara, L.; Isaac-Olivé, K.; Ocampo-García, B. E.; Morales-Ávila, E. *EXCLI J.* **2022,** *21,* 1028–1052. doi:10.17179/excli2022-4975
166. Zhang, R.; Han, Y.; Xie, W.; Liu, F.; Chen, S. *J. Agric. Food Chem.* **2022,** *70,* 6354–6367. doi:10.1021/acs.jafc.2c01936
167. Samrot, A. V.; Sean, T. C.; Kudaiyappan, T.; Bisyarah, U.; Mirarmandi, A.; Faradjeva, E.; Abubakar, A.; Ali, H. H.; Angalene, J. L. A.; Suresh Kumar, S. *Int. J. Biol. Macromol.* **2020,** *165,* 3088–3105. doi:10.1016/j.ijbiomac.2020.10.104
168. Alshawwa, S. Z.; Kassem, A. A.; Farid, R. M.; Mostafa, S. K.; Labib, G. S. *Pharmaceutics* **2022,** *14,* 883. doi:10.3390/pharmaceutics14040883
169. Luo, S.; Lv, Z.; Yang, Q.; Chang, R.; Wu, J. *Pharmaceutics* **2023,** *15,* 1928. doi:10.3390/pharmaceutics15071928
170. Eftekhari, A.; Kryschi, C.; Pamies, D.; Gulec, S.; Ahmadian, E.; Janas, D.; Davaran, S.; Khalilov, R. *Nanotheranostics* **2023,** *7,* 236–257. doi:10.7150/ntno.77564
171. Liu, L.; Wannemuehler, M. J.; Narasimhan, B. *Curr. Opin. Biomed. Eng.* **2021,** *20,* 100322. doi:10.1016/j.cobme.2021.100322
172. Dangkoub, F.; Sankian, M.; Tafaghodi, M.; Jaafari, M. R.; Badiee, A. *J. Controlled Release* **2021,** *339,* 274–283. doi:10.1016/j.jconrel.2021.09.037
173. Fan, D.; Cao, Y.; Cao, M.; Wang, Y.; Cao, Y.; Gong, T. *Signal Transduction Targeted Ther.* **2023,** *8,* 293. doi:10.1038/s41392-023-01536-y
174. Baeza, A. *Molecules* **2020,** *25,* 1508. doi:10.3390/molecules25071508
175. Elbagory, A. M.; Marima, R. M.; Dlamini, Z. *Cancers* **2021,** *13,* 5686. doi:10.3390/cancers13225686
176. AbdElhamid, A. S.; Zayed, D. G.; Heikal, L.; Khattab, S. N.; Mady, O. Y.; El-Gizawy, S. A.; Elzoghby, A. O. *Nanomedicine (London, U. K.)* **2021,** *16,* 1613–1625. doi:10.2217/nnm-2021-0037
177. Kumar, P.; Yadav, N.; Chaudhary, B.; Umakanthan, S.; Chattu, V. K.; Kazmi, I.; Al-Abbasi, F. A.; Alzarea, S. I.; Afzal, O.; Altamimi, A. S. A.; Gupta, G.; Gupta, M. M. *Curr. Pharm. Biotechnol.* **2024,** *25,* 268–284. doi:10.2174/1389201024666230523114350
178. Jayawardena, H. S. N.; Liyanage, S. H.; Rathnayake, K.; Patel, U.; Yan, M. *Anal. Chem. (Washington, DC, U. S.)* **2021,** *93,* 1889–1911. doi:10.1021/acs.analchem.0c05208
179. Lima, A. L.; Gratieri, T.; Cunha-Filho, M.; Gelfuso, G. M. *Methods* **2022,** *199,* 54–66. doi:10.1016/j.ymeth.2021.07.009
180. Zhou, Y.; Wang, P.; Wan, F.; Zhu, L.; Wang, Z.; Fan, G.; Wang, P.; Luo, H.; Liao, S.; Yang, Y.; Chen, S.; Zhang, J. *Nanomaterials* **2023,** *13,* 3125. doi:10.3390/nano13243125

181. Itzhaki, E.; Hadad, E.; Moskovits, N.; Stemmer, S. M.; Margel, S. *Pharmaceuticals* **2021,** *14,* 648. doi:10.3390/ph14070648
182. Xiao, X.; Teng, F.; Shi, C.; Chen, J.; Wu, S.; Wang, B.; Meng, X.; Essiet Imeh, A.; Li, W. *Front. Bioeng. Biotechnol.* **2022,** *10,* 1024143. doi:10.3389/fbioe.2022.1024143
183. Francis, D. M.; Manspeaker, M. P.; Archer, P. A.; Sestito, L. F.; Heiler, A. J.; Schudel, A.; Thomas, S. N. *Biomaterials* **2021,** *279,* 121184. doi:10.1016/j.biomaterials.2021.121184
184. Deng, S.; Gigliobianco, M. R.; Censi, R.; Di Martino, P. *Nanomaterials* **2020,** *10,* 847. doi:10.3390/nano10050847
185. Yıldırım, M.; Sessevmez, M.; Poyraz, S.; Düzgüneş, N. *Pharmaceutics* **2023,** *15,* 2566. doi:10.3390/pharmaceutics15112566
186. Vieira, I. R. S.; Tessaro, L.; Lima, A. K. O.; Velloso, I. P. S.; Conte-Junior, C. A. *Nutrients* **2023,** *15,* 3136. doi:10.3390/nu15143136
187. Penta, D.; Tripathi, P.; Rajarajan, D.; Natesh, J.; Mondal, P.; Meeran, S. M. *ACS Omega* **2022,** *7,* 43147–43160. doi:10.1021/acsomega.2c05832
188. Munakarmi, S.; Shrestha, J.; Shin, H.-B.; Lee, G.-H.; Jeong, Y.-J. *Cells* **2021,** *10,* 1178. doi:10.3390/cells10051178
189. Wang, W.; Wang, S.; Liu, Y.; Wang, X.; Nie, J.; Meng, X.; Zhang, Y. *Front. Aging Neurosci.* **2022,** *14,* 925855. doi:10.3389/fnagi.2022.925855
190. Duan, J.; Li, Y.; Gao, H.; Yang, D.; He, X.; Fang, Y.; Zhou, G. *Food Funct.* **2020,** *11,* 6332–6339. doi:10.1039/d0fo01177k
191. Yousuf, M.; Shamsi, A.; Khan, P.; Shahbaaz, M.; AlAjmi, M. F.; Hussain, A.; Hassan, G. M.; Islam, A.; Rizwanul Haque, Q. M.; Hassan, M. I. *Int. J. Mol. Sci.* **2020,** *21,* 3526. doi:10.3390/ijms21103526
192. Gholap, A. D.; Gupta, J.; Kamandar, P.; Bhowmik, D. D.; Rojekar, S.; Faiyazuddin, M.; Hatvate, N. T.; Mohanto, S.; Ahmed, M. G.; Subramaniyan, V.; Kumarasamy, V. *ACS Biomater. Sci. Eng.* **2024,** *10,* 271–297. doi:10.1021/acsbiomaterials.3c01247
193. Ma, L.; Zhang, M.; Zhao, R.; Wang, D.; Ma, Y.; Ai, L. *Molecules* **2021,** *26,* 933. doi:10.3390/molecules26040933
194. Lu, L.; Duong, V. T.; Shalash, A. O.; Skwarczynski, M.; Toth, I. *Vaccines (Basel, Switz.)* **2021,** *9,* 563. doi:10.3390/vaccines9060563
195. Hu, H.; Yang, C.; Zhang, F.; Li, M.; Tu, Z.; Mu, L.; Dawulieti, J.; Lao, Y.-H.; Xiao, Z.; Yan, H.; Sun, W.; Shao, D.; Leong, K. W. *Adv. Sci.* **2021,** *8,* 2002020. doi:10.1002/advs.202002020
196. Das, A.; Ali, N. *Expert Rev. Vaccines* **2021,** *20,* 1273–1290. doi:10.1080/14760584.2021.1984890
197. Liu, M.; Xie, D.; Hu, D.; Zhang, R.; Wang, Y.; Tang, L.; Zhou, B.; Zhao, B.; Yang, L. *Adv. Sci.* **2023,** *10,* 2207697. doi:10.1002/advs.202207697
198. Fang, X.; Lan, H.; Jin, K.; Gong, D.; Qian, J. *Cancers* **2022,** *14,* 3842. doi:10.3390/cancers14163842
199. Li, W.; Hu, X.; Wang, S.; Jiao, Z.; Sun, T.; Liu, T.; Song, K. *Int. J. Biol. Macromol.* **2020,** *145,* 985–997. doi:10.1016/j.ijbiomac.2019.09.189
200. Wang, Y.; Qian, J.; Yang, M.; Xu, W.; Wang, J.; Hou, G.; Ji, L.; Suo, A. *Carbohydr. Polym.* **2019,** *225,* 115206. doi:10.1016/j.carbpol.2019.115206
201. Rosales, T. K. O.; Fabi, J. P. Polysaccharide-Based Nanotechnology Approaches to Deliver Bioactive Compounds for Food Applications. *Advances in Chemical Engineering;* Academic Press: Cambridge, MA, USA, 2023; Vol. 62, pp 215–256. doi:10.1016/bs.ache.2023.08.001
202. Han, J.; Cui, Y.; Gu, Z.; Yang, D. *Biomaterials* **2021,** *273,* 120846. doi:10.1016/j.biomaterials.2021.120846
203. Mirrahimi, M.; Abed, Z.; Beik, J.; Shiri, I.; Shiralizadeh Dezfuli, A.; Mahabadi, V. P.; Kamran Kamrava, S.; Ghaznavi, H.; Shakeri-Zadeh, A. *Pharmacol. Res.* **2019,** *143,* 178–185. doi:10.1016/j.phrs.2019.01.005
204. Yang, Z.; Chen, Q.; Chen, J.; Dong, Z.; Zhang, R.; Liu, J.; Liu, Z. *Small* **2018,** *14,* 1803262. doi:10.1002/smll.201803262
205. Kandasamy, G.; Karuppasamy, Y.; Krishnan, U. M. *Vaccines (Basel, Switz.)* **2023,** *11,* 458. doi:10.3390/vaccines11020458
206. Sun, D.; Li, M.; Zhang, M.; Cui, R.; Yang, Z.; Yu, L.; Wang, D.; Yao, W. *ACS Omega* **2023,** *8,* 30474–30482. doi:10.1021/acsomega.3c03663
207. Palaniyappan, S.; Sridhar, A.; Kari, Z. A.; Téllez-Isaías, G.; Ramasamy, T. *Mar. Drugs* **2023,** *21,* 278. doi:10.3390/md21050278
208. Kleszcz, R.; Majchrzak-Celińska, A.; Baer-Dubowska, W. *Br. J. Pharmacol.* **2025,** *182,* 2075–2093. doi:10.1111/bph.16224
209. Ha, H.; Lee, H. Y.; Kim, J. H.; Kim, D. Y.; An, H. J.; Bae, S.; Park, H.-s.; Kang, J. H. *Cancer Res. Treat.* **2024,** *56,* 991–1013. doi:10.4143/crt.2024.128
210. *Acrotech Biopharma LLC; Withdrawal of Approval of New Drug Application For MARQIBO*. https://www.federalregister.gov/documents/2022/05/02/2022-09235/acrotech-biopharma-llc-withdrawal-of-approval-of-new-drug-application-for-marqibo-vincristine (accessed Aug 18, 2025).
211. Ahmad, A.; Imran, M.; Sharma, N. *Pharmaceutics* **2022,** *14,* 2463. doi:10.3390/pharmaceutics14112463
212. Medicines Agency - Heads of Medicines Agencies, E. *Nanotechnology-Based Medicinal Products for Human Use - EU-IN Horizon Scanning Report*. https://www.ema.europa.eu/en/documents/report/nanotechnology-based-medicinal-products-human-use-eu-horizon-scanning-report_en.pdf (accessed Aug 18, 2025).
213. Zeng, H.; Lv, Z.; Sun, X.; Tong, Y.; Wu, W.; Dong, S.; Mao, L. *Environ. Health* **2024,** *2,* 189–201. doi:10.1021/envhealth.3c00138
214. Oksel Karakus, C.; Bilgi, E.; Winkler, D. A. *Nanotoxicology* **2021,** *15,* 331–351. doi:10.1080/17435390.2020.1860265
215. Desai, A.; Gyawali, B. *eClinicalMedicine* **2020,** *20,* 100269. doi:10.1016/j.eclinm.2020.100269
216. McIntosh, S. A.; Alam, F.; Adams, L.; Boon, I. S.; Callaghan, J.; Conti, I.; Copson, E.; Carson, V.; Davidson, M.; Fitzgerald, H.; Gautam, A.; Jones, C. M.; Kargbo, S.; Lakshmipathy, G.; Maguire, H.; McFerran, K.; Mirandari, A.; Moore, N.; Moore, R.; Murray, A.; Newman, L.; Robinson, S. D.; Segaran, A.; Soong, C. N.; Walker, A.; Wijayaweera, K.; Atun, R.; Cutress, R. I.; Head, M. G. *Lancet Oncol.* **2023,** *24,* 636–645. doi:10.1016/s1470-2045(23)00182-1
217. Gil-Ramírez, A.; Rodriguez-Meizoso, I. *Sep. Purif. Rev.* **2021,** *50,* 32–52. doi:10.1080/15422119.2019.1617737
218. Ariani, M. D.; Zuhrotun, A.; Manesiotis, P.; Hasanah, A. N. *Polym. Adv. Technol.* **2024,** *35,* e6201. doi:10.1002/pat.6201
219. Roszczenko, P.; Szewczyk, O. K.; Czarnomysy, R.; Bielawski, K.; Bielawska, A. *Pharmaceutics* **2022,** *14,* 2286. doi:10.3390/pharmaceutics14112286
220. Jahangirian, H.; Ghasemian lemraski, E.; Webster, T. J.; Rafiee-Moghaddam, R.; Abdollahi, Y. *Int. J. Nanomed.* **2017,** *12,* 2957–2978. doi:10.2147/ijn.s127683
221. Beuguel, Q.; Tavares, J. R.; Carreau, P. J.; Heuzey, M.-C. *J. Colloid Interface Sci.* **2018,** *516,* 23–33. doi:10.1016/j.jcis.2018.01.035

222. Center for drug evaluation and research. *Pharmacology/toxicology review and evaluation of abraxane*. https://www.accessdata.fda.gov/drugsatfda_docs/nda/2005/21660_ABRAXANE_pharmr.PDF (accessed Aug 18, 2025).
223. Center for drug evaluation and research. *Aproval letter of abraxane*. https://www.accessdata.fda.gov/drugsatfda_docs/nda/2005/21660_AbraxaneTOC.cfm (accessed Aug 18, 2025).
224. Chou, P.-L.; Huang, Y.-P.; Cheng, M.-H.; Rau, K.-M.; Fang, Y.-P. *Int. J. Nanomed.* **2020,** *15,* 1731–1743. doi:10.2147/ijn.s231407

License and Terms

BEILSTEIN JOURNAL OF NANOTECHNOLOGY

Multifunctional anionic nanoemulsion with linseed oil and lecithin: a preliminary approach for dry eye disease

Niédja Fittipaldi Vasconcelos*§, Almerinda Agrelli, Rayane Cristine Santos da Silva, Carina Lucena Mendes-Marques, Isabel Renata de Souza Arruda, Priscilla Stela Santana de Oliveira, Mércia Liane de Oliveira and Giovanna Machado

Full Research Paper

Open Access

Address:
Centro de Tecnologias Estratégicas do Nordeste (CETENE), Avenida Professor Luiz Freire 01, Cidade Universitária, 50740-540, Recife, Pernambuco, Brazil

Email:
Niédja Fittipaldi Vasconcelos* - niedjafittipaldi@hotmail.com

* Corresponding author
§ Phone: +55 (85) 99127-7596

Keywords:
eye drops; micelles; low-energy method; ophthalmic vehicle; sample dilution; stability

Beilstein J. Nanotechnol. **2025,** *16,* 1711–1733.
https://doi.org/10.3762/bjnano.16.120

Received: 09 April 2025
Accepted: 17 September 2025
Published: 02 October 2025

This article is part of the thematic issue "Advances in nanotechnology applied to natural products".

Guest Editor: D. Dourado

Abstract

The treatment of dry eye disease (DED) often requires frequent use of artificial tear products. Because of their low permeability and limited ocular bioavailability, repeated applications are required for therapeutic effectiveness. In contrast to traditional drug delivery systems (DDS), a functional ophthalmic nanoemulsion was specifically designed to alleviate symptoms of DED by leveraging its antioxidant and osmoprotective properties. The study evaluated the optimal concentration of lecithin required to produce nanoemulsions with a uniform particle size and incorporated a co-surfactant to enhance the stability of the nanoformulation. A straightforward method was proposed, involving the dilution of the preformulation in an ophthalmic vehicle, followed by homogenization through ultrasonication, resulting in OphtNE-3.70% with a droplet diameter of 173 nm and a zeta potential of −44.7 mV. The addition of Kolliphor® HS15 in OphtNE-3.66%(K1%) initially reduced the droplet size to 70.8 nm and enhanced the antioxidant effect. Although the droplet size and polydispersity index increased after more than 60 days, the formulation remained physically quite stable without phase separation. Both nanoformulations contained 2.6% (w/v) linseed oil, providing a bioactive concentration compatible with ocular administration volumes (~50 µL). At a final concentration of 1.30 mg·mL^{-1}, OphtNE-3.66%(K1%) showed >75% cell viability in L929 cells and ~10% 2,2-diphenyl-1-picrylhydrazyl (DPPH) antioxidant effect. These findings support the multifunctional potential (cytocompatibility and antioxidant) of sterile OphtNE-3.66%(K1%) for the treatment of DED, emphasizing the need for in vivo studies to ensure its efficacy and safety for ocular administration.

Introduction

Dry eye disease (DED) is a multifactorial condition affecting the ocular surface, characterized by changes in tear fluid composition and/or insufficient tear production [1]. This condition can cause ocular discomfort, impair visual function, and promote inflammatory processes on the ocular surface, which could result in chronic complications and vision loss [2,3]. DED

affects approximately 11.6% of the global population [4], with this prevalence partly increasing due to the widespread use of screens and computers [5].

Systemic administration of medications for treating ocular diseases requires high doses to achieve therapeutic effects, which can increase the risk of toxicity [6]. Several barriers limit the penetration of ocular medications, such as rapid elimination by the precorneal layer and low retention of the ocular surface [7]. As a result, topical administration remains the primary treatment method despite its drawbacks, such as low bioavailability and the need for frequent applications [8,9]. Studies show that only a tiny fraction (approximately 5% or 1.5 μL) of the administered dose reaches the ocular chamber after topical application to the inferior conjunctival sac [10,11]. The topical use of artificial tears is the standard treatment for symptomatic relief from DED [12], while topical anti-inflammatory therapy is used in chronic disease cases [13]. Advances in nanomedicine have provided effective solutions, particularly for treating DED [1].

To address challenges in topical ocular drug delivery and to develop products that mimic tear film composition, ocular nanosystems (ONSs) with diameters ranging from 50 to 300 nm are being investigated as potential drug delivery technologies [14,15]. However, our formulation is not a drug delivery system (DDS) since it lacks pharmacological agents. Instead, it is a functional nanoemulsion designed to mimic the tear film's properties and provide antioxidant and osmoprotective benefits, aiming to reduce DED symptoms. ONSs include nanoparticles such as nanoemulsions, liposomes, nanomicelles, and dendrimers, which can serve as carriers for both lipophilic and hydrophilic drugs. This allows for smaller doses and more precise drug targeting [16]. Nanoemulsions (NEs) show promise in improving drug bioavailability after topical ocular instillation, offering several benefits such as reducing the administration frequency, optimizing pharmacokinetic parameters, protecting against enzymatic degradation, and enhancing the stability of bioactive molecules [14,17-19].

Currently, three ophthalmic products based on NEs, Restasis® (Allergan), Lacrinmune® (Bausch & Lomb), and Ikervis® (Santen). have been approved by regulatory agencies such as the FDA and EMA and are commercially available for treating DED [1]. These products are formulated with synthetic polymers and contain cyclosporine as the active ingredient [1]. NEs are designed as droplets that can potentially replenish the lipid layer in DED patients, mimicking the trilayered structure of the tear film, consisting of lipid, aqueous, and mucin layers [13,15,18,20]. According to the literature, the tear film compromises the stability of NE components. When NE is instilled, the oil nanodroplets merge with the lipid layer, the water in the formulation interacts with the aqueous layer of the tear film, and the surfactant interacts with the mucin layer [21-23].

The literature cites various lipids as components of the oily phase in nanoformulations of eye drops for treating DED [12,20,21,24-27]. These include mineral oil (found in Systane® Complete eye drops) [28], castor oil, phospholipids (phosphatidylcholine and/or hydrogenated phospholipids), polyunsaturated fatty acids (PFAs), and medium-chain triglycerides. Among these, PFAs such as the omega–3 fatty acid alpha-linolenic acid, the omega–6 fatty acid linoleic acid, and the omega–9 fatty acid oleic acid are recognized for their potent antioxidant and anti-inflammatory properties [29,30]. These fatty acids are predominantly found in linseed oil (*Linum usitatissimum*, LO), making it a promising ingredient for NE formulations [31-33]. Clinical studies have demonstrated that fatty acids derived from linseed oil are effective in alleviating DED, primarily by modulating inflammatory responses and downregulating key molecular markers, such as interleukin-1 beta, matrix metalloproteinase-9, intercellular adhesion molecule 1, and tumor necrosis factor [34-36]. Downie et al. reported strong clinical evidence supporting the efficacy of nanolipid carrier eye drops infused with omega–3 fatty acids in stabilizing the tear film in patients with meibomian gland dysfunction [31].

In addition to PFAs, phospholipids are notable for their structure, which includes a hydrophilic part (phosphate groups) and a hydrophobic part (fatty acid chains). This unique configuration allows phospholipids to interact at the interface between the lipid and aqueous layers of the tear film, increasing its thickness and improving its stability [1,37]. This leads to immediate relief for patients with DED [28,38]. Recently, promising clinical results have been observed using liposomal spray (Tears Again®) for DED treatment [39]. This product primarily contains phosphatidylcholine, making it an effective therapeutic option for this ocular condition.

Artificial tear products commonly used to alleviate symptoms of DED contain various ingredients that promote osmoprotective and antioxidant effects. In this context, this study proposes the development of an ophthalmic nanoemulsion with multifunctional action, formulated from linseed oil (rich in PFAs) and lecithin (rich in phosphatidylcholine). The focus is on developing a functional ophthalmic nanoemulsion with antioxidant and osmoprotective effects by optimizing physical properties and stability for potential use in DED treatment.

Experimental

Materials and reagents

Linseed oil (code 430021), egg lecithin or egg L-α-phosphatidylcholine (surfactant, ~60% TLC, code 61755), Kolliphor® HS15 (co-surfactant, code 42966), benzalkonium chloride (cationic detergent, code B4136), disodium EDTA ($C_{10}H_{14}N_2Na_2O_8$, code 114), DPPH (2,2-diphenyl-1-picrylhydrazyl, code D9132), triton-X100 (code T8787), phosphate buffered saline (PBS, code P4417), and F.A.M.E. Mix (C_8–C_{24} unsaturated, code 18918) were purchased from Merck®/Sigma-Aldrich® (Brazil). Hydrochloric acid (HCl, code R0101811000), sodium chloride (NaCl, code C1003460500), ethyl acetate ($CH_3COOCH_2CH_3$, code R2800491000), and ethanol (C_2H_5OH, code R0401701000) were purchased from CRQ Produtos Químicos. Disodium phosphate ($Na_2HPO_4{\cdot}2H_2O$, code P.10.0513.012.00.27), petroleum ether (code P.10.0450.000.04.81), sodium dodecyl sulfate ($C_{12}H_{25}SO_4Na$, code P.10.0645.000.00.27) were purchased from Dinâmica Química Contemporânea LTDA (Brazil). Potassium hydroxide (KOH, code HP09874RA), trypan blue (code AT06398SO), and methanol (CH_3OH, code AM07445RA) were purchased from Êxodo Científica® LTDA (Brazil). Monosodium phosphate (NaH_2PO_4, code 01414), phenolphthalein ($C_{20}H_{14}O_4$, code 317415), and citric acid ($C_6H_8O_7{\cdot}H_2O$, code 19228) were obtained from Neon LTDA (Brazil), Nuclear LTDA (Brazil), and AlphaQuimica LTDA (Brazil), respectively. Ascorbic acid ($C_6H_8O_6$, product batch 032121-CF) was purchased from CMS Impex LTDA (Brazil). Thiazolyl blue tetrazolium bromide (MTT, code 976360) was purchased from Ludwig Biotec (Brazil). All analytical grade reagents were used as received from the supplier without further purification.

Ultrapure water was obtained from a Milli-Q® (Merck Millipore) direct water purification system (18.2 MΩ·cm) and used for all aqueous solutions. L-929 cells (code 0188) were obtained from the Banco de Células do Rio de Janeiro (BCRJ)/ATCC (Brazil). RPMI Medium 1640 (code 31800022), fetal bovine serum (FBS, code 12657029), GlutaMAX (code 35050061), and penicillin–streptomycin (code 15140122) were purchased from GIBCO™ (Brazil).

Methodological basis: lecithin structure and emulsification process

Droplet size, homogeneity, and stability in colloidal systems are influenced by component proportions (surfactant, oil, and co-surfactant), emulsification methods (low-energy or high-energy techniques) [40-42], and intrinsic properties like linseed oil viscosity and lecithin's molecular structure [43]. These last factors are crucial for organizing amphiphilic molecules and influencing the uniformity of micellar dispersions in ophthalmic nanoformulations.

Lecithin is a mixture of phospholipids and consists mainly of phosphatidylcholine, which typically forms liposomes (concentric lipid bilayers) rather than micelles (single-layered lipid structures) [43]. The hydrophilic portion of lecithin consists of phospholipids, while the presence of unsaturated and/or saturated fatty acids determines its hydrophobic characteristics, thereby influencing its hydrophilic–lipophilic balance (HLB) values [44]. However, understanding the HLB value requires clarifying the arrangement of the hydrophilic portions of the surfactant molecules [43]. Previous research suggests that the behavior of lecithin in solutions is directly influenced by the proportion of phospholipids and fatty acids in its composition, as well as the type of fatty acids, whether they are saturated or unsaturated [45,46]. Lecithins rich in unsaturated fatty acids (especially those with cis-double bonds, which create molecular kinks) tend to form micellar or disordered colloidal structures because these conformational kinks hinder tight molecular packing, thus destabilizing bilayer formation. Conversely, lecithins with a higher proportion of saturated phospholipids are more likely to organize into stable bilayer vesicles like liposomes. These structural features of lecithin play a crucial role in determining the physicochemical properties of the resulting formulations, including their thermodynamic stability, size distribution, and optical clarity [47,48].

The packing parameter concept (PPC) provides a theoretical framework for predicting the geometry of amphiphilic systems, based on the ratio of the surfactant molecule's total volume, the area of its polar portions, and the length of its hydrophobic chain [49]. PPC values below 0.5 indicate the formation of monolayer micelles, whereas values between 0.5 and 1.0 favor liposome formation [49,50]. A value of $p \geq 0.5$ has been reported for phosphatidylcholine, indicating that lecithin can form micelles and liposomes [51]. Considering the approximately 60% phosphatidylcholine content in the egg lecithin utilized in this study, its dissolution in the aqueous phase was prioritized due to the predominance of its hydrophilic (polar) properties. However, mixed micellar systems (comprising lipid mono- and bilayers) form due to the diverse array of fatty acids in lecithin, the positioning and unsaturation of which are not provided by the manufacturer. Therefore, experimental tests on lecithin concentration are necessary to achieve a monolayer, nanometric, uniform, and stable micellar structural arrangement. Rupp et al. reported the successful translation of the theoretical approach (by PPC) into a practical methodology by investigating variations in surfactant concentration during the emulsification process, which was also carried out in our study [43].

Liposomes are widely studied in ophthalmology for treating anterior and posterior eye diseases, including dry eye, keratitis, transplant rejection, uveitis, endophthalmitis, and proliferative vitreoretinopathy [52]. They can encapsulate hydrophilic and lipophilic drugs, enhancing bioavailability and targeted delivery [53]. However, their clinical use can be limited by stability issues like drug leakage, lipid oxidation, and vesicle aggregation, which depend on drug properties and bilayer composition [54]. These challenges are significant regarding chronic topical use. Conversely, micellar nanoemulsions, such as those in this study, offer better stability, smaller droplet size, and improved solubilization of hydrophobic compounds, making them more suitable for superficial ocular conditions like dry eye, where sustained bioavailability and tear film compatibility are vital [53]. Liposomes may also face practical issues due to interactions between the drug and phospholipids, affecting stability [52,54].

Moreover, heating linseed oil to the formulation temperature of 75 °C offers specific advantages, such as enhanced phase interaction and improved solubilization potential for hydrophobic drugs, without compromising its chemical integrity or bioactivity. No signs of oxidation or thermal degradation were observed at this temperature. TGA and DSC analyses confirm that degradation processes begin only above 340 °C, ensuring that the oil's quality and functional properties are preserved during formulation. The optimal lecithin concentration was experimentally determined using a dilution method combined with a low-energy technique, ensuring the formation of uniform micelles ideal for ophthalmic applications, as detailed below.

Preparation of ophthalmic nanoformulations

To obtain nanoemulsions for ocular application, three progressive studies were conducted to determine (1) the appropriate amounts of surfactant in the pre-emulsions, (2) the nanoformulation prepared in an ophthalmic vehicle (OV), and (3) its stabilization with a co-surfactant. The formulations prepared in the OV were sterilized using a polyethersulfone (PES) membrane filter (0.22 µm pore size) and stored at room temperature. The hydrophilic nature of PES facilitates filtration of lipid-based nanoemulsions, while potential retention of larger or deformable droplets may occur without compromising overall stability.

Surfactant concentration in the pre-formulations

Pre-nanoemulsions (25 mL) were prepared by varying the egg lecithin concentration from 1% to 5% (w/w) in 8% (w/w) oil in water, resulting in pre-emulsions with five distinct concentrations (described in Table S1, Supporting Information File 1). The oil and aqueous phases were heated separately to 75 °C. The mass of egg lecithin was initially dissolved in the aqueous phase at the concentration specified for each experiment. Once the surfactant was fully solubilized, preheated linseed oil (75 °C) was gradually added, and the mixture was homogenized using an Ultra Turrax (IKA T18, Dispersion element S18N-19G) at 10,000 rpm for 5 min. Then, the system underwent further homogenization with a Q125 Sonicator (QSonica, USA), using the 4435 probe (QSonica, USA) for 15 min (three cycles of 5 min each), at 100% amplitude, with pulses of 10 s on and 2 s off.

Ophthalmic nanoformulation

The OV was initially prepared by dissolving 560 mg of monosodium phosphate, 284 mg of disodium phosphate, 500 mg of sodium chloride, 100 mg of disodium EDTA, and 0.1 mg of benzalkonium chloride in 100 mL of Milli-Q water (pH 7.3). To formulate 10 mL of ophthalmic nanoemulsion (OphtNE), 3.75 mL of the optimized pre-formulation (after 24 h at rest) was diluted with 6.25 mL of OV, resulting in a nanoemulsion with a 3.70% (w/w) final concentration of LO. This mixture was homogenized using a Q125 Sonicator (QSonica, USA) with a 4435 probe (QSonica, USA) for 10 min (two cycles of 5 min each), set at 100% amplitude with pulses of 10 s on and 2 s off. This formulation, designated as OphtNE-3.70%, was obtained by diluting the optimized pre-emulsion in the OV, resulting in a final concentration of 3.70% (w/w) with 2.6% (w/v) LO (equivalent to 26 $mg \cdot mL^{-1}$). The detailed mass composition of OphtNE-3.70% is provided in Table S2 (Supporting Information File 1).

Stabilization of ophthalmic nanoformulation with co-surfactant

The stabilization of the surfactant was enhanced by incorporating Kolliphor® HS15 as a co-surfactant at a concentration of 1% (w/v), as described in the study by Dukovski and colleagues [21]. For the preparation of a 10 mL ophthalmic nanoemulsion containing the co-surfactant (with a final concentration of 3.66% w/w), 3.75 mL of optimized pre-formulation (after 24 h of rest) was diluted in 6.25 mL of the OV, which had 100 mg of Kolliphor® HS15 pre-solubilized through magnetic stirring. The resulting formulation was then homogenized using a Q125 Sonicator (QSonica, USA), with a 4435 probe (QSonica, USA) for 10 min (two cycles of 5 min), set to 100% amplitude with 10 s on and 2 s off pulses. This nanoemulsion, designated as OphtNE-3.66%(K1%), was obtained by diluting the optimized pre-emulsion in the OV to a final concentration of 3.66% (w/w), containing 2.6% (w/v) LO (equivalent to 26 $mg \cdot mL^{-1}$ or 26,000 $\mu g \cdot mL^{-1}$) and added with 1% (w/v) Kolliphor® HS15 (indicated by the "K"). The detailed mass composition of OphtNE-3.66%(K1%) is provided in Table S2 (Supporting Information File 1).

Characterization techniques for linseed oil, pre-formulation, and ophthalmic nanoformulations

Linseed oil (LO), pre-formulations, and ophthalmic nanoformulations (OphtNE-3.70% and OphtNE-3.66%(K1%)) were characterized using the following techniques to assess their chemical, physical, biological (in vitro), and morphological properties. These characterizations were performed to ensure the quality and stability of the formulations and to evaluate their suitability for ophthalmic applications.

Gas chromatograph with flame ionization detection (GC-FID)

LO's fatty acid methyl esters were transesterified as described in [37,38]. Briefly, 1 g of LO was mixed with 100 mL methanolic KOH (2.5% w/v) and heated at 70 °C under magnetic stirring (3,000 rpm) for 1 h. Afterward, 100 mL of ethyl acetate was added, and the mixture was stirred at 3,000 rpm for 5 min. The resulting mixture was transferred to a separation funnel to remove the denser phase. The supernatant was washed three times with 10% (w/v) citric acid and then concentrated via rotary evaporation. A 2 µL aliquot of the supernatant was injected in split injection mode (1:10 in ethyl acetate) into a gas chromatograph with flame ionization detection (GC-FID) model 7290 A (Agilent Technologies, USA). The column used was a SP®-2560 capillary GC column (100 m × 0.25 mm × 0.20 µm) (Supelco). The injector temperature was maintained at 230 °C, with helium (He) serving as the carrier gas at a flow rate of 1 mL·min^{-1}. The oven temperature was programmed to increase from 150 to 300 °C at a rate of 5 K·min^{-1}. Peak identification was performed using the F.A.M.E Mix analytical standard (C_4–C_{24} unsaturated), and chromatogram analysis was carried out using OpenLab software (Agilent Technologies, USA). The fatty acid (FA) composition of linseed oil (LO) is summarized below in Table 1.

Viscosity and density

The viscosity and density of LO were measured using an SVM 3000/G2 kinematic viscometer (Anton Paar, USA). The measurements were performed at two temperatures: 25 °C (by ASTM D7042-21 standard) and 75 °C, with each measurement repeated in triplicate to determine the mean ± standard deviation.

Acid value for linseed oil

The acid value (AV) of LO was determined following the American Oil Chemists Society (AOCS) Cd 3d-63 method. For quantification, 5 g of LO was dissolved in 50 mL of a petroleum ether and ethanol mixture (1:1 v/v ratio) at 25 °C under magnetic stirring. The sample was titrated with a standardized ethanolic KOH solution (f = 1.07), using phenolphthalein (1%, w/v) as the indicator. The AV of the LO was calculated using Equation 1, with all determinations conducted in triplicate to obtain the mean ± standard deviation:

$$\text{acid value}\,[\text{mg}\cdot\text{g}^{-1}] = \frac{(V_A - V_B)\cdot[\text{KOH}]\cdot 56.1\ \text{g}\cdot\text{mol}^{-1}}{M_A}, \quad (1)$$

where V_A is the volume of KOH solution required for the titration of the LO sample (mL), V_B is the volume of KOH solution required for blank solvent titration (mL), [KOH] is the concentration of ethanolic KOH solution (0.093 mol·L^{-1}), M_A is the mass of the LO sample used (g), and 56.1 g·mol^{-1} is the molecular weight of KOH.

Thermal analysis

Thermogravimetric (TG) and differential scanning calorimetry (DSC) analyses of LO (20.5 mg) were performed using a Simultaneous Thermal Analyzer (STA) 449 F3 Jupiter (NETZSCH, Germany). The samples were scanned from 25 to 700 °C at a heating rate of 10 K·min^{-1} under a nitrogen (N_2) atmosphere with a flow rate of 50 mL·min^{-1}, using sealed aluminum pans (T181206 and T181128).

Droplet size, polydispersity index, zeta potential, and conductivity

Droplet size and polydispersity index (PdI) of the formulations were measured 24 h after preparation using dynamic light scattering with a Zetasizer Nano-ZS ZEN 3600 (Malvern Instruments, UK) at 25 °C. Before analysis, the samples were diluted 1:1000 with Milli-Q water, a standard dilution used to prevent multiple scattering without compromising micelle integrity. Measurements were performed at a 173° backscatter detection angle. Zeta potential and electrical conductivity were determined by electrophoretic mobility using the same instrument at 25 °C. Calculations were based on the Smoluchowski model. All measurements were performed in triplicate and expressed as mean ± standard deviation.

pH Value

The pH value of the pre-formulation and nanoformulations was measured using a digital pH meter (HI2221, Hanna Instruments, BR) equipped with a calibrated glass electrode and a temperature sensor. The electrode and sensor were immersed in the samples, and pH readings were recorded once the measurements stabilized.

Transmission electron microscopy

The morphology of the nanoemulsions was analyzed using transmission electron microscopy (TEM) with a MORGAGNI 268D (FEI Company, USA), operated at 80 kV. Before

imaging, the samples were sonicated in an ultrasound bath for 15 min, and a drop of the suspension was placed onto a copper grid (200 mesh) coated with formvar/carbon. Excess liquid was removed with filter paper, and the samples were counterstained with 2.5% uranyl acetate (w/v). The grids were then dried under vacuum for 24 h before TEM analysis.

Long-term stability test

The long-term stability of the nanoformulations was assessed by storing the samples in hermetically sealed glass vials at 25 °C, protected from light and kept at rest. The average droplet diameter (size-weighted), polydispersity index, and zeta potential were measured on days 1, 30, 45, and 60 after preparation, following the methodologies previously described. All measurements were performed in triplicate to calculate the mean ± standard deviation.

Antioxidant activity

The antioxidant activity of the linseed oil-based nanoformulation was assessed using the 2,2-diphenyl-1-picrylhydrazyl (DPPH) free radical photocolorimetry method [55,56]. A 100 µL aliquot of DPPH solution (0.3 mmol·L^{-1} in 99% ethanol) was mixed with 100 µL of ophthalmic nanoformulation, corresponding to linseed oil concentrations of 0.65 to 10.4 mg·mL^{-1} (corresponding to 25, 50, 100, 200, 300, and 400 µL of nanoformulation per mL of ethanol). The reaction mixture was incubated in a 96-well plate at 25 °C for 1 h, protected from light. Absorbance was then measured at 518 nm using a Multiskan Go UV spectrophotometer (Thermo Fisher Scientific, FI). Ascorbic acid (3% w/v, prepared in the ophthalmic vehicle) was used as the positive control. The experiment was performed in quadruplicate, and antioxidant activity (DPPH radical inhibition percentage) was calculated using Equation 2 [57]. The IC_{50} (the concentration required to achieve 50% inhibition) of the radical scavenging activity was determined via linear regression analysis [58].

$$\text{DPPH inhibition [\%]} = \frac{\text{Abs}_{\text{control}} - \left(\text{Abs}_{\text{sample}} - \text{Abs}_{\text{blank}}\right)}{\text{Abs}_{\text{control}}} \cdot 100, \quad (2)$$

where $\text{Abs}_{\text{control}}$, represents the absorbance of the DPPH radicals, $\text{Abs}_{\text{sample}}$, represents the absorbance of the nanoformulation, and $\text{Abs}_{\text{blank}}$ represents the absorbance of the sample without DPPH (sample + ethanol).

Cytotoxicity assay

L929 fibroblast cells were cultured in RPMI 1640 medium supplemented with 10% (v/v) fetal bovine serum (FBS), 1% (v/v) penicillin–streptomycin, and 1% (v/v) GlutaMAX, maintained under standard conditions (5% CO_2 at 37 °C). Cell viability was determined using the trypan blue exclusion method. The in vitro cytotoxicity of the sterile nanoformulations was evaluated according to the guidelines of the International Organization for Standardization (ISO 10993-5:2009) [59], using the MTT assay to assess cell viability based on metabolic activity.

L929 fibroblasts were seeded in 96-well plates at 2×10^4 cells per well. After 24 h, the medium was replaced with 100 µL of fresh medium containing sterile ophthalmic nanoformulations, providing final linseed oil concentrations of 0.65 to 13 mg·mL^{-1} (25, 50, 100, 200, 300, 400, and 500 µL nanoformulation per mL of medium).

After incubation for 24 and 72 h, the treatments were removed, and 100 µL of MTT solution (0.5 mg·mL^{-1}) was added to each well, followed by 3 h of incubation under standard culture conditions. To solubilize the blue-violet formazan crystals, 100 µL of 10% (w/v) sodium dodecyl sulfate solution, acidified with 0.1 mol·L^{-1} HCl, was added. After 24 h, the absorbance was measured at 570 nm using a Multiskan Go microplate reader (Thermo Fisher Scientific, FI). The positive control consisted of cells treated with 1% (v/v) Triton X, while the negative control comprised cells treated with only the supplemented RPMI medium.

The percentage of metabolically active cells was calculated by comparing the absorbance of the samples to that of the negative control. Linear regression analysis was used to determine the maximum non-cytotoxic concentration (MNCC70), defined as the concentration at which 70% cell viability was maintained. The assay was performed in triplicate across four independent experiments.

Graphs and statistical analysis

All data in tables and graphs are presented as mean ± standard deviation. Graphs were generated using OriginPro 2022 software (OriginLab Corporation, USA). The statistical analysis (StatSoft Inc., 2011, Tulsa, USA) was performed using analysis of variance (ANOVA), and mean differences were compared using the Tukey test. Statistical significance was set at $p < 0.05$.

For the cytotoxicity data analysis, technical replicates were collapsed using the median. Outliers were identified and excluded based on the interquartile range (IQR) method: values above Q3 + 1.5 × IQR or below Q1 − 1.5 × IQR were removed for each experimental group. Normality and homoscedasticity were assessed using the Shapiro–Wilk and Levene's tests, respectively. A three-way ANOVA was then performed, considering the factors exposure time (24 and 72 h), concentration (0.65 to 13 mg·mL^{-1}), and treatment (OphtNE-3.70% and

OphtNE-3.66%(K1%)). Two-way interactions were further examined using post hoc tests, including one-way ANOVA, estimated marginal means, and Tukey's honestly significant difference (HSD) test. When appropriate, the Bonferroni correction was applied for multiple comparisons. Statistical significance was defined as $p < 0.05$. Data processing and statistical analyses were performed using R v.4.5.1 [60], specifically the packages "tidyverse" v.2.0.0 [61] and "rstatix v.0.7.2 [62]. Supplementary statistical data are provided in spreadsheets and can be accessed in Supporting Information File 2.

Results and Discussion

Physicochemical properties of linseed oil

The identification and quantification of fatty acids (FAs) in linseed oil (LO) are presented in Table 1. Linolenic acid is the most abundant, constituting 46.7%, followed by oleic acid (17.7%), linoleic acid (14.5%), behenic acid (7.4%), erucic acid (5.6%), palmitic acid (5.0%), and stearic acid (3.3%). Heating LO to 75 °C did not significantly affect the relative quantities of these fatty acids. Unsaturated FAs (~79%) remained dominant over saturated FAs (~21%), consistent with the results reported by Qiu et al. [63] and Rahiminezhad and colleagues [64]. Among the FAs in LO, α-linolenic acid (ALA, omega–3), oleic acid (OA, omega–9), and linoleic acid (LA, omega–6) are recognized as essential bioactive compounds, making LO valuable for medicinal applications. Notably, ALA is metabolized into eicosapentaenoic acid (EPA, C20:5) and docosahexaenoic acid (DHA, C22:6), providing polyunsaturated fatty acids (PUFAs) that are vital for human health [65,66]. PUFAs are well-known for their therapeutic potential, particularly their anti-inflammatory and antioxidant properties [30], showing promising results in systemic and topical treatment [33,67,68], including for dry eye disease [35,36,69].

The viscosity, density, and AV of LO at both room temperature (25 °C) and elevated temperature (75 °C) are summarized in Table 2. Visually, heating LO to 75 °C did not result in any noticeable changes in color or turbidity; the oil maintained its original yellowish hue and translucent appearance, as shown in Figure 1a.

The observed density of LO at 25 °C was consistent with the values reported by Rahiminezhad and colleagues [64]. However, increasing temperature reduced LO density (by ca. 4%). This reduction can be attributed to the increased molecular motion of the oil's long fatty acid chains (saturated and unsaturated) when heated. The increased motion causes greater intermolecular spacing, leading to an increase in the oil's volume. As a result, the oil's mass-to-volume ratio (density) decreases, as observed for vegetable oils [70]. Raising the temperature of LO to 75 °C resulted in a statistically significant reduction (75.7%) in viscosity ($p < 0.05$). Linseed oil consists predominantly of

Table 1: Identification of fatty acid methyl esters, retention times, fatty acid profiles, carbon chain structures, and relative quantities in linseed oil (Sigma-Aldrich®).

Ester	Retention time (min)	Fatty acid	Carbon chain (carbon atoms:unsaturation)	Relative quantity (%)[a]
methyl palmitate	22.405	palmitic acid	16:0	4.9
methyl stearate	26.368	stearic acid	18:0	3.3
methyl oleate	27.581	oleic acid	18:1	17.7
methyl linoleate	29.336	linoleic acid	18:2	14.5
methyl linolenate	31.407	linolenic acid	18:3	46.7
methyl behenate	34.030	behenic acid	22:0	7.4
methyl erucate	35.271	eructic acid	22:1	5.6

[a]Determined from the relative peak area ([the peak area assigned to each fatty acid/the total peak areas of the fatty acids] × 100).

Table 2: Density, viscosity, and acid value of linseed oil (Sigma-Aldrich®) at 25 and 75 °C.

	Temperature (°C)	Density ($g \cdot cm^{-3}$)	Dynamic viscosity ($mPa \cdot s^{-1}$)[a]	Acid value ($mg \cdot g^{-1}$)[a]
linseed oil (Sigma-Aldrich®)	25	0.93	40.76 ± 0.22^{1}	1.74 ± 0.04^{1}
	75	0.89	9.91 ± 0.01^{2}	1.66 ± 0.07^{1}

[a]Values are expressed as mean ± standard deviation (n = 3), and equal superscript numbers indicate no statistically significant difference (α = 0.05) by Tukey's test.

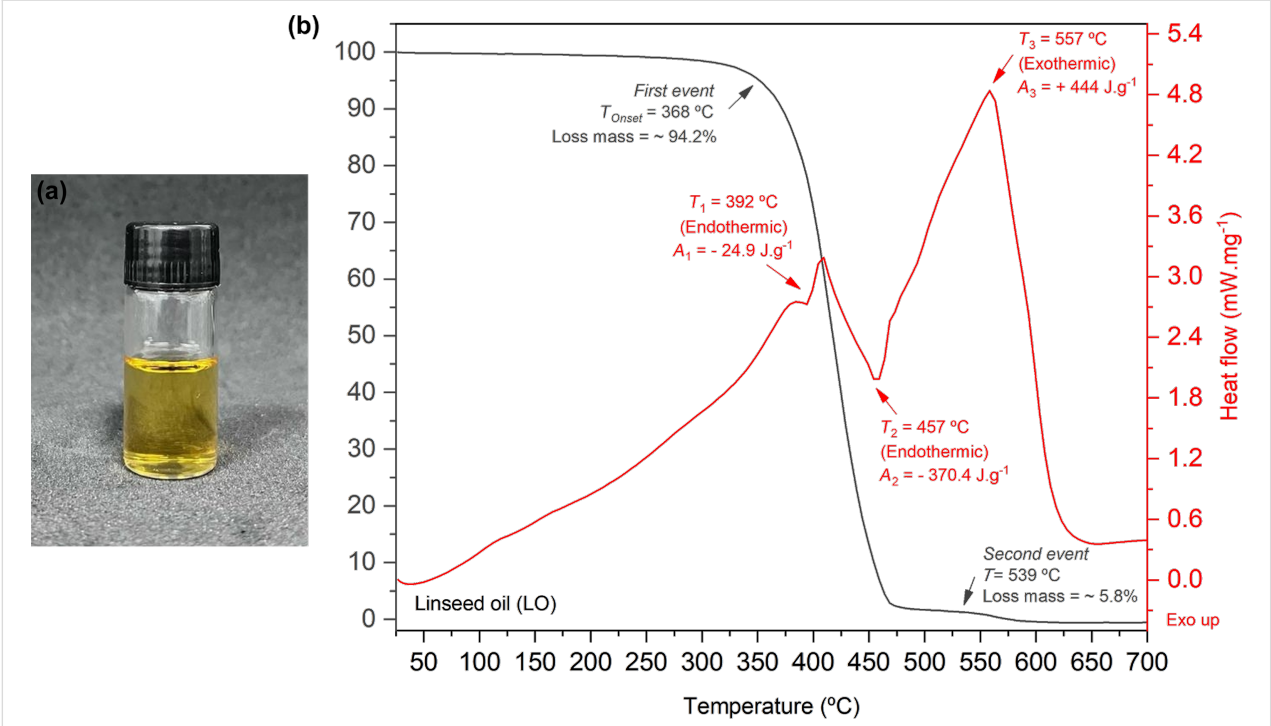

Figure 1: Linseed oil (Sigma-Aldrich®): (a) image of the oil after heating to 75 °C and (b) TGA/DSC curves.

unsaturated fatty acids, characterized by long hydrocarbon chains containing double bonds between carbon atoms. At higher temperatures, these double bonds relax and undergo configurational changes from cis to trans, leading to distortions in the molecular structure [71,72]. This results in weaker intermolecular interactions, reducing the oil's viscosity [73]. A lower viscosity in LO can facilitate the formation and stability of micelles by allowing surfactant molecules to move more freely, promoting their rapid formation and maintaining stability within the emulsion [74].

An important quality parameter of LO is the free fatty acid (FFA) content, determined by the AV. A lower AV signifies a reduced FFA content, indicating higher oil quality and enhanced bioactive functionality, making it well-suited for medical applications. The AV measured for LO at 25 °C was significantly lower than the value reported by Tariq et al. [75], indicating that the LO used in this study was of higher quality and free from deterioration, oxidation, and adulteration. Heating the LO to 75 °C had no significant impact on the AV, which remained stable at this temperature. This finding aligns with the results obtained through GC-FID analysis, confirming that heating to 75 °C did not affect the quality of the oil. To provide a comprehensive understanding of the thermal behavior of LO, the TG and DSC curves are presented in Figure 1b. The TGA curve for the LO revealed two distinct thermal mass loss events. The first event occurs between 340 and 490 °C, where a significant mass reduction (~94.2%) is observed, with the degradation temperature marked at 368 °C (T_{Onset}). This primary degradation phase involves lipolysis, the breakdown of triglycerides into fatty acids and glycerol. Following lipolysis, glycerol decomposes into acrolein, a compound known for its toxicity to humans, as well as the breakdown of unsaturated fatty acid chains. The second mass loss event (~5.8%) occurs between 539 and 600 °C and is attributed to the decomposition of saturated fatty acids and low-molecular-weight compounds generated during earlier thermal degradation processes.

The DSC curve for LO exhibited three distinct calorimetric events. The first endothermic peak (T_1 = 392 °C) is likely attributed to the presence of polyunsaturated fatty acids, as confirmed by GC-FID analysis. As the temperature rises, the double bonds in these unsaturated fatty acids undergo relaxation and changes from cis to trans configuration, distorting the molecular structure. This leads to weaker intermolecular interactions, which is reflected in a reduction in oil viscosity (as shown in Table 2) and a decrease in the oil's melting point. The second endothermic peak (T_2 = 457 °C) is attributed to the rupture of double bonds in the unsaturated fatty acids, resulting in the formation of glycerol and shorter-chain fatty acids. Finally, the third exothermic peak (T_3 = 557 °C) corresponds to the molecular rearrangement and decomposition of the oil into simpler compounds, such as aldehydes, ketones, and aromatic hydrocarbons.

These findings affirm the thermal stability of linseed oil at 75 °C, showing no significant changes in acid value or oxidation signs as per GC-FID analysis. TGA and DSC results reveal that degradation only occurs above 340 °C, ensuring that the formulation temperature does not affect the oil's quality or bioactivity. Overall, the oil's consistent thermal stability, fatty acid profile, and reduced viscosity under heat facilitate the formation of nanoemulsions, thereby enhancing its therapeutic benefits for DED, where antioxidant and anti-inflammatory effects are crucial.

Structural organization of micelles in the ophthalmic nanoformulations

To establish the stability of nanoemulsions, it is essential to identify a region in the ternary diagram where the concentrations of oil, water, and surfactant/co-surfactant are ideal for the formation of nanometer-sized droplets, minimizing the risk of coalescence or phase separation. A viable strategy to streamline the extensive series of formulations and to locate the optimized region in the ternary diagram involves diluting an emulsion, if the component proportions in its formulation are adjusted to enhance stability. In this context, as an initial approach, different concentrations of lecithin were evaluated in pre-formulations (pre-emulsions). The results for particle size, polydispersity index, electrical conductivity, zeta potential, and pH for all formulations (pre-formulations and ophthalmic nanoformulations) obtained are summarized in Table 3. The particle intensity distribution profiles of the pre-formulations are presented in Figure S1 of Supporting Information File 1.

The successful sterile filtration of nanoemulsions through 0.22 µm PES membranes demonstrates the viability of this method for ophthalmic use. PES membranes are hydrophilic, have low lipid affinity, reduce fouling, and are compatible with aqueous nanoemulsions. Although droplet size was below the pore size, larger or aggregated droplets might be retained due to deformability, causing minor phase loss or changes. Despite an initial droplet size larger than 220 nm, the surfactant-rich interface enables passage through the membrane. The filtration also helps exclude larger, unstable droplets, improving size uniformity. PES membranes are thus effective for sterilizing nanoemulsions without affecting stability or function [76-78].

The droplets in the pre-formulations exhibited a weighted average diameter ranging from 470 nm (lower surfactant content) to 222 nm (higher surfactant content), demonstrating the influence of lecithin concentration on the droplets' hydrodynamic diameter ($F = 67.34$, $p < 0.000001$, one-way ANOVA). Initially, when the surfactant content was 1% and 2% (w/w) in the 8% (w/w) pre-formulation, the droplet hydrodynamic diameter exceeded 300 nm, showing a multimodal distribution of intensities with PdI values above 0.3. This suggests that the lecithin content in the O/W(L-1%) and O/W(L-2%) pre-formulations is insufficient to effectively reduce surface tension, resulting in incomplete droplet coverage and subsequent coalescence. As the lecithin concentration in the pre-formulations was increased, the hydrodynamic diameter of the droplets and PdI values decreased, indicating improved uniformity. PdI values below 0.3 suggest greater size homogeneity [79]. Under the same ultra-

Table 3: Results of weighted average droplet diameter (nm), polydispersity index (PdI), electrical conductivity (µS·cm^{-1}), zeta potential (mV), and pH for pre-formulations and ophthalmic nanoformulations (with and without co-surfactant).

Procedures for manufacturing nanoformulations	Formulation code[a]	[Total] (%, w/w)[b]	LO (%, w/v)	Weighted mean of sizes (nm)[c] $F(5,18) = 15.24$, $p = 0.0023$	PdI	Conductivity (µS·cm^{-1})[c] $F(5,18) = 74.04$, $p < 0.0001$	Zeta potential (mV)[c] $F(5,18) = 67.34$, $p < 0.000001$	pH
pre-formulation (pre-emulsion)	O/W(L-1%)	8.2	8	470.2 ± 66.9^{1}	0.389	9.0 ± 0.8^{1}	–33.3 ± 0.8^{1}	4.7
	O/W(L-2%)	9.1	8	347.6 ± 1.5^{1,2}	0.383	9.3 ± 2.0^{1}	–40.7 ± 0.7^{2,3}	4.6
	O/W(L-3%)	9.9	8	308.0 ± 2.3^{3}	0.252	11.7 ± 0.1^{2}	–39.9 ± 0.2^{2}	4.6
	O/W(L-4%)	10.7	8	227.6 ± 2.8^{3,4}	0.238	14.8 ± 0.2^{3}	–41.6 ± 0.8^{2,3}	4.4
	O/W(L-5%)	11.5	8	222.3 ± 3.7^{3,4}	0.244	14.6 ± 0.7^{3}	–42.8 ± 1.5^{2,3}	4.5
ophthalmic nanoformulation	OphtNE-3.70%	3.70	2.6	173.1 ± 3.9^{5}	0.146	18.6 ± 0.7^{4}	–44.7 ± 0.2^{4}	6.9
ophthalmic nanoformulation with co-surfactant	OphtNE-3.66%(K1%)	3.66	2.6	70.8 ± 0.8^{6}	0.126	17.3 ± 0.8^{4}	–37.6 ± 0.8^{2}	6.8

[a]Lecithin is represented by L and Kolliphor® HS15 by K; [b][Total] = [(mass of LO + mass of L)/mass of water + mass of LO+ mass of L] × 100; [c]values are mean ± SD; equal superscript numbers (1–6) show no significant difference (α = 0.05) per Tukey's test.

sound emulsification conditions, the droplet diameter reaches an optimal point, indicating surfactant saturation at the droplet interface. This reduces surface tension by fully covering the interfacial surface area, thereby stabilizing the emulsion structure [80,81]. Among the pre-formulations, O/W(L-3%) demonstrated optimal performance, with a hydrodynamic diameter of approximately 300 nm and a PdI value of 0.252. This monomodal intensity distribution confirmed efficient surfactant coverage. Further lecithin additions, such as in O/W(L-4%) and O/W(L-5%), led to free micelle formation due to surfactant excess, resulting in smaller droplets but multimodal distributions. Similar results were reported in previous studies that reported the influence of surfactant concentration on the formation and stability of nanoemulsions [82-84].

In summary, variations in lecithin concentration assessed in pre-formulations containing linseed oil delineate distinct profiles concerning droplet diameter distribution, delineating three discernible phases. The initial phase (represented by pre-formulations O/W(L-1%) and O/W(L-2%)) exhibits inadequate lecithin levels to entirely coat the oil droplet interfaces. The subsequent phase (represented by pre-formulation O/W(L-3%)) reveals a saturation point of lecithin concentration at the oil droplet interfaces, ensuring optimal surfactant utilization. Finally, the third phase (illustrated by pre-formulations O/W(L-4%) and O/W(L-5%)) manifests an overabundance of lecithin, resulting in the formation of micellar structures within the pre-formulations.

As electrical conductivity is a physicochemical parameter modulated by surfactant concentration in emulsified systems [85]. The measured conductivity values corroborate earlier findings, with statistical significance confirmed by one-way ANOVA ($F = 74.04$, $p = 0.000026$), as shown in Table 3. In the initial phase, the electrical conductivity of pre-formulations O/W(L-1%) and O/W(L-2%) exhibited no significant changes with increasing lecithin concentration. Moving into the second phase, the O/W(L-3%) pre-formulation demonstrated a notable 21% increase in dispersion conductivity, indicating statistical significance compared to formulations with lower lecithin concentrations. Transitioning to the third phase, characterized by excess lecithin, both O/W(L-4%) and O/W(L-5%) pre-formulations exhibited a statistically significant 21% rise in electrical conductivity compared to O/W(L-3%). This elevation is attributed to free micelles capable of facilitating electron displacement within the aqueous dispersion. The enhanced conductivity facilitated by electron transport species can foster chemical interactions with contacting materials (such as primary packaging) or expedite degradation processes, particularly given the acidic nature of the pre-formulations.

Variations in zeta potential (−33.3 to −44.7 mV) reflect the influence of surface-active functional groups, particularly the phosphate groups in lecithin. This effect was statistically significant ($F = 15.24$, $p = 0.00235$, one-way ANOVA), as reported in Table 3. These groups impart a negative charge to the droplet surfaces, attributed to the amphiphilic nature of lecithin, whose polar head contains the phosphate anion ($[PO_4]^{3-}$). Müller [86] suggested that when the absolute value of the zeta potential exceeded 30 mV (in module), the droplets in the system would be stabilized by strong electrostatic repulsion. All pre-formulations exhibited zeta potential values exceeding −30 mV, as shown in Table 3.

The lecithin concentration significantly influenced the negative charge density on the droplets' surface. This effect was evident in the pre-formulation containing 2% (w/w) lecithin (O/W (L-2%)), where the surfactant coating begins to form on the droplet interface. While cationic and anionic nanoemulsions are commonly explored in drug delivery systems due to their distinct electrostatic properties, the present formulation was not designed as a drug delivery vehicle. Instead, it functions as a bioactive nanoemulsion intended to stabilize the tear film and provide antioxidant and osmoprotective effects. Cationic emulsions are known to enhance residence time on the ocular surface via electrostatic interactions with negatively charged mucins [25,87,88], while anionic nanoemulsions offer better compatibility with the components of tear fluid [2,89]. Based on this, an anionic profile was selected in this study to optimize retention and interaction with the ocular environment, aiming to support tear film function and alleviate dry eye symptoms through the multifunctional properties of LO. Although the physicochemical profile is compatible with nanosystems often used in drug delivery, no pharmacological agent was incorporated in this study.

All pre-formulations displayed a pH below 5, indicating their acidic nature. This acidity can be attributed mainly to LO, which has a pH of 4.1 and is the major component of pre-formulations at an 8% (w/w) concentration. The increase in lecithin concentration did not significantly impact the pH of the pre-formulations. While pH and ionic strength directly affect the electrical charge of system components [83,90], the observed zeta potential values were consistently related to the surfactant amount surrounding the droplets.

Several criteria were considered to determine the optimal lecithin concentration for forming coarse pre-emulsions: (1) achieving a mean hydrodynamic droplet diameter close to 300 nm to ensure the efficacy and safety of ocular administration [91,92]; (2) ensuring droplet uniformity with a monodisperse profile [93]; (3) maximizing lecithin's performance in

forming LO droplets through monolayer micelles [81]; (4) avoiding excess surfactant molecules to maintain biocompatibility [94,95]; and (5) maintaining a negative surface charge density greater than −30 mV for stability dispersion [84]. Based on these criteria, the O/W(L-3%) pre-formulation was identified as the most suitable candidate for further investigations in the development of ophthalmic nanoformulations for DED.

After optimizing the pre-formulation parameters, a simple dilution process of O/W(L-3%) combined with ultrasonic emulsification resulted in a reduction of the hydrodynamic diameter of the droplets by approximately 44%, leading to a decrease in the PdI values to 0.146 (see Table 3), thereby achieving a narrower monomodal distribution profile, a characteristic feature of nanoemulsions obtained through ultrasound [96].

The dilution process of the O/W(L-3%) system facilitated a more uniform distribution of lecithin molecules around the surface of the LO droplets, effectively reducing the interfacial tension. This process, coupled with low-energy ultrasound, allowed for the reduction of the droplet diameter [97]. Furthermore, diluting the pre-formulation increases the average distance between the droplets, thereby decreasing electrostatic repulsion interactions between them [83]. As a result, the OphtNE-3.70% nanoformulation produces smaller and more stable droplets, attributed to the reduced interfacial tension and the reorganization of lecithin molecules, which minimize aggregation over time.

However, a high density of ionic surfactants at the system interface requires careful consideration. Strong electrostatic repulsion within the dispersion can generate dipole moments between droplets, increasing surfactant mobility on their surfaces [98]. This mobility may create gaps at the interface, ultimately promoting coalescence and causing destabilization over time. To avoid this effect, Kolliphor® HS15, a non-ionic hydrophilic surfactant, was added as a second surfactant. The addition of this co-surfactant aimed to stabilize and slightly reduce the negative charge density in the droplet surface [99]. Furthermore, the combination of lecithin with another hydrophilic surfactant has a greater capacity to form micelles [43]. Kolliphor was selected due to its common use in ophthalmic products and FDA approval for concentrations up to 5% [88]. This co-surfactant reduced the zeta potential by approximately 16% compared to OphtNE-3.70%. Despite this reduction, OphtNE-3.66%(K1%) maintained zeta potential values below −30 mV, ensuring dispersion stability and supporting its use in ophthalmic nanoformulations.

After diluting the O/W(L-3%) pre-formulation in VO, a significant reduction of approximately 75% in droplet size was observed following the addition of Kolliphor® HS15. This substantial size reduction can be attributed to the surfactant's chemical structure, which effectively anchors onto the surfaces of the oil droplets. Additionally, the ultrasound process further contributes to size reduction by promoting droplet fragmentation. The smaller droplet size increases the surface-area-to-volume ratio, enhancing electrostatic shielding. This effect is particularly pronounced when the non-ionic co-surfactant occupies the droplet surface. These findings are consistent with Dukovski et al., who also highlighted the role of Kolliphor® HS15 in reducing droplet size in nanoemulsions [21].

The sterile nanoformulations OphtNE-3.70% and OphtNE-3.66%(K1%) exhibited droplet sizes ranging from larger than 50 nm to smaller than 300 nm, which are considered suitable for permeating the ocular barriers, indicating their potential as multifunctional systems for hydrophobic drug delivery to the eye [14,100]. Figure 2a and Figure 2b display the droplet diameter distribution plots for OphtNE-3.70% and OphtNE-3.66%(K1%), respectively.

The electrical conductivity of OphtNE-3.70% and OphtNE-3.66%(K1%) was higher than that of the O/W(L-3%) pre-formulation due to using VO as a diluent. VO contains electrolytes, particularly NaCl, which improves conductivity. In contrast, diluting the ophthalmic formulations in pure distilled water may cause variations in conductivity, which can compromise the consistency and effectiveness of your applications [101]. When preparing ophthalmic nanoformulations, VO guarantees more stable and reproducible conductivity conditions, with values consistently below 50 $\mu S \cdot cm^{-1}$ [102,103], compared to literature-reported nanoemulsions for DED treatment based on castor oil and 1,2-dimyristoyl-*sn*-glycerol-3-phosphocholine with a conductivity of 68.9 $\mu S \cdot cm^{-1}$ [20]. Another study described the development of a nanoemulsion-based gel containing moxifloxacin hydrochloride to treat conjunctivitis with a conductivity of 390 $\mu S \cdot cm^{-1}$ [104]. In comparison to both studies, the ophthalmic nanoformulations developed demonstrated lower conductivity, indicating good tolerance and no ocular irritation.

Preparing the OphtNE-3.70% and OphtNE-3.66%(K1%) nanoformulations involved diluting the O/W(L-3%) pre-formulation in OV. This process increased the pH of the nanoformulations by buffering salts such as $NaHPO_4$ and Na_2PO_4. Maintaining the pH within the range of 6.5–8.0 ensures ocular compatibility, avoiding irritation and enhancing drug absorption [92,105,106].

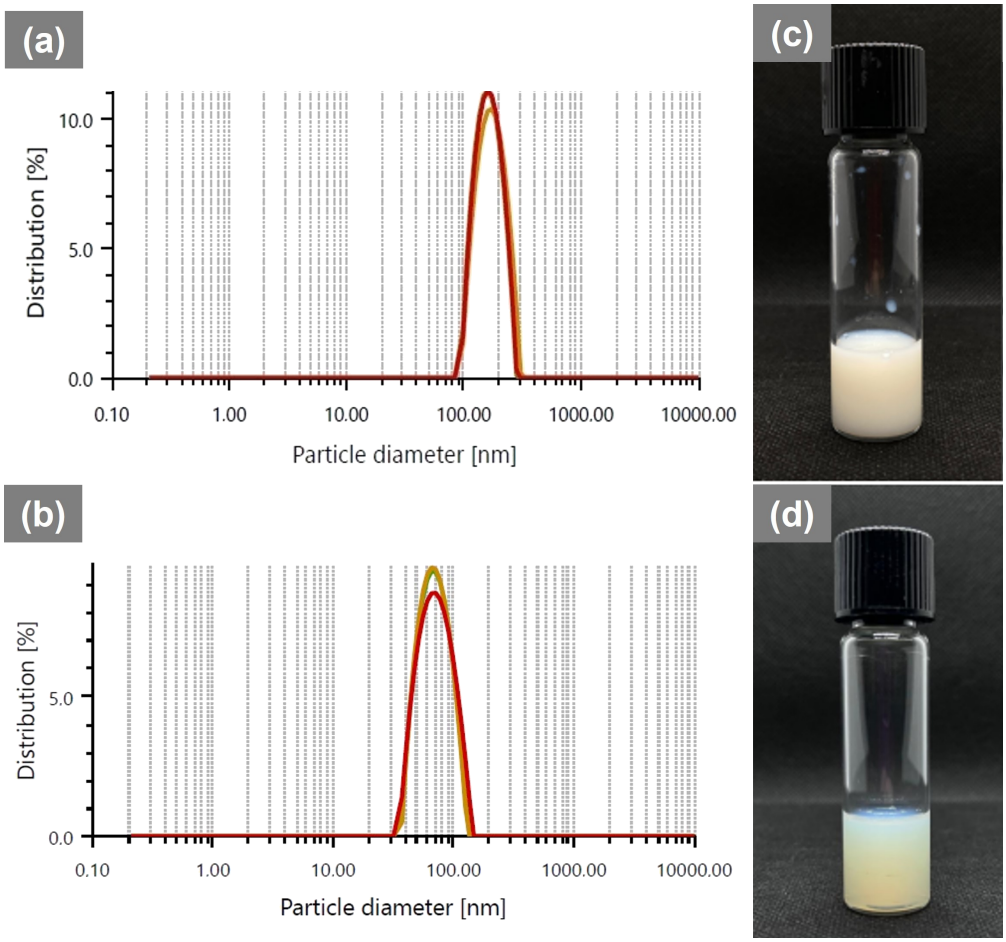

Figure 2: Droplet diameter distribution graphs and macroscopic appearance after 24 h at rest of sterile ophthalmic nanoformulations: (a, c) OphtNE-3.70%, and (b, d) OphtNE-3.66%(K1%).

Morphological, stability, and biological properties (in vitro) of ophthalmic nanoformulations

The pre-formulation emulsion (O/W systems with 1–5% lecithin) appeared homogeneous and milky white, typical of stable oil-in-water systems with fine droplets (Figure S2 in Supporting Information File 1). In contrast, the sterile ophthalmic nanoformulations OphtNE-3.70% and OphtNE-3.66%(K1%) (Figure 2c and Figure 2d, respectively) also exhibited a milky appearance but with distinct optical clarity, influenced by their smaller and more uniform nanodroplet size distributions. These visual attributes support the colloidal stability and successful transition from pre-formulation to nanoemulsion via ultrasonic processing.

The OphtNE-3.70% nanoformulation (containing only lecithin) forms a monomolecular film at the oil–water interface. When light interacts with this finely dispersed droplet system, it scatters in multiple directions, giving the nanoemulsion its characteristic milky opaque appearance. Similar optical properties have been documented in the literature for lecithin-based nanoemulsions with droplet sizes of approximately 150 nm [21,107]. The OphtNE-3.66%(K1%) nanoformulation appeared more translucent than the OphtNE-3.70% nanoformulation. This difference can be attributed to two main factors: (1) the significant reduction in droplet size and (2) the improved uniformity of the nanodroplets. These factors minimize light scattering, resulting in a more transparent nanoemulsion.

The macroscopic difference between the ophthalmic nanoformulations OphtNE-3.70% and OphtNE-3.66%(K1%) is further supported by the TEM micrographs presented in Figure 3a and Figure 3c, respectively. These micrographs reveal spherical droplets in both formulations, but distinct differences in size and dispersion uniformity are evident. OphtNE-3.70% displays larger and more heterogeneous particles, whereas OphtNE-3.66%(K1%) exhibits smaller, uniformly distributed droplets. This observation aligns with the PdI results shown in Table 3,

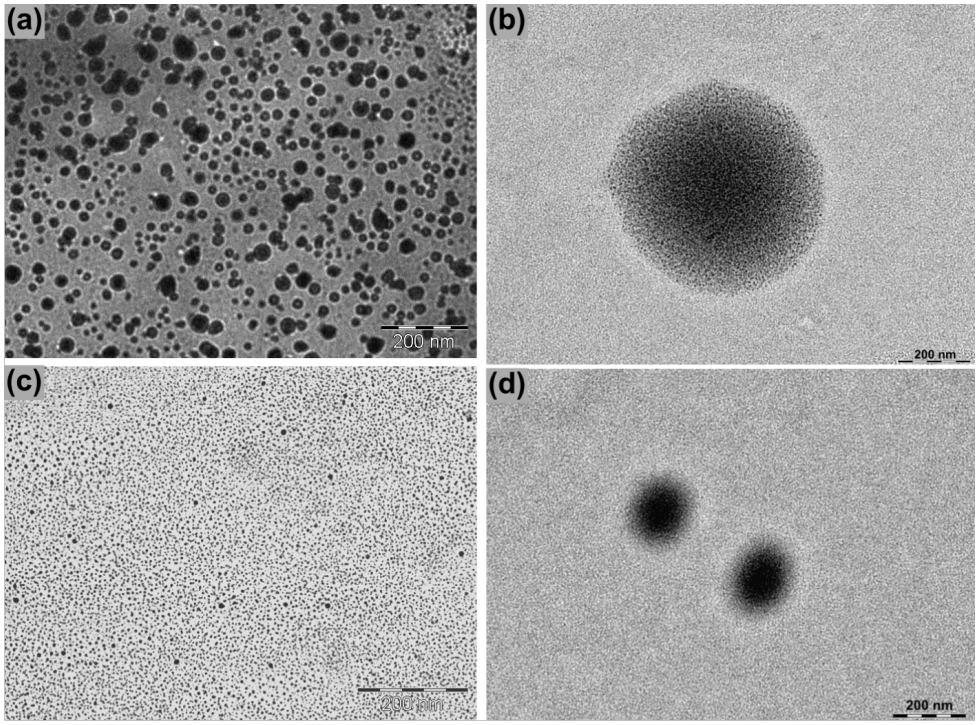

Figure 3: TEM micrographs of ophthalmic nanoformulations: OphtNE-3.70% (a, b) and OphtNE-3.66%(K1%) (c, d) at low (a, c) and high (b, d) magnification, showing nanodroplet and micellar morphology.

confirming that the addition of Kolliphor® HS15 improved both homogeneity and droplet size reduction. This feature is crucial for ensuring the stability of formulations and achieving uniformity in the dosage unit, a key requirement for ophthalmic applications [27]. The high-magnification images in Figure 3b and Figure 3d reveal the micellar structure, characterized by dense cores resulting from the presence of linseed oil and less dense peripheries formed by the interfacial layer, which consists of the surfactant and co-surfactant. This structural organization underscores the effective interaction between the formulation's components.

To ensure the prolonged stability of the OphtNE-3.70% and OphtNE-3.66%(K1%) nanoformulations, droplet size monitoring was carried out fortnightly for 60 days. Figure 4a and Figure 4b present the weighted means of particle size and PdI, respectively, during storage.

Emphasis should be placed on the phenomenon known as Ostwald ripening, commonly observed in colloidal systems, particularly in nanoemulsions [108,109]. During Ostwald ripening, smaller particles, which have a higher surface-area-to-volume ratio, diffuse and aggregate into larger droplets, leading to coalescence and an overall increase in droplet size. This dynamic process leads to a tendency for particle enlargement over time, as observed in both ophthalmic nanoformulations. However, this phenomenon was more pronounced in the first 15 days of OphtNE-3.66%(K1%) due to its smaller droplet size than OphtNE-3.70%.

For OphtNE-3.70%, relative stability was observed up to approximately 30 days of storage. After this period, a significant increase in the droplet size occurred, showing a 76% increase compared to the initial size, as depicted in the graph. This phenomenon can be attributed to the formation of induced dipole moments between negatively charged droplets of lecithin, creating repulsive forces that, over time, cause the droplets to coalesce due to the formation of interfacial gaps on their surfaces. However, the addition of Kolliphor® HS15 in OphtNE-3.66%(K1%) mitigated this effect by redistributing surface charges, improving interfacial organization. As a result, the formulation exhibited more consistent droplet size behavior over time, with only moderate increases in size and PdI. Although some variation occurred, no phase separation or macroscopic instability was observed, indicating acceptable colloidal stability under storage conditions. The PdI values of the ophthalmic nanoformulations remained relatively stable throughout the storage period, staying close to 0.2, indicating a uniform particle size distribution. This controlled droplet size profile in nanoemulsions can be attributed to the simple dilu-

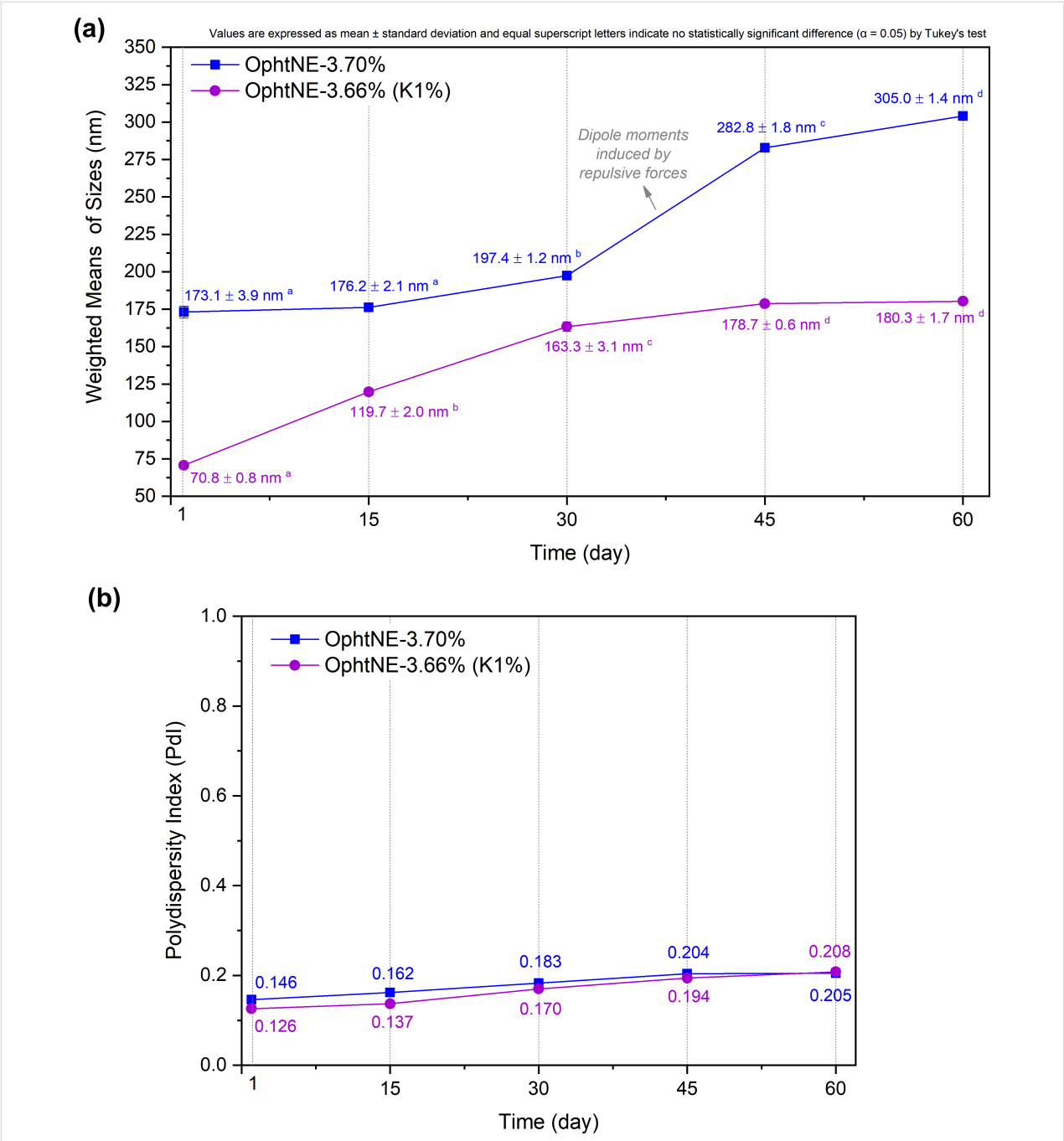

Figure 4: Changes in (a) average droplet size and (b) polydispersity index of OphtNE-3.70% and OphtNE-3.66%(K1%) nanoformulations over 60 days at room temperature. Data are shown as means ± standard deviation (n = 3) with statistical significance (p < 0.05).

tion process from pre-formulations. As reported in the literature, the storage of diluted nanoemulsions after treatment in a microfluidizer exhibited significantly greater stability compared to undiluted nanoemulsions [41].

The antioxidant potential of ophthalmic nanoformulations was evaluated using the DPPH assay, a well-established method for assessing the free radical-scavenging capacity of bioactive substances through a visible color change in the reaction medium. Typically, the greater a compound's ability to reduce DPPH radicals, the higher its antioxidant effect [55]. The antioxidant activity of OphtNE-3.70% and OphtNE-3.66%(K1%) nanoformulations was evaluated through these tests, as shown in Figure 5. The results demonstrated a statistically significant dose-dependent response. The antioxidant activity observed is attributed to the presence of linseed oil at 3% (w/v) in the

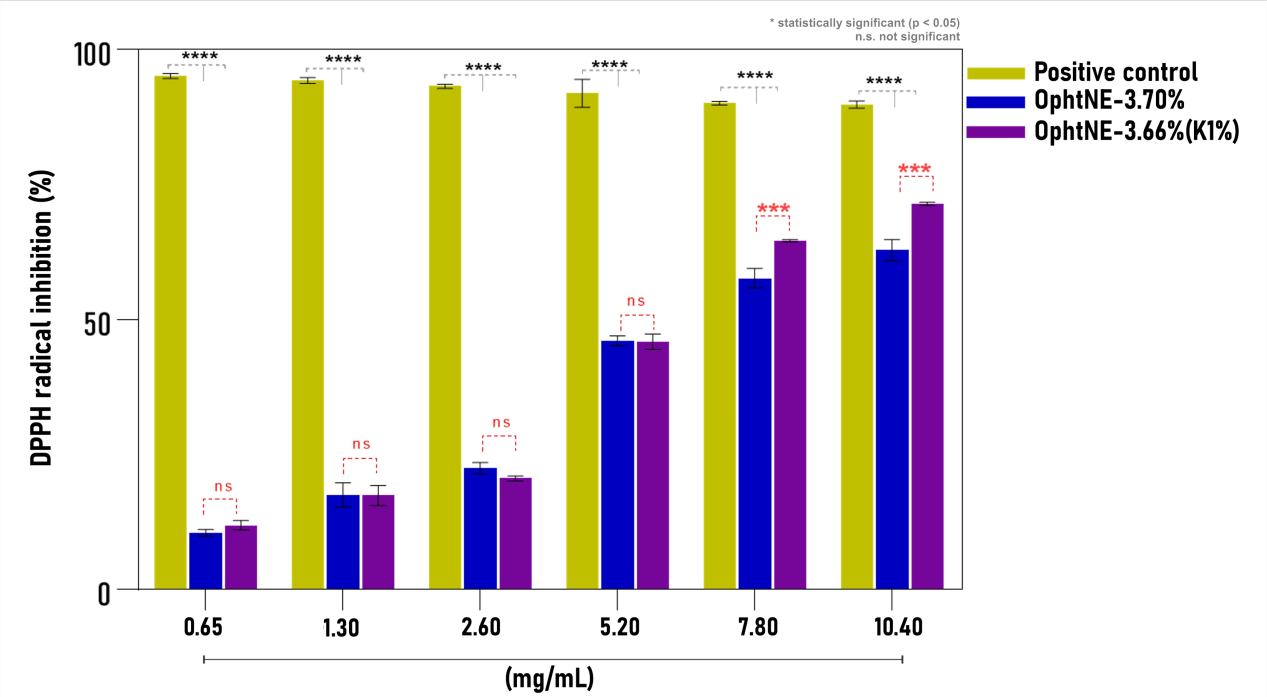

Figure 5: Antioxidant activity (DPPH assay) of OphtNE-3.70% and OphtNE-3.66%(K1%) at different concentrations (0.65–10.4 mg·mL^{-1}), with ascorbic acid as the positive control. Data are mean ± SD. *p < 0.05; n.s., not significant.

formulations, rich in α-linolenic acid and other bioactive components. As the concentration of nanoformulations increased, their antioxidant activity increased, compared to ascorbic acid (positive control). The essential omega–3 fatty acid is known for its ability to neutralize free radicals, which contributes to protection against cellular oxidative stress by synthesizing EPA and DHA [28,65,110]. Supporting these findings, a multicenter, double-blind, randomized clinical study conducted by Downie et al. developed a nanoemulsion-based tear formulation containing linseed oil and trehalose [31]. This nanoformulation provided additional ocular surface protection, highlighting its potential as a promising product for DED.

When comparing the nanoformulations, a statistically significant difference in antioxidant activity was observed beginning at an LO concentration of 7.80 mg·mL^{-1}, with OphtNE-3.66%(K1%) showing greater antioxidative potential due to its smaller nanodroplet size. The relationship between droplet size and antioxidant capacity has been highlighted in previous studies, where emulsified systems exhibited superior antioxidant performance compared to non-emulsified essential oils [55]. Additionally, antioxidant nanoemulsions containing α-tocopherol have been reported as effective strategies for glaucoma treatment [111].

The DPPH 50% inhibition activity (IC_{50}) was estimated at 9.56 mg·mL^{-1} for OphtNE-3.70% and 9.16 mg·mL^{-1} for OphtNE-3.66%(K1%). The linear regression equations used to determine the IC_{50} values for the antioxidant activity of ophthalmic nanoformulations are provided in Figure S3 in Supporting Information File 1. These antioxidant activities highlight the potential of OphtNE-3.70% and OphtNE-3.66%(K1%) to protect cells from oxidative damage caused by free radicals. This protection is essential for preserving cellular integrity and functionality, ensuring accurate and reliable results in cytotoxicity experiments. Notably, at LO concentrations lower than 7.80 mg·mL^{-1}, no statistical difference in antioxidant performance was observed between the two formulations, emphasizing their similar efficacy in cellular protection.

Given that the data satisfied the assumptions of normality and homoscedasticity, a three-way ANOVA was conducted to assess L929 cell viability based on absorbance measurements, which showed significant effects of concentration and time, as well as the interactions treatment:concentration and concentration:time (Table 4). Cell viability was influenced by the synergistic effects of nanoformulation concentration and exposure time. Increased absorbance values indicated cell proliferation, whereas decreased values signified cell death.

The two-way ANOVA applied to the treatment:concentration interaction was statistically significant at all analyzed levels (Table S3 in Supporting Information File 1), supporting the trends observed in the graphical representation. The results of

Table 4: Three-way ANOVA of the effects of treatment, concentration, and time, and their interactions, on MTT assay absorbance in L929 cells.[a]

Effect	DF_n	DF_d	*F*	*p*	$p < 0.05$	ges
treatment (OphtNE-3.70% and OphtNE-3.66%(K1%))	1	99	82.887	$9.83\ 10^{-15}$	*	0.456
concentration ($mg{\cdot}mL^{-1}$)	8	99	60.025	$1.39\ 10^{-34}$	*	0.829
time (h)	1	99	0.107	0.744	ns	0.001
treatment:concentration	8	99	8.734	$5.81\ 10^{-9}$	*	0.414
treatment:time	1	99	1.595	0.21	ns	0.016
concentration:time	8	99	2.924	0.006	*	0.191
treatment:concentration:time	8	99	0.797	0.607	ns	0.060

[a]*: significant (p <0.05); ns: not significant.

the one-way ANOVA for the significance levels are presented in Table S4 in Supporting Information File 1.

The boxplot in Figure 6a displays a characteristic dose-dependent response pattern, where increasing concentrations of the nanoformulations lead to a progressive decrease in absorbance values and, consequently, in cell viability, observed at both 24 and 72 h of exposure. This behavior is indicative of a cytotoxic effect, likely associated with the accumulation of nanoformulation components in the extracellular environment.

OphtNE-3.70% maintained high cell viability, comparable to the negative control, up to a concentration of 7.80 $mg{\cdot}mL^{-1}$ (300 $\mu L{\cdot}mL^{-1}$), suggesting good tolerability after 24 h of exposure. This observation aligns with previous reports indicating that lecithin-containing formulations are generally well tolerated by non-tumor cells, due to their structural similarity to plasma membrane phospholipids [42,112]. Such compatibility may facilitate spontaneous fusion with the membrane or passive endocytosis without triggering inflammatory or apoptotic responses. However, at concentrations of 10.40 $mg{\cdot}mL^{-1}$ and above, a marked reduction in absorbance values and, consequently, in cell viability was observed. This effect may be primarily attributed to: (i) the relatively high sample volume applied to the wells (400 $\mu L{\cdot}mL^{-1}$), potentially limiting oxygen and nutrient diffusion; and (ii) lipid overload, which could disrupt local osmotic balance and alter membrane fluidity and integrity, thereby promoting necrosis or delayed apoptosis [113,114].

From a biochemical perspective, this high lipid load may enhance lipid peroxidation and disrupt membrane lipid domain organization, affecting associated proteins and the cytoskeleton, thereby further compromising cell viability. These effects become particularly evident at higher concentrations, such as 13 $mg{\cdot}mL^{-1}$, where absorbance values approach those observed in the positive control (non-viable cells). Under this condition, the high proportion of formulation relative to the RPMI medium (500 µL of formulation per well) amplifies the physicochemical stress on the cells, impairing the maintenance of homeostasis and promoting irreversible loss of membrane integrity.

In contrast, OphtNE-3.66%(K1%), which contains Kolliphor® HS15 as a co-surfactant, exhibited more pronounced cytotoxicity even at lower concentrations. Cell viability was comparable to the negative control only at 1.30 $mg{\cdot}mL^{-1}$, decreasing sharply at higher concentrations. This effect may be attributed to the smaller size of the nanodroplets, which increases the specific surface area, thereby enhancing interactions with the cell membrane and facilitating particle internalization via endocytosis [115]. Previous studies have linked colloidal nanosystems to increased mitochondrial instability and the activation of apoptotic pathways, even in normal cells [116,117].

Regarding the concentration:time interaction, the two-way ANOVA revealed statistical significance only for OphtNE-3.70% (Table S5 in Supporting Information File 1). This effect was further examined through a one-way ANOVA, pooling exposure times to assess the influence of concentration, which confirmed the significance of this factor (Table S6 in Supporting Information File 1). This finding suggests that, for this nanoformulation, exposure time exerts a more pronounced influence on the cellular response compared with the OphtNE-3.66%(K1%) (containing Kolliphor® HS15). The boxplot in Figure 6b illustrates an upward trend in absorbance values over time, particularly at lower concentrations, which may indicate either cellular recovery following initial exposure or adaptation to the external stimulus. This pattern was also observed in the negative control, supporting the experimental consistency. Notably, at LO concentrations of 7.80 and 10.40 $mg{\cdot}mL^{-1}$, a reduction in absorbance value and, consequently, in L929 cell viability was detected at 72 h but not at 24 h. This observation indicates a delayed cytotoxic effect, potentially associated with intracellular accumulation of nanoemulsion components, mitochondrial dysfunction, or oxidative stress induced by prolonged

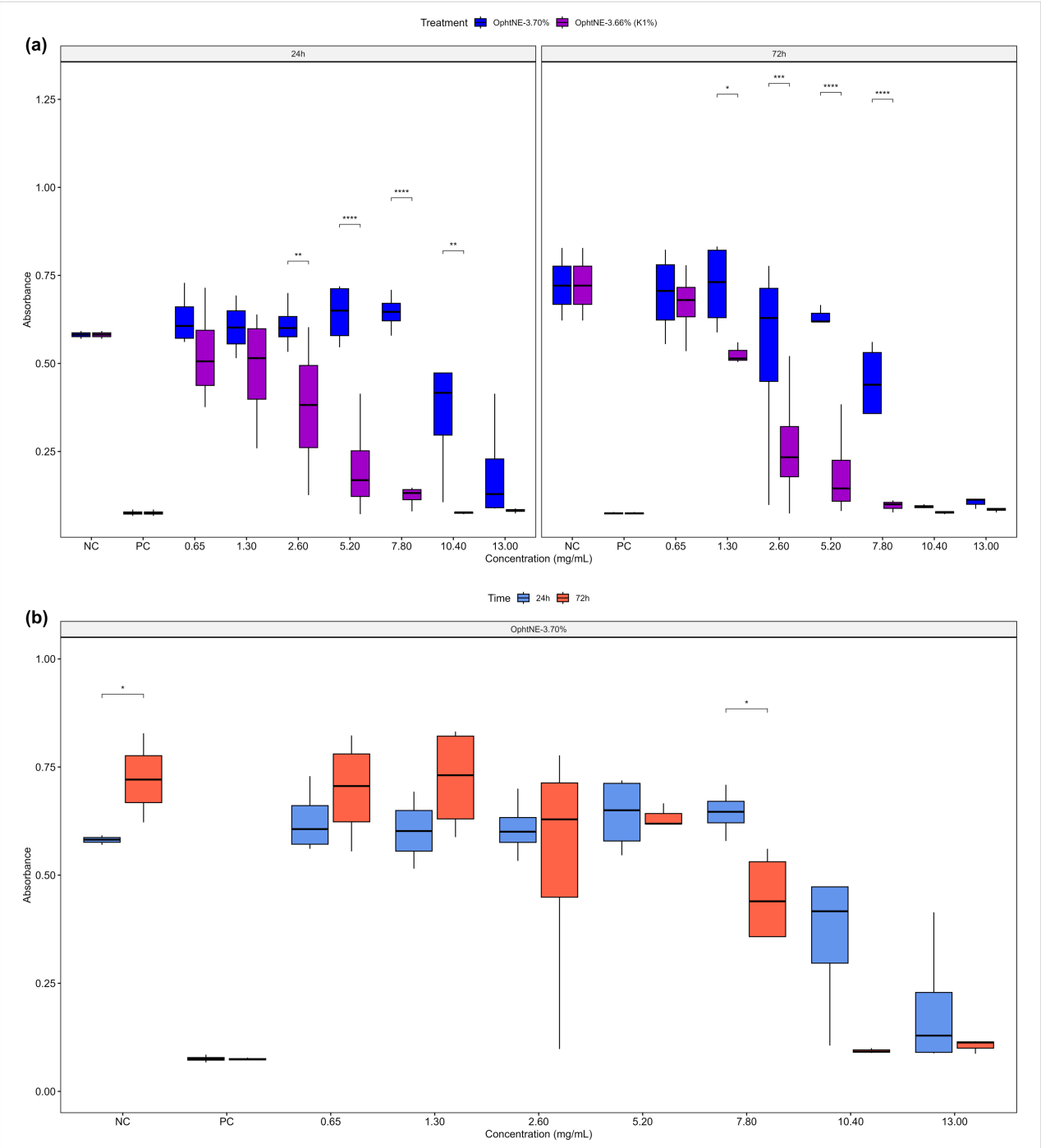

Figure 6: MTT assay absorbance for L929 cells: (a) boxplots for OphtNE-3.70% and OphtNE-3.66%(K1%) by treatment:concentration interaction at 24 and 72 h; (b) boxplots for OphtNE-3.70% by concentration:time interaction. *$p < 0.05$; n.s., not significant.

exposure [118]. Collectively, these findings underscore the importance of considering multiple parameters in the development of ophthalmic nanoformulations, including lipid concentration, application volume, exposure time, and formulation composition. Fine-tuning these variables is essential to ensure therapeutic efficacy without compromising cellular safety. Furthermore, the relevance of long-term in vivo studies is highlighted as a means to predict potential adverse events that may arise from repeated topical clinical applications.

Cell viability results above 70% are generally considered acceptable by the ISO 10993-5:2009. [59]. Table 5 summarizes the maximum non-cytotoxic concentration (MNCC) for L929 cells exposed to the developed ophthalmic nanoformulations. A

Table 5: Results for 70% maximum non-cytotoxic concentration ($MNCC_{70}$) of nanoformulations OphtNE-3.70% and OphtNE-3.66%(K1%) after 24 and 72 h of culture.

Ophthalmic nanoformulations	Maximum Non-Cytotoxic Concentration (MNCC)			
	24 h (short exposure)		72 h (long exposure)	
	$MNCC_{70}$ ($mg \cdot mL^{-1}$)	$MNCC_{70}$ ($\mu L \cdot mL^{-1}$)	$MNCC_{70}$ ($mg \cdot mL^{-1}$)	$MNCC_{70}$ ($\mu L \cdot mL^{-1}$)
OphtNE-3.70%	7.80	300	7.80	300
OphtNE-3.66%(K1%)	1.30	50	2.60	100

comparative analysis of the results revealed that only the OphtNE-3.66%(K1%) nanoformulation showed decreased tolerance, despite a slight increase in its MNCC with prolonged exposure.

Cell-based assays are widely accepted alternatives to Draize tests (in vivo), given the evidence of the correlation between cytotoxicity and ocular damage, particularly ocular irritation [119]. The scientific community strongly advocates integrating in vitro tests to generate robust data, developing alternative methods, and reducing reliance on animal testing [120]. The biocompatibility and safety of linseed oil have been consistently demonstrated in biomedical applications, particularly in ophthalmology [121-123]. In a randomized clinical trial involving patients with dry eye disease, a nanoemulsion containing linseed oil was associated with a significantly lower incidence of treatment-related adverse events compared to a conventional artificial tear formulation [121]. These findings support the therapeutic potential of linseed oil-based formulations in the management of ocular surface disorders.

Beyond its lubricating properties, linseed oil has also been investigated as a vehicle for ocular drug delivery, showing the capacity to prolong pre-corneal residence time and enhance local bioavailability [122]. Although specific concentrations of linseed oil within nanoemulsions are rarely disclosed, efficacy is largely attributed to nanotechnology-driven production of ultrafine, stable oil droplets.

Oral supplementation with linseed oil capsules (1–2 g/day) has further demonstrated clinical benefits in patients with Sjögren's syndrome, reducing ocular surface inflammation and alleviating disease-related symptoms [123]. In addition, a novel artificial tear nanoemulsion enriched with linseed oil produced significant improvements in ocular staining parameters, including corneal and conjunctival staining scores [123]. Preclinical evidence also supports these findings. In a rabbit model, a linseed oil-containing formulation exerted a robust inhibitory effect on experimentally induced ocular inflammation, reinforcing both its biocompatibility and therapeutic value [122].

However, correlating the concentration of nanoformulations with their actual application volume is essential, particularly for topical applications such as eye drops. Considering that the average volume of an ophthalmic drop is approximately 50 µL [9,11,27], the resulting concentration of active components administered per dose would be around 1.30 $mg \cdot mL^{-1}$. Notably, cytotoxic effects in L929 cells were observed only at concentrations exceeding this limit, suggesting satisfactory in vitro biocompatibility at the intended dose. Furthermore, both nanoformulations contain 2.6% (w/v) linseed oil, a bioactive lipid rich in polyunsaturated fatty acids with recognized anti-inflammatory and antioxidant activities. This concentration ensures sufficient delivery of the oil's functional components while maintaining physicochemical and biological stability. Therefore, the observed multifunctional behavior (antioxidant capacity and cytocompatibility) can be attributed, at least in part, to the presence of linseed oil at this optimized level, reinforcing its therapeutic potential in the DED treatment.

The nanoformulations have several benefits: (i) antioxidant activity shown by DPPH assays, crucial for reducing oxidative stress in DED; (ii) high compatibility with fibroblasts, indicating safety for the eye; (iii) nanoscale size with low polydispersity, improving penetration and stability; (iv) negative zeta potential, promoting stability and interaction with mucins; and (v) a pH value close to that of natural tears, ensuring tolerability. These features make them promising carriers for treating DED.

Conclusion

This study presents a scalable pre-formulation strategy based on lecithin-stabilized pre-emulsions refined by tip ultrasound. This approach enabled the development of two sterile ophthalmic nanoformulations, namely, OphtNE-3.70% (lecithin only) and OphtNE-3.66%(K1%) (lecithin with Kolliphor® HS15). Both nanoemulsions demonstrated antioxidant activity and cytocompatibility, supporting their potential use in the DED treatment.

Linseed oil was characterized by GC-FID, acid value, viscosity, and thermal analyses (TGA/DSC), confirming its identity,

purity, and thermal stability (even after mild heating), thus validating its suitability for nanoemulsion preparation. This preformulation ensures effective emulsification and regulation of droplet size, thereby supporting multifunctional properties (such as antioxidant and cytocompatible responses), while also facilitating sterile and scalable manufacturing suitable for ophthalmic drug products. Both nanoformulations were developed with 2.6% (w/v) (equivalent to 26 mg·mL^{-1}) of the linseed oil, a bioactive lipid known for its antioxidant and anti-inflammatory effects. This optimized concentration ensures therapeutic relevance within the typical ocular drop volume (~50 µL), while maintaining cytocompatibility. The multifunctional behavior observed in vitro is thus closely associated with the preserved activity of the oil in its nanoformulated form.

Although this study focused on formulation design and in vitro characterization, future work should include comparative biological assays between the native and nanoformulated oil to better elucidate their respective contributions. Two methodological limitations were also noted: osmolality was not assessed, and in vitro inflammatory markers were not analyzed. These aspects should be addressed in future studies to confirm ocular tolerability and to explore the anti-inflammatory potential of the nanoemulsions, particularly considering the bioactivity of linseed oil fatty acids.

Supporting Information

Supporting Information File 1 contains a detailed table of the mass composition of the pre-formulations (O/W(L-1%), O/W(L-2%), O/W(L-3%), O/W(L-4%), and O/W(L-5%)) and ophthalmic nanoformulations (OphtNE-3.70% and OphtNE-3.66%(K1%)), along with visual and experimental data supporting the article. Included are macroscopic images of the pre-formulations, particle size distribution profiles, and linear regression curves used to determine antioxidant activity (IC_{50}). Also, this file contains the two-way and one-way ANOVA tables for the statistically significant treatment:concentration and concentration:time interactions identified in the three-way ANOVA, based on MTT assay absorbance data from L929 cells. Supporting Information File 2 contains the data processing workflow and statistical analyses, including the Shapiro–Wilk test for assessing normality, outlier removal, and Levene's test for evaluating homoscedasticity.

Supporting Information File 1

Supplementary tables and figures.
[https://www.beilstein-journals.org/bjnano/content/supplementary/2190-4286-16-120-S1.pdf]

Supporting Information File 2

Complementary statistical data.
[https://www.beilstein-journals.org/bjnano/content/supplementary/2190-4286-16-120-S2.xlsx]

Acknowledgements

The authors gratefully acknowledge the Ministry of Science, Technology, and Innovation (MCTI, Brazil) for institutional support. The authors also thank Dr. Ronald Rodrigues de Moura, from the Istituto di Ricovero e Cura a Carattere Scientifico (IRCCS) Burlo Garofolo, for statistical assistance using the R software. The drawings representing the beakers, pipette, hotplate stirrer, sonication probe, dropper bottles, and process arrows presented in the Graphic Abstract were adapted from Servier Medical Art (https://smart.servier.com/), licensed under CC BY 4.0 (https://creativecommons.org/licenses/by/4.0/).

Funding

This research was financially supported by the Foundation for Support of Science and Technology of the State of Pernambuco (FACEPE, Process no. BFP-0136-1.06/21), and the Brazilian Funding Agency for Studies and Projects (FINEP, Contract no. 01.22.0149.00 - Ref. 0071/21).

Author Contributions

Niédja Fittipaldi Vasconcelos: conceptualization; formal analysis; investigation; methodology; writing – original draft. Almerinda Agrelli: formal analysis; writing – original draft. Rayane Cristine Santos da Silva: formal analysis; investigation; methodology. Carina Lucena Mendes-Marques: formal analysis; methodology. Isabel Renata de Souza Arruda: formal analysis; methodology. Priscilla Stela Santana de Oliveira: formal analysis; investigation; methodology. Mércia Liane de Oliveira: supervision; writing – review & editing. Giovanna Machado: funding acquisition; project administration; supervision; writing – review & editing.

ORCID® iDs

Niédja Fittipaldi Vasconcelos - https://orcid.org/0000-0002-2440-0039
Almerinda Agrelli - https://orcid.org/0000-0002-9908-742X
Carina Lucena Mendes-Marques - https://orcid.org/0000-0002-3111-7063
Giovanna Machado - https://orcid.org/0000-0002-9058-3056

Data Availability Statement

All data that supports the findings of this study is available in the published article and/or the supporting information of this article.

References

1. Lv, Z.; Li, S.; Zeng, G.; Yao, K.; Han, H. *Adv. Ophthalmol. Pract. Res.* **2024,** *4,* 23–31. doi:10.1016/j.aopr.2024.01.008
2. Meshksar, S.; Hadipour Jahromy, M.; Qomi, M.; Sami, N.; Faali, F. *Phytomed. Plus* **2024,** *4,* 100541. doi:10.1016/j.phyplu.2024.100541
3. Nelson, J. D.; Craig, J. P.; Akpek, E. K.; Azar, D. T.; Belmonte, C.; Bron, A. J.; Clayton, J. A.; Dogru, M.; Dua, H. S.; Foulks, G. N.; Gomes, J. A. P.; Hammitt, K. M.; Holopainen, J.; Jones, L.; Joo, C.-K.; Liu, Z.; Nichols, J. J.; Nichols, K. K.; Novack, G. D.; Sangwan, V.; Stapleton, F.; Tomlinson, A.; Tsubota, K.; Willcox, M. D. P.; Wolffsohn, J. S.; Sullivan, D. A. *Ocul. Surf.* **2017,** *15,* 269–275. doi:10.1016/j.jtos.2017.05.005
4. Papas, E. B. *Ophthalmic Physiol. Opt.* **2021,** *41,* 1254–1266. doi:10.1111/opo.12888
5. Tovar, A. A.; Frankel, S. T.; Galor, A.; Sabater, A. L. *Ophthalmol. Ther.* **2023,** *12,* 2219–2226. doi:10.1007/s40123-023-00736-7
6. Andrés-Guerrero, V.; Bravo-Osuna, I.; Pastoriza, P.; Molina-Martinez, I. T.; Herrero-Vanrell, R. *J. Drug Delivery Sci. Technol.* **2017,** *42,* 181–192. doi:10.1016/j.jddst.2017.07.001
7. Ramsay, E.; del Amo, E. M.; Toropainen, E.; Tengvall-Unadike, U.; Ranta, V.-P.; Urtti, A.; Ruponen, M. *Eur. J. Pharm. Sci.* **2018,** *119,* 83–89. doi:10.1016/j.ejps.2018.03.034
8. Patel, A.; Cholkar, K.; Agrahari, V.; Mitra, A. K. *World J. Pharmacol.* **2013,** *2,* 47–64. doi:10.5497/wjp.v2.i2.47
9. Gause, S.; Hsu, K.-H.; Shafor, C.; Dixon, P.; Powell, K. C.; Chauhan, A. *Adv. Colloid Interface Sci.* **2016,** *233,* 139–154. doi:10.1016/j.cis.2015.08.002
10. Adibkia, K.; Shadbad, M. R. S.; Nokhodchi, A.; Javadzedeh, A.; Barzegar-Jalali, M.; Barar, J.; Mohammadi, G.; Omidi, Y. *J. Drug Targeting* **2007,** *15,* 407–416. doi:10.1080/10611860701453125
11. Agrahari, V.; Mandal, A.; Agrahari, V.; Trinh, H. M.; Joseph, M.; Ray, A.; Hadji, H.; Mitra, R.; Pal, D.; Mitra, A. K. *Drug Delivery Transl. Res.* **2016,** *6,* 735–754. doi:10.1007/s13346-016-0339-2
12. Markoulli, M.; Wong, K.; Jia, T.; Siddireddy, J. S.; Briggs, N.; Tan, J. *Contact Lens Anterior Eye* **2022,** *45,* 101736. doi:10.1016/j.clae.2022.101736
13. Jones, L.; Downie, L. E.; Korb, D.; Benitez-del-Castillo, J. M.; Dana, R.; Deng, S. X.; Dong, P. N.; Geerling, G.; Hida, R. Y.; Liu, Y.; Seo, K. Y.; Tauber, J.; Wakamatsu, T. H.; Xu, J.; Wolffsohn, J. S.; Craig, J. P. *Ocul. Surf.* **2017,** *15,* 575–628. doi:10.1016/j.jtos.2017.05.006
14. Nagai, N.; Otake, H. *Adv. Drug Delivery Rev.* **2022,** *191,* 114582. doi:10.1016/j.addr.2022.114582
15. Aswathanarayan, J. B.; Vittal, R. R. *Front. Sustainable Food Syst.* **2019,** *3,* 95. doi:10.3389/fsufs.2019.00095
16. Natarajan, J. V.; Darwitan, A.; Barathi, V. A.; Ang, M.; Htoon, H. M.; Boey, F.; Tam, K. C.; Wong, T. T.; Venkatraman, S. S. *ACS Nano* **2014,** *8,* 419–429. doi:10.1021/nn4046024
17. Alvarez-Trabado, J.; Diebold, Y.; Sanchez, A. *Int. J. Pharm.* **2017,** *532,* 204–217. doi:10.1016/j.ijpharm.2017.09.017
18. Lallemand, F.; Schmitt, M.; Bourges, J.-L.; Gurny, R.; Benita, S.; Garrigue, J.-S. *Eur. J. Pharm. Biopharm.* **2017,** *117,* 14–28. doi:10.1016/j.ejpb.2017.03.006
19. Prasad, M.; Lambe, U. P.; Brar, B.; Shah, I.; J, M.; Ranjan, K.; Rao, R.; Kumar, S.; Mahant, S.; Khurana, S. K.; Iqbal, H. M. N.; Dhama, K.; Misri, J.; Prasad, G. *Biomed. Pharmacother.* **2018,** *97,* 1521–1537. doi:10.1016/j.biopha.2017.11.026
20. Chávez-Hurtado, P.; Pesqueda-Pinedo, L.; Ceballos-Delgadillo, H. A.; Liñán-Segura, A.; Figueroa-Ponce, H.; Quintana-Hau, J. D. *Contact Lens Anterior Eye* **2022,** *45,* 101428. doi:10.1016/j.clae.2021.02.014
21. Jurišić Dukovski, B.; Juretić, M.; Bračko, D.; Randjelović, D.; Savić, S.; Crespo Moral, M.; Diebold, Y.; Filipović-Grčić, J.; Pepić, I.; Lovrić, J. *Int. J. Pharm.* **2020,** *576,* 118979. doi:10.1016/j.ijpharm.2019.118979
22. Gan, L.; Wang, J.; Jiang, M.; Bartlett, H.; Ouyang, D.; Eperjesi, F.; Liu, J.; Gan, Y. *Drug Discovery Today* **2013,** *18,* 290–297. doi:10.1016/j.drudis.2012.10.005
23. Walenga, R. L.; Babiskin, A. H.; Zhang, X.; Absar, M.; Zhao, L.; Lionberger, R. A. *J. Pharm. Sci.* **2019,** *108,* 620–629. doi:10.1016/j.xphs.2018.10.034
24. Tran, V. N.; Strnad, O.; Šuman, J.; Veverková, T.; Sukupová, A.; Cejnar, P.; Hynek, R.; Kronusová, O.; Šach, J.; Kaštánek, P.; Ruml, T.; Viktorová, J. *Int. J. Pharm.* **2023,** *643,* 123202. doi:10.1016/j.ijpharm.2023.123202
25. Attia, M. A.; Eleraky, N. E.; Abdelazeem, K.; Safwat, M. A. *J. Drug Delivery Sci. Technol.* **2024,** *92,* 105406. doi:10.1016/j.jddst.2024.105406
26. Toragall, V.; Srirangam, P.; Jayapala, N.; Baskaran, V. *Mater. Today Commun.* **2021,** *28,* 102522. doi:10.1016/j.mtcomm.2021.102522
27. Choradiya, B. R.; Patil, S. B. *J. Mol. Liq.* **2021,** *339,* 116751. doi:10.1016/j.molliq.2021.116751
28. Maulvi, F. A.; Desai, D. T.; Kalaiselvan, P.; Dumpati, S.; Kuppusamy, R.; Masoudi, S.; Shah, D. O.; Willcox, M. D. P. *Contact Lens Anterior Eye* **2024,** *47,* 102154. doi:10.1016/j.clae.2024.102154
29. Baboota, S.; Rahman, M. u.; Kumar, A.; Sharma, S.; Sahni, J.; Ali, J. *J. Dispersion Sci. Technol.* **2012,** *33,* 1259–1266. doi:10.1080/01932691.2011.596339
30. Bardaa, S.; Turki, M.; Ben Khedir, S.; Mzid, M.; Rebai, T.; Ayadi, F.; Sahnoun, Z. *BioMed Res. Int.* **2020,** 5643465. doi:10.1155/2020/5643465
31. Downie, L. E.; Hom, M. M.; Berdy, G. J.; El-Harazi, S.; Verachtert, A.; Tan, J.; Liu, H.; Carlisle-Wilcox, C.; Simmons, P.; Vehige, J. *Ocul. Surf.* **2020,** *18,* 148–157. doi:10.1016/j.jtos.2019.11.004
32. Deinema, L. A.; Vingrys, A. J.; Wong, C. Y.; Jackson, D. C.; Chinnery, H. R.; Downie, L. E. *Ophthalmology* **2017,** *124,* 43–52. doi:10.1016/j.ophtha.2016.09.023
33. Kildaci, I.; Budama-Kilinc, Y.; Kecel-Gunduz, S.; Altuntas, E. *J. Drug Delivery Sci. Technol.* **2021,** *64,* 102652. doi:10.1016/j.jddst.2021.102652
34. Rashid, S.; Jin, Y.; Ecoiffier, T.; Barabino, S.; Schaumberg, D. A.; Dana, M. R. *Arch. Ophthalmol. (Chicago, IL, U. S.)* **2008,** *126,* 219–225. doi:10.1001/archophthalmol.2007.61
35. Dasyani, M.; Gao, F.; Xu, Q.; Van Fossan, D.; Zhang, E.; Pinto, A. F. M.; Saghatelian, A.; Skowronska-Krawczyk, D.; Chao, D. L. *Cells* **2020,** *9,* 2583. doi:10.3390/cells9122583
36. Hachem, M.; Bermudez, J. R.; Ali, A. H.; Murtaza, F. F.; Rommala, M.; Corridon, P. R. *Heliyon* **2024,** *10,* e38148. doi:10.1016/j.heliyon.2024.e38148
37. Guimarães, D.; Cavaco-Paulo, A.; Nogueira, E. *Int. J. Pharm.* **2021,** *601,* 120571. doi:10.1016/j.ijpharm.2021.120571

38. Garrigue, J.-S.; Amrane, M.; Faure, M.-O.; Holopainen, J. M.; Tong, L. *J. Ocul. Pharmacol. Ther.* **2017,** *33,* 647–661. doi:10.1089/jop.2017.0052
39. Pult, H.; Khatum, F. S.; Trave-Huarte, S.; Wolffsohn, J. S. *Eye Contact Lens* **2021,** *47,* 445–448. doi:10.1097/icl.0000000000000788
40. Zhang, M.; Cao, Q.; Yuan, Y.; Guo, X.; Pan, D.; Xie, R.; Ju, X.; Liu, Z.; Wang, W.; Chu, L. *Chin. Chem. Lett.* **2024,** *35,* 108710. doi:10.1016/j.cclet.2023.108710
41. Yun, S.; Kim, G. W.; Jang, J.; Lee, J. B.; Kim, S. Y. *Colloids Surf., A* **2024,** *691,* 133845. doi:10.1016/j.colsurfa.2024.133845
42. Vater, C.; Adamovic, A.; Ruttensteiner, L.; Steiner, K.; Tajpara, P.; Klang, V.; Elbe-Bürger, A.; Wirth, M.; Valenta, C. *Int. J. Pharm.* **2019,** *566,* 383–390. doi:10.1016/j.ijpharm.2019.05.078
43. Rupp, C.; Steckel, H.; Müller, B. W. *Int. J. Pharm.* **2010,** *387,* 120–128. doi:10.1016/j.ijpharm.2009.12.018
44. Zheng, Y.; Zheng, M.; Ma, Z.; Xin, B.; Guo, R.; Xu, X. Sugar Fatty Acid Esters. *Polar lipids;* AOCS Press: Urbana, IL, USA, 2015; pp 215–243. doi:10.1016/b978-1-63067-044-3.50012-1
45. Cohen, D. E.; Carey, M. C. *J. Lipid Res.* **1991,** *32,* 1291–1302. doi:10.1016/s0022-2275(20)41959-5
46. Booker, M. L.; LaMorte, W. W.; Ahrendt, S. A.; Lillemoe, K. D.; Pitt, H. A. *J. Lipid Res.* **1992,** *33,* 1485–1492. doi:10.1016/s0022-2275(20)41403-8
47. Torchilin, V. P. *Nat. Rev. Drug Discovery* **2005,** *4,* 145–160. doi:10.1038/nrd1632
48. Bozzuto, G.; Molinari, A. *Int. J. Nanomed.* **2015,** *10,* 975–999. doi:10.2147/ijn.s68861
49. Israelachvili, J. N.; Mitchell, D. J.; Ninham, B. W. *Biochim. Biophys. Acta, Biomembr.* **1977,** *470,* 185–201. doi:10.1016/0005-2736(77)90099-2
50. Corkery, R. W. *Colloids Surf., B* **2002,** *26,* 3–20. doi:10.1016/s0927-7765(02)00034-6
51. Šegota, S.; Težak, D. *Adv. Colloid Interface Sci.* **2006,** *121,* 51–75. doi:10.1016/j.cis.2006.01.002
52. Ebrahim, S.; Peyman, G. A.; Lee, P. J. *Surv. Ophthalmol.* **2005,** *50,* 167–182. doi:10.1016/j.survophthal.2004.12.006
53. Mirchandani, Y.; Patravale, V. B.; S., B. *J. Controlled Release* **2021,** *335,* 457–464. doi:10.1016/j.jconrel.2021.05.032
54. Priyadarshini, S.; Bora, S.; Kulhari, H. Lipid-Based Nanocarriers for the Delivery of Phytoconstituents. In *Nanotechnology Based Delivery of Phytoconstituents and Cosmeceuticals;* Pooja, D.; Kulhari, H., Eds.; Springer Nature: Singapore, 2024; pp 125–167. doi:10.1007/978-981-99-5314-1_5
55. Sundararajan, B.; Moola, A. K.; Vivek, K.; Kumari, B. D. R. *Microb. Pathog.* **2018,** *125,* 475–485. doi:10.1016/j.micpath.2018.10.017
56. Brand-Williams, W.; Cuvelier, M. E.; Berset, C. *Lebensm.-Wiss. Technol. (1968-2004)* **1995,** *28,* 25–30. doi:10.1016/s0023-6438(95)80008-5
57. Gulcin, İ.; Alwasel, S. H. *Processes* **2023,** *11,* 2248. doi:10.3390/pr11082248
58. AlMotwaa, S. M.; Al-Otaibi, W. A. *J. Drug Delivery Sci. Technol.* **2022,** *75,* 103664. doi:10.1016/j.jddst.2022.103664
59. ISO 10993-5:2009 - Biological evaluation of medical devices — Part 5: Tests for in vitro cytotoxicity. https://www.iso.org/standard/36406.html (accessed Sept 17, 2025).
60. R: The R Project for Statistical Computing. https://www.R-project.org/ (accessed Sept 17, 2025).
61. Wickham, H.; Averick, M.; Bryan, J.; Chang, W.; McGowan, L. D.; François, R.; Grolemund, G.; Hayes, A.; Henry, L.; Hester, J.; Kuhn, M.; Pedersen, T. L.; Miller, E.; Bache, S. M.; Müller, K.; Ooms, J.; Robinson, D.; Seidel, D. P.; Spinu, V.; Takahashi, K.; Vaughan, D.; Wilke, C.; Woo, K.; Yutani, H. *J. Open Source Software* **2019,** *4,* 1686. doi:10.21105/joss.01686
62. Pipe-Friendly Framework for Basic Statistical Tests – rstatix. https://rpkgs.datanovia.com/rstatix/ (accessed Sept 17, 2025).
63. Qiu, C.; Wang, H.; Guo, Y.; Long, S.; Wang, Y.; Abbasi, A. M.; Guo, X.; Jarvis, D. I. *Oil Crop Sci.* **2020,** *5,* 136–141. doi:10.1016/j.ocsci.2020.08.001
64. Rahiminezhad, Z.; Hashemi Gahruie, H.; Esteghlal, S.; Mesbahi, G. R.; Golmakani, M.-T.; Hosseini, S. M. H. *LWT-Food Sci. Technol.* **2020,** *127,* 109392. doi:10.1016/j.lwt.2020.109392
65. DiNicolantonio, J. J.; O'Keefe, J. H. *Nutrients* **2020,** *12,* 2333. doi:10.3390/nu12082333
66. Kauser, S.; Hussain, A.; Ashraf, S.; Fatima, G.; Ambreen; Javaria, S.; Abideen, Z. U.; Kabir, K.; Yaqub, S.; Akram, S.; Shehzad, A.; Korma, S. A. *Food Chem. Adv.* **2024,** *4,* 100573. doi:10.1016/j.focha.2023.100573
67. Lee-Okada, H.-C.; Xue, C.; Yokomizo, T. *Biochim. Biophys. Acta, Mol. Cell Biol. Lipids* **2025,** *1870,* 159564. doi:10.1016/j.bbalip.2024.159564
68. Andressa Caetano, R.; Alves, J.; Smaniotto, T. A.; Daroda Dutra, F.; de Assis, E. Z. B.; Soares Pedroso, L.; Peres, A.; Machado, A. G.; Krolow, R.; Maciel August, P.; Matté, C.; Seady, M.; Leite, M. C.; Machado, B. G.; Marques, C.; Saraiva, L.; de Lima, R. M. S.; Dalmaz, C. *Brain Res.* **2025,** *1846,* 149268. doi:10.1016/j.brainres.2024.149268
69. Al Mahmood, A. M.; Al-Swailem, S. A. *Saudi J. Ophthalmol.* **2014,** *28,* 195–197. doi:10.1016/j.sjopt.2014.06.004
70. Ustra, M. K.; Silva, J. R. F.; Ansolin, M.; Balen, M.; Cantelli, K.; Alkimim, I. P.; Mazutti, M. A.; Voll, F. A. P.; Cabral, V. F.; Cardozo-Filho, L.; Corazza, M. L.; Vladimir Oliveira, J. *J. Chem. Thermodyn.* **2013,** *58,* 460–466. doi:10.1016/j.jct.2012.10.007
71. Meiri, N.; Berman, P.; Colnago, L. A.; Moraes, T. B.; Linder, C.; Wiesman, Z. *Biotechnol. Biofuels* **2015,** *8,* 96. doi:10.1186/s13068-015-0280-5
72. Roufegarinejad, L.; Dehghani, S.; Bakhshi, S.; Toker, O. S.; Pirouzian, H. R.; Khiabani, A. H. *Food Chem.* **2024,** *437,* 137745. doi:10.1016/j.foodchem.2023.137745
73. Xue, S.; Hou, K.; Zhang, Z.; Liu, H.; Zhu, C.; Liu, X.; He, M. *J. Mol. Liq.* **2021,** *341,* 117374. doi:10.1016/j.molliq.2021.117374
74. Yi, L.; Wang, C.; van Vuren, T.; Lohse, D.; Risso, F.; Toschi, F.; Sun, C. *J. Fluid Mech.* **2022,** *951,* A39. doi:10.1017/jfm.2022.881
75. Tariq, M.; Qureshi, A. K.; Karim, S.; Sirajuddin, M.; Abbas, N.; Imran, M.; Shirazi, J. H. *Energy* **2021,** *222,* 120014. doi:10.1016/j.energy.2021.120014
76. Rosi Cappellani, M.; Perinelli, D. R.; Pescosolido, L.; Schoubben, A.; Cespi, M.; Cossi, R.; Blasi, P. *Appl. Nanosci.* **2018,** *8,* 1483–1491. doi:10.1007/s13204-018-0829-2
77. Espinosa-Olivares, M. A.; Delgado-Buenrostro, N. L.; Chirino, Y. I.; Trejo-Márquez, M. A.; Pascual-Bustamante, S.; Ganem-Rondero, A. *Eur. J. Pharm. Sci.* **2020,** *155,* 105533. doi:10.1016/j.ejps.2020.105533
78. Kapila, S.; Soukup, R. J.; Bradley, M. E.; Zydney, A. L. *J. Membr. Sci.* **2025,** *713,* 123370. doi:10.1016/j.memsci.2024.123370

79. Saberi, A. H.; Fang, Y.; McClements, D. J. *J. Colloid Interface Sci.* **2013,** *391,* 95–102. doi:10.1016/j.jcis.2012.08.069
80. Kentish, S.; Wooster, T. J.; Ashokkumar, M.; Balachandran, S.; Mawson, R.; Simons, L. *Innovative Food Sci. Emerging Technol.* **2008,** *9,* 170–175. doi:10.1016/j.ifset.2007.07.005
81. Lamaallam, S.; Bataller, H.; Dicharry, C.; Lachaise, J. *Colloids Surf., A* **2005,** *270–271,* 44–51. doi:10.1016/j.colsurfa.2005.05.035
82. Lee, G. W. J.; Tadros, T. F. *Colloids Surf.* **1982,** *5,* 105–115. doi:10.1016/0166-6622(82)80066-8
83. Azmi, N. A. N.; Elgharbawy, A. A. M.; Motlagh, S. R.; Samsudin, N.; Salleh, H. M. *Processes* **2019,** *7,* 617. doi:10.3390/pr7090617
84. Tadros, T.; Izquierdo, P.; Esquena, J.; Solans, C. *Adv. Colloid Interface Sci.* **2004,** *108–109,* 303–318. doi:10.1016/j.cis.2003.10.023
85. Rizzatti, I. M.; Zanette, D. R.; Mello, L. C. *Quim. Nova* **2009,** *32,* 518–521. doi:10.1590/s0100-40422009000200041
86. Müller, R. H. *Zetapotential*. *Zetapotential und Partikelladung in der Laborpraxis;* Wissenschaftliche Verlagsgesellschaft: Stuttgart, Germany, 1996; pp 19–99.
87. Bazán Henostroza, M. A.; Curo Melo, K. J.; Nishitani Yukuyama, M.; Löbenberg, R.; Araci Bou-Chacra, N. *Colloids Surf., A* **2020,** *597,* 124755. doi:10.1016/j.colsurfa.2020.124755
88. Jurišić Dukovski, B.; Ljubica, J.; Kocbek, P.; Safundžić Kučuk, M.; Krtalić, I.; Hafner, A.; Pepić, I.; Lovrić, J. *Int. J. Pharm.* **2023,** *633,* 122622. doi:10.1016/j.ijpharm.2023.122622
89. Jadhav, A.; Salave, S.; Rana, D.; Benival, D. *Drug Delivery Lett.* **2023,** *13,* 196–212. doi:10.2174/2210303113666230309151048
90. Marinova, K. G.; Alargova, R. G.; Denkov, N. D.; Velev, O. D.; Petsev, D. N.; Ivanov, I. B.; Borwankar, R. P. *Langmuir* **1996,** *12,* 2045–2051. doi:10.1021/la950928i
91. Katzer, T.; Chaves, P.; Bernardi, A.; Pohlmann, A.; Guterres, S. S.; Ruver Beck, R. C. *J. Microencapsulation* **2014,** *31,* 519–528. doi:10.3109/02652048.2013.879930
92. Imperiale, J. C.; Acosta, G. B.; Sosnik, A. *J. Controlled Release* **2018,** *285,* 106–141. doi:10.1016/j.jconrel.2018.06.031
93. Bouchemal, K.; Briançon, S.; Perrier, E.; Fessi, H. *Int. J. Pharm.* **2004,** *280,* 241–251. doi:10.1016/j.ijpharm.2004.05.016
94. Bellantone, R. A.; Shah, K. B.; Patel, P. G.; Kaplan, M.; Xu, X.; Li, V.; Newman, B.; Abul Kaisar, M. *Int. J. Pharm.* **2022,** *615,* 121521. doi:10.1016/j.ijpharm.2022.121521
95. Petrochenko, P. E.; Pavurala, N.; Wu, Y.; Yee Wong, S.; Parhiz, H.; Chen, K.; Patil, S. M.; Qu, H.; Buoniconti, P.; Muhammad, A.; Choi, S.; Kozak, D.; Ashraf, M.; Cruz, C. N.; Zheng, J.; Xu, X. *Int. J. Pharm.* **2018,** *550,* 229–239. doi:10.1016/j.ijpharm.2018.08.030
96. Li, Y.; Liu, B.; Jiang, L.; Regenstein, J. M.; Jiang, N.; Poias, V.; Zhang, X.; Qi, B.; Li, A.; Wang, Z. *Food Hydrocolloids* **2019,** *87,* 814–829. doi:10.1016/j.foodhyd.2018.09.006
97. Tayeb, H. H.; Sainsbury, F. *Nanomedicine (London, U. K.)* **2018,** *13,* 2507–2525. doi:10.2217/nnm-2018-0088
98. Lyra, L. P. d. S. Desenvolvimento de nanoemulsão de geraniol e óleo essencial da palmarosa (Cymbopogon martinii) e sua ação inibitória sobre linhagens de Cutibacterium acnes. Master's Thesis, Universidade Estadual de São Paulo "Júlio de Mesquita Filho", Botucatu, Brazil. https://hdl.handle.net/11449/181641
99. Trotta, M.; Pattarino, F.; Ignoni, T. *Eur. J. Pharm. Biopharm.* **2002,** *53,* 203–208. doi:10.1016/s0939-6411(01)00230-2
100. Onugwu, A. L.; Nwagwu, C. S.; Onugwu, O. S.; Echezona, A. C.; Agbo, C. P.; Ihim, S. A.; Emeh, P.; Nnamani, P. O.; Attama, A. A.; Khutoryanskiy, V. V. *J. Controlled Release* **2023,** *354,* 465–488. doi:10.1016/j.jconrel.2023.01.018
101. Singh, M.; Bharadwaj, S.; Lee, K. E.; Kang, S. G. *J. Controlled Release* **2020,** *328,* 895–916. doi:10.1016/j.jconrel.2020.10.025
102. Klang, V.; Matsko, N.; Zimmermann, A.-M.; Vojnikovic, E.; Valenta, C. *Int. J. Pharm.* **2010,** *393,* 153–161. doi:10.1016/j.ijpharm.2010.04.029
103. Ibrahim, S. S.; Awad, G. A. S.; Geneidi, A.; Mortada, N. D. *Colloids Surf., B* **2009,** *69,* 225–231. doi:10.1016/j.colsurfb.2008.11.034
104. Prajapati, B. G.; Patel, A. G.; Paliwal, H. *Food Hydrocolloids Health* **2021,** *1,* 100045. doi:10.1016/j.fhfh.2021.100045
105. López-Alemany, A.; Montés-Micó, R.; Garcia-Valldecabres, M. *J. Am. Optom. Assoc.* **1999,** *70,* 455–460.
106. Mohanty, B.; Mishra, S. K.; Majumdar, D. K. *J. Adv. Pharm. Technol. Res.* **2013,** *4,* 210–216. doi:10.4103/2231-4040.121416
107. Klang, V.; Valenta, C. *J. Drug Delivery Sci. Technol.* **2011,** *21,* 55–76. doi:10.1016/s1773-2247(11)50006-1
108. Çinar, K. *Trakya Univ. J. Eng. Sci.* **2017,** *18,* 73–83.
109. Taylor, P. *Adv. Colloid Interface Sci.* **1998,** *75,* 107–163. doi:10.1016/s0001-8686(98)00035-9
110. Bhargava, R.; Kumar, P.; Phogat, H.; Kaur, A.; Kumar, M. *Contact Lens Anterior Eye* **2015,** *38,* 206–210. doi:10.1016/j.clae.2015.01.007
111. Guo, X.; Zhang, J.; Liu, X.; Lu, Y.; Shi, Y.; Li, X.; Wang, S.; Huang, J.; Liu, H.; Zhou, H.; Li, Q.; Luo, L.; You, J. *J. Controlled Release* **2023,** *361,* 534–546. doi:10.1016/j.jconrel.2023.08.004
112. Nguyen, T. T. L.; Edelen, A.; Neighbors, B.; Sabatini, D. A. *J. Colloid Interface Sci.* **2010,** *348,* 498–504. doi:10.1016/j.jcis.2010.04.053
113. Zhang, L.; Gu, F. X.; Chan, J. M.; Wang, A. Z.; Langer, R. S.; Farokhzad, O. C. *Clin. Pharmacol. Ther. (Hoboken, NJ, U. S.)* **2008,** *83,* 761–769. doi:10.1038/sj.clpt.6100400
114. Fröhlich, E. *Int. J. Nanomed.* **2012,** 5577–5591. doi:10.2147/ijn.s36111
115. Hassanabadi, N.; Mahdavi Meymand, Z.; Ashrafzadeh, A.; Sharififar, F. *Ann. Pharm. Fr.* **2024,** *82,* 645–653. doi:10.1016/j.pharma.2024.01.005
116. Sola, F.; Montanari, M.; Fiorani, M.; Barattini, C.; Ciacci, C.; Burattini, S.; Lopez, D.; Ventola, A.; Zamai, L.; Ortolani, C.; Papa, S.; Canonico, B. *Int. J. Mol. Sci.* **2022,** *23,* 3069. doi:10.3390/ijms23063069
117. Misra, S. K.; Rosenholm, J. M.; Pathak, K. *Molecules* **2023,** *28,* 4701. doi:10.3390/molecules28124701
118. Okoampah, E.; Mao, Y.; Yang, S.; Sun, S.; Zhou, C. *Colloids Surf., B* **2020,** *196,* 111312. doi:10.1016/j.colsurfb.2020.111312
119. Lotz, C.; Schmid, F. F.; Rossi, A.; Kurdyn, S.; Kampik, D.; De Wever, B.; Walles, H.; Groeber, F. K. *ALTEX* **2016,** *33,* 55–67. doi:10.14573/altex.1508241
120. Bonneau, N.; Baudouin, C.; Brignole-Baudouin, F. *Regul. Toxicol. Pharmacol.* **2021,** *125,* 105021. doi:10.1016/j.yrtph.2021.105021
121. Downie, L. E.; Hom, M. M.; Berdy, G. J.; El-Harazi, S.; Verachtert, A.; Tan, J.; Liu, H.; Carlisle-Wilcox, C.; Simmons, P.; Vehige, J. *Ocul. Surf.* **2020,** *18,* 148–157. doi:10.1016/j.jtos.2019.11.004
122. Katara, R.; Sachdeva, S.; Majumdar, D. K. *Pharm. Dev. Technol.* **2018,** *23,* 240–246. doi:10.1080/10837450.2017.1337794
123. Al-Madhagy, S.; Ashmawy, N. S.; Mamdouh, A.; Eldahshan, O. A.; Farag, M. A. *Eur. J. Med. Res.* **2023,** *28,* 240. doi:10.1186/s40001-023-01203-6

BEILSTEIN JOURNAL OF NANOTECHNOLOGY

Phytol-loaded soybean oil nanoemulsion as a promising alternative against *Leishmania amazonensis*

Victória Louise Pinto Freire[1], Mariana Farias Alves-Silva[1], Johny W. de Freitas Oliveira[2], Matheus de Freitas Fernandes-Pedrosa[1], Alianda Maira Cornélio[3], Marcelo de Souza-Silva[2], Thayse Silva Medeiros[*1] and Arnóbio Antônio da Silva Junior[*1]

Full Research Paper

Open Access

Address:
[1]Laboratory of Pharmaceutical Technology and Biotechnology, Department of Pharmacy, Federal University of Rio Grande do Norte-UFRN, Natal, RN, Brazil, [2]Immunoparasitology Laboratory, Department of Clinical and Toxicological Analysis, Centre of Health Sciences, Federal University of Rio Grande do Norte-UFRN, Natal, RN, Brazil and [3]Department of Morphology, Federal University of Rio Grande do Norte-UFRN, Natal, RN, Brazil

Email:
Thayse Silva Medeiros[*] - thaysesmfarma@gmail.com;
Arnóbio Antônio da Silva Junior[*] - arnobio.silva@ufrn.br

* Corresponding author

Keywords:
cutaneous leishmaniasis; *Leishmania amazonensis*; nanoemulsion; negleted tropical disease; phytol

Beilstein J. Nanotechnol. **2025,** *16,* 1826–1836.
https://doi.org/10.3762/bjnano.16.126

Received: 26 May 2025
Accepted: 26 September 2025
Published: 21 October 2025

This article is part of the thematic issue "Advances in nanotechnology applied to natural products".

Guest Editor: D. Dourado

Abstract

Leishmaniasis, caused by protozoa of the genus *Leishmania* spp., is a neglected tropical disease that poses a significant challenge to the public health in tropical and subtropical regions, affecting mainly low-income individuals. Current therapies are limited due to severe adverse reactions to currently available drugs, high cost, low patient adherence, and even the emergence of resistant strains. Examining safer and more effective alternatives, natural compounds such as phytol – a diterpene derived from chlorophyll – have attracted attention due to their broad biological activities. To increase their solubility, stability, and cell delivery, nanotechnology-based systems, such as nanoemulsions (NEs), represent a promising approach. In this study, soybean oil nanoemulsions loaded with phytol (PHYT-NE) were developed using the phase inversion composition (PIC) method, and then characterized and evaluated. The PHYT-NE had a mean droplet diameter close to 200 nm, a polydispersity index of less than 0.2, spherical shape, and a pH value compatible with cutaneous application. The formulation showed high colloidal stability for at least 30 days of storage and at least 15 days even under stress conditions, with no signs of macroscopic instability or changes in droplet size. The cytocompatibility of NEs was confirmed in 3T3 fibroblasts at the concentrations tested, indicating potential safety for in vivo trials. Notably, PHYT-NE exhibited significant time-dependent leishmanicidal activity against *Leishmania amazonensis* promastigotes, with lower IC_{50} values (up to five times lower at 48 hours) and up to 75% parasite death after 48 hours, showing greater antiparasitic activity compared to that of free phytol. Although the use of promastigotes represents a limitation, this model was used as a proof-of-concept, with promising evidence of the potential of PHYT-NE. Future studies in macrophage models infected with intracellular amastigotes will

be essential to confirm the observed efficacy and validate the potential of PHYT-NE as a safe and effective topical therapy for cutaneous leishmaniasis.

Introduction

Leishmaniasis is one of the 20 listed neglected tropical diseases (NTDs), affecting over 350 million people globally, with an alarming 700,000 to 1 million new cases reported annually [1-3]. It is caused by protozoan parasites of the genus *Leishmania* spp., and transmitted through the bite of infected female phlebotomine sandflies. During its life cycle, the parasite exhibits two main morphological forms: the promastigote, which resides in the insect vector and represents the infective stage, and the amastigote, the intracellular form found in vertebrate hosts [4,5].

Different *Leishmania* spp. species are responsible for distinct clinical manifestations, including (i) cutaneous leishmaniasis, (ii) mucocutaneous leishmaniasis, and (iii) visceral leishmaniasis. In cutaneous leishmaniasis, the infection triggers an immune-inflammatory cascade that produces painless ulcerative lesions. Depending on the immune status of the host and the infecting species, these lesions can progress to extensive tissue damage (i.e., from the cutaneous to the mucocutaneous form [6], particularly involving the nasal septum and ears) resulting in scarring, anatomical disfigurement, and consequent social stigmatization [7-9].

Current therapeutic strategies for leishmaniasis rely on pentavalent antimonial compounds (first-line therapy), amphotericin B, miltefosine, and paromomycin. Although these drugs are effective, their use is often limited by serious adverse effects such as cardiotoxicity, nephrotoxicity, hepatotoxicity, pancreatic toxicity, and teratogenicity. Moreover, resistance to antileishmanial agents, particularly pentavalent antimonials, has been increasingly reported [10,11].

As a result, plant-derived natural compounds have been extensively investigated as alternative therapeutic agents [12]. There are currently no herbal medicines used in the treatment of cutaneous leishmaniasis. However, previous studies have reported that diterpenes exhibit promising antileishmanial activity while displaying low toxicity to host cells [13-15]. One such compound is a phytol, a highly lipophilic, acyclic monounsaturated diterpene alcohol derived from chlorophyll metabolism in plants [16], and has demonstrated promising antileishmanial potential. For example, da Silva and colleagues (2015) [17] showed that a phytol-rich fraction extracted from *Lacistema pubescens* exhibited potent activity against *Leishmania amazonensis* promastigotes and intracellular amastigotes. However, the high lipophilicity of the phytol significantly limits its pharmaceutical application by reducing bioavailability [18]. To overcome these limitations, the incorporation of phytol into nanostructured delivery systems, has been proposed to improve its solubility, stability, and intracellular delivery efficiency [19].

Nanotechnology-based drug delivery systems that encapsulate bioactive molecules have proven effective against trypanosomatids [20,21] especially *Leishmania* spp. [22,23]. Among these systems, nanoemulsions (NEs) are one of the most common types. They are colloidal dispersions of two immiscible liquids – typically oil and water – stabilized by emulsifying agents such as surfactants and co-surfactants, forming a kinetically stable system. With droplet sizes ranging from 20 to 500 nm, NEs can significantly enhance drug permeability and bioavailability [24-27].

Therefore, the present study aimed to develop a nanoemulsion containing phytol, produced via the low-energy emulsification method, as a novel potential pharmacological alternative for the treatment of cutaneous leishmaniasis.

Results

Phytol-loaded soybean-oil nanoemulsion

Blank-NE and soybean oil nanoemulsions loaded with phytol (PHYT-NE) were successfully prepared using the phase inversion composition (PIC) method (Figure 1a), and exhibited droplet diameters of approximately 140 and 210 nm, respectively. An increase in droplet size was observed upon PHYT incorporation ($p < 0.05$). The polydispersity index (PdI) of the samples was below 0.2, indicating a monodisperse distribution, as shown in the size distribution graph (Figure 1b). Moreover, the zeta potential (ZP) of both samples was around −20 mV, with no significant changes upon phytol loading.

To evaluate the shape and morphological characteristics of the nanoemulsions, transmission electron microscopy (TEM) analysis was performed. The results revealed nanodroplets with spherical and oval shapes and a homogeneous size distribution, with diameters up to 250 nm, consistent with the dynamic light scattering (DLS) data (Figure 1c,d).

Colloidal and physicochemical stability

The colloidal and physicochemical stability of the NEs was evaluated over a period of 30 days by monitoring droplet size, PdI, zeta potential, and pH values. In parallel, the samples were subjected to centrifugation at two different speeds (960 and

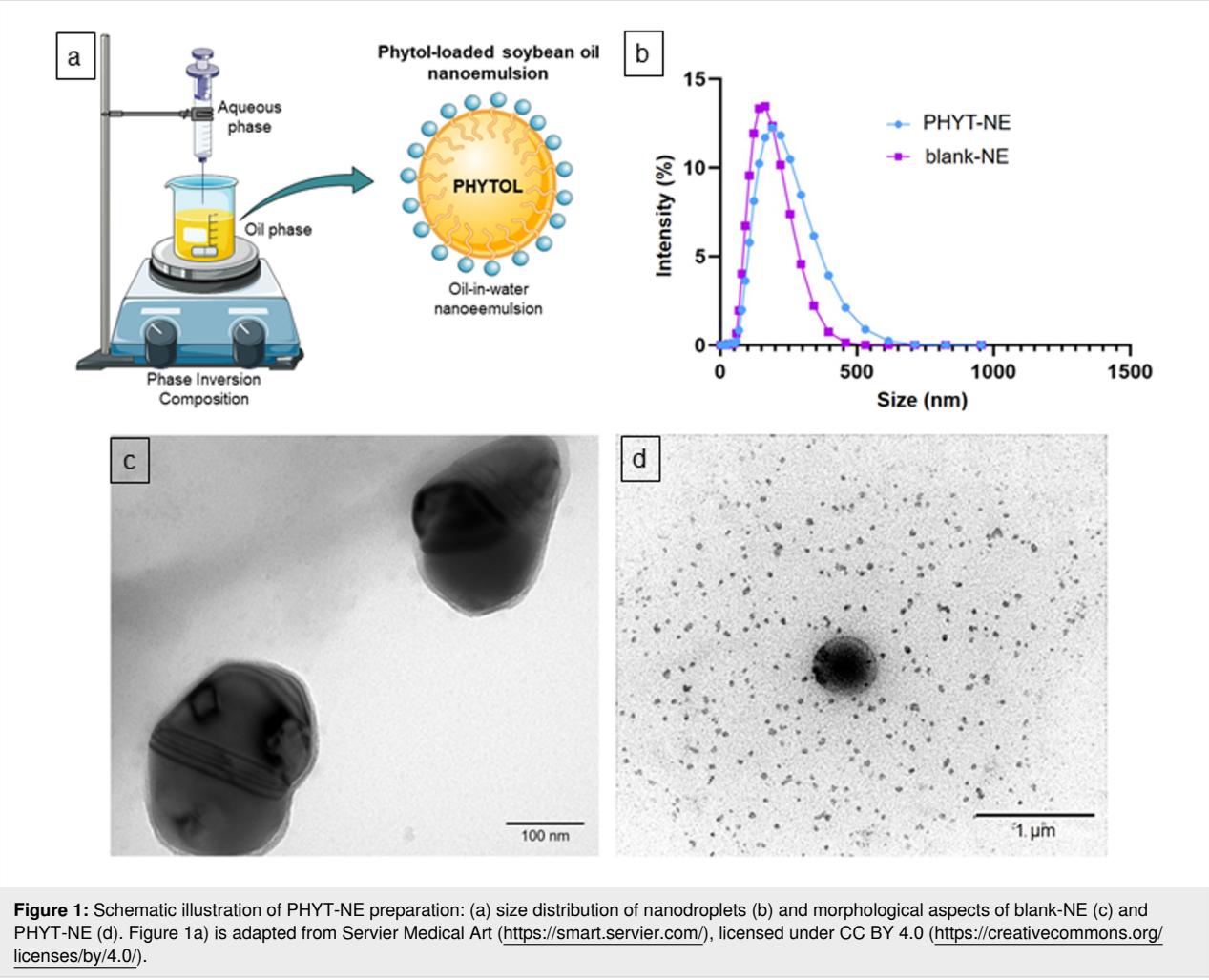

Figure 1: Schematic illustration of PHYT-NE preparation: (a) size distribution of nanodroplets (b) and morphological aspects of blank-NE (c) and PHYT-NE (d). Figure 1a) is adapted from Servier Medical Art (https://smart.servier.com/), licensed under CC BY 4.0 (https://creativecommons.org/licenses/by/4.0/).

8600*g*) to simulate stress conditions. After centrifugation, droplet size, PdI, and ZP were assessed over a period of up to 15 days.

At the end of the 30-day stability study, both blank-NE and PHYT-NE remained stable with no changes in their initial macroscopic appearance (opaque, white, milky, and with low viscosity) and remained unchanged even after centrifugation. Among the physicochemical parameters evaluated, only the zeta potential showed a significant reduction at day 30 ($p < 0.05$), while no significant changes were observed in the other parameters, as shown in Figure 2a,b. Similarly, the formulations maintained their stability under all centrifugation conditions and time points analyzed, as presented in Table 1.

3T3 fibroblast-like cell viability

Cell viability in mammalian cells was assessed using 3T3 fibroblast-like cells at 24 and 48 hours (Figure 3). Our results showed that none of the treatments induced significant cytotoxicity in this cell type at 24 hours. However, at 48 hours, cytotoxicity was observed in cells treated with free PHYT and blank-NE at a concentration of 200 µg/mL, resulting in 67% and 71% cell viability, respectively. Interestingly, PHYT-NE remained safe at all tested concentrations and time points, with cell viability above 80% even at the highest concentration.

In vitro leishmanicidal effects

The leishmanicidal effect of blank-NE, PHYT-NE, and free-PHYT was evaluated against the promastigote forms of *Leishmania amazonensis*. The PHYT-NE exhibited superior efficacy compared to that of free-PHYT at both time points at the same concentrations tested, with estimated IC_{50} values of 289.7 µg/mL at 24 hours and 127.7 µg/mL at 48 hours. In contrast, free-PHYT showed IC_{50} values of 480.5 µg/mL and 713.5 µg/mL at 24 and 48 hours, respectively (Table 2, Figure 4). After 48 hours, the PHYT-NE treatment resulted in approximately 75% of parasite death – nearly double the effect observed after 24 hours. In contrast, the free-PHYT treatment induced less than 30% of parasite death at both 24 and 48 hours (Figure 4).

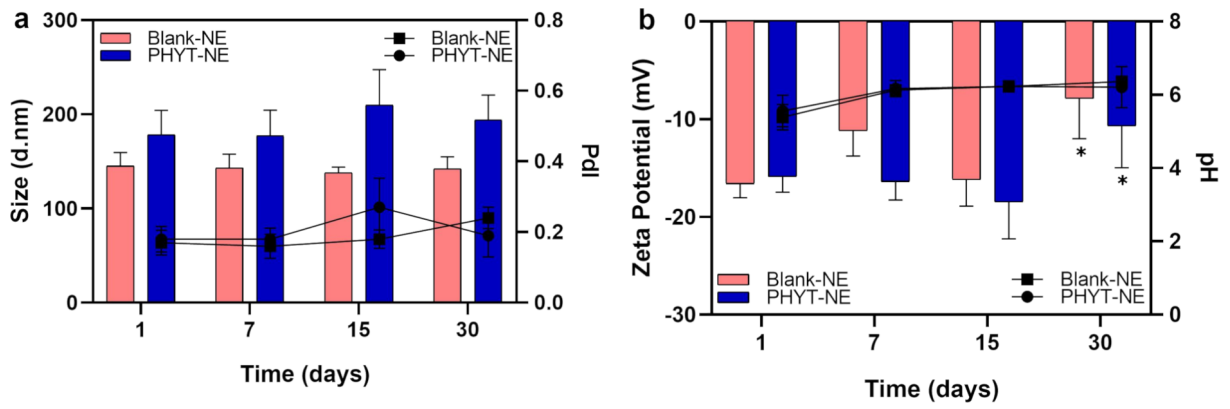

Figure 2: Colloidal and physicochemical stability of nanoemulsions regarding size, PdI (a), zeta potential and pH (b) over 30 days.

Table 1: Physicochemical properties of nanoemulsions after centrifugation stability assessment over 15 days.

Samples	Rotation (*g*)	Time (days)	Size (nm) ± SD	PdI ± SD	ZP (mV) ± SD
blank-NE	960	7	143.2 ± 3.27	0.19 ± 0.022	−18.4 ± 0.72
	8600	7	142.6 ± 3.15	0.16 ± 0.025	−18.2 ± 0.64
	960	15	145.8 ± 1.90	0.18 ± 0.019	−19.5 ± 0.58
	8600	15	144.5 ± 1.30	0.15 ± 0.010	−19.6 ± 0.61
PHYT-NE	960	7	208.5 ± 2.45	0.18 ± 0.027	−19.1 ± 0.58
	8600	7	205.2 ± 2.25	0.15 ± 0.041	−19.5 ± 0.52
	960	15	218.5 ± 1,29	0.19 ± 0,008	−24.2 ± 0.61
	8600	15	203.1 ± 1.12	0.13 ± 0.020	−21.9 ± 0.64

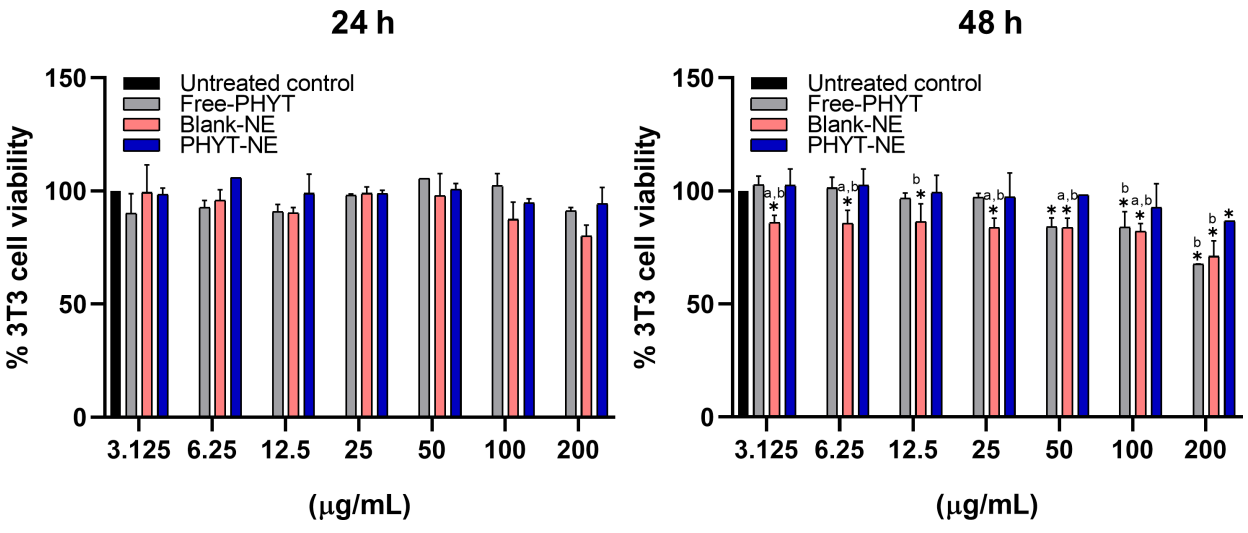

Figure 3: Effects of NEs and free-PHYT treatment on mammalian cells after exposure for 24 and 48 hours. The values represent the mean ± standard deviation of three independent experiments. * Represents significant differences at $p < 0.05$ compared to untreated control; a,b significant differences at $p < 0.05$ between treated groups.

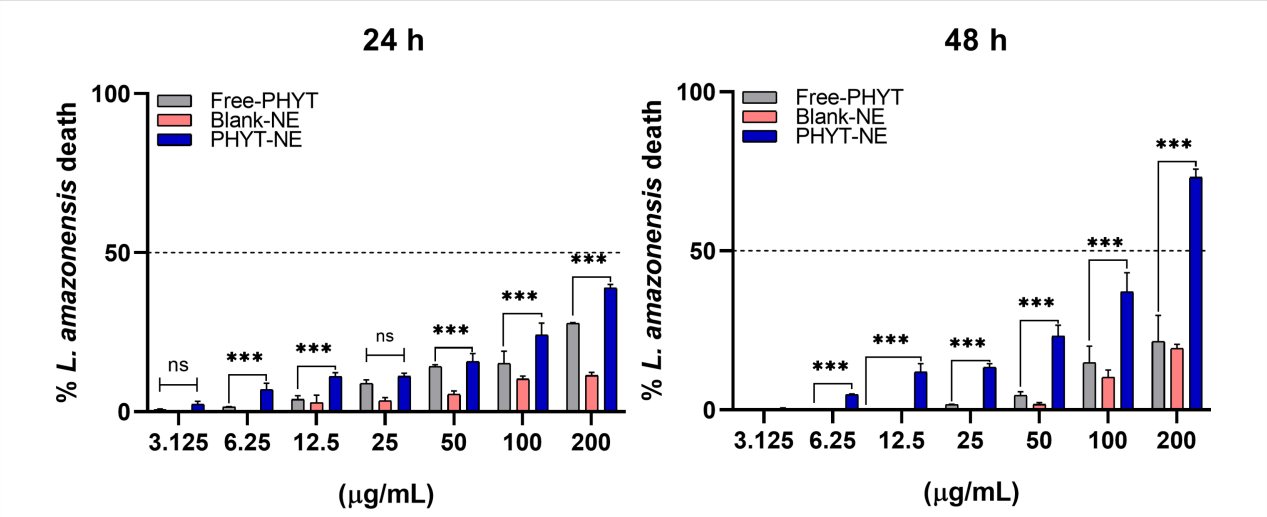

Figure 4: Effect of NEs and free-PHYT on promastigote forms of *L. amazonensis* after exposure for 24 and 48 hours. The values represent the mean ± standard deviation of three independent experiments. *** Represents significant differences at $p < 0.01$.

Table 2: IC_{50} values of free-PHYT and PHYT-NE on promastigote forms of *L. amazonensis*.

Samples	IC_{50} 24 h (μg/mL)	IC_{50} 48 h (μg/mL)
free-PHYT	480.5	713.5
PHYT-NE	289.7	127.7

Discussion

The topical administration of drugs for various diseases offers several advantages over other routes of application, especially in the treatment of cutaneous leishmaniasis [28,29]. To address a promising candidate to this, we developed a stable soybean oil-based nanoemulsion capable of encapsulating PHYT, using the phase inversion composition (PIC) nanoemulsification method. This is a low-shear technique that allows for easy scale-up and helps prevent thermal degradation of sensitive compounds, as well as excessive loss of volatile substances such as PHYT [30].

The small droplet size results in a large surface area, which enables effective interaction with biological membranes and consequently enhances drug penetration and retention [31]. Key formulation parameters – such as drug miscibility with the oil phase, droplet size, and size uniformity – have been directly correlated with permeation efficiency across the skin barrier [32,33]. Specifically, the encapsulation of lipophilic compounds like phytol in finely dispersed droplets within oil-in-water (O/W) nanoemulsions is more effective when the droplets are spherical and have diameters close to 200 nm. This enhanced effect has been attributed to increased Laplace pressure, which refers to the pressure difference between the interior and exterior of a curved interface, and leads to higher surface curvature and increased solute concentration at the droplet interface in the aqueous phase. Such structural features can promote a higher drug flux and localized delivery in the skin layers [34-36].

Chiu et al. (2024) reported a significant increase in curcumin skin permeability when carried by nanoemulsions with a mean diameter between 84.3 and 241.6 nm [37]. In this context, PHYT-NE exhibits suitable droplet size, low PdI, spherical shape, and a pH value within the physiological range of human skin, which suggests that it is a promising formulation for transdermal administration route in the treatment against cutaneous leishmaniasis. Although no permeation assay was conducted in the present study, the physicochemical profile of PHYT-NE supports its potential for efficient skin interaction and warrants further investigation in permeation studies. As a future perspective, ex vivo permeation studies using porcine ear skin or synthetic membranes in Franz diffusion cells could be employed to further evaluate the cutaneous permeation profile of the phytol-loaded nanoemulsion.

In addition to forming nanodroplets, nanoemulsions must maintain their structural and physicochemical integrity over time to ensure consistent performance. In our study, both blank-NE and PHYT-NE remained stable for at least 30 days, with no significant alterations in most evaluated parameters – except the zeta potential – even under centrifugation at different speeds. This behavior can be attributed to the kinetic stabilization achieved through the optimized composition of the surfactant pair, which likely contributed to a robust interfacial film that prevented coalescence and Ostwald ripening [38-40]. Although colloidal

stability has been demonstrated, chemical stability studies are still needed to fully confirm the long-term stability and therapeutic reliability of the formulation.

Additionally, the presence of glycerin as a co-solvent may have contributed to the reduction in interfacial tension and improved droplet uniformity, factors known to enhance long-term stability [41]. Importantly, the incorporation of poloxamer 407 increased the viscosity of the external aqueous phase, thereby reducing Brownian motion and droplet collision frequency – mechanisms that are often associated with delayed creaming and phase separation [42,43]. Taken together, these compositional strategies demonstrate the effectiveness of PHYT-NE in maintaining colloidal stability under storage and stress conditions.

For pharmaceutical applications and the intended therapeutic purpose, nanoemulsions must not only be functional but also safe and selective. That is, they should effectively damage the parasite without causing toxicity to host cells – especially intracellular amastigote forms [44].

Previous studies have shown that fibroblasts can act as alternative host cells and have been used to evaluate cytotoxic activity against *Leishmania* spp. in contexts involving epithelial cells and fibroblasts [45]. In addition, reviews on cytotoxicity in cutaneous leishmaniasis highlight the immunological interactions involving multiple cell types beyond macrophages, as well as the role of cytotoxic cells in disease progression and tissue damage, supporting the relevance of studying different cellular models, including fibroblasts [46]. Therefore, the metabolic activity of the fibroblast-like 3T3 cell line was assessed following treatment with the NEs to predict their cytocompatibility and, consequently, their safety. Similarly, promastigote forms of *Leishmania amazonensis* were subjected to the same treatments and conditions to evaluate the leishmanicidal potential of these nanoemulsions.

As PHYT-NE concentrations and exposure times increased, the leishmanicidal activity also improved. Importantly, this formulation did not induce a reduction in cell viability sufficient to indicate cytotoxicity to 3T3 cells, even at the highest concentration and longest exposure time tested. In contrast, this same outcome was not observed with free-PHYT. When both host cells and parasites were treated with free-PHYT, cytotoxicity to fibroblasts was observed at the highest concentration and time point, without a corresponding increase in efficacy against *L. amazonensis* promastigotes compared to the 24-hour exposure. Altogether, these results indicate that incorporating PHYT into the nanoemulsion enhances the selectivity of the molecule, potentiating its therapeutic effect while reducing its toxicity toward mammalian cells. This is supported by a 1.65-fold decrease in the PHYT-NE IC_{50} values at 24 hours, and approximately a 5.6-fold decrease at 48 hours when compared to free-PHYT.

A study conducted by da Silva et al. (2015) [17] demonstrated that the leishmanicidal activity of phytol is associated with induction of mitochondrial membrane depolarization, consequently leading to the generation of reactive oxygen species (ROS) and oxidative stress in promastigotes. It is noteworthy that *Leishmania*, like other trypanosomatids, possesses a single mitochondrion, which is responsible for multiple essential metabolic processes and is crucial for parasite survival; therefore, to exert its effect, the compound must be taken up and accumulate in the cytosol [47]. In the free-living promastigote form, nanoemulsions may facilitate drug access to the intracellular target by more efficiently permeating the membrane of the parasite – either due to their nanoscale size, lipid fusion with membrane components, or disruption of the plasma membrane structure [48,49].

However, several studies have also highlighted the remarkable potential of nanoemulsions against intracellular amastigote forms. In addition to enhancing cutaneous penetration, nanoemulsions also can improve the cellular uptake of various drugs and can facilitate targeted delivery to the intracellular parasites [50,51]. Since the amastigote forms of *Leishmania* spp. reside within the phagolysosomes of macrophages, the phagocytic uptake of nanodroplets significantly increases the intracellular concentration of the drug, thereby enhancing its leishmanicidal efficacy [1,52].

For instance, Mousavi and collaborators (2022) [53] reported that a nanoemulsion loaded with resveratrol effectively inhibited both promastigote and amastigote forms of *Leishmania major*, with an IC_{50} value 2.32-fold lower than that observed for free resveratrol. Similarly, a study conducted by Nahanji et al. (2024) [54] achieved comparable success using fluconazole-loaded NEs against *L. major*, demonstrating a 3-fold and 9-fold reduction in IC_{50} for the promastigote and amastigote forms, respectively, compared to that of free fluconazole. More recently, Cunha et al. (2024) [55] developed NEs containing amphotericin B and paromomycin, and upon evaluating their efficacy against *L. amazonensis* amastigotes, observed that nanoemulsification did not enhance the activity of amphotericin B. In contrast, paromomycin-loaded NEs outperformed the free drug.

All of these studies are in agreement with our results and further underscore the potential of nanoemulsions as effective carriers for antileishmanial agents. Although promastigotes were employed as a proof of concept in this study, it is reasonable to

propose that a similar efficacy may also be expected against amastigotes, given the comparable cellular biology and mitochondrial activity between the two stages. The major challenge, however, is the intracellular localization of amastigotes, which requires not only uptake of the nanoemulsion by macrophages but also subsequent internalization by the parasite. Importantly, previous studies have demonstrated that nanoemulsions are efficiently internalized by macrophages, which reinforces the potential of our formulation to also target intracellular amastigotes. Taken together, our results pave the way for further in vitro assays on amastigotes forms, in vivo validation, and clinical translation of PHYT-NE as a safe and effective topical therapy for cutaneous leishmaniasis.

Conclusion

This is the first time that a soybean oil-based nanoemulsion containing phytol with antileishmanial potential has been reported. The results of this study demonstrate that the phytol-loaded nanoemulsion, developed through a low-energy PIC method, is a stable and physicochemical suitable system for topical and transdermal administration in the future. The PHYT-NE exhibited enhanced leishmanicidal activity against *Leishmania amazonensis* promastigotes in a time- and concentration-dependent manner, while also showing reduced cytotoxicity toward mammalian cells when compared to that of free phytol.

Further studies are still required to strongly support our hypotheses, including evaluation against amastigote forms, safety in macrophages, and confirmation of skin permeation. Nevertheless, the present findings indicate that entrapment enhances selectivity and therapeutic efficacy of phytol. Therefore, PHYT-NE emerges as a promising and safe alternative for the treatment of cutaneous leishmaniasis, warranting additional evaluations to access the scalability potential and in vivo investigations to confirm its efficacy, tissue distribution, and mechanism of action.

Experimental

Material

L-α-Phosphatidylcholine (95%) (Avanti Polar lipids, United States); polaxamer 407 (Sigma-Aldrich, Brazil); glycerin (Vetec, Brazil); phytol (97%), mixture of isomers (Sigma-Aldrich, Brazil); soybean oil (Sigma-Aldrich, Brazil); Tween® 80 (Sigma-Aldrich, Brazil); purified water (obtained from a reverse osmosis purification equipment, model OS50 LX, Gehaka, Brazil) were used for nanoemulsion preparation. Mammalian cells were cultured in DMEM, High Glucose (Life Technologies, Cat. 12800-058, Bleiswijk, The Netherlands) supplemented with 10% fetal bovine serum (FBS, Life Technologies, Cat. 12657029, Bleiswijk, The Netherlands) and maintained in an atmosphere of 5% CO_2 at 37 °C. Cell viability was assessed using MTT reagent (Sigma-Aldrich, Cat. M5655, St. Louis, MO, USA), with formazan solubilization in ethanol (Sigma-Aldrich, Brazil) when required. In vitro antileishmanial activity was performed in RPMI 1640 medium (Sigma-Aldrich, Brazil) supplemented with FBS and streptomycin antibiotic 100 IU/mL, with parasite viability measured using resazurin solution (Sigma-Aldrich, Brazil).

Nanoemulsion preparation and composition

Nanoemulsions were prepared using the phase inversion composition method, a low-energy technique wherein the aqueous phase (AP) was gradually added dropwise to the oil phase (OP) under continuous magnetic stirring at 1500 rpm, using a magnetically stirrer (IKA® C-MAG HS7) at a temperature of 25 ± 2 °C. Following the complete addition of the AP, the mixtures were stirred for an additional 30 min to ensure homogeneity. The AP consisted of purified water and poloxamer 407 (POL), as a stabilizing agent, while the OP was composed of soybean oil (SO), glycerin, as a co-solvent, Tween® 80, and L-α-phosphatidylcholine (PC), as surfactants. For nanoemulsions containing phytol, 10 mg/g of the drug was added to OP. Subsequent to the nanoemulsification step, the nanoemulsions were transferred into hermetically sealed glass vials and stored at room temperature for further analysis. All samples were prepared in triplicate and data were expressed as mean ± standard deviation. The NEs composition was described in Table 3.

Physicochemical characterization

Droplet size, polydispersity index and zeta potential evaluation

The droplet size was determined by dynamic light scattering using a Zetasizer Nano ZS instrument (Malvern Instruments, UK) at 25 ± 2 °C, with a detection wavelength of 633 nm and a backscattering angle of 173°. The zeta potential was assessed via electrophoretic mobility measurements using the same equipment under identical temperature conditions. For both

Table 3: Composition of the nanoemulsion (per 10 g).

	SO (g)	Tween® 80 (g)	PC (g)	Glycerin (g)	POL 407 (g)	PHYT (g)	Water (mL)
blank-NE	0.5	0.4	0.1	1.0	1.0	–	7.0
PHYT-NE	0.5	0.4	0.1	1.0	1.0	0.1	6.9

analyses, samples were appropriately diluted at a 1:100 (v/v) ratio.

Assessment of hydrogenic potential (pH)

The pH value was determined by the potentiometric method by inserting the electrode (Digimed, mod. DM-22) directly into the samples. In this assay, the NE were used in triplicates at room temperature (24 ± 2 °C).

Colloidal and physicochemical stability

For accelerated stability analysis, 1 mL aliquots of the nanoemulsion were transferred to Eppendorf tubes and subjected to three centrifugation cycles at 960 and 8600*g* for 15 min, each using a mini centrifuge (Fisherbrand®, model Gusto, Illinois, USA), following a protocol adapted from Saberi et al. (2013) [41]. After centrifugation, samples were analyzed regarding droplet size, PdI, and ZP. All measurements were performed in triplicates at room temperature (25 ± 2 °C).

In addition, colloidal stability of non-centrifuged nanoemulsions was evaluated over a 30-day period by monitoring droplet size, PdI, ZP, and pH using the same methodologies previously described.

Morphology

The morphology of the nanoemulsion droplets was examined by transmission electron microscopy using a FEI Tecnai G2 Spirit Biotwin microscope operating at 120 kV (FEI Company, Hillsboro, OR, USA). The samples were diluted in purified water at a 1:20 (v/v) ratio, and a drop of the diluted suspension was deposited onto square-mesh copper grids and allowed to adsorb for 2 min. The grids were then air-dried at room temperature prior to imaging.

Cytocompatibility

Mammalian cell culture

The mouse embryonic fibroblast cell line 3T3 cells (ATCC® CRL-1658) were cultured in 25 cm^2 culture flasks with Dulbecco's Modified Eagle Culture Medium (DMEM, Life Technologies, Cat. 12800-058, Bleiswijk, The Netherlands), supplemented with 10% fetal bovine serum (FBS, Life Technologies, Cat. 12657029, Bleiswijk, The Netherlands), remaining in an atmosphere of 5% CO_2 at 37 °C.

Cell viability assay

The 3T3 cells maintained in culture were treated with trypsin, centrifuged at 200*g* for 5 min, resuspended in DMEM, and seeded at a concentration of 5×10^4 cells/mL in 96-well microplates and incubated for 24 h at 37 °C and atmosphere at 5% CO_2. Subsequently, the cells were deprived of serum for 24 h with serum-free DMEM. After the deprivation period, cells were treated with the test formulations diluted in DMEM containing 10% FBS to restore normal growth conditions. The nanoemulsions were filtered through a 0.45 µm Millipore filter, and drug solutions were filtered through a 0.22 µm Millipore filter. Then, cells were treated with blank nanoemulsions and PHYT in serial dilutions, considering the concentration of drugs in the formulations (200 to 3.125 µg/mL) and incubated for 24 and 48 h. These incubation times were selected to evaluate the acute response, focusing on immediate effects.

After this period, the supernatant was removed, and 100 µL of an MTT solution in DMEM (final concentration 1 mg/mL) was added to each well. The plates were incubated at 37 °C with 5% CO_2 for 4 h. After this time, the MTT solution was removed, and 100 µL of ethanol was added to each well. The plates were protected from light and agitated for 20 min. The absorbance was measured at 570 nm using an ELISA microplate reader (Biotek® Epoch), and the obtained values were applied following Equation 1. Cells grown under the same conditions and that did not receive treatment with the systems were used as negative control.

$$\%\text{cell viability} = \frac{\text{Abs}_{\text{sample}}}{\text{Abs}_{\text{control}}} \times 100, \quad (1)$$

where $\text{Abs}_{\text{sample}}$ is the absorbance of cells treated with the sample and $\text{Abs}_{\text{control}}$ is the absorbance of untreated control cells. The statistical analysis performed in the in vitro cytocompatibility assay was the two-way ANOVA, followed by Tukey's post hoc test.

In vitro antileishmanial activity

Parasite cell culture

The cultures of *Leishmania amazonensis* promastigotes were carried out in 25 cm^2 flasks containing RPMI medium (Sigma-Aldrich, Brazil) supplemented with 10% FBS and 10% streptomycin antibiotic (100 IU/mL) at 27 °C. For the tests, cultures were used after the 4th day of supplementation, obtaining parasites at the end of the log phase, that is, with the greatest possible growth potential.

Antiparasitic activity of nanoemulsions on *Leishmania amazonensis* promastigotes

To assess the antiparasitic activity, *Leishmania amazonensis* promastigotes after the 4th days of growing in RPMI medium were counted using a Neubauer chamber, diluted in RPMI medium supplemented with 10% FBS and 10% streptomycin antibiotic (100 IU/mL) at 27 °C, and adjusted to a concentration of 1×10^7 parasites/mL. Afterward, the aliquots of 200 µL were dispensed in 96-well plates in triplicates and treated with differ-

ent concentrations of free-PHYT, blank-NE, and PHYT-NE (200 to 3.125 µg/mL); moreover, amphotericin B (2.5 µg/mL) was used as the positive control (100% death). After 24 and 48 h of exposure at 26 °C, the parasite viability was determined by the resazurin reduction assay. For that, 20 µL of 3 mM resazurin solution (Sigma-Aldrich, Brazil) was added to each well and plates were incubated for 24 h. The absorbance was read at 570 and 600 nm (Epoch, BioTek). The results of antiparasitic activity were determinate by Equation 2:

$$\%\text{inhibition} = 100 - \left[\frac{\text{A570t} - (\text{A600t} \times \text{R0})}{\text{A570c} - (\text{A600c} \times \text{R0})} \times 100\right], \quad (2)$$

where A570t = absorbance of the treatment at a wavelength of 570 nm; A600t = absorbance of the treatment at a wavelength of 600 nm; A570c = absorbance of the control at a wavelength of 570 nm; A600c = absorbance of the control at a wavelength of 600 nm; R0 = correction factor of the medium interacting with resazurin, obtained using the following formula: R0 = $C_{medium}570nm/C_{medium}600nm$, with $C_{medium}570nm$ = absorbance of the medium at a wavelength of 570 nm and $C_{medium}600nm$ = absorbance of the medium at a wavelength of 600 nm.

Statistical analysis

Samples were prepared and analyzed in triplicates. Results were expressed as mean ± standard deviation. Initially, the normality test was performed, followed by Student's t test for paired analysis of two or one-way analysis of variance (ANOVA) when applicable, using the GraphPad Prism 8 software. The results were considered statistically significant for $p < 0.05$.

Supporting Information

Supporting Information File 1

Additional figure.
[https://www.beilstein-journals.org/bjnano/content/supplementary/2190-4286-16-126-S1.pdf]

Acknowledgements

The Graphical Abstract was created from elements from the Servier Medical Art collection (https://smart.servier.com/), licensed under CC BY 4.0 (https://creativecommons.org/licenses/by/4.0/).

Funding

The authors wish to thank the Brazilian National Council for Scientific and Technological Development (CNPq) for financial support (Grant: 308382/2017-0, 311209/2020-3) and Coordination for the Improvement of Higher Education Personal (CAPES) (code 01).

Author Contributions

Victória Louise Pinto Freire: investigation; methodology; writing – original draft. Mariana Farias Alves-Silva: investigation. Johny W. de Freitas Oliveira: methodology. Matheus de Freitas Fernandes-Pedrosa: investigation; methodology; resources. Alianda Maira Cornélio: visualization; writing – review & editing. Marcelo de Souza-Silva: conceptualization; formal analysis; resources; writing – review & editing. Thayse Silva Medeiros: conceptualization; investigation; methodology; supervision; writing – original draft; writing – review & editing. Arnóbio Antônio da Silva Junior: conceptualization; funding acquisition; project administration; supervision; writing – review & editing.

ORCID® iDs

Mariana Farias Alves-Silva - https://orcid.org/0000-0001-9373-3585
Johny W. de Freitas Oliveira - https://orcid.org/0000-0002-3100-0420
Matheus de Freitas Fernandes-Pedrosa - https://orcid.org/0000-0003-4221-9580
Alianda Maira Cornélio - https://orcid.org/0000-0001-5762-2538
Marcelo de Souza-Silva - https://orcid.org/0000-0002-1000-0149
Thayse Silva Medeiros - https://orcid.org/0000-0002-8069-5871
Arnóbio Antônio da Silva Junior - https://orcid.org/0000-0002-7516-1787

Data Availability Statement

All data that supports the findings of this study is available in the published article and/or the supporting information of this article.

References

1. Abpeikar, Z.; Safaei, M.; Akbar Alizadeh, A.; Goodarzi, A.; Hatam, G. *Int. J. Pharm.* **2023,** *633,* 122615. doi:10.1016/j.ijpharm.2023.122615
2. Hotez, P. J.; Aksoy, S.; Brindley, P. J.; Kamhawi, S. *PLoS Negl. Trop. Dis.* **2020,** *14,* e0008001. doi:10.1371/journal.pntd.0008001
3. WHO: Leishmaniasis. https://www.who.int/news-room/fact-sheets/detail/leishmaniasis.
4. Borghi, S. M.; Fattori, V.; Conchon-Costa, I.; Pinge-Filho, P.; Pavanelli, W. R.; Verri, W. A., Jr. *Parasitol. Res.* **2017,** *116,* 465–475. doi:10.1007/s00436-016-5340-7
5. Kammona, O.; Tsanaktsidou, E. *Int. J. Pharm.* **2021,** *605,* 120761. doi:10.1016/j.ijpharm.2021.120761
6. Symptoms, transmission, and current treatments for cutaneous leishmaniasis | DNDi. https://dndi.org/diseases/cutaneous-leishmaniasis/facts/.
7. Goonoo, N.; Laetitia Huët, M. A.; Chummun, I.; Karuri, N.; Badu, K.; Gimié, F.; Bergrath, J.; Schulze, M.; Müller, M.; Bhaw-Luximon, A. *R. Soc. Open Sci.* **2022,** *9,* 220058. doi:10.1098/rsos.220058
8. Joshi, G.; Quadir, S. S.; Yadav, K. S. *J. Controlled Release* **2021,** *339,* 51–74. doi:10.1016/j.jconrel.2021.09.020

9. Holanda, V. N.; da Silva, W. V.; do Nascimento, P. H.; Silva, S. R. B.; Cabral Filho, P. E.; de Oliveira Assis, S. P.; da Silva, C. A.; de Oliveira, R. N.; de Figueiredo, R. C. B. Q.; de Menezes Lima, V. L. *Bioorg. Chem.* **2020,** *105,* 104437. doi:10.1016/j.bioorg.2020.104437
10. Chakravarty, J.; Sundar, S. *Expert Opin. Pharmacother.* **2019,** *20,* 1251–1265. doi:10.1080/14656566.2019.1609940
11. Pradhan, S.; Schwartz, R. A.; Patil, A.; Grabbe, S.; Goldust, M. *Clin. Exp. Dermatol.* **2022,** *47,* 516–521. doi:10.1111/ced.14919
12. dos Santos, D. B.; Lemos, J. A.; Miranda, S. E. M.; Di Filippo, L. D.; Duarte, J. L.; Ferreira, L. A. M.; Barros, A. L. B.; Oliveira, A. E. M. F. M. *Pharmaceutics* **2022,** *14,* 2339. doi:10.3390/pharmaceutics14112339
13. Raimundo, V. D.; Carvalho, R. P. R.; Machado-Neves, M.; Marques-da-Silva, E. d. A. *Pharmacol. Res.* **2022,** *177,* 106117. doi:10.1016/j.phrs.2022.106117
14. Troncoso, M. E.; Germanó, M. J.; Arrieta, V. J.; García Bustos, M. F.; Cifuente, D.; Cargnelutti, D. E.; Lozano, E. S. *J. Nat. Prod.* **2023,** *86,* 797–803. doi:10.1021/acs.jnatprod.2c00976
15. Araújo, I. A. C.; De Paula, R. C.; Alves, C. L.; Faria, K. F.; de Oliveira, M. M.; Takarada, G. G. M.; Dias, E. M. F. A.; de Oliveira, A. B.; da Silva, S. M. *Exp. Parasitol.* **2022,** *242,* 108383. doi:10.1016/j.exppara.2022.108383
16. Gutbrod, K.; Romer, J.; Dörmann, P. *Prog. Lipid Res.* **2019,** *74,* 1–17. doi:10.1016/j.plipres.2019.01.002
17. da Silva, J. M.; Antinarelli, L. M. R.; Ribeiro, A.; Coimbra, E. S.; Scio, E. *Exp. Parasitol.* **2015,** *159,* 143–150. doi:10.1016/j.exppara.2015.09.009
18. Islam, M. T.; Ali, E. S.; Uddin, S. J.; Shaw, S.; Islam, M. A.; Ahmed, M. I.; Chandra Shill, M.; Karmakar, U. K.; Yarla, N. S.; Khan, I. N.; Billah, M. M.; Pieczynska, M. D.; Zengin, G.; Malainer, C.; Nicoletti, F.; Gulei, D.; Berindan-Neagoe, I.; Apostolov, A.; Banach, M.; Yeung, A. W. K.; El-Demerdash, A.; Xiao, J.; Dey, P.; Yele, S.; Jóźwik, A.; Strzałkowska, N.; Marchewka, J.; Rengasamy, K. R. R.; Horbańczuk, J.; Kamal, M. A.; Mubarak, M. S.; Mishra, S. K.; Shilpi, J. A.; Atanasov, A. G. *Food Chem. Toxicol.* **2018,** *121,* 82–94. doi:10.1016/j.fct.2018.08.032
19. García, D. J.; Fernández-Culma, M.; Upegui, Y. A.; Ríos-Vásquez, L. A.; Quiñones, W.; Ocampo-Cardona, R.; Echeverri, F.; Vélez, I. D.; Robledo, S. M. *Arch. Pharm. (Weinheim, Ger.)* **2023,** *356,* 2300108. doi:10.1002/ardp.202300108
20. Medeiros, T. S.; Bezerra de Lima, L. E.; Alves-Pereira, E. L.; Alves-Silva, M. F.; Dourado, D.; Fernandes-Pedrosa, M. d. F.; Figueiredo, R. C. B. Q. d.; da Silva-Junior, A. A. *Biomed. Pharmacother.* **2025,** *183,* 117782. doi:10.1016/j.biopha.2024.117782
21. Morilla, M. J.; Ghosal, K.; Romero, E. L. *Beilstein J. Nanotechnol.* **2024,** *15,* 333–349. doi:10.3762/bjnano.15.30
22. Verçoza, B. R. F.; Bernardo, R. R.; de Oliveira, L. A. S.; Rodrigues, J. C. F. *Beilstein J. Nanotechnol.* **2023,** *14,* 893–903. doi:10.3762/bjnano.14.73
23. Das, S.; Ghosh, S.; De, A. K.; Bera, T. *Int. J. Biol. Macromol.* **2017,** *102,* 996–1008. doi:10.1016/j.ijbiomac.2017.04.098
24. Duarte, J. L.; Di Filippo, L. D.; de Faria Mota Oliveira, A. E. M.; Sábio, R. M.; Marena, G. D.; Bauab, T. M.; Duque, C.; Corbel, V.; Chorilli, M. *Beilstein J. Nanotechnol.* **2024,** *15,* 104–114. doi:10.3762/bjnano.15.10
25. Moghassemi, S.; Dadashzadeh, A.; Azevedo, R. B.; Amorim, C. A. *J. Controlled Release* **2022,** *351,* 164–173. doi:10.1016/j.jconrel.2022.09.035
26. Pahwa, R.; Sharma, G.; Chhabra, J.; Haider, T.; Anitha, K.; Mishra, N. *J. Drug Delivery Sci. Technol.* **2024,** *101,* 106227. doi:10.1016/j.jddst.2024.106227
27. Souto, E. B.; Cano, A.; Martins-Gomes, C.; Coutinho, T. E.; Zielińska, A.; Silva, A. M. *Bioengineering* **2022,** *9,* 158. doi:10.3390/bioengineering9040158
28. Bashir, S.; Shabbir, K.; Din, F. u.; Khan, S. U.; Ali, Z.; Khan, B. A.; Kim, D. W.; Khan, G. M. *Heliyon* **2023,** *9,* e21939. doi:10.1016/j.heliyon.2023.e21939
29. Severino, P.; Santana, W.; Lisboa, E. S.; dos Santos, V. L. S.; dos Santos Lima, E. T.; Cardoso, J. C.; de Albuquerque-Junior, R. L. C.; Naveros, B. C.; Santini, A.; Souto, E. B.; Jain, S. *Microbiol. Res.* **2022,** *13,* 836–852. doi:10.3390/microbiolres13040059
30. Graván, P.; Aguilera-Garrido, A.; Marchal, J. A.; Navarro-Marchal, S. A.; Galisteo-González, F. *Adv. Colloid Interface Sci.* **2023,** *314,* 102871. doi:10.1016/j.cis.2023.102871
31. Dhorm Pimentel de Moraes, A. R.; Tavares, G. D.; Soares Rocha, F. J.; de Paula, E.; Giorgio, S. *Exp. Parasitol.* **2018,** *187,* 12–21. doi:10.1016/j.exppara.2018.03.005
32. Wilson, R. J.; Li, Y.; Yang, G.; Zhao, C.-X. *Particuology* **2022,** *64,* 85–97. doi:10.1016/j.partic.2021.05.009
33. Rai, V. K.; Mishra, N.; Yadav, K. S.; Yadav, N. P. *J. Controlled Release* **2018,** *270,* 203–225. doi:10.1016/j.jconrel.2017.11.049
34. McClements, D. J. *Soft Matter* **2012,** *8,* 1719–1729. doi:10.1039/c2sm06903b
35. de Meneses, A. C.; Sayer, C.; Puton, B. M. S.; Cansian, R. L.; Araújo, P. H. H.; de Oliveira, D. *J. Food Process Eng.* **2019,** *42,* e13209. doi:10.1111/jfpe.13209
36. Musakhanian, J.; Osborne, D. W. *AAPS PharmSciTech* **2025,** *26,* 31. doi:10.1208/s12249-024-02997-2
37. Chiu, C.-S.; Huang, P.-H.; Chan, Y.-J.; Li, P.-H.; Lu, W.-C. *J. Agric. Food Res.* **2024,** *15,* 100932. doi:10.1016/j.jafr.2023.100932
38. Ho, T. M.; Razzaghi, A.; Ramachandran, A.; Mikkonen, K. S. *Adv. Colloid Interface Sci.* **2022,** *299,* 102541. doi:10.1016/j.cis.2021.102541
39. Chen, Y.; Narayan, S.; Dutcher, C. S. *Langmuir* **2020,** *36,* 14904–14923. doi:10.1021/acs.langmuir.0c02476
40. Singh, Y.; Meher, J. G.; Raval, K.; Khan, F. A.; Chaurasia, M.; Jain, N. K.; Chourasia, M. K. *J. Controlled Release* **2017,** *252,* 28–49. doi:10.1016/j.jconrel.2017.03.008
41. Saberi, A. H.; Fang, Y.; McClements, D. J. *J. Colloid Interface Sci.* **2013,** *411,* 105–113. doi:10.1016/j.jcis.2013.08.041
42. Nooshkam, M.; Varidi, M.; Zareie, Z.; Alkobeisi, F. *Food Chem.: X* **2023,** *18,* 100725. doi:10.1016/j.fochx.2023.100725
43. Boostani, S.; Aminlari, M.; Moosavi-nasab, M.; Niakosari, M.; Mesbahi, G. *Int. J. Biol. Macromol.* **2017,** *102,* 297–307. doi:10.1016/j.ijbiomac.2017.04.019
44. Caldeira, L. R.; Fernandes, F. R.; Costa, D. F.; Frézard, F.; Afonso, L. C. C.; Ferreira, L. A. M. *Eur. J. Pharm. Sci.* **2015,** *70,* 125–131. doi:10.1016/j.ejps.2015.01.015
45. de Queiroz Filho, T. N.; Costa, B. F.; Rodrigues, A. P. D. *BMC Microbiol.* **2025,** *25,* 495. doi:10.1186/s12866-025-04098-x
46. Campos, T. M.; Costa, R.; Passos, S.; Carvalho, L. P. *Mem. Inst. Oswaldo Cruz* **2017,** *112,* 733–740. doi:10.1590/0074-02760170109
47. Pegoraro, C.; Domingo-Ortí, I.; Conejos-Sánchez, I.; Vicent, M. J. *Adv. Drug Delivery Rev.* **2024,** *207,* 115195. doi:10.1016/j.addr.2024.115195

48. Zarenezhad, E.; Agholi, M.; Ghanbariasad, A.; Ranjbar, A.; Osanloo, M. *J. Parasit. Dis.* **2021,** *45,* 441–448. doi:10.1007/s12639-020-01318-1
49. de Mattos, C. B.; Argenta, D. F.; de Lima Melchiades, G.; Cordeiro, M. N. S.; Tonini, M. L.; Moraes, M. H.; Weber, T. B.; Roman, S. S.; Nunes, R. J.; Teixeira, H. F.; Steindel, M.; Koester, L. S. *Int. J. Nanomed.* **2015,** 5529. doi:10.2147/ijn.s83929
50. Chatzidaki, M. D.; Mitsou, E. *Pharmaceutics* **2025,** *17,* 337. doi:10.3390/pharmaceutics17030337
51. Preeti; Sambhakar, S.; Malik, R.; Bhatia, S.; Al Harrasi, A.; Rani, C.; Saharan, R.; Kumar, S.; Geeta; Sehrawat, R. *Scientifica* **2023,** 1–25. doi:10.1155/2023/6640103
52. Dourado, D.; Silva Medeiros, T.; do Nascimento Alencar, É.; Matos Sales, E.; Formiga, F. R. *Beilstein J. Nanotechnol.* **2024,** *15,* 37–50. doi:10.3762/bjnano.15.4
53. Mousavi, P.; Rahimi Esboei, B.; Pourhajibagher, M.; Fakhar, M.; Shahmoradi, Z.; Hejazi, S. H.; Hassannia, H.; Nasrollahi Omran, A.; Hasanpour, H. *BMC Microbiol.* **2022,** *22,* 56. doi:10.1186/s12866-022-02455-8
54. Nahanji, M. K.; Mahboobian, M. M.; Harchegani, A. L.; Mohebali, M.; Fallah, M.; Nourian, A.; Motavallihaghi, S.; Maghsood, A. H. *Biomed. Pharmacother.* **2024,** *178,* 117109. doi:10.1016/j.biopha.2024.117109
55. Cunha, N. F. C.; de Oliveira de Siqueira, L. B.; Garcia, A. R.; Rodrigues, I. A.; dos Santos Matos, A. P.; Júnior, E. R.; de Souza Bustamante Monteiro, M. S. *Acta Trop.* **2024,** *254,* 107189. doi:10.1016/j.actatropica.2024.107189

License and Terms

BEILSTEIN JOURNAL OF NANOTECHNOLOGY

On the road to sustainability – application of metallic nanoparticles obtained by green synthesis in dentistry: a scoping review

Lorena Pinheiro Vasconcelos Silva[1], Joice Catiane Soares Martins[2], Israel Luís Carvalho Diniz[1], Júlio Abreu Miranda[3], Danilo Rodrigues de Souza[4,5], Éverton do Nascimento Alencar[6], Moan Jéfter Fernandes Costa[‡1,2] and Pedro Henrique Sette-de-Souza[*,‡1,2]

Review

Open Access

Address:
[1]Programa de Pós-Graduação em Odontologia, Universidade de Pernambuco, Av. Norte Miguel Arraes de Alencar, 80 – Zip Code: 52071-035 - Santo Amaro, Recife/PE, Brazil, [2]Programa de Pós-Graduação em Saúde e Desenvolvimento Socioambiental, Universidade de Pernambuco, R. Cap. Pedro Rodrigues, 105 – Zip Code: 55294-902 - São José, Garanhuns/PE, Brazil, [3]Graduate Program in Health Sciences, Federal University of Rio Grande do Norte, R. Gen. Gustavo Cordeiro de Farias, s/n – Zip Code: 59078-970 - Natal/RN, Brazil, [4]Programa de Pós-Graduação em Ciências dos Materiais, Universidade Federal do Oeste da Bahia, Rua da Prainha, 1326 – Zip Code: 47805-100 - Morada Nobre, Barreiras/BA, Brazil, [5]Programa de Pós-Graduação em Química Pura e Aplicada, Universidade Federal do Oeste da Bahia, Rua da Prainha, 1326 – Zip Code: 47805-100 - Morada Nobre, Barreiras/BA, Brazil and [6]Laboratory of Micro and Nanostructured Systems, College of Pharmaceutical Sciences, Food and Nutrition, Federal University of Mato Grosso do Sul, Avenida Costa e Silva, s/n – Zip Code: 79070-900 – Bairro Universitário, Campo Grande/MS, Brazil

Email:
Pedro Henrique Sette-de-Souza[*] - pedro.souza@upe.br

* Corresponding author ‡ Equal contributors

Keywords:
dentistry; green chemistry technology; metal nanoparticles; nanotechnology; sustainable development

Beilstein J. Nanotechnol. **2025,** *16,* 1851–1862.
https://doi.org/10.3762/bjnano.16.128

Received: 01 June 2025
Accepted: 24 September 2025
Published: 22 October 2025

This article is part of the thematic issue "Advances in nanotechnology applied to natural products".

Associate Editor: J. Lahann

Abstract

The growing interest in green-synthesized metallic nanoparticles reflects a global shift toward sustainable, eco-friendly technologies in biomedical innovation, particularly in dentistry. This scoping review examines the rising focus on these nanoparticles regarding their antimicrobial, regenerative, and therapeutic potential in dental applications. Among the metals studied, silver and zinc oxide nanoparticles dominate because of their broad-spectrum antimicrobial activity and enhanced biocompatibility, achieved

through phytochemically mediated synthesis. Conventional nanoparticle production often relies on toxic reagents and energy-intensive processes, posing environmental and clinical challenges. In contrast, green synthesis, using plant extracts, fungi, or bacteria, offers a sustainable alternative by leveraging natural reducing agents like polyphenols and flavonoids. These bioactive compounds not only facilitate nanoparticle formation but also improve stability and biological efficacy, making them ideal for dental applications such as caries prevention, endodontic disinfection, and periodontal regeneration. Our analysis of 98 studies reveals India as the leading contributor (78.6%), driven by its rich biodiversity and strong research infrastructure. Key plant families including Lamiaceae and Fabaceae were frequently employed due to their high phenolic content. Despite promising results, gaps remain, such as the predominance of in vitro studies (68.7%) and insufficient cytotoxicity assessments (47.8%), underscoring the need for translational research. This review highlights the transformative potential of green-synthesized nanoparticles in dentistry, merging technological advancement with ecological responsibility. Future work should prioritize clinical trials, long-term safety evaluations, and standardized protocols to fully realize their therapeutic benefits.

Introduction

Nanotechnology is an interdisciplinary field of science that involves the manipulation of materials at the nanoscale, typically ranging from 1 to 100 nm in inorganic nanomaterials, to generate structures with unique physicochemical properties [1-3]. Among the most widely studied nanomaterials are metallic nanoparticles, particularly silver (AgNPs), gold (AuNPs), and copper (CuNPs), and various metal oxide nanoparticles such as zinc oxide (ZnO-NPs), due to their high surface-to-volume ratio, chemical stability, and distinctive optical and antimicrobial properties [4-6]. These nanomaterials have been successfully applied in diverse fields, such as medicine, agriculture, cosmetics, electronics, the food industry, and, more recently, dentistry [5,6]. However, conventional chemical and physical synthesis routes often involve toxic organic solvents, high energy consumption, and hazardous reducing agents; also, they result in environmental waste, in addition to producing nanoparticles that may be toxic and poorly biocompatible [3,7].

Given the limitations of conventional synthesis methods, the green synthesis of nanoparticles has emerged as a sustainable, safe, and economically viable alternative [8,9]. This approach employs biological agents, such as plant extracts, fungi, bacteria, and algae, which contain bioactive compounds capable of acting as reducing and stabilizing agents in the formation of metallic nanoparticles [10,11]. In the case of plant extracts, several compounds, such as phenols, flavonoids, terpenoids, alkaloids, and proteins, play crucial roles in reducing metal ions and stabilizing nanoparticles, thereby eliminating the need for harsh chemical catalysts [12-14]. This technique is widely regarded as a clean technology as it significantly reduces the generation of toxic waste, occupational risks, and environmental impacts [13-15]. Furthermore, green-synthesized nanoparticles demonstrate enhanced biocompatibility, improved bioavailability, and reduced cytotoxicity, which broadens their applicability in fields such as dental biomaterials [16,17]. Owing to their high adaptability to various metals, including silver, zinc, iron, and platinum, their operational simplicity, and the ability to control nanoparticle size and morphology by selecting plant extracts and reaction conditions, green synthesis is gaining increasing prominence in health-related nanotechnology [8,10]. It is considered a promising approach that integrates technological innovation, biological safety, and environmental responsibility [8,10,16].

An interesting example are silver nanoparticles, particularly those synthesized via green methods, which have recently become the focus of significant attention [18,19]. The eco-friendly applications of AgNPs in the biomedical, pharmaceutical, cosmetic, sanitation, and electronic sectors have driven extensive research into their biosynthesis [20-22]. Silver nanoparticles exhibit unique physical and chemical properties that enhance their versatility across multiple applications [23-25]. Biosynthesized AgNPs have been assessed regarding their antimicrobial, antioxidant, and anticancer effects, as well as for their therapeutic potential in treating dermatitis and other conditions [26]. Studies have demonstrated that these nanoparticles exhibit low toxicity, effectiveness against antibiotic-resistant microorganisms, and strong colloidal stability, ensuring long-term dispersion [26,27]. Additionally, they exhibit antioxidant activity and selective cytotoxic effects on tumor cells, including oral cancer cell lines [24,28]. In dentistry, green-synthesized nanoparticles have been explored in various clinical applications. They are effective in preventing biofilm formation and growth of key oral pathogens, such as *Streptococcus mutans* and *Candida albicans*, particularly when incorporated into dental materials or applied to prosthetic and restorative surfaces [8,25,26].

Despite the potential for application in dentistry, there is a lack of reviews integrating recent advances in the green synthesis of metallic nanoparticles in this field. Therefore, this scoping review employed the “population, concept, context” (PCC) strategy to explore how these metallic nanoparticles (population) obtained through green synthesis (concept) are being applied in dentistry (context).

Review

We identified 1606 non-duplicate articles, from which 1,506 articles were excluded for not meeting the eligibility criteria. The full texts of 100 articles were assessed, with two further exclusions due to insufficient methodological data. The final sample consisted of 98 articles included for qualitative synthesis (Figure 1).

Where and when are articles from?

Of the 98 articles selected for this review, 77 (78.6%) originated from India (Figure 2). It is important to highlight that the combined number of publications from all other countries does not surpass India's contribution to this topic.

The predominance of India in the number of published articles related to the green synthesis of metallic nanoparticles in dentistry can be attributed to a combination of scientific, cultural, and socioeconomic factors. First, India possesses a rich biodiversity, with a variety of endemic medicinal plants traditionally used in Ayurvedic and Unani medicine [10]. The country's long-standing cultural familiarity with plant-based therapeutics provides a robust foundation for research into

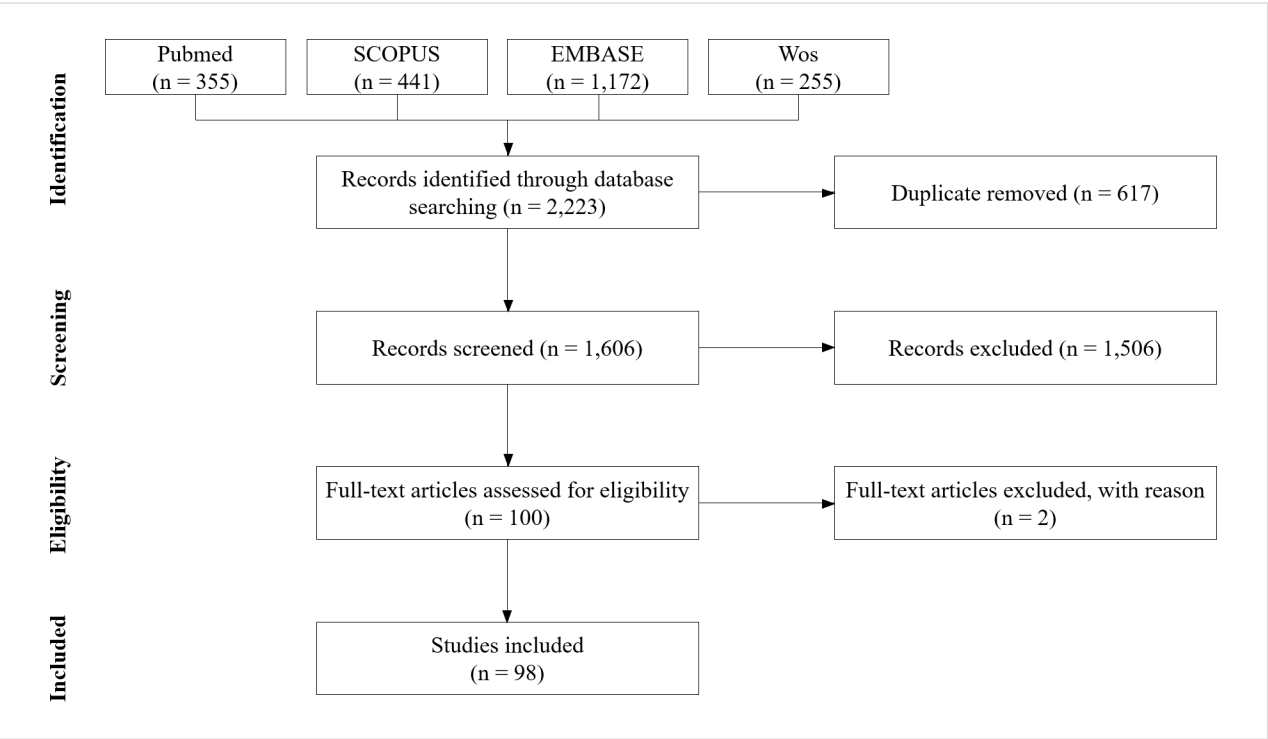

Figure 1: Flowchart summarizing the data management process to obtain the study articles.

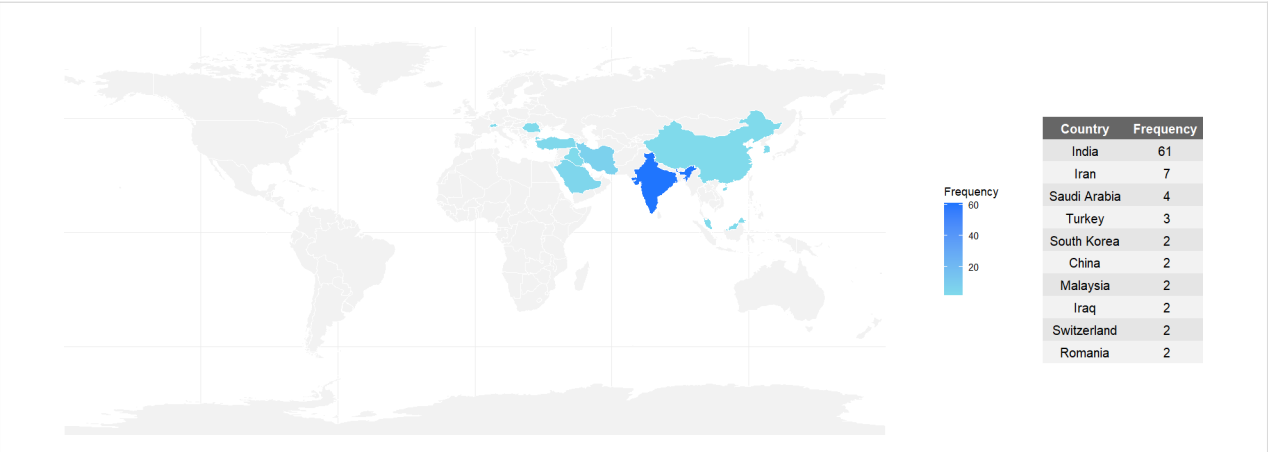

Figure 2: Number of publications about green-synthesized metallic nanoparticles by country.

botanical extracts as reducing and stabilizing agents in nanoparticle synthesis [29].

Additionally, India has significantly invested in scientific research over the past decades, particularly in nanotechnology, biotechnology, and pharmaceutical sciences. The country is home to a large number of public and private universities, research institutes, and government-funded agencies (e.g., "Council of Scientific & Industrial Research" (CSIR), "Indian Council of Medical Research" (ICMR), and "Department of Biotechnology" (DBT)), which actively promote low-cost, eco-friendly innovation, particularly in healthcare [30,31]. The economic feasibility and simplicity of green synthesis methods also align well with the resource-limited infrastructure often encountered in academic laboratories across developing nations.

India's high burden of oral and systemic infectious diseases, particularly in underserved populations, has also contributed to increased research efforts seeking affordable and sustainable alternatives to conventional antimicrobial therapies. In this context, the green synthesis of metal nanoparticles becomes a strategic research focus that addresses local public health needs while offering potential for low-cost translational applications [32]. In summary, India's leadership in this domain is the result of an interplay between cultural heritage, biodiversity, public health priorities, institutional infrastructure, and scientific dissemination practices, which together create fertile ground for prolific research on green-synthesized nanoparticles in dentistry.

It is also important to highlight that, throughout the 2020s, studies involving metallic nanoparticles obtained via green synthesis in dentistry have shown a consistent year-by-year increase (Figure 3). This increase may be primarily related to the recent pursuit of sustainable and biocompatible methods.

Plants, metals, and methods used in green synthesis

The predominance of plant families such as Lamiaceae (n = 15), Fabaceae (n = 12), Myrtaceae (n = 8), Asteraceae (n = 7), and Zingiberaceae (n = 6) among the species used in green synthesis (Figure 4) reflects their rich phytochemical profiles, particularly their high content of phenolic compounds [33]. These secondary metabolites, including flavonoids, tannins, phenolic acids, and terpenoids, act as both reducing and stabilizing agents during the biosynthesis of metallic nanoparticles [34,35].

For instance, plants from the Lamiaceae family (e.g., *Ocimum* spp., *Rosmarinus officinalis,* and *Salvia rosmarinus*) are extensively documented for their abundant polyphenols such as rosmarinic acid and caffeic acid, which facilitate the reduction of metal ions and promote the nucleation and capping of nanoparticles [36,37]. Similarly, species within the Fabaceae family (e.g., *Glycyrrhiza glabra*, *Clitoria ternatea*, and *Cassia fistula*) produce significant quantities of isoflavones and tannins that contribute to controlled nanoparticle morphology and size, which are crucial for optimizing biological activity [8,38]. The Myrtaceae family, particularly *Syzygium aromaticum*, is a well-established source of eugenol, a potent phenolic compound with

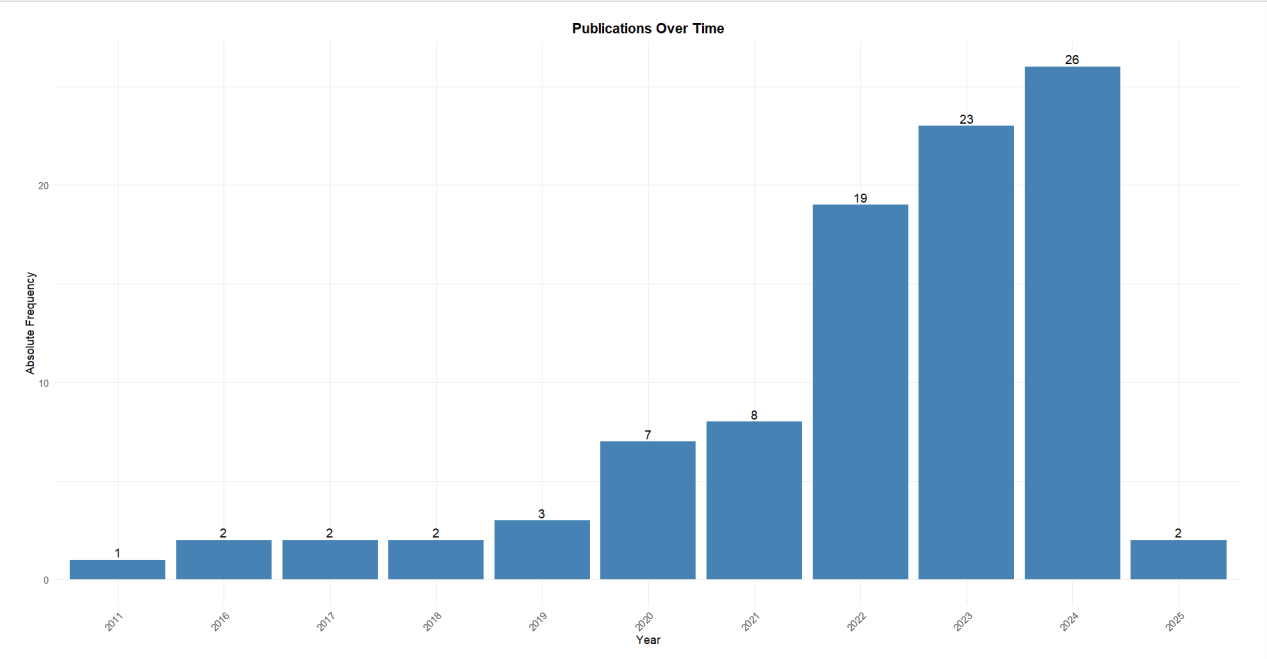

Figure 3: Publications in green-synthesized metallic nanoparticles used in the dental field over the years (2011–2025).

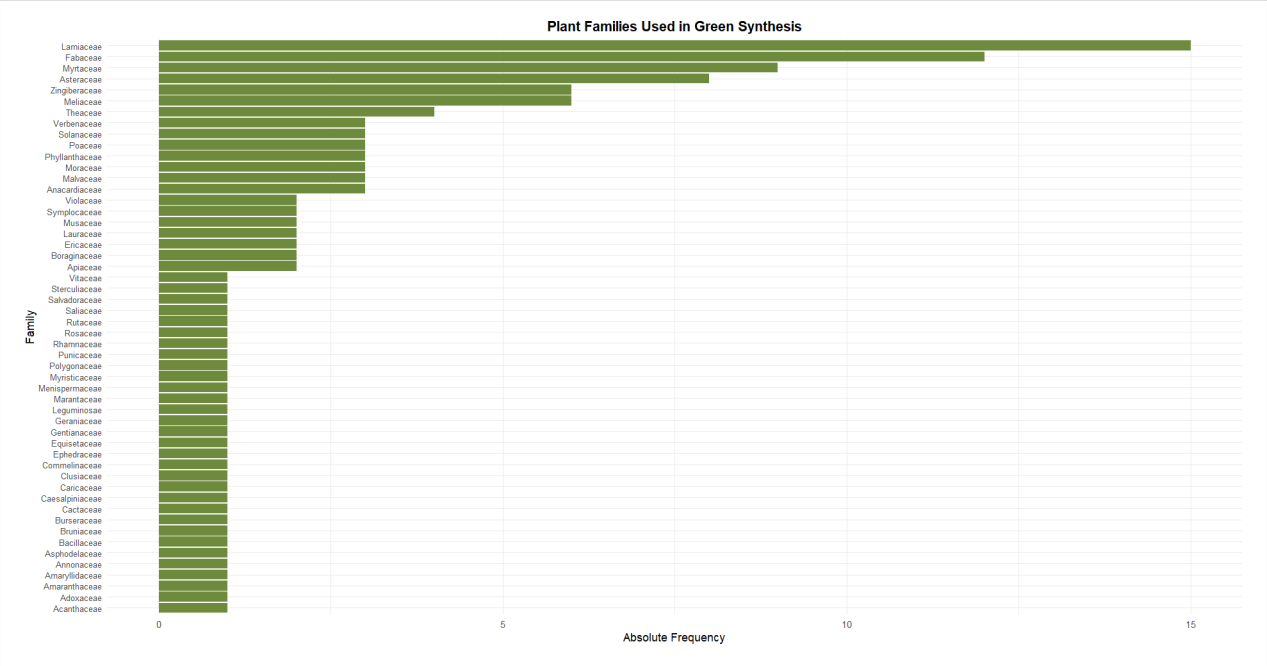

Figure 4: Botanical families used in green-synthesized metallic nanoparticles used in dentistry.

known antimicrobial and antioxidant properties, enhancing the bioactivity of synthesized nanoparticles [39,40]. The Asteraceae family includes species rich in flavonoids like quercetin and luteolin, and sesquiterpene lactones, which have been associated with both nanoparticle synthesis and broad-spectrum biological effects, such as antibiofilm and anticancer activities [36,41]. Plants from the Zingiberaceae family, especially *Zingiber officinale*, provide gingerols and shogaols, phenolic compounds known not only for their anti-inflammatory and antioxidant effects, but also for their ability to support nanoparticle synthesis under mild conditions [42].

This review identified that two botanical families, Fabaceae and Lamiaceae, stood out as recurrent sources of phytochemicals used in the green synthesis of metallic nanoparticles [9,43]. Nanoparticles derived from these families have been incorporated into dental applications such as restorative materials and endodontic medicaments. In cariology, plant-mediated AgNPs and ZnO-NPs demonstrated significant antibacterial activity against *Streptococcus mutans* biofilms [8,9,43], whereas in endodontics, their integration into irrigants and sealers improved disinfection efficiency against *Enterococcus faecalis* [44]. These findings underscore the translational potential of plant-based nanotechnology in core areas of dentistry.

The high frequency of these families in the reviewed articles indicates a strategic phytochemical selection that maximizes both synthetic feasibility and therapeutic potential. This correlation highlights the critical role of phenolic-rich botanical species in enabling the eco-friendly, scalable production of biofunctional nanoparticles suitable for applications in oral health, including antimicrobial, antibiofilm, and tissue-regenerative uses.

A consistent observation across the reviewed studies was the superior biological behavior of nanoparticles synthesized through green chemistry compared to those obtained via conventional methods. This enhanced activity is frequently attributed to the presence of plant-derived bioactive compounds, such as flavonoids, polyphenols, and terpenoids, that act as both reducing and capping agents [13]. These phytochemicals not only facilitate the formation of stable colloidal nanostructures but also contribute synergistically to their bioactivity, enhancing their interaction with microbial membranes and disrupting biofilm formation [10,24].

In this study, silver (66%) was the main metal used in nanoparticle synthesis with an eco-friendly approach (Figure 5). The wide predominance of AgNPs can be attributed to their well-documented antimicrobial, antifungal, and anti-inflammatory properties, making them especially attractive for applications in dental materials aimed at infection prevention and biofilm control [45,46].

Besides silver, zinc, copper, and nickel, other metals have been used to a lesser extent. The significant representation of ZnO-NPs, known for their biocompatibility, UV-blocking capacity, and antibacterial efficacy, aligns with their growing use in restorative and preventive dentistry, including cements, sealants,

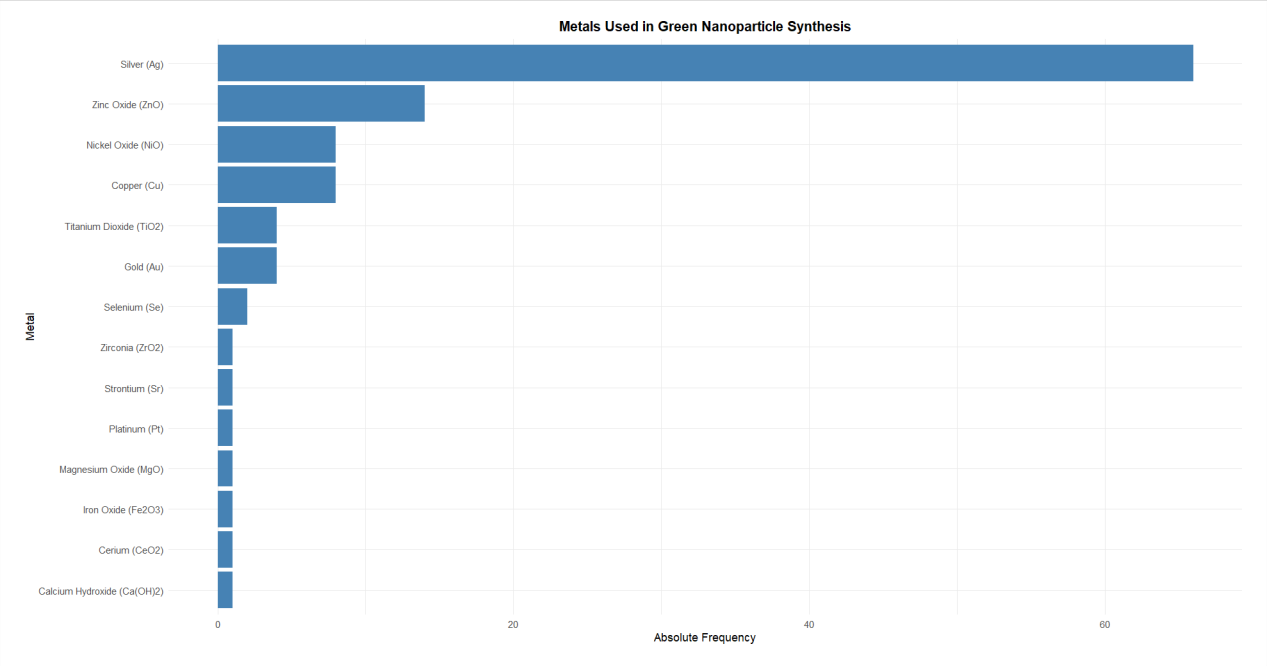

Figure 5: Metals used in nanoparticles green synthesis in the dental field.

and mouthwashes [8,45]. CuNPs and nickel oxide nanoparticles, though less frequent, are also gaining attention for their antimicrobial activity, despite some concerns regarding cytotoxicity [46,47]. The presence AuNPs and titanium dioxide nanoparticles highlights an interest in optical and photocatalytic applications, particularly in regenerative procedures and dental coatings [48,49]. The sparse use of other metals such as magnesium, iron, selenium, and cerium oxides suggests ongoing exploration of less conventional materials with niche properties, possibly linked to targeted therapeutic functions or synergistic effects when combined with more established agents [50,51]. Overall, the choice of metal reflects a balance between desired biological activity, safety profile, and the feasibility of green synthesis, all critical for clinical translation in dental practice.

We highlighted that 68.80% (n = 51) of the studies describing nanoparticle synthesis methods employed stirring. Other reported methods included heating (27.30%; n = 21) and cooling (3.90%; n = 3). Stirring is a widely used method in the green synthesis of metallic nanoparticles because it plays a crucial role in ensuring efficient nucleation, growth, and stabilization of nanoparticles. Once plant extracts are commonly used as reducing and capping agents, stirring promotes the homogeneous mixing of the metal ions and the bioactive compounds in the extract. This enhances the frequency of collisions between them and results in more uniform nucleation and better control over particle size and morphology. Moreover, continuous stirring prevents aggregation of the nanoparticles, contributing to their colloidal stability. Studies have shown that variations in stirring speed can significantly impact the yield and characteristics of the resulting nanoparticles, making it an essential parameter for optimizing reproducibility and ensuring eco-friendly synthesis processes [52,53].

Metallic nanoparticles characterization

The studies characterize the nanoparticles obtained through green synthesis in terms of both physicochemical properties and biological effects (Figure 6). The most frequently reported biological activity among the selected studies was the inhibition of microbial growth (80.0%; n = 44), highlighting its prominence as a primary target in antimicrobial research. The studies primarily evaluated antimicrobial effects against *Streptococcus mutans* (69.10%; n = 38), *Candida albicans* (50.90%; n = 28), and *Enterococcus faecalis* (32.70%; n = 18), demonstrating the broad versatility of green-synthesized metallic nanoparticles in targeting various biofilm-associated oral diseases [54,55]. The investigation of antimicrobial activity against these microorganisms indicates the potential dental applications of green-synthesized metallic nanoparticles.

To characterize the green-synthesized metallic nanoparticles, the selected studies used mainly Fourier-transform infrared spectroscopy (FTIR, 36.73%; n = 36), ultraviolet–visible spectroscopy (UV–vis, 34.69%; n = 35), and X-ray diffraction (XRD, 25.48%; n = 27). They are among the most commonly used techniques for the characterization of metallic nanoparticles synthesized via green routes due to their complementary abilities to elucidate key structural, optical, and chemical prop-

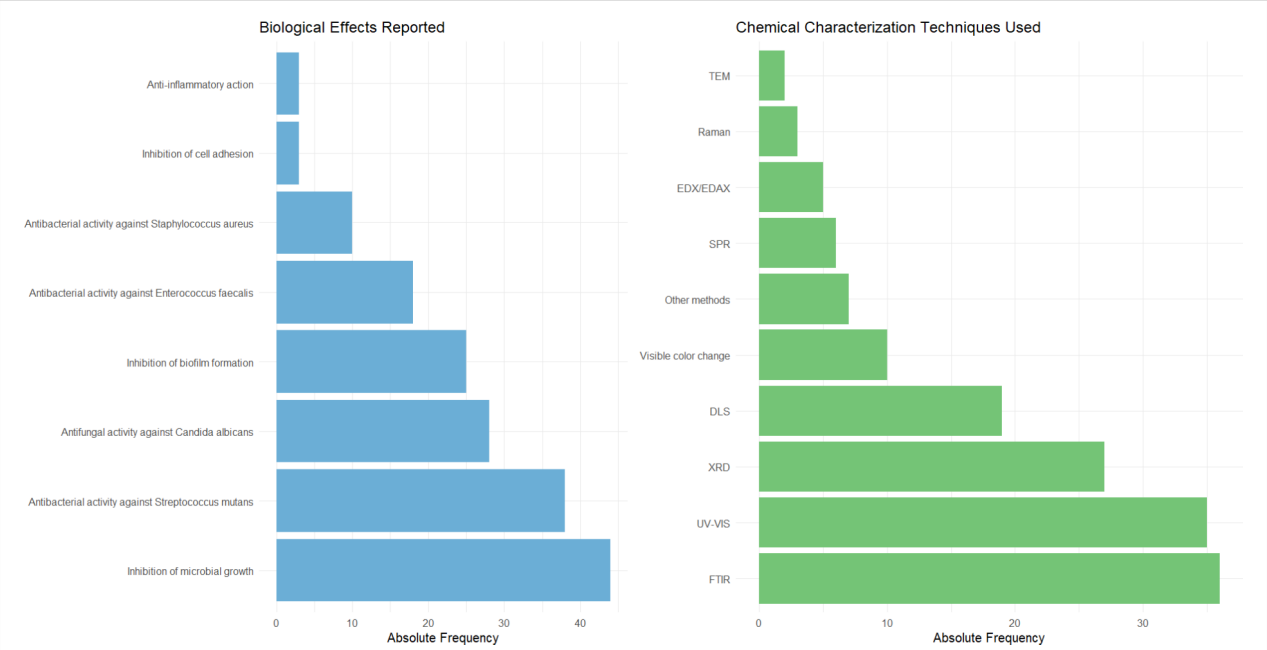

Figure 6: Biological and chemical characterization of nanoparticles used in the selected studies.

erties. FTIR enables the identification of functional groups involved in the reduction and stabilization of nanoparticles, typically derived from phytochemicals in plant extracts used as reducing agents [52,56]. UV–vis spectroscopy is widely employed to monitor nanoparticle formation in real time by detecting surface plasmon resonance bands, which provide insight into particle size and distribution [57]. XRD offers detailed information on the crystalline structure and phase composition of the nanoparticles, confirming successful synthesis and purity [53]. Together, these techniques form a robust analytical toolkit that supports the eco-friendly and scalable production of metal nanoparticles in green nanotechnology.

Limitations concerning selected studies

The analysis of study limitations revealed that the vast majority (68.7%; n = 67) of the reviewed articles conducted exclusively in vitro experiments, with no progression to in vivo experimentation in 53.7% (n = 53) of cases. Moreover, 47.8% (n = 45) lacked cytotoxicity assessments or evaluations in human cells. This gap raises important concerns regarding the long-term biocompatibility, biodistribution, and potential cytotoxicity of these nanoparticles within the complex and dynamic oral environment [15,20]. A significant number of selected studies (n = 23; 24.1%) also failed to perform advanced physicochemical characterizations, such as FTIR, SEM, or XRD, which are essential for confirming nanoparticle properties.

Only a minority of studies investigated mechanisms of action (18.9%; n = 16) or addressed the scalability and reproducibility of the synthesis process (17.6%; n = 15), which are crucial for industrial and clinical translation. Comparisons with conventional treatments or commercial products were absent in 16.2% (n = 14) of the works, while 9.5% (n = 8) did not replicate their experiments. Limitations also included restricted animal modeling (8.1%; n = 7) and absence of long-term effect assessments (8.1%; n = 7).

Altogether, these findings indicate that while green-synthesized nanoparticles hold great promise for dental applications, there is still a substantial need for methodological thoroughness, translational progression, and standardized protocols to advance their clinical implementation and proper systematic efficacy comparisons. These limitations are herein represented in the variability of plant sources, extraction methods, synthesis parameters, and nanoparticle characterization techniques.

Applications in the dental science field

Preventive and restorative dentistry represents the field that most extensively utilizes green synthesis of nanoparticles (Table 1), particularly in the development of antimicrobial compounds such as oral antiseptics and toothpastes with prolonged antimicrobial action, restorative materials (including composite resins and cements) with antibacterial properties, nanoparticle-reinforced sealants and fluoride varnishes for caries prevention, and antibiofilm coatings for dental and orthodontic surfaces.

Beyond the initial findings, nanoparticles have also been incorporated into a wide range of preventive and restorative dental

Table 1: Summary of green-synthesized nanoparticle applications in dentistry.

Dentistry area	Applications with green synthesis of nanoparticles
preventive and restorative dentistry	mouthwashes [4,12,13,15,16,20,41,44,60,61], toothpastes [15,20,44,58,59], composites [61]
endodontics	irrigants [15,61-63], filling [62], intracanal medicament [4], nonspecific [64,65]
periodontics	gels [66], systems with controlled release of nanoparticles [67], dental floss [68], nonspecific [69-71]
implantology	coating of implants with nanoparticles [72], nonspecific [59]
orthodontics	nonspecific [15,59,72], orthodontic wire [73], brackets with antimicrobial coatings [19]

materials. Composite resins and glass ionomer cements reinforced with silver or zinc oxide nanoparticles exhibit enhanced antimicrobial activity, reducing bacterial colonization at restoration margins and thereby minimizing secondary caries risk [9]. Additionally, fluoride varnishes and dental sealants containing biogenic nanoparticles demonstrate antibiofilm effects and prolonged ion release, making them promising adjuncts in caries prevention strategies, especially in high-risk populations [8].

Within the dental sciences, green-synthesized nanoparticles have demonstrated considerable potential across multiple domains. In cariology and periodontology, these nanoparticles have been effectively incorporated into toothpastes, mouthwashes, and composite resins to inhibit or reduce microbial colonization by key oral pathogens such as *Streptococcus mutans*, *Lactobacillus* spp., and *Candida albicans* [27,28]. Their antimicrobial efficacy contributes to disrupting biofilm formation and controlling infection processes fundamental to dental caries and periodontal disease progression.

In periodontal therapy, green-synthesized nanoparticles have been formulated into bioadhesive gels, local delivery systems, and coated dental flosses to sustain antimicrobial release in periodontal pockets [18]. Such approaches improve the control of periodontopathogens such as *Porphyromonas gingivalis* and *Aggregatibacter actinomycetemcomitans*, reducing inflammation and supporting adjunctive treatment to scaling and root planing. Regenerative strategies are also being developed, in which nanoparticle-functionalized membranes have shown potential to modulate host immune response and stimulate periodontal tissue repair [72].

In the field of endodontics, biosynthesized AgNPs and ZnO-NPs have been employed as adjuvants to conventional irrigants and intracanal dressings, thereby enhancing the disinfection efficacy of root canal systems [21]. The nanoscale properties of these particles facilitate deeper penetration into complex canal anatomies and improve antimicrobial action against resistant endodontic pathogens, which is critical for preventing reinfection and ensuring treatment success.

The incorporation of biogenic nanoparticles into irrigating solutions, intracanal medicaments, and filling materials enhances their penetration and antibacterial action against resistant microorganisms, including *Enterococcus faecalis* [8,43,44]. Green-synthesized AgNPs and ZnO-NPs are particularly relevant due to their ability to disrupt biofilm architecture within dentinal tubules [8,43]. Moreover, their use in nanoparticle-coated guttapercha cones has been proposed to improve long-term disinfection and reduce reinfection risks [44].

Furthermore, within dental tissue engineering, recent studies have reported promising outcomes using biogenic nanoparticles incorporated into scaffolds and regenerative membranes designed to stimulate osteogenesis and promote periodontal tissue regeneration [16,17]. These nanoparticles not only provide antimicrobial protection but also actively modulate cellular behavior, such as proliferation and differentiation, thereby enhancing the regenerative potential of biomaterials applied in clinical settings.

Implantology is another emerging area of application, where nanoparticle-based coatings are used to reduce peri-implant biofilm formation and enhance osseointegration [9,19]. Titanium implants functionalized with green-synthesized AgNPs or iron oxide nanoparticles doped with silver (Ag-Fe_2O_3) exhibited dual properties, that is, antimicrobial protection and stimulation of osteoblastic activity. In prosthodontics, biogenic nanoparticles have been incorporated into denture base resins and soft liners, demonstrating significant antifungal activity against *Candida albicans*, which is crucial for denture stomatitis management [18,59].

In orthodontics, nanoparticles have been applied as antimicrobial coatings on brackets and archwires to mitigate plaque accu-

mulation and white spot lesions during treatment. Additionally, mouth rinses and gels containing biogenic AgNPs are being investigated as adjunctive therapies to improve oral hygiene in patients with fixed orthodontic appliances [8,37,44]. These strategies aim to balance microbial control while preserving the mechanical performance of orthodontic devices.

Green-synthesized nanoparticles also hold promise in regenerative dentistry. Incorporated into scaffolds, membranes, and hydrogels, they have demonstrated the ability to enhance osteogenesis and angiogenesis while simultaneously reducing microbial contamination [19]. These multifunctional biomaterials not only support bone and periodontal regeneration but also represent sustainable alternatives for next-generation regenerative therapies [8].

Conclusion

In conclusion, this review emphasizes the growing significance of green nanotechnology in dentistry while underscoring the imperative for interdisciplinary collaboration and stringent regulatory oversight. The prominent use of silver and zinc oxide nanoparticles, produced through environmentally sustainable phytochemical-mediated synthesis, underscores a convergence of advanced antimicrobial functionality, enhanced biocompatibility, and alignment with global sustainability goals. These findings affirm that green nanotechnology represents a paradigm shift in dental material innovation, offering promising avenues to enhance oral health outcomes while integrating ecological responsibility. Future research must prioritize translational approaches, including comprehensive clinical trials and toxicological assessments, to validate the safety and efficacy of these innovative materials and facilitate their responsible integration into routine dental practice, as green-synthesized nanoparticles are pioneering agents on the verge of redefining the future of dental therapeutics and biomaterials.

Review Guidelines

Review protocol and objective

This scoping review followed the PRISMA guidelines for systematic reviews and was registered in “Open Science Framework” (https://osf.io/n3htg/). The main objective was to identify and analyze studies on the application of metallic nanoparticles synthesized via green chemistry in dentistry.

Search strategy and information sources

This review was guided by the PCC framework, that is, population (P): metallic nanoparticles (e.g., silver, gold, copper, zinc oxide); concept (C): green synthesis using plant-based extracts or eco-friendly biosynthetic routes; context (C): dental applications (e.g., oral microbiology, materials science, cariology, periodontology, endodontics). Thus, we used a combination of Boolean expressions that correspond to the PCC (Table 2).

Eligibility criteria

Inclusion criteria were original research articles evaluating the use of green-synthesized metallic nanoparticles in dental contexts, articles published in English, studies with experimental or in vitro/in vivo design, full publication until May 2025, and peer-reviewed publications. Exclusion criteria included reviews, editorials, letters to the editor, conference abstracts, and studies not focused on dentistry.

Study selection and data management

A total of 2,223 articles were retrieved (PubMed = 355; Scopus = 441; Embase = 1,172; Web of Science = 255). After removal of 617 duplicates using Rayyan QCRI (RRID:SCR_017584), 1,606 studies were screened based on titles and abstracts by two independent reviewers.

Data extraction

Data were extracted regarding authorship, publication year, country, type of metal used, part of the plant, synthesis method, nanoparticle characterization techniques, biological evaluations, and application within dentistry.

Acknowledgements

To improve the clarity and fluency of the English writing, we used the assistance of ChatGPT-4.1, a large language model developed by OpenAI. As non-native English speakers, this tool supported us in refining the textual coherence of the manuscript. Nonetheless, all content was critically reviewed and validated

Table 2: Boolean expression used in this scoping review.

Category	Keywords / Terms
population	metal OR metallic OR ZnO OR Gold OR Silver OR Copper OR Cobalt OR Niquel AND nanoparticle
concept	"biosynthesis" OR "green synthesis" OR ecofriendly OR "eco-friendly" OR "plant extracts" OR "herbal extracts" OR "phytochemicals"
context	dentistry OR mouth OR oral OR teeth OR tooth OR tongue OR odontology OR 'oral science'

by the authors to ensure scientific accuracy, originality, and integrity.

Author Contributions

Lorena Pinheiro Vasconcelos Silva: data curation; formal analysis; investigation; writing – original draft. Joice Catiane Soares Martins: data curation; formal analysis; investigation; writing – original draft. Israel Luís Carvalho Diniz: data curation; formal analysis; investigation; writing – original draft. Júlio Abreu Miranda: data curation; formal analysis; investigation; writing – original draft. Danilo Rodrigues de Souza: conceptualization; formal analysis; methodology; writing – review & editing. Éverton do Nascimento Alencar: conceptualization; formal analysis; methodology; writing – review & editing. Moan Jéfter Fernandes Costa: conceptualization; formal analysis; investigation; methodology; writing – review & editing. Pedro Henrique Sette-de-Souza: conceptualization; data curation; methodology; project administration; supervision; visualization; writing – review & editing.

ORCID® iDs

Lorena Pinheiro Vasconcelos Silva - https://orcid.org/0009-0007-6948-2211
Israel Luís Carvalho Diniz - https://orcid.org/0000-0003-1678-6960
Júlio Abreu Miranda - https://orcid.org/0000-0003-0783-7447
Danilo Rodrigues de Souza - https://orcid.org/0000-0001-5346-7972
Éverton do Nascimento Alencar - https://orcid.org/0000-0002-6148-6804
Moan Jéfter Fernandes Costa - https://orcid.org/0000-0002-7250-5863
Pedro Henrique Sette-de-Souza - https://orcid.org/0000-0001-9119-8435

Data Availability Statement

Data sharing is not applicable as no new data was generated or analyzed in this study.

References

1. Sanfelice, R. C.; Pavinatto, A.; Corrêa, D. S. Introdução à Nanotecnologia. ***Nanotecnologia aplicada a polímeros****;* Blucher: São Paulo, Brazil, 2022; pp 27–48. doi:10.5151/9786555502527-01
2. Bayda, S.; Adeel, M.; Tuccinardi, T.; Cordani, M.; Rizzolio, F. *Molecules* **2019,** *25,* 112. doi:10.3390/molecules25010112
3. García-Quintero, A.; Palencia, M. *Sci. Total Environ.* **2021,** *793,* 148524. doi:10.1016/j.scitotenv.2021.148524
4. Nnaji, N.; Nwaji, N.; Mack, J.; Nyokong, T. *J. Mol. Struct.* **2021,** *1236,* 130279. doi:10.1016/j.molstruc.2021.130279
5. Contaldo, M.; Di Stasio, D.; Romano, A.; Fiori, F.; Della Vella, F.; Rupe, C.; Lajolo, C.; Petruzzi, M.; Serpico, R.; Lucchese, A. *Curr. Drug Delivery* **2023,** *20,* 441–456. doi:10.2174/1567201819666220418104042
6. Yang, R.; Wang, M.; Ma, X.; Gao, Q. *Comb. Chem. High Throughput Screening* **2023,** *26,* 2030–2038. doi:10.2174/1386207326666221116101621
7. Iravani, S. *Green Chem.* **2011,** *13,* 2638–2650. doi:10.1039/c1gc15386b
8. Bozer, B. D.; Dede, A.; Güven, K. *Indian J. Microbiol.* **2024,** *64,* 1903–1911. doi:10.1007/s12088-024-01276-9
9. Varghese, R. M.; S, A. K.; Shanmugam, R. *Cureus* **2024,** *16,* e54994. doi:10.7759/cureus.54994
10. Yazdanian, M.; Rostamzadeh, P.; Rahbar, M.; Alam, M.; Abbasi, K.; Tahmasebi, E.; Tebyaniyan, H.; Ranjbar, R.; Seifalian, A.; Yazdanian, A. *Bioinorg. Chem. Appl.* **2022,** 2311910. doi:10.1155/2022/2311910
11. Tanwar, S. N.; Parauha, Y. R.; There, Y.; Swart, H. C.; Dhoble, S. J. *ChemBioEng Rev.* **2024,** *11,* e202400012. doi:10.1002/cben.202400012
12. Gaikwad, S.; Torane, R.; Parthibavarman, M. *Nanotechnol. Russ.* **2020,** *15,* 760–769. doi:10.1134/s199507802006021x
13. Dikshit, P. K.; Kumar, J.; Das, A.; Sadhu, S.; Sharma, S.; Singh, S.; Gupta, P. K.; Kim, B. S. *Catalysts* **2021,** *11,* 902. doi:10.3390/catal11080902
14. Latif, M. S.; Abbas, S.; Kormin, F.; Mustafa, M. K. *Asian J. Pharm. Clin. Res.* **2019,** 75–84. doi:10.22159/ajpcr.2019.v12i7.33211
15. Salman, B. N.; Gheidari, M. M.; Zeighami, H.; Nejad, A. Y.; Mohammadi, A.; Shabestari, S. B. *Med. J. Islam. Repub. Iran* **2022,** *36,* 1174–1181. doi:10.47176/mjiri.36.154
16. Manna, I.; Das, D.; Mondal, S.; Bandyopadhyay, M. Use of Nanoparticles in the Delivery of Plant-Based Therapeutics. In *Advances in Phytonanotechnology for Treatment of Various Diseases;* Kesharwani, P.; Gajbhiye, V., Eds.; CRC Press: Boca Raton, FL, USA, 2023; pp 67–126. doi:10.1201/9781003231721-3
17. Rohaľová, S.; Wolaschka, T.; Balážová, Ľ.; Paulovičová, K.; Tóthová, J.; Pavloková, S.; Stahorský, M.; Gajdziok, J. *Eur. J. Pharm. Sci.* **2024,** *193,* 106683. doi:10.1016/j.ejps.2023.106683
18. Klein, W.; Ismail, E.; Maboza, E.; Hussein, A. A.; Adam, R. Z. *J. Funct. Biomater.* **2023,** *14,* 379. doi:10.3390/jfb14070379
19. Anand, B. G.; Shejale, K. P.; Rajesh Kumar, R.; Thangam, R.; Prajapati, K. P.; Kar, K.; Mala, R. *Biomater. Adv.* **2023,** *148,* 213346. doi:10.1016/j.bioadv.2023.213346
20. Al-Dahmash, N. D.; Al-Ansari, M. M.; Al-Otibi, F. O.; Singh, A. J. A. R. *J. Drug Delivery Sci. Technol.* **2021,** *61,* 102337. doi:10.1016/j.jddst.2021.102337
21. Chandraker, S. K.; Kumar, R. *Biotechnol. Genet. Eng. Rev.* **2024,** *40,* 3113–3147. doi:10.1080/02648725.2022.2106084
22. Kaushik, A.; Singh, R. K.; Tyagi, P. K. *Precis. Nanomed.* **2023,** *6,* 1109–1131. doi:10.33218/001c.89165
23. Alsubki, R.; Tabassum, H.; Abudawood, M.; Rabaan, A. A.; Alsobaie, S. F.; Ansar, S. *Saudi J. Biol. Sci.* **2021,** *28,* 2102–2108. doi:10.1016/j.sjbs.2020.12.055
24. Alhadrami, H. A.; Alkhatabi, H.; Abduljabbar, F. H.; Abdelmohsen, U. R.; Sayed, A. M. *Pharmaceutics* **2021,** *13,* 1846. doi:10.3390/pharmaceutics13111846
25. Naganthran, A.; Verasoundarapandian, G.; Khalid, F. E.; Masarudin, M. J.; Zulkharnain, A.; Nawawi, N. M.; Karim, M.; Che Abdullah, C. A.; Ahmad, S. A. *Materials* **2022,** *15,* 427. doi:10.3390/ma15020427
26. Thiyagarajan, S.; Kanchana, S. *Braz. J. Pharm. Sci.* **2022,** *58,* e19898. doi:10.1590/s2175-97902022219898
27. Klein, W.; Ismail, E.; Maboza, E.; Hussein, A. A.; Adam, R. Z. *J. Funct. Biomater.* **2023,** *14,* 379. doi:10.3390/jfb14070379

28. Kandwal, A.; Parveen, S.; Bachheti, R. K.; Bachheti, A.; Khajuria, A. K. Green Synthesis of Silver and Silver Oxide Nanoparticles From Plants and Their Characterization. In *Metal and Metal-Oxide Based Nanomaterials;* Bachheti, R. K.; Bachheti, A.; Husen, A., Eds.; Springer: Singapore, 2024; pp 1–24. doi:10.1007/978-981-99-7673-7_1
29. Villagrán, Z.; Anaya-Esparza, L. M.; Velázquez-Carriles, C. A.; Silva-Jara, J. M.; Ruvalcaba-Gómez, J. M.; Aurora-Vigo, E. F.; Rodríguez-Lafitte, E.; Rodríguez-Barajas, N.; Balderas-León, I.; Martínez-Esquivias, F. *Resources* **2024,** *13,* 70. doi:10.3390/resources13060070
30. Bhatia, P.; Vasaikar, S.; Wali, A. *Nanotechnol. Rev.* **2018,** *7,* 131–148. doi:10.1515/ntrev-2017-0196
31. Department of Biotechnology (DBT), Ministry of Science & Technology, Government of India. Annual Report 2024–25. https://dbtindia.gov.in/sites/default/files/DBT%20Annual%20Report%202024-25.pdf.
32. Ashwini, D.; Mahalingam, G. *Res. J. Pharm. Technol.* **2020,** *13,* 468–474. doi:10.5958/0974-360x.2020.00091.8
33. Ahmed, S.; Ahmad, M.; Swami, B. L.; Ikram, S. *J. Adv. Res.* **2016,** *7,* 17–28. doi:10.1016/j.jare.2015.02.007
34. Khalil, A. T.; Ovais, M.; Ullah, I.; Ali, M.; Shinwari, Z. K.; Khamlich, S.; Maaza, M. *Nanomedicine (London, U. K.)* **2017,** *12,* 1767–1789. doi:10.2217/nnm-2017-0124
35. Singh, P.; Kim, Y.-J.; Zhang, D.; Yang, D.-C. *Trends Biotechnol.* **2016,** *34,* 588–599. doi:10.1016/j.tibtech.2016.02.006
36. Abdelsattar, A. S.; Hakim, T. A.; Rezk, N.; Farouk, W. M.; Hassan, Y. Y.; Gouda, S. M.; El-Shibiny, A. *J. Inorg. Organomet. Polym. Mater.* **2022,** *32,* 1951–1965. doi:10.1007/s10904-022-02234-y
37. Harsha, L.; Jain, R. K.; Prasad, A. S. *J. Adv. Pharm. Technol. Res.* **2022,** *13* (Suppl. 1), S272–S276. doi:10.4103/japtr.japtr_181_22
38. Barma, M. D.; Doraikanan, S. *Int. J. Health Sci.* **2022,** *6,* 2529–2538. doi:10.53730/ijhs.v6ns1.5316
39. Devanesan, S.; AlSalhi, M. S. *Int. J. Nanomed.* **2021,** *16,* 3343–3356. doi:10.2147/ijn.s307676
40. Mohapatra, S.; Leelavathi, L.; Meignana, A. I.; Arumugham, I.; Pradeep, K. R.; Rajeshkumar, S. *J. Evol. Med. Dent. Sci.* **2020,** *9,* 2034–2039. doi:10.14260/jemds/2020/445
41. Kumar, P. V.; Jelastin Kala, S. M.; Prakash, K. S. *J. Environ. Chem. Eng.* **2019,** *7,* 103146. doi:10.1016/j.jece.2019.103146
42. Hussain, Z.; Jahangeer, M.; Rahman, S. u.; Ihsan, T.; Sarwar, A.; Ullah, N.; Aziz, T.; Alharbi, M.; Alshammari, A.; Alasmari, A. F. *Pol. J. Chem. Technol.* **2023,** *25* (3), 23–30. doi:10.2478/pjct-2023-0021
43. Cinthura, C.; Rajasekar, A. *Plant Cell Biotechnol. Mol. Biol.* **2020,** *21,* 11–17.
44. Mehrabkhani, M.; Movahhed, T.; Bagheri, H.; Tajzadeh, P.; Hamedi, S. S.; Goli, M.; Dehghanitafti, S. *J. Dent. Mater. Tech.* **2024,** *13,* 121–126. doi:10.22038/jdmt.2024.79223.1623
45. Blessy, S.; Priyadharshini, R.; Rajeshkumar, S.; Sinduja, P. In Vitro Anticariogenic Effects of a Mouthwash Containing Zinc Oxide Nanoparticles Infused with Chamomile and Ginger. In *Case Studies on Holistic Medical Interventions;* Oruganti, S. K.; Karras, D.; Thakur, S. S.; Nagpal, K.; Gupta, S. K., Eds.; CRC Press: London, UK, 2025; pp 467–471. doi:10.1201/9781003596684-84
46. Radulescu, D.-M.; Surdu, V.-A.; Ficai, A.; Ficai, D.; Grumezescu, A.-M.; Andronescu, E. *Int. J. Mol. Sci.* **2023,** *24,* 15397. doi:10.3390/ijms242015397
47. Sadeghi, B.; Gholamhoseinpoor, F. *Spectrochim. Acta, Part A* **2015,** *134,* 310–315. doi:10.1016/j.saa.2014.06.046
48. Rónavári, A.; Igaz, N.; Adamecz, D. I.; Szerencsés, B.; Molnar, C.; Kónya, Z.; Pfeiffer, I.; Kiricsi, M. *Molecules* **2021,** *26,* 844. doi:10.3390/molecules26040844
49. Sirelkhatim, A.; Mahmud, S.; Seeni, A.; Kaus, N. H. M.; Ann, L. C.; Bakhori, S. K. M.; Hasan, H.; Mohamad, D. *Nano-Micro Lett.* **2015,** *7,* 219–242. doi:10.1007/s40820-015-0040-x
50. Nadeem, M.; Abbasi, B. H.; Younas, M.; Ahmad, W.; Khan, T. *Green Chem. Lett. Rev.* **2017,** *10,* 216–227. doi:10.1080/17518253.2017.1349192
51. Durán, N.; Silveira, C. P.; Durán, M.; Martinez, D. S. T. *J. Nanobiotechnol.* **2015,** *13,* 55. doi:10.1186/s12951-015-0114-4
52. Soundarajan, S.; Rajasekar, A. *Dent. Med. Probl.* **2023,** *60,* 445–451. doi:10.17219/dmp/150728
53. Ahmed, S.; Saifullah; Ahmad, M.; Swami, B. L.; Ikram, S. *J. Radiat. Res. Appl. Sci.* **2016,** *9,* 1–7. doi:10.1016/j.jrras.2015.06.006
54. Sette-de-Souza, P. H.; Amorim, R. d. S.; Cartaxo, R. d. O.; Silvério, S. I. C.; Amorim de Lima, L. R.; Costa, M. J. F. *Odovtos – Int. J. Dent. Sci.* **2025,** *27,* 48–58. doi:10.15517/ijds.2025.65258
55. Sette-De-Souza, P. H.; De Santana, C. P.; Sousa, I. M. O.; Foglio, M. A.; De Medeiros, F. D.; De Medeiros, A. C. D. *An. Acad. Bras. Cienc.* **2020,** *92,* e20200408. doi:10.1590/0001-3765202020200408
56. Ibrahim, H. M. M. *J. Radiat. Res. Appl. Sci.* **2015,** *8,* 265–275. doi:10.1016/j.jrras.2015.01.007
57. Sharma, D.; Kanchi, S.; Bisetty, K. *Arabian J. Chem.* **2019,** *12,* 3576–3600. doi:10.1016/j.arabjc.2015.11.002
58. Ghabban, H.; Alnomasy, S. F.; Almohammed, H.; Al Idriss, O. M.; Rabea, S.; Eltahir, Y. *J. Nanomater.* **2022,** 9721736. doi:10.1155/2022/9721736
59. Deena Dayal, S.; Pushpa Rani, V.; Antony Prabhu, D.; Rajeshkumar, S.; David, D.; Francis, J. *Microb. Pathog.* **2024,** *197,* 107033. doi:10.1016/j.micpath.2024.107033
60. Manikandan, V.; Velmurugan, P.; Park, J.-H.; Chang, W.-S.; Park, Y.-J.; Jayanthi, P.; Cho, M.; Oh, B.-T. *3 Biotech* **2017,** *7,* 72. doi:10.1007/s13205-017-0670-4
61. Basha, S. B. A.; Soundhararajan, R.; Srinivasan, H. *Discover Appl. Sci.* **2025,** *7,* 67. doi:10.1007/s42452-025-06469-5
62. Navayath, M.; Ramesh, S. R.; Kalaiselvam, R.; Ashok, R.; Rajendran, M. R.; Balaji, L. *J. Contemp. Dent. Pract.* **2023,** *24,* 459–466. doi:10.5005/jp-journals-10024-3530
63. Saygi, K. O.; Bayram, H. M.; Bayram, E. *Biomass Convers. Biorefin.* **2024,** *14,* 5531–5539. doi:10.1007/s13399-022-02857-8
64. VA, M.; Ramesh, S.; Muthukrishnan, L. *Plant Nano Biol.* **2023,** *3,* 100023. doi:10.1016/j.plana.2022.100023
65. Ahmed, O. A. K.; Sibuyi, N. R. S.; Fadaka, A. O.; Maboza, E.; Olivier, A.; Madiehe, A. M.; Meyer, M.; Geerts, G. *Pharmaceutics* **2023,** *15,* 871. doi:10.3390/pharmaceutics15030871
66. Barik, B.; Satapathy, B. S.; Pattnaik, G.; Bhavrao, D. V.; Shetty, K. P. *Front. Chem. (Lausanne, Switz.)* **2024,** *12,* 1489253. doi:10.3389/fchem.2024.1489253
67. Mathew, C. A.; Veena, H. R.; Shubha, P.; Daniel, R. A. *J. Appl. Oral Sci.* **2023,** *31,* e20230271. doi:10.1590/1678-7757-2023-0271
68. Renganathan, S.; Shenoy, A.; Ganapathy, D. *J. Phys.: Conf. Ser.* **2024,** *2837,* 012048. doi:10.1088/1742-6596/2837/1/012048

69. Lahiri, D.; Ray, R. R.; Sarkar, T.; Upadhye, V. J.; Ghosh, S.; Pandit, S.; Pati, S.; Edinur, H. A.; Abdul Kari, Z.; Nag, M.; Ahmad Mohd Zain, M. R. *Front. Microbiol.* **2022,** *13,* 939390. doi:10.3389/fmicb.2022.939390
70. Andor, B.; Tischer (Tucuina), A. A.; Berceanu-Vaduva, D.; Lazureanu, V.; Cheveresan, A.; Poenaru, M. *Rev. Chim.* **2019,** *70,* 781–783. doi:10.37358/rc.19.3.7006
71. El-Rab, S. M. F. G.; Basha, S.; Ashour, A. A.; Enan, E. T.; Alyamani, A. A.; Felemban, N. H. *J. Microbiol. Biotechnol.* **2021,** *31,* 1656–1666. doi:10.4014/jmb.2106.06008
72. Thomas, A. A.; Varghese, R. M.; Rajeshkumar, S. *bioinformation* **2022,** *18,* 284–288. doi:10.6026/97320630018284
73. Farheen, S.; Oanz, A. M.; Khan, N.; Umar, M. S.; Jamal, F.; Altaf, I.; Kashif, M.; Alshameri, A. W.; Somavarapu, S.; Wani, I. A.; Khan, S.; Owais, M. *Front. Nanotechnol.* **2022,** *4,* 780783. doi:10.3389/fnano.2022.780783

License and Terms

BEILSTEIN JOURNAL OF NANOTECHNOLOGY

Targeting the vector of arboviruses *Aedes aegypti* with nanoemulsions based on essential oils: a review with focus on larvicidal and repellent properties

Laryssa Ferreira do Nascimento Silva[‡1], Douglas Dourado[*,‡1], Thayse Silva Medeiros[1], Mariana Alice Gonzaga Gabú[1], Maria Cecilia Queiroga dos Santos[1], Daiane Rodrigues dos Santos[1], Mylena Lemos dos Santos[1], Gabriel Bezerra Faierstein[2], Rosângela Maria Rodrigues Barbosa[2] and Fabio Rocha Formiga[*1,3]

Review

Open Access

Address:
[1]Department of Immunology, Aggeu Magalhães Institute (IAM), Oswaldo Cruz Foundation (FIOCRUZ), 50670-420 Recife, PE, Brazil, [2]Department of Entomology, Aggeu Magalhães Institute (IAM), Oswaldo Cruz Foundation (FIOCRUZ), 50670-420 Recife, PE, Brazil and [3]Faculty of Medical Sciences (FCM), University of Pernambuco (UPE), 50100-130, Recife, PE, Brazil

Email:
Douglas Dourado[*] - ddourado.science@gmail.com;
Fabio Rocha Formiga[*] - fabio.formiga@fiocruz.br

* Corresponding author ‡ Equal contributors

Keywords:
Aedes aegypti; arboviruses; mosquito vector; nanoemulsion; nanotechnology; natural products

Beilstein J. Nanotechnol. **2025,** *16,* 1894–1913.
https://doi.org/10.3762/bjnano.16.132

Received: 04 June 2025
Accepted: 09 October 2025
Published: 28 October 2025

This article is part of the thematic issue "Advances in nanotechnology applied to natural products".

Associate Editor: K. Koch

Abstract

Mosquitoes of the *Aedes* genus are responsible for the transmission of arboviruses that seriously affect public health. Given the increasing resistance to traditional insecticides and their negative environmental impacts, the need for safer alternatives arises. In this context, natural produts such as essential oils (EOs) have been studied for their larvicidal and repellent properties against *Aedes aegypti*, due to the presence of compounds such as terpenoids and phenols. However, the usage of EOs is limited due to some properties such as poor water solubility, high volatility, and intrinsic oxidation sensitivity. Thus, the development of novel formulations to efficiently deliver bioactives represents an innovative approach for *Aedes aegypti* control. In this context, nanothecnology provides smart formulations with improved drug solubility, controlled release, and protection against degradation. Nanoemulsions are colloidal systems with droplets of 20 to 500 nm, which improve the dispersion of the compounds, protect their active properties, and enhance their efficacy. This review addresses the potential of nanoemulsions as efficient carriers of EOs, and how this approach could emerge as ecological alternatives to synthetic insecticides. Herein, the focus was kept on targeting larvicidal and repellent activities against *Ae. aegypti*. For that, 23 studies were analyzed, which demonstrated a significant increase in the efficacy of nanoemulsions with EOs compared to that of free EOs, in both activities. However, the repellent activity has been less explored,

present in only three of the studies evaluated, in the last 10 years. Correlatingh with this, other aspects such as botanical species of EOs, mechanisms of action, composition, and characteristics of nanoemulsions are discussed. In addition, this review highlights challenges and perspectives on pharmaceutical nanotechnology towards nanoemulsions as safe, effective, and eco-friendly tools for controlling *Ae. Aegypti.*

Introduction

Arboviruses (arthropod-borne viruses) are viruses transmitted by arthropods, including mosquitoes, sandflies, and ticks. Currently, more than 615 arboviruses have been recognized and reported in the literature. Their transmission cycle typically begins when a vector, such as a mosquito, feeds on the blood of an infected host [1]. Thus, the virus undergoes a replication process in the midgut of the mosquito, being disseminated to different organs, mainly the salivary glands. Upon contact with a new host, the virus is inoculated through the bite of the vector, continuing the transmission cycle [2,3]. Most diseases caused by arboviruses are zoonoses, meaning they are primarily infections of vertebrates which can occasionally trigger incidental infections in humans [3,4].

The main vectors are mosquitoes of the *Aedes* genus, primarily *Aedes aegypti* and *Aedes albopictus*, which are capable of transmitting various arboviruses on a global scale [5]. *Ae. aegypti* is generally considered the most efficient and important vector for the transmission of these viral diseases, due to its evolutionary adaptations, its strong association with human environments, and its high vector competence [5,6]. However, *Ae. albopictu*s has been reported as the main or even the sole vector responsible for arbovirus transmission in certain regions of the world, demonstrating significant epidemiological relevance under specific ecological conditions [7]. Therefore, these arthropods play a crucial role in the transmission of arboviruses of global epidemiological relevance, such as dengue (DENV), yellow fever (YFV), zika (ZIKV), and chikungunya (CHIKV).

In these diseases, high morbidity and mortality rates are observed, and they have a global distribution, particularly in tropical and subtropical regions, where climatic conditions favor the reproduction and proliferation of mosquitoes. Due to the growing threat posed by arboviruses, the Global Arbovirus Initiative [8] highlights integrated vector control as a critical pillar for reducing transmission risks worldwide, advocating for the use of multiple complementary approaches as an essential strategy for effective disease control. These include the rational use of chemical insecticides, aimed at minimizing the development of resistance; biological control, through the use of natural predators and larvicidal microorganisms such as *Bacillus thuringiensis israelensis* (Bti); mechanical control, based on improving basic sanitation and infrastructure to eliminate breeding sites; and behavioral control, which promotes the adoption of practices such as the use of traps to capture mosquitoes at different life stages [9-12]. In this context, the development of nanoemulsions based on essential oils emerges as a promising innovation within integrated control strategies, offering environmentally friendly larvicidal and repellent alternatives specifically targeted at *Aedes aegypti* [12-14].

Although chemical insecticides are important tools in vector control, the development of resistance and the consequent decrease in their effectiveness have become a major concern [15-18]. Several cases of resistance to pyrethroids, carbamates, organochlorines, and organophosphates have been reported over the years [11,19]. Additionally, repellents based on DEET (*N*,*N*-diethyl-meta-toluamide) are recognized as the gold standard for mosquito repellents; however, these repellents are not widely used in regions at risk for arbovirus transmission, mainly due to accessibility issues, cost, and concerns about long-term safety. Additionally, commonly used components have been associated with allergic reactions, skin irritation, and adverse effects on the nervous, cardiovascular, and respiratory systems of humans because these chemicals are highly toxic to non-target organisms and are not selective for the vector [11,20,21]. Furthermore, these products also contribute to environmental pollution [14]. Given this scenario, the search for more sustainable alternatives, such as the use of natural products, becomes a promising strategy to tackle these challenges [22].

Among natural products are essential oils, secondary metabolites with complex chemical composition extracted from different parts of plants [23]. They stand out for their efficiency in combating the vector at different stages of the evolutionary cycle, especially as larvicides, wherein the mosquito is at its most vulnerable stage [24]. In addition, they can act as insecticides, ovicides, pupicides, oviposition deterrents, and repellents [25,26]. The main advantages include low toxicity, biodegradability, and action in multiple locations due to the variety of compounds [12,19].

On the other hand, essential oils in their natural form are not stable under environmental stress, being easily degradable or evaporated upon exposure to air, light, heat, and humidity during processing, use, or storage [27,28]. Their volatile nature, susceptibility to oxidation, and insolubility in water limit their industrial application [29]. To overcome these limitations,

nanotechnological strategies have been used, such as polymeric nanocarriers [30], solid lipid nanoparticles [31], liposomes [32], and nanoemulsions [13,14,33].

Among these strategies, nanoemulsions, kinetically stable nanometric dispersions (20–500 nm) of two immiscible liquids, stabilized by surfactants, have stood out [34]. These are not affected by moderate changes in pH or temperature, making them ideal for the protection of solubilized bioactives [35]. They also promote the protection of essential oils against oxidation caused by external factors, maintaining or increasing their functional properties [28]. Furthermore, they increase the water solubility of poorly soluble compounds, improve the dispersion of essential oils in vector control, and provide a controlled release of the bioactives. Finally, these systems can be obtained at low cost and through more sustainable technologies [36].

Given these advantages, nanoemulsions containing essential oils have been used as a promising strategy for mosquito control [33]. These systems can improve the efficacy of essential oils (EOs) against these vectors, providing the abundance of these bioactives in their structures at different stages of their cycle [37]. Therefore, this review focuses on mapping nanoemulsions based on essential oils and their potential as an innovative strategy for controlling *Aedes aegypti* and consequently related arboviruses.

Review

Aedes aegypti: General aspects and control strategies

Insects are important vectors in the transmission of bacteria and viruses, contributing to the spread of various diseases in humans. Among these pathogens, arboviruses form a diverse group of viruses primarily transmitted by arthropods such as mosquitoes, ticks, and flies [38]. More than 500 arboviruses have been identified globally, but only about 150 cause diseases in humans. Among them, the *Flaviviridae* family includes pathogens such as dengue (DENV) and zika (ZIKV) viruses, while *Alphaviruses* include the chikungunya virus (CHIKV) [39,40]. These viruses are primarily transmitted by the *Ae. aegypti* mosquito, which relies on humans as its main amplification hosts [2,41,42].

Aedes aegypti is a species of mosquito of the *Culicidae* family, order *Diptera*, native to Africa and distributed throughout various regions of the world. This extensive distribution occurs due to the sum of several factors, such as dispersion favored by high temperatures and high humidity, and inefficient urban and rural development planning measures. Thus, due to climatic and social conditions, tropical and subtropical regions are considered favorable for the development of this mosquito [43].

Ae. aegypti mosquitoes are small in size, black in color, and have white spots [44]. Regarding their life cycle, they present complete metamorphosis, including the egg, larva, pupa, and adult stages (Figure 1) [45]. The complete cycle, which takes approximately seven to 14 days, encompasses the transition from an *Ae. aegypti* mosquito egg to an adult mosquito, and it is influenced by environmental factors such as temperature, nutrient availability, water quality, and ecological interactions. Higher temperatures accelerate growth, while food scarcity and competition can prolong this phase [46-48].

The life cycle of *Ae. aegypti* (Figure 1) begins with the deposition of eggs by adult female mosquitoes. These eggs are capable of surviving for a prolonged period in the absence of water and can withstand extreme environmental conditions, thereby persisting in aridand/or cold environments [20,48]. Upon contact with water, the eggs hatch, resulting in the hatching of larvae corresponding to the 1st instar stage (L1). Larvae rapidly progress to the 2nd instar stage (L2), and subsequently to the 3rd instar stage (L3) larvae. The transition from L3 to the 4th instar stage (L4) occurs more gradually, as larvae must achieve sufficient size and weight to initiate metamorphosis into pupae. Pupae also live exclusively in aquatic habitats and represent a transitional phase of metamorphosis between larval and adult stages. During this phase, pupae develop into adult mosquitoes, which are capable of flying short distances. *Aedes aegypti* mosquitoes generally disperse within 50 to 100 meters from their emergence site [49], although in less populated areas this range may extend up to 560 meters in rural or more open environments [45,48,50,51].

Environmental factors, such as improper water storage and climatic conditions, influence the proliferation of *Ae. aegypti,* increasing arbovirus transmission. According to data from the World Health Organization [52], arboviroses are seen as a major obstacle to public health, especially to dengue, zika, and chikungunya viruses, especially in subtropical and tropical countries [3]. In this scenarium, DENV causes more than 400 million infections annually, presenting symptoms such as high fever, headaches, and, in severe cases, hemorrhagic shock [53]. CHIKV, present in over 100 countries, leads to fever, severe joint pain, and, in critical cases [54,55], to neurological and cardiac complications [55]. Initially overlooked, ZIKV gained global attention after outbreaks in the Americas, being linked to severe complications such as congenital zika syndrome and Guillain–Barré syndrome [56]. In addition to mosquito transmission, ZIKV can spread through sexual contact [57], blood transfusions [58], and from mother to child [59].

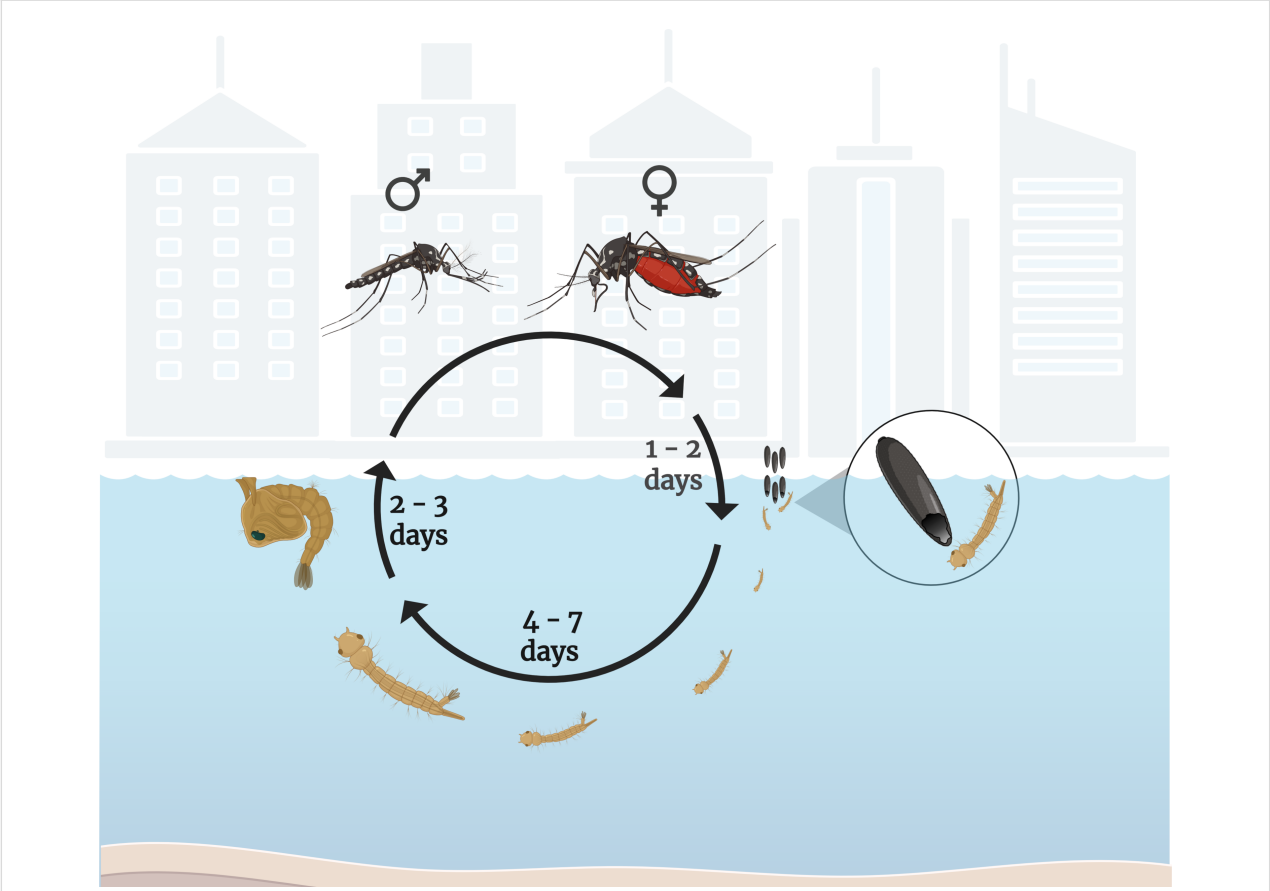

Figure 1: Life cycle of *Aedes aegypti* mosquitoes. After oviposition, the eggs hatch into larvae within one to two days. Larvae develop through four instar stages over four to seven days before becoming pupae. Pupae mature into adult mosquitoes within two to three days. Males usually emerge first. Only females need to feed on blood to develop their eggs and continue the cycle. The scale of the image in cm provides a reference for the approximate size of the mosquitoes and their stages of development. Created in BioRender. Rocha Formiga, F. (2025) https://BioRender.com/ssghykj. This content is not subject to CC BY 4.0.

Given the persistence and severity of arboviral diseases, effective strategies to control *Ae. aegypti* are crucial for preventing their spread. The absence of vaccines and effective treatments for most arboviruses further reinforces the importance of vector control as an important strategy to reduce the transmission of these diseases [60]. For that, a variety of methods targeting different stages of the mosquito life cycle have been employed to control their populations. Traditional strategies focus on eliminating breeding sites, such as water containers and discarded tires that collect rainwater, which serve as ideal habitats for mosquito larvae. Additionally, the application of larvicides, including chemical and biological agents, insect growth regulators, and bacterial toxins, has been widely used to reduce mosquito populations. Internal residual spraying to eliminate adult mosquitoes and the use of insecticide-treated nets are also common control measures [61,62].

Historically, the Pan American Health Organization (PAHO), in collaboration with Latin American governments, led efforts to eradicate *Ae. aegypti* in the Americas during the 1950s and 1960s, primarily using dichloro-diphenyl-trichloroethane (DDT) and other persistent insecticides. Although effective at the time, DDT use was discontinued due to its environmental persistence and the emergence of resistance in mosquito populations [60,63]. Another widely used insecticide is temephos, an organophosphate larvicide applied in water reservoirs to control mosquito reproduction. However, its direct correlation with reduced dengue cases remains inconclusive [60].

Despite their effectiveness, the excessive use of chemical insecticides poses health risks and contributes to the development of resistance in mosquito populations [63]. These concerns highlight the need for safer, more sustainable vector control strategies that minimize risks to human health and delay the onset of insecticide resistance. In this context, natural products have emerged as a promising alternative for mosquito control, particularly as larvicides, given that many insecticides are derived from natural compounds [64]. Various classes of natural prod-

ucts and secondary metabolites have been evaluated, with a particular focus on plant essential oils and their constituents [65,66].

Essential oils in vector control

Essential oils are hydrophobic, aromatic, volatile liquid compounds mainly secreted by glandular trichomes, which are the secretory tissues present in different vegetative parts of plants, such as leaves, flowers, roots, fruits, or stems [67]. These can be obtained by distillation with water or steam, microwave or ultrasound assisted extraction, or from the epicarp of fruits by a mechanical process, or by "dry distillation". They and are made of a complex mixture of low molecular weight chemical substances including terpenes, terpenoids, phenylpropanoids, aldehydes, ketones, and ethers which are directly related to the defense of plants against different pathogens [68-70].

The chemical compounds present in the essential oils of some plant species (such as *Cymbopogon excavatus*, *Mentha piperita*, *Azadirachta indica*, *Eucalyptus maculata*, and *Cymbopogon nardus*) [62,66], exhibit, either alone or in synergy, larvicidal, ovicidal, pupicidal, and repellent properties. These characteristics make these oils sustainable and effective alternatives for controlling disease-carrying insects, including *Ae. aegypti* [71,72]. Chemical components such as limonene, menthol, linalool, thymol, eugenol, citral, and camphor are widely used in commercial insecticide and repellent formulations around the world [67,73,74]. These constituents and others have been found in the composition of different species producing EOs, presenting significant biological activities against *Ae. aegypti* [72,75-77].

The action of these components consists of interfering with larval physiology, preventing its development and contributing to the reduction of the adult mosquito population. Ovicidal activities are also reported, which prevent eggs from hatching, interrupting the life cycle of the vector. Furthermore, essential oils exhibit repellent properties that keep mosquitoes away, reducing the incidence of bites and, consequently, the transmission of diseases [10,24].

Despite the potential of essential oils, their use in vector control faces several limitations. The high volatility of the active compounds can reduce long-term efficacy, requiring frequent reapplications. In addition, the low polarity of the components of essential oils makes their use unfeasible in aqueous environments, which are common for larval development. Furthermore, chemical instability and variation in the consistency of the composition of the oils can affect the efficacy of the products [78].

To overcome these limitations, pharmaceutical nanotechnology strategies such as nanoemulsions have been used as tools for vector control [79]. Numerous studies have shown that nanoemulsions can increase the solubility and prolong the larvicidal and/or repellent activity of essential oils, making them a promising solution to improve the efficacy of herbal products for mosquito control [80,81].

Nanoemulsions: Concepts and applications in larvicides and repellents

Pharmaceutical nanotechnology offers innovative solutions for the delivery and targeting of molecules for therapeutic, prophylactic, or diagnostic purposes [82]. In 1995, the Food and Drug Administration (FDA) agency approved the first nanomedicine, Doxil® (doxorubicin-loaded liposomes) for chemotherapy. Over the past 30 years, research and development in nanotechnology have expanded significantly, with more than 70 nanomedicines approved by FDA or EMA [83-86].

Beyond liposomes, other lipid-based nanosystems have gained prominence, such as nanoemulsions (NEs) [87]. NEs are kinetically stable dispersed systems composed of two immiscible phases, typically an oil and aqueous phases, with droplets (20–500 nm) stabilized by surfactants. NEs can be classified as oil-in-water (O/W), water-in-oil (W/O), or multiple emulsions (W/O/W or O/W/O) (Figure 2), depending on the preparation techniques and the choice and interaction of formulation components [34,88,89].

Nanoemulsions exhibit several advantages, making them promising systems for pharmaceutical and biomedical applications. These include: (a) superior stability during storage compared to that of macroemulsions, attributed to their small droplet size, which prevents flocculation, creaming, and sedimentation; (b) enhanced bioavailability and improved aqueous solubility of lipophilic molecules; (c) increased cutaneous permeability of various molecules; (d) reduced emulsifier concentrations compared to that of macro- and microemulsions; (e) protection of molecules from adverse environmental conditions such as pH-induced hydrolysis and oxidation; and (f) versatile applications allowing administration in various forms, including gels, creams, aerosols, and sprays, via oral, topical, intravenous, pulmonary, and ocular routes [88,90-93].

Given these numerous advantages, nanoemulsions have been successfully explored for the treatment of diverse cancers [94], inflammatory processes [95], photodynamic therapy [96], antimicrobial applications [97], intracellular parasites such as *Trypanosoma cruzi* and *Leishmania spp*. [98,99], and for antioxidant potential [100], larvicidal, and repellent activities against arthropod vectors [101]. Nanotechnology has shown the

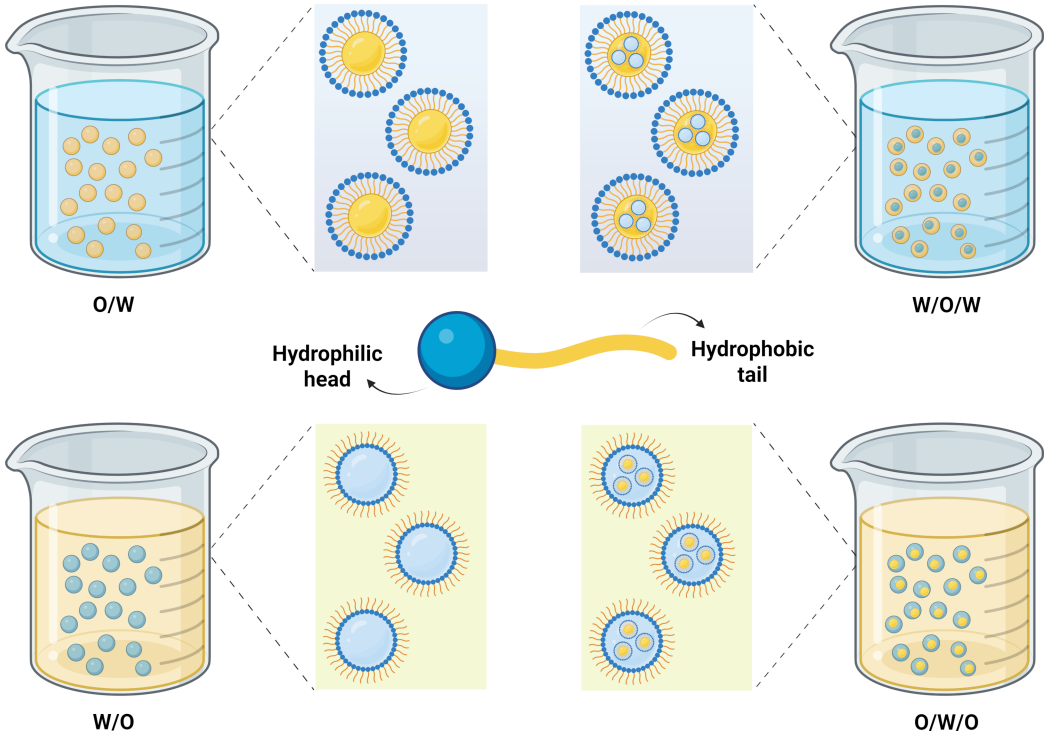

Figure 2: Nanoemulsion classification. Created in BioRender. Rocha Formiga, F. (2025) https://BioRender.com/mcdrou6. This content is not subject to CC BY 4.0.

potential to enhance the performance and significantly improve the physical, chemical, and biological properties of essential oils, phytocompounds, and other insecticidal materials [102].

Wei et al. (2023) demonstrated the larvicidal potential of fenpropathrin NEs against *Helicoverpa armigera* larvae at the L3 stage, reporting superior efficacy compared to commercial emulsions, along with lower toxicity to non-target organisms and improved environmental compatibility [103].

Similarly, Shaari et al. (2021) developed palm-oil-based nanoemulsions containing deltamethrin, which exhibited enhanced insecticidal performance against *Ae. aegypti* mosquitoes using thermal fogging techniques in outdoor environments [104]. This superior performance was attributed to the reduced droplet size, which facilitates penetration through mesothoracic spiracles and into the inner walls of the mesothoracic trachea, thereby increasing insect mortality.

Against the *Ae. aegypti* vector, Duarte et al. (2024) developed NEs loaded with two monoterpenes, cymene and myrcene, and evaluated their larvicidal potential against L3 larvae [36]. The NEs showed significant lethality to *Ae. aegypti* larvae, with insecticidal activity equal to or greater than that of free terpenes but with enhanced safety for *Galleria mellonella* larvae and human keratinocyte cells (HaCaT). Additionally, NEs facilitated dispersion in aqueous environments.

In conclusion, nanoemulsions are safe, eco-friendly, and effective nanosystems capable of enhancing the larvicidal and insecticidal effects of various compounds. Developing essential oil-based nanoemulsions represents an intelligent and promising alternative for vector control, as further detailed in the following sections.

Nanoemulsions based on essential oils to control *Aedes aegypti*

There have been reports in recent years regarding the use of nanoemulsions as effective active EO carriers. In this review, we compiled studies of nanoemulsions containing essential oils against *Ae. aegypti*, a vector of arboviruses such as zika, chikungunya, and dengue. We found 23 studies with different types of nanoemulsified essential oils. Most of the studies were related to larvicidal activity, with less investigation regarding repellent potential in recent years. These aspects are detailed and discussed in the sections below.

Larvicidal properties

Essential oils have gained attention due to their larvicidal properties against different vector larvae, including *Ae. aegypti*, and

have been enhanced in nanoemulsions thanks to their properties [105-107]. Nanostructured plant-based larvicides could be associated with larvae morphological alterations, formation of reactive oxygen species that cause genotoxicity, and inhibition of acetylcholinesterase (Figure 3).

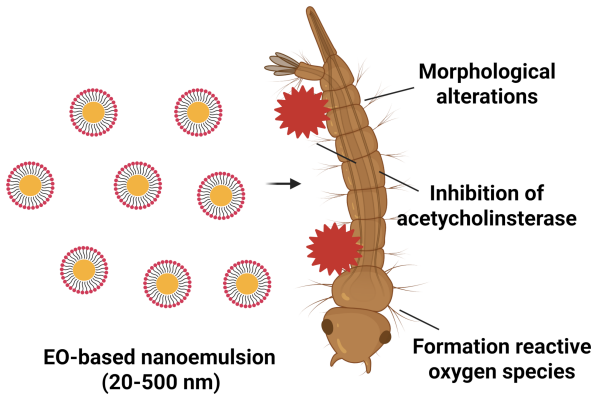

Figure 3: Schematic representation of the larvicidal mechanism of nanoemulsions based on essential oils against *Aedes aegypti* larvae. Created in BioRender. Rocha Formiga, F. (2025) https://BioRender.com/qu9l3j9. This content is not subject to CC BY 4.0.

In this context, Romano et al. (2024) investigated the use of a nanoemulsion formulated with an essential oil extracted from the leaves of *Murraya koenigii* to evaluate its efficacy as a larvicide against the *Ae. aegypti* mosquito [108]. This plant, known as curry in India, is widely distributed in tropical and subtropical regions of the world and has culinary and medicinal applications [109]. Its leaves can be used to extract essential oils rich in sesquiterpenes, whose major components are β-phellandrene (38.3%), α-fenchene (10.5%), and sabinene (9.6%), which are important for its larvicidal activity [108]. Thus, a nanoemulsion with an average droplet size of 140 nm containing 1% of essential oils was evaluated on third-instar larvae (treated for 24 hours) at 1:100 and 1:200 (v:v) dilutions. The results reveal high mortality at different concentrations, with LC_{50} values of 11.8 µg/mL and 12.5 µg/mL, LC_{90} values of 22.6 µg/mL and 21.6 µg/mL for laboratory and field, respectively. In comparison to the unformulated essential oil, the nanoemulsion maintained its effectiveness for an extended period of up to 29 days. While genotoxic effects were not observed in *Allium cepa* cells, a decrease in cellular proliferation was evidenced.

De Sousa dos Santos et al. (2024) investigated the larvicidal effects of a nanoemulsion containing essential oil from *Ocimum basilicum* [76]. This species is known as basil or alfavaca and it is native to tropical regions of Africa and Asia [110]. It presents high levels of linalool (32.66%) and anethole (32.48%), in addition to α-selinene (0.82%) in their composition, which showed promising molecular affinity in in silico studies, despite its low concentration [76]. The oil was obtained by hydrodistillation and incorporated into the nanoemulsion through a low-energy method, using polysorbate 20 as a surfactant. The formulation presented an average droplet size ranging from 244.6 to 280.4 nm, a polydispersity index of less than 0.25, and a negative zeta potential (−15.7 to −18.6 mV), maintaining stability for 14 days. In the bioassays, fourth-stage larvae (L4) of *Aedes aegypti* and *Culex quinquefasciatus* were exposed to concentrations of 10 to 50 mg/L for 24 and 48 hours. LC_{50} values ranged from 38 to 42 mg/L for both vectors throughout the evaluated periods. Distilled water, polysorbate 20, and commercial larvicides (Temephos and Pyriproxyfen) were used as controls. It should be noted that the study did not perform comparisons with the free essential oil nor did it evaluate the formulation in non-target species [111,112].

Machado et al. (2023) developed an oil-in-water nanoemulsion containing 5% of surfactants and 5% of the essential oil of *Ocotea indecora* leaves and evaluated the larvicidal activity against *Ae. Aegypti* [113]. This species is an endemic plant native to Brazil found in the remaining Atlantic Forest in the southern and southeastern regions of Brazil [113,114]. Among these metabolites, there are reports of bicyclogermacrene, valerianol, β-pinene, and sesquirosefuran being the major substances in the essential oil of leaves (81.4%), suggesting a key role of this metabolites in larvicidal activity [113,115]. The oil was extracted using hydrodistillation and incorporated into the nanoemulsion by the low-energy method by phase inversion, using polysorbate 80 and sorbitan monooleate 20 as surfactants. The NE presented an average size of 105.3 nm (±1.36) and a polydispersity index of 0.263 (± 0.004). The larvicidal bioassays against third-stage *Aedes aegypti* larvae produced an LC_{50} of 61.4 µg/mL at 48 hours and 26.8 µg/mL at 144 hours. The toxicity of NE in *Apis mellifera* was evaluated, proving that the formulated nanoemulsion did not present toxicity for this non-target species.

Viana et al. (2023) explored the larvicidal activity of a nanoemulsion formulated with an essential oil extracted from the leaves of *Xylopia ochrantha*, a plant native to the restinga ecosystem of Brazil [111]. The oil has a composition rich in sesquiterpenes, the main ones being germacrene D (17.8%), bicyclogermacrene (17.4%), and δ-elemene (13.9%). The extraction was performed by hydrodistillation, and the nanoemulsion was prepared using a low-energy method with sorbitan monooleate 80 and polysorbate 20. The NE presented an average droplet size of 74.5 nm (±1.939) and a polydispersity index of 0.271 (±0.007), remaining physicochemically stable for up to 180 days. Larvicidal bioassays against third-stage *Aedes aegypti* larvae produced an LC_{50} of 192.5 µg/mL at 48 hours. Further-

more, acute oral toxicity tests in *Danio rerio* (zebrafish), a non-target model organism, showed no adverse effects. Although the study did not compare the nanoemulsion to the corresponding free essential oil, it highlights the potential of this formulation as a safe and environmentally friendly bioinsecticide for the control of arbovirus vectors.

Subaharan et al. (2022) evaluated the larvicidal efficacy of nanoemulsions of *Trachyspermum ammi* essential oil and its main component, thymol, against *Ae. aegypti*. The plant, native to India, has seeds rich in thymol (54.22%), p-cymene (15.04%), and γ-terpinene (10.46%) [116,117]. The oil was extracted by hydrodistillation (1.8% yield), and the nanoemulsions were prepared with 5% of oil or thymol, 5% of Tween® 80, and 90% of water by ultrasound at 50 °C. The nanoemulsions presented average sizes of 65 to 83 nm (oil) and 167 to 230 nm (thymol), with stability of up to 60 days. In bioassays with third-instar larvae, thymol nanoemulsion demonstrated greater efficacy (LC_{50} = 34.89 ppm), followed by oil (LC_{50} = 46.73 ppm), both outperforming conventional emulsions. Electron microscopy revealed damage to the larvae, and enzymatic analysis showed that thymol nanoemulsion inhibited 83.48% of acetylcholinesterase, while oil inhibited 53.62%, suggesting multiple mechanisms of action.

Gupta et al. (2022) investigated the larvicidal efficacy of a *Thymus vulgaris* essential oil nanoemulsion against *Ae. Aegypti* [118]. Thyme, a plant native to the Mediterranean, has antimicrobial and insecticidal properties, with main compounds such as 1,3,8-p-menthatriene (45.58%) and 2-ethyl-4,5-dimethylphenol (41.50%) [119]. The essential oil was extracted by steam distillation. The nanoemulsion was prepared by ultrasound, with a ratio of 1:0.5 (oil/surfactant, polysorbate 80) and Milli-Q water. It presented an average size of 52.18 nm (±4.53), a polydispersity index of 0.237 (±0.006), and thermal stability. In bioassays, third instar larvae exposed to concentrations between 5 and 150 ppm showed LC_{50} of 58.72 ppm after 24 hours. Morphological analysis revealed significant damage to the larvae, such as cuticular deformations, especially in the anal segment. The rapid release of the essential oil (91.68% in 48 hours) indicated high bioavailability, contributing to the efficacy of the nanoemulsion.

Bosly et al. (2022) developed an oil-in-water nanoemulsion containing *Santalum album* (sandalwood) essential oil and evaluated its larvicidal activity against *Ae. aegypti* [120]. The essential oil was extracted by hydrodistillation from the wood and roots of *Santalum album*, a tree native to India, East Asia, northern Australia, and the Hawaiian Islands [121]. This oil is rich in sesquiterpene alcohols, such as α-santalol (24.27%) and β-santalol (27.65%) [120,122]. The NE presented an average droplet size of 195.7 nm, a polydispersity index of 0.342, and a negative zeta potential (−20.1 mV). Third-instar larvae were exposed to concentrations ranging from 62.5 to 1500 ppm. The nanoemulsion showed LC_{50} values of 232.18 and 182.37 ppm after 24 and 48 hours, showing greater efficacy than that of the free essential oil, which required higher concentrations. Furthermore, the nanoemulsion significantly reduced the activity of the enzymes α-esterase, β-esterase, and glutathione S-transferase (GST) in the larvae, suggesting interference in the detoxification mechanisms and indicating the involvement of enzymatic pathways in the larvicidal action.

Almadiy and Nenaah (2022) developed an oil-in-water nanoemulsion containing *Origanum vulgare* essential oil, composed mainly of carvacrol, thymol, γ-terpinene, and p-cymene – monoterpenes widely present in species from the mediterranean and temperate regions of Asia [72,123]. The formulation was composed of EO, polysorbate 80 (surfactant), and purified water, and it was stabilized at 25 °C for 30 days. The nanoemulsion showed physicochemical stability with an initial average size of 64.1 nm (±6.3), polydispersity index of 0.21 (±0.04), and initial pH of 5.8. After 30 days, the average size increased to 71.8 ± 8.3 nm, with a polydispersity index of 0.18 ± 0.03 and pH of 4.9 ± 0.06. In larvicidal bioassays with *Ae. aegypti* (exposure: 24 hours), the nanoemulsion presented a LC_{50} of 13.9 μg/mL, higher than that of isolated EO (29.2 μg/mL) and pure terpenes (carvacrol: 31.9 μg/mL; thymol: 45.3 μg/mL; γ-terpinene: 50.4 μg/mL; *p*-cymene: 75.7 μg/mL). The 40 μg/mL dose of the nanoemulsion eliminated 100% of the larvae tested. No toxicity data for non-target organisms were reported.

Rodrigues et al. (2021) evaluated the larvicidal potential of nanoemulsions formulated with essential oils from two morphotypes of *Ayapana triplinervis*, a plant native to South America and widely distributed in Brazil, Ecuador, Peru, and other countries [124,125]. The plant material was collected in the state of Amapá (Brazil), and the morphotypes were differentiated by morphological characteristics and chemical composition determined by GC-MS. The morphotype A presented β-caryophyllene (45.93%) and thymohydroquinone dimethyl ether (32.93%) as the main constituents, while the morphotype B was dominated by the latter compound (84.53%). Nanoemulsions were obtained by the low-energy method, with average sizes of 101.4 nm (morphotype A) and 104.6 nm (morphotype B), polydispersity < 0.17, and zeta potentials between −19.3 and −27.7 mV. Third-instar larvae of *Aedes aegypti* were treated with concentrations of 50–150 μg/mL (A) and 20–100 μg/mL (B), with the morphotype B formulation being the most effective (LC_{50} = 35.57 μg/mL in 48 hours), surpassing the free essential oil. Acute oral toxicity tests in *Mus musculus* mice

(2000 mg/kg) did not result in mortality, although inflammatory changes were observed in the lungs and liver.

Faustino et al. (2021) investigated the larvicidal potential of a nanoemulsion formulated with an essential oil extracted from the resin of *Protium heptaphyllum*, a species native to the Amazon region. The chemical composition of the oil was dominated by p-cymene (27.70%) and α-pinene (22.31%), compounds recognized for their insecticidal activity [126,127]. The nanoemulsion was obtained by a low-energy method, presenting ideal physicochemical characteristics, with an average diameter of 109.7 nm (±0.75), a polydispersity index of 0.29 (±0.007), and a zeta potential of −21.7 mV (±1.10), conferring stability to the system. The larvicidal tests were performed with third-stage larvae of *Ae. aegypti,* exposed to the samples for a period of 24 and 48 hours. The nanoemulsion demonstrated high efficacy, with a LC_{50} of 2.91 μg/mL after 48 hours, outperforming the free essential oil. Finally, tests with zebrafish revealed only mild changes in the gills at concentrations higher than those used in the bioassays, demonstrating low toxicity of the nanoemulsion.

Folly et al. (2021) developed a nanoemulsion with an essential oil from the leaves of *Annona acutiflora*, a plant native to tropical regions of South America, with occurrences recorded in Brazil, Colombia, Peru, Ecuador, and Venezuela. The chemical composition of the essential oil is rich in sesquiterpenes, with α-santalene, bicyclogermacrene, and α-zingiberene as the main constituents [128,129]. The nanoemulsion was prepared with essential oil, polysorbate 20, and distilled water using magnetic stirring and aqueous titration, followed by emulsification. The resulting formulation had an average size of 171.1 nm (±1.2), a polydispersity index of 0.171 (±0.011), and a zeta potential of −15.0 mV (±0.53). In larvicidal bioassays performed with third-instar larvae of *Ae. aegypti*, concentrations of 12.5, 25.0, and 50.0 ppm were evaluated, with exposure times of 24 and 48 hours. The LC_{50} values were 36 ppm (24 hours) and 21.2 ppm (48 hours), with maximum mortality of 100% being observed at the concentration of 50 ppm after 48 hours.

Martins et al. (2021) prepared a nanoemulsion containing essential oil from the leaves of *Aeollanthus suaveolens* to evaluate its larvicidal efficacy against *Ae. aegypti* and its toxicity to non-target organisms [130]. This species belongs to the Lamiaceae family, native to Africa, and is also distributed in the north and northeast of Brazil [131,132]. The main constituents of its essential oil are massoialactone (64.79%), linalool (7.83%), and (E)-β-farnesene (6.17%) [130]. The NE presented an average size of 104.3 nm (±0.47), a polydispersity index of 0.156 (±0.01), and a zeta potential of −13.63 mV (±0.83). The L3 larvae were treated with NE (100, 80, 60, 40, and 20 μg/mL) in a 100 mL container. An aqueous dispersion with the surfactant was used as the negative control and sbiotrin as the positive control. The larvicidal bioassay demonstrated that the concentration of 100 mg/mL resulted in 98% mortality in 24 hours and 100% after 48 hours. The LC_{50} was 54.23 mg/mL after 24 hours and 46.06 mg/mL at 48 hours.

De Oliveira et al. (2020) developed a nanoemulsion containing *Piper alatipetiolatum* essential oil and evaluated its ovicidal, larvicidal and pupicidal efficacy against *Aedes aegypti* [133]. This native brazilian species presented essential oil compositions mainly consisting of ishwarona (78.6%), ishwarol (8.2%), β-elemene (6.9%), selin-11-en-4α-ol (2.9%), and ishwaran (2.4%), which have been reported to possess biological activities such as larvicidal effects [134]. Based on this, a nanoemulsion was prepared and evaluated against eggs, L3 larvae, and pupae. The NE presented a size of 316 nm (±8), a polydispersity index of 0.44 (±0.01), and a zeta potential of −8.5 mV (±0.14). The essential oil showed lower ovicidal (19 to 100%), larvicidal (LC_{50} of 33.74 ppm), and pupicidal (LC_{50} of 65.06 ppm) activity when compared to those of the nanoemulsion containing this oil. The formulation showed higher ovicidal (47.7 to 100%), larvicidal (LC_{50} of 6.37 ppm), and pupicidal (LC_{50} of 9.33 ppm) activity against *Aedes aegypti.*

Rodriguez Amado et al. (2020) developed a nanoemulsion with 5% of essential oils extracted from the leaves of *Croton linearis*, a species widely distributed throughout the Americas [135,136]. The oil, with a yield of 1.5%, is mainly composed of eucalyptol (26.66%), sabinene (9.37%), and 10-epi-γ-eudesmol (6.83%) [135]. The NE presented an average size of 175 nm, a polydispersity index of 0.074, and a negative zeta potential (−27.02 mV). In bioassays, fourth-instar larvae of *Ae. aegypti* were exposed to concentrations of 10 to 100 μg/mL of the free essential oil and the nanoemulsion in distilled water. The nanoformulation presented an LC_{50} of 17.86 μg/mL after 24 hours, demonstrating superior efficacy to the free oil (LC_{50} = 64.24 μg/mL). Controls included surfactant-treated water and temephos (12 μg/L). Finally, toxicity was evaluated in Vero (*Chlorocebus sabaeus*) kidney cells and in adult Wistar rats via oral administration. The assays revealed no hemolytic, cytotoxic, or toxic effects, with IC_{50} above 2000 mg/kg, indicating a good environmental safety profile of the formulation.

Suresh et al. (2020) investigated the use of nanoemulsions containing *Crithmum maritimum* essential oil to control *Ae. aegypti*. The plant, typical of coastal areas, is widely distributed along the Mediterranean coast, including countries in Europe, North Africa, and regions of Western Asia [137,138]. Chemical analysis of the oil revealed compounds with insecticidal activity, such as dillapiole, myristicin, γ-terpinene, and

thymol methyl ether. The nanoemulsion was prepared using a low-energy method, combining 5% of essential oil, 5% of polysorbate 20, and 90% of water. The most stable formulation was obtained with a 1:3 ratio between oil and surfactant, presenting droplets with a diameter between 50 and 70 nm and a zeta potential of −18.3 mV, indicating good stability. In biological tests, the nanoemulsion demonstrated efficacy against the immature stages of the vector. The LC_{50} values ranged from 27.467 to 63.134 µL/L for larvae and from 49.662 to 96.436 µL/L for pupae, with greater toxicity observed in the larval stage. In addition, tests were conducted with *Artemia salina*, a non-target species, which showed mortality below 10%, even at high concentrations of the formulation. This suggests a low ecotoxicological risk and potential for safe application in mosquito control.

Ferreira et al. (2020) investigated the larvicidal effects of a nanoemulsion containing essential oil from *Siparuna guianensis,* a native Brazilian plant rich in oxygenated sesquiterpenes, the major components being curzerenone (18.86%) and α-muurolol (11.75%), in addition to the presence of the compounds curzerene and γ-muurolene [112]. The oil was extracted by hydrodistillation and incorporated into the nanoemulsion using a low-energy method, without heating and without solvents, using polysorbate 80 as the surfactant. The nanoemulsion had an average droplet size of 176.0 nm (±12.3) and a polydispersity index of 0.38 (±0.004). In the bioassays, third-stage larvae of *Aedes aegypti* were exposed for 24 and 48 hours. The nanoemulsion demonstrated significantly superior efficacy to the free essential oil, with CL_{50} values of 24.75 µg/mL after 24 hours and CL_{90} of 54.17 µg/mL after 48 hours, while the free essential oil presented CL_{50} of 86.52 µg/mL and CL_{90} of 134.81 µg/mL after 24 hours, and CL_{50} of 82.81 µg/mL and CL_{90} of 128.39 µg/mL after 48 hours. It is noteworthy that the formulation was not tested in non-target organisms.

Kaur et al. (2019) developed an optimized nanoemulsion containing *Eucalyptus globulus* essential oil for larvicidal control of *Ae. Aegypti* [139]. The plant, originally from Australia, is widely cultivated in tropical and subtropical regions. Although the oil used was not characterized in the study, its composition is known to be rich in compounds such as eucalyptol (1,8-cineole), gamma-terpinene, globulol, and gamma-pinene, with eucalyptol being considered the main agent responsible for the larvicidal action [139,140]. The nanoemulsion formulation was obtained in a 1:2 (v/v) ratio between the oil phase (oil + polysorbate 20) and water, prepared by magnetic stirring followed by ultrasonication (40 kHz). This formulation demonstrated physicochemical stability, with good optical transparency and absence of phase separation. Characterization by TEM revealed spherical droplets with sizes between 20 and 40 nm. In the larvicidal bioassay, fourth-instar larvae of *Ae. aegypti* were exposed to different concentrations of the nanoemulsion. The dose of 70 µg/mL was the most effective, promoting 100% mortality within 24 hours. The LC_{50} and LC_{90} values were 60.33 and 92.29 µg/mL, respectively.

Mishra et al. (2018) developed a nanoemulsion using *Azadirachta indica* (neem) oil, urea, and Tween® 20 as surfactant, by microfluidization [141]. Neem, originating from the Indian subcontinent and widely distributed in tropical and subtropical regions, has as its major constituents azadirachtin, nimbin, and salanin, recognized for their bioinsecticidal properties. The nanoemulsion presented an average droplet size of 12.3 ± 0.06 nm, polydispersity index of 0.249, and zeta potential of −21.7 ± 1.22 mV. In larvicidal bioassays with L3 larvae of *Aedes aegypti* (exposure: 24 hours), the LC_{50} value was 99.26 µg/mL, lower than that of the neem oil alone (123.59 µg/mL) and Tween 20 (169.30 µg/mL), indicating greater efficacy of the nanoformulation. No toxicological tests on non-target organisms were reported.

Balasubramani et al. (2017) developed a nanoemulsion with essential oil from *Vitex negundo* L., an Asian plant used for medicinal purposes [69,142]. The oil, rich in compounds such as 2*R*-acetoxymethyl-1,3,3-trimethylcyclohexanol (27.2%), nerolidol (14.6%), and β-caryophyllene (11.9%), was extracted by hydrodistillation (0.5% yield) [69,143]. The nanoemulsion was formulated with 5% essential oil, 5% polysorbate 80, and 90% water, resulting in droplets smaller than 200 nm and stability for 30 days. In bioassays with *Ae. aegypti* larvae, concentrations of 25 to 400 ppm of the nanoemulsion and free oil showed greater larvicidal efficacy of the nanoemulsion, with LC_{50} of 28.84 µg/mL (second instar, 24 hours) and 43.29 µg/mL (third instar, 24 hours), compared to the free oil, which presented LC_{50} of 77.35 µg/mL and 56.13 µg/mL, respectively.

Botas et al. (2017) developed a nanoemulsion based on the essential oil of *Baccharis reticularia*, a plant native to Brazil, also found in Paraguay, Bolivia, and Argentina. The oil is mainly composed of mono- and sesquiterpenes, including D-limonene, a key precursor in the biosynthesis of monoterpenes [73,144]. The formulation was obtained by a low-energy method, presenting an average droplet diameter of 92.9 nm (±0.4), polydispersity index of 0.412 (±0.009), and zeta potential of −20.4 mV (±0.6). In larvicidal tests with fourth-instar larvae of *Ae. aegypti* for 24 hours and 48 hours, the LC_{50} was 221.273 µg/mL and 144.685 µg/mL, respectively. Histological damage, such as changes in intestinal cells, was observed, indicating a potentially harmful effect on the larvae. Tests in non-target species were not performed.

Oliveira et al. (2016) prepared a nanoemulsion based on *Pterodon emarginatu*s essential oil and evaluated its larvicidal activity [145]. This species *Pterodon emarginatus*, popularly known as white sucupira or faveira, is a tree which is native to the Brazilian Cerrado [145,146]. The diterpenes methyl 6α,7β-dihydroxyvouacapan-17-β-oate (MHV), geranylgeraniol, and the sesquiterpene β-caryophyllene, reported in the literature for their larvicidal activity, stand out as constituents [145]. The formulation was tested against fourth-instar *Ae. aegypti* larvae at concentrations ranging from 12.5 to 250 µg/mL, with assessments conducted at 24 and 48 hours. Maximum mortality occurred at 250 µg/mL, while a notable increase in efficacy at 75 ppm was observed over extended exposure. Toxicological evaluation in *Mus musculus* revealed no signs of systemic toxicity, supporting the selective action of the formulation and safety for non-target organisms.

The studies (Table 1) suggest that nanoemulsions enhance the larvicidal properties of essential oils against *Ae. aegypti*, with efficacy varying according to the plant, composition, and formulation method. Many nanoemulsions have demonstrated stability over time and low toxicity to non-target species, making them a promising and sustainable solution for mosquito control.

Repellent properties

Essential oils have repellent properties against mosquitoes such as *Ae. aegypti.* Their efficacy has been enhanced when incorporated into nanoemulsions [147-150]. These nanostructured systems improve the stability, volatility, and skin permeation of the active compounds, prolonging the repellent effect due to the controlled release of these compounds [151,152]. The mechanism of action may involve interference with the olfactory system of the mosquitoes, masking host signals and disrupting orientation behavior [147] (Figure 4).

Despite the increased efficacy and potential of nanoemulsions containing essential oils against this vector, only three studies have evaluated the repellent efficacy of these nanoformulations in the last 10 years, the data for which are compiled in Table 2 and detailed below.

In addition to the larvicidal efficacy reported by Faustino and collaborators (2021), the authors also evaluated the efficacy of a nanoemulsion containing *Protium heptaphyllum e*ssential oil

Table 1: Overview of studies on the use of nanoemulsions with essential oils in the larvicidal control of *Aedes aegypti*.

Species	Nanoemulsion characterizations (size, polydispersity index, and zeta potential)	Larval stage of the *Ae. aegypti* tested	Time (hours)	LC_{50}	LC_{90}	Ref.
Murraya koenigii	size = 140.00 nm PdI = 0.24 ZP = –16.10 mV	L3	24	11.80 µg/mL (lab) 12.50 µg/mL (field)	22.60 µg/mL (lab) 21.60 µg/mL (field)	[108]
Ocimum basilicum	size = 244.60 to 280.40 PdI = Less than 0.25 ZP = –15.70 to –18.60 mV	L4	24 48	42.15 µg/mL 40.94 µg/mL	50.35 µg/mL 48.87 µg/mL	[76]
Ocotea indecora	size = 105.30 nm (±1.36) PdI = 0.26 (±0.004) ZP = –23.8 mV (±2.01)	L3	48 144	61.40 µg/mL 26.80 µg/mL	ND	[113]
Xylopia ochrantha	size = 74.50 nm (±1.939) PdI = 0.27 (±0.007) ZP = –25.15 mV (±0.65)	L3	48	192.50 µg/mL	ND	[111]
Trachyspermum ammi	size = 65.00 nm (±0.7) to 83.00 nm (±0.09) PdI = between 0.18 (±0.003) and 0.20 (±0.07)	L3	24	46.73 µg/mL	ND	[117]
Thymus vulgaris	size = 52.18 nm (±4.53) PdI = 0.23 (±0.006) ZP = 1.62 mV (±0.052)	L3	24	58.70 µg/mL	ND	[118]

Table 1: Overview of studies on the use of nanoemulsions with essential oils in the larvicidal control of *Aedes aegypti*. (continued)

Santalum album	size = 195.70 nm PdI = 0.34 ZP = –20.10 mV	L3	24 48	232.18 µg/mL 182.37 µg/mL	ND	[120]
Origanum vulgare	size = 64.10 nm (±6.3) PdI = 0.21 (±0.04)	L3	24	13.90 µg/mL	21.60 µg/mL	[72]
Ayapana triplinervis	size = 88.83 nm (±0.948) to morphotype A and 99.637 nm (±0.529) to morphotype B PdI = 0.138 (±0.012) to morphotype A and 0.213 (±0.011) to morphotype B ZP = –23.20 mV (±0.458) to morphotype A and –22.00 mV (±1.153) to morphotype B	L3	24 48	96.23 µg/mL (morphotype A) and 44.76 µg/mL (morphotype B) 87.43 µg/mL (morphotype A) and 35.57 µg/mL (morphotype B)	202.04 µg/mL (morphotype A) and 100.47 µg/mL (morphotype B) 177.21 µg/mL (morphotype A) and 117.45 µg/mL (morphotype B)	[125]
Protium heptaphyllum	size = 109.7 nm (±0.75) PdI = 0.29 (±0.007) ZP = –21.7 mV (±1.10)	L3	24 48	2.91 µg/mL 12.44 µg/mL	0.17 µg/mL and 8.87 µg/mL	[127]
Annona acutiflora	size = 171.10 nm (±1.2) PdI = 0.17 (±0.011) ZP = –15.0 mV (±0.53)	L3	24 48	36.00 µg/mL 21.20 µg/mL	ND	[128]
Aeollanthus suaveolens	size = 104.83 nm (±0.47) PdI = 0.16 (±0.01) ZP = –13.63 mV (±0.83)	L3	24 48	54.23 µg/mL 46.06 µg/mL	96.96 µg/mL 75.31 µg/mL	[130]
Piper alatipetiolatum	size = 316.0 nm (±8) PdI = 0.44 (±0.01) ZP = –8.50 mV (±0.14)	L3	24	6.370 µg/mL	21.70 µg/mL	[133]
Croton linearis	size = 175.0 nm PdI = 0.074 ZP = –27.02 mV	L4	24	17.86 µg/mL	ND	[135]
Crithmum maritimum	size = 50.0 and 70.0 nm ZP = –18.3 mV	Larval stage Pupae	24	27.47 to 48.94 µL/L 63.13 µL/L	65.80 to 105.14 µL/L 121.95 µL/L	[138]
Siparuna guianensis	size = 176.0 nm (±12.3) PdI = 0.381 (±0.004)	L3	24 48	24.75 µg/mL NI	75.24 µg/mL 54.17 µg/mL	[112]
Eucalyptus globulus	sizes between 20 and 40 nm	L4	12	60.33 µg/mL	92.29 µg/mL	[139]
Azadirachta indica	size = 12.30 nm (±0.06) PdI = 0.25 ZP = –21.70 mV (±1.22)	L3	24	99.26 µg/mL	ND	[141]
Vitex negundo	size = smaller than 200 nm	L2 L3	24	28.84 µg/mL 43.29 µg/mL	ND	[69]
Baccharis reticularia	size = 92.9 nm (±0.4) PdI = 0.412 (±0.009) ZP = –20.4 mV (±0.6)	L4	24 48	221.27 µg/mL 144.69 µg/mL	ND	[73]
Pterodon emarginatus	size = 135.8 nm (±0.2) PdI = 0.173 (±0.002) ZP = –27.2 (±0.6)	L4	24 48	– 34.75 µg/mL	ND	[145]

ND: not defined;
PdI: polydispersity index;
ZP: zeta potential.

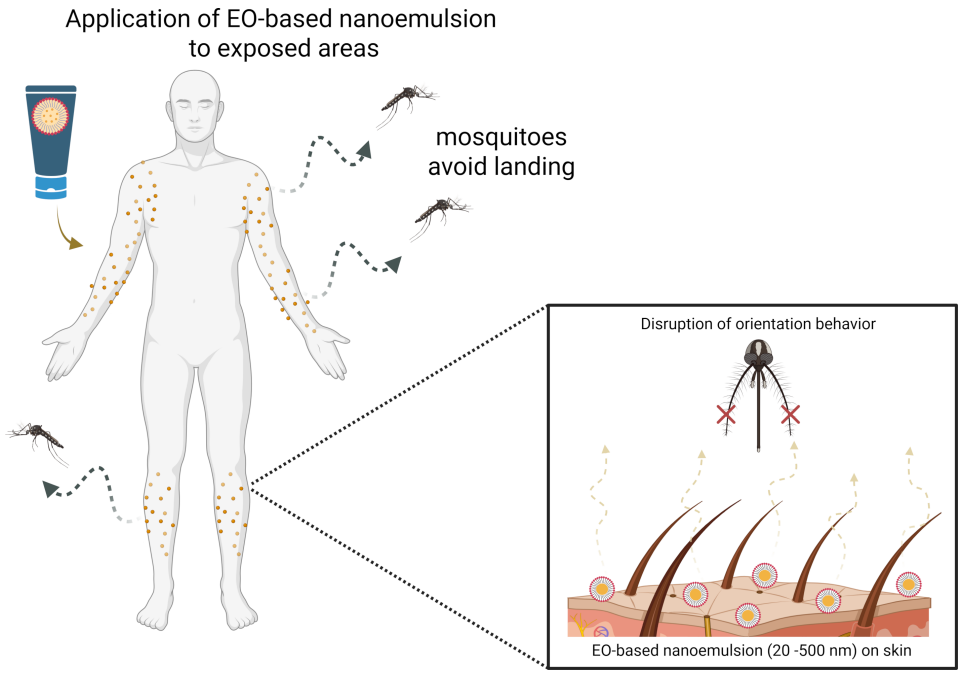

Figure 4: Schematic representation of the repellent mechanism of essential oil-based nanoemulsions against *Aedes aegypti* mosquitoes. Created in BioRender. Rocha Formiga, F. (2025) https://BioRender.com/7d1odbe. This content is not subject to CC BY 4.0.

Table 2: Recent studies (last 10 years) evaluating the repellent efficacy of nanoemulsions containing essential oils against *Aedes aegypti*.

Species	Nanoemulsion characterizations (size, polydispersity index, and zeta potential)	Concentration	Protection (percentage)	Time	Release	Ref.
Protium heptaphyllum	size = 109.00 nm (±0.75) PdI = 0.29 (±0.007) ZP = –21.70 mV (±1.10)	200 µg/mL	77.67%	3 h	ND	[150]
Myristica fragrans	size = 217.00 nm PdI = 0.25 ZP = –44.20 mV	ND	87.81%	8 h	53.3% in 8 h and 71.5% after 24 h	[148]
Mentha piperita and *Eucalyptus globulus*	size = 137.00 nm PdI = 0.28 ZP = –43.10 mV	ND	85.40%	8 h	51.7% after 8 h and 69.6% after 24 h	[149]

ND: not defined;
PdI: polydispersity index;
ZP: zeta potential.

[150]. This demonstrated significant repellent activity against adult females of *Ae. aegypti*. The repellency tests were conducted in a laboratory under controlled conditions, where samples of the nanoemulsion were applied to simulated human skin (using an artificial membrane) and exposed to previously fasted adult females of *Ae. aegypti*. The formulation, at a concentration of 200 µg/mL, provided a protection rate of 77.67% over 180 minutes (3 hours), demonstrating prolonged effect in relation to the free essential oil, which showed rapid loss of activity due to volatilization.

Mohd Narawi et al. (2020) developed a nanoemulsion with nutmeg essential oil (*Myristica fragrans*), an aromatic plant native to the Moluccan Islands and widely cultivated in tropical regions [148,153]. The oil, rich in α-pinene, safrole, and terpinen-4-ol, was encapsulated with Montanov 82, glycerol, and distilled water, resulting in droplets of approximately 217 nm, with a PdI of 0.248 and a zeta potential of −44.2 mV. The incorporation efficiency reached 85.4%, according to gas chromatography analysis. In the tests, Sprague Dawley rats received the formulation applied to their backs before being

exposed to 50 female *Ae. aegypti* for 8 hours. The average protection was 87.81%, surpassing the pure oil (54.57%) and falling below DEET (100%). The study also demonstrated controlled release of the active ingredient, with 53.3% released in 8 hours (33.31 mg/mL) and 71.5% after 24 hours. Finally, cytotoxicity tests were conducted, wherein the nanoemulsion maintained high cellular compatibility, with viability greater than 97% in murine fibroblasts (L929) up to concentrations of 400 µg/mL.

Finally, Mohammadi and colleagues (2020) evaluated the repellent efficacy of a nanoemulsion containing *Mentha piperita* and *Eucalyptus globulus* essential oils against *Ae. aegypti* [149]. These oils are widely found in tropical and temperate regions and are used for their aromatic and medicinal properties [154]. The chemical profiles of the oils include major constituents such as D-limonene, thymol, and carvacrol in *M. piperita*, and 1,8-cineole and γ-terpinene in *E. globulus* [149]. Thus, the oils were combined and incorporated using the high-pressure homogenization method, resulting in droplets with an average size of 137 nm, PdI of 0.279, and zeta potential of −43.1 mV.

Unlike previous authors, they verified the repellent efficacy in humans. The nanoemulsion was applied to the skin of volunteers before exposure to 50 female *Ae. aegypti* for 8 hours. The treatment obtained 85.4% protection, compared to that of the pure essential oil, which had a 57.4% efficacy. In addition, the formulation demonstrated a controlled release of the active compounds, with 51.7% released after 8 hours and 69.6% after 24 hours. Regarding safety, the cell viability of murine fibroblast cultures (L929 cells) was greater than 90% up to concentrations of 400 µg/mL, indicating low toxicity to human cells.

In summary, nanoemulsions improved the repellent efficacy of essential oils against *Aedes aegypti*, with efficacy varying according to the plant and the composition of the essential oils. Furthermore, these nanoemulsions demonstrate low toxicity given the high cell viability in tests with murine fibroblasts and safety in rats and humans, which makes them a promising and safe option for mosquito control.

General discussion and final considerations

This review gathered recent advances in the use of nanoemulsions containing essential oils as an alternative and eco-friendly tool for controlling *Aedes aegypti*.

Botanical diversity and chemical composition of essential oils

Regarding the plant species used, a wide botanical and geographic diversity was observed, including plants native to South America, Asia, and Europe. This variety is reflected in the chemical richness of the essential oils used, in which compounds such as thymol, carvacrol, β-caryophyllene, citronellol, and α-santalol stand out as the main agents responsible for the larvicidal and repellent effects. These metabolites act in a multifactorial manner, including inhibition of acetylcholinesterase, generation of reactive oxygen species, morphological damage, and impairment of the larval cuticular barriers.

In addition to the technical and methodological gaps, the challenges associated with the seasonality of the plant species used stand out. The variation in the chemical composition of essential oils throughout the year, influenced by environmental and phenological factors, can significantly impact the biological efficacy of formulations and hinder standardization on an industrial scale. This factor represents a significant practical obstacle, especially when seeking reproducibility of results and stability of products over time.

Surfactants composition of nanoemulsions

Among the technical and formulation aspects observed, the recurring use of nonionic surfactants, such as polysorbate 20, polysorbate 80, and sorbitan monoleate 80, stands out. These agents are widely used due to their low toxicity and high emulsifying capacity [155]. These agents promote the emulsification and stabilization of nanoemulsions. They can also influence aspects such as entrapment efficiency and release of active ingredients, aspects that still lack standardization in the studies evaluated. Additionally, nonionic surfactants can present zeta potential values below −30 mV, conferring steric stability on part of their chains, as observed in most studies reported in dilutions in purified water. Values above −30 mV may reflect EO compounds with ionizable groups, which confer electrical double layers and/or a diluent rich in salts, not reported by the authors [155]. Furthermore, although not evaluated by studies, the concentration and size of surfactant chains may influence droplet size distribution [156].

Challenges in the development of repellent nanoformulations

Despite the emphasis on the larvicidal activity, only three studies have addressed the repellent potential of these formulations, revealing a critical gap in the literature. The scarcity of data on repellency may be linked to the limitations imposed by ethics committees when conducting tests with humans and animals. In view of this, there is an urgent need to develop alternative and ethical approaches, such as predictive computational models (QSAR), diffusion systems with synthetic membranes, and automated bioassays to assess mosquito behavior.

The lack of studies on skin permeation and photostability also represents an important limitation. Repellent products intended

for topical application require validation regarding their ability to cross the epidermal barrier and resist degradation induced by sunlight. These characteristics are essential to ensure prolonged efficacy and user safety, especially under real-world conditions of use. The lack of such tests in the publications analyzed reveals a critical point that needs to be overcome in order to enable the translation of these nanostructured systems for commercial applications.

Another fundamental point is the lack of data on incorporation efficiency and in vitro release tests. These variables are crucial to ensuring the stability of the system, the maintenance of the content of bioactive compounds over time, and the correlation between the release of the active ingredient and the time of protection or larvicidal action. The lack of methodological standardization in this regard compromises not only the reproducibility of studies, but also the scalability of the products developed.

Assessment in non-target species

Additionally, the environmental and biological safety of formulations is a dimension that deserves greater attention. Although some authors have evaluated toxicity in non-target organisms such as *Danio rerio*, *Apis mellifera*, *Mus musculus*, *Galleria mellonella*, and *Artemia salina*, these tests are still isolated and do not predominate in the literature. Similarly, some studies have performed in vitro tests with human and murine cell lines, such as HaCaT (human keratinocytes) and L929 (murine fibroblasts), demonstrating low cytotoxicity at certain concentrations. However, these cellular safety assessments are still not prevalent among the reviewed studies, being treated more as complements than as fundamental validation steps.

Finally, even in view of the demonstrated potential, nanotechnology products such as nanoemulsions face considerable translational barriers. The lack of clear and specific regulations for the registration of nanostructured formulations for entomological purposes makes their regulation and commercialization difficult. This regulatory gap generates legal uncertainty and limits the advancement of innovative technologies in the market. Therefore, it is essential that regulatory frameworks be updated and adapted to contemplate the specific safety, efficacy and quality requirements of these new technological platforms.

Therefore, although nanoemulsions with essential oils show promising performance in controlling *Aedes aegypti*, the consolidation of this strategy requires an interdisciplinary effort aimed at standardizing critical parameters, deepening the mechanisms of action, validating safety and efficacy, and overcoming technical, regulatory, and environmental barriers. Future studies should prioritize the integration of physicochemical, biological, and toxicological data, as well as strategies for standardizing plant raw materials to ensure the development of effective, safe, and sustainable products.

Conclusion

The use of nanoemulsions based on essential oils is emerging as a viable and environmentally responsible alternative for controlling the *Aedes aegypti* vector. In addition to gathering evidence on their effectiveness, this review highlights the need for a paradigm shift in the way nanobiotechnological products are developed and evaluated. The future of this approach will depend not only on technical and scientific advances, but also on a regulatory environment prepared to welcome innovations with safety, transparency, and real applicability. This will consolidate the foundations for the development of safer and more efficient solutions that are compatible with current global public health challenges.

Acknowledgements

The Graphical Abstract was created in BioRender. Rocha Formiga, F. (2025) https://BioRender.com/flppu3h. This content is not subject to CC BY 4.0.

Funding

This work was supported by Programa Inova Fiocruz (VPPIS-004-FIO-22-2-91), FACEPE (BCT-0722-4.03/22; IBPG-2291-2.10/22; IBPG-0652-4.03/24), PIBIC-Fiocruz/CNPq and CNPq (313931/2021-6). In addition, this study was financed in part by the Coordenação de Aperfeiçoamento de Pessoal de Nível Superior – Brasil (CAPES) – Finance Code 001.

Conflict of Interest

The authors declare that they have no known competing financial interests or personal relationships that could have appeared to influence the work reported in this paper.

Author Contributions

Laryssa Ferreira do Nascimento Silva: conceptualization; investigation; methodology; visualization; writing – original draft; writing – review & editing. Douglas Dourado: conceptualization; investigation; methodology; project administration; supervision; visualization; writing – original draft; writing – review & editing. Thayse Silva Medeiros: investigation; methodology; supervision; visualization; writing – original draft; writing – review & editing. Mariana Alice Gonzaga Gabú: investigation; methodology; visualization; writing – original draft. Maria Cecilia Queiroga dos Santos: investigation; methodology; visualization; writing – original draft. Daiane Rodrigues dos Santos: investigation; methodology; visualization; writing – original draft. Mylena Lemos dos Santos: methodology; validation; vi-

sualization; writing – original draft. Gabriel Bezerra Faierstein: visualization; writing – original draft; writing – review & editing. Rosângela Maria Rodrigues Barbosa: supervision; visualization; writing – review & editing. Fabio Rocha Formiga: conceptualization; project administration; supervision; validation; visualization; writing – review & editing.

ORCID® iDs

Laryssa Ferreira do Nascimento Silva - https://orcid.org/0000-0002-6001-6659
Douglas Dourado - https://orcid.org/0000-0003-3445-5217
Mariana Alice Gonzaga Gabú - https://orcid.org/0009-0008-2029-3839
Maria Cecilia Queiroga dos Santos - https://orcid.org/0000-0001-7605-7300
Daiane Rodrigues dos Santos - https://orcid.org/0000-0003-1767-9892
Mylena Lemos dos Santos - https://orcid.org/0009-0001-3125-9352
Gabriel Bezerra Faierstein - https://orcid.org/0000-0002-1663-7642

Data Availability Statement

Data sharing is not applicable as no new data was generated or analyzed in this study.

References

1. Huang, Y.; Wang, S.; Liu, H.; Atoni, E.; Wang, F.; Chen, W.; Li, Z.; Rodriguez, S.; Yuan, Z.; Ming, Z.; Xia, H. *Sci. Data* **2023,** *10,* 305. doi:10.1038/s41597-023-02226-8
2. Huang, Y.-J. S.; Higgs, S.; Vanlandingham, D. L. *Curr. Opin. Virol.* **2019,** *34,* 104–109. doi:10.1016/j.coviro.2019.01.001
3. Côrtes, N.; Lira, A.; Prates-Syed, W.; Dinis Silva, J.; Vuitika, L.; Cabral-Miranda, W.; Durães-Carvalho, R.; Balan, A.; Cabral-Marques, O.; Cabral-Miranda, G. *Front. Immunol.* **2023,** *14,* 1281667. doi:10.3389/fimmu.2023.1281667
4. Young, P. R.; Ng, L. F. P.; Hall, R. A.; Smith, D. W.; Johansen, C. A. Arbovirus Infections. *Manson's Tropical Infectious Diseases;* Elsevier: Amsterdam, Netherlands, 2014; pp 129–161.e3. doi:10.1016/b978-0-7020-5101-2.00015-7
5. Patterson, J.; Sammon, M.; Garg, M. *West. J. Emerg. Med.* **2016,** *17,* 671–679. doi:10.5811/westjem.2016.9.30904
6. Gómez, M.; Martinez, D.; Muñoz, M.; Ramírez, J. D. *Parasites Vectors* **2022,** *15,* 287. doi:10.1186/s13071-022-05401-9
7. Kraemer, M. U. G.; Reiner, R. C., Jr.; Brady, O. J.; Messina, J. P.; Gilbert, M.; Pigott, D. M.; Yi, D.; Johnson, K.; Earl, L.; Marczak, L. B.; Shirude, S.; Davis Weaver, N.; Bisanzio, D.; Perkins, T. A.; Lai, S.; Lu, X.; Jones, P.; Coelho, G. E.; Carvalho, R. G.; Van Bortel, W.; Marsboom, C.; Hendrickx, G.; Schaffner, F.; Moore, C. G.; Nax, H. H.; Bengtsson, L.; Wetter, E.; Tatem, A. J.; Brownstein, J. S.; Smith, D. L.; Lambrechts, L.; Cauchemez, S.; Linard, C.; Faria, N. R.; Pybus, O. G.; Scott, T. W.; Liu, Q.; Yu, H.; Wint, G. R. W.; Hay, S. I.; Golding, N. *Nat. Microbiol.* **2019,** *4,* 854–863. doi:10.1038/s41564-019-0376-y
8. World Health Organization (WHO). Report on the global arbovirus surveillance and response capacity survey 2021-2022. https://www.who.int/publications/i/item/9789240107380 (accessed April 27, 2025).
9. World Health Organization (WHO). Global vector control response: progress in planning and implementation. https://www.who.int/publications/i/item/9789240007987 (accessed April 27, 2025).
10. Abbas, M. G.; Azeem, M.; Bashir, M. U.; Ali, F.; Mozūratis, R.; Binyameen, M. *Molecules* **2024,** *29,* 2657. doi:10.3390/molecules29112657
11. Parveen, A.; Abbas, M. G.; Keefover-Ring, K.; Binyameen, M.; Mozūraitis, R.; Azeem, M. *Molecules* **2024,** *29,* 1359. doi:10.3390/molecules29061359
12. de Andrade Silva, J. R.; de Oliveira, A. A.; França, L. P.; da Cruz, J. D.; Amaral, A. C. F. *Molecules* **2024,** *29,* 2240. doi:10.3390/molecules29102240
13. Radwan, I. T.; Khater, H. F.; Mohammed, S. H.; Khalil, A.; Farghali, M. A.; Mahmoud, M. G.; Selim, A.; Manaa, E. A.; Bagato, N.; Baz, M. M. *Sci. Rep.* **2024,** *14,* 6884. doi:10.1038/s41598-024-56802-y
14. Sonter, S.; Dwivedi, M. K.; Mishra, S.; Singh, P.; Kumar, R.; Park, S.; Jeon, B.-H.; Singh, P. K. *Sci. Rep.* **2024,** *14,* 16325. doi:10.1038/s41598-024-67148-w
15. Akoton, R.; Sovegnon, P. M.; Djihinto, O. Y.; Medjigbodo, A. A.; Agonhossou, R.; Saizonou, H. M.; Tchigossou, G. M.; Atoyebi, S. M.; Tossou, E.; Zeukeng, F.; Lagnika, H. O.; Mousse, W.; Adegnika, A. A.; Djouaka, R.; Djogbénou, L. S. *Malar. J.* **2023,** *22,* 385. doi:10.1186/s12936-023-04815-9
16. Abbasi, E.; Daliri, S. *PLoS Negl. Trop. Dis.* **2024,** *18,* e0011991. doi:10.1371/journal.pntd.0011991
17. Carrera, L. C.; Piedra, L.; Torres-Cosme, R.; Castillo, A. M.; Bruno, A.; Ramírez, J. L.; Martínez, D.; Rodríguez, M. M.; Bisset, J. A. *Trop. Med. Health* **2024,** *52,* 69. doi:10.1186/s41182-024-00637-w
18. Estep, A. S.; Sanscrainte, N. D.; Okech, B. A. *J. Am. Mosq. Control Assoc.* **2024,** *40,* 102–108. doi:10.2987/23-7160
19. Farag, S. M.; Moustafa, M. A. M.; Fónagy, A.; Kamel, O. M. H. M.; Abdel-Haleem, D. R. *Parasitol. Res.* **2024,** *123,* 110. doi:10.1007/s00436-024-08118-z
20. Priya, S. S.; Vasantha-Srinivasan, P.; Altemimi, A. B.; Keerthana, R.; Radhakrishnan, N.; Senthil-Nathan, S.; Kalaivani, K.; Chandrasekar, N.; Karthi, S.; Ganesan, R.; Alkanan, Z. T.; Pal, T.; Verma, O. P.; Proćków, J. *Molecules* **2023,** *28,* 2386. doi:10.3390/molecules28052386
21. Dutta, R. S.; Sahu, S.; Baishya, R.; Pachuau, L.; Kakoti, B. B.; Mazumder, B. *J. Vector Borne Dis.* **2024,** *61,* 107–116. doi:10.4103/0972-9062.392256
22. Tavares, M.; da Silva, M. R. M.; de Oliveira de Siqueira, L. B.; Rodrigues, R. A. S.; Bodjolle-d'Almeida, L.; dos Santos, E. P.; Ricci-Júnior, E. *Int. J. Pharm.* **2018,** *539,* 190–209. doi:10.1016/j.ijpharm.2018.01.046
23. Khan, S.; Sahar, A.; Tariq, T.; Sameen, A.; Tariq, F. Essential Oils in Plants: Plant Physiology, the Chemical Composition of the Oil, and Natural Variation of the Oils (Chemotaxonomy and Environmental Effects, Etc.). *Essential Oils;* Academic Press: London, UK, 2023; pp 1–36. doi:10.1016/b978-0-323-91740-7.00016-5
24. Tang, Y.; Li, H.; Song, Q. *Parasitol. Res.* **2024,** *123,* 315. doi:10.1007/s00436-024-08338-3
25. Fikru, S.; Tolossa, K.; Lindemann, P.; Bucar, F.; Asres, K. *J. Trop. Med.* **2024,** 1051086. doi:10.1155/2024/1051086
26. Vilvest, J.; Milton, M. C. J.; Yagoo, A.; Balakrishna, K. *Exp. Parasitol.* **2024,** *267,* 108858. doi:10.1016/j.exppara.2024.108858
27. Liñán-Atero, R.; Aghababaei, F.; García, S. R.; Hasiri, Z.; Ziogkas, D.; Moreno, A.; Hadidi, M. *Antioxidants* **2024,** *13,* 488. doi:10.3390/antiox13040488
28. Medeleanu, M. L.; Fărcaș, A. C.; Coman, C.; Leopold, L.; Diaconeasa, Z.; Socaci, S. A. *Food Chem.: X* **2023,** *20,* 100960. doi:10.1016/j.fochx.2023.100960

29. Moreira da Silva, T. L.; Beltrame, F. L.; Ferrari, P. C. *Arch. Pharm. (Weinheim, Ger.)* **2024,** *357,* 2300726. doi:10.1002/ardp.202300726
30. Khandehroo, F.; Moravvej, G.; Farhadian, N.; Ahmadzadeh, H. *Sci. Rep.* **2024,** *14,* 18567. doi:10.1038/s41598-024-69318-2
31. Sanei-Dehkordi, A.; Agholi, M.; Shafiei, M.; Osanloo, M. *Acta Parasitol.* **2022,** *67,* 1265–1272. doi:10.1007/s11686-022-00580-y
32. Sanei-Dehkordi, A.; Heiran, R.; Montaseri, Z.; Elahi, N.; Abbasi, Z.; Osanloo, M. *Acta Parasitol.* **2024,** *69,* 216–226. doi:10.1007/s11686-023-00735-5
33. AnnaDurai, K. S.; Chandrasekaran, N.; Velraja, S.; Hikku, G. S.; Parvathi, V. D. *Acta Trop.* **2024,** *257,* 107290. doi:10.1016/j.actatropica.2024.107290
34. de Souza, R. L.; Dantas, A. G. B.; Melo, C. d. O.; Felício, I. M.; Oliveira, E. E. *J. Drug Delivery Sci. Technol.* **2022,** *76,* 103834. doi:10.1016/j.jddst.2022.103834
35. Rehman, M.; Tahir, N.; Sohail, M. F.; Qadri, M. U.; Duarte, S. O. D.; Brandão, P.; Esteves, T.; Javed, I.; Fonte, P. *Pharmaceutics* **2024,** *16,* 1376. doi:10.3390/pharmaceutics16111376
36. Duarte, J. L.; Di Filippo, L. D.; de Faria Mota Oliveira, A. E. M.; Sábio, R. M.; Marena, G. D.; Bauab, T. M.; Duque, C.; Corbel, V.; Chorilli, M. *Beilstein J. Nanotechnol.* **2024,** *15,* 104–114. doi:10.3762/bjnano.15.10
37. Theochari, I.; Giatropoulos, A.; Papadimitriou, V.; Karras, V.; Balatsos, G.; Papachristos, D.; Michaelakis, A. *Insects* **2020,** *11,* 740. doi:10.3390/insects11110740
38. Lorenz, C.; Chiaravalloti-Neto, F. *Travel Med. Infect. Dis.* **2022,** *49,* 102428. doi:10.1016/j.tmaid.2022.102428
39. Stiasny, K.; Kiermayr, S.; Heinz, F. X. Entry Functions and Antigenic Structure of Flavivirus Envelope Proteins. *New Treatment Strategies for Dengue and Other Flaviviral Diseases;* Novartis Foundation Symposium, Vol. 277; John Wiley & Sons. doi:10.1002/0470058005.ch5
40. Musso, D.; Gubler, D. J. *Clin. Microbiol. Rev.* **2016,** *29,* 487–524. doi:10.1128/cmr.00072-15
41. Holmes, A. C.; Basore, K.; Fremont, D. H.; Diamond, M. S. *PLoS Pathog.* **2020,** *16,* e1008876. doi:10.1371/journal.ppat.1008876
42. Brown, R. S.; Wan, J. J.; Kielian, M. *Viruses* **2018,** *10,* 89. doi:10.3390/v10020089
43. Carvalho, F. D.; Moreira, L. A. *Neotrop. Entomol.* **2017,** *46,* 243–255. doi:10.1007/s13744-017-0520-4
44. Ferreira, Q. R.; Lemos, F. F. B.; Moura, M. N.; Nascimento, J. O. d. S.; Novaes, A. F.; Barcelos, I. S.; Fernandes, L. A.; Amaral, L. S. d. B.; Barreto, F. K.; Melo, F. F. d. *Viruses* **2023,** *15,* 779. doi:10.3390/v15030779
45. Rodrigues dos Santos, D.; Lopes Chaves, L.; Couto Pires, V.; Soares Rodrigues, J.; Alves Siqueira de Assunção, M.; Bezerra Faierstein, G.; Gomes Barbosa Neto, A.; de Souza Rebouças, J.; Christine de Magalhães Cabral Albuquerque, E.; Alexandre Beisl Vieira de Melo, S.; Costa Gaspar, M.; Maria Rodrigues Barbosa, R.; Elga Medeiros Braga, M.; Cipriano de Sousa, H.; Rocha Formiga, F. *Int. J. Pharm.* **2023,** *643,* 123221. doi:10.1016/j.ijpharm.2023.123221
46. Reinhold, J.; Lazzari, C.; Lahondère, C. *Insects* **2018,** *9,* 158. doi:10.3390/insects9040158
47. Edillo, F.; Ymbong, R. R.; Bolneo, A. A.; Hernandez, R. J.; Fuentes, B. L.; Cortes, G.; Cabrera, J.; Lazaro, J. E.; Sakuntabhai, A. *Parasites Vectors* **2022,** *15,* 74. doi:10.1186/s13071-022-05186-x
48. Oliveira, L. M. S.; Brito, T. B.; de Sena Filho, J. G.; Cavalcanti, S. C. d. H. *Rev. Bras. Farmacogn.* **2023,** *34,* 48–64. doi:10.1007/s43450-023-00445-z
49. David, M. R.; Lourenço-de-Oliveira, R.; Freitas, R. M. d. *Mem. Inst. Oswaldo Cruz* **2009,** *104,* 927–932. doi:10.1590/s0074-02762009000600019
50. Harrington, L. C.; Scott, T. W.; Lerdthusnee, K.; Coleman, R. C.; Costero, A.; Clark, G. G.; Jones, J. J.; Kitthawee, S.; Kittayapong, P.; Sithiprasasna, R.; Edman, J. D. *Am. J. Trop. Med. Hyg.* **2005,** *72,* 209–220. doi:10.4269/ajtmh.2005.72.209
51. Mundim-Pombo, A. P. M.; de Carvalho, H. J. C.; Rodrigues Ribeiro, R.; León, M.; Maria, D. A.; Miglino, M. A. *Parasites Vectors* **2021,** *14,* 531. doi:10.1186/s13071-021-05024-6
52. World Health Organization. Global Arbovirus Initiative. https://www.who.int/initiatives/global-arbovirus-initiative (accessed April 27, 2025).
53. Roy, S. K.; Bhattacharjee, S. *Can. J. Microbiol.* **2021,** *67,* 687–702. doi:10.1139/cjm-2020-0572
54. Vairo, F.; Haider, N.; Kock, R.; Ntoumi, F.; Ippolito, G.; Zumla, A. *Infect. Dis. Clin. North Am.* **2019,** *33,* 1003–1025. doi:10.1016/j.idc.2019.08.006
55. Goupil, B. A.; Mores, C. N. *Open Rheumatol. J.* **2016,** *10,* 129–140. doi:10.2174/1874312901610010129
56. Leta, S.; Beyene, T. J.; De Clercq, E. M.; Amenu, K.; Kraemer, M. U. G.; Revie, C. W. *Int. J. Infect. Dis.* **2018,** *67,* 25–35. doi:10.1016/j.ijid.2017.11.026
57. D'Ortenzio, E.; Matheron, S.; de Lamballerie, X.; Hubert, B.; Piorkowski, G.; Maquart, M.; Descamps, D.; Damond, F.; Yazdanpanah, Y.; Leparc-Goffart, I. *N. Engl. J. Med.* **2016,** *374,* 2195–2198. doi:10.1056/nejmc1604449
58. Ferraris, P.; Yssel, H.; Missé, D. *Microbes Infect.* **2019,** *21,* 353–360. doi:10.1016/j.micinf.2019.04.005
59. Besnard, M.; Lastere, S.; Teissier, A.; Cao-Lormeau, V. M.; Musso, D. *Eurosurveillance* **2014,** *19,* 20751. doi:10.2807/1560-7917.es2014.19.13.20751
60. Achee, N. L.; Grieco, J. P.; Vatandoost, H.; Seixas, G.; Pinto, J.; Ching-NG, L.; Martins, A. J.; Juntarajumnong, W.; Corbel, V.; Gouagna, C.; David, J.-P.; Logan, J. G.; Orsborne, J.; Marois, E.; Devine, G. J.; Vontas, J. *PLoS Negl. Trop. Dis.* **2019,** *13,* e0007275. doi:10.1371/journal.pntd.0007275
61. Callaway, E. *Nature* **2016,** *539,* 17–18. doi:10.1038/nature.2016.20878
62. Aliota, M. T.; Walker, E. C.; Uribe Yepes, A.; Dario Velez, I.; Christensen, B. M.; Osorio, J. E. *PLoS Negl. Trop. Dis.* **2016,** *10,* e0004677. doi:10.1371/journal.pntd.0004677
63. Gubler, D. J.; Vasilakis, N. The Arboviruses: Quo Vadis?. *Arboviruses: Molecular Biology, Evolution and Control;* Caister Academic Press, 2016; pp 1–6. doi:10.21775/9781910190210.01
64. Newman, D. J.; Cragg, G. M. *J. Nat. Prod.* **2016,** *79,* 629–661. doi:10.1021/acs.jnatprod.5b01055
65. Asbahani, A. E.; Miladi, K.; Badri, W.; Sala, M.; Addi, E. H. A.; Casabianca, H.; Mousadik, A. E.; Hartmann, D.; Jilale, A.; Renaud, F. N. R.; Elaissari, A. *Int. J. Pharm.* **2015,** *483,* 220–243. doi:10.1016/j.ijpharm.2014.12.069
66. Mohamed, A. A.; Alotaibi, B. M. *J. Umm Al-Qura Univ. Appl. Sci.* **2023,** *9,* 40–49. doi:10.1007/s43994-022-00018-1
67. Movahedi, F.; Nirmal, N.; Wang, P.; Jin, H.; Grøndahl, L.; Li, L. *J. Anim. Sci. Biotechnol.* **2024,** *15,* 110. doi:10.1186/s40104-024-01067-8

68. Sharma, A. D.; Kaur, I.; Chauhan, A. *J. Umm Al-Qura Univ. Appl. Sci.* **2024,** *10,* 313–329. doi:10.1007/s43994-023-00108-8
69. Balasubramani, S.; Rajendhiran, T.; Moola, A. K.; Diana, R. K. B. *Environ. Sci. Pollut. Res.* **2017,** *24,* 15125–15133. doi:10.1007/s11356-017-9118-y
70. Maurya, A.; Prasad, J.; Das, S.; Dwivedy, A. K. *Front. Sustainable Food Syst.* **2021,** *5,* 653420. doi:10.3389/fsufs.2021.653420
71. Nascimento, A. M. D.; Maia, T. D. S.; Soares, T. E. S.; Menezes, L. R. A.; Scher, R.; Costa, E. V.; Cavalcanti, S. C. H.; La Corte, R. *Neotrop. Entomol.* **2017,** *46,* 223–230. doi:10.1007/s13744-016-0457-z
72. Almadiy, A. A.; Nenaah, G. E. *J. Essent. Oil Res.* **2022,** *34,* 424–438. doi:10.1080/10412905.2022.2091673
73. Botas, G.; Cruz, R.; De Almeida, F.; Duarte, J.; Araújo, R.; Souto, R.; Ferreira, R.; Carvalho, J.; Santos, M.; Rocha, L.; Pereira, V.; Fernandes, C. *Molecules* **2017,** *22,* 1990. doi:10.3390/molecules22111990
74. Manh, H. D.; Tuyet, O. T. *Insects* **2020,** *11,* 198. doi:10.3390/insects11030198
75. Zhu, J.; Zeng, X.; Liu, T.; Qian, K.; Han, Y.; Xue, S.; Tucker, B.; Schultz, G.; Coats, J.; Rowley, W.; Zhang, A. *J. Am. Mosq. Control Assoc.* **2006,** *22,* 515–522. doi:10.2987/8756-971x(2006)22[515:aralao]2.0.co;2
76. de Sousa dos Santos, E. L. V.; Cruz, J. N.; da Costa, G. V.; de Sá, E. M. F.; da Silva, A. K. P.; Fernandes, C. P.; de Faria Mota Oliveira, A. E. M.; Duarte, J. L.; Bezerra, R. M.; Tavares, J. F.; da Costa, T. S.; dos Anjos Ferreira, R. M.; dos Santos, C. B. R.; Souto, R. N. P. *Separations* **2024,** *11,* 97. doi:10.3390/separations11040097
77. Muturi, E. J.; Ramirez, J. L.; Doll, K. M.; Bowman, M. J. *J. Med. Entomol.* **2017,** *54,* 1684–1691. doi:10.1093/jme/tjx168
78. Pavela, R.; Benelli, G. *Trends Plant Sci.* **2016,** *21,* 1000–1007. doi:10.1016/j.tplants.2016.10.005
79. Yi, T.; Wan, J.; Xu, H.; Yang, X. *Eur. J. Pharm. Biopharm.* **2008,** *70,* 439–444. doi:10.1016/j.ejpb.2008.05.001
80. Singh, Y.; Meher, J. G.; Raval, K.; Khan, F. A.; Chaurasia, M.; Jain, N. K.; Chourasia, M. K. *J. Controlled Release* **2017,** *252,* 28–49. doi:10.1016/j.jconrel.2017.03.008
81. Oliveira, A. E. M. F. M.; Bezerra, D. C.; Duarte, J. L.; Cruz, R. A. S.; Souto, R. N. P.; Ferreira, R. M. A.; Nogueira, J.; da Conceição, E. C.; Leitão, S.; Bizzo, H. R.; Gama, P. E.; Carvalho, J. C. T.; Fernandes, C. P. *Sustainable Chem. Pharm.* **2017,** *6,* 1–9. doi:10.1016/j.scp.2017.06.001
82. Duarte, J.; Sharma, A.; Sharifi, E.; Damiri, F.; Berrada, M.; Khan, M. A.; Singh, S. K.; Dua, K.; Veiga, F.; Mascarenhas-Melo, F.; Pires, P. C.; Paiva-Santos, A. C. *Appl. Mater. Today* **2023,** *35,* 102001. doi:10.1016/j.apmt.2023.102001
83. Jia, Y.; Jiang, Y.; He, Y.; Zhang, W.; Zou, J.; Magar, K. T.; Boucetta, H.; Teng, C.; He, W. *Pharmaceutics* **2023,** *15,* 774. doi:10.3390/pharmaceutics15030774
84. Chen, J.; Zhao, Z.; Alantary, D.; Huang, J. *Eur. J. Pharm. Biopharm.* **2025,** *207,* 114597. doi:10.1016/j.ejpb.2024.114597
85. Haftcheshmeh, S. M.; Jaafari, M. R.; Mashreghi, M.; Mehrabian, A.; Alavizadeh, S. H.; Zamani, P.; Zarqi, J.; Darvishi, M. H.; Gheybi, F. *J. Drug Delivery Sci. Technol.* **2021,** *62,* 102351. doi:10.1016/j.jddst.2021.102351
86. Zhang, X.; Chan, H. W.; Shao, Z.; Wang, Q.; Chow, S.; Chow, S. F. *Int. J. Pharm.* **2025,** *671,* 125202. doi:10.1016/j.ijpharm.2025.125202
87. Graván, P.; Aguilera-Garrido, A.; Marchal, J. A.; Navarro-Marchal, S. A.; Galisteo-González, F. *Adv. Colloid Interface Sci.* **2023,** *314,* 102871. doi:10.1016/j.cis.2023.102871
88. Moghassemi, S.; Dadashzadeh, A.; Azevedo, R. B.; Amorim, C. A. *J. Controlled Release* **2022,** *351,* 164–173. doi:10.1016/j.jconrel.2022.09.035
89. Pahwa, R.; Sharma, G.; Chhabra, J.; Haider, T.; Anitha, K.; Mishra, N. *J. Drug Delivery Sci. Technol.* **2024,** *101,* 106227. doi:10.1016/j.jddst.2024.106227
90. de Souza, M. L.; Oliveira, D. D.; Pereira, N. d. P.; Soares, D. M. *Int. J. Dermatol.* **2018,** *57,* 894–900. doi:10.1111/ijd.14028
91. Musakhanian, J.; Osborne, D. W. *AAPS PharmSciTech* **2025,** *26,* 31. doi:10.1208/s12249-024-02997-2
92. Begum JP, S.; Sahu, P.; Vinode, R.; Patel, A.; Alomary, M. N.; Begum, M. Y.; Jamous, Y. F.; Siddiqua, A.; Al Fatease, A.; Ansari, M. A. *J. Saudi Chem. Soc.* **2024,** *28,* 101896. doi:10.1016/j.jscs.2024.101896
93. Preeti; Sambhakar, S.; Malik, R.; Bhatia, S.; Al Harrasi, A.; Rani, C.; Saharan, R.; Kumar, S.; Geeta; Sehrawat, R. *Scientifica* **2023,** 6640103. doi:10.1155/2023/6640103
94. Meghani, N.; Patel, P.; Kansara, K.; Ranjan, S.; Dasgupta, N.; Ramalingam, C.; Kumar, A. *Colloids Surf., B* **2018,** *166,* 349–357. doi:10.1016/j.colsurfb.2018.03.041
95. de Souza, R. L.; Opretzka, L. C. F.; de Morais, M. C.; de Oliveira Melo, C.; de Oliveira, B. E. G.; de Sousa, D. P.; Villarreal, C. F.; Oliveira, E. E. *Pharmaceuticals* **2023,** *17,* 17. doi:10.3390/ph17010017
96. Ma, H. L.; Varanda, L. C.; Perussi, J. R.; Carrilho, E. *J. Photochem. Photobiol., B* **2021,** *223,* 112303. doi:10.1016/j.jphotobiol.2021.112303
97. Jiang, H.; Zhong, S.; Schwarz, P.; Chen, B.; Rao, J. *Food Chem.* **2023,** *400,* 134016. doi:10.1016/j.foodchem.2022.134016
98. Streck, L.; Sarmento, V. H. V.; de Menezes, R. P. R. P. B.; Fernandes-Pedrosa, M. F.; Martins, A. M. C.; da Silva-Júnior, A. A. *Int. J. Pharm.* **2019,** *555,* 36–48. doi:10.1016/j.ijpharm.2018.11.041
99. Kawakami, M. Y. M.; Zamora, L. O.; Araújo, R. S.; Fernandes, C. P.; Ricotta, T. Q. N.; de Oliveira, L. G.; Queiroz-Junior, C. M.; Fernandes, A. P.; da Conceição, E. C.; Ferreira, L. A. M.; Barros, A. L. B.; Aguiar, M. G.; Oliveira, A. E. M. F. M. *Biomed. Pharmacother.* **2021,** *134,* 111109. doi:10.1016/j.biopha.2020.111109
100. Tan, T. N.; Mnocaran, Y. P. A.; Ramli, M. E.; Utra, U.; Ariffin, F.; Yussof, N. S. *ACS Food Sci. Technol.* **2023,** *3,* 150–160. doi:10.1021/acsfoodscitech.2c00296
101. Duarte, J. L.; Duchon, S.; Di Filippo, L. D.; Chorilli, M.; Corbel, V. *PLoS One* **2024,** *19,* e0293124. doi:10.1371/journal.pone.0293124
102. Sharma, S.; Loach, N.; Gupta, S.; Mohan, L. *Environ. Nanotechnol. Monit. Manage.* **2020,** *14,* 100331. doi:10.1016/j.enmm.2020.100331
103. Wei, N.; Hou, C.; Liu, Z.; Liang, Q.; Lv, Z.; Meng, X.; Feng, J. *Colloids Surf., A* **2023,** *656,* 130442. doi:10.1016/j.colsurfa.2022.130442
104. Shaari, A.; Yunus, R.; Raman, I. A.; Omar, D.; Shahar, M. K.; Awang Biak, D. R.; Kania, D.; Aulia, A. *Acta Trop.* **2021,** *224,* 106107. doi:10.1016/j.actatropica.2021.106107
105. Firooziyan, S.; Osanloo, M.; Basseri, H. R.; Moosa-Kazemi, S. H.; Mohammadzadeh Hajipirloo, H.; Amani, A.; Sedaghat, M. M. *Arabian J. Chem.* **2022,** *15,* 104064. doi:10.1016/j.arabjc.2022.104064

106. Wardani, A. T.; Kusumaningsih, T.; Ainurofiq, A. *Biodiversitas* **2024,** *25,* 990–997. doi:10.13057/biodiv/d250311
107. Bendjazia, R.; Dris, D.; Seghier, H.; Essid, R.; Jallouli, S.; Tabbene, O.; Bouabida, H. *S. Afr. J. Bot.* **2025,** *180,* 512–519. doi:10.1016/j.sajb.2025.03.029
108. Romano, C. A.; de Oliveira Neto, J. R.; da Cunha, L. C.; dos Santos, A. H.; de Paula, J. R. *Ind. Crops Prod.* **2024,** *208,* 117836. doi:10.1016/j.indcrop.2023.117836
109. Balakrishnan, R.; Vijayraja, D.; Jo, S.-H.; Ganesan, P.; Su-Kim, I.; Choi, D.-K. *Antioxidants* **2020,** *9,* 101. doi:10.3390/antiox9020101
110. Etsassala, N. G. E. R.; Hussein, A. A.; Nchu, F. *Plants* **2021,** *10,* 279. doi:10.3390/plants10020279
111. Viana, V. C. R.; Machado, F. P.; Esteves, R.; Duarte, J. A. D.; Enríquez, J. J. S.; Campaz, M. L. M.; Oliveira, E. E.; Santos, M. G.; Ricci-Junior, E.; Ruppelt, B. M.; Rocha, L. *Sustainable Chem. Pharm.* **2023,** *32,* 100992. doi:10.1016/j.scp.2023.100992
112. Ferreira, R. M. d. A.; D'haveloose, N. P.; Cruz, R. A. S.; Araújo, R. S.; Carvalho, J. C. T.; Rocha, L.; Fernandes, L. P.; Da Costa, T. S.; Fernandes, C. P.; Souto, R. N. P. *J. Med. Entomol.* **2020,** *57,* 788–796. doi:10.1093/jme/tjz221
113. Pinto, L. d. A.; Machado, F. P.; Esteves, R.; Farias, V. M.; Köptcke, F. B. N.; Ricci-Junior, E.; Rocha, L.; Keller, L. A. M. *Molecules* **2023,** *28,* 3437. doi:10.3390/molecules28083437
114. Paiva Machado, F.; da Silva Rangel, L.; Nunes Farias Gomes, K.; Albuquerque dos Santos, J. A.; Xavier Faria, R.; Santos, M. G.; Fernandes, C. P.; Rocha, L. *Exp. Parasitol.* **2024,** *259,* 108717. doi:10.1016/j.exppara.2024.108717
115. de Almeida Gonçalves, R.; Pinheiro, A. B.; de Oliveira, M. A.; do Nascimento, R. T.; Rosalem, P. F.; Garcia, V. L.; Martins, A. R. *Rev. Bras. Farmacogn.* **2018,** *28,* 1–8. doi:10.1016/j.bjp.2017.11.008
116. Hosseinizadeh, Z.; Osanloo, M.; Alipour, H.; Heiran, R.; Shahriari-Namadi, M.; Moemenbellah-Fard, M. D. *Exp. Parasitol.* **2023,** *255,* 108644. doi:10.1016/j.exppara.2023.108644
117. Subaharan, K.; Senthamarai Selvan, P.; Subramanya, T. M.; Senthoorraja, R.; Manjunath, S.; Das, T.; Pragadheesh, V. S.; Bakthavatsalam, N.; Mohan, M. G.; Senthil-Nathan, S.; Uragayala, S.; Samuel, P. P.; Govindarajan, R.; Eswaramoorthy, M. *Environ. Sci. Pollut. Res.* **2022,** *29,* 71326–71337. doi:10.1007/s11356-022-20870-2
118. Gupta, P.; Preet, S.; Ananya; Singh, N. *Sci. Rep.* **2022,** *12,* 4335. doi:10.1038/s41598-022-07676-5
119. Vassiliou, E.; Awoleye, O.; Davis, A.; Mishra, S. *Int. J. Mol. Sci.* **2023,** *24,* 6936. doi:10.3390/ijms24086936
120. Bosly, H. A. E.-K. *Saudi J. Biol. Sci.* **2022,** *29,* 103455. doi:10.1016/j.sjbs.2022.103455
121. Pullaiah, T.; Karuppusamy, S. Botany of Sandalwood (Santalum Album L.). *Sandalwood: Silviculture, Conservation and Applications;* Springer: Singapore, 2021; pp 21–48. doi:10.1007/978-981-16-0780-6_3
122. Misra, B. B.; Dey, S. *Trees (Heidelberg, Ger.)* **2013,** *27,* 1071–1086. doi:10.1007/s00468-013-0858-0
123. Khan, M.; Khan, S. T.; Khan, N. A.; Mahmood, A.; Al-Kedhairy, A. A.; Alkhathlan, H. Z. *Arabian J. Chem.* **2018,** *11,* 1189–1200. doi:10.1016/j.arabjc.2018.02.008
124. Bhattacharyya, M.; Easmin, S.; Pal, K.; Sahu, R.; Nandi, G.; Sahariah, B. J.; Dutta, K. N.; Deka, M. K.; Maiti, P. P.; Dua, T. K. *Pharmacol. Res. Nat. Prod.* **2023,** *1,* 100002. doi:10.1016/j.prenap.2023.100002
125. Lobato Rodrigues, A. B.; Martins, R. L.; Rabelo, É. d. M.; Tomazi, R.; Santos, L. L.; Brandão, L. B.; Faustino, C. G.; Ferreira Farias, A. L.; dos Santos, C. B. R.; de Castro Cantuária, P.; Galardo, A. K. R.; de Almeida, S. S. M. d. S. *PLoS One* **2021,** *16,* e0254225. doi:10.1371/journal.pone.0254225
126. Mobin, M.; De Lima, S. G.; Almeida, L. T. G.; Takahashi, J. P.; Teles, J. B.; Szeszs, M. W.; Martins, M. A.; Carvalho, A. A.; Melhem, M. S. C. *Rev. Bras. Plant. Med.* **2016,** *18,* 531–538. doi:10.1590/1983-084x/15_110
127. Faustino, C. G.; de Medeiros, F. A.; Ribeiro Galardo, A. K.; Lobato Rodrigues, A. B.; Lopes Martins, R.; de Medeiros Souza Lima, Y.; Fechine Tavares, J.; Alves de Medeiros, M. A.; dos Santos Cruz, J.; Almeida, S. S. M. d. S. d. *Molecules* **2020,** *25,* 5333. doi:10.3390/molecules25225333
128. Folly, D.; Machado, F. P.; Esteves, R.; Duarte, J. L.; Cruz, R. A. S.; Oliveira, A. E. M. F. M.; Ferreira, R. M. A.; Souto, R. N. P.; Santos, M. G.; Carvalho, J. C. T.; Ruppelt, B. M.; Fernandes, C. P.; Rocha, L. *J. Essent. Oil Res.* **2021,** *33,* 559–566. doi:10.1080/10412905.2021.1966847
129. Joseph, S. M.; Dev, A. R. A.; A, K. *J. Mol. Struct.* **2023,** *1292,* 136082. doi:10.1016/j.molstruc.2023.136082
130. Lopes Martins, R.; Bruno Lobato Rodrigues, A.; de Menezes Rabelo, É.; Lima Santos, L.; Barreto Brandão, L.; Gomes Faustino, C.; Luzia Ferreira Farias, A.; Maria da Cunha Sá, D.; de Castro Cantuária, P.; Kardec Ribeiro Galardo, A.; Susan Moreira da Silva de Almeida, S. *Arabian J. Chem.* **2021,** *14,* 103148. doi:10.1016/j.arabjc.2021.103148
131. Martins, R. L.; Simões, R. C.; Rabelo, É. d. M.; Farias, A. L. F.; Rodrigues, A. B. L.; Ramos, R. d. S.; Fernandes, J. B.; Santos, L. d. S.; de Almeida, S. S. M. d. S. *PLoS One* **2016,** *11,* e0166684. doi:10.1371/journal.pone.0166684
132. Simionatto, E.; Porto, C.; Stüker, C. Z.; Dalcol, I. I.; Silva, U. F. d. *Quim. Nova* **2007,** *30,* 1923–1925. doi:10.1590/s0100-40422007000800024
133. de Oliveira, A. C.; Sá, I. S. C.; Mesquita, R. S.; Pereira, B. L.; Pocrifka, L. A.; de Souza, T. P.; Rodriguez Amado, J. R.; Azevedo, S. G.; Sanches, E. A.; Nunomura, S. M.; Roque, R. A.; Tadei, W. P.; Nunomura, R. C. S. *Rev. Bras. Farmacogn.* **2020,** *30,* 667–677. doi:10.1007/s43450-020-00092-8
134. da Costa, M. L. L.; de Oliveira, A. C.; Roque, R. A. *Pestic. Biochem. Physiol.* **2024,** *200,* 105809. doi:10.1016/j.pestbp.2024.105809
135. Amado, J. R. R.; Prada, A. L.; Diaz, J. G.; Souto, R. N. P.; Arranz, J. C. E.; de Souza, T. P. *Environ. Sci. Pollut. Res.* **2020,** *27,* 9410–9423. doi:10.1007/s11356-020-07608-8
136. García Díaz, J.; Tuenter, E.; Escalona Arranz, J. C.; Llauradó Maury, G.; Cos, P.; Pieters, L. *J. Ethnopharmacol.* **2019,** *236,* 250–257. doi:10.1016/j.jep.2019.01.049
137. Vuković, D.; Božović, M.; Caković, D.; Petrović, D.; Živković, V. *Nat. Prod. Res.* **2024,** 1–4. doi:10.1080/14786419.2024.2440514
138. Suresh, U.; Murugan, K.; Panneerselvam, C.; Aziz, A. T.; Cianfaglione, K.; Wang, L.; Maggi, F. *Ind. Crops Prod.* **2020,** *158,* 113033. doi:10.1016/j.indcrop.2020.113033
139. Kaur, N.; Kocher, D. K.; Sidhu, A. *Afr. Entomol.* **2019,** *27,* 433. doi:10.4001/003.027.0433
140. Yip, S. C.; Ho, L. Y.; Wu, T.-Y.; Sit, N. W. *Ind. Crops Prod.* **2024,** *222,* 120118. doi:10.1016/j.indcrop.2024.120118

141. Mishra, P.; Samuel, M. K.; Reddy, R.; Tyagi, B. K.; Mukherjee, A.; Chandrasekaran, N. *Environ. Sci. Pollut. Res.* **2018,** *25,* 2211–2230. doi:10.1007/s11356-017-0591-0
142. Kamal, N.; Mio Asni, N. S.; Rozlan, I. N. A.; Mohd Azmi, M. A. H.; Mazlan, N. W.; Mediani, A.; Baharum, S. N.; Latip, J.; Assaw, S.; Edrada-Ebel, R. A. *Plants* **2022,** *11,* 1944. doi:10.3390/plants11151944
143. Issa, M.; Chandel, S.; Pal Singh, H.; Rani Batish, D.; Kumar Kohli, R.; Singh Yadav, S.; Kumari, A. *Ind. Crops Prod.* **2020,** *145,* 112083. doi:10.1016/j.indcrop.2019.112083
144. Lima, L. A.; Ferreira-Sá, P. S.; Garcia, M. D. N., Jr.; Pereira, V. L. P.; Carvalho, J. C. T.; Rocha, L.; Fernandes, C. P.; Souto, R. N. P.; Araújo, R. S.; Botas, G.; Cruz, R. A. S. *Ind. Crops Prod.* **2021,** *162,* 113282. doi:10.1016/j.indcrop.2021.113282
145. Oliveira, A. E. M. F. M.; Duarte, J. L.; Amado, J. R. R.; Cruz, R. A. S.; Rocha, C. F.; Souto, R. N. P.; Ferreira, R. M. A.; Santos, K.; da Conceição, E. C.; de Oliveira, L. A. R.; Kelecom, A.; Fernandes, C. P.; Carvalho, J. C. T. *PLoS One* **2016,** *11,* e0145835. doi:10.1371/journal.pone.0145835
146. Costa-Singh, T.; Jorge, N. *Braz. Arch. Biol. Technol.* **2019,** *62,* e19170758. doi:10.1590/1678-4324-2019170758
147. Sakulku, U.; Nuchuchua, O.; Uawongyart, N.; Puttipipatkhachorn, S.; Soottitantawat, A.; Ruktanonchai, U. *Int. J. Pharm.* **2009,** *372,* 105–111. doi:10.1016/j.ijpharm.2008.12.029
148. Mohd Narawi, M.; Chiu, H. I.; Yong, Y. K.; Mohamad Zain, N. N.; Ramachandran, M. R.; Tham, C. L.; Samsurrijal, S. F.; Lim, V. *Front. Pharmacol.* **2020,** *11,* 214. doi:10.3389/fphar.2020.00214
149. Mohammadi, R.; Khoobdel, M.; Talebi, A. A.; Negahban, M.; Norani, M.; Moradi, M.; Dehghan, O. *Open Biotechnol. J.* **2020,** *14,* 145–152. doi:10.2174/1874070702014010145
150. Faustino, C. G.; de Medeiros, F. A.; Galardo, A. K. R.; Rodrigues, A. B. L.; da Costa, A. L. P.; Martins, R. L.; Brandão, L. B.; Santos, L. L.; de Medeiros, M. A. A.; de Castro Cantuária, P.; Farias, A. L. F.; Cruz, J. S.; da Silva de Almeida, S. S. M. *Molecules* **2021,** *26,* 6439. doi:10.3390/molecules26216439
151. Nwagwu, C.; Onugwu, A.; Echezona, A.; Uzondu, S.; Agbo, C.; Kenechukwu, F.; Ogbonna, J.; Ugorji, L.; Nwobi, L.; Nwobi, O.; Mmuotoo, O.; Ezeibe, E.; Loretz, B.; Tarirai, C.; Mbara, K. C.; Agumah, N.; Nnamani, P.; Ofokansi, K.; Lehr, C.-M.; Attama, A. *Nanoscale Adv.* **2024,** *6,* 4751–4780. doi:10.1039/d4na00474d
152. Dubey, A. K.; Mostafavi, E. *Curr. Opin. Green Sustainable Chem.* **2023,** *41,* 100827. doi:10.1016/j.cogsc.2023.100827
153. Ashokkumar, K.; Simal-Gandara, J.; Murugan, M.; Dhanya, M. K.; Pandian, A. *Phytother. Res.* **2022,** *36,* 2839–2851. doi:10.1002/ptr.7491
154. Hudz, N.; Kobylinska, L.; Pokajewicz, K.; Horčinová Sedláčková, V.; Fedin, R.; Voloshyn, M.; Myskiv, I.; Brindza, J.; Wieczorek, P. P.; Lipok, J. *Molecules* **2023,** *28,* 7444. doi:10.3390/molecules28217444
155. Zhao, S.; Wang, Z.; Wang, X.; Kong, B.; Liu, Q.; Xia, X.; Liu, H. *Foods* **2023,** *12,* 3183. doi:10.3390/foods12173183
156. Algahtani, M. S.; Ahmad, M. Z.; Ahmad, J. *Bioengineering* **2022,** *9,* 384. doi:10.3390/bioengineering9080384

License and Terms

BEILSTEIN JOURNAL OF NANOTECHNOLOGY

Beyond the shell: exploring polymer–lipid interfaces in core–shell nanofibers to carry hyaluronic acid and β-caryophyllene

Aline Tavares da Silva Barreto[‡1,2], Francisco Alexandrino-Júnior[‡3], Bráulio Soares Arcanjo[‡2,4], Paulo Henrique de Souza Picciani[‡5] and Kattya Gyselle de Holanda e Silva[*,‡1,2,§]

Full Research Paper

Open Access

Address:
[1]Laboratório de Sistemas Híbridos, Faculdade de Farmácia, Universidade Federal do Rio de Janeiro (UFRJ), Av. Carlos Chagas Filho, 373 - Cidade Universitária, Rio de Janeiro - RJ, 21941-170, Brasil, [2]Programa de Pós-Graduação em Nanobiossistemas, Universidade Federal do Rio de Janeiro, Duque de Caxias, Brasil, [3]Laboratório de Micro e Nanotecnologia (LMN), CDTS, Fundação Oswaldo Cruz (Fiocruz), Brasil Av., 4036, 107 - Maré, Rio de Janeiro - RJ, 21040-361, Brasil, [4]Divisão de Metrologia e Materiais Instituto Nacional de Metrologia, Qualidade e Tecnologia (INMETRO), Xerém, RJ, Brasil and [5]Laboratório de Biomateriais, Instituto de Macromoléculas Heloisa Mano, Universidade Federal do Rio de Janeiro (UFRJ) – Av. Horácio Macedo, 2030, Rio de Janeiro, Brasil

Email:
Kattya Gyselle de Holanda e Silva[*] - gyselle@farmacia.ufrj.br

* Corresponding author ‡ Equal contributors
§ Email: gysaholanda@me.com

Keywords:
co-axial nanofibers; electrospinning; hybrid nanosystem; nanofibers; nanoemulsion; poly(lactic acid)

Beilstein J. Nanotechnol. **2025,** *16,* 2015–2033.
https://doi.org/10.3762/bjnano.16.139

Received: 20 June 2025
Accepted: 14 October 2025
Published: 12 November 2025

This article is part of the thematic issue "Advances in nanotechnology applied to natural products".

Guest Editor: D. Dourado

Abstract

Hyaluronic acid (HA) and β-caryophyllene (βCp) are two promising agents in biomedical research, each offering unique therapeutic benefits. The successful integration of these compounds into a single, functional nanofiber system presents a significant technical challenge, demanding innovative strategies to ensure their compatibility and sustained activity. This study addresses this critical challenge through the rational design and fabrication of hybrid core–shell nanofibers manufactured via coaxial electrospinning. Poly(lactic acid) (PLA) was used as an outer shell providing structural integrity and effectively encapsulating a core comprising a nanoemulsion containing β-caryophyllene (NE-βCp) alongside HA. A rigorous optimization of the electrospinning process was critical, involving the systematic evaluation of key parameters. This optimization successfully identified the optimal core formulation (1% w/w HA, 2% w/w NE) and process parameters (17 kV applied voltage, 6.25 flow rate ratio (0.04 mL/h inner; 0.25 mL/h outer), 12 cm needle-to-collector distance). These conditions provided highly uniform fibers with an average diameter of 439 ± 100 nm, notably 37% larger than fibers without the lipid core. Furthermore, maintaining ambient relative humidity below 45% proved essen-

tial for processing stability. Comprehensive morphological characterization via scanning electron microscopy confirmed the uniformity of the fibers. At the same time, confocal microscopy, cross-sectional imaging, and attenuated total reflectance with Fourier transform infrared (ATR-FTIR) spectroscopy provided compelling evidence for the successful formation of the intended core–shell structure. The resulting nanofibers exhibited surface hydrophobicity, suggesting potential for anti-adhesive membrane applications. Thermal and crystalline analyses demonstrated improved thermal stability upon NE-βCp incorporation. Collectively, these results provide robust evidence for the feasibility of producing multifunctional nanofiber membranes that successfully integrate a polymer–lipid hybrid core encapsulated within a PLA shell, highlighting substantial potential for biomedical applications by overcoming key material integration hurdles.

Introduction

Driven by the significant potential of biomaterials, recent decades have seen intensive research into novel therapeutic strategies for regenerative medicine [1-4]. Within this scenario, a pivotal current strategy in formulation development focuses on integrating nanocarriers with nanoscale three-dimensional biomaterials, enabling major advancements in the controlled release of diverse bioactive compounds [5-10].

Among the various nanostructured platforms explored for these purposes, nanofibers have gained attention due to their high surface area, adjustable porosity, and robust mechanical properties, which set them apart from conventional fibrous materials. Their flexibility in fabrication allows for integration into a broad range of applications, from drug delivery scaffolds to composite biomaterials, contributing to their increasing relevance in both scientific research and industrial development [11-14].

To leverage the properties of nanofibers and create advanced structures with enhanced functionality, coaxial electrospinning can be used to generate nanofibers allowing for the building of a core–shell structure with desirable properties, taking advantage of the positive characteristics of each component (core and shell materials) [15]. However, achieving high-quality structures for biomedical use with tailored properties requires careful management of various processes, materials, and environmental parameters [16], necessitating thorough optimization of the electrospinning conditions. This includes precise control over process variables, such as high voltage, flow rate, and the distance from the Taylor cone to the collector, which significantly impacts nanofiber morphology [17]. Furthermore, selection of the material to be electrospun is crucial, requiring control over key attributes such as molecular weight, polymer concentration, surface tension, conductivity, and solvent volatility, alongside careful consideration of electrospinning conditions, such as temperature and humidity [18,19].

The polymer selection of nanofibers intended for biomedical applications must prioritize not only mechanical strength, controlled degradation, and moderate hydrophilicity, but also biocompatibility, non-toxicity, and non-carcinogenicity [5].

Adhering to these critical quality requirements for biomedical products, polylactic acid (PLA) was selected for nanofiber production. This biotechnologically derived aliphatic polyester is a rigid thermoplastic known for its biodegradability, biocompatibility, and bioabsorbability [20,21]. Highly attractive due to its versatile physical, chemical, and biological properties, PLA is a suitable option for manufacturing tissue engineering scaffolds, implantable devices, and drug delivery systems, holding recognition as safe and approved for human use by the U.S. Food and Drug Administration (FDA). While PLA exhibits relatively high modulus and strength, it possesses limitations such as low toughness, a slow degradation rate, and high hydrophobicity [18,22,23]. Nevertheless, PLA fibers effectively provide mechanical strength, assist in managing wound exudates, and maintain a moist wound bed. Its properties can also be tailored through blends with different forms of PLA or other biopolymers to achieve desired tensile strength, release profiles, or biodegradation characteristics [24,25]. The growing commercial interest in biopolymers such as PLA is, in part, driven by environmental concerns, climate change, and the depletion of fossil fuel resources, as PLA is derived from renewable sources and is both readily and completely biodegradable.

Hyaluronic acid (HA) is an extensively used component in wound healing applications and naturally occurring in vertebrates [26,27]. It is a key element of the extracellular matrix, providing a gelatinous structure where collagen and elastin fibers are embedded. As an endogenous molecule, it demonstrates ideal biocompatibility and full absorption by human tissues. Its natural origin, high structural conservatism across species, and minimal interaction with blood components make HA and HA-based materials exceptionally biocompatible, a non-negotiable prerequisite for biomedical use. Hyaluronic acid is also recognized and listed in the US FDA inactive ingredient database for various biomedical applications [28,29].

Complementing the regenerative and biocompatible profile of HA, β-caryophyllene (βCp) is another critical component of significant pharmaceutical potential. Among the array of attributes exhibited by βCp, it notably possesses potent analgesic, antioxi-

dant, antimicrobial, and anti-inflammatory effects [30,31]. It is also currently been evaluated as a candidate for skin regeneration due to its effect as a cannabinoid receptor 2 (CB2) ligand, with studies suggesting that CB2 activation by selective agonists can enhance re-epithelialization, reduce pain, and improve inflammatory response during wound healing [32,33]. Chemically, βCp is characterized as a natural bicyclic sesquiterpene found in several plants and essential oils, and as expected for compounds of this class, it exhibits characteristic volatility and low solubility in water [34]. To address these limitations for effective pharmaceutical use, βCp is often formulated within lipid liquid dispersions, such as nanoemulsions, to enhance its stability and improve therapeutic properties [35-38].

While lipid nanosystems offer undeniable advances for the delivery of active compounds, their inherent liquid nature can present formulation challenges, particularly when seeking integration into solid scaffolds like nanofibers. The strategic combination of polymers and lipids in hybrid systems has emerged as a promising approach to overcome these limitations. Incorporating polymer–lipid interfaces within core–shell nanofibers can enhance the system in various scenarios (e.g., improving formulation stability, increasing the encapsulation efficiency, and tailoring the controlled release of therapeutically active molecules [39,40]). This approach has demonstrated promising results, especially for topical drug administration via dressings made of biocompatible polymers containing lipid nanosystems [41-43]. Numerous researchers have successfully encapsulated nanoemulsions into nanofibers for diverse applications, including studies by Kaur et al. (2024) showing superior wound healing with bakuchiol nanoemulsion-loaded electrospun scaffolds compared to that of the gel formulation [44], and Coelho et al. (2021) reporting PVA nanofibers containing chalcone NE as a potential treatment for cutaneous leishmaniasis [45].

Despite these advances in nanofiber composite structures incorporating various nanosystems, a critical gap persists in thoroughly understanding the complex polymer–lipid interactions, particularly in systems designed for the simultaneous co-encapsulation of compounds with vastly different physicochemical properties, such as hydrophilic HA and lipophilic βCp. An in-depth understanding of these specific interactions is essential for precise modulation of encapsulation efficiency, ensuring system stability and achieving tailored kinetic release. Therefore, the primary objective of this study was to thoroughly investigate lipid–polymer interactions within coaxially electrospun PLA nanofibers engineered for hyaluronic acid and βCp co-delivery. The insights gained from this investigation are crucial for bridging this specific knowledge gap and may guide the design of optimized hybrid therapeutic platforms.

Results and Discussion

This study aimed to develop and investigate PLA nanofibers impregnated with HA and βCp nanoemulsion. The use of βCp in practice is questioned due to its low aqueous solubility, low viscosity, extreme volatility, and sensitivity to temperature, oxygen, and light [38]. The production of a nanoemulsion was developed as a nanocarrier system designed to enhance both the stability and bioavailability [35] of the compound and enable its incorporation into nanofibers. In this study, a Box–Behnken design was applied to develop an optimized βCp nanoemulsion (NE-βCp). This experimental design employed ultrasonication as the manufacturing method with the oil: βCp ratio (0–80%), surfactant concentration (2–20%), and HLB (10–15) as the independent variables (data not shown). Based on the preliminary results, a sample was selected for this study. It can be observed that formulations exhibited droplet mean sizes in the nanoscale range, varying from 58 nm. The formulations showed a unimodal distribution with a polydispersity index (PDI) range of 0.218. Most of the formed nanoemulsions are small in size and well distributed (Figure 1).

The most favorable processing conditions for obtaining uniform fibers – free of surface roughness and with fewer beads – were determined based on morphological analysis. Varying the process parameters and the concentration of the constituent(s) seems to be an effective way to control the morphology of the electrospun mats, especially the diameter of the fibers, as demonstrated by Coelho et al. [45]. This study investigated the influence of core composition on fiber formation by analyzing the concentrations of the core components and the process flow rate as variables.

It was observed that the concentration of NE-βCp in the core had a significant impact on fiber morphology, as illustrated in Figure 2. The presence of NE-βCp led to an increase in the number of beads and the formation of fibers with a more dispersed structure, likely reflecting insufficient polymer chain entanglement and Taylor cone instability. This behavior appears to result from interactions between NE-βCp droplets and HA chains, which may disrupt the jet and hinder solvent evaporation within the core, as also reported by Ricaurte et al. (2022) [46]. Air relative humidity was additionally found to influence solvent evaporation and the formation of uniform HA fibers. Similar to the observations reported by Yao et al. (2013), a stable process without interruptions was only achieved when the relative humidity was below 45% [47].

Regarding the NE-βCp concentration, it was evident that values above 2% (Figure 2B) led to the formation of more heterogeneous fibers with a higher density of beads, likely because the increased droplet content hindered proper flow and elongation of

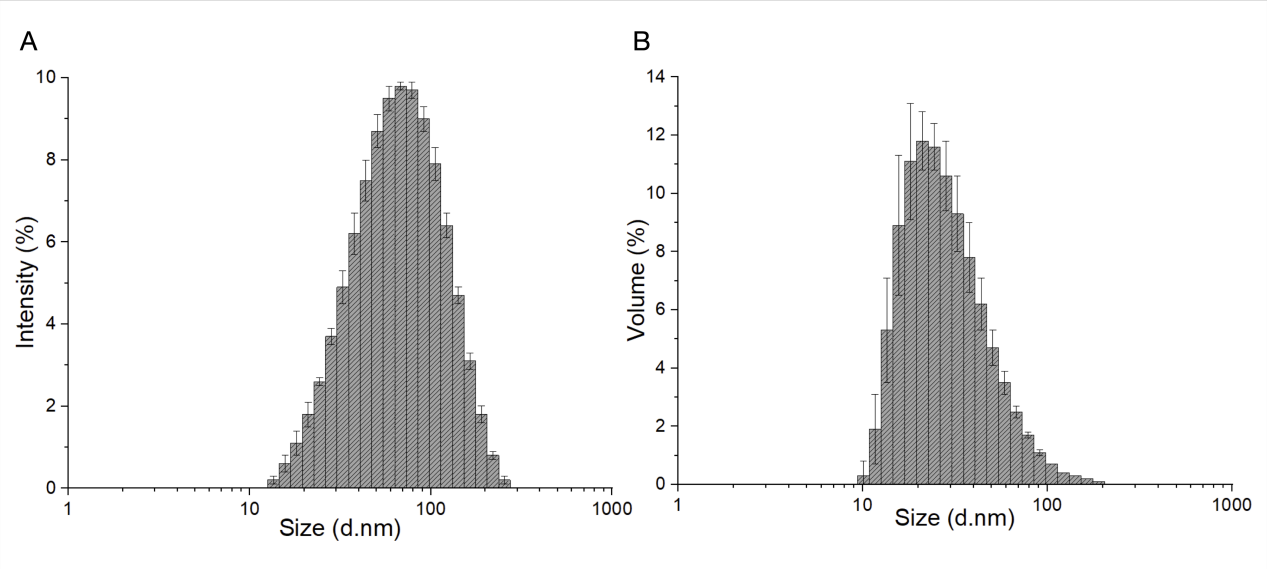

Figure 1: Hydrodynamic diameter distribution of β-caryophyllene nanoemulsion measured by DLS: (A) intensity distribution and (B) volume distribution.

the polymer jet. Based on these preliminary results, the NE concentration and flow rates (outer flow rate: 0.25 mL/h; inner flow rate: 0.04 mL/h) were fixed in subsequent experiments to investigate the influence of HA concentration on nanofiber formation. Given that HA is a high-viscosity polymer [48], its concentration in the core significantly affects the overall viscosity of the solution, potentially causing instability in the Taylor cone and leading to bead formation and other morphological defects in the fibers [49]. Micrographs revealed the morphological changes resulting from different HA concentrations. Figure 3 shows that no significant variations in the average fiber diameter were observed with increasing HA concentrations: diameters of 257 ± 111 nm, 250 ± 74 nm, and 242 ± 94 nm were obtained for HA concentrations of 0.75%, 1.00%, and 1.25%, respectively. However, the micrograph corresponding to 0.75% HA showed a higher density of beads, suggesting insufficient polymer chain entanglement, which may have impaired fiber stretching during the electrospinning process. Among the tested concentrations, 1.00% HA yielded the most uniform fibers. This effect may result from a more favorable balance between chain entanglement and viscosity: compared to 0.75%, the solution exhibited increased entanglement, while its viscosity remained lower than that of the 1.25% solution, facilitating better core dragging by the shell solution.

In the coaxial electrospinning process, the optimal ratio between the shell and core flow rates is crucial to ensure proper incorporation of the core material. When this ratio is excessively high, the core flow becomes insufficient relative to the shell flow, resulting in fibers with a discontinuous or poorly defined core [50]. Conversely, when the core flow is too high, structural instability and bead formation may occur, as the shell solution may not efficiently envelop or drag the core solution [51,52]. In this study, a flow rate ratio of 12.5 (outer flow rate: 0.50 mL/h; inner flow rate: 0.04 mL/h) was associated with the formation of thinner fibers and numerous beads, likely due to limited core incorporation and the generation of fine PLA nanofibers with bead-like structures containing core material. Upon reducing the ratio, the resulting fibers were thicker and exhibited fewer beads, suggesting improved core incorporation. Therefore, for sample preparation, a flow rate ratio of 6.25 was maintained, with an outer flow rate of 0.25 mL/h and an inner flow rate of 0.04 mL/h, as this ratio prevented severe dripping and ensured a more stable Taylor cone. Having characterized the influence of core composition on fiber formation, the next step involved evaluating the effects of electric field intensity, which is responsible for polymer chain stretching and the speed of fiber deposition, on fiber morphology. Specifically, the impact of varying the needle-to-collector distance (12 and 15 cm) and the applied voltage (15, 17, and 19 kV) was assessed. The important physicochemical properties of these structures are highly related to conformational changes in the polymeric chain caused by the spinning process [49,53].

Initially, the influence of the travel distance of the polymer jet on fiber formation was examined (Figure 4). This critical parameter exerts a notable influence on the characteristics of the resultant nanofibers. A reduction in the needle-to-collector distance from 15 (Figure 4D) to 12 cm (Figure 4B) resulted in a significant increase in the average fiber diameter, from 250 ± 74 to 439 ± 100 nm. This phenomenon is likely associated with the enhancement of the electric field strength at shorter distances,

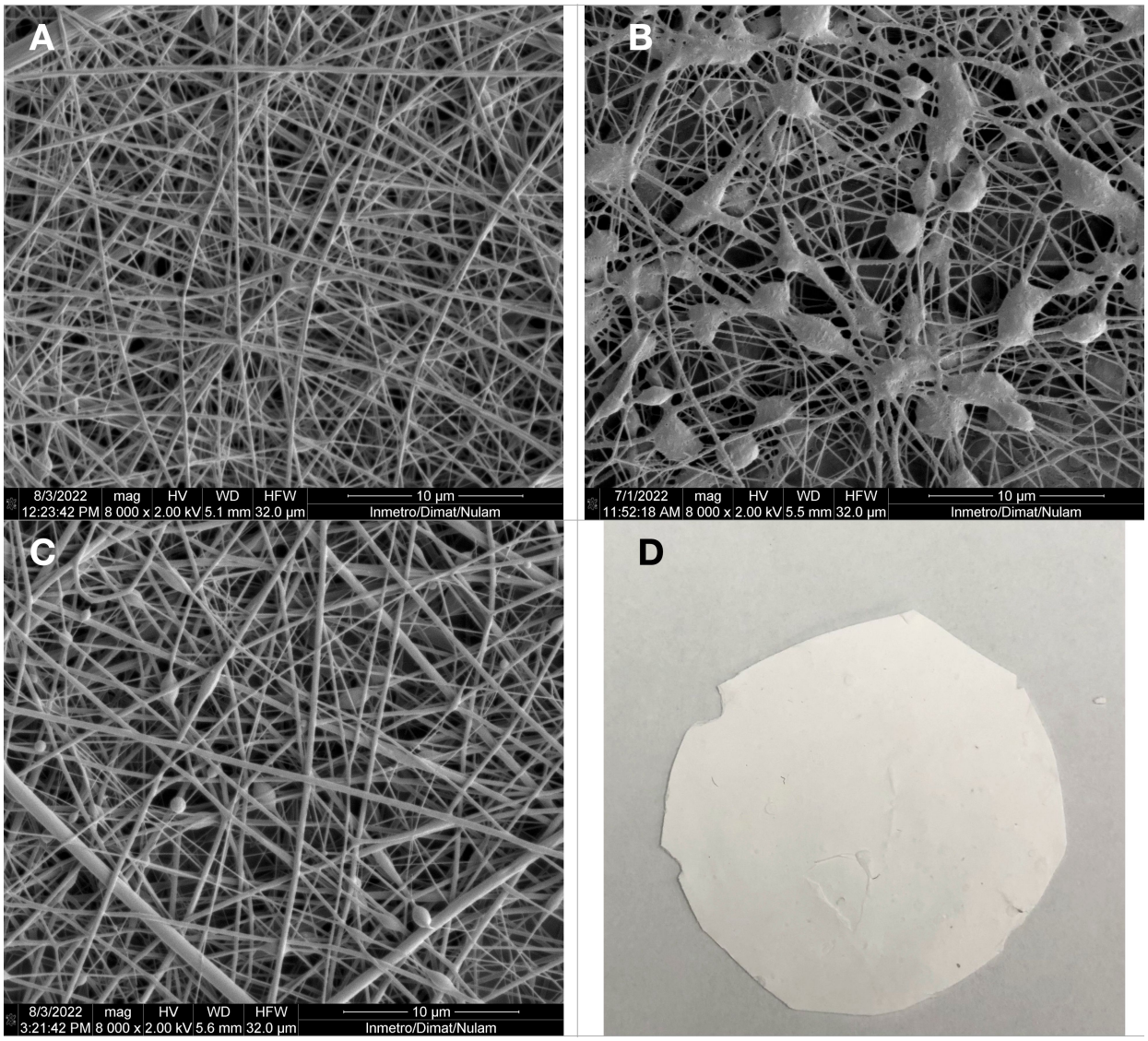

Figure 2: SEM images of nanofibers obtained from the composition: (A) PLA 20%$_{(w/w)}$ and HA 1%$_{(w/w)}$; (B) PLA 20%$_{(w/w)}$, HA 1%$_{(w/w)}$, and NE 5%$_{(w/w)}$; (C) PLA 20%$_{(w/w)}$, HA 1%$_{(w/w)}$, and NE 2%$_{(w/w)}$; and (D) picture of a nanofiber mat. The scale bars are 10 µm and the magnification is 8000×.

which accelerates fiber deposition and reduces the time available for jet elongation, ultimately leading to the formation of thicker fibers. Additionally, a stronger electric field may reduce Rayleigh instability and stabilize the Taylor cone [49]. Although the diameter distribution was narrower at 15 cm, the 12 cm distance was selected for subsequent experiments due to the enhanced Taylor cone stability and reduced bead formation. The influence of the distance between the needle and the collector is dependent on the polymer system used. For this study, we determined the optimal distance required to maximize the flight time for solvent evaporation, without compromising the applied electric field, to favor the formation of fibers with adequate morphology and uniformity.

With a fixed distance of 12 cm between the needle and the collector, the influence of voltage variation on fiber morphology was then investigated. Similar to other process parameters, the critical voltage varies among different polymer systems, and optimizing this value is crucial for achieving optimal morphology in the resulting fibers [54]. Increasing the voltage from 17 (Figure 4B) to 19 kV (Figure 4A) resulted in the formation of thinner fibers (292 ± 117 nm), probably due to the amplified repulsive forces which consequently induced stretching. However, it was also observed that more beads and a broader diameter distribution were present, suggesting that the critical voltage threshold may have been exceeded, resulting in the formation of two separate jets: one from the core and another from the shell,

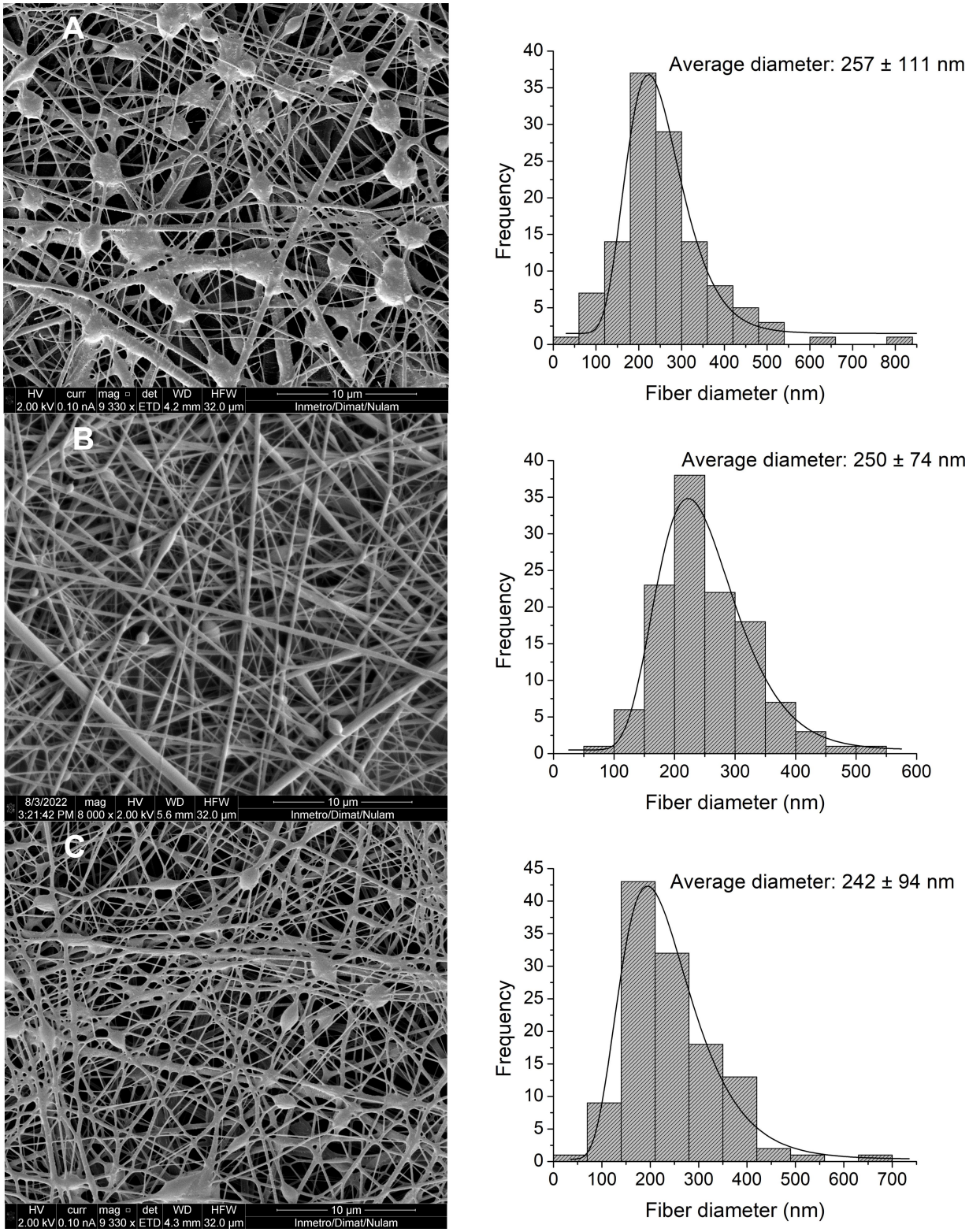

Figure 3: SEM images and histograms with diameter frequencies of nanofibers obtained from the composition: NE 2%$_{(w/w)}$, PLA 20%$_{(w/w)}$, and (A) HA 0.75%$_{(w/w)}$; (B) HA 1.00%$_{(w/w)}$; and (C) HA 1.25%$_{(w/w)}$. The scale bars are 10 µm. In picture (B), the magnification is different (8000×).

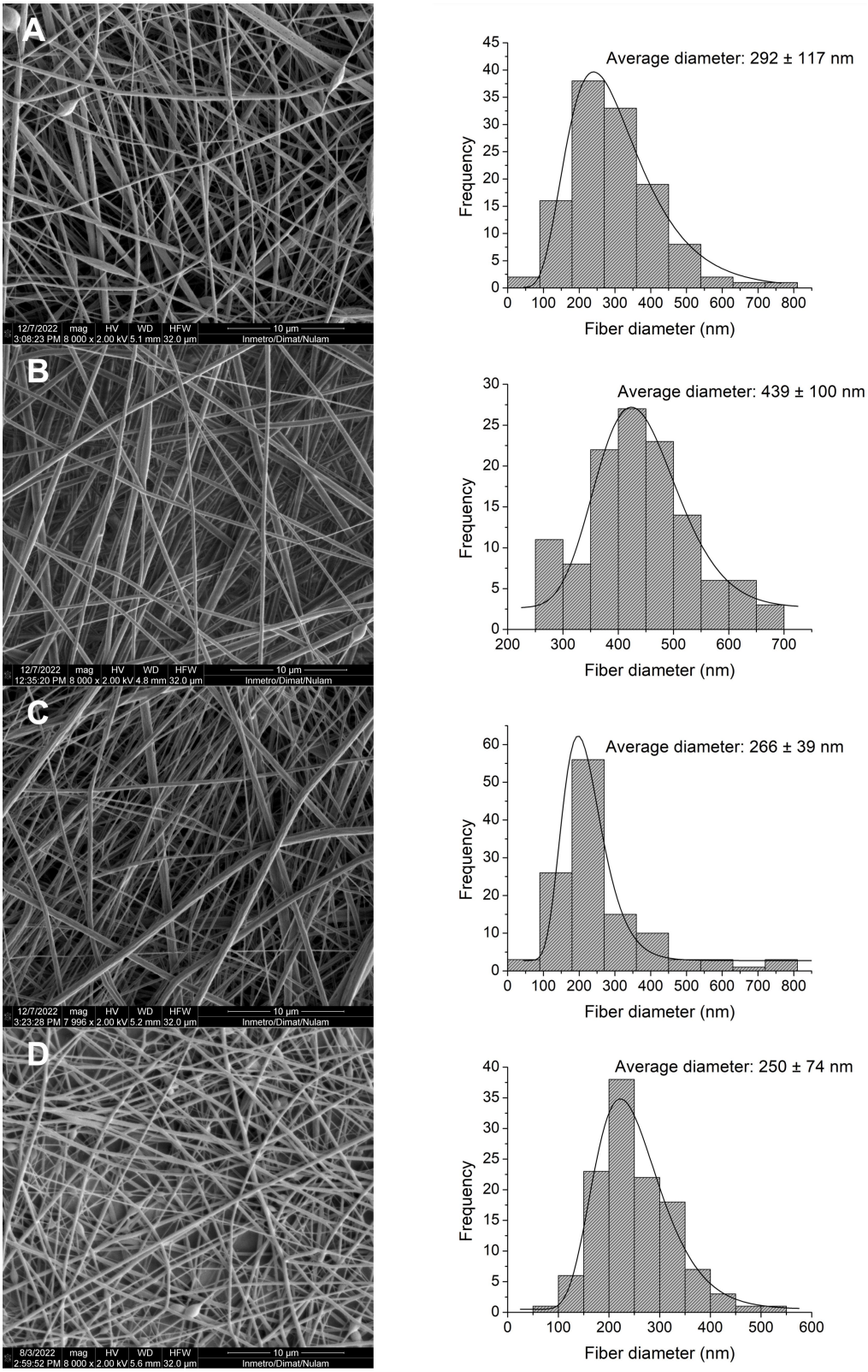

Figure 4: SEM images and histograms with diameter frequencies of nanofibers obtained from the composition: HA 1%$_{(w/w)}$, NE 2%$_{(w/w)}$, and PLA 20%$_{(w/w)}$ electrospun at (A) 12 cm and 19 kV, (B) 12 cm and 17 kV, (C) 12 cm and 15 kV, and (D) 15 cm and 17 kV. The scale bars are 10 µm, and the magnification is 8000×.

ultimately producing monolithic fibers. Reducing the voltage to 15 kV (Figure 4C) yielded fibers with an average diameter of 266 ± 139 nm, no observable beads, and a heterogeneous diameter distribution.

Structural characterization of nanofibers

Core–shell nanofibers create a protective environment for bioactive agents within the core, preserving their activity while enabling controlled release. By tailoring the shell architecture, the release profile can be modulated, and the initial burst release minimized [7]. Beyond drug delivery, an ideal biomedical scaffold should support cellular attachment while providing effective drug release; balancing these functions is crucial for promoting tissue formation. Achieving this balance in electrospun scaffolds remains challenging, as modifications that improve release kinetics or protect the core can sometimes compromise biocompatibility or cellular interactions [55].

To evaluate the structure of the nanofibers produced, confocal microscopy was used under a fluorescent filter to study the morphologies of scaffold types throughout their thickness and assess the core structure of HA+NE2/PLA nanofibers. Fluorescein, a fluorescent dye, was added to the HA+NE mixture to facilitate its encapsulation within the core during the electrospinning process. As shown in Figure 5, the presence of fluorescein was confirmed by its fluorescence emission under incident light, indicating that the electrospun fibers predominantly displayed continuous cores. This suggests that the established coaxial electrospinning parameters successfully supported the formation of nanofibers with HA+NE cores. The limited discontinuities identified in the fiber structure were attributed to instabilities in the electrospinning process, likely resulting from the low core flow rate (0.04 mL/h). Despite these minor defects, the majority of the fibers exhibited continuous and well-defined cores, confirming the consistency of the process and their potential suitability for subsequent applications. The observed discontinuities could act as preferential sites for accelerated diffusion and burst release of encapsulated compounds, potentially compromising a sustained release profile while being advantageous for applications requiring an initial burst. To improve fiber homogeneity, strategies such as fine-tuning the core–shell flow rate ratio and optimizing solution viscosities can be employed, enhancing coaxial jet stability and promoting more continuous cores [16].

The evaluation of the cross-section before and after core removal is a key technique for assessing the core–shell structure of coaxial fibers. This method provides insight into the structural changes resulting from the release of hydrophilic core content and potential pore formation on the shell surface. For this study, the HA+NE2/PLA sample was analyzed before and after core removal.

Before core removal, the fibers exhibited a filled core structure, as depicted in Figure 6A. Sequential washing with water and ethanol, followed by drying and cryofracture, effectively solubilized and removed the core material, yielding hollow fiber structures (Figure 6B). These observations confirmed the suc-

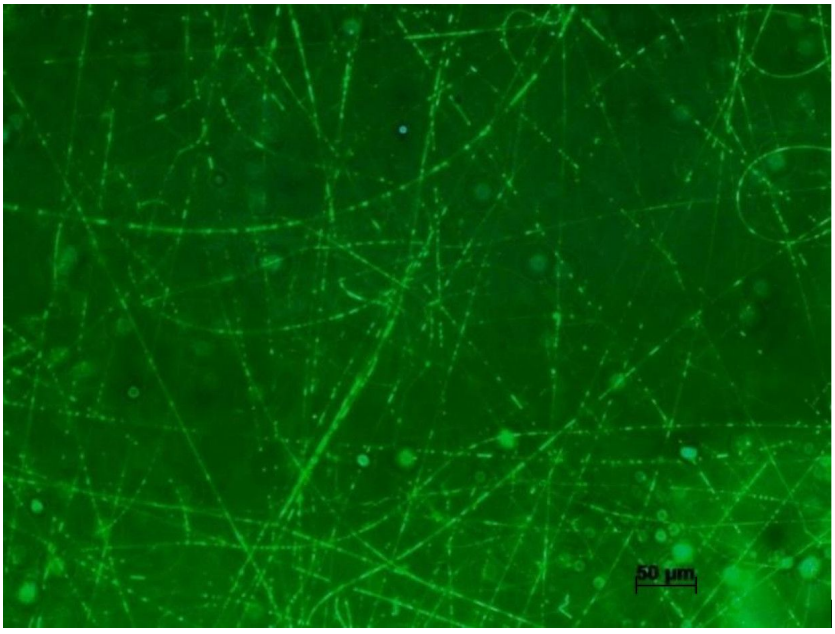

Figure 5: Confocal microscopy images of nanofibers containing fluorescein. The scale bar is 50 µm.

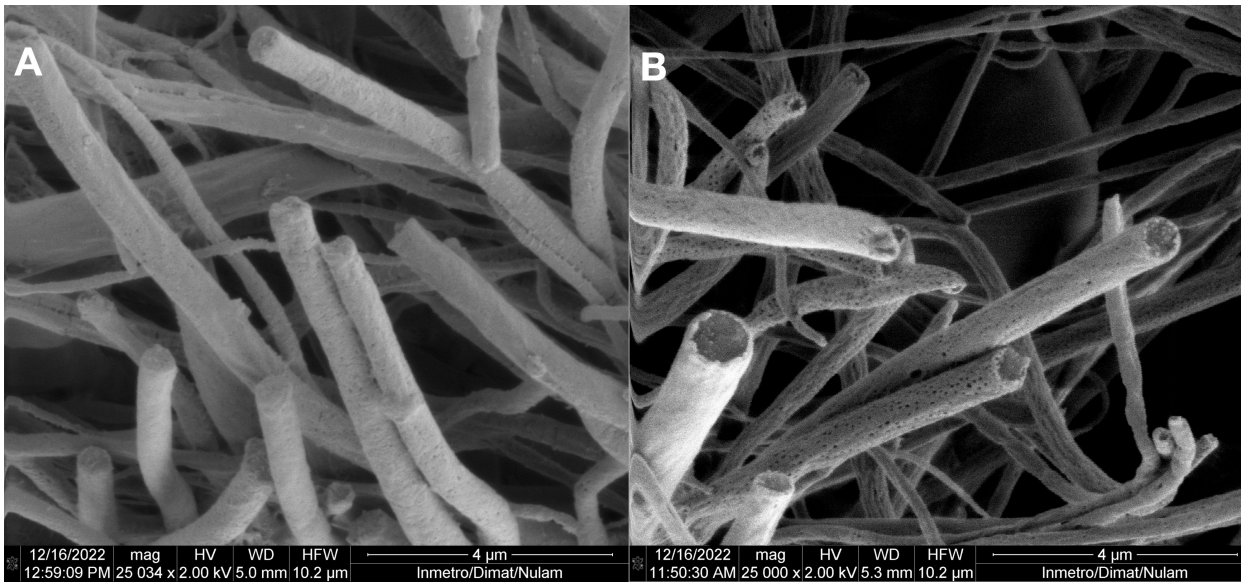

Figure 6: SEM images of the cross-section of nanofibers obtained before (A) and after (B) core removal. The scale bars are 4 µm, and the magnification is 25000×.

cessful formation of a core–shell structure via coaxial electrospinning, using the optimized parameters from the morphology study. Additionally, Figure 6B highlights the presence of pores on the PLA shell surface after washing, suggesting that core removal occurred through diffusion facilitated by these pores. The pore formation on the shell surface is a potential mechanism for regulating the release of the core content [56,57]. A biomedical scaffold must possess suitable pore size and a high level of porosity. The porosity of the scaffold in tissue engineering applications should be adequate. A study by Nguyen et al. (2012) compared the release profiles of salicylic acid encapsulated within cores protected by porous and nonporous PLA shells. Over a period of five days, the release from fibers with porous shells was approximately five times greater than that from nonporous counterparts, likely due to increased water ingress through the pores, facilitating access to the core [58]. This possibility is also described by Wang and Xu (2018), who successfully prepared tea polyphenol-loaded porous core–shell fibers by controlling coaxial electrospinning parameters [56].

ATR-FTIR spectroscopy has been widely used to evaluate the integrity of core–shell structures and confirm the presence of the core material within electrospun fibers. A well-formed core–shell structure is indicated by FTIR spectra showing the absence of characteristic core bands and the exclusive presence of shell bands [59-61]. As reported by da Silva et al. (2019), inadequate flow rates during the production of coaxial nanofibers can lead to incomplete core incorporation, resulting in monolithic fibers that are identifiable by their spectral signatures [61]. To evaluate the surface composition of nanofiber membranes, ATR-FTIR analysis was performed on PLA (monolithic), HA/PLA, and HA+NE2/PLA nanofiber samples, along with pure HA powder.

The obtained spectra (Figure 7) confirmed effective shell coating, as only the characteristic bands of PLA were detected in the core–shell nanofibers. All three nanofiber membranes (NF-PLA, NF-HA/PLA, and NF-HA+NE2/PLA) exhibited PLA-specific bands at 2995, 2946, 1759, and 1089 cm^{-1}, corresponding to the asymmetric stretching vibration of $–CH_3$, symmetric stretching of $–CH_3$, and stretching vibrations of C=O and C–O, respectively [62]. The HA powder spectrum displayed bands at 3300, 1605, 1410, and 1030 cm^{-1}, which were attributed to the overlapping O–H and N–H stretching of hydroxyl and amide groups, the amide I C=O stretching, the symmetric stretching of C=O, and the C–O stretching, respectively [63,64]. In comparison, the absence of HA-specific bands at 3300 and 1605 cm^{-1} in the nanofiber spectra confirmed the complete encapsulation of the core material by the PLA shell. This observation aligns with the cross-sectional analysis results, where a coated core–shell structure was evident following the removal of the HA+NE2 core.

Thermal behavior and crystallinity of nanofibers

The thermal properties and crystallinity of NF-PLA (monolithic), NF-HA/PLA, and NF-HA+NE2/PLA nanofibers were analyzed using thermogravimetric analysis (TGA), X-ray

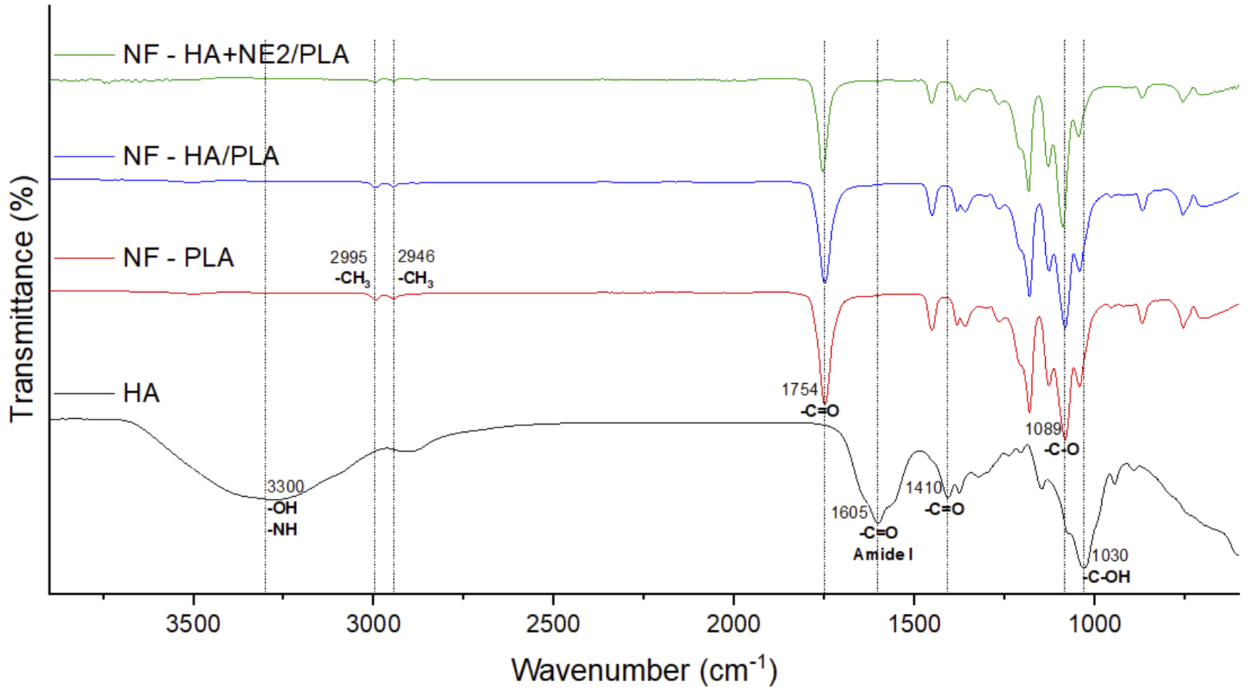

Figure 7: FTIR spectra of bulk HA (black), PLA nanofiber (red), nanofiber composed of HA 1%$_{(w/w)}$ and PLA 20%$_{(w/w)}$ (blue), and nanofiber composed of HA 1%$_{(w/w)}$, NE 2%$_{(w/w)}$, and PLA 20%$_{(w/w)}$ (green).

diffraction (XRD), and differential scanning calorimetry (DSC). Thermal behavior and crystallinity of the nanofibers mats of βCp nanoemulsion-loaded PLA are displayed in Figure 8. The TGA and DTG curves provide insights into the thermal stability and decomposition behavior of the nanofibers [65]. At the same time, the DSC and XRD analyses complement the study by elucidating the crystallinity and thermal transitions of the samples. Figure 8A and Figure 8B illustrate the mass variation curves as a function of temperature, along with the first derivative of mass variation concerning temperature (DTG), obtained from TGA. In the TGA curve of the HA bulk, a degradation profile with three main stages of mass loss was observed, as previously described by Ahire et al. [66]. The first stage of mass loss occurred at temperatures up to 220 °C. In this stage, approximately 21% of the mass was lost due to the dehydration of HA chains, resulting from the evaporation of water molecules. HA polymer chains are characterized by a high capacity for water adsorption and retention, owing to their large number of pendant hydrophilic groups and atoms capable of forming hydrogen bonds, such as nitrogen and oxygen. The second and third stages corresponded to the degradation and cleavage of the HA chains, resulting in mass losses of approximately 40% between 220 and 300 °C, and 13% between 300 and 700 °C [66,67]. Therefore, about 26% of the HA remained thermally stable up to 700 °C, yielding a residual mass that did not decompose at the analyzed temperature.

Regarding the nanofibers, the TGA and DTG curves indicated a single decomposition stage associated with the cleavage of polymer chains. No significant differences were observed in the T_{onset} and T_{max} temperatures among the different nanofiber groups, likely due to the high PLA content (≈99%). Monolithic PLA nanofibers exhibited a T_{onset} of 286.8 °C and a T_{max} of 322.5 °C, values consistent with those reported by Vidal et al. [68]. The incorporation of an AH core into the PLA nanofibers led to an increase in T_{onset} to 301.2 C and T_{max} to 337.4 °C. Similarly, the addition of the HA+NE core also increased the T_{onset} to 294.7 °C and the T_{max} to 343.6 °C. These results indicate that the presence of the core did not reduce the thermal stability of the nanofibers, suggesting that the hybrid HA+NE core may have enhanced this stability, likely due to an interaction between the core and the shell.

Complementing the thermal analysis performed by TGA, DSC was used to obtain detailed information on the thermal and crystallinity properties of the nanofibers through the values of T_g, T_{cc}, T_m, ΔH_m, ΔH_{cc}, and X_c%. The DSC analysis provided heating curves and thermal transitions for the first and second heating cycles of the nanofibers. The first heating cycle offers insights into the polymers after processing by electrospinning, while the second heating cycle reveals characteristics of the material before processing. The values for each thermal event are presented in Table 1 (first heating) and Table 2 (second

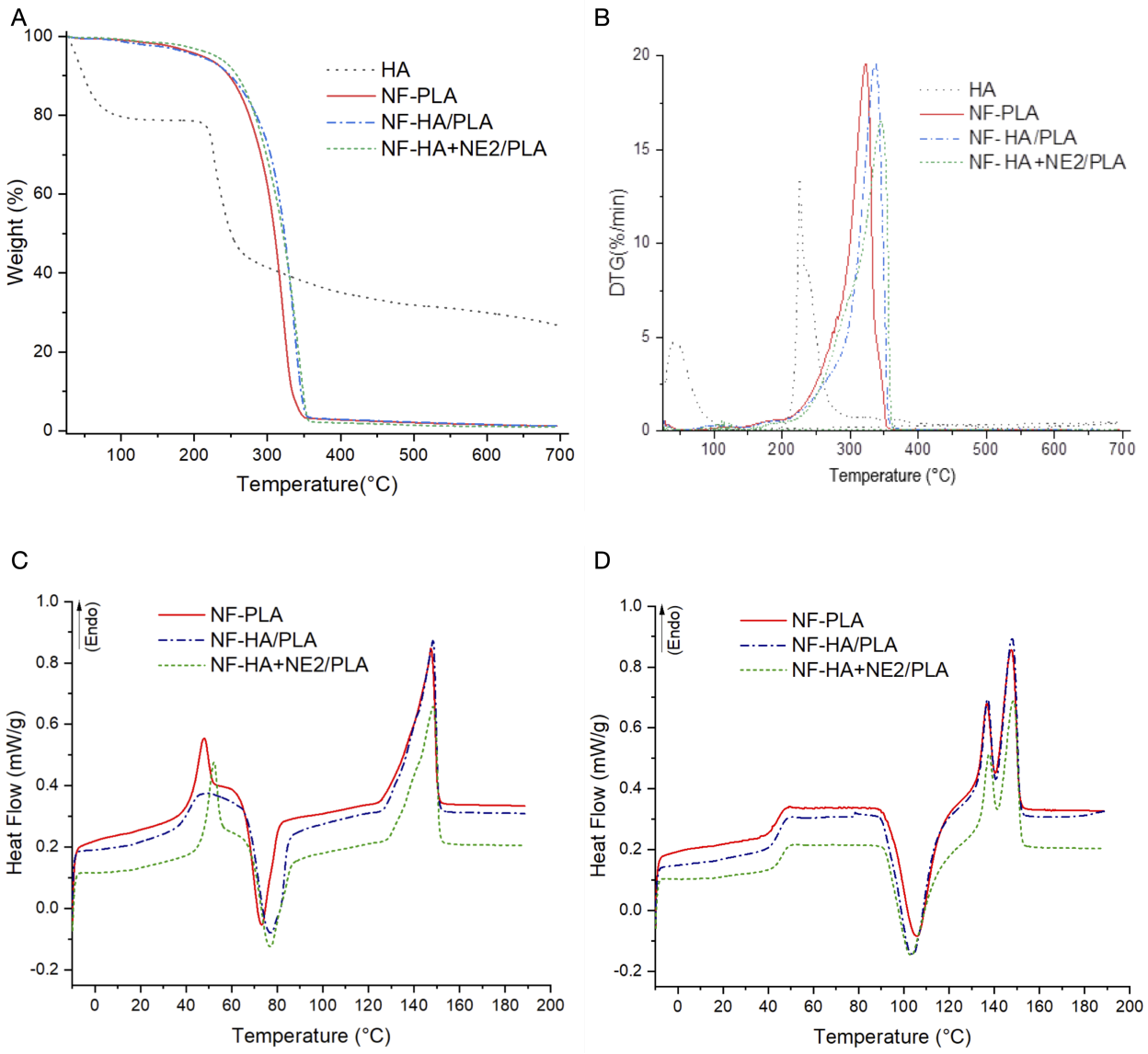

Figure 8: Thermal characterization plots of neat HA, PLA, and nanofiber compositions. Thermogravimetric analysis (A), DTG curves (B), and DSC thermograms: (C) first heating and (D) second heating.

Table 1: DSC data corresponding to the first heating.[a]

Sample	T_g (°C)	T_{cc} (°C)	ΔH_{cc} (J/g)	T_{m1} (°C)	T_{m2} (°C)	ΔH_m (J/g)
NF-PLA	43.7	105.9	37.9	136.6	147.5	33.5
NF-HA/PLA	44.3	104.2	42.7	137.4	148.0	35.7
NF-HA+NE2/PLA	45.6	103.4	33.0	137.8	148.5	29.6

[a]Glass transition temperature (T_g), crystallization temperature upon cooling (T_{cc}), melting temperature of the α crystalline form (T_{m1},), melting temperature of the β crystalline form (T_{m2}), melting enthalpy (ΔH_m), and crystallization enthalpy (ΔH_{cc}).

heating). All fibers exhibited a typical semicrystalline polymer profile, featuring an endothermic peak corresponding to the melting of crystallites, an exothermic peak related to the crystallization of polymer chains into spherulites, and a baseline shift indicative of the glass transition of the amorphous regions. Due to the high PLA content in the fibers, all three analyzed sam-

Table 2: DSC data corresponding to the second heating.[a]

Sample	T_{cc} (°C)	ΔH_{cc} (J/g)	T_m (°C)	ΔH_m (J/g)	X_c% (PLA)
NF-PLA	72.8	23.8	147.3	35.4	12.4
NF-HA/PLA	76.2	30.5	148.3	38.3	8.4
NF-HA+NE2/PLA	76.3	22.0	148.4	31.0	9.8

[a]Crystallization temperature upon cooling (T_{cc}), melting temperature (T_m), melting enthalpy (ΔH_m), crystallization enthalpy (ΔH_{cc}), and degree of crystallinity (X_c%).

ples exhibited thermal behavior similar to that of monolithic PLA nanofibers.

In the first heating cycle (Figure 8C), all three samples displayed an exothermic peak between 72–77 °C, corresponding to the cold crystallization temperature (T_{cc}), which indicates the crystallization of chains that were not fully crystallized during the electrospinning process. Additionally, an endothermic peak at approximately 148 °C was observed in all samples, characteristic of the PLA melting temperature (T_m). The appearance of two melting peaks between 135–150 °C during the second heating cycle (Figure 8D) is associated with two distinct crystalline forms of PLA, the α-form and a metastable β-form. The latter may have formed through recrystallization and reordering of α-crystals upon remelting [69,70]. In the second heating cycle (Figure 8D), a baseline shift was observed between 43–45 °C, corresponding to the glass transition temperature (T_g) of PLA and related to enthalpic relaxations in the amorphous regions.

X-ray diffraction (XRD) analysis was also performed to compare the crystallinity and characteristic peaks of the produced nanofibers. Figure 9 presents the diffractograms of the NF-PLA, NF-HA/PLA, and NF-HA+NE2/PLA nanofibers, as well as the HA and PLA powders for comparison purposes. As expected, the HA powder exhibited the typical profile of an amorphous polymer, with a broad amorphous halo between 2θ = 15° and 30°. The PLA powder displayed a characteristic semicrystalline PLA diffraction pattern, with four prominent peaks at 2θ = 14.7°, 16.6°, 18.9°, and 22.2° [22,71], along with

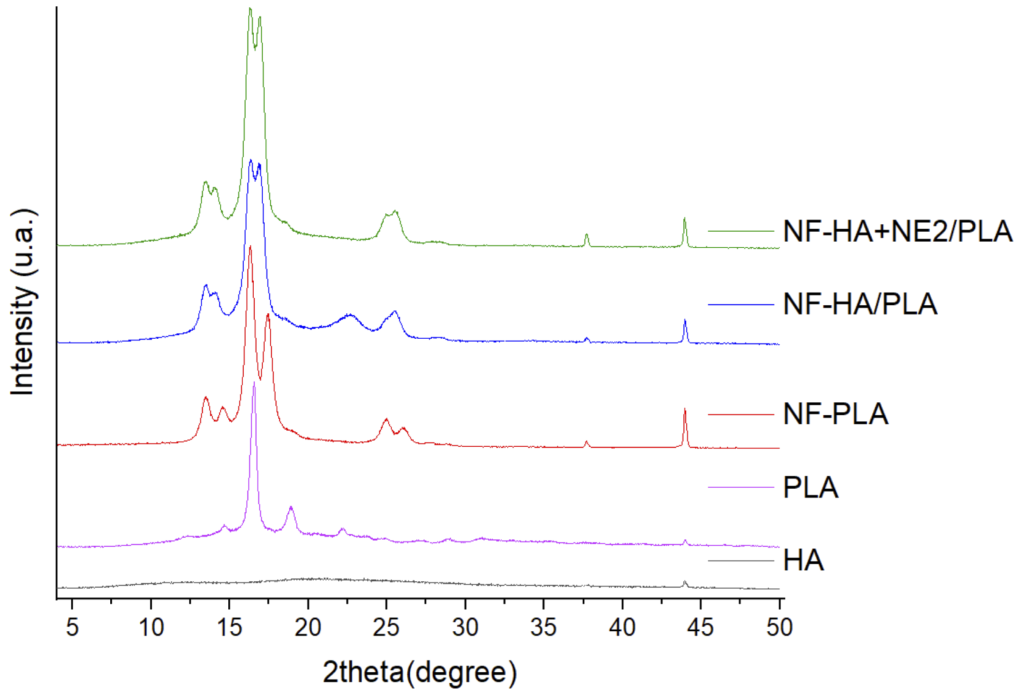

Figure 9: X-ray diffractograms of bulk HA (black), bulk PLA (rose), PLA nanofiber (red), nanofiber composed of HA 1%$_{(w/w)}$ and PLA 20%$_{(w/w)}$ (blue), and nanofiber composed of HA 1%$_{(w/w)}$, NE 2%$_{(w/w)}$, and PLA 20%$_{(w/w)}$ (green).

lower-intensity peaks at 2θ = 24.9°, 27.3°, 29.0°, and 31.0°. In the NF-PLA diffractogram, three additional peaks were observed at 2θ = 13.5°, 26.1°, and 37.7°, as well as an increase in intensity and a shift of the 2θ = 18.9° peak to 2θ = 17.5°, along with the disappearance of the 2θ = 22.2° peak. The core–shell nanofiber samples exhibited very similar diffraction patterns, indicating that the polymers adopted the same structural characteristics during processing. The common peaks between the two coaxial fiber conditions were observed at 2θ = 13.5°, 14.1°, 16.3°, 16.9°, 25.5°, 37.7°, and 43.9°, all of which were also present in the NF-PLA pattern. Additionally, the NF-HA/PLA sample exhibited a peak at 2θ = 22.6°, which is also present in the PLA powder pattern.

No crystalline phases of HA or NE were detected. The degree of crystallinity of the nanofibers and PLA, calculated from the crystalline fraction area obtained by integration of the diffraction peaks, is presented in Table 3 using the OriginLab software. The crystalline fraction refers to the portion of the material that exhibits crystallinity relative to the total material. It can be determined by measuring the area of the diffraction peaks corresponding to the crystalline structure, excluding the area attributed to the amorphous portion [72]. The PLA powder exhibited a crystallinity degree of 27%, whereas the PLA nanofibers showed a crystallinity degree of 53%. This increase in crystallinity after the electrospinning process can be attributed to the stretching of polymer chains, resulting in greater molecular organization [69].

Table 3: Degree of crystallinity obtained by XRD.

Sample	X_c%
PLA	27
NF-PLA	53
NF-HA/PLA	44
NF-HA+NE2/PLA	52

As also observed in the DSC analysis, the XRD patterns revealed lower crystallinity for the nanofibers containing an HA core compared to the monolithic PLA fibers. The prominent peaks, centered at approximately 2θ = 13°, 16°, and 19°, appeared broadened and merged when the amorphous HA core was incorporated. This reduction in crystallinity, resulting from an increase in amorphous regions within the material, may be attributed to the presence of an amorphous core and/or a decrease in the available space for PLA molecular organization within the shell structure.

The crystallinity of the PLA shell can be correlated with its hydrolytic degradation behavior and, consequently, with its ability to control the release of the active compound incorporated in the core. These findings indicate that the crystallinity of the material can be modulated to tailor the degradation rate for specific applications. The semicrystalline nature of PLA results in the formation of both crystalline and amorphous regions, and the arrangement of these two phases directly influences its degradation behavior.

Studies have shown that PLA with higher crystallinity, in both film [73,74] and fiber forms [65], exhibits a higher rate of hydrolytic degradation in phosphate-buffered saline (PBS) at pH 7.4. This is attributed to the higher density of hydrophilic (carboxyl –COOH and hydroxyl –OH) and catalytic (carboxyl –COOH) end groups in the amorphous regions between crystalline domains. These terminal groups reduce chain packing in the amorphous regions between crystallites, making them less densely packed than amorphous polymers and more prone to defects due to crystallization within a confined space [75]. As a result, water diffusion in these amorphous regions increases, and the catalytic effect of the carboxyl groups may accelerate the hydrolytic degradation of semicrystalline samples [20,65,73].

Furthermore, the crystallinity of the encapsulated drug also impacts its release profile. Uncontrolled crystallization of the drug can affect its distribution, leading to the formation of crystals on the fiber surface. In contrast, an amorphous form tends to be more uniformly incorporated into the fiber matrix. Such nonuniform surface distribution may compromise encapsulation efficiency and alter release kinetics [76].

Surface hydrophilicity

The hydrophilicity of the membranes was evaluated through contact angle measurements. Figure 10 shows photographs of a water droplet in contact with the surface of the samples: (a) monolithic PLA, (b) HA/PLA, and (c) HA+NE2/PLA. All samples exhibited a hydrophobic surface, with contact angles ranging between 90° and 150°, attributed to the PLA surface. This result corroborates other characterizations demonstrating that the shell effectively coats the hydrophilic core.

As expected, the monolithic PLA nanofiber sample showed a contact angle of 117.1° ± 11.3°. For core–shell samples, contact angles of 126.9° ± 9.8° and 129.8° ± 1.3° were observed for the samples without NE (HA/PLA) and with NE (HA+NE2/PLA), respectively. The maintenance of surface hydrophobicity with the formation of the core–shell structure indicates the absence of core material at the surface, and that the shell structure does not possess pores that would allow permeation or direct contact of water molecules with the core, as evidenced by scanning electron microscopy (SEM) images.

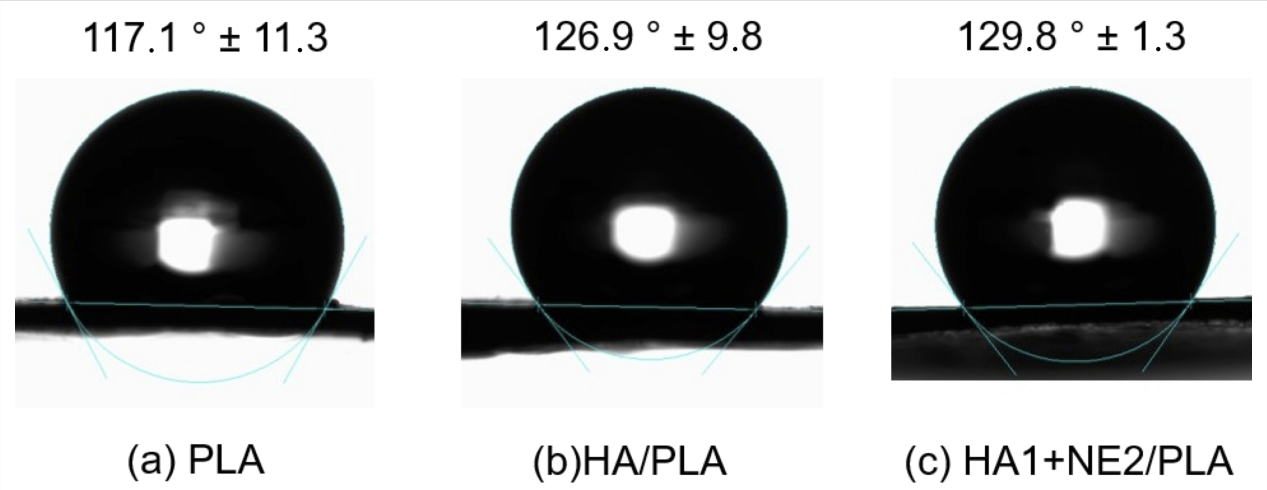

Figure 10: Water contact angles of electrospun nanofibers from the surface of the samples: (A) monolithic nanofiber composed of PLA 20%$_{(w/w)}$, (B) nanofiber composed of HA 1%$_{(w/w)}$ and PLA 20%$_{(w/w)}$, and (C) nanofiber composed of HA 1%$_{(w/w)}$, NE 2%$_{(w/w)}$ and PLA 20%$_{(w/w)}$ electrospun.

Electrospun nanofibers organize into an interconnected nanoarchitecture, forming a membrane with porosity that enhances surface hydrophobicity and promotes strong adhesion forces with water [61]. In core–shell nanofibers, the use of PLA as the shell inherently implies that the nanofibers will exhibit a hydrophobic surface due to the high hydrophobicity of this polymer. In cases where not all the hydrophilic core content is fully coated by the shell, a reduction in membrane hydrophobicity is observed due to the presence of hydrophilic nanofibers [77].

Surface hydrophilicity assays revealed that the produced nanofibers exhibit high hydrophobicity, indicating strong antibioadhesive properties. This feature is particularly advantageous for preventing membrane adhesion to tissues, such as in tendon and abdominal surgeries [78], and can also reduce bacterial adhesion [79], enhance resistance to moisture, and protect the hydrophilic core from premature degradation. Although such high hydrophobicity may limit direct cell interactions, it can be controllably modulated through surface modifications, such as plasma treatment [80], photopolymerization [81], or chemical grafting [82]. These approaches introduce polar functional groups and tune wettability without altering the internal fiber composition. When combined with the presence of hyaluronic acid in the core, which provides biofunctional potential, these strategies broaden the scope of possible biomedical applications, ranging from wound healing and tissue engineering to the controlled release of bioactive molecules [83-85].

Conclusion

The results of this study demonstrate the potential of PLA coaxial nanofibers as hybrid systems for the controlled release of bioactive compounds, particularly in topical administration of both hydrophilic and lipophilic agents, such as hyaluronic acid and β-caryophyllene. The application of coaxial electrospinning allowed the formation of well-defined core–shell structures, as confirmed by morphological, spectroscopic, and thermal analyses. Efficient core encapsulation was evidenced by confocal microscopy, FTIR spectroscopy, and selective core removal tests, which indicated the effective isolation of the bioactive components by the PLA shell. From a physicochemical perspective, the fibers presented good thermal stability without compromising the properties of the base polymer. The variation of electrospinning parameters revealed that small changes in core flow rate, HA, and NE-βCp concentration, as well as electrical voltage, directly influence the morphology of the fibers, affecting their uniformity and the presence of structural defects in the form of beads.

Additionally, the presence of porosities in the shell, resulting from the removal of the core, suggests a viable mechanism for the controlled release of active ingredients through diffusion. The high surface hydrophobicity of the nanofibers, confirmed by contact angle measurements, reinforces their potential use in applications that require low tissue adhesion, such as non-adherent dressings. However, for applications where cell adhesion is desired, surface modifications may be necessary. Thus, the data presented here significantly contribute to the understanding of polymer–lipid interactions in coaxial systems and pave the way for the development of multifunctional nanofibers in tissue engineering and controlled drug delivery. Despite these promising results, the present study has some limitations. The encapsulation efficiency and release kinetics of the bioactive compounds were not quantified, and biological assessments were not performed at this stage. Furthermore, morphological instabilities observed at higher core flow rates limited the range of processing conditions which could be explored. These limita-

tions underscore the need for further investigations to establish the translational potential of the proposed nanofiber systems. Future studies will therefore focus on evaluating encapsulation efficiency and conducting in vitro release assays, employing transmission electron microscopy for more detailed visualization of the core–shell structure, and performing biological assessments such as cytocompatibility and scratch wound healing tests to validate the performance of these nanofibers as bioactive dressings. Additionally, surface modification strategies may be explored to tailor adhesion properties according to the intended biomedical application.

Experimental

Materials

Tween® 80 (polyoxyethylene (20) sorbitan monooleate), Span® 80 (sorbitan monooleate), β-caryophyllene (purity ≥80%), fluorescein, poly(lactic acid) (M_w ≈ 93,156 Da), anhydrous chloroform (PA), and PBS tablets (pH 7.2–7.6) were obtained from Sigma-Aldrich (USA). Captex® 300 was kindly provided by ABITEC Corporation (USA). Pharmaceutical-grade hyaluronic acid (95% purity) was purchased from Shandong Focuschem Biotech Co. (China), saline solution (0.9% sodium chloride) from Needs (Brazil), and *N*,*N*-dimethylformamide (DMF, PA) from Vetec Química Fina Ltda (Brazil).

Manufacturing nanoemulsion via the sonication method

βCp-loaded nanoemulsions were prepared by the sonication method. Briefly, an aqueous and an oil phase were prepared under magnetic stirring, with their composition specified in Table 4. Subsequently, the aqueous phase was carefully added to the oil phase. The mixture was subjected to vortex (IKA) mixing for 5 min, followed by ultrasonication for 5 min at an amplitude of 40% using an ultrasonic device (Eco-sonics/Brazil).

Table 4: Composition of the β-caryophyllene-loaded nanoemulsions.

Excipients	% (w/w)
β-caryophyllene	2.5
Captex® 300	2.5
Span® 80	1.4
Tween® 80	3.6
distilled water	90.0

Electrospinning of nanofibers

Coaxial electrospinning setup

The coaxial electrospinning apparatus consisted of an acrylic enclosure to isolate the system, a high-voltage power supply (positioned atop the enclosure) connected to the tip of a core–shell needle, two independent syringe pumps, and a grounded collector. The relative humidity within the enclosure was maintained between 39% and 60% using a dehumidifier and an air conditioning system, ensuring consistent fiber formation conditions.

Preparation of polymer solutions

For the shell solution, a 20% (w/v) PLA solution was prepared by dissolving PLA in a 2:8 (v/v) mixture of DMF and chloroform. The core solution was composed of HA at varying concentrations, solubilized in 0.9% (w/v) sodium chloride solution (physiological saline) under constant stirring at room temperature until fully dissolved. To incorporate the nanoemulsion into the fiber core, 2% and 5% (w/w), of NE relative to the total core solution were added to the HA solution and stirred for 1 h to ensure homogeneity.

Fabrication of coaxial nanofibers

Coaxial nanofibers were produced using two plastic syringes – one loaded with the PLA shell solution and the other with the HA solution or a mix of HA+NE to the core. Each syringe was connected to an individual syringe pump for independent control of flow rate. The coaxial needle assembly comprised two stainless steel needles concentrically aligned, with an 18G outer needle for the shell solution and a 20G inner needle for the core solution, coaxially fixed.

Fabrication of monolithic PLA nanofibers

For comparative purposes, monolithic PLA nanofibers were produced using the same 20% (w/v) PLA solution. An 18-gauge needle connected to a 5 mL plastic syringe was used, operated with a single syringe pump. Electrospinning parameters were as follows: an applied voltage of 17 kV, a flow rate of 0.25 mL/h, a needle-to-collector distance of 12 cm, and a processing time of 5 h.

Physicochemical characterizations

Droplet size

NE-βCp were characterized for hydrodynamic diameter (*z*-average) and PDI using dynamic light scattering (DLS) with a Zetasizer Nano ZS (Malvern Instruments, UK) at 25 °C. The measurements were based on a refractive index of 1.34 for the material. Prior to analysis, the samples were diluted at a ratio of 1:10 (βCp/distilled water). The reported parameters represent the average of readings performed in triplicate for each sample analyzed using the ZetaSizer software 7.11.

Scanning electron microscopy

The morphology of the obtained nanofibers (porosity, average diameter, uniformity, and roughness) was evaluated using a

scanning electron microscope under different production conditions. This evaluation allowed for the observation of the cross-sectional structure before and after core removal. The nanofibers were coated with approximately 10 nm of gold via sputter deposition for 1 min at 30 mA. Micrographs were acquired using an acceleration voltage of 2 kV and 0.21 nA on a Nova 600 NanoLab system (FEI Company, Thermo Fisher Scientific, USA). The average diameter of the nanofibers (n = 120) was calculated using the SizeMeter software. Forty fibers were measured in three distinct regions of the same sample, and the mean value was obtained.

Cross-sectional analysis

SEM imaging of the cross-section of the HA+NE2/PLA sample was performed before and after core removal to observe the core–shell structure. For core removal, a portion of the sample was washed multiple times with distilled water, followed by ethanol, and then dried at room temperature. Samples, both before and after washing, were immersed in liquid nitrogen and fractured using tweezers. The fractured samples were mounted on 45 degree stubs to capture cross-sectional images without requiring the sample holder to be moved.

Confocal microscopy

Confocal microscopy was conducted to observe the distribution of the core within nanofibers produced via coaxial electrospinning. A disk scanning unit confocal microscope (Olympus, Japan) was utilized for this analysis. Fluorescein was added to the core solution (1% HA + 2% NE) to enable fluorescence imaging during microscopic observation.

Thermogravimetric analysis

The thermal stability of the nanofibers was investigated using a Q500 thermogravimetric analyzer (TA Instruments, USA) equipped with platinum (Pt) crucibles. Mass loss as a function of temperature was recorded from 30 to 700 °C at a heating rate of 10 °C/min under a nitrogen atmosphere. Samples analyzed included monolithic PLA nanofibers, HA/PLA, HA+NE2/PLA, and HA powder.

Differential scanning calorimetry

DSC analysis was performed using a Q2000 differential scanning calorimeter (TA Instruments, USA) to assess the impact of core–shell formation and NE incorporation on the thermal properties of the nanofibers. Key parameters evaluated included: glass transition temperature (T_g), crystallization temperature upon cooling (T_{cc}), melting temperature (T_m), melting enthalpy (ΔH_m), and crystallization enthalpy (ΔH_{cc}). Furthermore, the degree of crystallinity (X_c%) of PLA within the nanofibers was calculated. Samples (monolithic PLA, HA/PLA, and HA+NE2/PLA) were subjected to three heating/cooling cycles. Each cycle involved heating to 200 °C at a rate of 10 °C/min under nitrogen, holding for 1 min, and then cooling at the same rate. The crystallinity of the PLA shell (X_c%) was calculated using the following equation:

$$X_c\% = \frac{\Delta H_m - \Delta H_{cc}}{X_{PLA} - \Delta H_{m0}}, \quad (1)$$

where ΔH_{m0} is the melting enthalpy of fully crystalline PLA (93.1 J/g), and X_{PLA} is the mass fraction of PLA in the fiber (Vidal et al., 2022) [68].

Fourier transform infrared spectroscopy

FTIR analysis was conducted to examine the surface composition of the nanofibers and confirm core encapsulation within the PLA shell. An ATR-FTIR spectrometer (Frontier FT-IR/FIR, PerkinElmer, USA) was used to acquire spectra in the range of 4000–600 cm^{-1} with a resolution of 4 cm^{-1} and 60 scans. Samples analyzed included monolithic PLA nanofibers, HA/PLA, HA+NE2/PLA, and HA powder.

X-ray diffraction

XRD analyses of PLA nanofibers (monolithic), HA/PLA, HA+NE2/PLA, and HA and PLA powders were performed to investigate and characterize the crystalline structure of the samples and their polymers. Nanofiber samples were cut into circular shapes with a diameter of 2.5 cm and placed on the sample holder. For polymer powders, sieving was conducted using an ASTM 70 mesh (212 µm) before compressing the powders onto the sample holder to ensure grain homogeneity. The analyses were carried out using a LabX XRD-6100 diffractometer (Shimadzu, Japan) in an angle ranging from 2° to 50° (2θ), using a step size of 0.02° (2θ), and Cu Kα radiation (λ = 1.5418 Å) with a voltage of 40 kV and a current of 30 mA. The degree of crystallinity (X_c%) of each sample was calculated from the diffractogram using Equation 2 (Madsen et al., 2011) [72]. The areas of the peaks in the diffractograms were determined using OriginPro 8.5 software (OriginLab Corporation).

$$X_c\% = \left(\frac{\text{CrystallineArea}}{\text{CrystallineArea}+\text{AmorphousArea}}\right)\times 100. \quad (2)$$

Contact angle analysis

Contact angle measurements were conducted to evaluate the surface wettability of PLA nanofiber samples, including monolithic PLA, HA/PLA, and HA+NE2/PLA, using an OCA 15EC optical contact angle tensiometer (Dataphysics Instruments, Germany). Samples were cut into 1.5 cm × 2 cm sections and fixed to a metal holder. Afterward, a droplet of distilled water

was placed on three distinct regions on the surface of each sample, and images were captured to determine the contact angle. The final contact angle value of each sample was calculated as the average of the three measurements.

Statistical analysis

All samples were produced in triplicate. Statistical analysis was performed using OriginPro 8.5 software (OriginLab Corporation). The diameters of the obtained nanofibers were quantified from the micrographs using SizeMeter.

Funding

This work was supported by Foundation for Research Support in the State of Rio de Janeiro (FAPERJ) - Brazil:

1. Rede Rio de Inovação em Nanossistemas para a Saúde, Rio de Janeiro, RJ, Brazil [grant numbers: E-26/010.000983/2019].

2. Apoio aos Programas e Cursos de Pós-Graduação stricto sensu do estado do Rio de Janeiro - 2021 [grant numbers: E_29/2021].

3. This study was financed in part by the Coordenação de Aperfeiçoamento de Pessoal de Nível Superior – Brasil (CAPES) – Finance Code 001.

Author Contributions

Aline Tavares da Silva Barreto: conceptualization; investigation; writing – original draft. Francisco Alexandrino-Júnior: project administration; writing – original draft; writing – review & editing. Bráulio Soares Arcanjo: methodology; project administration; supervision. Paulo Henrique de Souza Picciani: conceptualization; formal analysis; investigation; project administration. Kattya Gyselle de Holanda e Silva: conceptualization; funding acquisition; project administration; resources; supervision; writing – original draft; writing – review & editing.

ORCID® iDs

Aline Tavares da Silva Barreto - https://orcid.org/0000-0002-2712-0913
Bráulio Soares Arcanjo - https://orcid.org/0000-0001-8145-7712
Kattya Gyselle de Holanda e Silva - https://orcid.org/0000-0002-8750-1726

Data Availability Statement

Data generated and analyzed during this study is available from the corresponding author upon reasonable request.

References

1. Rahmati, M.; Mills, D. K.; Urbanska, A. M.; Saeb, M. R.; Venugopal, J. R.; Ramakrishna, S.; Mozafari, M. *Prog. Mater. Sci.* **2021,** *117,* 100721. doi:10.1016/j.pmatsci.2020.100721
2. Zhao, L.; Li, X.; Yang, L.; Sun, L.; Mu, S.; Zong, H.; Li, Q.; Wang, F.; Song, S.; Yang, C.; Zhao, C.; Chen, H.; Zhang, R.; Wang, S.; Dong, Y.; Zhang, Q. *Mater. Sci. Eng.: C* **2021,** *118,* 111441. doi:10.1016/j.msec.2020.111441
3. Banerjee, S.; Banerjee, S.; Mondal, A. Nanomaterials regenerative medicine and tissue engineering. *Nanostructured Materials for Tissue Engineering;* Elsevier: Amsterdam, Netherlands, 2023; pp 3–53. doi:10.1016/b978-0-323-95134-0.00001-8
4. Jonidi Shariatzadeh, F.; Currie, S.; Logsetty, S.; Spiwak, R.; Liu, S. *Prog. Mater. Sci.* **2025,** *147,* 101350. doi:10.1016/j.pmatsci.2024.101350
5. Ding, J.; Zhang, J.; Li, J.; Li, D.; Xiao, C.; Xiao, H.; Yang, H.; Zhuang, X.; Chen, X. *Prog. Polym. Sci.* **2019,** *90,* 1–34. doi:10.1016/j.progpolymsci.2019.01.002
6. Ilomuanya, M. O.; Okafor, P. S.; Amajuoyi, J. N.; Onyejekwe, J. C.; Okubanjo, O. O.; Adeosun, S. O.; Silva, B. O. *Beni-Suef Univ. J. Basic Appl. Sci.* **2020,** *9,* 31. doi:10.1186/s43088-020-00057-9
7. Chen, X.; Li, H.; Lu, W.; Guo, Y. *Nanomaterials* **2021,** *11,* 1316. doi:10.3390/nano11051316
8. El-Naggar, M. E.; Shalaby, E. S.; Abd-Al-Aleem, A. H.; Abu-Saied, M. A.; Youssef, A. M. *J. Mater. Res. Technol.* **2021,** *15,* 3447–3460. doi:10.1016/j.jmrt.2021.09.136
9. Razzaq, A.; Khan, Z. U.; Saeed, A.; Shah, K. A.; Khan, N. U.; Menaa, B.; Iqbal, H.; Menaa, F. *Pharmaceutics* **2021,** *13,* 349. doi:10.3390/pharmaceutics13030349
10. Abboud, H. A.; Zelkó, R.; Kazsoki, A. *Drug Delivery* **2025,** *32,* 2445259. doi:10.1080/10717544.2024.2445259
11. Pant, B.; Park, M.; Park, S.-J. *Pharmaceutics* **2019,** *11,* 305. doi:10.3390/pharmaceutics11070305
12. Lugoloobi, I.; Yuanhao, W.; Marriam, I.; Hu, J.; Tebyetekerwa, M.; Ramakrishna, S. *Curr. Opin. Biomed. Eng.* **2022,** *24,* 100418. doi:10.1016/j.cobme.2022.100418
13. Hiwrale, A.; Bharati, S.; Pingale, P.; Rajput, A. *Heliyon* **2023,** *9,* e18917. doi:10.1016/j.heliyon.2023.e18917
14. Rajabifar, N.; Rostami, A.; Afshar, S.; Mosallanezhad, P.; Zarrintaj, P.; Shahrousvand, M.; Nazockdast, H. *Polymers (Basel, Switz.)* **2024,** *16,* 2526. doi:10.3390/polym16172526
15. Zhao, J.; Chen, L.; Ma, A.; Bai, X.; Zeng, Y.; Liu, D.; Liu, B.; Zhang, W.; Tang, S. *Mater. Today Bio* **2024,** *29,* 101309. doi:10.1016/j.mtbio.2024.101309
16. Abdullah, M. F.; Nuge, T.; Andriyana, A.; Ang, B. C.; Muhamad, F. *Polymers (Basel, Switz.)* **2019,** *11,* 2008. doi:10.3390/polym11122008
17. Ahmadi Bonakdar, M.; Rodrigue, D. *Macromol* **2024,** *4,* 58–103. doi:10.3390/macromol4010004
18. Xue, J.; Wu, T.; Dai, Y.; Xia, Y. *Chem. Rev.* **2019,** *119,* 5298–5415. doi:10.1021/acs.chemrev.8b00593
19. Ji, D.; Lin, Y.; Guo, X.; Ramasubramanian, B.; Wang, R.; Radacsi, N.; Jose, R.; Qin, X.; Ramakrishna, S. *Nat. Rev. Methods Primers* **2024,** *4,* 1. doi:10.1038/s43586-023-00278-z
20. Gorrasi, G.; Pantani, R. Hydrolysis and Biodegradation of Poly(lactic acid). *Advances in Polymer Science;* Springer: Cham, Switzerland, 2017; pp 119–151. doi:10.1007/12_2016_12
21. Khouri, N. G.; Bahú, J. O.; Blanco-Llamero, C.; Severino, P.; Concha, V. O. C.; Souto, E. B. *J. Mol. Struct.* **2024,** *1309,* 138243. doi:10.1016/j.molstruc.2024.138243
22. Carrasco, F.; Pagès, P.; Gámez-Pérez, J.; Santana, O. O.; Maspoch, M. L. *Polym. Degrad. Stab.* **2010,** *95,* 116–125. doi:10.1016/j.polymdegradstab.2009.11.045

23. Tyler, B.; Gullotti, D.; Mangraviti, A.; Utsuki, T.; Brem, H. *Adv. Drug Delivery Rev.* **2016,** *107,* 163–175. doi:10.1016/j.addr.2016.06.018
24. Trivedi, A. K.; Gupta, M. K.; Singh, H. *Adv. Ind. Eng. Polym. Res.* **2023,** *6,* 382–395. doi:10.1016/j.aiepr.2023.02.002
25. Habibi, S.; Ghajarieh, A.; Ahmadi, S. *Russ. J. Appl. Chem.* **2024,** *97,* 803–818. doi:10.1134/s1070427224110016
26. Graça, M. F. P.; Miguel, S. P.; Cabral, C. S. D.; Correia, I. J. *Carbohydr. Polym.* **2020,** *241,* 116364. doi:10.1016/j.carbpol.2020.116364
27. Roehrs, H.; Stocco, J. G. D.; Pott, F.; Blanc, G.; Meier, M. J.; Dias, F. A. L. *Cochrane Database Syst. Rev.* **2023,** CD012215. doi:10.1002/14651858.cd012215.pub2
28. Carton, F.; Malatesta, M. *Int. J. Mol. Sci.* **2024,** *25,* 3975. doi:10.3390/ijms25073975
29. Salih, A. R. C.; Farooqi, H. M. U.; Amin, H.; Karn, P. R.; Meghani, N.; Nagendran, S. *Future J. Pharm. Sci.* **2024,** *10,* 63. doi:10.1186/s43094-024-00636-y
30. Di Sotto, A.; Mancinelli, R.; Gullì, M.; Eufemi, M.; Mammola, C. L.; Mazzanti, G.; Di Giacomo, S. *Cancers* **2020,** *12,* 3034. doi:10.3390/cancers12103034
31. Gyrdymova, Y. V.; Rubtsova, S. A. *Chem. Pap.* **2022,** *76,* 1–39. doi:10.1007/s11696-021-01865-8
32. Koyama, S.; Purk, A.; Kaur, M.; Soini, H. A.; Novotny, M. V.; Davis, K.; Kao, C. C.; Matsunami, H.; Mescher, A. *PLoS One* **2019,** *14,* e0216104. doi:10.1371/journal.pone.0216104
33. Parikh, A. C.; Jeffery, C. S.; Sandhu, Z.; Brownlee, B. P.; Queimado, L.; Mims, M. M. *Health Sci. Rep.* **2024,** *7,* e1908. doi:10.1002/hsr2.1908
34. Collado, I. G.; Hanson, J. R.; Macías-Sánchez, A. J. *Nat. Prod. Rep.* **1998,** *15,* 187–204. doi:10.1039/a815187y
35. Santos, P. S.; Oliveira, T. C.; Júnior, L. M. R.; Figueiras, A.; Nunes, L. C. C. *Curr. Pharm. Des.* **2018,** *24,* 3440–3453. doi:10.2174/1381612824666180912151412
36. de Oliveira Neves, J. K.; Apolinário, A. C.; Alcantara Saraiva, K. L.; da Silva, D. T. C.; de Freitas Araújo Reis, M. Y.; de Lima Damasceno, B. P. G.; Pessoa, A., Jr.; Moraes Galvão, M. A.; Soares, L. A. L.; Veiga Júnior, V. F. d.; Silva, J. A. d.; Converti, A. *Ind. Crops Prod.* **2018,** *111,* 185–192. doi:10.1016/j.indcrop.2017.10.025
37. Parisotto-Peterle, J.; Bidone, J.; Lucca, L. G.; Araújo, G. d. M. S.; Falkembach, M. C.; da Silva Marques, M.; Horn, A. P.; dos Santos, M. K.; da Veiga, V. F., Jr.; Limberger, R. P.; Teixeira, H. F.; Dora, C. L.; Koester, L. S. *Eur. J. Pharm. Sci.* **2020,** *148,* 105318. doi:10.1016/j.ejps.2020.105318
38. Baranda, E. R.; Santos, J. S.; Toledo, A. L. M. M.; Barradas, T. N. *Beilstein Arch.* **2025,** 202536. doi:10.3762/bxiv.2025.36.v1
39. Huang, Y.; Huang, H.; Wu, J.; Feng, Q.; Li, Y.; Li, Q.; Sun, T. *Food Res. Int.* **2024,** *194,* 114817. doi:10.1016/j.foodres.2024.114817
40. Kenawy, E.-R.; Hemdan, B. A.; Abdel-Sattar, R.; Khairallah, M. R.; Shendy, S.; Morsy, O. M.; El-Naggar, M. E. *Polym. Adv. Technol.* **2024,** *35,* e6594. doi:10.1002/pat.6594
41. Farahani, H.; Barati, A.; Arjomandzadegan, M.; Vatankhah, E. *Int. J. Biol. Macromol.* **2020,** *162,* 762–773. doi:10.1016/j.ijbiomac.2020.06.175
42. El-Naggar, M. E.; Abdelgawad, A. M.; Abdel-Sattar, R.; Gibriel, A. A.; Hemdan, B. A. *Eur. Polym. J.* **2023,** *184,* 111782. doi:10.1016/j.eurpolymj.2022.111782
43. Kaur, K.; Singh, A.; Rajput, N.; Bhullar, V.; Monga, A.; Mahajan, A.; Gahlay, G. K.; Bedi, N. *J. Drug Delivery Sci. Technol.* **2024,** *92,* 105311. doi:10.1016/j.jddst.2023.105311
44. Kaur, K.; Kant, S.; Chaudary, T. K.; Mehra, A.; Singh, A.; Attri, S.; Gasso, S.; Mahajan, A.; Bedi, N. *Naunyn-Schmiedeberg's Arch. Pharmacol.* **2024,** *397,* 6075–6091. doi:10.1007/s00210-024-03011-z
45. Coelho, D.; Veleirinho, B.; Mazzarino, L.; Alberti, T.; Buzanello, E.; Oliveira, R. E.; Yunes, R. A.; Moraes, M.; Steindel, M.; Maraschin, M. *Colloids Surf., B* **2021,** *198,* 111390. doi:10.1016/j.colsurfb.2020.111390
46. Ricaurte, L.; Perea-Flores, M. d. J.; Méndez-Méndez, J. V.; Santagapita, P. R.; Quintanilla-Carvajal, M. X. *Colloids Surf., A* **2022,** *636,* 128148. doi:10.1016/j.colsurfa.2021.128148
47. Yao, S.; Wang, X.; Liu, X.; Wang, R.; Deng, C.; Cui, F. *J. Nanosci. Nanotechnol.* **2013,** *13,* 4752–4758. doi:10.1166/jnn.2013.7197
48. Castro, K. C.; Campos, M. G. N.; Mei, L. H. I. *Int. J. Biol. Macromol.* **2021,** *173,* 251–266. doi:10.1016/j.ijbiomac.2021.01.100
49. Abdulhussain, R.; Adebisi, A.; Conway, B. R.; Asare-Addo, K. *J. Drug Delivery Sci. Technol.* **2023,** *90,* 105156. doi:10.1016/j.jddst.2023.105156
50. Tarmizie Hassim, M.; Prabhakar, M. N.; Song, J.-i. *Composites, Part A* **2023,** *173,* 107661. doi:10.1016/j.compositesa.2023.107661
51. Li, Y.; Lim, C. T.; Kotaki, M. *Polymer* **2015,** *56,* 572–580. doi:10.1016/j.polymer.2014.10.073
52. Li, M.; Zheng, Y.; Xin, B.; Xu, Y. *Ind. Eng. Chem. Res.* **2020,** *59,* 6301–6308. doi:10.1021/acs.iecr.9b05866
53. Rêgo, T. R. S.; Toledo, A. L. M. M.; Dias, M. L. *Processes* **2025,** *13,* 1837. doi:10.3390/pr13061837
54. Jacobs, V.; Anandjiwala, R. D.; Maaza, M. *J. Appl. Polym. Sci.* **2010,** *115,* 3130–3136. doi:10.1002/app.31396
55. Lai, H.-J.; Kuan, C.-H.; Wu, H.-C.; Tsai, J.-C.; Chen, T.-M.; Hsieh, D.-J.; Wang, T.-W. *Acta Biomater.* **2014,** *10,* 4156–4166. doi:10.1016/j.actbio.2014.05.001
56. Wang, Y.; Xu, L. *Polymers (Basel, Switz.)* **2018,** *10,* 144. doi:10.3390/polym10020144
57. Yang, J.; Xu, L. *Materials* **2023,** *16,* 6021. doi:10.3390/ma16176021
58. Nguyen, T. T. T.; Ghosh, C.; Hwang, S.-G.; Chanunpanich, N.; Park, J. S. *Int. J. Pharm.* **2012,** *439,* 296–306. doi:10.1016/j.ijpharm.2012.09.019
59. Augustine, R.; Zahid, A. A.; Hasan, A.; Wang, M.; Webster, T. J. *Int. J. Nanomed.* **2019,** *14,* 8573–8588. doi:10.2147/ijn.s224047
60. Fang, Y.; Zhu, X.; Wang, N.; Zhang, X.; Yang, D.; Nie, J.; Ma, G. *Eur. Polym. J.* **2019,** *116,* 30–37. doi:10.1016/j.eurpolymj.2019.03.050
61. da Silva, T. N.; Gonçalves, R. P.; Rocha, C. L.; Archanjo, B. S.; Barboza, C. A. G.; Pierre, M. B. R.; Reynaud, F.; de Souza Picciani, P. H. *Mater. Sci. Eng.: C* **2019,** *97,* 602–612. doi:10.1016/j.msec.2018.12.020
62. Chieng, B. W.; Ibrahim, N. A.; Yunus, W. M. Z. W.; Hussein, M. Z. *Polymers (Basel, Switz.)* **2014,** *6,* 93–104. doi:10.3390/polym6010093
63. Chen, G.; Guo, J.; Nie, J.; Ma, G. *Polymer* **2016,** *83,* 12–19. doi:10.1016/j.polymer.2015.12.002
64. Séon-Lutz, M.; Couffin, A.-C.; Vignoud, S.; Schlatter, G.; Hébraud, A. *Carbohydr. Polym.* **2019,** *207,* 276–287. doi:10.1016/j.carbpol.2018.11.085
65. Leonés, A.; Peponi, L.; Lieblich, M.; Benavente, R.; Fiori, S. *Polymers (Basel, Switz.)* **2020,** *12,* 2975. doi:10.3390/polym12122975

66. Ahire, J. J.; Robertson, D.; Neveling, D. P.; van Reenen, A. J.; Dicks, L. M. T. *RSC Adv.* **2016,** *6,* 34791–34796. doi:10.1039/c6ra01996j
67. Kim, S. J.; Shin, S. R.; Lee, S. M.; Kim, I. Y.; Kim, S. I. *J. Macromol. Sci., Part A: Pure Appl. Chem.* **2003,** *40,* 807–815. doi:10.1081/ma-120022272
68. Vidal, C. P.; Velásquez, E.; Galotto, M. J.; López de Dicastillo, C. *Polym. Test.* **2021,** *93,* 106937. doi:10.1016/j.polymertesting.2020.106937
69. Oliveira, J. E.; Mattoso, L. H. C.; Orts, W. J.; Medeiros, E. S. *Adv. Mater. Sci. Eng.* **2013,** 409572. doi:10.1155/2013/409572
70. Radusin, T.; Torres-Giner, S.; Stupar, A.; Ristic, I.; Miletic, A.; Novakovic, A.; Lagaron, J. M. *Food Packag. Shelf Life* **2019,** *21,* 100357. doi:10.1016/j.fpsl.2019.100357
71. Kaczmarek, H.; Nowicki, M.; Vuković-Kwiatkowska, I.; Nowakowska, S. *J. Polym. Res.* **2013,** *20,* 91. doi:10.1007/s10965-013-0091-y
72. Madsen, I. C.; Scarlett, N. V. Y.; Kern, A. *Z. Kristallogr. - Cryst. Mater.* **2011,** *226,* 944–955. doi:10.1524/zkri.2011.1437
73. Tsuji, H.; Del Carpio, C. A. *Biomacromolecules* **2003,** *4,* 7–11. doi:10.1021/bm020090v
74. Cifuentes, S. C.; Lieblich, M.; Saldaña, L.; González-Carrasco, J. L.; Benavente, R. *Materialia* **2019,** *6,* 100270. doi:10.1016/j.mtla.2019.100270
75. Tsuji, H.; Mizuno, A.; Ikada, Y. *J. Appl. Polym. Sci.* **2000,** *77,* 1452–1464. doi:10.1002/1097-4628(20000815)77:7<1452::aid-app7>3.0.co;2-s
76. Seif, S.; Franzen, L.; Windbergs, M. *Int. J. Pharm.* **2015,** *478,* 390–397. doi:10.1016/j.ijpharm.2014.11.045
77. Gonçalves, R. P.; da Silva, F. F. F.; Picciani, P. H. S.; Dias, M. L. *Mater. Sci. Appl.* **2015,** *06,* 189–199. doi:10.4236/msa.2015.62022
78. Shalumon, K. T.; Sheu, C.; Chen, C.-H.; Chen, S.-H.; Jose, G.; Kuo, C.-Y.; Chen, J.-P. *Acta Biomater.* **2018,** *72,* 121–136. doi:10.1016/j.actbio.2018.03.044
79. Chanda, A.; Adhikari, J.; Ghosh, A.; Chowdhury, S. R.; Thomas, S.; Datta, P.; Saha, P. *Int. J. Biol. Macromol.* **2018,** *116,* 774–785. doi:10.1016/j.ijbiomac.2018.05.099
80. Nandakumar, A.; Tahmasebi Birgani, Z.; Santos, D.; Mentink, A.; Auffermann, N.; van der Werf, K.; Bennink, M.; Moroni, L.; van Blitterswijk, C.; Habibovic, P. *Biofabrication* **2013,** *5,* 015006. doi:10.1088/1758-5082/5/1/015006
81. Ahmadipour, Z.; Seyed Dorraji, M. S.; Ashjari, H. R.; Dodangeh, F.; Rasoulifard, M. H. *Sci. Rep.* **2023,** *13,* 9741. doi:10.1038/s41598-023-36893-9
82. Baraka, F.; Santos, J. I.; Langari, M. M.; Rivilla, I.; Labidi, J. *Chem. Eng. J.* **2025,** *506,* 160349. doi:10.1016/j.cej.2025.160349
83. Qian, Y.; Li, L.; Jiang, C.; Xu, W.; Lv, Y.; Zhong, L.; Cai, K.; Yang, L. *Int. J. Biol. Macromol.* **2015,** *79,* 133–143. doi:10.1016/j.ijbiomac.2015.04.059
84. Knopf-Marques, H.; Pravda, M.; Wolfova, L.; Velebny, V.; Schaaf, P.; Vrana, N. E.; Lavalle, P. *Adv. Healthcare Mater.* **2016,** *5,* 2841–2855. doi:10.1002/adhm.201600316
85. Martin, A. R.; Patel, J. M.; Locke, R. C.; Eby, M. R.; Saleh, K. S.; Davidson, M. D.; Sennett, M. L.; Zlotnick, H. M.; Chang, A. H.; Carey, J. L.; Burdick, J. A.; Mauck, R. L. *Acta Biomater.* **2021,** *126,* 170–182. doi:10.1016/j.actbio.2021.03.013

License and Terms

BEILSTEIN JOURNAL OF NANOTECHNOLOGY

Quality by design optimization of microemulsions for topical delivery of *Passiflora setacea* seed oil

Daniel T. Pereira[1,2], Douglas Dourado[1], Danielle T. Freire[1,3], Dayanne L. Porto[4], Cícero F. S. Aragão[4], Myla L. de Souza[5], Guilherme R. S. de Araujo[6], Ana Maria Costa[7], Wógenes N. Oliveira[1], Anne Sapin-Minet[2], Éverton N. Alencar[1,3] and Eryvaldo Sócrates T. Egito[*1,§]

Full Research Paper

Open Access

Address:
[1]Graduate Program in Health Sciences, Federal University of Rio Grande do Norte (UFRN), R. Gen. Gustavo Cordeiro de Farias, s/n, Natal-RN, 59012-520, Brazil, [2]CITHEFOR, Université de Lorraine, Nancy, F-54000, France, [3]Laboratory of Micro and Nanostructured Systems, College of Pharmaceutical Sciences, Food and Nutrition, Federal University of Mato Grosso do Sul (UFMS), Cidade Universitária, s/n, Campo Grande-MS, 79070-900, Brazil, [4]Department of Pharmacy, Federal University of Rio Grande do Norte, R. Gen. Gustavo Cordeiro de Farias, s/n, Natal-RN, 59012-570, Brazil, [5]Laboratório de Tecnologia dos Medicamentos, Department of Pharmaceutical Sciences, Federal University of Pernambuco (UFPE), Av. Prof. Moraes Rego, 1235, Recife-PE, 50670-901, Brazil, [6]Department of Pharmaceutical Sciences, Federal University of Sergipe (UFS), Av. Marcelo Deda Chagas, s/n, São Cristóvão-SE, 49100-000, Brazil and [7]Embrapa Cerrados, Laboratory of Food Science, BR-020, km 18, s/n, Planaltina-DF, 73310-970, Brazil

Email:
Eryvaldo Sócrates T. Egito[*] - socratesegito@gmail.com

* Corresponding author
§ Phone: +55 84 99431 8816

Keywords:
design of experiments (DoE); microemulsions; nanotechnology; natural products; passion fruit; quality by design; skin delivery

Beilstein J. Nanotechnol. **2025,** *16,* 2116–2131.
https://doi.org/10.3762/bjnano.16.146

Received: 18 June 2025
Accepted: 31 October 2025
Published: 20 November 2025

This article is part of the thematic issue "Advances in nanotechnology applied to natural products".

Associate Editor: Y. Corvis

Abstract

Passiflora setacea seed oil is a natural source of bioactive unsaturated fatty acids, notably linoleic acid (ω-6) and oleic acid (ω-9), with promising antioxidant and anti-inflammatory potential for dermatological applications. However, its direct use is limited by poor physicochemical and organoleptic properties. This study aimed to develop and optimize a topical microemulsion (ME) system incorporating *P. setacea* seed oil using quality by design principles to address formulation challenges. The oil was extracted via Soxhlet and characterized by gas chromatography–mass spectrometry and thermal analysis. A full factorial design, followed by a Box–Behnken design, was employed to optimize the formulation based on critical quality attributes and the defined quality target

product profile. The optimized ME presented a hydrodynamic diameter of approximately 22 nm and polydispersity index below 0.2 and remained stable for 60 days. The ME was gelled with sodium carboxymethyl cellulose, while vitamin E and Liquid Germall® Plus were incorporated as antioxidant and preservative agents, respectively, yielding the final topical gel formulation. Cytocompatibility assays demonstrated high cell viability for ME at concentrations below 2 mg/mL in RAW 264.7 macrophages and 0.5 mg/mL in human umbilical vein endothelial cells. Overall, this work presents a promising nanotechnology-based topical delivery platform for *P. setacea* seed oil, employing quality by design principles to ensure formulation performance, stability, and skin cell compatibility.

Introduction

Species of the *Passiflora* genus are known for their rich composition of fixed oils and bioactive compounds, including flavonoids and alkaloids, which exhibit significant therapeutic potential [1]. While *Passiflora edulis*, *P. alata*, and *P. incarnata* have been extensively studied in phytopharmaceutical research, recent investigations have turned attention toward underexplored wild species, such as *Passiflora setacea* [2,3].

Notably, seed oil extracted from *P. setacea* (OPS) is particularly rich in unsaturated fatty acids, predominantly linoleic acid (ω-6) and oleic acid (ω-9). Compared to other wild *Passiflora* species, OPS exhibits a markedly higher antioxidant capacity. De Santana et al. (2015) [3] reported that this enhanced activity, reflected in both radical scavenging and oxygen radical absorption capacities, is associated with the elevated levels of tocopherol isomers and total phenolic compounds in *P. setacea* samples. Overall, the composition of OPS has been linked to diverse biological effects, including anti-inflammatory, antioxidant, and skin-regenerative activities, underscoring its potential for dermatological applications [4].

Despite these promising attributes, the direct use of natural oils in topical applications is often limited by their undesirable physicochemical and organoleptic properties. These include (i) unfavorable sensorial characteristics (e.g., greasy texture, poor spreadability), (ii) strong odor, and (iii) susceptibility to oxidative degradation, which can negatively impact patient compliance and therapeutic efficacy [5].

To address these challenges, nanotechnology-based delivery systems, particularly microemulsions (MEs), offer a promising solution. Microemulsions are thermodynamically stable, isotropic mixtures typically composed of oil, water, surfactants, and co-surfactants [6]. Their spontaneous formation, high solubilization capacity, ability to enhance dermal permeation, and cost-effectiveness make microemulsions attractive carriers compared with other delivery systems [6,7]. Nevertheless, conventional microemulsions typically require high concentrations of surfactants, which may raise safety concerns such as cytotoxicity and skin irritation [8]. Furthermore, the optimization of microemulsion formulations may be time-consuming and costly, and their stability is often sensitive to environmental factors (e.g., pH, salinity, and temperature). These challenges highlight the importance of a comprehensive understanding of the physicochemical properties and interactions of their constituents [7,9].

In this context, the quality by design (QbD) framework provides a systematic and scientifically grounded approach for pharmaceutical formulation development. QbD emphasizes predefined quality objectives, product and process understanding, and risk management [10]. Key elements include the definition of a quality target product profile (QTPP), identification of critical quality attributes (CQAs), and comprehensive risk assessment (RA) [10]. The QTPP establishes the desired characteristics of the final product to ensure safety, efficacy, and patient acceptability, whereas the CQAs comprise physical, chemical, biological, and microbiological characteristics that must remain within appropriate limits to guarantee product quality [11]. In turn, RA tools complement this framework by identifying potential sources of variability and supporting the systematic optimization of the formulation [10,12].

Therefore, the present study aimed to develop and optimize a low-surfactant microemulsion containing PEG-30 castor oil and Span® 80, based on the approach described by Dourado et al. (2022) [13], as a topical delivery system for *Passiflora setacea* seed oil. QbD principles and experimental design methodologies were employed to guide formulation development. The microemulsion was designed to enhance physicochemical stability, improve skin application performance, and support future therapeutic applications.

Results and Discussion

Oil extraction and characterization

OPS was extracted using the Soxhlet method with *n*-hexane as the solvent, yielding 30.5 ± 0.8% (w/w) relative to the initial seed mass. After extraction, the oil was dried using a rotary evaporator to remove residual solvent, filtered through a PTFE membrane (0.45 μm), and stored under refrigerated conditions (4 ± 2 °C) in amber glass bottles to preserve its quality and minimize oxidative degradation and microbiological contamination.

The extraction yield aligns with values reported in the literature for the same species, which range from ≈32% with ethyl ether to ≈34% with hexane [3-5]. Such variations are commonly influenced by parameters including solvent type, moisture content of the seeds, extraction time, and temperature conditions [6].

The chemical profile of OPS was determined after transesterification to fatty acid methyl esters (FAME), followed by gas chromatography coupled with mass spectroscopy (GC–MS) analysis. The relative composition of fatty acids is presented in Table 1, and the corresponding chromatogram is provided in Figure S1 (Supporting Information File 1).

The major constituents identified in OPS were linoleic acid (64.69%), oleic acid (20.67%), palmitic acid (9.32%), and stearic acid (3.36%). Additional compounds, including isopropyl myristate, isopropyl 14-methylpentadecanoate, 10-octadecenoic acid, and isoarachidic acid, were also detected and are reported here for the first time in this *Passiflora* species. It is important to note that the transesterification process used for GC–MS analysis may yield different proportions of free fatty acids, triglycerides, and transesterified *N*-acyl lipids, potentially affecting the observed lipid profile [14].

The four predominant fatty acids in OPS (i.e., oleic, palmitic, stearic, and linoleic acids) are physiologically relevant to skin health. Oleic, palmitic, and stearic acids are the major components of the epidermal and dermal lipid matrix [15]. The balance among these fatty acids is associated with skin homeostasis, influencing the activity of enzymes that regulate keratinocyte and fibroblast proliferation [15,16]. Furthermore, linoleic acid and oleic acid serve as precursors to various lipid mediators, including prostaglandins, leukotrienes, and lipoxins, which are essential for modulating inflammatory responses and coordinating immune cell activity during wound healing [17-19].

In addition to its chemical characterization, the thermal stability in inert atmosphere (N_2) of OPS was assessed. Thermogravimetric analysis (TGA) revealed an initial mass loss of less than 1% (T_{onset} = 60 °C), likely associated with the evaporation of residual solvent entrapped in the oil matrix. A second thermal event began (T_{onset} = 384 °C) corresponding to the thermal degradation of the oil (Figure 1). This thermal behavior is consistent with that reported for *P. edulis* seed oil, which exhibited a similar decomposition profile [20].

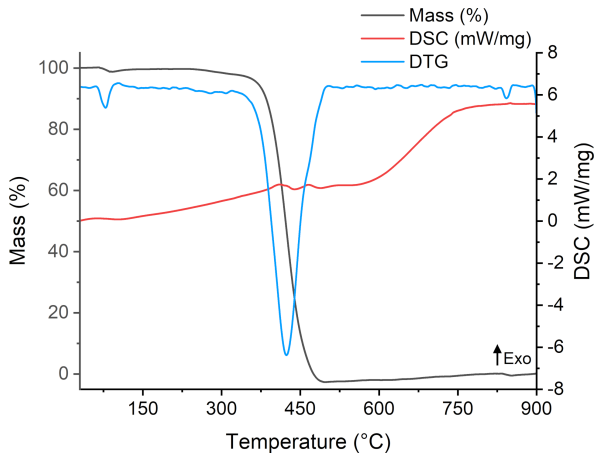

Figure 1: Thermogravimetric analysis, derivative thermogravimetry (DTG), and differential scanning calorimetry (DSC) of *P. setacea* seed oil. Legend: The black line indicates the TGA curve (% mass loss); the blue line corresponds to the DTG; and the red line shows the DSC signal (mW/mg).

Quality by design approach

Defining the product profile and critical quality attributes

In this study, the QTPP and associated CQAs were established during the pre-formulation phase, guiding the formulation strategy (Table 2) [21].

Table 1: Chemical composition of fatty acid methyl esters (FAMEs) derived from *Passiflora setacea* seed oil (OPS) as determined by GC–MS.

Compound	Retention time (min)	Composition (%)	Similarity index
impurity	24.17	0.07	–
isopropyl myristate	31.15	0.06	852
palmitic acid	33.17	9.32	967
isopropyl 14-methylpentadecanoate	35.06	1.66	881
linoleic acid	36.42	64.69	968
oleic acid	36.50	20.67	954
10-octadecenoic acid	36.57	0.11	910
stearic acid	36.93	3.36	957
isoarachidic acid	40.38	0.05	801

Table 2: Quality target product profile and corresponding justification for the microemulsion system.

QTPP	Target	Justification
dosage form	microemulsion and gelled microemulsion	thermodynamically stable systems with high permeability and biodistribution suitable for topical delivery
route of administration	topical	appropriate for skin conditions; minimizes systemic toxicity due to limited absorption and distribution
delivery type	modified-release topical system	enables rapid permeation with minimal systemic absorption, enhancing local therapeutic effect
appearance	clear, yellowish, homogeneous	ensures aesthetic appeal and uniformity, reflecting formulation quality
active pharmaceutical ingredient (API) strength	higher oil content	vegetable oil-based API is well tolerated and may enhance therapeutic outcomes
shelf stability	minimum of two months at room temperature (25 ± 2 °C)	maintains formulation integrity and therapeutic potential during preliminary storage period
safety	skin-compatible	formulation must preserve skin barrier functions, including pH and cytocompatibility
efficacy	enhanced local bioavailability	nanostructures improve drug release kinetics and skin permeation

Based on the QTPP, preformulation-level CQAs were systematically identified by assessing how their potential directly or indirectly influences the performance and quality of the final products (Table 3). These attributes encompass physicochemical, biological, and microbiological properties that must remain within defined limits to ensure the desired quality, safety, and efficacy of the microemulsion system [11].

To further assess potential formulation and process risks, an Ishikawa (fishbone) diagram was constructed to visualize and categorize possible sources of variability affecting the identified CQAs (Figure 2) [22]. Following this qualitative analysis, a risk estimation matrix (REM) was employed to quantitatively evaluate these risks. A three-level interdependence scale (1: low, 3: medium, 9: high) was applied to assess the relationship between the QTPP and CQAs (Supporting Information File 1, Table S1), as well as between the CQAs and the critical material attributes (CMAs) and critical process parameters (CPPs, Supporting Information File 1, Tables S2 and S3) [23].

To quantify the overall influence of each CMA and CPP on the final product quality, the two-risk estimation matrices (QTPP–CQA and CQA–CMA/CPP) were mathematically combined. The resulting composite scores are presented as a heatmap in Figure 3, where darker regions indicate variables

Table 3: Preformulation-level CQAs and their justification for inclusion.

Quality attribute	Target value	CQA?	Justification
hydrodynamic diameter	<100 nm	yes	microemulsions are characterized by droplet sizes below 100 nm, which directly impacts system definition and performance
polydispersity index (PdI)	<0.2	yes	a narrow size distribution (low PdI) indicates uniform droplet size and improved stability, reducing risks like Ostwald ripening
pH value	neutral to slightly acidic	yes	ensures compatibility with skin physiology and prevents irritation; pH shifts may signal degradation or instability
viscosity	$>10^3$ cP	yes	sufficient viscosity promotes appropriate spreadability, skin adherence, and user acceptability for topical formulations
appearance	transparent	yes	transparency reflects nanoscale droplet size and formulation homogeneity
surface tension	ultralow	yes	low surface tension facilitates spontaneous formation of microemulsions and affects drug solubilization and interfacial behavior
physicochemical stability	thermodynamic, oxidative, and microbiological stability	yes	ensures shelf life, safety, and preservation of the therapeutic properties of a product throughout its use

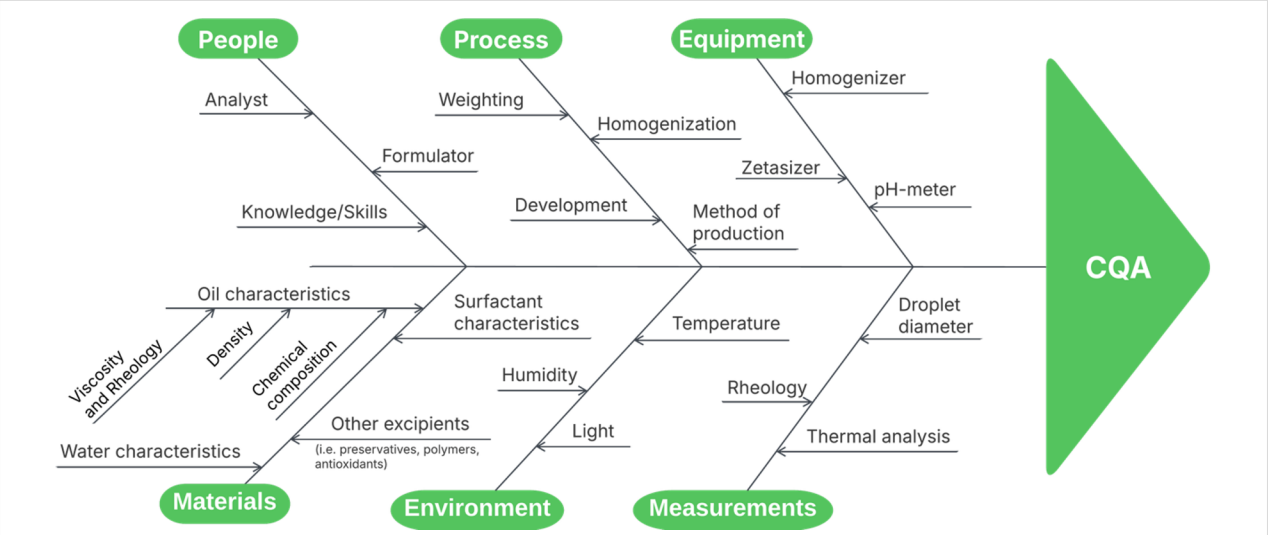

Figure 2: Ishikawa (fishbone) diagram illustrating potential sources of variability affecting CQAs in the development of the microemulsion system. Key influencing categories include people, process, equipment, materials, environment, and measurements, each contributing to formulation performance and quality consistency.

with a higher potential to compromise the ability of the product to meet the predefined QTPP. This risk prioritization informed the selection of input variables for the design of experiments (DoE) and future control strategies. Specifically, OPS concentration, surfactant mixture (S_{mix}) ratio (PEG-30 castor oil/Span® 80), and S_{mix} concentration were identified as high-risk factors and selected for the DoE due to their significant impact on the CQAs. Other high-risk variables, while not included in the DoE, were flagged for strict monitoring during formulation to ensure quality consistency.

Experimental design for the development and optimization of *Passiflora setacea* microemulsion

An initial exploratory 2^3 full factorial applied was employed to evaluate the effects and interactions among key formulation variables (see Supporting Information File 1, Tables S4 to S6). However, the presence of significant higher-order interactions limited the predictive capability and overall fit of the model. These limitations indicated the need for a more refined strategy with higher resolution and reduced confounding effects. There-

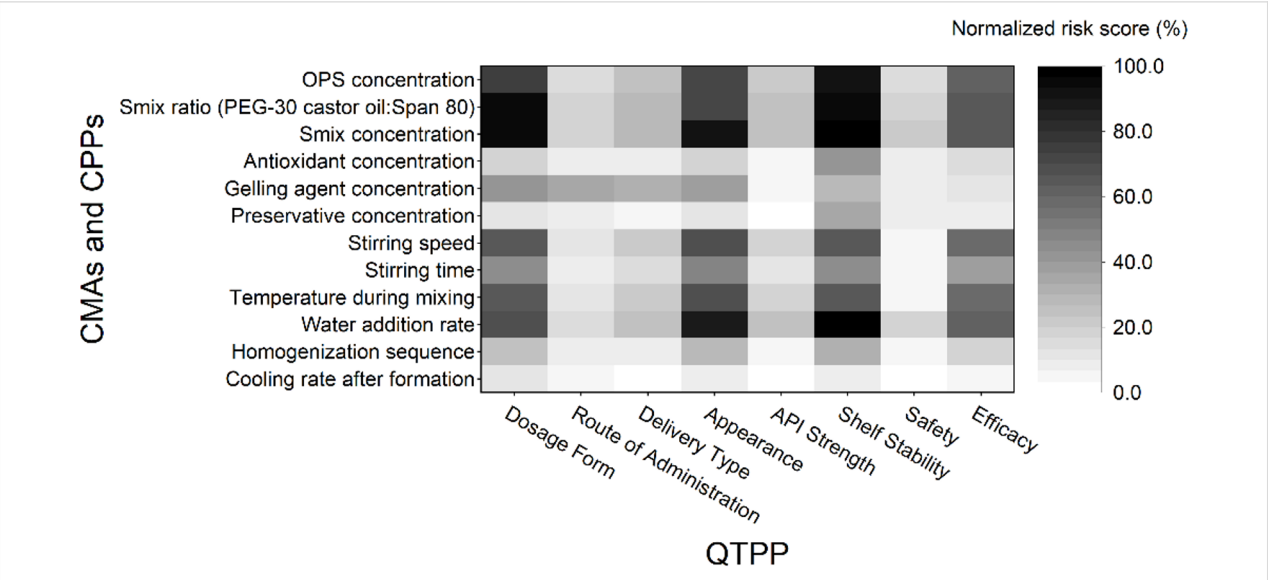

Figure 3: Heatmap of the normalized risk scores (%) illustrating the impact of CMAs and CPPs on each element of the QTPP. Higher risk scores (darker shades) indicate stronger influence on final product quality and guide prioritization in formulation control strategies. OPS concentration, S_{mix} ratio (PEG-30 castor oil/Span® 80), and S_{mix} concentration emerged as key high-risk variables.

fore, a Box–Behnken design (BBD) was selected for the subsequent optimization phase [24].

The BBD employs three levels for each factor: in each experiment, two factors vary between their upper (+1) and lower (−1) levels, while the third remains at the center point (0) [24]. Using this approach, 17 experimental combinations were generated to systematically explore the formulation space. The specific combinations and corresponding response results for all experimental runs are summarized in Table 4.

Although the BBD does not include extreme combinations of variables, it improved precision and accuracy for predictions near the center of the experimental space. The prepared formulations corresponding to the experimental design runs are shown in Figure 4, and a summary of the BBD is presented in Table 5.

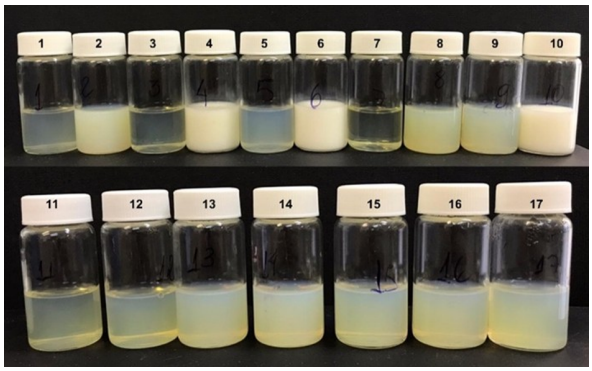

Figure 4: Microemulsion systems obtained from Box–Behnken design experimental runs. Each formulation is labeled according to its standard order in the design matrix.

Table 4: Experimental execution and responses from the Box–Behnken design[a].

Standard order	Execution order	Factor A (%)	Factor B (mass ratio)	Factor C (%)	Response 1 (nm)	Response 2 (PdI)	Response 3 (visual class)
1	9	5	7:3	15	23.7	0.10	2
2	6	15	7:3	15	59.9	0.21	3
3	15	5	9:1	15	20.3	0.07	1
4	13	15	9:1	15	246.2	0.32	4
5	11	5	8:2	10	27.4	0.10	2
6	8	15	8:2	10	201.2	0.16	4
7	2	5	8:2	20	19.6	0.05	1
8	3	15	8:2	20	45.9	0.19	3
9	17	10	7:3	10	47.0	0.18	3
10	7	10	9:1	10	182.7	0.30	4
11	16	10	7:3	20	24.0	0.16	2
12	12	10	9:1	20	30.1	0.14	2
13	4	10	8:2	15	38.5	0.16	3
14	1	10	8:2	15	41.0	0.14	3
15	10	10	8:2	15	36.4	0.12	3
16	5	10	8:2	15	37.1	0.20	3
17	14	10	8:2	15	33.4	0.18	3

[a]Factor A: oil concentration (*P. setacea*); Factor B: surfactant mixture ratio (PEG 30 castor oil:Span® 80); Factor C: surfactant mixture concentration. Response 1: hydrodynamic diameter (nm); Response 2: polydispersity index; Response 3: visual classification (1–clear to 4–turbid).

Table 5: Summary of Box–Behnken design responses and model fitting[a].

Response	Min.	Max.	Avg.	SD	Ratio	Transformation	Model type
Dh (nm)	19.6	246.2	65.6	70.7	12.54	$\sqrt{}$(Dh)	reduced cubic
PdI	0.05	0.32	0.16	0.07	6.59	1/$\sqrt{}$(PdI)	reduced quadratic
visual score	1	4	2.71	0.99	4.00	none	reduced quadratic

[a]Abbreviations: Dh = hydrodynamic diameter; PdI = polydispersity index; SD = standard deviation; Ratio = Max/Min; Transformation = Box–Cox transformation applied for model fitting.

To refine the model and improve predictive accuracy, the response data were subjected to Box–Cox transformation, an essential step when non-normal distribution is detected [25]. Following transformation, analysis of variance (ANOVA) was conducted to evaluate the statistical significance of the overall model and the individual formulation factors. To enhance model parsimony, backward regression elimination was applied to remove nonsignificant terms ($p > 0.1$), while preserving model hierarchy where required [26]. A detailed summary of these findings is available in the Supporting Information File 1 (Tables S7 to S9).

The final regression models for hydrodynamic diameter, polydispersity index, and visual classification exhibited strong statistical performance. Lack-of-fit tests were nonsignificant for both Dh (p = 0.632) and PdI (p = 0.665), confirming good model–data agreement. The R^2 values for Dh, PdI, and visual classification were 0.99, 0.94, and 0.97, respectively, with adjusted R^2 values of 0.99, 0.89, and 0.95. These metrics indicate that the models account for a high proportion of the variability in the measured responses (Figure 5).

These findings confirm that the selected formulation variables had a statistically significant and predictable impact on key microemulsion attributes. The strength of the fitted models supports their use in optimizing the formulation through the DoE approach. The predictive models for hydrodynamic diameter, polydispersity index, and visual classification were expressed as a polynomial function of the encoded factor as follows:

$$\sqrt{\mathrm{Dh}} = 6.10 + 3.51\mathrm{A} + 1.85\mathrm{B} - 2.50\mathrm{C} + 2.08\mathrm{AB} - 1.65\mathrm{AC} - 1.52\mathrm{BC} + 1.03\mathrm{A}^2 + 1.06\mathrm{B}^2 + 0.52\mathrm{C}^2 + 0.44\mathrm{A}^2\mathrm{C} - 0.69\mathrm{AC}^2, \quad (1)$$

$$\frac{1}{\sqrt{\mathrm{PdI}}} = 2.57 - 0.72\mathrm{A} - 0.05\mathrm{B} + 0.26\mathrm{C} - 0.23\mathrm{AB} - 0.39\mathrm{AC} + 0.48\mathrm{A}^2 - 0.30\mathrm{B}^2, \quad (2)$$

$$\text{Visual classification} = 2.89 + 1.00\mathrm{A} + 0.13\mathrm{B} - 0.63\mathrm{C} + 0.50\mathrm{AB} - 0.25\mathrm{BC} - 0.39\mathrm{A}^2. \quad (3)$$

These equations were then used to generate 3D response surface plots for each response, as shown in Figure 6. The axes were selected based on the most significant interactions identified through ANOVA, while the third factor was held constant at its central level. The resulting plots provide a visual representation of the individual and interactive effects of the formulation variables. As expected, increasing oil concentration was associated with higher hydrodynamic diameter, PdI, and visual classification scores. In contrast, higher concentrations of the S_{mix} led to reductions in all three response values, indicating microemulsion uniformity and clarity.

The objective of this experimental design was to develop a microemulsion that meets CQAs, specifically achieving a smaller hydrodynamic diameter, lower polydispersity index, and improved visual classification. Additionally, minimizing the concentration of S_{mix} was a priority, given the potential cytotoxic effects of high surfactant levels. Based on these criteria, numerical optimization was applied to predict the optimal combination of formulation factors. This approach relies on a mathematical desirability function, in which each factor and response is assigned a value between 0 (unacceptable) and 1 (fully desirable). The relative importance of each goal is then weighted on a scale from 1 to 5, allowing for balanced multiresponse optimization. These predefined parameters are subsequently processed by the software algorithm to identify the optimal combination of responses [27]. The

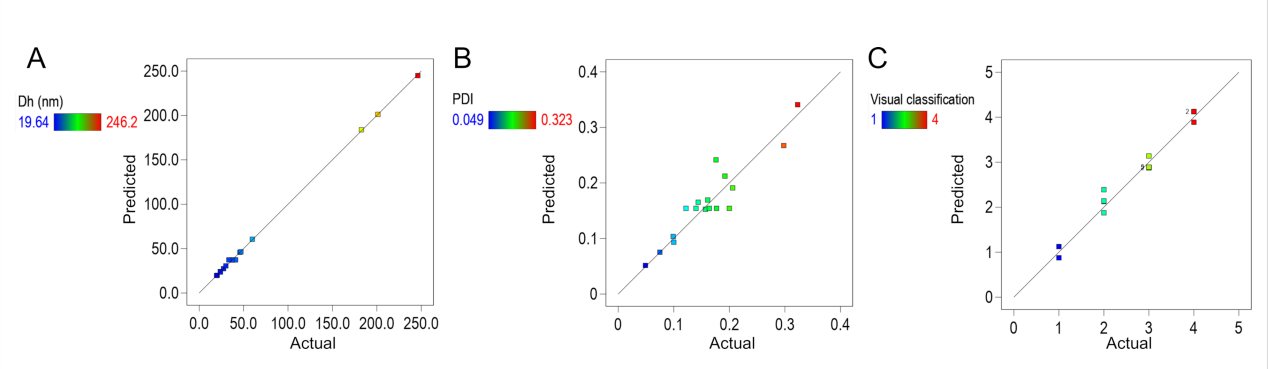

Figure 5: Linear regression plots of actual versus predicted values for: (A) hydrodynamic diameter, (B) polydispersity index, and (C) visual classification. The high degree of correlation between predicted and experimental values supports the robustness and predictive capability of the fitted models.

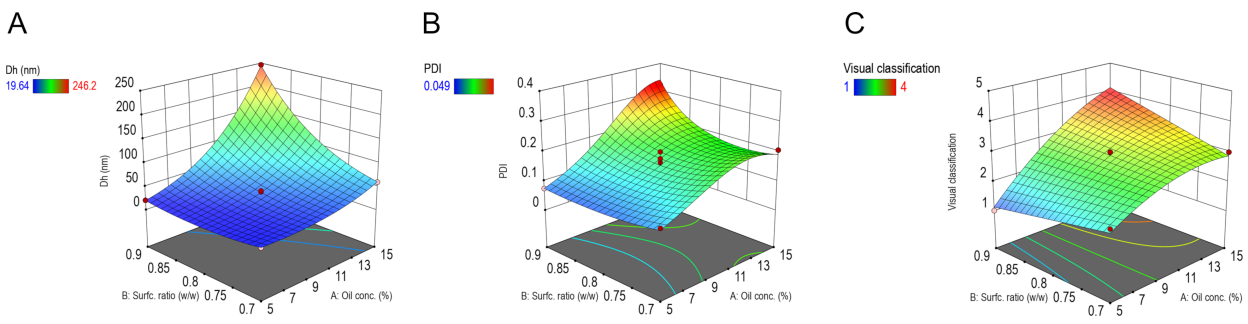

Figure 6: Surface plots derived from the Box–Behnken design showing the effects of formulation variables on: (A) hydrodynamic diameter, (B) polydispersity index, and (C) visual classification. The plots illustrate the interaction between key input variables, with the third variable held constant at its central level.

constraints and results of the microemulsion optimization process are summarized in Table 6.

The optimized microemulsion system, selected based on predefined criteria, comprised 5% of oil, a 9:1 (w/w) S_{mix} ratio of PEG-30 castor oil to Span® 80, and 15% of this S_{mix}. Microemulsions typically require high surfactant and/or co-surfactant concentrations to sufficiently reduce interfacial tension and promote spontaneous formation of stable nanodroplets [6,28]. However, a previous study from our group (Dourado et al. (2022) [13]) successfully developed stable microemulsion regions using the same surfactant blend at similar concentrations (13.2% of PEG-30 castor oil and 1.8% of Span® 80), for curcumin delivery in a Miglyol® 812N (medium chain triglycerides) oil phase. These findings support the feasibility of developing microemulsions with reduced surfactant content, in alignment with safety considerations and current best practices in nanocarrier formulation [29].

The application of experimental design in microemulsion development is well established, with several studies employing DoE strategies to obtain and optimize microemulsified systems, particularly for topical use [30-34]. The primary advantage of this approach lies in its regulatory relevance within the QbD framework, as it allows the identification of operational factor ranges that ensure compliance with CQAs.

Gelled microemulsion

For topical administration, the incorporation of adjuvants is necessary to enhance the performance of the formulation. One of the main limitations of microemulsions for this route is their inherently low viscosity, which is undesirable for cutaneous application. Moreover, polyunsaturated fatty acids are prone to oxidative degradation, compromising their biological efficacy. Another frequent issue in emulsified systems is microbial contamination, which can result in physical and chemical instability, such as pH shifts, turbidity, degradation of active components (e.g., fatty acids), and phase separation [35].

To address these challenges and improve topical suitability, additional excipients were incorporated into the formulation within their commonly employed concentration ranges [36]. Sodium carboxymethylcellulose (NaCMC, 1.5% w/w) was added as a gelling agent owing to its excellent biocompatibility, ease of dispersion in aqueous systems, and ability to enhance viscosity without compromising droplet stability [37]. Vitamin E at 0.05% w/w was included as a lipophilic antioxidant to protect the unsaturated fatty acids in OPS oil from oxidative

Table 6: Constraints and results of numerical optimization for microemulsion development.

Variable/response	Goal	Lower limit	Upper limit	Importance (1–5)	Optimized result
A: oil concentration (%)	in range	5	15	3	5
B: proportion of surfactants (S_{mix})	in range	7:3	9:1	3	9:1
C: S_{mix} concentration (%)	minimize	10	20	3	15
hydrodynamic diameter (nm)	minimize	19.6	246.2	5	19.9
polydispersity index	minimize	0.05	0.32	5	0.08
visual classification	target = 1	1	4	5	1

degradation, thereby improving formulation stability [38]. Additionally, 0.2% of Liquid Germall® Plus was selected as a broad-spectrum preservative for the aqueous phase, with regulatory approval for topical applications.

Characterization of microemulsions and physicochemical stability

Physicochemical stability

As prove of the model prediction capabilities, the optimized formulation identified through numerical optimization, the base microemulsion, was produced and characterized to confirm its quality and alignment with the CQAs. On the first day post-production, the formulation exhibited a hydrodynamic diameter of approximately 22.0 nm and a PdI of 0.14, both of which fall within the acceptable CQA criteria.

The stability of the system was evaluated over a 60 day period (Figure 7A). Throughout this time, no significant changes were detected in particle size, with the hydrodynamic diameter consistently remaining below 100 nm, and the PdI remaining below 0.20, confirming the physical stability of the base microemulsion and its preservation of desirable nanostructural features over time [39].

It is important to note, however, that NaCMC forms polymeric networks when dispersed in aqueous media, which scatter light and may artificially increase the measured hydrodynamic diameter [40]. Consequently, dynamic light scattering (DLS) data may not accurately reflect the true droplet size distribution in the MEgel. This phenomenon is evident from the apparent increase in mean hydrodynamic diameter to 45.1 nm and PdI to 0.27, which is attributed to NaCMC matrix scattering rather than actual droplet growth [40]. A comparison of the hydrodynamic diameter distributions for both systems is provided in Figure S2 (Supporting Information File 1). The stability profile of the MEgel formulation is presented in Figure 7B.

Furthermore, as shown in Figure 8, both ME and MEgel formulations maintained stable pH values throughout the storage period, with mean values of 6.3 ± 0.3 and 6.8 ± 0.1, respectively. The slightly acidic pH of healthy skin (typically ranging from 4 to 6) plays a key role in supporting physiological functions such as keratinocyte differentiation, lipid mantle formation of the stratum corneum, and preservation of the skin microbiome. In contrast, compromised or sensitive skin often exhibits a shift toward neutral pH [41]. Given their stability and proximity to the natural skin pH, the observed pH values for ME and MEgel are considered appropriate for topical application.

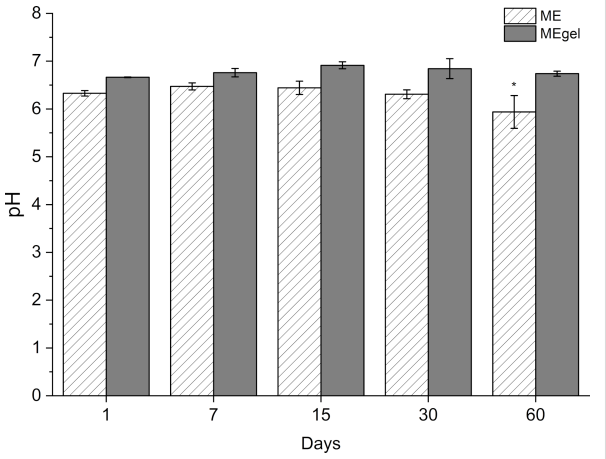

Figure 8: pH values of ME and MEgel formulations over a 60 day storage period. Data are presented as mean ± SD (n = 3). *p < 0.05 indicates a statistically significant difference.

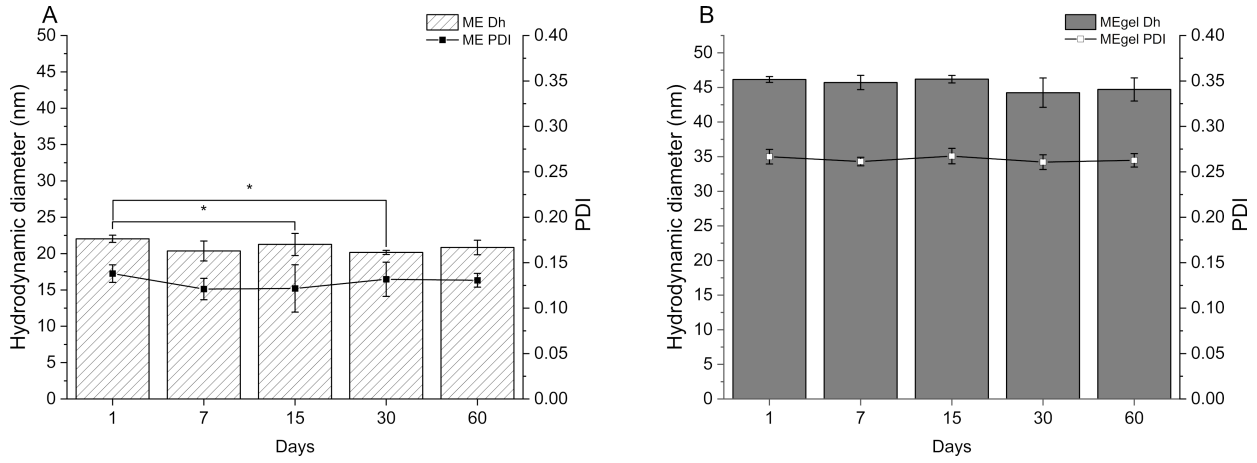

Figure 7: Hydrodynamic diameter over a 60 day period for (A) the optimized microemulsion (ME) and (B) the gelled microemulsion (MEgel). Data are presented as mean ± SD (n = 3). *p < 0.05 indicates statistically significant difference.

Nevertheless, on day 60 the ME formulation exhibited a statistically significant difference ($p < 0.05$) in pH compared with earlier time points. Although the reduction was modest, from pH 6.4 ± 0.1 to 5.9 ± 0.3, it is hypothesized to result from a combination of physicochemical and microbiological factors [42]. One possible explanation involves the oxidative or hydrolytic degradation of the oil phase, particularly the fatty acids in OPS, as well as the surfactants. In particular, the autoxidation of the polyoxyethylene (POE) chains in the hydrophilic head group of the PEG-30 castor oil and the hydrolysis of the surfactant hydrophobic tails may have contributed to the observed pH shift [42,43]. These findings underscore the importance of incorporating preservatives into the MEgel formulation to mitigate such instability.

It is worth noting that although microemulsified systems are thermodynamically stable, their individual excipients remain vulnerable to instability phenomena such as chemical degradation and microbial contamination. These processes can compromise the thermodynamic stability and overall performance of the system [6].

Thermal analysis

The thermal characteristics of the formulations were also evaluated (Figure 9). The thermograms revealed no evidence of incompatibility among the excipients, such as the lowering of degradation temperatures. The thermal events observed in the DTG and DSC curves correspond to the loss of free water (≈98 °C), solvation water (≈110 °C), and thermal degradation of the oil phase (≈417 °C), overlapping with the degradation profiles of other components such as NaCMC and vitamin E [44,45].

Surface tension

The surface tension of the microemulsion was characterized through six replicates, yielding an average value of 40.27 ± 0.22 $mN \cdot m^{-1}$. Similar surface tension values have been reported for microemulsions in the literature [46,47]. This range is considerably favorable for topical formulations, as lower surface tension enhances spreadability and promotes interaction with the stratum corneum and its lipidic barrier. Due to instrumental limitations associated with the high viscosity resulting from NaCMC addition, the surface tension of the MEgel could not be determined. However, NaCMC solutions exhibit negligible surface activity and typically maintain surface tension values close to that of water [48].

Rheological analysis

Rheological profiling provides key insights into the behavior of formulations under applied stress or strain, offering critical information about viscosity, flow characteristics, and structural stability. According to the proposed QTPP, a higher viscosity with pseudoplastic (shear-thinning) behavior is preferred for topical formulations, as it ensures ease application and good retention on the skin. Accordingly, the microemulsions were evaluated for their shear stress and viscosity at both room temperature (25 ± 2 °C) and skin temperature (32.5 ± 2 °C). Microemulsions can exhibit diverse rheological behaviors depending on their type, structure, droplet density, and interdroplet interactions [49]. As shown in Figure 10A, the base ME demonstrated Newtonian behavior, with viscosity remaining constant regardless of shear rate or temperature. This is consistent with microemulsions that possess globular or discontinuous droplet structures, which typically exhibit Newtonian flow characteristics [50,51].

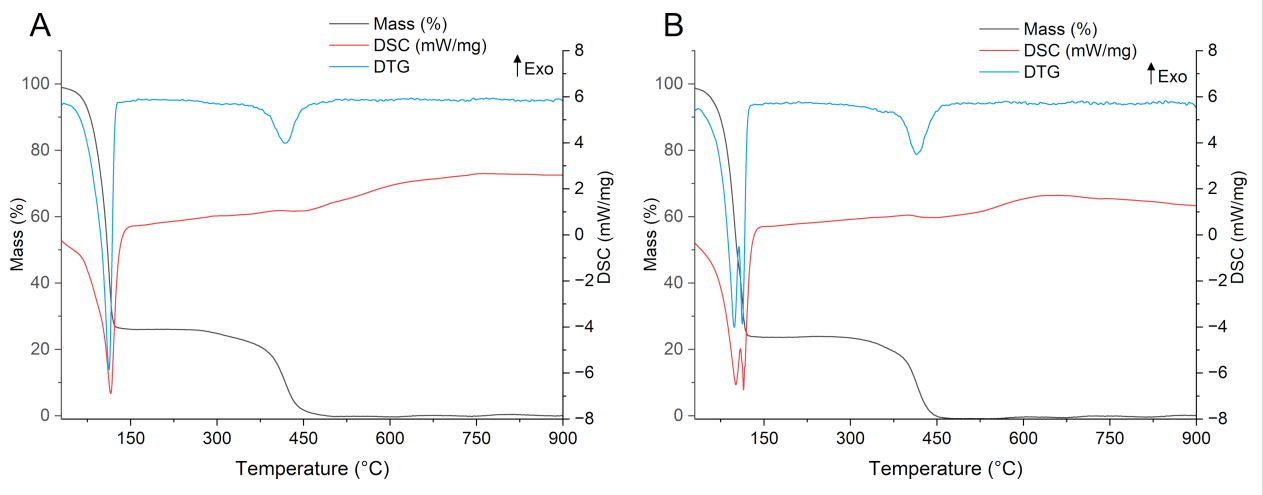

Figure 9: Thermal analysis of ME and MEgel. (A) Differential thermal and thermogravimetric profiles of the base microemulsion. (B) Differential thermal and thermogravimetric profiles of the gelled microemulsion.

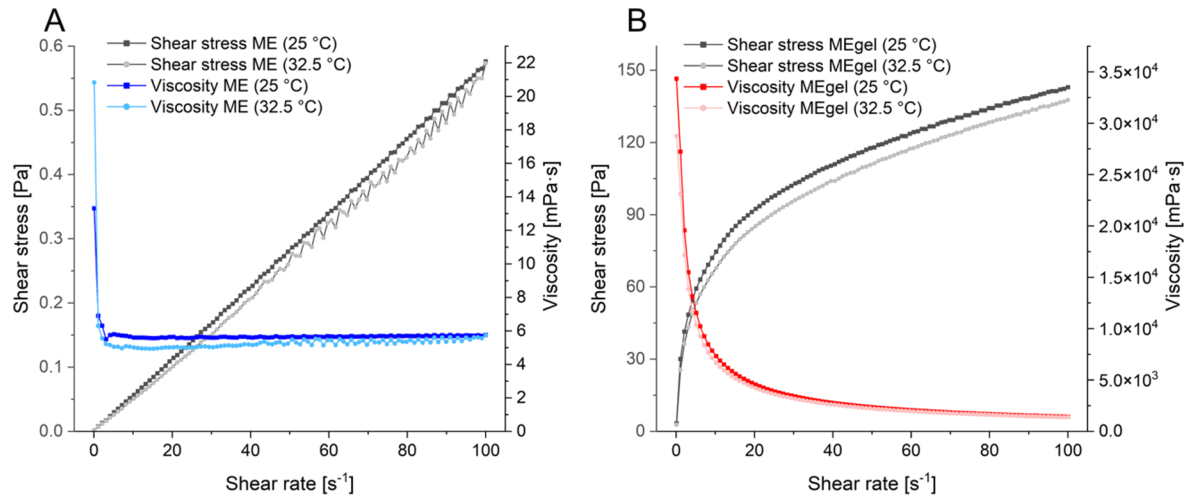

Figure 10: Shear stress and viscosity profiles of (A) the base microemulsion, and (B) the gelled microemulsion at 25 and 32.5 °C.

However, MEgel exhibited a pseudoplastic, shear-thinning behavior, as demonstrated by a decrease in viscosity from approximately 3.0×10^4 to 1.4×10^3 mPa•s. with increasing shear rate (Figure 10B). This rheological profile enhances the residence time of the formulation on the skin and minimizes runoff, thereby improving patient compliance.

In vitro cytocompatibility

To assess the safety of the ME formulation for potential topical use, a proof-of-concept cytocompatibility evaluation was conducted using the MTT assay, which measures mitochondrial metabolic activity. The assay was performed on two cell lines relevant to wound healing and topical application: murine macrophages (RAW 264.7) and human umbilical vein endothelial cells (HUVECs) (Figure 11). According to ISO 10993-13 guidelines, the base ME was considered cytocompatible up to concentrations of 2 mg/mL for RAW cells and 0.5 mg/mL for HUVECs. The observed cytotoxicity at higher concentrations is likely due to the increase proportion of surfactants in the formulation. Additionally, under certain experimental conditions, fatty acids may induce lipid peroxidation and trigger pro-inflammatory responses in endothelial cells such as HUVECs, potentially offsetting the proliferative effects typically observed in keratinocytes such as HaCaT cells [2,52,53].

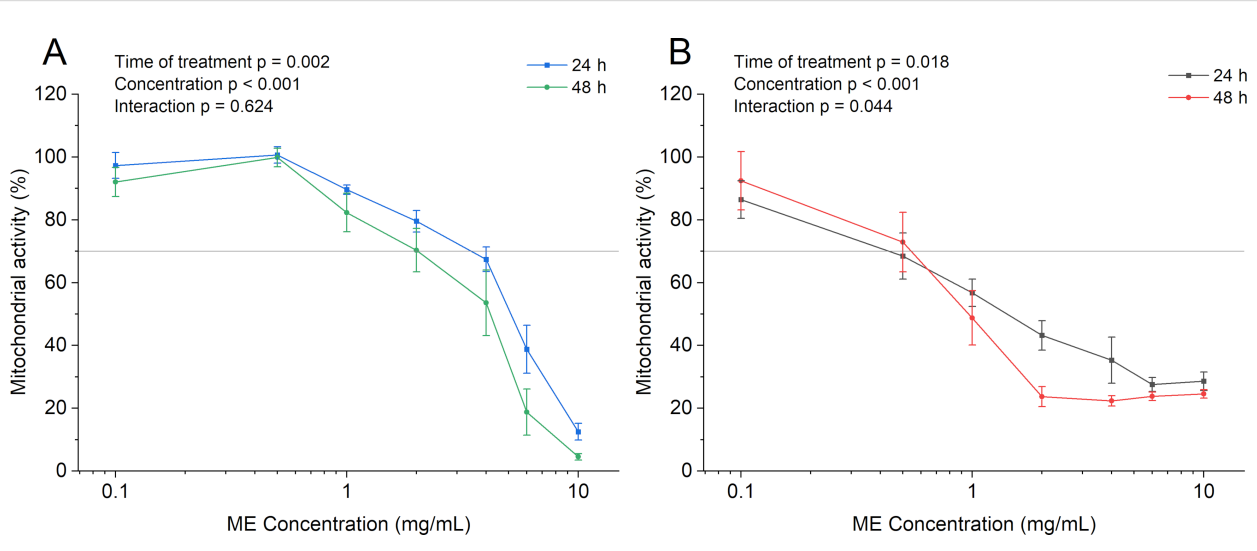

Figure 11: Mitochondrial activity of (A) RAW 264.7 murine macrophages and (B) HUVECs after 24 h and 48 h of exposure to different concentrations of the microemulsion, assessed by the MTT assay. Data are presented as mean ± SD (n = 3).

To gain a more comprehensive understanding of the therapeutic potential of OPS and its ME formulation in wound healing and topical applications, it is crucial to extend cytocompatibility assessments to include additional cell types, particularly keratinocytes and dermal fibroblasts, which are key players in skin regeneration and re-epithelialization [17]. Although the MTT assay is a widely accepted and convenient method for preliminary cytotoxicity screening, it offers limited insight into the complex biological processes involved in wound healing. Specifically, it does not evaluate critical mechanisms such as cell migration, proliferation, extracellular matrix remodeling, or the modulation of inflammatory mediators. Therefore, future investigations should incorporate complementary assays that capture these dimensions. Ultimately, in vivo models remain the gold standard for assessing wound healing efficacy, as they replicate the dynamic, multicellular, and inflammatory nature of living tissue, providing crucial translational insights that cannot be obtained through in vitro testing alone [54].

Conclusion

Passiflora setacea seed oil was successfully extracted using the Soxhlet method, yielding 30.5 ± 0.8% (w/w). The oil is rich in polyunsaturated fatty acids, primarily ω-6 (64.7%) and ω-9 (20.7%), which are associated with anti-inflammatory, antioxidant, and regenerative properties, key attributes for dermatological applications. For topical administration, the base microemulsion was supplemented with vitamin E and Liquid Germall® Plus and subsequently gelled with NaCMC, resulting in a pseudoplastic system with suitable viscosity for skin application. In cytocompatibility assays, the ME preserved mitochondrial activity at concentrations up to 0.5 mg/mL in HUVEC and 2 mg/mL in RAW 264.7 cells after 48 h. Toxicity observed at higher concentrations was attributed to increased surfactant content, highlighting the importance of formulation optimization. Despite these promising results, further studies are required to address the limitations identified, including droplet size characterization of MEgel, comprehensive cytotoxicity assessments, and wound healing assays. Overall, the developed microemulsion system represents a promising nanocarrier-based strategy for topical delivery, effectively combining the functional benefits of *P. setacea* seed oil with a QbD-guided formulation process.

Experimental

Materials

Seeds of *Passiflora setacea* BRS Pérola do Cerrado were kindly provided by EMBRAPA (Brasília, DF, Brazil – SisGen Registration Nº. A51F883). *n*-Hexane was purchased from LabSynth Ltda. (Diadema, Brazil), and HPLC grade *n*-heptane (Neon Ltda. – Suzano, Brazil) was donated by the Agricultural School of Jundiaí (EAJ-UFRN). The following excipients were donations: Vitamin E (Galena – Campinas, Brazil), Liquid Germall® plus (Mapric – São Paulo, SP), ALKEST® CSO 300 (polyethoxylated castor oil 30 mol, "PEG 30", Oxiteno – São Paulo, SP) and sodium carboxymethyl cellulose (NaCMC – All chemistry, São Paulo, Brazil). Span® 80 was obtained from Sigma-Aldrich Inc. (St. Louis, MO – USA).

Extraction of *Passiflora setacea* oil

Oil extraction was performed using a Soxhlet apparatus with 4:1 ratio of *n*-hexane to *P. setacea* seeds, following the methodology recommended by the Association of Official Analytical Chemists [55]. Prior to extraction, dried seeds were grounded, placed in folded filter paper, and inserted into the Soxhlet extractor. The extraction was carried out for 6 h at 60 °C. Afterward, the solvent was removed using a rotary evaporator under reduced pressure at a water bath temperature of 40 °C. The obtained oil was then filtered through a 0.45 μm PTFE membrane and stored in amber glass bottles under refrigeration (4 °C) until use. The oil yield was calculated using the following equation:

$$\text{Yield}(\%\ \text{w/w}) = \left(\frac{\text{weight of oil}}{\text{weight of dried seeds}}\right) \times 100 \qquad (4)$$

Characterization of *Passiflora setacea* oil

Oil composition

The chemical composition of *Passiflora setacea* oil was determined through the analysis of its fatty acids methyl esters (FAMEs) [14,56]. Briefly, 10 mg of oil was solubilized in 1 mL of freshly prepared 0.5 M methanolic potassium hydroxide. The base-catalyzed transesterification reaction was carried out at 60 °C for 15 min. After cooling, the reaction was quenched with 20 μL of acetic acid. To extract the FAMEs, 1 mL of *n*-hexane and water were added, followed by vigorous agitation. Once phase separation occurred, the organic (*n*-hexane) layer was collected and washed three times with saturated NaCl solution to remove residual reagents. A 200 μL aliquot of the organic phase was then dried at room temperature in pre-weighted vials.

FAME quantification was performed using a gas chromatograph (GC Agilent 8860, Agilent – Santa Clara, USA) coupled with a mass spectrometer (5977B GC/MSD, Agilent – Santa Clara, USA). Prior to injection, samples were dissolved in 1 mL of *n*-heptane. The GC system operated with helium as the carrier gas at a flow rate of 1 $mL \cdot min^{-1}$. The injection and detection temperatures were set at 270 °C and 250 °C, respectively. The oven temperature program ranged from 70 °C to 300 °C, increasing at a rate of 3 $°C \cdot min^{-1}$. Compound identification was conducted by matching the mass spectra to those in the NIST17.

Simultaneous thermal analysis

The thermal behavior of *P. setacea* oil was evaluated using a simultaneous thermal analysis (STA 449 F3 Jupiter®, NETZSCH – Selb, Germany). Samples were weighed in alumina crucibles and analyzed with a heating rate of 10 °C·min^{-1}, under nitrogen flow of 10 mL·min^{-1}, over a temperature range of 25 °C to 900 °C. Microemulsion systems were analyzed under the same conditions for comparative purposes.

Quality by design framework

The development of the microemulsion system was guided by a QbD strategy, aligned with ICH Q8(R2) guidelines [57]. This framework was employed to define the QTPP and CQAs, CMAs, and CPPs relevant to the topical delivery of *P. setacea* seed oil.

A risk assessment was conducted to identify and prioritize factors most likely to affect the CQAs. This included the construction of an Ishikawa diagram followed by a REM [58]. The REM was based on interdependence scores between QTPP-CQA and CQA-CMA/CPP relationships, using a three-level scale (1 = low, 3 = moderate, 9 = high). The multiplication of the matrices resulted in a final risk score linking each QTPP element to the corresponding CMA and CPPs, enabling the identification of high-risk variables for subsequent optimization steps.

Experimental design for development and optimization of *Passiflora setacea* microemulsion

Experimental design is a valuable strategy for minimizing the number of experiments while maximizing the understand of how each factor influences a dependent variable [59]. Based on variables identified during risk assessment, DoE was applied to investigate the effects of OPS concentration, the surfactants mixture ratio (S_{mix}), and S_{mix} concentration on the formation of a microemulsified system with desirable hydrodynamic diameter and transparency (Table 7).

Initially, a full factorial design (2^3) with three central points was employed to explore the experimental domain. Subsequently, a three-level Box–Behnken design was used to refine the model and enhance resolution. Microemulsion clarity was visually classified into four categories: (1) transparent, (2) slightly cloudy, (3) slightly milky, and (4) milky. The experimental matrix and statistical analyses were conducted using Design-Expert® software (M/s Stat-Ease Inc.).

Table 7: Independent and dependent variables used in the experimental planning for the development of *P. setacea* oil-based microemulsions.

Variable	Level (coded)		
Independent variable	lower (–1)	central (0)	upper (+1)
X1: OPS concentration	5%	10%	15%
X2: surfactant ratio (PEG 30 Castor Oil/Span® 80)	7:3	8:2	9:1
X3: S_{mix} concentration	10%	15%	20%
Dependent variables	Desired outcomes		
Y1: hydrodynamic diameter (nm)	less than 100 nm		
Y2: polydispersity index	less than 0.2		
Y3: visual classification[a]	category 1 (transparent)		

[a]Y3 was used only on the Box–Behnken design.

Production method for *Passiflora setacea* oil-based systems

The formulations were prepared using the phase inversion composition method [60]. Component proportions were defined according to the experimental matrix (Table 7). Briefly, accurately weighed amounts of OPS and surfactants were homogenized under magnetic stirring for 2 min. Ultrapure water was then added dropwise (≈0.5 mL/min) under continuous stirring (≈900 rpm, IKA® C-MAG HS7 – Staufen, Germany). The entire process was conducted at 75 ± 3 °C. After water addition, the mixture was stirred for an additional 15 min to ensure system stabilization.

For the preparation of the topical microemulsion, the same method was followed with slight modifications. Initially, vitamin E (0.05% w/w) was solubilized in the oil phase. The microemulsion was then prepared as previously described. Subsequently, Liquid Germall® Plus (0.2% w/w) and sodium carboxymethylcellulose (1.5% w/w) were added under mechanical stirring to obtain the gelled topical microemulsion.

Characterization of the emulsified systems

Hydrodynamic diameter distribution

The hydrodynamic diameter and polydispersity index of the microemulsions were determined by dynamic light scattering using a Zetasizer® Nano ZS (Malvern Panalytical Ltd. – Malvern, United Kingdom) at 25 °C with a fixed backscattering angle of 173°. Prior to analysis, samples were diluted in purified water (1:40 v/v) [13]. All measurements were performed in triplicate.

Surface tension

Surface tension was measured using the pendant droplet method with a drop-shape analyzer (DAS-100, KRÜSS GmbH,

Hamburg, Germany). Microemulsion droplets (17 µL) were formed at the tip of a stainless-steel needle and analyzed by image capture and subsequent software processing to calculate surface tension [13].

Rheological analysis

The rheological behavior of the ME formulations was evaluated using an MCR-302 rheometer (Anton Paar) equipped with a cone-plate geometry (50 mm diameter, 1° angle, and 96 µm gap). Samples were subjected to a shear rate ranging from 0.1 to 100 s^{-1} at both room temperature (25 °C) and skin temperature (32.5 °C) [13]. All measurements were carried out in triplicate.

Microemulsion stability tests

The physicochemical stability of the optimized microemulsion and its gelled form was monitored over 60 days at room temperature (25 ± 2 °C). Stability parameters included visual appearance (e.g. signs of haze, creaming, or phase separation), hydrodynamic diameter distribution, and pH. The pH was measured using a pre-calibrated PG 2000 pH meter (Gehaka, São Paulo, Brazil). Due to its high viscosity, MEgel samples were diluted with purified water (1:40 w/w) prior to analysis. All tests were conducted in triplicate.

In vitro cytocompatibility

The cytocompatibility the ME was evaluated using the MTT [3(4,5-dimethylthiazol-2-yl)-2,5-diphenyltetrazolium bromide] assay. Assays were performed on murine macrophage cells (RAW 264.7 TIB-71™) and human umbilical vein endothelial cells (HUVEC, C12203).

RAW cells were cultured in Dulbecco's modified eagle medium (DMEM, Sigma-Aldrich, D0822) supplemented with 10% (v/v) fetal bovine serum. HUVEC cells were maintained in endothelial cell growth medium (Sigma-Aldrich, C22110). Cells were seeded in 96-well plates at densities of 3×10^4 (RAW) and 1.9×10^4 for (HUVEC) cells/well and incubated for 24 h at 37 °C in a humidified atmosphere with 5% (v/v) CO_2 before treatment.

Cells were then treated with varying concentrations of ME (0.1 to 10 mg/mL) for 24 or 48 h (n = 3 plates, each with 3 wells per concentration). Compatibility was assessed by mitochondrial metabolic activity, based on the conversion of MTT salt into insoluble formazan crystals. After incubation, formazan crystals were solubilized in DMSO, and absorbance was measured at 570 nm with a reference at 630 nm using a microplate reader (EL 800, Bio-TEK Instrument, Inc®, France). Cell viability was calculated normalizing untreated controls as 100%, according to the equation:

$$\text{Mitochondrial activity}(\%) = \frac{\text{OD}_{570-630}\text{sample}}{\text{OD}_{570-630}\text{control}} \times 100. \quad (5)$$

Statistical analysis

Statistical analyses, excluding those related to DoE, were performed using the Prism® 10 software (GraphPad, California, USA). Two-way ANOVA followed by Tukey's pos hoc test was used to assess statistical significance. Differences were considered significant when $p < 0.05$.

Supporting Information

Supporting Information File 1

Additional figures and tables.
[https://www.beilstein-journals.org/bjnano/content/supplementary/2190-4286-16-146-S1.pdf]

Acknowledgements

The authors thank the Federal University of Rio Grande do Norte (UFRN), Université de Lorraine, and the Federal University of Sergipe (UFS) for providing the research infrastructure. Special thanks are extended to Alexandra Kleinclauss and Isabelle Fries (Université de Lorraine) for their valuable contributions to the cell culture and cytocompatibility assays. The graphical abstract was composed by the authors using Microsoft PowerPoint® and additional licensed figures. The image of the beaker was provided by Servier Medical Art (https://smart.servier.com/), licensed under CC BY 4.0 (https://creativecommons.org/licenses/by/4.0/); The image of the GC–MS was adapted from https://commons.wikimedia.org/wiki/File:Gas_chromatographs_with_functional_detectors_in_CAFIA_laboratory,_Czech_Republic.jpg, © 2021 by Sarka Na kopci, distributed under the terms of the Creative Commons Attribution-Share Alike 4.0 International License, https://creativecommons.org/licenses/by-sa/4.0/. This content is not subject to CC BY 4.0; The image of "Thermal analysis" was reproduced from https://commons.wikimedia.org/wiki/File:Netzsch_STA_449_F1.jpg, © 2012 by Technex, distributed under the terms of the Creative Commons Attribution-Share Alike 3.0 Unported License, https://creativecommons.org/licenses/by-sa/3.0/. This content is not subject to CC BY 4.0.

Funding

This research was funded by the Conselho Nacional de Desenvolvimento Científico e Tecnológico (CNPq) and Coordenação de Aperfeiçoamento de Pessoal de Nível superior–Brasil (CAPES)–Finance Code 001, and the Franco-Brazilian Cooperation Program (COFECUB).

Conflict of Interest

The authors confirm that there is no conflict of interest.

Author Contributions

Daniel T. Pereira: conceptualization; data curation; formal analysis; investigation; methodology; validation; visualization; writing – original draft; writing – review & editing. Douglas Dourado: conceptualization; data curation; investigation; supervision; writing – review & editing. Danielle T. Freire: data curation; investigation. Dayanne L. Porto: data curation; investigation; validation. Cícero F. S. Aragão: funding acquisition; project administration; resources. Myla L. de Souza: conceptualization; methodology; resources. Guilherme R. S. de Araujo: data curation; investigation; methodology. Ana Maria Costa: funding acquisition; project administration; resources; writing – review & editing. Wógenes N. Oliveira: project administration; writing – review & editing. Anne Sapin-Minet: funding acquisition; resources; supervision; writing – review & editing. Éverton N. Alencar: conceptualization; project administration; supervision; writing – review & editing. Eryvaldo Sócrates T. Egito: conceptualization; funding acquisition; project administration; resources; supervision; writing – review & editing.

ORCID® iDs

Daniel T. Pereira - https://orcid.org/0000-0002-4374-1947
Douglas Dourado - https://orcid.org/0000-0003-3445-5217
Ana Maria Costa - https://orcid.org/0000-0003-4456-7802
Eryvaldo Sócrates T. Egito - https://orcid.org/0000-0002-2180-3991

Data Availability Statement

Additional research data generated and analyzed during this study is not shared.

References

1. R, S.; M, D.; K, A.; Ravi, M. *J. Adv. Biomed. Pharm. Sci.* **2021,** *4,* 45–55. doi:10.21608/jabps.2020.44321.1105
2. Lôbo de Souza, M.; Dourado, D.; Pinheiro Lôbo, I.; Couto Pires, V.; Nunes de Oliveira Araújo, S.; de Souza Rebouças, J.; Costa, A. M.; Pinho Fernandes, C.; Machado Tavares, N.; de Paula Pereira, N.; Rocha Formiga, F. *J. Drug Delivery Sci. Technol.* **2022,** *67,* 102803. doi:10.1016/j.jddst.2021.102803
3. de Santana, F. C.; Shinagawa, F. B.; Araujo, E. d. S.; Costa, A. M.; Mancini-Filho, J. *J. Food Sci.* **2015,** *80,* C2647–C2654. doi:10.1111/1750-3841.13102
4. Criollo-Mendoza, M. S.; Contreras-Angulo, L. A.; Leyva-López, N.; Gutiérrez-Grijalva, E. P.; Jiménez-Ortega, L. A.; Heredia, J. B. *Molecules* **2023,** *28,* 598. doi:10.3390/molecules28020598
5. Spence, C.; Zhang, T. *Int. J. Cosmet. Sci.* **2024,** *46,* 833–849. doi:10.1111/ics.12975
6. Egito, E. S. T.; Amaral-Machado, L.; Alencar, E. N.; Oliveira, A. G. *Drug Delivery Transl. Res.* **2021,** *11,* 2108–2133. doi:10.1007/s13346-020-00872-8
7. Ait-Touchente, Z.; Zine, N.; Jaffrezic-Renault, N.; Errachid, A.; Lebaz, N.; Fessi, H.; Elaissari, A. *Nanomaterials* **2023,** *13,* 1688. doi:10.3390/nano13101688
8. Callender, S. P.; Mathews, J. A.; Kobernyk, K.; Wettig, S. D. *Int. J. Pharm.* **2017,** *526,* 425–442. doi:10.1016/j.ijpharm.2017.05.005
9. Rao, J.; McClements, D. J. *Food Hydrocolloids* **2011,** *25,* 1413–1423. doi:10.1016/j.foodhyd.2011.02.004
10. Yu, L. X.; Amidon, G.; Khan, M. A.; Hoag, S. W.; Polli, J.; Raju, G. K.; Woodcock, J. *AAPS J.* **2014,** *16,* 771–783. doi:10.1208/s12248-014-9598-3
11. Beg, S.; Rahman, M.; Kohli, K. *Drug Discovery Today* **2019,** *24,* 717–725. doi:10.1016/j.drudis.2018.12.002
12. Pawar, S. S.; Mahale, Y. S.; Kalamkar, P. A.; Satdive, R. A.; Sonawane, S. K.; Bhapkar, S. P. *Curr. Pharm. Anal.* **2023,** *19,* 677–686. doi:10.2174/1573412919666230914103355
13. Dourado, D.; Oliveira, M. C. d.; Araujo, G. R. S. d.; Amaral-Machado, L.; Porto, D. L.; Aragão, C. F. S.; Alencar, E. d. N.; Egito, E. S. T. d. *Colloids Surf., A* **2022,** *652,* 129720. doi:10.1016/j.colsurfa.2022.129720
14. Aldai, N.; Murray, B. E.; Nájera, A. I.; Troy, D. J.; Osoro, K. *J. Sci. Food Agric.* **2005,** *85,* 1073–1083. doi:10.1002/jsfa.2110
15. Kiezel-Tsugunova, M.; Kendall, A. C.; Nicolaou, A. *Biochem. Soc. Trans.* **2018,** *46,* 119–129. doi:10.1042/bst20160469
16. Lin, M.-H.; Khnykin, D. *Biochim. Biophys. Acta, Mol. Cell Biol. Lipids* **2014,** *1841,* 362–368. doi:10.1016/j.bbalip.2013.09.016
17. Rodrigues, M.; Kosaric, N.; Bonham, C. A.; Gurtner, G. C. *Physiol. Rev.* **2019,** *99,* 665–706. doi:10.1152/physrev.00067.2017
18. Caputa, G.; Flachsmann, L. J.; Cameron, A. M. *Immunol. Cell Biol.* **2019,** *97,* 268–278. doi:10.1111/imcb.12237
19. Krzyszczyk, P.; Schloss, R.; Palmer, A.; Berthiaume, F. *Front. Physiol.* **2018,** *9,* 419. doi:10.3389/fphys.2018.00419
20. dos Santos, O. V.; Vieira, E. L. S.; Soares, S. D.; da Conceição, L. R. V.; do Nascimento, F. d. C. A.; Teixeira-Costa, B. E. *Cienc. Tecnol. Aliment. (Campinas, Braz.)* **2021,** *41* (Suppl. 1), 218–225. doi:10.1590/fst.16220
21. Upadhyay, M.; Ghori, V.; Soniwala, M. M. *J. Pharm. Negat. Results* **2022,** *13,* 765–776. doi:10.47750/pnr.2022.13.s09.088
22. Grangeia, H. B.; Silva, C.; Simões, S. P.; Reis, M. S. *Eur. J. Pharm. Biopharm.* **2020,** *147,* 19–37. doi:10.1016/j.ejpb.2019.12.007
23. Németh, Z.; Pallagi, E.; Dobó, D. G.; Kozma, G.; Kónya, Z.; Csóka, I. *Pharmaceutics* **2021,** *13,* 1071. doi:10.3390/pharmaceutics13071071
24. Dean, A.; Morris Last Nam, M.; Stufken, J.; Bingham, D., Eds. *Handbook of Design and Analysis of Experiments,* 1st ed.; Chapman & Hall/CRC: New York, NY, USA, 2015. doi:10.1201/b18619
25. Box, G. E. P.; Cox, D. R. *J. R. Stat. Soc.: Ser. B* **1964,** *26,* 211–243. doi:10.1111/j.2517-6161.1964.tb00553.x
26. Barker, T. B.; Milivojevich, A. *Quality by Experimental Design,* 4th ed.; Chapman & Hall/CRC: New York, NY, USA, 2016. doi:10.1201/b19616
27. Derringer, G.; Suich, R. J. *Qual. Technol.* **1980,** *12,* 214–219. doi:10.1080/00224065.1980.11980968
28. Tartaro, G.; Mateos, H.; Schirone, D.; Angelico, R.; Palazzo, G. *Nanomaterials* **2020,** *10,* 1657. doi:10.3390/nano10091657
29. Souto, E. B.; Cano, A.; Martins-Gomes, C.; Coutinho, T. E.; Zielińska, A.; Silva, A. M. *Bioengineering* **2022,** *9,* 158. doi:10.3390/bioengineering9040158
30. Hajjar, B.; Zier, K.-I.; Khalid, N.; Azarmi, S.; Löbenberg, R. *J. Pharm. Invest.* **2018,** *48,* 351–362. doi:10.1007/s40005-017-0327-7

31. Jeirani, Z.; Mohamed Jan, B.; Si Ali, B.; Mohd. Noor, I.; Chun Hwa, S.; Saphanuchart, W. *Chemom. Intell. Lab. Syst.* **2012,** *112,* 1–7. doi:10.1016/j.chemolab.2011.10.008
32. Negi, P.; Singh, B.; Sharma, G.; Beg, S.; Raza, K.; Katare, O. P. *Drug Delivery* **2016,** *23,* 941–957. doi:10.3109/10717544.2014.923067
33. Shah, V.; Sharma, M.; Pandya, R.; Parikh, R. K.; Bharatiya, B.; Shukla, A.; Tsai, H.-C. *Mater. Sci. Eng., C* **2017,** *75,* 1231–1241. doi:10.1016/j.msec.2017.03.002
34. Sood, J.; Sapra, B.; Tiwary, A. K. *AAPS PharmSciTech* **2017,** *18,* 1901–1916. doi:10.1208/s12249-016-0658-0
35. Dao, H.; Lakhani, P.; Police, A.; Kallakunta, V.; Ajjarapu, S. S.; Wu, K.-W.; Ponkshe, P.; Repka, M. A.; Narasimha Murthy, S. *AAPS PharmSciTech* **2018,** *19,* 60–78. doi:10.1208/s12249-017-0875-1
36. Rowe, C. R.; Sheskey, P. J.; Quinn, M. E. *Handbook of pharmaceutical excipients,* 6th ed.; Pharmaceutical Press: London, UK, 2009.
37. Costa, E. M.; Pereira, C. F.; Ribeiro, A. A.; Casanova, F.; Freixo, R.; Pintado, M.; Ramos, O. L. *Appl. Sci.* **2022,** *12,* 6560. doi:10.3390/app12136560
38. Jerzykiewicz, M.; Ćwieląg-Piasecka, I.; Jezierski, A. *J. Am. Oil Chem. Soc.* **2013,** *90,* 803–811. doi:10.1007/s11746-013-2227-y
39. Solans, C.; Solé, I. *Curr. Opin. Colloid Interface Sci.* **2012,** *17,* 246–254. doi:10.1016/j.cocis.2012.07.003
40. Behra, J. S.; Mattsson, J.; Cayre, O. J.; Robles, E. S. J.; Tang, H.; Hunter, T. N. *ACS Appl. Polym. Mater.* **2019,** *1,* 344–358. doi:10.1021/acsapm.8b00110
41. Lukić, M.; Pantelić, I.; Savić, S. D. *Cosmetics* **2021,** *8,* 69. doi:10.3390/cosmetics8030069
42. Amaral-Machado, L.; Xavier-Júnior, F. H.; Rutckeviski, R.; Morais, A. R. V.; Alencar, É. N.; Dantas, T. R. F.; Cruz, A. K. M.; Genre, J.; Da Silva-Junior, A. A.; Pedrosa, M. F. F.; Rocha, H. A. O.; Egito, E. S. T. *Molecules* **2016,** *21,* 585. doi:10.3390/molecules21050585
43. Weber, J.; Buske, J.; Mäder, K.; Garidel, P.; Diederichs, T. *Int. J. Pharm.: X* **2023,** *6,* 100202. doi:10.1016/j.ijpx.2023.100202
44. Ahmad, N.; Wahab, R.; Al-Omar, S. Y. *Eur. J. Chem.* **2014,** *5,* 247–251. doi:10.5155/eurjchem.5.2.247-251.971
45. Arora, S.; Bagoria, R.; Kumar, M. *J. Therm. Anal. Calorim.* **2010,** *102,* 375–381. doi:10.1007/s10973-009-0460-2
46. Rastogi, V.; Yadav, P.; Verma, A.; Pandit, J. K. *Eur. J. Pharm. Sci.* **2017,** *107,* 168–182. doi:10.1016/j.ejps.2017.07.014
47. Zeng, Z.; Zhou, G.; Wang, X.; Huang, E. Z.; Zhan, X.; Liu, J.; Wang, S.; Wang, A.; Li, H.; Pei, X.; Xie, T. *Int. J. Nanomed.* **2010,** *5,* 567–572. doi:10.2147/ijn.s12485
48. Yang, J.; Pal, R. *Polymers (Basel, Switz.)* **2020,** *12,* 2302. doi:10.3390/polym12102302
49. Acharya, D. P.; Hartley, P. G. *Curr. Opin. Colloid Interface Sci.* **2012,** *17,* 274–280. doi:10.1016/j.cocis.2012.07.002
50. Mohammed, A. N.; Ishwarya, S. P.; Nisha, P. *Food Bioprocess Technol.* **2021,** *14,* 133–150. doi:10.1007/s11947-020-02562-2
51. Subramanian, N.; Ghosal, S. K.; Acharya, A.; Moulik, S. P. *Chem. Pharm. Bull.* **2005,** *53,* 1530–1535. doi:10.1248/cpb.53.1530
52. Bass, V. L.; Soukup, J. M.; Ghio, A. J.; Madden, M. C. *Lipids Health Dis.* **2020,** *19,* 128. doi:10.1186/s12944-020-01296-6
53. Harvey, K. A.; Walker, C. L.; Pavlina, T. M.; Xu, Z.; Zaloga, G. P.; Siddiqui, R. A. *Clin. Nutr.* **2010,** *29,* 492–500. doi:10.1016/j.clnu.2009.10.008
54. Ud-Din, S.; Bayat, A. *Wound Repair Regen.* **2017,** *25,* 164–176. doi:10.1111/wrr.12513
55. AOCS, *Am 5-04: Rapid Determination of Oil/Fat Utilizing High-Temperature Solvent Extraction.* 2024. https://library.aocs.org/Am-5-04 (accessed Sept 18, 2025).
56. Ferreira, L. D. S.; Turatti, I. C. C.; Lopes, N. P.; Guaratini, T.; Colepicolo, P.; Oliveira Filho, E. C.; Garla, R. C. *Int. J. Anal. Chem.* **2012,** 431954. doi:10.1155/2012/431954
57. ICH, *Q8(R2): Pharmaceutical Development,* 2009.
58. ICH, *Q9: Quality Risk Management,* 2005.
59. Fukuda, I. M.; Pinto, C. F. F.; Moreira, C. d. S.; Saviano, A. M.; Lourenço, F. R. *Braz. J. Pharm. Sci.* **2018,** *54,* e01006. doi:10.1590/s2175-97902018000001006
60. McClements, D. J. *Soft Matter* **2012,** *8,* 1719–1729. doi:10.1039/c2sm06903b

License and Terms

BEILSTEIN JOURNAL OF NANOTECHNOLOGY

Development and in vitro evaluation of liposomes and immunoliposomes containing 5-fluorouracil and R-phycoerythrin as a potential phototheranostic system for colorectal cancer

Raissa Rodrigues Camelo[‡1], Vivianne Cortez Sombra Vandesmet[‡1], Octavio Vital Baccallini[1], José de Brito Vieira Neto[2], Thais da Silva Moreira[1], Luzia Kalyne Almeida Moreira Leal[1], Claudia Pessoa[2], Daniel Giuliano Cerri[3], Maria Vitória Lopes Badra Bentley[3], Josimar O. Eloy[1], Ivanildo José da Silva Júnior[4] and Raquel Petrilli[*1,§]

Full Research Paper

Open Access

Address:
[1]Federal University of Ceará, Faculty of Pharmacy, Dentistry and Nursing, Department of Pharmacy, Fortaleza, Ceará, Brazil, [2]Federal University of Ceará, College of Medicine, Department of Physiology and Pharmacology, Fortaleza, Ceará, Brazil, [3]School of Pharmaceutical Sciences of Ribeirao Preto, University of São Paulo, Ribeirão Preto, São Paulo, Brazil and [4]Federal University of Ceará, Center of Technology, Department of Chemical Engineering, Fortaleza, Ceará, Brazil

Email:
Raquel Petrilli[*] - petrilliraquel@ufc.br

* Corresponding author ‡ Equal contributors
§ Email: petrilliraquel@gmail.com

Keywords:
colorectal cancer; immunoliposomes; photodynamic therapy; R-phycoerythrin; 5-fluorouracil

Beilstein J. Nanotechnol. **2026,** *17,* 97–121.
https://doi.org/10.3762/bjnano.17.7

Received: 08 July 2025
Accepted: 04 December 2025
Published: 09 January 2026

This article is part of the thematic issue "Advances in nanotechnology applied to natural products".

Guest Editor: D. Dourado

Abstract

5-Fluorouracil (5-FU) is the first-line drug for the treatment of colorectal cancer (CRC), which is considered the third most prevalent type of cancer in the world. R-phycoerythrin (R-PE) is a phycobiliprotein isolated from red algae such as *Solieria filiformis*, with fluorescent properties, photodynamic activity and potential for cancer treatment. However, 5-FU toxicity promotes several side effects and R-PE low stability hampers its clinical use. Thus, the present work aimed to develop co-encapsulated liposomes system for co-delivery of 5-FU and R-PE as theranostic nanosystems for CRC, as well as immunoliposomes targeted with the anti-EGFR monoclonal antibody, cetuximab, as a strategy for targeted delivery to EGFR-positive CRC. To the best of our knowledge, this is the first study to report the development and in vitro evaluation of liposomes and immunoliposomes co-encapsulating 5-FU and R-PE. Thus, liposomes containing 25 mg or 50 mg of soybean phosphatidylcholine (SPC), diesterolphosphatidylcholine (DSPC),

dipalmitoylphosphatidylcholine (DPPC), hydrogenated soybean phosphatidylcholine (HSPC) with cholesterol (Chol) and 1,2-distearol-*sn*-glycero-3-phosphoethanolamine-*N*-[amino(polyethylene glycol)-2000] (DSPE-PEG 2000) were prepared and characterized. Among the liposomes, those containing HSPC lipid at 50 mg showed a low polydispersity index (PDI) (0.100 ± 0.022), small size (103.43 ± 1.31 nm), and slightly negative zeta potential (−12.23 ± 0.35 mV). The encapsulation efficiency (EE%) was 94 ± 2.4% for R-PE and 42 ± 2.8% for 5-FU. Regarding the stability study, the liposomes maintained vesicle size, PDI and zeta potential values in a stable range. From the choice of the 50 mg HSPC liposome, the immunoliposomes were developed. The selected immunoliposomes, composed HSPC/DOPE/Chol/DSPE-PEG-Mal in a ratio of 64:10:22.2:3.7, were named HSPC IM 07. This formulation presented low PDI (0.185 ± 0.01), small vesicle size (99.45 ± 1.81 nm), negative zeta potential (−14.8 ± 0.81 mV) and antibody conjugation efficiency of 34.4%. Topographical AFM analysis showed that HSPC-IM-R-PE presented significantly higher surface roughness and viscoelastic contrast, indicating successful antibody anchoring. For cell viability in the HCT-116 CCR cell line, the IC_{50} values for immunoliposomes were higher than those for liposomes. Also, for phototoxicity experiments it was found a reduction in IC_{50} for all groups tested. The internalization of R-PE was verified, highlighting a greater internalization in the immunoliposome within 24 h. Thus, the HSPC 50 formulation containing R-PE and 5-FU, functionalized with cetuximab, is a promising alternative for the development of co-encapsulation delivery systems as a phototheranostic nanocarriers.

1 Introduction

Colorectal cancer (CRC) consists in malignant neoplasms related to several histologic types along the colon and rectum. In 2020, worldwide, colorectal cancer is the 3rd most prevalent type of cancer, corresponding to around 10% of the total cases of this disease. Regarding mortality numbers, this kind of cancer reaches the 2nd position, having approximately 900,000 deaths per year [1]. A diversity of factors may contribute, to a greater or lesser extent, to CRC incidence such as genetic mutations and lifestyle. The prognosis, in general, depends on the disease stage and gene affected [2,3]. Among the treatment options for CRC, there are oxaliplatin, irinotecan, mitomycin C and fluoropyrimidines, such as 5-fluSousa et al.orouracil (5-FU), in addition to radiotherapy and anti-EGFR monoclonal antibodies, such as cetuximab [2].

Even though these options are classic treatments for CRC and are well known for improving patient survival, they have numerous side effects, such as immunosuppression, nausea, vomiting, diarrhea, neurological, renal, and cardiac damage [4]. In addition, classic chemotherapy faces another challenge, which is multiple drug resistance (MDR), considering that approximately half of metastatic CRC cases are resistant to 5-FU treatments, contributing to decrease the survival rate of patients [5]. In this context, nanotechnology has emerged as a promising therapeutic strategy for cancer treatment. Nanostructured drug delivery systems enable preferential drug accumulation in tumor tissue through the enhanced permeability and retention (EPR) effect, thereby reducing cytotoxic exposure to healthy tissues and minimizing side effects [6]. Liposomes have promising characteristics due to their biocompatibility and their ability to carry both hydrophilic and lipophilic substances. Furthermore, liposomes can also act as a protein delivery system, reducing enzymatic degradation of proteins and enhancing their stability and their permeability through cell membranes [7].

Immunoliposomes provide many advantages by surface functionalization with targeting biomolecules. These systems are formed by monoclonal antibodies linked to the lipid bilayer, allowing the nanoparticle to recognize and specifically bind to receptors overexpressed in the membrane of tumor cells. This active functionalization expands the therapeutic potential of liposomes by promoting greater intratumor accumulation with higher cellular internalization. In addition, the use of immunoliposomes contributes to reducing systemic toxicity, since their delivery is concentrated in the tumor microenvironment, avoiding exposure of healthy tissues [8].

In colorectal cancer, the epidermal growth factor receptor (EGFR) has been widely explored as a therapeutic target, given its high expression in tumors, especially the most aggressive and metastatic ones [9]. Functionalization with anti-EGFR antibodies, such as cetuximab, allows the construction of immunoliposomes capable of selectively recognizing these tumor cells, enhancing the internalization of the system and promoting greater cytotoxic activity compared to conventional therapies [10]. By combining selective cytotoxicity with the potential to label cancer tissue using an imaging probe, EGFR-targeted immunoliposomes represent an integrated approach for more effective, safer, and personalized theranostic treatment of colorectal cancer [11].

R-phycoerythrin (R-PE) is a phycobiliprotein isolated from red algae *Solieria filiformis*, which is cultivated on the Brazilian coast [12]. Several pre-clinical studies have shown that this protein has potential application in cancer treatment, ranging from in vitro cell programmed death induction in the liver, lung, and gastric cancer cells [12] to in vivo reduction in nodule number and liver weight in rats [13]. In addition, R-PE also has a photosensitizing role that can be explored in photodynamic therapy. Another characteristic of this molecule is its fluorescence activi-

ty, which is important for use as a diagnosis tool [14]. Recently, our research group has demonstrated the potential of using the fluorescent properties of R-PE in 4T1 (triple-negative breast murine cancer) and PC3 (human prostate cancer) cells [15].

Furthermore, as previously mentioned, 5-FU is a drug used to treat colorectal cancer, an analogue of the uracil nucleotide, capable of inhibiting the synthesis of DNA and RNA, in addition to inhibiting thymidylate synthase. This drug is the first line of the treatment of colorectal cancer, but there are cellular mechanisms of resistance, such as membrane transporters, which lower the therapeutic response rate. However, when the treatment with 5-FU was evaluated, associated with photodynamic therapy using Foslip® as a liposomal system, it was found that this treatment was effective for cells resistant to 5-FU and for those that are not resistant [16].

In this work, the proposal was to develop nanostructured delivery systems with therapeutic and diagnostic activity by co-encapsulating R-PE and 5-FU in liposomes and immunoliposomes. For this, different lipid compositions were evaluated, and the systems were thoroughly characterized. Finally, in vitro experiments in a CRC cell line were conducted for the evaluation of cytotoxicity, photo toxicity, and uptake. Some studies have sought to demonstrate that dual-drug nanosystems can result in synergistic antitumor effects or reduce adverse effects [17]. This can be considered the first report on the use of liposomes and immunoliposomes containing co-encapsulated 5-FU and R-PE, which may represent a promising strategy for theranostics and allow early tumor treatment.

2 Materials and Methods

2.1 Materials

The Rhodophyte macroalgae *Solieria filiformis* were collected from cultivation ropes positioned about 200 meters from the shoreline. These activities were overseen by the Association of Algae Producers of Flecheiras and Guajiru (APAFG), situated on the western coast of Ceará State, Brazil (SisGen approval: A41C95F and AA3CF48). R-PE was obtained using a previously reported protocol [15]. 5-Fluorouracil, cholesterol (Chol), Sepharose CL-4B, bovine serum albumin, RPMI medium, trypsin, and 3-[4,5-dimethylthiazol-2-yl]-2,5-diphenyltetrazolium bromide (MTT) were obtained from Sigma-Aldrich (St. Louis, MO). 1,2-Dipalmitoylphosphatidylcholine (DPPC), 1,2-disteasteroyl-*sn*-glycero-3-phosphocholine (DSPC), soja 1,2-disteasteroyl-*sn*-glycero-3-phosphocholine (SPC), hydrogenated soy phosphatidylcholine (HSPC), 1,2-distearol-*sn*-glycero-3-phosphoethanolamine-*N*-[amino(polyethylene glycol)-2000], (DSPE–PEG 2000), and DOPE were obtained from LIPOID (Lipoid GmbH, Germany). DSPE–PEG–MAL was obtained from LaySan Bio, United States. Chloroform (CAS 67-66-3) was obtained from Contemporary Chemical Dynamics (Brazil). Dimethyl sulfoxide (DMSO, CAS 67-68-5), was obtained from NEON (Suzano, Brazil). The cell line HCT-116 (ATCC® CCL-247™) was provided by the National Cancer Institute (USA).

2.2 Formulation development

2.2.1 Liposomes

Liposomes were prepared by the lipid film hydration method as previously described [18], based on phospholipid/Chol/DSPE–PEG 2000 (70:20:5) with eight different compositions varying the lipid type (HSPC, DSPC, DPPC, SPC) and amount (25 and 50 mg) followed by sonication. In summary, the lipids were solubilized in 5 mL of chloroform and evaporated for 30 min at 65 °C. In the next step, the lipid film was hydrated with 5 mL of phosphate buffer saline (PBS, pH 7.4) during 60 min at 100 rpm and 37 °C or with PBS, pH 7.4 containing 5-FU and/or R -PE, respectively, at final concentrations of 260 µg/mL and 1 mg/mL. Subsequently, the formulations were subjected to an ultrasonic bath for 15 min. To reduce the size of the vesicles, the sonication method with a probe ultrasound was applied (Qsonica Sonicator – Model: Q500) at a 20% amplitude, for 5 min, under an ice bath [19].

2.2.2 Immunoliposomes

Immunoliposomes were developed from the chosen liposome formulation (HSPC/DOPE/Chol/DSPE–PEG–MAL in a ratio of 64:10:22.2:3.7), with adaptations for better antibody conjugation. Cetuximab (2.0 mg/mL) was thiolated using Traut's reagent, in a molar ratio of 40:1 (Traut/cetuximab), in PBS/EDTA buffer (5 mM, pH 8.0), under incubation at 37 °C for 1 h. The excess Traut's reagent was removed by chromatography on a disposable PD-10 desalting column, collecting 1 mL fractions eluted with PBS/EDTA (5 mM, pH 8.0). The cetuximab concentration was quantified by the BCA assay, according to the specifications of the manufacturer, and the fractions containing thiolated cetuximab (fractions 4–6) were combined. For antibody conjugation, DSPE–PEG–MAL was used as a lipid anchor for cetuximab fixation. Immunoliposomes were prepared by the lipid film evaporation method, as previously described. The fractions containing thiolated cetuximab (fractions 4–6) were then combined with the liposomes and the mixture was incubated overnight for 20 h, at room temperature, stirred at 200 rpm. Unconjugated antibodies were removed by chromatography on a Sepharose CL-4B column eluted with PBS (pH 7.4) [19].

2.3 Sample characterization

2.3.1 Particle size, polydispersity and zeta potential

The hydrodynamic vesicle size and polydispersity index (PDI) were performed by dynamic light scattering (DLS), and the zeta

potential by electrophoretic light scattering (ELS) techniques using the Zetasizer Nano ZS device (Malvern Instruments). The vesicle size and PDI were evaluated with noninvasive backscatter with an incidence angle of 173°, and the zeta potential was determined by the forward scatter (13°) ELS technique. The samples were diluted (1:200) in Milli-Q water. Given that PBS from the original formulation remains associated with the vesicles and maintains their colloidal stability, no additional saline was required during dilution. The measurements were performed in triplicate at 25 °C using an optical 4 mW HeNe at a wavelength of 633 nm. The results (n = 3) were expressed as mean ± standard deviation [20].

2.3.2 Encapsulation efficiency

To determine the encapsulation efficiency (EE%) of 5-FU, an indirect method was employed using ultrafiltration technique and quantification by spectrophotometry. To quantify the free/purified drug, a 1000 µL aliquot of the samples was added to a 50 kDa Amicon®, and subsequently centrifuged at 3000 rcf/g for 15 min. Then, a 50 µL aliquot collected from the filtrate was pipetted and the volume was made up to 5 mL with PBS buffer pH 7.4 and subjected to filtration through PVDF with a pore size of 0.45 µm. The samples were analyzed in a spectrophotometer at 265 nm [19]. The amount of total 5-FU corresponds to the theoretical amount of the drug present in the formulation. The results obtained were applied to Equation 1:

$$\mathrm{EE\%} = \frac{[\text{purified fraction}]}{[\text{total fraction}]} \times 100. \quad (1)$$

For this, a spectrophotometric method was previously validated [21]. Initially, a stock solution of 1.3 mg/mL of 5-FU in PBS buffer pH 7.4 was prepared. After that, dilutions were carried out obtaining the working solutions used to validate the analytical control: 0.25, 0.5, 1.0, 2.0, 4.0, and 5.0 µg/mL in triplicate. The data obtained was analyzed for precision, linearity, limit of detection (LD), and limit of quantification (LQ) based on ICH Q2(R2) on validation of analytical procedures [22].

For R-PE, an indirect method was used to determine the free/purified fraction. To quantify free/purified drug, a 1000 µL aliquot was removed from the sample and eluted on a CL-4B molecular exclusion gel column. As the sample was eluting, a 1 mL aliquot was collected, and 1 mL of PBS pH 7.4 buffer eluent was added. Finally, a total of twenty fractions were obtained. With the free/purified fraction (eluted fractions), quantification was done by fluorescence (excitation at 495 nm, emission range between 515 and 700 nm) using PBS buffer pH 7.4 as the blank and a 5 nm slit. For this, a spectrophotometric method was previously validated [15]. Initially, a stock solution of 0.05 mg/mL of R-PE in PBS buffer pH 7.4 was prepared. After that, dilutions were carried out obtaining the working solutions used to validate the analytical method: 0.5, 2.0, 4.0, 6.0, 8.0, and 10.0 µg/mL in triplicate.

The method for both molecules was analyzed for precision, accuracy, linearity, LD, and LQ based on ICH Q2(R2) on validation of analytical procedures [22]. Linearity was evaluated using three independent series of calibration curves for 5-FU and R-PE. Linearity was assessed by least-squares linear regression (calibration equation and correlation coefficient). Precision and accuracy were determined by the analysis of replicates of different concentrations. The detection limit and the quantification limit were determined from the calibration curve parameters, standard deviation, and slope of the curve.

The amount of total R-PE corresponds to the theoretical amount of the drug present in the formulation. The results of the concentrations obtained were applied to Equation 1.

The drug loading rate (DL%) of the molecules was determined as a percentage based on the mass of the liposomes obtained after lyophilization, according to Equation 2 [23].

$$\mathrm{DL\%} = \frac{\text{Amount of encapsulated molecule}}{\text{Amount of lyophilized formulation}}. \quad (2)$$

In vitro release

2.3.4.1 In vitro release of 5-FU. To evaluate the drug release profile, 250 µL of each sample was diluted in 7 mL of phosphate buffer (pH 7.4) and incubated in sealed Erlenmeyer flasks under continuous stirring (150 rpm) at 37 °C (n = 5). The assay was performed independently for each release interval (0, 0.5, 2, 4, 6, 8, and 24 h). At predetermined time points, aliquots were withdrawn and filtered through an Amicon® tube (50 kDa), in the centrifugal rotation of 3000g. The resulting filtrate was subsequently diluted in phosphate buffer (pH 7.4) and analyzed by UV–vis spectrophotometry at 265 nm [19]. The release profiles of free 5-FU solution, 5-FU-loaded liposomes, and 5-FU-loaded immunoliposomes were comparatively analyzed under the same conditions.

2.3.4.2 In vitro release of R-PE. Aliquots of the selected formulations with both molecules were diluted in PBS/azide 0.01% w/v buffer (pH 7.4) to a final R-PE concentration of 125 µg/mL and a final volume of 5 mL, and maintained under agitation at 150 rpm and 37 °C. At 1, 2, 4, 6, 24, 48, and 72 h, samples were ultracentrifuged at 18.000 rpm for 10 min. The supernatant was collected and quantified using a micro BCA assay, following the instructions of the manufacturer. The nanoparticle precipitate was re-dispersed in fresh PBS/azide buffer

and agitated until the next time point, as previously described [24].

2.3.4.3 Release profile of R-PE and 5-FU. The release profile of R-PE and 5-FU from liposomes and immunoliposomes was analyzed using the Korsmeyer–Peppas (Equation 3) model, commonly employed in drug release kinetics studies, using the DDSolver software [24].

The Korsmeyer–Peppas is a semi-empirical model that encompasses release profiles of drugs through polymeric chains when the governing mechanism is a combination of Fickian and non-Fickian mechanisms:

$$Q = k \cdot t^n \tag{3}$$

where Q is the amount of dose released at time t, k is the release rate constant, and n is the exponent.

2.3.5 Atomic force microscopy

The topographical characterization of liposomal formulations was performed by using atomic force microscopy (AFM) with a Nanosurf® FlexAFM system. The samples analyzed included liposomes and immunoliposomes containing R-PE. Briefly, to avoid vesicle deformation or disruption, liposomes and immunoliposomes were first stabilized by adding 5% glutaraldehyde for 2 h [25]. After fixation, the formulations were diluted at a ratio of 1:750 in deionized distilled water (ddH_2O). A 3.0 µL aliquot of the diluted sample was deposited onto a freshly cleaved mica substrate, followed by vacuum drying for 15 min at room temperature. The analyses were conducted in air, using the tapping mode to prevent damage to the sample surface, by using a PPP-NCSTAu probe (Nanosensors®, Switzerland), with frequency resonance of 125 kHz and spring constant of 5.0 N/m. The scan rate was 1.5 s per line. The images were captured using the Nanosurf C3000i software and subsequently processed and analyzed with the Gwyddion v 2.66 software, which was used for image leveling, coloring, 3D visualization of the specimens, and roughness analysis [26].

2.3.5.1 Atomic force microscopy roughness calculation. Roughness analyses were done by using the Gwyddion software. Each z-axis (height) of the image was previously processed to level it, which included shifting the minimum data value to zero, mean plane subtraction, and row alignment using the median of the differences function. After these steps, the statistical quantities tool provided in the Gwyddion software calculated single values for R_q and R_a (the root mean square roughness and arithmetic mean roughness, respectively) for each image obtained, considering the entire scanned area without any masking. These values and their standard deviation were calculated from [e.g., n = 507] HSPC-50-R-PE control liposomes and [e.g., n = 788] HSPC-IM-R-PE immunoliposomes, which were obtained from six and eight independent AFM images, respectively.

2.4 Fourier transform infrared spectroscopy

Drug–nanoparticle interactions were studied by subjecting the previously lyophilized samples to Fourier-transform infrared (FTIR) spectroscopy in an FTIR spectrophotometer (IRTracer-100, Shimazdzu, Japan), with a horizontal attenuated total reflectance accessory. The scan was performed in the range of 500 to 4000 cm^{-1} [27].

2.5 Stability study

After physicochemical characterization, the selected formulations were 30 days. The samples were kept at 4 °C in plastic containers wrapped in aluminum protected from light, and characterized for vesicle size, PDI, and zeta potential.

2.5.1 Stability of nanoparticles in serum

The stability of the nanoparticles in bovine serum was assessed following an adapted method [28]. Liposomes and immunoliposomes (with and without 5-FU and R-PE) were diluted in 10% serum and incubated at 4 °C for 12 h, 24 h, and 48 h. The samples were vortexed and analyzed for vesicle size, polydispersity index, and zeta potential using a Malvern Nanosizer ZS equipment (Malvern Instruments, UK) at the corresponding incubation times [28].

2.6 Phototoxicity and cytotoxicity

The HCT-116 cell line was cultivated in RPMI 1640M medium, supplemented with 10% Fetal Bovine Serum (FBS), and 1% antibiotic/antimycotic solution at 37 °C with 5% CO_2, in accordance with ATCC recommendations.

The photocytotoxicity and cytotoxicity were evaluated by 3-[4,5-dimethyl-thiazol-2-yl]-2,5-diphenyltetrazolium bromide (MTT) assay, which assesses cellular metabolic activity by quantifying mitochondrial dehydrogenase activity in viable cells, serving as an indicator of cell viability and, consequently, cytotoxicity [29]. For this, the cells were plated onto 96-well plates with 7×10^4 cells per well at 37 °C in 5% CO_2. After 24 h, the cells were treated with the formulations: liposome (HSPC/Chol/DSPE–PEG2000; 70:20:5; 50 mg of HSPC) and immunoliposome (HSPC/Chol/DOPE/DSPE–PEG–MAL; 64:10:22.2:3.7) containing 5-FU, R-PE, 5-FU/R-PE co-encapsulated and blank formulations. R-PE and/or 5-FU and RPMI medium were used as control solutions. The treatments were diluted in incomplete RPMI medium to obtain curve concentrations according to Table 1.

Table 1: Concentration for the MTT method of control and test samples: solution, liposome, and immunoliposome with 5-FU and/or R-PE.

Molecule	Concentration (μM)
5-FU	50.0; 25.0; 12.5; 6.25; 3.15; 1.56
R-PE	0.1; 0.05; 0.025; 0.012; 0.006; 0.003

The microplates were incubated at 37 °C in the presence of 5% CO_2, for 69 h for cytotoxicity assays, while for phototoxicity assays they remained incubated for 48 h, followed by 2 h of green light irradiation, γ = 525 nm, dose of 14.4 J/cm^2 and incubated again until completing the 69 h period. After incubation for 69 h, 20 μL of the MTT solution (0.5 mg/mL) was added, followed by incubation for 3 h (for a total 72 h of incubation) at 37 °C. After this period, the medium containing MTT was discarded from the wells and DMSO was added to dissolve the formazan crystals. Finally, the colored solution was quantified by measuring the absorbance at 562 nm on a plate spectrophotometer (Nivo-Perkinelmer). The cellular viability was calculated as the percentage of viable cells compared to the control group and half maximum inhibitory concentration (IC_{50}).

2.6.1 Competitive EGFR-binding of anti-EGFR immunoliposome and EGF in HCT-116 cells using flow cytometry

The experimental procedure was based on previous studies [30] with minor modifications detailed below. HCT-116 colorectal carcinoma cells were seeded at a density of 7×10^4 cells/mL in appropriate culture medium and incubated overnight at 37 °C with 5% CO_2. The following day, the cells were chilled on ice for 10 min and washed with live cell buffer (phosphate-buffered saline supplemented with 20 mM glucose and 1% bovine serum albumin). Cells were then treated with Alexa Fluor™ 488-labeled EGF (Thermo Fisher Scientific, E13345, 2 μg/mL) alone or following a sequential pre-incubation with either anti-EGFR immunoliposomes HSPC IM 07 (25 μg/mL) or cetuximab (Erbitux, 25 μg/mL) for 5 min. Each treatment was followed by a 20 min incubation at 37 °C. After incubation, the cells were washed twice, detached with trypsin-EDTA, centrifuged, and resuspended in a live cell buffer containing DAPI (3 μM) for viable cell selection. Flow cytometry analyses were conducted on a CytoFLEX (Beckman Coulter) using 405 nm and 488 nm lasers to detect DAPI and Alexa Fluor™ 488 signals, respectively. Competitive binding to EGFR was quantified by measuring the cellular fluorescence intensity of Alexa Fluor™ 488.

2.7 Cellular uptake

Cellular internalization was assessed by confocal microscopy. For confocal microscopy, 1×10^6 cells were seeded onto 6-well plates containing sterile cover slides and 1 mL of culture medium per well. After allowing cell adhesion overnight, the culture medium was removed and 1 mL of the liposome and immunoliposome nanoparticle suspension (containing R-PE) diluted to a concentration of 1000 nM in serum-free RPMI medium was added. The treatments were kept during 3, 6, or 24 h. After the internalization periods, the cells on the cover slides were rinsed and fixed using a 2% paraformaldehyde solution. For cell nucleus labeling, a DAPI solution (3 mg/mL) and fluoromount-G were used to preserve fluorescence. The slides were photographed using a Leica TCS SP8 confocal fluorescence microscope, using a 40× magnification objective. The wavelengths used were 488 nm for excitation and 575–585 nm for emission of R-PE, and 405 nm with emission between 413–472 nm for DAPI.

The fluorescence intensity quantified from confocal images was performed using the Zeiss Zen 3.12 software integrated with the confocal microscope. For each experimental group, the mean fluorescence intensity and corresponding standard deviation (SD) were determined from the selected regions of interest within the software. The resulting values were exported to GraphPad Prism 8 for statistical analysis.

2.8 Statistical analysis

The results were processed using Excel and analyzed in PRISM 8.0 software, and $p < 0.05$ was considered the minimum value of significance using TwoAway ANOVA test with Tukey's post-test. Competitive EGFR binding assay was analyzed using one-way ANOVA followed by Tukey's multiple comparisons test.

3 Results and Discussion

3.1 Liposomes development and characterization

Drug encapsulation in liposomes occurs passively during the formation of vesicles. For water-soluble drugs, such as those used in this study, loading occurs through interactions with the intraliposomal aqueous core. For hydrophilic drugs, encapsulation efficiency tends to be low, so the drug/lipid ratio is usually lower, between 10 and 50% [31]. The EE% results for both 5-FU and R-FE are shown in Figure 1.

The EE% significantly varied depending on the lipid composition and the nature of the encapsulated compound. Formulations containing HSPC exhibited statistically different EE% values for 5-FU and R-PE. However, no significant differences were observed when formulations containing SPC 25 or DSPC 50 were compared to HSPC 50, suggesting that for certain lipid

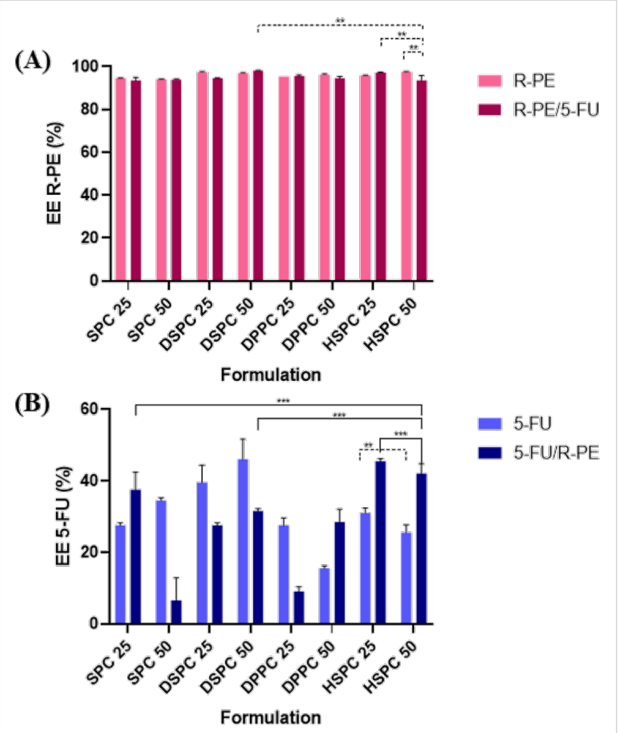

Figure 1: EE% of formulations. (A) Comparison between liposomes containing R-PE alone and those co-encapsulated with 5-FU. (B) Comparison between liposomes containing 5-FU alone and those co-encapsulated with R-PE. (Two-way-ANOVA with Tukey's test $^{**}p < 0.05$; $^{***}p > 0.05$).

types and concentrations, the EE% may reach a plateau or become less responsive to compositional changes.

A statistically significant difference was observed in the EE% of R-PE between the same HSPC-based formulations. The enhanced encapsulation of R-PE with increasing HSPC content may reflect improved bilayer stability or more favorable partitioning into the aqueous core or thebilayer interface.

In all formulations analyzed, the EE% of R-PE exceeded 90%, indicating a remarkably high level of protein encapsulation. These values are significantly higher than those reported in the literature, where the EE% for the β-subunit of R-PE typically remains around 50% [32]. The high EE% observed in this study may be attributed to the presence of carbohydrates, which are known to reduce pore formation in lipid bilayers and thus enhance vesicle integrity [33]. Such carbohydrates are likely present in the dispersion medium of the liposomes, as the R-PE used was extracted from the red algae *Solieria filiformis*, a species known to produce carrageenan. Additionally, the purity index of the extracted R-PE (0.73) suggests the presence of other biomolecules – such as polysaccharides and residual proteins – which may further contribute to membrane stabilization during liposome formation [15].

For 5-FU, no significant difference was observed between the HSPC 25 and HSPC 50 formulations, which may be explained by small size and high hydrophilicity of the drug – features that hinder its retention in the aqueous core of liposomes. These findings are in line with previous studies: Petrilli et al. (2018) reported EE% values of 45.8 ± 2.0 using DSPC and cholesterol [19], while Crisóstomo et al. (2022) achieved 61.73 ± 0.65 using SPC and cholesterol, which decreased to 50.20 ± 10.20 upon Span 20 addition [34].

Formulations with DSPC showed an improvement in EE%, likely due to its higher phase transition temperature and longer acyl chains, which enhance bilayer rigidity and stability [35]. Literature data support these results, with DSPC/cholesterol (55:45) liposomes showing EE% around 49.9% for 5-FU [21]. The difference in EE% between DSPC 25 and DSPC 50 may be attributed to vesicle size variation, as hydrophilic drug loading is directly related to aqueous volume and vesicle size [36].

Conversely, this trend was not observed in DPPC-based liposomes. DPPC has a lower phase transition temperature (41 °C) than DSPC (55 °C), leading to higher permeability. It has been reported that DPPC liposomes may leak encapsulated compounds even before reaching their transition temperature. Given that film hydration and 5-FU encapsulation were performed at 37 °C, this may explain the reduced EE% observed with DPPC formulations [37,38].

Regarding HSPC, the EE% for 5-FU was 26% for HSPC 50 and 30% for HSPC 25. Although other studies report EE% values of 75–80% for HSPC-based liposomes, those formulations often involve particles up to four times larger than those in the present study [39]. Notably, co-loading of 5-FU and R-PE in HSPC liposomes improved EE% to 46% and 42% for HSPC 25 and HSPC 50, respectively. This suggests a possible interaction between the protein and the drug, enhancing 5-FU retention. Furthermore, the HSPC 50 formulation was the only one to present both high EE% values and a PDI of 0.1 when co-loading both agents, indicating high homogeneity and stability. Thus, HSPC 50 was selected for subsequent immunoliposome preparation, characterization, and efficacy studies against CRC cells.

These findings highlight the importance of optimizing lipid composition not only according to the general hydrophilicity or lipophilicity of the drug, but also considering the molecular size, structure, and specific interactions with lipid components.

The stability of formulations containing HSPC 50 was evaluated over 30 days (Figure 2A–C). The vesicle size and zeta potential values showed a small increase in relation to storage

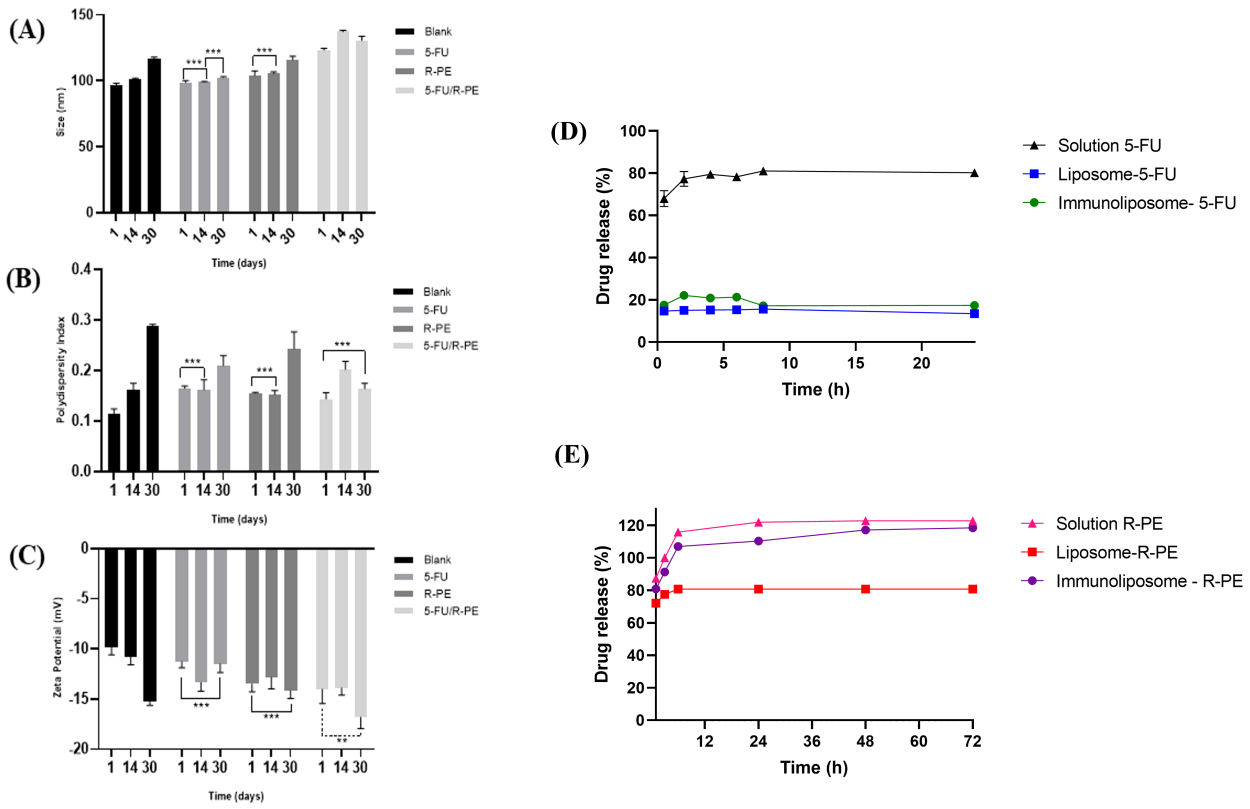

Figure 2: Physicochemical parameters of liposome formulations containing HSPC 50 (with and without 5-FU and/or R-PE) during the stability study at 4 °C for 30 days. (A) Vesicle size, (B) PDI, and (C) zeta potential (Two-way-ANOVA with Tukey's test $^{**}p < 0.05$; $^{***}p > 0.05$). (D) In vitro release profile of 5-FU from solution, liposome–5-FU, and immunoliposome–5-FU at different time points (0.5–24 h). Data are expressed as mean ± standard deviation ($n = 3$). Statistical analysis was performed by Tukey's multiple comparisons test: solution vs liposome or immunoliposome, $p < 0.0001$ at all time points; immunoliposome vs liposome, $p < 0.001$ (2 h), $p < 0.01$ (4 h), $p < 0.001$ (6 h), nonsignificant (ns) at other time points. (E) In vitro release profile of R-PE from solution, liposomes, and immunoliposomes in phosphate buffer (pH 7.4) over 72 h ($n = 3$; mean ± SD).

time, although they are not considered harmful to the stability of the formulation, as they remained in the expected range for liposomes and the PDI remained lower than 0.3. Furthermore, for PDI, no variability was observed when compared with the result of the 1st day of the formulation with 5-FU and R-PE with the last day. Regarding the zeta potential, there was no statistical difference between the days of analysis for samples containing only R-PE and for liposomes with only 5-FU. However, the stability was not shown in the formulations containing 5-FU/R-PE when correlating the zeta potential values from the last day with the previous ones.

Vesicle size is one of the first characteristics to be evaluated in a nanoparticle, as it influences clearance by the mononuclear phagocytic system and affects the drug release rate. Furthermore, smaller particles have greater stability against gravity, due to the Brownian effect [40]. Thus, liposomes around 100 nm are commonly used. Table 2 presents the results obtained herein for different liposomal compositions. The majority of the formulations presented vesicle size smaller than 200 nm, an acceptable value for the intended purpose, with which the EPR effect for therapy is expected tumor [41].

Based on the results, most formulations showed significant differences. However, no difference was observed in certain comparisons. For SPC 25, the vesicle size values of R-PE and R-PE/5-FU formulations were equivalent to the blank. A similar pattern occurred for HSPC 50 when comparing the blank with the 5-FU-only formulation, and for DPPC 25 both the 5-FU-only and R-PE/5-FU formulations matched the blank. Finally, variations in the proportion of constituents in the blank formulations, such as DSPC and SPC, also did not cause differences in vesicle size.

From the results shown in Table 2, in most cases, a difference in vesicle size values can be observed, depending on the encapsulated molecule. The exception is the formulation that contains the lipid SPC, which generated liposomes around 80 nm. However, SPC 50 formulations with encapsulated R-PE and 5-FU and with encapsulated SPC 25 5-FU were larger, with

Table 2: Physicochemical characterization of liposome formulations, containing Phospholipid/Chol/DSPE–PEG 2000 (70:30:5), where SPC, DSPC, DPPC, and HSPC were used at 25 or 50 mg.

Sample	Blank			5-FU		
	Size (nm)	PDI	ZP (mV)	Size (nm)	PDI	ZP (mV)
SPC 25	82.66 ± 0.20	0.208 ± 0.014	−15.47 ± 1.65	92.06 ± 1.13	0.261 ± 0.003	−10.87 ± 0.75
SPC 50	82.16 ± 0.55	0.190 ± 0.008	−13.47 ± 0.64	81.72 ± 0.71	0.188 ± 0.015	−9.79 ± 1.03
DSPC 25	113.77 ± 1.26	0.134 ± 0.020	−12.20 ± 0.98	124.83 ± 0.50	0.275 ± 0.015	−10.49 ± 0.90
DSPC 50	112.07 ± 1.40	0.153 ± 0.019	−12.77 ± 0.64	133.40 ± 4.90	0.270 ± 0.034	−9.66 ± 1.15
DPPC 25	104.67 ± 0.21	0.157 ± 0.018	−13.80 ± 1.13	94.48 ± 1.77	0.154 ± 0.014	−10.18 ± 0.54
DPPC 50	164.00 ± 2.70	0.309 ± 0.007	−12.07 ± 0.90	100.40 ± 1.52	0.174 ± 0.020	−11.11 ± 1.30
HSPC 25	96.86 ± 0.10	0.160 ± 0.011	−12.03 ± 0.90	116.50 ± 2.31	0.241 ± 0.007	−13.10 ± 1.51
HSPC 50	114.10 ± 1.85	0.159 ± 0.016	−12.27 ± 0.45	113.37 ± 0.81	0.188 ± 0.015	−12.77 ± 0.91
	R-PE			5-FU/R-PE		
Sample	Size (nm)	PDI	Size (mV)	Size (nm)	PDI	ZP (mV)
SPC 25	86.22 ± 1.61	0.260 ± 0.002	−22.23 ± 0.45	81.29 ± 0.18	0.202 ± 0.022	−15.03 ± 2.23
SPC 50	84.04 ± 2.09	0.237 ± 0.005	−18.47 ± 0.91	109.63 ± 0.55	0.321 ± 0.030	−16.33 ± 0.81
DSPC 25	141.4 ± 1.11	0.247 ± 0.007	−14.93 ± 1.31	160.57 ± 1.26	0.288 ± 0.010	−13.70 ± 1.51
DSPC 50	148.90 ± 1.06	0.218 ± 0.015	−11.97 ± 0.75	186.80 ± 4.43	0.310 ± 0.040	−13.97 ± 0.61
DPPC 25	120.53 ± 1.20	0.189 ± 0.016	−13.47 ± 1.14	96.87 ± 0.17	0.117 ± 0.014	−18.97 ± 0.61
DPPC 50	176.60 ± 0.56	0.226 ± 0.013	−11.57 ± 0.68	121.63 ± 1.42	0.147 ± 0.018	−11.30 ± 0.56
HSPC 25	132.13 ± 0.91	0.169 ± 0.007	−14.53 ± 0.49	122.30 ± 1.04	0.249 ± 0.007	−14.17 ± 1.19
HSPC 50	125.53 ± 1.82	0.127 ± 0.023	−11.77 ± 0.76	103.43 ± 1.31	0.100 ± 0.022	−12.23 ± 0.35

vesicle size values of 109.63 nm and 92.06 nm, respectively. It was also verified that, in most formulations that contained R-PE, the vesicle size increased. Regarding the vesicle size results of 5-FU with SPC, a study obtained a vesicle size of 97.2 ± 1.25 nm, for liposomes with the same lipid/cholesterol ratio of this work (70:30), similar to those herein (92.1 ± 1.1 nm and 81.7 ± 0.7 nm for SPC 25 and SPC 50, respectively). A slight reduction in vesicle size compared to previous reports can be possibly due to the presence of DSPE–PEG [34].

The incorporation of hydrophilic molecules into liposomal formulations does not necessarily result in an increase in vesicle size [42]. For instance, liposomes composed of HSPC 50 and encapsulating 5-FU did not exhibit a significant change in particle diameter when compared to blank formulations. This behavior may be attributed to the structural instability inherent to liposomes, as their size can vary depending on the lipid composition. Notably, formulations containing HSPC, DPPC, and DSPC exhibited larger vesicle sizes than those composed of SPC. A plausible explanation is that these phospholipids possess a higher bending modulus of the lipid bilayer at room temperature, rendering the membrane less flexible and more rigid compared to SPC, which is known for forming more fluid and deformable bilayers [38,43,44].

The vesicle size distribution graphs obtained by DLS show that the presence of bimodal peaks in the liposome formulations is associated with higher PDI values. For example, the blank formulation of DPPC 50 exhibited a PDI of 0.31, with two distinct populations: one with an average hydrodynamic diameter of 160.9 nm (89.9%) and another of 4401 nm (10.1%). In contrast, the HSPC 50 formulation containing both 5-FU and R-PE showed a monodisperse profile, with a PDI of 0.10 and a mean diameter of 112.8 nm (100%), which is considered satisfactory (PDI ≤ 0.3), indicating a homogeneous particle population [45].

When carrying out a statistical evaluation of the PDI values obtained, in the case of the formulation with 5-FU and R-FE encapsulated in HSPC 50-based liposomes, the lowest PDI value refers to the combination of the two encapsulated molecules when compared with the DPPC formulations, which were not statistically different under the same conditions. Previous reports show that with the DSPC lipid there is greater heterogeneity when compared to DPPC [46].

As expected, all liposomal formulations exhibited a negative zeta potential due to the presence of phosphate groups in the phospholipid headgroups. However, significant differences in

zeta potential values were observed between some blank and drug-loaded liposomes, particularly in SPC 25 and DPPC 25 formulations. The presence of R-PE notably influenced the zeta potential, especially in formulations containing SPC 50, DPPC 25, and DSPC 25 and 50. This increase in negative surface charge may be attributed to changes in the distribution of surrounding counterions, possibly caused by the adsorption or ionization of functional groups at the liposomal surface [47]. Additionally, the exposure of the phosphate moiety to the aqueous environment may further contribute to the observed surface charge differences [48].

Among the zeta potential values described in Table 1, only some formulations encapsulated with 5-FU were in the neutrality range, which is −10 to +10 mV. However, some authors consider values greater than −30 to +30 mV to be ideal for the nanoparticle stability to avoid aggregation. The results can be justified by the neutral pH in which these liposomes are dispersed, since in a more acidic medium, it is expected that the amines, present in the lipids, are protonated, decreasing the zeta potential [49].

The DL% rates of the liposome formulations that showed the best performance are described in Table 3. Therefore, the increase in 5-FU encapsulation in liposomes upon adding R-PE was confirmed.

Table 3: Drug loading (DL%) of the best performance liposome formulations.

Formulation	DL%
Lipossome 5-FU	0.34 ± 0.03
Lipossome R-PE	5.62 ± 0.01
Liposome 5-FU/R-PE (5-FU)	0.58 ± 0.04
Liposome 5-FU/R-PE (R-PE)	5.05 ± 0.13

3.2 Development and characterization of immunoliposomes

Table 4 presents the physicochemical characterization of immunoliposome formulations developed under different preparation conditions, evaluating vesicle size, PDI, zeta potential, and conjugation efficiency. Among the formulations, HSPC IM-07 stands out with the highest conjugation rate.

The HSPC IM 07 formulation achieved the highest conjugation efficiency, at 34.4%, standing out among the formulations analyzed. This result is likely related to the presence of 10% DOPE in its composition, as well as the preparation conditions – antibody conjugation at room temperature with agitation speed at 200 rpm – which may have contributed to the best conjugation. DOPE promotes rearrangements in the lipid bilayer, increasing its fluidity and consequently facilitating the insertion of ligands onto the surface, in agreement with previous findings [50]. However, increasing the DOPE concentration did not enhance conjugation efficiency. In the IM-D08 formulation, where the DOPE concentration was 20%, the conjugation drastically decreased, indicating that excessive DOPE may compromise the bilayer organization, possibly due to increased instability, thus hindering ligand binding [51].

Moreira et al. (2023) [27] prepared immunoliposomes with DOPE, CHEMS, and DSPE–PEG-PEG to functionalize cetuximab and obtained 14.06% conjugation efficiency with a high percentage of cellular internalization in prostate cancer cells overexpressing EGFR. Souza et al. (2024) [52] also conjugated cetuximab to liposomes based on SPC, cholesterol, and DSPE–PEG–PEG with 40.9% conjugation efficiency.

Regarding vesicle size, HSPC IM 07 presented an average value of 99.45 ± 1.81 nm, within the ideal range, which favors prolonged circulation time and reduced phagocytosis. On the other hand, the polydispersity index was 0.185, slightly higher

Table 4: Physicochemical characterization of immunoliposomes for vesicle size, polydispersity index, zeta potential, and conjugation efficiency. All formulations contained fixed amounts of cholesterol (7.34 mg) and DSPE–PEG–MAL (10.75 mg).

Formulations	Hspc (mg)	Dope (%)	Temperature (°C)	Agitation (rpm)	Particle size (nm)	Pdi	Zeta potential (mV)	Conjugation efficiency (%)
HSPC IM-01	50	–	37	–	118.83 ± 2.43	0.168 ± 0.018	–22.6 ± 1.04	19.49
HSPC IM-02	50	–	RT	100	127.13 ± 2.81	0.211 ± 0.004	–20.2 ± 1.00	22.46
HSPC IM-03	50	–	37	100	114.9 ± 3.33	0.120 ± 0.006	–19.4 ± 0.16	20.42
HSPC IM-04	50	–	45	–	100.77 ± 2.81	0.133 ± 0.004	–14.9 ± 0.65	12.15
HSPC IM-05	50	–	RT	200	103.86 ± 0.65	0.115 ± 0.005	–16.1 ± 0.57	25.22
HSPC IM-06	50	–	45	200	100.44 ± 2.13	0.126 ± 0.01	–16.1 ± 0.81	19.29
HSPC IM-07	43.25	10	RT	200	99.45 ± 1.81	0.185 ± 0.01	–14.8 ± 0.81	34.4
HSPC IM-08	36.5	20	RT	200	100.44 ± 2.13	0.126 ± 0.01	–16.1 ± 0.81	11.59

than that of other formulations, such as IM-D05 (PDI: 0.115) [53]. However, since PDI values up to 0.2 are still considered satisfactory, this parameter is within the expected range [54]. The zeta potential of the selected formulation IM-D07 was −14.8 mV, which is acceptable for ensuring stability, although it does not fall within the ideal range of −20 to −30 mV reported to be more effective for maintaining colloidal stability [55]. The formulations IM-D01 and HSPC IM 02 presented zeta potentials of −22.6 mV and −20.2 mV, respectively, both within the ideal range. However, their conjugation efficiencies were significantly lower – 19.49% and 22.46%, respectively – further supporting the selection of HSPC IM 07 as the optimal formulation.

Another relevant aspect concerns the impact of preparation temperature. A comparison between HSPC IM 05 (room temperature) and HSPC IM 06 (45 °C), both under 200 rpm agitation speed and without DOPE, showed better conjugation efficiency than the formulation prepared at room temperature (25.22% vs 19.29%). This finding is supported by other studies, which demonstrated that elevated temperatures could alter the bilayer structure, negatively affecting ligand orientation and compromising functionalization efficiency [56].

Thus, the HSPC IM 07 formulation exhibits the most favorable characteristics for application in delivery systems, balancing nanoscale size, acceptable PDI, and high conjugation efficiency.

3.3 Atomic force microscopy assays

Atomic force microscopy assays were used to characterize the surface topography of nonfunctionalized liposomes (HSPC-50-R-PE) and immunoliposomes (HSPC-IM-R-PE), as shown in Figure 3 and Figure 4. It is worth noting the good quality of the AFM images by analyzing amplitude (Figure 3A and Figure 3D), which presented no noticeable noise artifacts, providing pseudo-3D contrast in both samples. In the case of HSPC-50-R-PE, the *z*-axis and 3D projection images (Figure 3B and Figure 3G, respectively) showed predominantly spherical vesicles, although slightly flattened. This aspect is typical of analyses performed in dried conditions on solid substrates such as mica and is mainly due to the dehydration process and adhesion forces onto the substrate [57,58]. On the other hand, the *z*-axis and 3D projections for HSPC-IM-R-PE (Figure 3E and Figure 3H, respectively) demonstrated a more irregular nanoparticle surface, with visibly rougher and more heterogeneous topography, a result consistent with previous studies [27,59,60].

To complement the topographic data, when comparing phase images of both formulations (Figure 3C and Figure 3F for HSPC-50-R-PE and HSPC-IM-R-PE, respectively), we observe

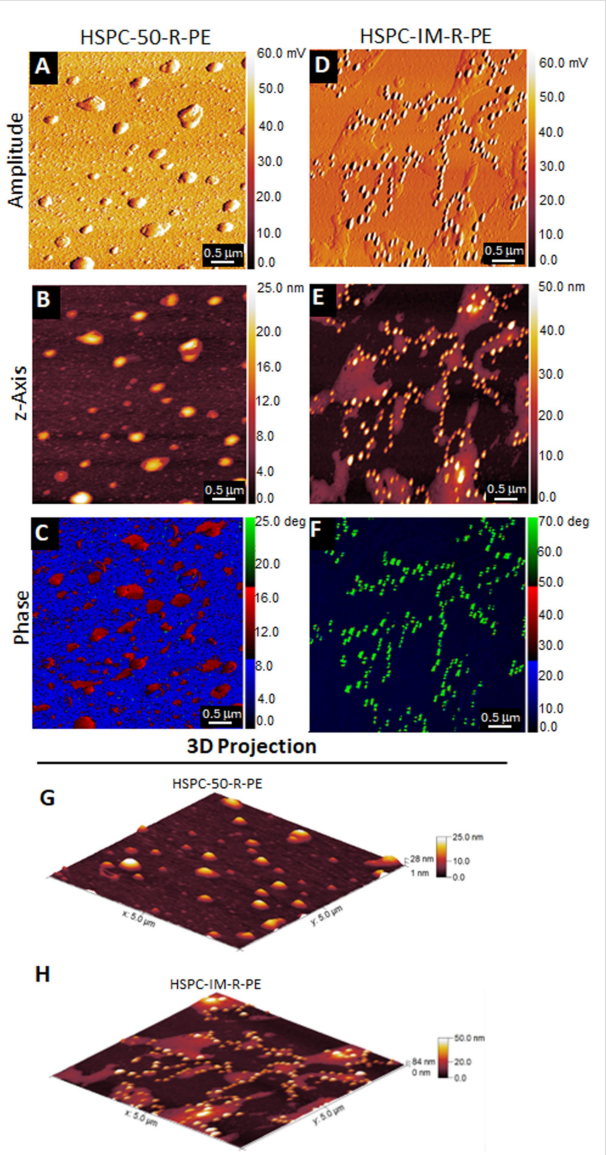

Figure 3: AFM analysis of liposomes (HSPC-50-R-PE) and immunoliposomes (HSPC-IM-R-PE) containing R-PE. Representative AFM images of HSPC-50-R-PE (A, B, C, and G) and HSPC-IM-R-PE (D, E, F, and H). (A, D) Amplitude images showing high-quality imaging without noise artifacts. (B, E) 2D Topographic profile of height (*z*-axis). (C, F) Phase images revealing distinct phase contrast between formulations, see text for further details. (G, H) 3D topographic projections.

further evidence of consistent structural alterations in the membrane of immunoliposomes, which aligns with the presence of anchored cetuximab on the lipid membrane, promoting changes in the surface organization of the nanoparticle. This is reflected in the relatively low phase angle of approximately 16° for all HSPC-50-R-PE (as indicated by red-colored liposomes) compared to approximately 70° for HSPC-IM-R-PE (as indicated by green-colored immunoliposomes). The lower phase angle indicates a more elastic, stiffer, and homogeneous lipid membrane, whereas the higher phase angle of HSPC-IM-R-PE is consis-

tent with a more dissipative tip–sample interaction, which is characteristic of softer, flexible, and viscoelastic materials [61,62]. The decoration of liposomes with cetuximab may result in a softer outer surface than the underlying lipid bilayer, explaining the observed increase in energy dissipation. These data strongly support that the surface properties of this liposome formulation were indeed altered following antibody functionalization, leading to distinct nanomechanical profiles, further reinforced by the observed changes in surface roughness, as follows.

Herein, we highlighted that AFM roughness measurements were uniquely used to confirm antibody decoration onto the liposome surface, with no correlation to nanoparticle size obtained by DLS, since both assays were performed in different conditions (hydrodynamic vs dried samples for DLS and AFM, respectively). The surface roughness showed a significant difference when both formulations were compared (Figure 4A–4C). Herein, we used the arithmetic roughness (R_a) and the root-mean-square roughness (R_q) as parameters to evaluate surface features [26]. Regarding R_a, as shown in Figure 4A (left pair of bars), the nonfunctionalized liposomes exhibited a notably low value of 2.016 ± 0.5081 nm, indicating a more uniform surface. In contrast, immunoliposomes exhibited a significantly higher R_a of 17.22 ± 2.487 nm (p = 0.0002 vs liposomes). This increase in R_a is a direct consequence of successful cetuximab conjugation onto the liposomal surface, which introduces irregularities and elevated features, as previously described in proteoliposome membranes [25,59]. This difference is also evident in the profile analysis of selected nanoparticles (Figure 3J and Figure 3K). Irregularities are clearly visible only in HSPC-IM-R-PE (Figure 4C, arrowheads in the right panel), which can be due to cetuximab decoration. In addition to the R_a results, the R_q values also support these findings (Figure 4A, right pair of bars). HSPC-50-R-PE maintained a low R_q of 3.874 ± 0.9706 nm, reinforcing the existence of a smooth topography without extreme height variations. In contrast, HSPC-IM-R-PE reached 23.61 ± 2.225 nm (p < 0.0001 vs liposomes), suggesting more distinct surface peaks and valleys, consistent with the functionalization process, which increase roughness

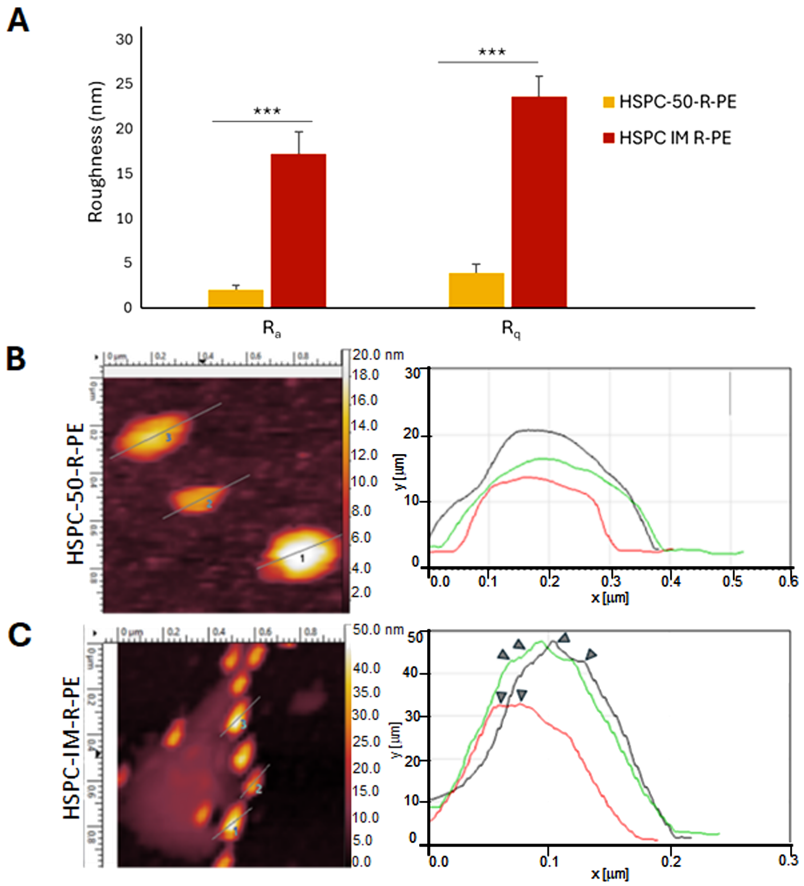

Figure 4: Graphical roughness analysis by AFM of liposomes (HSPC-50-R-PE) and immunoliposomes (HSPC-IM-R-PE) containing R-PE. (A) Quantitative roughness comparison between the two formulations, based on arithmetic roughness (R_a) and root-mean-square roughness (R_q) parameters. (B, C) Profile traces of representative liposomes from each formulation. Arrows in (C) indicate that surface irregularities in HSPC-IM-R-PE are likely resulting from the cetuximab functionalization.

and significant topographical variations caused by the conjugated biomolecules. As seen above, the differences between formulations were statistically significant, it is noteworthy that when comparing R_a and R_q within each liposome formulation, no statistical significance was observed (HSPC-50-R-PE, $p = 0.1208$ vs R_q; HSPC-IM-R-PE, $p = 0.0761$ vs R_q), indicating sample uniformity within each group.

Taken together, the topographic data, phase angle variations, and quantitative roughness analyses provide strong evidence of liposome functionalization. The transition from a smooth surface in HSPC-50-R-PE to a rougher HSPC-IM-R-PE topography is likely to impact biological interactions such as cellular uptake mechanisms, biodistribution, clearance by the reticuloendothelial system, and even protein corona formation under physiological conditions [63]. These findings highlight the importance of surface characterization by AFM in the development and optimization of nanoparticles.

3.4 Fourier-transform infrared spectroscopy assays

The FTIR spectra obtained for the formulations showed the characteristic bands of both R-PE and 5-FU, confirming their incorporation into liposomes and immunoliposomes (Figure 5). For R-PE, typical amide vibrations were observed: amide I (C=O) around 1650 cm^{-1} and amide II (N–H) near 1540 cm^{-1}, along with a broad N–H/O–H stretching between 3200–3400 cm^{-1}, attributed to the polypeptide backbone of the protein. For 5-FU, bands associated with C=O stretching (≈1670 cm^{-1}), N–H stretching (≈3120 cm^{-1}) [64-66], and the characteristic C–F vibration (≈1240 cm^{-1}) were also detected [66].

When the spectra of the formulations were compared with those of the free molecules, changes in relative intensity and slight shifts in the amide and carbonyl bands were noted, suggesting intermolecular interactions between R-PE, 5-FU, and the lipid matrix. These spectral shifts are indicative of hydrogen bonding and rearrangement of the molecular microenvironment, phenomena commonly associated with the encapsulation process, as previously reported for protein–lipid systems [67,68].

Similar alterations have been described in liposomal formulations containing therapeutic agents and biomolecules, where spectral changes were consistent with stabilization of the encapsulated compounds and reduced molecular mobility within the lipid bilayer [67]. Specifically for 5-FU, Ezekiel et al. (2021) [66] confirmed the preservation of its characteristic bands after

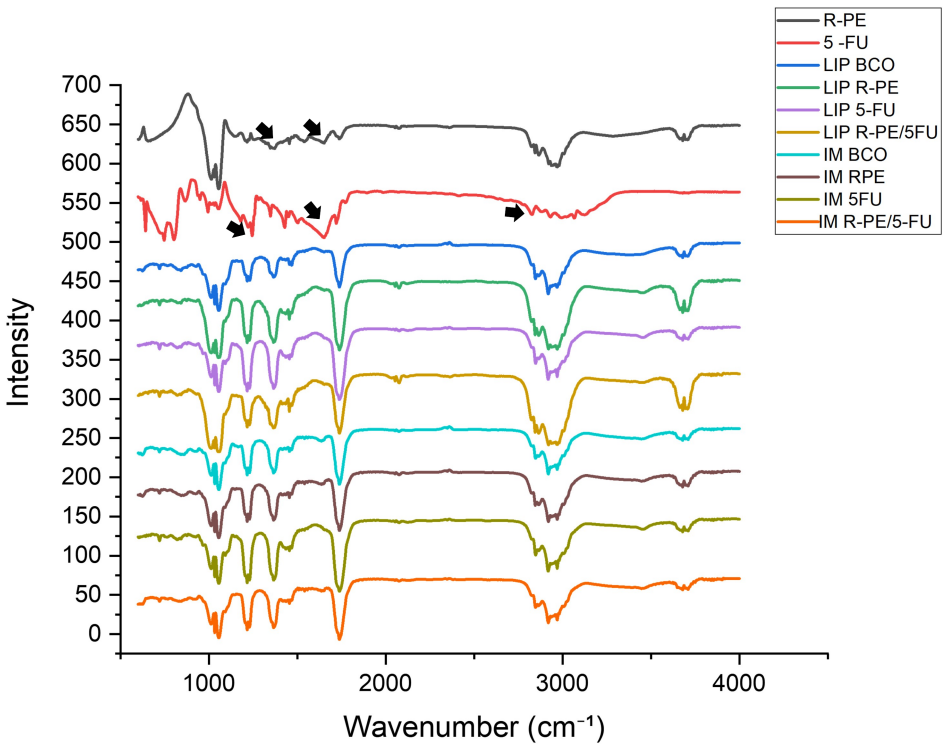

Figure 5: FTIR spectra of R-PE, 5-FU, liposomes, and immunoliposomes. Characteristic bands of R-PE were identified, including amide I (≈1650 cm^{-1}), amide II (≈1540 cm^{-1}), and the broad N–H/O–H stretching between 3200–3400 cm^{-1}. In the spectra of 5-FU, typical vibrations of C=O (≈1670 cm^{-1}), N–H (≈3120 cm^{-1}), and C–F (≈1240 cm^{-1}) were observed.

encapsulation in soybean lecithin liposomes, reinforcing that the presence of these peaks in our formulations indicates successful incorporation. Likewise, Udofot et al. (2015) [64] reported subtle FTIR spectral changes in pH-sensitive liposomes loaded with 5-FU, attributing these modifications to drug–lipid interactions that enhance the stability of the delivery system.

Taken together, these results are consistent with previous literature and demonstrate that both R-PE and 5-FU were effectively incorporated into the nanocarriers. Moreover, the observed spectral modifications suggest that the lipid bilayer not only acted as a physical barrier to immediate diffusion but also provided a stabilizing microenvironment that preserved the structural and functional integrity of the bioactive compounds.

3.5 Stability of nanoparticles in serum

Assessing colloidal stability in bovine serum is a critical parameter for inferring the in vivo behavior of nanostructured systems, as the presence of plasma proteins can induce adsorption on the particle surface, aggregation, or changes in surface charge [28]. In this study, liposomes and immunoliposomes containing or not 5-FU and R-PE were incubated in 10% bovine serum for up to 48 h, and the parameters of size, polydispersity index, and zeta potential were monitored.

In general, conventional liposomes exhibited greater colloidal stability, with slight variations in hydrodynamic size and PDI throughout the incubation period. This behavior suggests that the lipid composition employed provided an efficient steric barrier, minimizing nonspecific interactions with serum proteins. The presence of the PEG polymer is known to reduce protein corona formation and confer greater stability in biological media [69,70].

In immunoliposomes, a tendency for size and PDI to increase after 24–48 h of incubation was observed, suggesting possible adsorption of serum proteins and/or reorganization of antibody chains on the surface. This effect is consistent with the literature describing immunoliposomes as more susceptible to interactions with plasma proteins due to the presence of exposed protein domains [71].

The incorporation of 5-FU and R-PE did not promote instability, although small changes in zeta potential were recorded. The shift in zeta potential to less negative values after incubation indicates partial neutralization of surface charges by the serum components, a typical phenomenon in physiological environments. This change, however, did not significantly compromise the physicochemical stability of the formulations, as PDI values remained within the acceptable range (<0.3 for monodisperse systems) [72].

Therefore, the results demonstrate that the developed formulation presents adequate stability under conditions that simulate the biological environment, an essential requirement for in vivo applications. The presence of PEG in the lipid composition and the control of the initial size are probably important factors in maintaining stability, even after 48 h of exposure to bovine serum.

3.6 In vitro release

The release profiles of 5-FU and R-PE were evaluated using the Korsmeyer–Peppas model (Table 5).

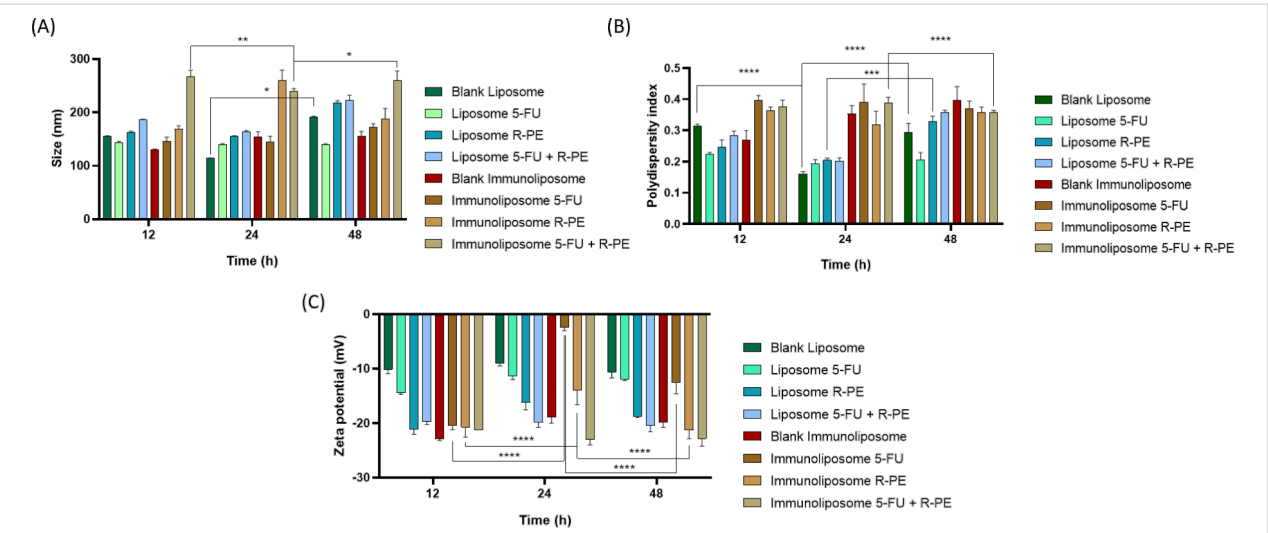

Figure 6: Physicochemical parameters of liposome and immunoliposome formulations during stability in serum study at 4 °C for 48 h. (A) Particle size, (B) PDI, and (C) zeta potential (Two-way-ANOVA with Tukey's test ****$p < 0.001$).

Table 5: Kinetic parameters obtained from the application of the Korsmeyer–Peppas model to the release profiles of 5-FU and R-PE. The table presents the determination coefficient (R^2), root mean square error (RMSE), release rate constant (k), and release exponent (n) values corresponding to the solution, liposome, and immunoliposome formulations.

	5-FU			R-PE		
	Solution	Liposome	Immunoliposome	Solution	Liposome	Immunoliposome
R^2	0.994	0.984	0.926	0.986	0.997	0.991
RMSE	0.281	0.459	0.839	6.134	1.714	4.661
k	9.238	9.669	7.880	117.072	93.085	106.271
n	0.040	0	0	0.072	0.012	0.082

For 5-FU, the R^2 values ranged from 0.926 to 0.994, with RMSE between 0.281 and 0.839, indicating excellent correlation between the experimental and calculated data. The kinetic constants (k) ranged from 7.880 to 9.669, while the release exponents (n) remained low (0.00 to 0.04).

Similarly, for R-PE, high R^2 values (0.986–0.997) and low RMSE values (1.714–6.134) were observed, with k ranging from 93.085 to 117.072 and n between 0.012 and 0.082.

According to Kozik et al. (2023), $n \leq 0.43$ values are characteristic of a Fickian release mechanism, in which diffusion is the main process responsible for the release of the active compound through the liposomal matrix. Thus, the obtained low n values indicate that both 5-FU and R-PE follow a predominantly diffusional release process, consistent with the behavior described for liposomal systems [23].

In addition, as reported by de Jesús Martín-Camacho et al. (2023), the parameter k represents the release constant and reflects the rate at which the compound is released from the system. Higher k values correspond to a faster release, whereas lower values indicate a more controlled profile. Therefore, the formulations containing R-PE, which showed higher k values (93–117), exhibited a more pronounced release rate compared with the 5-FU formulations ($k \approx 7$–9), possibly due to the hydrophilic nature of R-PE and its lower interaction with the lipid matrix [23,73].

These results are consistent with the literature, demonstrating that the Korsmeyer–Peppas model adequately describes the release kinetics of the formulations, revealing a sustained and controlled release profile, mainly influenced by diffusion through the liposomal matrix [23,73].

3.6.1 In vitro release of 5-FU

The 5-FU solution showed substantially higher release percentages compared to the nanoformulations at all time points (0.5–24 h; $p < 0.0001$) as shown in Figure 2D. Between 0.5 h and the subsequent times (2–24 h), a significant increase was observed ($p < 0.0001$), whereas no differences were detected between 2, 4, 6, 8, and 24 h (ns), indicating a plateau after 2 h.

The release profile observed for the 5-FU solution evidenced rapid drug diffusion, reaching approximately 70% at 0.5 h and remaining stable around 80% up to 24 h. This behavior was expected, given the hydrophilic character and low molecular weight of 5-FU, which favors its immediate dissolution in an aqueous medium. Similar results were reported by Wang et al. (2022) [74], who highlighted the high release rate of free 5-FU compared to controlled-release systems.

Both 5-FU liposomes and immunoliposomes exhibited controlled and low release (≈15–22%), significantly lower than the solution at all times ($p < 0.0001$). Within each nanoformulation, liposomes remained stable over time (ns). In immunoliposomes, modest increases were observed from 2 to 8 h ($p < 0.05$) and from 2 to 24 h ($p < 0.05$); other comparisons were not significant. Both liposome and immunoliposome formulations demonstrated a significantly lower and sustained release (≈15–22%) throughout the 24 h period.

Direct comparison between liposomes and immunoliposomes was mostly not statistically different (0.5, 8, and 24 h). However, immunoliposomes showed slightly higher release at 2 h ($p < 0.001$), 4 h ($p < 0.01$), and 6 h ($p < 0.001$). In summary, the solution promoted rapid and high release, while the nanoformulations provided sustained and low release, with punctual differences in favor of immunoliposomes between 2–6 h and temporal stability in liposomes. This controlled profile is consistent with other studies that identified liposomal encapsulation as an efficient strategy to prolong 5-FU availability, reduce plasma peaks, and minimize adverse effects [75,76]. Li et al. (2024) [77] also demonstrated that lipid composition, particularly the presence of cholesterol, plays a critical role in decreasing bilayer permeability, thereby slowing drug diffusion [78].

Statistical analysis confirmed significant differences between the 5-FU solution and both liposomal formulations at all evaluated time points ($p < 0.0001$). These findings reinforce that the incorporation of 5-FU into lipid vesicles creates a physical barrier to immediate release, which can be clinically exploited for sustained-release regimens. In contrast, no statistically relevant differences were found between liposomes and immunoliposomes at most time points, suggesting that antibody conjugation to the surface did not significantly alter the in vitro release pattern. This result was also reported by Petrilli et al. (2017) [21], who observed similar release profiles between 5-FU liposomes and immunoliposomes, with more notable differences only in studies of cellular internalization and antitumor efficacy [79].

Although the in vitro release was not modified by the presence of antibodies, immunoliposomes have the recognized advantage of active targeting and enhanced cellular uptake. Previous studies with cetuximab-conjugated immunoliposomes, for example, showed a significant improvement in intracellular delivery of 5-FU and a consequent stronger cytotoxic effect in EGFR-positive tumor cells [21]. Similarly, Scavo et al. (2020) [79] demonstrated that immunoliposomes decorated with antibodies enhanced tumor delivery of 5-FU in sarcoma models, even without differences in in vitro release kinetics.

3.6.2 In vitro release of R-PE

The R-PE release profiles markedly differed among the three tested formulations (Figure 2E). The R-PE solution exhibited significantly higher release at all time points (1–72 h; $p < 0.0001$). A progressive increase was observed between 1 and 24 h ($p < 0.0001$), followed by a plateau from 24 to 72 h (ns). This behavior was expected because R-PE is a hydrophilic protein that rapidly diffuses in aqueous media without structural barriers. Similar findings have been reported for free phycocyanin, which undergoes fast degradation and diffusion compared to encapsulated systems [80].

In contrast, R-PE liposomes displayed a slower and more sustained release, reaching a maximum of ≈80% at 72 h. Significant release was observed only up to 6 h ($p < 0.0001$), after which the profile stabilized and reached a plateau until 72 h. This stable behavior suggests that the lipid bilayer acts as a diffusion barrier for the protein, a phenomenon also reported in liposomal systems containing phycocyanin, where cholesterol content and membrane organization reduced permeability and prolonged pigment availability [81,82].

The R-PE immunoliposome showed an intermediate profile, with release significantly higher than that of liposomes at all time points ($p < 0.0001$), but still lower than that of the solution ($p < 0.0001$). A gradual and continuous increase was observed from 1 to 48 h ($p < 0.0001$), followed by a plateau between 48 and 72 h (ns). These results indicate that antibody conjugation to the vesicle surface may have partially altered the bilayer organization, allowing for slightly greater diffusion. Similar patterns have been described for functionalized immunoliposomes, where surface biomolecules influence stability and release kinetics [83].

The sustained and gradual release observed for both liposomes and immunoliposomes is consistent with previous findings on nanoencapsulated microalgae proteins. Pereira Martins et al. (2023) [15] demonstrated that encapsulation of R-PE in polymeric nanoparticles drastically reduced its release rate compared to that of the free protein, extending its stability in aqueous medium. Similarly, Frota Reis et al. (2025) [24] showed that polymer composition plays a critical role in modulating R-PE release kinetics, with less permeable formulations producing more sustained profiles. Although the systems described in these studies are polymeric, while the present work focuses on liposomal formulations, the results converge in highlighting nanoencapsulation as an effective physical barrier against immediate protein diffusion.

Furthermore, Kopp et al. (2017) [84] demonstrated that the mere presence of free R-PE does not ensure biological efficacy, as the protein undergoes rapid intracellular degradation following internalization. Thus, although the present results indicate that antibody conjugation does not markedly alter in vitro release, immunoliposomes may represent a future clinical advantage by combining a sustained-release profile with active targeting and enhanced cellular uptake. Recent reviews have also emphasized that R-PE bioconjugates exhibit superior stability and more robust functional properties compared to that of the free protein [85].

The results show that the free solution promotes rapid and high release, liposomes provide sustained and stable release, and immunoliposomes maintain this sustained profile but with a slightly higher release than that of liposomes. These findings, in agreement with the literature, reinforce the importance of nanoencapsulation strategies to enhance the stability and modulate the release kinetics of R-PE, while also highlighting the potential of immunoliposomes for therapeutic and bioimaging applications.

3.7 Phototoxicity and cytotoxicity

The cytotoxic effect of the selected liposomal formulation with the lipid HSPC 50, with R-PE and 5-FU, as well as the HSPC IM-07 immunoliposome with R-PE and 5-FU were tested by evaluating the inhibition of cell growth in the CRC HCT-116

cell line. Figure 7 and Table 6 show the results in the absence and presence of light irradiation.

It was found that the toxicity of 5-FU is similar across all groups, being slightly more toxic in the liposome formulation with 5-FU, reaching the IC50 at a concentration 0.79 times lower than that in solution. The opposite occurred in the formulation with liposomes containing 5-FU and R-PE, since IC_{50} was reached at a concentration 1.4 times higher than the solution with the free drug. Therefore, R-PE may be influencing the release of 5-FU into the intracellular environment. It is noteworthy that the lack of difference in cytotoxicity between the groups with 5-FU in studies on HCT-116 cells may be due to the development of resistance in these cells. Overexpression of the anti-apoptotic tumor protein, translationally controlled by this factor, has already been observed in HCT-116 cells during combined therapy based on 5-FU [86].

The immunoliposomal formulation containing only 5-FU showed an IC_{50} value of 44.44 µM for cytotoxicity, the highest among all formulations analyzed. This result contrasts with that observed for the liposome with 5-FU, whose IC_{50} was 5.47 µM, indicating that, without irradiation, the presence of targeting antibodies did not provide an immediate cytotoxic advantage. However, this difference may be associated with the time required for receptor-mediated internalization, as well as with the more stable nature of the immunoliposome structure, characteristics previously associated with systems functionalized with

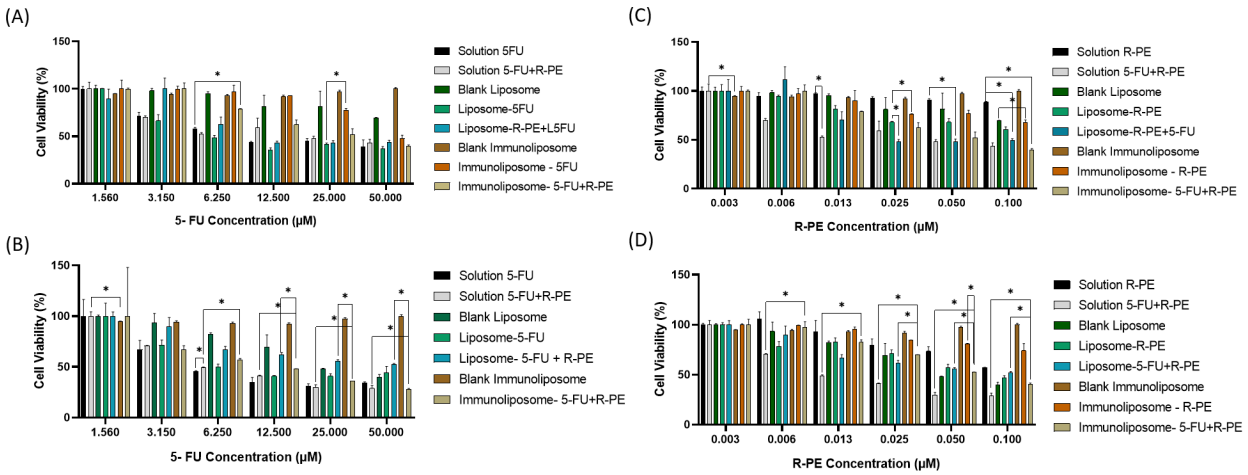

Figure 7: Cellular viability of the formulations in the HCT-116 cell line. (A) Cytotoxicity at different 5-FU concentrations. (B) Phototoxicity at different 5-FU concentrations. (C) Cytotoxicity at different R-PE concentrations. (D) Phototoxicity at different R-PE concentrations.

Table 6: IC_{50} in the cytotoxicity and phototoxicity evaluations of the formulations and the compounds 5-FU and R-PE evaluated in the HCT-116 cell line, with the respective confidence intervals.

Group	Cytotoxicity		Phototoxicity	
	IC_{50} (µM)	Confidence interval (µM)	IC_{50} (µM)	Confidence interval (µM)
Solution 5-FU	6.914	5.537 to 8.609	–	–
Solution R-PE	0.424	0.220 to 1.512	0.055	0.037 to 0.098
Solution 5-FU/R-PE (IC_{50} 5-FU)	6.812	5.592 to 8.263	3.659	2.478 to 4.969
Solution 5-FU/R-PE (IC_{50} R-PE)	0.0131	0.011 to 0.016	0.007	0.005 to 0.010
Liposome 5-FU	5.479	4.483 to 6.646	–	–
Liposome R-PE	0.331	0.181 to 1.086	0.069	0.048 to 0.121
Liposome 5-FU/R-PE (IC_{50} 5-FU)	10.010	8.162 to 12.280	–	–
Liposome 5-FU/R-PE (IC_{50} R-PE)	0.020	0.016 to 0.025	0.017	0.013 to 0.024
Immunoliposome 5-FU	44.44	32.77 to 73.10	–	–
Immunoliposome R-PE	1.307	1.252 to 1.404	1.390	1.336 to 1.480
Immunoliposome 5-FU/R-PE (IC_{50} 5-FU)	27.63	20.10 to 41.78	–	–
Immunoliposome 5-FU/R-PE (IC_{50} R-PE)	0.07842	0.05269 to 0.1463	0.06562	0.05478 to 0.08122

anti-EGFR antibodies in HCT-116 cells. The high expression of EGFR in this cell line, in fact, is one of the main factors that favor the selective internalization of immunoliposomes, although this process may not be immediate, with time being an important interfering factor [87].

The IC_{50} value obtained for the liposome containing 5-FU (5.5 μM) is within the range observed by other authors for modified liposomal formulations in HCT-116 cells [88]. In contrast, the immunoliposome presented an IC_{50} of 44 μM in the absence of light. This result is not necessarily indicative of worse intrinsic performance, as it may reflect slower internalization kinetics (receptor-mediated) or greater stability/delay in intracellular drug release, as reported by Moreira et al. (2023) [27] and de Sousa et al. (2024) [89]. Previous studies show that immunoliposomes may exhibit less immediate cytotoxicity in vitro if endosome/lysosome-dependent release is slow. In vivo, however, this greater stability may translate into better tumor delivery and lower systemic toxicity [90].

For R-PE, the cytotoxic effect was observed in the presence of 5-FU and was also slightly greater when the molecules were in solution. In the groups with only R-PE, IC_{50} values were not reached for the concentrations tested herein. This corroborates the findings of Sousa et al. (2024), as the IC_{50} for R-PE was found at a concentration of 500 μg/mL [89].

For phototoxicity experiments, a reduction in IC_{50} was found for all groups tested. The R-PE solution revealed a 7.7-fold reduction in IC_{50} upon light irradiation, whereas for R-PE liposomes the reduction was near 4.8 fold. When R-PE was co-administered with 5-FU, the solution provided a higher reduction in IC_{50} compared to that of the liposomes. Previously, it was also observed that the concentration of the photosensitizer also interferes with the cytotoxic effect on the cell, as at the highest concentration the liposome and the R-PE solution (0.1 μM) presented the lowest rate of viable cells. This situation was also observed when comparing phthalocyanine treatments in HCT-116 cells with or without PDT. In this study, the lowest dosage of phthalocyanine to reach the IC_{50} was 0.5 μM, indicating, as in cytotoxicity assays, that R-PE needs to be in a higher concentration, as it is a molecule with hydrophilic properties that will require higher concentrations to reach the IC_{50} value [91].

When we observed the immunoliposomes effect on phototoxicity, the 5-FU immunoliposome in association with R-PE showed a marked reduction in IC_{50}, reaching 0.065 μM compared to 0.078 μM for cytotoxicity. Light, in this case, acts as an activating factor, intensifying the action of R-PE and potentiating the cytotoxic effect of encapsulated 5-FU.

The most relevant benefit of the developed system lies in the phototoxic condition (PDT + 5-FU), with an IC_{50} of 0.065 μM for the immunoliposome + 5-FU/R-PE, demonstrating remarkable efficacy and synergism between PDT and active drug release. This result aligns with recent literature showing that encapsulating photosensitizers and combining them with chemotherapeutics in functionalized nanoformulations increases phototherapeutic efficacy and may reduce effective doses [92,93].

This pattern corroborates the data of Chiu et al. (2005) [94] and Song et al. (2020) [95], who reported a significant increase in the sensitivity of HCT-116 cells after exposure to compounds associated with photodynamic stimuli [94]. Furthermore, Ghaddar et al. (2024) [96] reinforce that the combination of localized drug release and induced production of reactive oxygen species (ROS) represents one of the main mechanisms for increasing therapeutic efficacy in light-activation-dependent therapies [96]. Yalçın et al. (2020), in turn, highlights that the encapsulation of photosensitizers in functionalized nanosystems increases the specificity of the therapeutic action and reduces damage to healthy tissues, a scenario consistent with the results obtained for the immunoliposome functionalized with R-PE [97].

The comparison between the formulations with R-PE reinforces this behavior. In the cytotoxicity analysis without light irradiation, both the liposome with R-PE and the immunoliposome with R-PE did not reach the IC_{50} value at the concentrations tested, which was expected for a photosensitizer whose activity depends on light activation. However, after irradiation, the liposome with R-PE reached an IC_{50} of 0.069 μM, while the immunoliposome containing R-PE and 5-FU presented an IC_{50} of 0.065 μM, a value almost twice as low. This significant gain can be attributed to the greater internalization promoted by the functionalization of the system and to the synergistic action between R-PE and 5-FU after activation. This behavior is consistent with the findings of Deng et al. (2023) [98], who demonstrated greater tumor accumulation and photodynamic efficacy of nanoparticles containing photosensitizers in HCT-116 [98]. Similar results were reported by Soriano et al. (2013), who observed increased phototoxicity in liposomal formulations functionalized with m-THPC in colorectal cancer cells [99]. Yalçın et al. (2020) [97] also highlighted that functionalized nanosystems promoted greater production of reactive species and lower toxicity in healthy tissues [97].

Encapsulation of drugs in liposomes and immunoliposomes helps reduce free drug exposure to healthy tissues, increases tumor accumulation (EPR effect) and promotes receptor-mediated internalization, thus lowering the required systemic dose.

Moreover, the combination of locally activatable PDT (R-PE) and 5-FU allows more precise tumor targeting via localized irradiation, minimizing toxicity to adjacent tissues [100,101]. Therefore, the data obtained indicate that, although the immunoliposomal formulation containing only 5-FU did not outperform the nonfunctionalized liposome in terms of cytotoxicity, the association with R-PE and the use of light resulted in significantly superior performance. This improvement is directly related to the active targeting capacity of the system, the use of an effective photosensitizer, and the spatiotemporal control provided by light activation – central elements in therapeutic strategies based on multifunctional nanosystems.

Upon light activation, R-PE generates ROS, inducing oxidative damage to lipids, proteins, and DNA and triggering cell death primarily through the intrinsic (mitochondrial) apoptosis pathway and/or necrosis, depending on the ROS load. Recent studies indicate that PDT may also activate autophagy or ferroptosis in specific contexts [102]. In parallel, 5-FU acts as an antimetabolite, inhibiting thymidylate synthase and incorporating into RNA/DNA, triggering replication stress and pro-apoptotic signaling [103]. The combination of both drugs with the targeting agent cetuximab likely induces cell death through the synergy of these mechanisms, with immediate ROS-driven damage accelerating apoptosis and intracellularly released 5-FU exacerbating replicative stress [104]. This dual mechanism can explain the markedly lower IC_{50} observed under phototoxic conditions.

3.8 Competitive EGFR-binding of anti-EGFR immunoliposome and EGF in HCT-116 cells using flow cytometry

The competitive binding of HSPC IM 07 and EGF to EGFR was evaluated in HCT-116 cells using flow cytometry. Treatment with Alexa Fluor™ 488-labeled EGF resulted in approximately 65% of the cell population being positive for EGF binding, indicating robust EGFR expression on the cell surface. In contrast, co-treatment with the anti-EGFR antibody cetuximab led to a marked reduction in EGF-positive cells, with binding levels decreasing to approximately 1% ($p < 0.0001$ vs EGF group; demonstrating effective competition for EGFR binding sites (Figure 8F). Similarly, pre-incubation with anti-EGFR immunoliposomes followed by EGF exposure significantly reduced the proportion of EGF-positive cells from 65% to 55% ($p < 0.001$ vs EGF group), showing that the immunoliposome also competes with EGF for EGFR binding in HCT-116 cells (Figure 8F).

The comparatively lower inhibition by HSPC IM 07 may be attributable to steric hindrance related to the spatial arrangement and density of antibodies or PEG chains on the liposome surface [105,106]. Additionally, variations in internalization pathways including endocytosis, phagocytosis, and macropinocytosis may influence nanoparticle entry into cancer cells, sometimes independently of receptor-mediated pathways [107]. A recent study has shown that anti-EGFR immunoliposomes are internalized via multiple mechanisms, suggesting that direct EGFR competition may not be their exclusive cellular entry route [108]. These findings align with recent literature advocating the potential of immunoliposomes for nanoparticle-mediated drug delivery.

3.9 Cellular uptake

The evaluation of the internalization of the R-PE liposome and R-PE immunoliposome formulations, performed by confocal analysis, showed differences over the incubation time. For this, R-PE was used as a fluorescent marker.

In the first time analyzed, 3 h (Figure 8A and B), a similar uptake was observed for both formulations, corroborating the study by Garanina et al. (2024), who reported the same initial peak of internalization, relating this to the endocytosis pathways [109]. According to de Souza et al. 2024, the increase in cellular uptake promoted by cetuximab-functionalized immunoliposomes occurs in a time-dependent manner, being more evident in longer incubation periods. At shorter times, such as up to 3 h, the receptor-mediated internalization process is still ongoing, which may result in confocal microscopy images that do not show significant differences between conventional liposomes and immunoliposomes. Furthermore, the passive internalization of conventional liposomes contributes to this similar initial uptake, masking possible differences in specific EGFR-mediated internalization [52].

At the end of 24 h, the internalization levels increased for both the liposome and the immunoliposome. At this stage, Figure 8C and Figure 8D show an increase for the fluorescence of the immunoliposome, which is higher than that of the liposome, which may indicate that the cellular uptake is dependent on the presence of cetuximab and the incubation time. In the study carried out by Alshaer et al. (2025), better internalization was observed in shorter times, followed by a decrease and subsequent increase, and showing that this is likely due to a common regulation mechanism of the cell, where the cell needs an intermediate time to restart internalization [110]. In studies with EGFR-positive cells (A431 cell line), confocal microscopy revealed higher fluorescence intensities after 24 h of treatment with immunoliposomes, indicating a more efficient cellular uptake of these targeted nanoparticles compared to nonfunctionalized liposomes, corroborating the present study which showed a greater internalization within 24 h in immunoliposomes in EGFR-positive HCT116 cells [19].

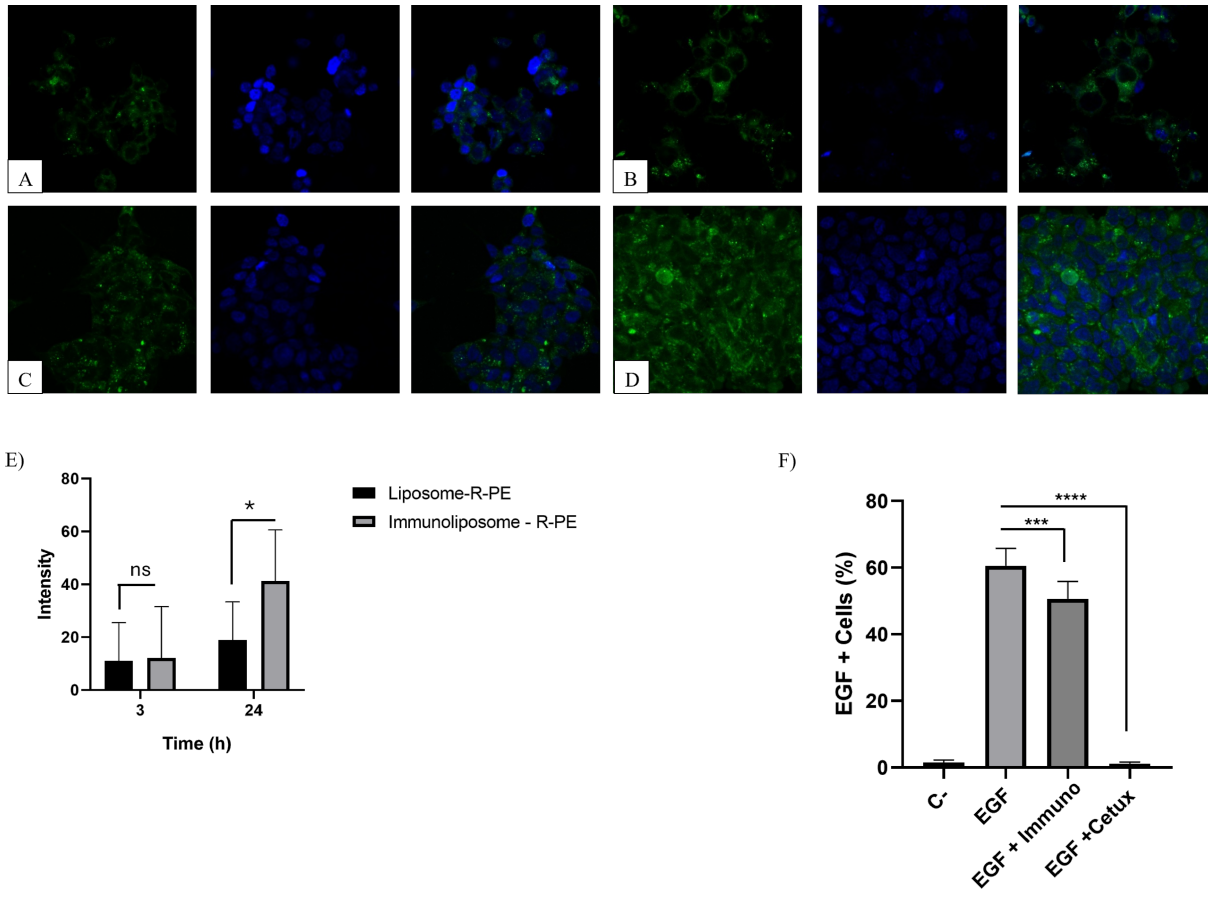

Figure 8: Results of the confocal studies after incubation for 3 h (A and B), and 24 h (C and D) for R-PE liposomes and R-PE immunoliposomes, respectively. The nuclei were stained using DAPI and imaged using a 40× magnification objective. The wavelengths used were 488 nm for excitation and 575–585 nm for emission for R-PE, and 405 nm with emission between 413–472 nm for DAPI. (E) Quantification of R-PE fluorescence intensity after incubation of liposomes and immunoliposomes in HCT-116 cells for 3 and 24 h. (F) Competitive inhibition of EGF binding to EGFR by anti-EGFR immunoliposomes in HCT-116 Cells. C_: Negative control, cells treated only with buffer. EGF: Cells treated only with Alexa Fluor™ 488 EGF. EGF+Immuno: Cells treated with HSPC IM 07 and EGF EGF+Cetux: Cells treated with cetuximab and EGF. The values represent the mean ± SD of two independent experiments. Statistical significance was determined using one-way ANOVA followed by Tukey's multiple comparisons test (ns, not statistically significant; ***p < 0,001, ****p < 0,0001 compared to the EGF treatment group).

Therefore, internalization data showed that the cetuximab-functionalized immunoliposome presented a higher intracellular R-PE signal after 24 h in HCT-116 cells, while at short time points (3 h), the uptake was similar between liposomes and immunoliposomes. This indicates a typical pattern of receptor-mediated internalization: an initial uptake by passive internalization/nonspecific endocytosis, followed by a receptor-dependent increase over time, consistent with several studies describing EGFR-mediated internalization and time-dependent accumulation in EGFR-positive cells [109,110].

The relative increase in fluorescence in immunoliposomes at 24 h corroborates that cetuximab conjugation favors EGFR-dependent recognition and internalization – this is essential for the theranostic strategy since it increases the probability of intracellular delivery of the photosensitizer R-PE and 5-FU to the target site, improving tumor specificity and reducing systemic exposure [111].

Regarding the relevance for the developed system, the observed kinetics suggest that the maximum therapeutic effect (especially the photodynamic effect mediated by R-PE) should be planned considering the time window in which the internalization of immunoliposomes is maximized, a common procedure in PDT studies combined with targeting [101].

The quantitative fluorescence analysis (Figure 8E) corroborated the results qualitatively observed in the confocal images. After 3 h of incubation, no significant differences were found between liposomes and immunoliposomes ($p > 0.05$), indicating similar initial internalization for both formulations. However, after 24 h, a significant increase in fluorescence intensity

was observed for R-PE immunoliposomes compared to that of liposomes at the same time point ($p < 0.05$).

These results reinforce that the cellular internalization of immunoliposomes occurs in a time- and antibody-dependent manner, leading to a greater intracellular accumulation of R-PE after 24 h. The alignment between the qualitative and quantitative results demonstrated that cetuximab functionalization enhanced EGFR-mediated recognition and facilitated a more efficient internalization of immunoliposomes than conventional liposomes.

Conclusion

All the developed liposomes exhibited nanoscale vesicle sizes (above 200 nm) and low polydispersity indices, indicating good homogeneity. The liposomal formulation containing HSPC 50 was selected due to its higher encapsulation efficiency of 5-FU and R-PE, as well as a lower PDI, reflecting greater colloidal stability. These formulations also demonstrated spherical morphology and adequate physicochemical stability. Based on this, immunoliposomes were developed, maintaining nanoscale characteristics and satisfactory polydispersity indices. Among them, the HSPC IM-07 formulation stood out for presenting the highest conjugation efficiency, and was therefore chosen for further studies. In vitro cytotoxicity assays using the HCT-116 colorectal cancer cell line, both the HSPC 50 liposomal formulation and the HSPC IM immunoliposomal formulation containing both molecules showed efficacy comparable to that of free-form drugs. In the presence of light, a significant potentiation of the cytotoxic effect of R-PE was observed, especially when associated with 5-FU in liposomes and immunoliposomes, evidencing a synergistic effect and greater therapeutic efficacy. Thus, the HSPC IM formulation, co-encapsulating R-PE and 5-FU, emerges as a promising alternative. The results obtained through confocal microscopy reinforce the potential of functionalized immunoliposomes for efficient and sustained cellular internalization, suggesting the involvement of a time-dependent regulatory mechanism that favors recycling and intracellular retention of the nanosystems. This behavior is particularly advantageous for applications in phototheranostic therapies, where system selectivity and stability are key determinants of therapeutic success. Moreover, in vitro release assays revealed distinct profiles for 5-FU and R-PE, with liposomes and immunoliposomes promoting sustained and controlled release compared to solutions, thereby reducing premature diffusion and supporting prolonged therapeutic availability. FTIR analyses confirmed the successful incorporation of both molecules into the lipid matrix, as well as intermolecular interactions that likely contributed to their stabilization within the nanosystem. In conclusion, this study highlights the potential of cetuximab-functionalized liposomal systems co-encapsulating R-PE and 5-FU for colorectal cancer therapy, combining selective targeting, photodynamic action, and chemotherapy. These findings advance the field of multifunctional nanocarriers for future clinical applicability of such nanosystems.

Acknowledgements

The authors thank the Multi-User Facility of Drug Research and Development Center of Federal University of Ceará. We also acknowledge Algae Producers Association of Flecheiras and Guajiru cities for algae supply. We also thank João Isaac Silva Miranda lab and Federal Institute of Education, Science and Technology, Ceará, Brazil for light application instruments. The Graphical Abstract was created in the Mind the Graph Platform, available at https://www.mindthegraph.com. It is distributed under the terms of the Attribution-ShareAlike 4.0 International Deed (https://creativecommons.org/licenses/by-sa/4.0/). This content is not subject to CC BY 4.0.

Funding

The authors would like to thank the funding agency FUNCAP (grant MLC-0191-00296.01.00/22 and PS1-0186-00043.01.00/21) and Conselho Nacional de Desenvolvimento Científico e Tecnológico (CNPq) Process No. 440639/2022-0/ 2022-9. Also, FUNCAP, CAPES and FAPESP (process no. 2023/14018-0) for scholarships. The authors would like to thank the Central Analítica-UFC (funded by Finep-CT-INFRA, CAPES-Pró-Equipamentos, and MCTI-CNPq-SisNano2.0).

Author Contributions

Raissa Rodrigues Camelo: investigation; writing – original draft. Vivianne Cortez Sombra Vandesmet: investigation; writing – original draft. Octavio Vital Baccallini: investigation. José de Brito Vieira Neto: investigation; writing – original draft. Thais da Silva Moreira: investigation; writing – original draft. Luzia Kalyne Almeida Moreira Leal: formal analysis. Claudia Pessoa: methodology. Daniel Giuliano Cerri: investigation; methodology; writing – original draft. Maria Vitória Lopes Badra Bentley: methodology; writing – review & editing. Josimar O. Eloy: methodology; writing – review & editing. Ivanildo José da Silva Júnior: methodology; writing – review & editing. Raquel Petrilli: conceptualization; funding acquisition; supervision; writing – review & editing.

ORCID® iDs

Claudia Pessoa - https://orcid.org/0000-0002-4344-4336
Daniel Giuliano Cerri - https://orcid.org/0009-0001-4898-5924
Raquel Petrilli - https://orcid.org/0000-0003-2305-8566

Data Availability Statement

Data generated and analyzed during this study is available from the corresponding author upon reasonable request.

References

1. WHO. Colorectal cancer – IARC 2024. International Agency for Research on Cancer, World Health Organization. 2024. https://www.iarc.who.int/cancer-type/colorectal-cancer/ (accessed Oct 16, 2025).
2. Aran, V.; Victorino, A. P.; Thuler, L. C.; Ferreira, C. G. *Clin. Colorectal Cancer* **2016,** *15,* 195–203. doi:10.1016/j.clcc.2016.02.008
3. Sartor, I. T. S.; Recamonde-Mendoza, M.; Ashton-Prolla, P. *PLoS One* **2019,** *14,* e0210762. doi:10.1371/journal.pone.0210762
4. Almeida de Sousa, Â. M.; Pienna Soares, C.; Chorilli, M., Eds. *Cancer Nanotechnology;* Springer International Publishing: Cham, Switzerland, 2023. doi:10.1007/978-3-031-17831-3
5. Chen, L.; Tian, B.; Liu, W.; Liang, H.; You, Y.; Liu, W. *Front. Oncol.* **2022,** *12,* 855674. doi:10.3389/fonc.2022.855674
6. Kalyane, D.; Raval, N.; Maheshwari, R.; Tambe, V.; Kalia, K.; Tekade, R. K. *Mater. Sci. Eng.: C* **2019,** *98,* 1252–1276. doi:10.1016/j.msec.2019.01.066
7. Thapa Magar, K.; Boafo, G. F.; Li, X.; Chen, Z.; He, W. *Chin. Chem. Lett.* **2022,** *33,* 587–596. doi:10.1016/j.cclet.2021.08.020
8. Liu, Y.; Li, X.; Pen, R.; Zuo, W.; Chen, Y.; Sun, X.; Gou, J.; Guo, Q.; Wen, M.; Li, W.; Yu, S.; Liu, H.; Huang, M. *BioMed. Eng. OnLine* **2022,** *21,* 53. doi:10.1186/s12938-022-01012-8
9. Naishima, N. L.; Faizan, S.; Raju, R. M.; Sruthi, A. S. V. L.; NG, V.; Sharma, G. K.; Vasanth, K. S.; Shivaraju, V. K.; Ramu, R.; Kumar, B. R. P. *J. Mol. Struct.* **2023,** *1277,* 134848. doi:10.1016/j.molstruc.2022.134848
10. Doleschal, B.; Petzer, A.; Rumpold, H. *Front. Oncol.* **2022,** *12,* 1048166. doi:10.3389/fonc.2022.1048166
11. Bofinger, R.; Weitsman, G.; Evans, R.; Glaser, M.; Sander, K.; Allan, H.; Hochhauser, D.; Kalber, T. L.; Årstad, E.; Hailes, H. C.; Ng, T.; Tabor, A. B. *Nanoscale* **2021,** *13,* 18520–18535. doi:10.1039/d1nr02770k
12. Tan, H.; Gao, S.; Zhuang, Y.; Dong, Y.; Guan, W.; Zhang, K.; Xu, J.; Cui, J. *Mar. Drugs* **2016,** *14,* 166. doi:10.3390/md14090166
13. Senthilkumar, N.; Thangam, R.; Murugan, P.; Suresh, V.; Kurinjimalar, C.; Kavitha, G.; Sivasubramanian, S.; Rengasamy, R. *J. Food Biochem.* **2018,** *42,* e12695. doi:10.1111/jfbc.12695
14. Kawczyk-Krupka, A.; Bartusik-Aebisher, D.; Latos, W.; Cieślar, G.; Sieroń, K.; Kwiatek, S.; Oleś, P.; Kwiatek, B.; Aebisher, D.; Krupka, M.; Wiench, R.; Skaba, D.; Olek, M.; Kasperski, J.; Czuba, Z.; Sieroń, A. *Photochem. Photobiol.* **2020,** *96,* 539–549. doi:10.1111/php.13243
15. Pereira Martins, J. R.; Linhares de Aguiar, A. L.; Barros Nogueira, K. A.; Uchôa Bastos Filho, A. J.; da Silva Moreira, T.; Lima Holanda Araújo, M.; Pessoa, C.; Eloy, J. O.; da Silva Junior, I. J.; Petrilli, R. *J. Microencapsulation* **2023,** *40,* 37–52. doi:10.1080/02652048.2023.2168081
16. Wu, R. W. K.; Yow, C. M. N.; Law, E.; Chu, E. S. M.; Huang, Z. *Photodiagn. Photodyn. Ther.* **2020,** *31,* 101945. doi:10.1016/j.pdpdt.2020.101945
17. Corte-Real, M.; Veiga, F.; Paiva-Santos, A. C.; Pires, P. C. *Pharmaceutics* **2024,** *16,* 1200. doi:10.3390/pharmaceutics16091200
18. Bangham, A. D.; Standish, M. M.; Watkins, J. C. *J. Mol. Biol.* **1965,** *13,* 238–252. doi:10.1016/s0022-2836(65)80093-6
19. Petrilli, R.; Eloy, J. O.; Saggioro, F. P.; Chesca, D. L.; de Souza, M. C.; Dias, M. V. S.; daSilva, L. L. P.; Lee, R. J.; Lopez, R. F. V. *J. Controlled Release* **2018,** *283,* 151–162. doi:10.1016/j.jconrel.2018.05.038
20. Eloy, J. O.; Ruiz, A.; de Lima, F. T.; Petrilli, R.; Raspantini, G.; Nogueira, K. A. B.; Santos, E.; de Oliveira, C. S.; Borges, J. C.; Marchetti, J. M.; Al-Jamal, W. T.; Chorilli, M. *Colloids Surf., B* **2020,** *194,* 111185. doi:10.1016/j.colsurfb.2020.111185
21. Petrilli, R.; Eloy, J.; Lopez, R.; Lee, R. *Anti-Cancer Agents Med. Chem.* **2017,** *17,* 301–308. doi:10.2174/1871520616666160526110913
22. ICH Harmonised Guideline. Validation of Analytical Procedures Q2(R2), 2023, pp 1–36.. https://database.ich.org/sites/default/files/ICH_Q2-R2_Document_Step2_Guideline_2022_0324.pdf (accessed Oct 16, 2025).
23. Kozik, V.; Pentak, D.; Paździor, M.; Zięba, A.; Bąk, A. *Int. J. Mol. Sci.* **2023,** *24,* 11686. doi:10.3390/ijms241411686
24. Frota Reis, A. V.; de Sousa, A. C. C.; de Freitas, J. V. B.; Arruda, B. R.; Ferreira Lima, R. M.; de Araujo Nobre, A. R.; Holanda Araújo, M. L.; da Silva Júnior, I. J.; Eloy, J. O.; Petrilli, R. *Int. J. Pharm.* **2025,** *682,* 125966. doi:10.1016/j.ijpharm.2025.125966
25. Bolean, M.; Borin, I. A.; Simão, A. M. S.; Bottini, M.; Bagatolli, L. A.; Hoylaerts, M. F.; Millán, J. L.; Ciancaglini, P. *Biochim. Biophys. Acta, Biomembr.* **2017,** *1859,* 1911–1920. doi:10.1016/j.bbamem.2017.05.010
26. Eaton, P.; West, P. *Atomic Force Microscopy;* Oxford University Press: Oxford, UK, 2010. doi:10.1093/acprof:oso/9780199570454.001.0001
27. da Silva Moreira, T.; Silva, A. D. O.; Vasconcelos, B. R. F.; da Silva Santos, E.; de Sousa, A. C. C.; de Freitas, J. V. B.; de Oliveira, Y. S.; Vidal, L. M. T.; de Oliveira Silva Ribeiro, F.; de Araújo, A. R.; de Brito Vieira Neto, J.; do Ó Pessoa, C.; Petrilli, R.; Eloy, J. O. *Pharmaceutics* **2023,** *15,* 915. doi:10.3390/pharmaceutics15030915
28. de Queiróz Carvalho Silva, L.; Raspantini, G. L.; Abriata, J. P.; Luiz, M. T.; de Sousa, A. C. C.; da Silva Moreira, T.; Magalhães, E. P.; de Menezes, R. R. P. P. B.; Petrillic, R.; Marchetti, J. M.; Eloy, J. O. *J. Pharm. Sci.* **2025,** *114,* 103766. doi:10.1016/j.xphs.2025.103766
29. Mosmann, T. *J. Immunol. Methods* **1983,** *65,* 55–63. doi:10.1016/0022-1759(83)90303-4
30. Comez, D.; Glenn, J.; Anbuhl, S. M.; Heukers, R.; Smit, M. J.; Hill, S. J.; Kilpatrick, L. E. *Front. Immunol.* **2022,** *13,* 1006718. doi:10.3389/fimmu.2022.1006718
31. Abbasi, H.; Kouchak, M.; Mirveis, Z.; Hajipour, F.; Khodarahmi, M.; Rahbar, N.; Handali, S. *Adv. Pharm. Bull.* **2023,** *13,* 7–23. doi:10.34172/apb.2023.009
32. Hu, L.; Huang, B.; Zuo, M.-m.; Guo, R.-y.; Wei, H. *Acta Pharmacol. Sin.* **2008,** *29,* 1539–1546. doi:10.1111/j.1745-7254.2008.00886.x
33. Makyła-Juzak, K.; Chachaj-Brekiesz, A.; Dynarowicz-Latka, P.; Dąbczyński, P.; Zemla, J. *J. Membr. Biol.* **2018,** *251,* 641–651. doi:10.1007/s00232-018-0041-z
34. Crisóstomo, L. C. C. F.; Carvalho, G. S. G.; Leal, L. K. A. M.; de Araújo, T. G.; Nogueira, K. A. B.; da Silva, D. A.; de Oliveira Silva Ribeiro, F.; Petrilli, R.; Eloy, J. O. *AAPS PharmSciTech* **2022,** *23,* 212. doi:10.1208/s12249-022-02356-z
35. Aygun, A.; Torrey, K.; Kumar, A.; Stephenson, L. D. *Appl. Biochem. Biotechnol.* **2012,** *167,* 743–757. doi:10.1007/s12010-012-9724-6
36. Aghaei, H.; Solaimany Nazar, A. R.; Varshosaz, J. *Colloids Surf., A* **2021,** *614,* 126166. doi:10.1016/j.colsurfa.2021.126166

37. Chen, J.; Cheng, D.; Li, J.; Wang, Y.; Guo, J.-x.; Chen, Z.-p.; Cai, B.-c.; Yang, T. *Drug Dev. Ind. Pharm.* **2013,** *39,* 197–204. doi:10.3109/03639045.2012.668912
38. Chen, W.; Duša, F.; Witos, J.; Ruokonen, S.-K.; Wiedmer, S. K. *Sci. Rep.* **2018,** *8,* 14815. doi:10.1038/s41598-018-33107-5
39. Liang, B.; Shahbaz, M.; Wang, Y.; Gao, H.; Fang, R.; Niu, Z.; Liu, S.; Wang, B.; Sun, Q.; Niu, W.; Liu, E.; Wang, J.; Niu, J. *Clin. Cancer Res.* **2015,** *21,* 1183–1195. doi:10.1158/1078-0432.ccr-14-1194
40. Hou, L.; Sun, X.; Pan, L.; Gu, K. *J. Oleo Sci.* **2021,** *70,* 1295–1306. doi:10.5650/jos.ess21033
41. Bi, H.; Xue, J.; Jiang, H.; Gao, S.; Yang, D.; Fang, Y.; Shi, K. *Asian J. Pharm. Sci.* **2019,** *14,* 365–379. doi:10.1016/j.ajps.2018.07.006
42. Romero-Arrieta, M. R.; Uria-Canseco, E.; Perez-Casas, S. *Thermochim. Acta* **2020,** *687,* 178462. doi:10.1016/j.tca.2019.178462
43. Ulker, D.; Barut, I.; Şener, E.; Bütün, V. *Eur. Polym. J.* **2021,** *146,* 110270. doi:10.1016/j.eurpolymj.2021.110270
44. Oh, E.; Jackman, J. A.; Yorulmaz, S.; Zhdanov, V. P.; Lee, H.; Cho, N.-J. *Langmuir* **2015,** *31,* 771–781. doi:10.1021/la504267g
45. Paolino, D.; Accolla, M. L.; Cilurzo, F.; Cristiano, M. C.; Cosco, D.; Castelli, F.; Sarpietro, M. G.; Fresta, M.; Celia, C. *Colloids Surf., B* **2017,** *155,* 266–275. doi:10.1016/j.colsurfb.2017.04.018
46. van Rooij, T.; Luan, Y.; Renaud, G.; van der Steen, A. F. W.; Versluis, M.; de Jong, N.; Kooiman, K. *Ultrasound Med. Biol.* **2015,** *41,* 1432–1445. doi:10.1016/j.ultrasmedbio.2015.01.004
47. Jiang, H.; Zhang, H.; Yin, S.-J.; Lu, M.; Wang, X.; Yang, F.-Q. *Electrophoresis* **2021,** *42,* 1436–1449. doi:10.1002/elps.202000382
48. Chotphruethipong, L.; Battino, M.; Benjakul, S. *Food Chem.* **2020,** *328,* 127127. doi:10.1016/j.foodchem.2020.127127
49. Dymek, M.; Sikora, E. *Adv. Colloid Interface Sci.* **2022,** *309,* 102757. doi:10.1016/j.cis.2022.102757
50. Bozzuto, G.; Molinari, A. *Int. J. Nanomed.* **2015,** *10,* 975–999. doi:10.2147/ijn.s68861
51. Amador, G. J.; van Dijk, D.; Kieffer, R.; Aubin-Tam, M.-E.; Tam, D. *Proc. Natl. Acad. Sci. U. S. A.* **2021,** *118,* e2100156118. doi:10.1073/pnas.2100156118
52. Carolina Cruz de Sousa, A.; da Silva Santos, E.; da Silva Moreira, T.; Gabriela Araújo Mendes, M.; Rodrigues Arruda, B.; de Jesus Guimarães, C.; de Brito Vieira Neto, J.; de Oliveira, Y. S.; Ayala, A. P.; da Costa, M. D. R.; Sampaio, T. L.; Alves, A. P. N. N.; Pessoa, C.; Petrilli, R.; Eloy, J. O. *Int. J. Pharm.* **2024,** *661,* 124439. doi:10.1016/j.ijpharm.2024.124439
53. Danaei, M.; Dehghankhold, M.; Ataei, S.; Hasanzadeh Davarani, F.; Javanmard, R.; Dokhani, A.; Khorasani, S.; Mozafari, M. R. *Pharmaceutics* **2018,** *10,* 57. doi:10.3390/pharmaceutics10020057
54. Jain, S.; Kumar, N.; Tahir, M.; Garg, S. Nanoparticle synthesis, characterization and applications. *The Impact of Nanoparticles on Agriculture and Soil;* Academic Press: London, UK, 2023; pp 13–40. doi:10.1016/b978-0-323-91703-2.00007-5
55. Napolitano, S.; Martini, G.; Ciardiello, D.; Del Tufo, S.; Martinelli, E.; Troiani, T.; Ciardiello, F. *Lancet Gastroenterol. Hepatol.* **2024,** *9,* 664–676. doi:10.1016/s2468-1253(23)00479-x
56. Gregoriadis, G. *Trends Biotechnol.* **1995,** *13,* 527–537. doi:10.1016/s0167-7799(00)89017-4
57. Ruozi, B.; Belletti, D.; Tombesi, A.; Tosi, G.; Bondioli, L.; Forni, F.; Vandelli, M. A. *Int. J. Nanomed.* **2011,** *6,* 557–563. doi:10.2147/ijn.s14615
58. Liang, X.; Mao, G.; Ng, K. Y. S. *Colloids Surf., B* **2004,** *34,* 41–51. doi:10.1016/j.colsurfb.2003.10.017
59. Anabousi, S.; Laue, M.; Lehr, C.-M.; Bakowsky, U.; Ehrhardt, C. *Eur. J. Pharm. Biopharm.* **2005,** *60,* 295–303. doi:10.1016/j.ejpb.2004.12.009
60. Sitterberg, J.; Gaspar, M. M.; Ehrhardt, C.; Bakowsky, U. Atomic Force Microscopy for the Characterization of Proteoliposomes. *Methods in molecular biology;* Humana Press: Totowa, NJ, USA, 2010; Vol. 106, pp 351–361. doi:10.1007/978-1-60761-447-0_23
61. Dufrêne, Y. F.; Ando, T.; Garcia, R.; Alsteens, D.; Martinez-Martin, D.; Engel, A.; Gerber, C.; Müller, D. J. *Nat. Nanotechnol.* **2017,** *12,* 295–307. doi:10.1038/nnano.2017.45
62. Butt, H.-J.; Cappella, B.; Kappl, M. *Surf. Sci. Rep.* **2005,** *59,* 1–152. doi:10.1016/j.surfrep.2005.08.003
63. Salvati, A.; Pitek, A. S.; Monopoli, M. P.; Prapainop, K.; Bombelli, F. B.; Hristov, D. R.; Kelly, P. M.; Åberg, C.; Mahon, E.; Dawson, K. A. *Nat. Nanotechnol.* **2013,** *8,* 137–143. doi:10.1038/nnano.2012.237
64. Udofot, O.; Affram, K.; Israel, B.; Agyare, E. *Integr. Cancer Sci. Ther.* **2015,** *2,* 245–252. doi:10.15761/icst.1000150
65. Zare-Zardini, H.; Soltaninejad, H.; Ghorani-Azam, A.; Nafisi-Moghadam, R.; Haddadzadegan, N.; Ansari, M.; Saeed-Banadaki, S. H.; Sobhan, M. R.; Mozafari, S.; Zahedi, M. *Prog. Biomater.* **2022,** *11,* 311–320. doi:10.1007/s40204-022-00197-4
66. Ezekiel, C. I.; Bapolisi, A. M.; Walker, R. B.; Krause, R. W. M. *Pharmaceutics* **2021,** *13,* 821. doi:10.3390/pharmaceutics13060821
67. Zong, W.; Hu, Y.; Su, Y.; Luo, N.; Zhang, X.; Li, Q.; Han, X. *J. Microencapsulation* **2016,** *33,* 257–262. doi:10.3109/02652048.2016.1156176
68. Xu, Y.; Hou, Y.; Wang, Y.; Wang, Y.; Li, T.; Song, C.; Wei, N.; Wang, Q. *Ecotoxicol. Environ. Saf.* **2019,** *168,* 356–362. doi:10.1016/j.ecoenv.2018.10.102
69. Sainaga Jyothi, V. G. S.; Bulusu, R.; Venkata Krishna Rao, B.; Pranothi, M.; Banda, S.; Kumar Bolla, P.; Kommineni, N. *Int. J. Pharm.* **2022,** *624,* 122022. doi:10.1016/j.ijpharm.2022.122022
70. Caddeo, C.; Pucci, L.; Gabriele, M.; Carbone, C.; Fernàndez-Busquets, X.; Valenti, D.; Pons, R.; Vassallo, A.; Fadda, A. M.; Manconi, M. *Int. J. Pharm.* **2018,** *538,* 40–47. doi:10.1016/j.ijpharm.2017.12.047
71. Navarro-Marchal, S. A.; Martín-Contreras, M.; Castro-Santiago, D.; del Castillo-Santaella, T.; Graván, P.; Jódar-Reyes, A. B.; Marchal, J. A.; Peula-García, J. M. *Int. J. Mol. Sci.* **2023,** *24,* 16759. doi:10.3390/ijms242316759
72. Adler, A.; Inoue, Y.; Ekdahl, K. N.; Baba, T.; Ishihara, K.; Nilsson, B.; Teramura, Y. *J. Mater. Chem. B* **2022,** *10,* 2512–2522. doi:10.1039/d1tb01485d
73. Martín-Camacho, U. d. J.; Rodríguez-Barajas, N.; Sánchez-Burgos, J. A.; Pérez-Larios, A. *Int. J. Pharm.* **2023,** *640,* 123017. doi:10.1016/j.ijpharm.2023.123017
74. Wang, W.; Joyce, P.; Bremmell, K.; Milne, R.; Prestidge, C. A. *Pharmaceutics* **2022,** *14,* 221. doi:10.3390/pharmaceutics14020221
75. Ali, M. S.; Jha, S. K.; Gupta, G.; Alsayari, A.; Wahab, S.; Kesharwani, P. *J. Drug Delivery Sci. Technol.* **2024,** *96,* 105730. doi:10.1016/j.jddst.2024.105730
76. Alrbyawi, H. *Pharmaceutics* **2024,** *16,* 966. doi:10.3390/pharmaceutics16070966
77. Li, Y.; Sun, Q.; Hao, L.; Shan, H.; Jiang, Z.; Wang, Y.; Chen, Z.; Zhu, W.; Zhao, S. *Int. J. Nanomed.* **2024,** *19,* 7353–7365. doi:10.2147/ijn.s466221
78. Amărandi, R.-M.; Marin, L.; Drăgoi, B.; Neamțu, A. *Mol. Pharmaceutics* **2024,** *21,* 6137–6152. doi:10.1021/acs.molpharmaceut.4c00328

79. Scavo, M. P.; Cutrignelli, A.; Depalo, N.; Fanizza, E.; Laquintana, V.; Gasparini, G.; Giannelli, G.; Denora, N. *Pharmaceutics* **2020,** *12,* 650. doi:10.3390/pharmaceutics12070650
80. Li, Y.; Li, X.; Liang, Z.-P.; Chang, X.-Y.; Li, F.-T.; Wang, X.-Q.; Lian, X.-J. *Molecules* **2022,** *27,* 5854. doi:10.3390/molecules27185854
81. Anderson, M.; Omri, A. *Drug Delivery* **2004,** *11,* 33–39. doi:10.1080/10717540490265243
82. Manconia, M.; Pendás, J.; Ledón, N.; Moreira, T.; Sinico, C.; Saso, L.; Fadda, A. M. *J. Pharm. Pharmacol. (Oxford, U. K.)* **2009,** *61,* 423–430. doi:10.1211/jpp.61.04.0002
83. Nasr, G.; Greige-Gerges, H.; Elaissari, A.; Khreich, N. *Int. J. Pharm.* **2020,** *580,* 119198. doi:10.1016/j.ijpharm.2020.119198
84. Kopp, M.; Rotan, O.; Papadopoulos, C.; Schulze, N.; Meyer, H.; Epple, M. *PLoS One* **2017,** *12,* e0178260. doi:10.1371/journal.pone.0178260
85. Bekasova, O. *Int. J. Biol. Macromol.* **2024,** *255,* 128181. doi:10.1016/j.ijbiomac.2023.128181
86. Ugorji, O. L.; Umeh, O. N. C.; Agubata, C. O.; Adah, D.; Obitte, N. C.; Chukwu, A. *Heliyon* **2022,** *8,* e12369. doi:10.1016/j.heliyon.2022.e12369
87. Mahajan, U. M.; Li, Q.; Alnatsha, A.; Maas, J.; Orth, M.; Maier, S. H.; Peterhansl, J.; Regel, I.; Sendler, M.; Wagh, P. R.; Mishra, N.; Xue, Y.; Allawadhi, P.; Beyer, G.; Kühn, J.-P.; Marshall, T.; Appel, B.; Lämmerhirt, F.; Belka, C.; Müller, S.; Weiss, F.-U.; Lauber, K.; Lerch, M. M.; Mayerle, J. *Gastroenterology* **2021,** *161,* 996–1010.e1. doi:10.1053/j.gastro.2021.05.055
88. Rah, B.; Shafarin, J.; Karim, A.; Bajbouj, K.; Hamad, M.; Muhammad, J. S. *Cell Biochem. Biophys.* **2024,** *82,* 3763–3780. doi:10.1007/s12013-024-01463-x
89. de Sousa, A. C. S. P.; Martins, J. R. P.; Alves, A. A. A.; Sant'Anna Maranhão, S.; Pessoa, C.; Feitosa, F. X.; de Sant'Ana, H. B.; da Silva, I. J., Jr. *Algal Res.* **2024,** *80,* 103493. doi:10.1016/j.algal.2024.103493
90. Paramshetti, S.; Angolkar, M.; Talath, S.; Osmani, R. A. M.; Spandana, A.; Al Fatease, A.; Hani, U.; Ramesh, K. V. R. N. S.; Singh, E. *Life Sci.* **2024,** *346,* 122616. doi:10.1016/j.lfs.2024.122616
91. Sarı, C.; Eyüpoğlu, F. C.; Değirmencioğlu, İ.; Bayrak, R. *Photodiagn. Photodyn. Ther.* **2018,** *23,* 83–88. doi:10.1016/j.pdpdt.2018.05.009
92. Zhang, X.; Ma, Y.; Shi, Y.; Jiang, L.; Wang, L.; ur Rashid, H.; Yuan, M.; Liu, X. *Biomed. Pharmacother.* **2024,** *174,* 116586. doi:10.1016/j.biopha.2024.116586
93. Huang, L.; Chen, X.; Bian, Q.; Zhang, F.; Wu, H.; Wang, H.; Gao, J. *J. Controlled Release* **2020,** *328,* 325–338. doi:10.1016/j.jconrel.2020.08.062
94. Chiu, S.-M.; Xue, L.-Y.; Azizuddin, K.; Oleinick, N. L. *Apoptosis* **2005,** *10,* 1357–1368. doi:10.1007/s10495-005-2217-0
95. Song, C.; Xu, W.; Wu, H.; Wang, X.; Gong, Q.; Liu, C.; Liu, J.; Zhou, L. *Cell Death Dis.* **2020,** *11,* 938. doi:10.1038/s41419-020-03136-y
96. Ghaddar, S.; Pinon, A.; Gallardo-Villagran, M.; Massoud, J.; Ouk, C.; Carrion, C.; Diab-Assaf, M.; Therrien, B.; Liagre, B. *Int. J. Mol. Sci.* **2024,** *25,* 10847. doi:10.3390/ijms251910847
97. Yalçın, C. Ö.; Barut, B.; Barut, E. N.; Demirbaş, Ü.; Dinçer, T.; Engin, S.; Özel, A.; Sezen, F. S. *Photodiagn. Photodyn. Ther.* **2020,** *32,* 101975. doi:10.1016/j.pdpdt.2020.101975
98. Deng, J.; Xia, X.; Yuan, H.; Chen, Z.; Jiang, X.; Zou, D.; Wang, Q. *Mater. Adv.* **2023,** *4,* 4835–4842. doi:10.1039/d3ma00400g
99. Soriano, J.; García-Díaz, M.; Mora, M.; Sagristá, M. L.; Nonell, S.; Villanueva, A.; Stockert, J. C.; Cañete, M. *Biochim. Biophys. Acta, Gen. Subj.* **2013,** *1830,* 4611–4620. doi:10.1016/j.bbagen.2013.05.021
100. Warszyńska, M.; Repetowski, P.; Dąbrowski, J. M. *Coord. Chem. Rev.* **2023,** *495,* 215350. doi:10.1016/j.ccr.2023.215350
101. Chen, J.; Hu, S.; Sun, M.; Shi, J.; Zhang, H.; Yu, H.; Yang, Z. *Eur. J. Pharm. Sci.* **2024,** *193,* 106688. doi:10.1016/j.ejps.2023.106688
102. Zhou, X.; An, B.; Lin, Y.; Ni, Y.; Zhao, X.; Liang, X. *Biomed. Pharmacother.* **2023,** *165,* 115036. doi:10.1016/j.biopha.2023.115036
103. Sethy, C.; Kundu, C. N. *Biomed. Pharmacother.* **2021,** *137,* 111285. doi:10.1016/j.biopha.2021.111285
104. Handali, S.; Moghimipour, E.; Rezaei, M.; Ramezani, Z.; Kouchak, M.; Amini, M.; Angali, K. A.; Saremy, S.; Dorkoosh, F. A. *Biomed. Pharmacother.* **2018,** *108,* 1259–1273. doi:10.1016/j.biopha.2018.09.128
105. Botosoa, E. P.; Maillasson, M.; Mougin-Degraef, M.; Remaud-Le Saëc, P.; Gestin, J.-F.; Jacques, Y.; Barbet, J.; Faivre-Chauvet, A. *J. Drug Delivery* **2011,** 368535. doi:10.1155/2011/368535
106. Saha, B.; Evers, T. H.; Prins, M. W. J. *Anal. Chem. (Washington, DC, U. S.)* **2014,** *86,* 8158–8166. doi:10.1021/ac501536z
107. Toscano, F.; Torres-Arias, M. *Curr. Res. Immunol.* **2023,** *4,* 100073. doi:10.1016/j.crimmu.2023.100073
108. Galvão, G. F.; Petrilli, R.; Arfelli, V. C.; Carvalho, A. N.; Martins, Y. A.; Rosales, R. R. C.; Archangelo, L. F.; daSilva, L. L. P.; Lopez, R. F. V. *Colloids Surf., B* **2025,** *248,* 114459. doi:10.1016/j.colsurfb.2024.114459
109. Garanina, A.; Vishnevskiy, D.; Chernysheva, A.; Malinovskaya, J.; Lazareva, P.; Semkina, A.; Abakumov, M.; Naumenko, V. *Biomedicines* **2024,** *12,* 2180. doi:10.3390/biomedicines12102180
110. Alshaer, W.; Lafi, Z.; Nsairat, H.; AlQuaissi, B.; Alqudah, D. A.; Zureigat, H.; Hamad, I. *Molecules* **2025,** *30,* 1549. doi:10.3390/molecules30071549
111. Matusewicz, L.; Filip-Psurska, B.; Psurski, M.; Tabaczar, S.; Podkalicka, J.; Wietrzyk, J.; Ziółkowski, P.; Czogalla, A.; Sikorski, A. F. *Int. J. Pharm.* **2019,** *569,* 118605. doi:10.1016/j.ijpharm.2019.118605